THE CATHOLIC UNIVERSITY OF AMERICA

Experimental Study of 3D Failure Surface for Cross-Anisotropic Sand Deposits During Stress Rotation

A DISSERTATION

Submitted to the Faculty of the

Department of Civil Engineering

School of Engineering

Of The Catholic University of America

In Partial Fulfillment of the Requirements

For the Degree

Doctor of Philosophy

By

Nina Maria Rodriguez

Washington, D.C.

2012

Experimental Study of 3D Failure Surface Location for Cross-Anisotropic Sand Deposits During Stress Rotation

Nina Maria Rodriguez, Ph.D.

Director: Poul V. Lade, Ph.D.

A torsion shear apparatus developed at The Catholic University of America, Washington, DC was used to conduct experiments on Fine Nevada Sand in order to study the effects of cross-anisotropy, shear banding and stress rotation under three independent principal stresses on stress-strain behavior. Drained torsion shear tests were performed with constant b-values, major principal stress directions and mean confining stress. A series of 18 drained tests using a true triaxial apparatus were conducted for comparison with certain torsion shear results. Drained triaxial tests with varying mean confining stress were also performed. Additional drained conventional triaxial tests were also performed to determine parameters needed for modeling. The 3D failure surface of Fine Nevada sand is presented. Shear banding patterns and analysis is presented for the true triaxial and torsion shear tests. The failure conditions from the torsion shear results are compared to a newly developed failure criterion. The effects of the intermediate principal stress on the failure surface are analyzed. Results clearly show the effects of cross-anisotropy in Fine Nevada Sand. This is seen in variation of friction angle with differing conditions and from strain analysis in different stress paths. Non-associated flow is observed and shear band inclinations in torsion shear specimens, although scattered, follow the Coulomb equation prediction. Data from these tests provide a solid foundation for future developments of cross-anisotropic constitutive models for frictional materials.

This dissertation by Nina Maria Rodriguez fulfills the dissertation requirement for the doctoral degree in Civil Engineering approved by Poul V. Lade, Ph.D. as Director, and by George Mavroeidis, Ph.D. and Biprodas Dutta, Ph.D. as Readers.

Poul V. Lade, Ph.D., Director

George Mavroeidis, Ph.D., Reader

Biprodas Dutta, Ph.D., Reader

This thesis is dedicated to my mom and dad for their unconditional love, faith and guidance my entire life. You have been by my side in all the decisions that I have made and have shown me the true definition of love and sacrifice. You both have provided me with the foundations for a successful life and I am eternally grateful. Thank you for instilling in me the values and confidence that makes me the person I am today. I love you with all my heart. Los quiero muchisimo.

Table of Contents

List of Figures

List of Tables

Acknowledgements

First and foremost, I would like to thank Dr. Poul Lade for making this thesis possible. His patience, enthusiasm, knowledge, passion, creativity, experience and continuing curiosity of geotechnical engineering are inspiring. Over countless hours of discussion and analysis of results and experimentation, he has taught me all that I know about research and geotechnical engineering. I would also like to thank my thesis readers, Dr. Dutta and Dr. Mavroeidis for their feedback and advice in preparing this thesis.

Negar Mohrammi-Garghari was instrumental in helping refresh and relearn much of the mathematics that went into analyzing my results. Her patience and helpfulness at every moment that I had a "math question" is greatly appreciated. I also want to thank Afshin Nabili for always being there to help me carry the top lid off of the torsion shear apparatus and Don Smolley who was always so cheerful, helpful and creative whenever I needed something from the machine shop! Thanks to Gene Van Dyke for all the lab time spent together in that basement! Gracias, Jania for all the cleaning supplies and more specifically, for your smiling face each day. Thank you to Leo Dwyer and Annette Parlade for always knowing when I needed a break, for your help and especially, your friendship. I would also like to thank my parents, brother and friends, both near and far, for asking and listening to me speak about my PhD over the past years. Even at times when the subject matter was not super exciting, you all nodded your heads and let me go on and on about my sand castles. Thank you!

1. Introduction

The study of cross-anisotropy in sands has been of great interest for the past several decades. The definition of anisotropy can be written as a material whose properties are directionally dependent. Experiments have been performed traditionally under two dimensional conditions in the laboratory. These tests, mainly done on triaxial apparatuses, only have control of two independent stresses in two different scenarios: First, in compression testing where $\sigma_1>\sigma_2=\sigma_3$ and second, in extension testing where $\sigma_1=\sigma_2>\sigma_3$. In order to fully study cross-anisotropy, the effects of σ_2 should be isolated and three independent stresses must be applied to the specimen. Certain apparatuses exist in the laboratory for these conditions to be produced. In this experimental study, the use of both a true triaxial apparatus and a torsion shear machine was required. The advantages and disadvantages of both will be discussed in further detail. Test results of a comprehensive study on Fine Nevada sand will be presented and a detailed analysis of the effects that cross-anisotropy has on the failure surface of this sand under a variety of conditions is presented.

While the cross-anisotropic behavior of sand plays a crucial role in the strength behavior of soil, shear banding is also an area that should not be overlooked. This experimental study also presents, analyzes and compares shear bands that develop in the testing program for both apparatuses.

1.1. Overview of Research

The aim of this research is to perform a comprehensive study of the cross-anisotropic effects on the failure surface of Fine Nevada Sand. In order to study this cross-anisotropy, a testing program was devised consisting of true triaxial and torsion shear tests. Under the true triaxial apparatus testing program, the aim was to determine the cross-anisotropy present under different loading conditions in the three sectors of the octahedral plane. The torsion shear experimental program consisted of looking at the failure surface under constant b-value (in which $b=(\sigma_2-\sigma_3)/(\sigma_1-\sigma_3)$), constant inclination of principal stresses and constant mean principal stress. With both sets of data, points that overlap between the true triaxial and torsion shear tests were to be compared and studied for similar trends and results. Study of shear bands as well as the angle at which they develop was also a major aim of this research program. By analyzing shear bands in two different apparatuses over a variety of conditions, greater knowledge from the experimental data collected would be attained.

1.2. Experimental Program

The experimental program is separated into three main research areas: Triaxial Tests, True Triaxial Tests and Torsion Shear Tests. All tests were performed on Fine Nevada Sand. Fine Nevada Sand was chosen in order to minimize membrane penetration effects. A true triaxial apparatus was used to shear tall prismatic specimens with dimensions 7.6cm in width, 7.6cm in length and 19cm in height. A series of 10 triaxial compression tests and one conventional extension test were performed with both horizontal and vertical bedding planes in order to attain parameters for an already developed cross-anisotropic failure criterion (Lade 2007). Specimens were sheared at a variety of constant confining pressures and the stress-strain behavior was analyzed. The parameters determined were used and compared to the experimental results. Fourteen tests were performed in a of series triaxial compression experiments with varying stress paths. This set of experiments in a triaxial apparatus studied the effects that stress paths may have on the strength behavior of the soil by changing the confining pressure to follow the predetermined stress path. A series of 18 tests were performed in a true triaxial apparatus (Lade 1978). Tests were performed in all three sectors of the octahedral plane. A horizontal loading machine was used to maintain constant, but different b-values at an increment of 0.25 from 0 to 1 for each of the three sectors. These tests produced the data needed to successfully plot all points along the octahedral plane and visually see the effects of cross-anisotropy for conditions of no stress rotation.

A torsion shear apparatus was used for an additional 22 tests performed on hollow cylinder specimens. These 22 tests were used to study effects of stress rotation when compared with existing data previously attained from the true triaxial tests. The tests were performed with changing inner and outer pressures and vertical load applied to the hollow cylinder specimens, allowing for different b-values (also at increments of 0.25 from 0 to 1) and varying alpha values (the angle of major principal stress with the vertical axis). Alpha values ranged from 0 to 90 degrees in 22.5 degree increments. In this manner, a 3D plot showing the failure surface from the tests in torsion shear of friction angle/stress ratio at various points along constant b-values and constant alpha could be attained. Looking at the failure surface of Fine Nevada sand over a series of conditions allows for a final and complete picture of the effect that cross-anisotropy has on the failure surface of soil. In addition, strain analyses were performed to study cross-anisotropy.

Shear banding was also studied extensively and its effect on the failure of sand in the two different testing apparatuses. As will be shown in the chapters to come, shear banding can occur both in the hardening and softening regime. With shear banding occurring in the hardening regime, the strength of the soil may be affected. This was seen in most torsion shear tests. For true triaxial tests, shear banding occurred mainly in the softening regime, following the peak stress.

By testing the same soil in two different apparatuses, a complete comparison between the true triaxial and torsion shear results is presented. The stress-strain behavior, dilation angles and strain increment directions, as well as the shear band directions are analyzed and presented in the pages that follow.

2. Previous Studies

2.1. Background and Introduction

There are many engineering situations, anywhere from the application to shallow foundations to complicated earthquake engineering problems, where soil is subjected to multi-axial loads. These loads may create increases in shear stress levels and cause the rotation of principal stress directions. One common example is that of a shallow spread footing. In this situation, there can be rotations of up to 40° about the vertical direction with increasing shear stresses. This creates a highly stressed zone below the footing that is subjected to a vertical static load. Figure 2.1.1 shows stress states along a rupture area for a situation similar to what was just described. In naturally deposited soils, cross-anisotropy can be found. The axis of symmetry is most often aligned in the vertical direction of deposition. Because of this anisotropy, soils have deformations due to both the changes in magnitudes of the principal stresses as well as their orientation. There is a well-recognized need to investigate the response of soil deformation under stress changes where there is control of orientation and rotation of principal stress directions. Situations where one can isolate the influence of the rotation of principal stresses, while other parameters are held constant can be studied in the laboratory. This of course needs the help of laboratory devices that can control both the direction and magnitudes of the principal stresses. True triaxial as well as torsion shear devices have been used for many years in order to study these conditions. With these devices that allow for the creation of three principal stresses, it is possible to create continuous controlled increments and/or rotations of principal stresses in the vertical plane of the soil specimen that is being studied and then apply it to real world conditions.

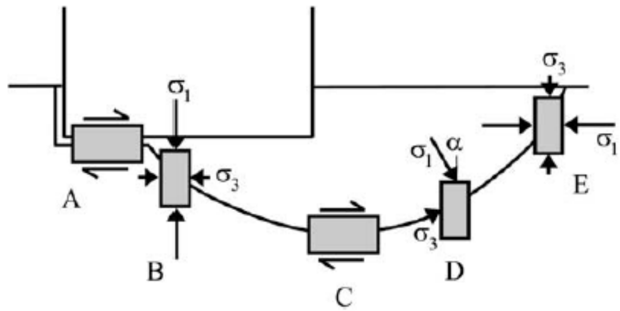

Figure 2.1.1. Stress states along rupture surface (after O'Kelly and Naughton 2009).

In the following sections, this literature review will explain true triaxial and torsion shear devices, as well as past research concerning anisotropy, shear banding, and failure surfaces that have been researched, providing the necessary background for the experimental programs that have been performed.

2.2. True Triaxial Apparatuses

In order to conduct three-dimensional experiments on soils in the laboratory, the conventional triaxial setup cannot be used. Traditional triaxial cells only have two acting principal stresses. In cases of triaxial compression, the intermediate principal stress, σ_2 is equal to the minor principal stress, σ_3. For triaxial extension tests, the major principal stress, σ_1 is equal to the intermediate principal stress, σ_2. Due to this shortcoming of the conventional triaxial setup, the influence of the intermediate principal stress cannot be studied. In order to have three independent principal stresses, true triaxial devices must be designed and used. In the pages that follow, the principles of true triaxial testing will be explained, as well as several designs that have been used in the past to study the behavior of soils with three independent principal stresses. It is important to note that true triaxial testing does not allow for rotation of principal stresses. However, as will be seen in later chapters, certain techniques can be employed on the specimen, such as freezing, to rotate the bedding planes of a specimen so that the major principal stress direction can be changed from 0° to 90°.

Principles of True Triaxial Apparatuses

Lade, in 1978, laid out some key criteria for successful testing in true triaxial apparatuses. First, it is required that the apparatus be able to handle strains in the three directions up to the point of failure. This will allow for uniform stress and strain conditions on the specimen and not create non-uniform stresses and strains, which may affect the data. Second, the apparatus also has to have the capability of creating uniform stresses on the specimen without creating any significant shear stresses to the surfaces of the specimen, which can also affect the results.

Arthur (1988) described certain features of cubical devices with flexible boundaries. As he noted, the cubical shape is very practical on which to apply principal stresses independently. He mentioned that two ideal boundary faces, flexible and rigid could be used for cubical testing. Cubical specimens can also be stressed through a combination of flexible and rigid boundaries. Arthur (1988) summarizes the capabilities of certain cubical sample apparatuses in the following Table 2.2.1.

Early designs of certain types with flexible, rigid and mixed boundaries are worth describing. Figure 2.2.1 shows different boundary conditions for true triaxial apparatuses. A classic example of a rigid boundary type is Hambly's design (Hambly 1969) (see Figure 2.2.2). Both Ko and Scott (1967) and Lomize and Kryzhanovsky (1967) used flexible type boundaries. Designs with mixed boundary types were used by Green (1971) and Lade and Duncan (1973). In these designs, a pair of vertical stiff platens replaced the flexible rubber bags where the horizontal deviator stress is applied. Lade's design will be described in detail in Section 2.2.3 as it is the true triaxial apparatus used in part of the experimental program.

Hambly's design, shown in the Figure 2.2.2 allows for unlimited boundary displacement in all three axes. In this design, all six faces of the cubical specimen are loaded rigid boundaries and can slide relative to each other. However, because of its complexity only limited stress ranges can be reached. Tests on this design are done with constant mean normal stress and constant b-value.

Table 2.2.1. Capabilities of cubical sample apparatus (after Arthur 1988).

Cubical Sample Apparatus		Boundary Surfaces Condition	All Rigid	All Flexible	Mixed Surfaces
Boundary control capabilities	Stress	Average normal stress	Yes	Yes	Yes
		Average shear stress	Yes	Yes	Yes
		Uniform normal stress	Restricted	Yes	Yes/no according to surfaces concerned
		Uniform shear stress	No	Yes	
	Deformation	Uniform boundary displacement	Yes	Restricted	
		Uniform sample strain	Cannot be assumed	Cannot be assumed	Cannot be assumed
Study applications	Material type	Homogeneous strain hardening	Yes	Yes	Yes
		Homogeneous strain hardening (→softening)	Yes	Yes	Yes
		Inhomogeneous sample or material	Restricted R[a]	Yes R	Restricted R
	Stress–strain behavior	Drained or undrained shear	Either	Either	Either
		Independent variation of principal stresses	Yes	Yes	Yes
		Principal stress direction rotation	Very restricted	Planar restriction only	According to surface
		Post peak strain (after rupture layer formed)	Restricted R	Restricted R	Restricted R
		Exceptional stress levels High	Yes	Yes	Yes
		Exceptional stress levels Low	Difficult	Yes	Difficult
	Failure	Shear strength measurement	R Yes	R Yes	R Yes
		Rupture layer formation (bifurcation phenomena)	Restricted R	Yes R	Yes R

[a] R = Radiography needed.

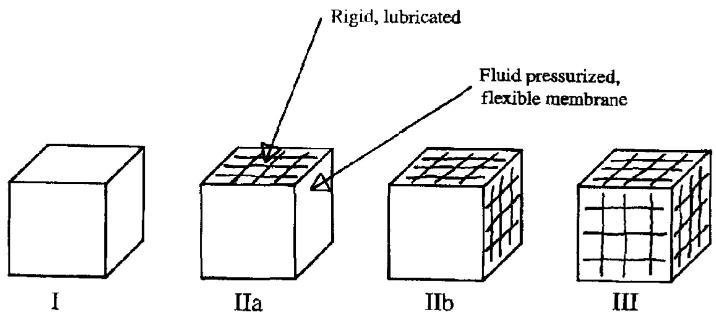

Figure 2.2.1. Types of boundary conditions employed in different true triaxial apparatus for soil testing (after Lade 2006).

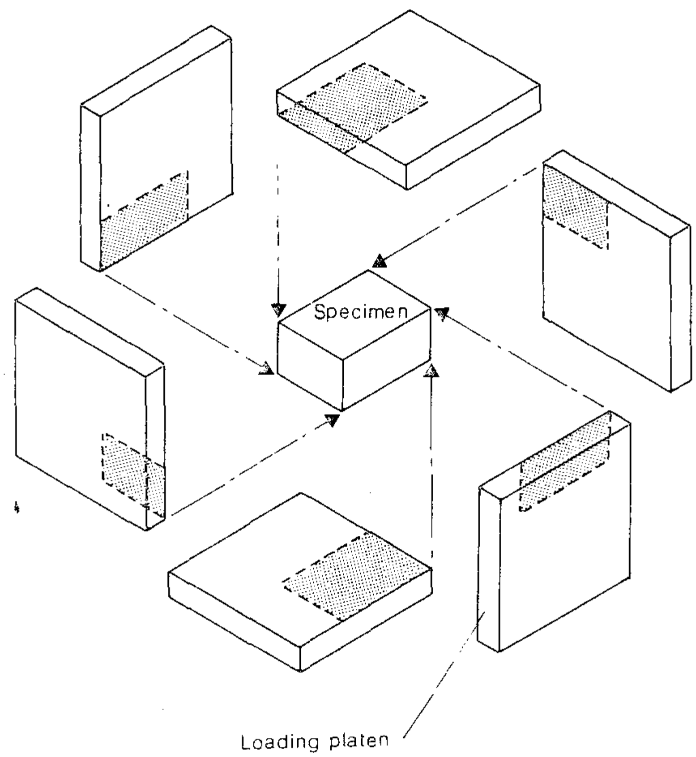

Figure 2.2.2. Hambly's rigid boundary true triaxial concept (after Arthur 1988).

For tests with high stress levels, Meier et al. (1985) designed a flexible boundary device, as seen in Figure 2.2.3, where the stresses were transmitted through a vinyl membrane and then through a pad of polyurethane, followed by another pad of material which depended on the material being tested. Yamada and Ishihara (1979) designed an apparatus based on Ko and Scott's design (1967) for intermediate stress levels where they were able to study the effects of anisotropy. These types of apparatuses where all six faces of the cubical specimen are loaded by flexible boundaries are usually used to perform tests with constant mean stress and constant b-values. Yamada and Ishihara's design, shown in Figure 2.2.4. may create very high stresses along the edges if the strain of the specimen drives its edges into the frame's edge. The rigidity of the frame allows for the possibility of unlimited stress concentrations. Flexible membranes may also create very low stresses along the edges if the pressure membrane does not exert the right amount of pressure on the sample edge.

Directional shear devices have been designed to apply uniform normal and shear stresses to opposite sides of the specimen normal to the plain of strain. Varying σ_a, σ_b, τ_a, and τ_b controls the direction of the principal stress relative to the plane of strain. This can be seen in the apparatus developed by Arthur et al. (1977) in Figure 2.2.5.

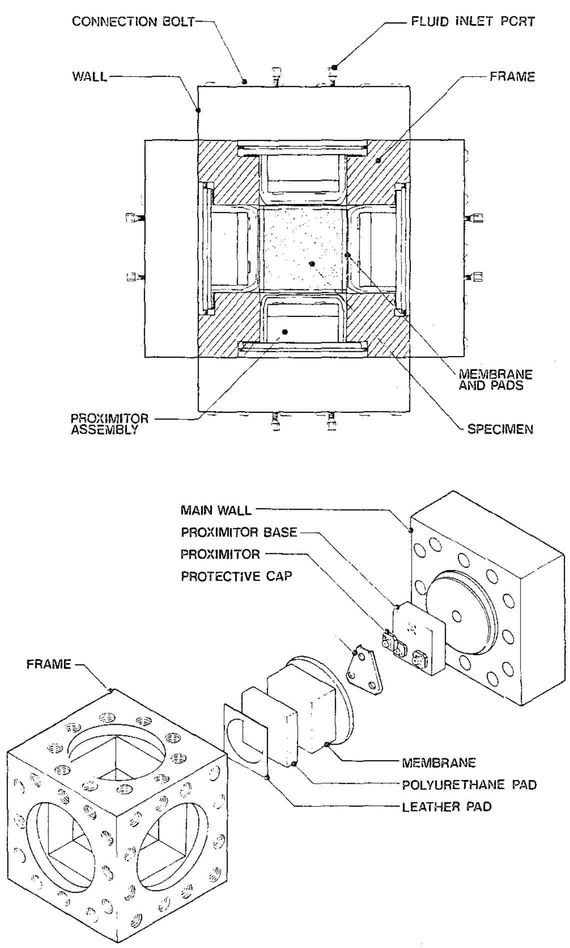

Figure 2.2.3. High stress flexible boundary true triaxial (after Meier et al. 1985).

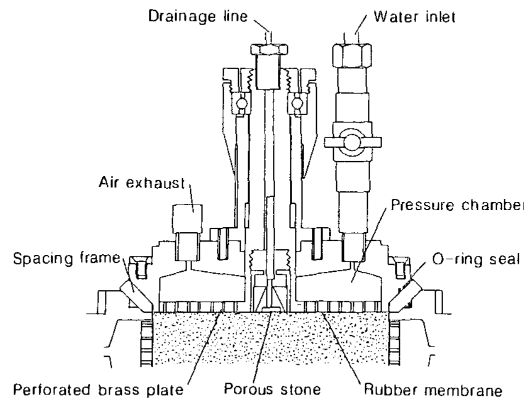

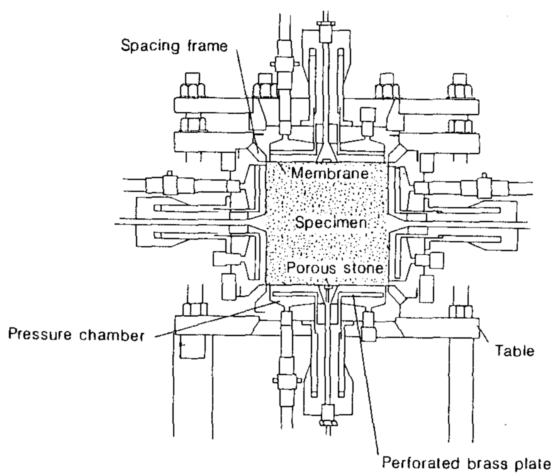

Figure 2.2.4. Flexible boundary true triaxial (after Yamada and Ishihara 1979).

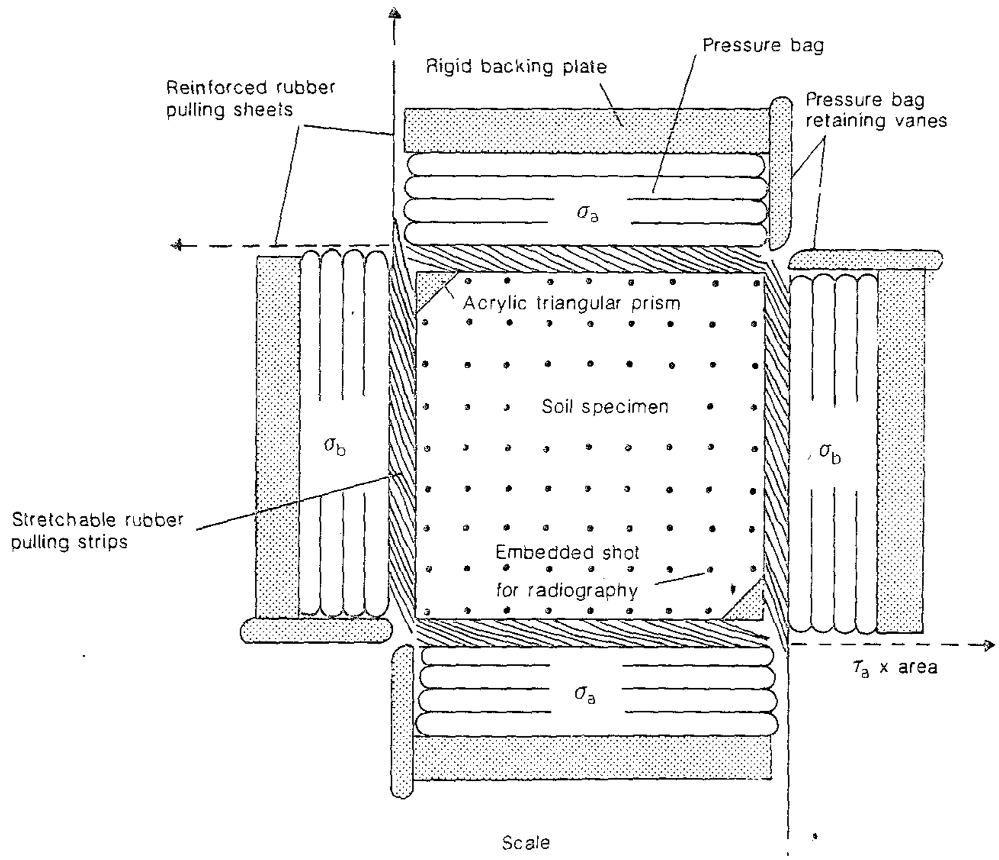

Figure 2.2.5. Directional Shear Cell (after Arthur et al. 1977).

True Triaxial Design used in Experimentation

Lade's cubical triaxial apparatus (1978) was designed so that two different horizontal stresses could be applied to the specimen. One is applied via the confining pressure, the second through a horizontal deviator stress via a horizontal loading system. The vertical load applied to the specimen's cap and base is transferred through a piston. The setup is in a triaxial chamber. In this chamber, the cell pressure acts as the minor principal stress, σ_3. The deviator stress created by the vertical load applied to the specimen and the cell pressure act as the major principal stress, σ_1. The horizontal deviator stress and the cell pressure create the intermediate principal stress, σ_2. A schematic of the entire assembly is seen in Figure 2.2.6.

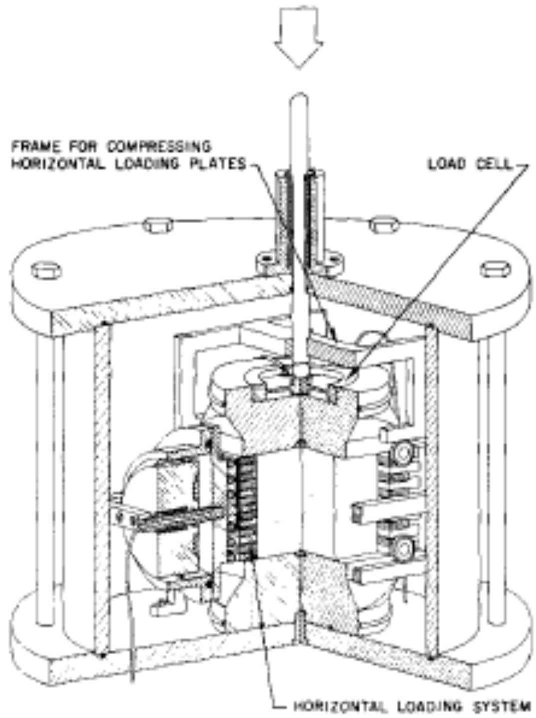

Figure 2.2.6. Cubical Triaxial Apparatus (after Lade 1978).

A brief description of the setup is as follows. More details can be found in Lade and Duncan (1973) and Lade (1978) where the entire assembly is described and illustrated. Two loading plates are connected at opposite sides of the specimen. One side is connected to an oil-filled pressure cylinder which, when compressed, allows the plates to move freely on the rails that the bottom wheels sit on. The compressibility of the plates creates an independent straining in the horizontal direction. The plates are made to be compressible in the vertical direction by alternating steel and pre-stressed balsa wood laminae. The balsa wood is pre-compressed and presoaked in water in order to decrease the strength in the directions perpendicular to the fibers. This ensures that there is no interference with the cap and base during compression of the specimen. Lubricated ends made of 0.03-cm rubber sheets, which are separated by a thin layer of silicon grease are also placed on the specimen base and cap, as well as on the sides of the horizontal loading plates to provide frictionless surfaces and avoid significant shear stresses. A beryllium copper load cell is embedded in the top cap, which has strain gages connected in a full bridge configuration. The wires lead through the triaxial cell and are connected to a measurement device. When loaded, the flat edge of the piston applies load to a steel ball, which sits in a ball socket on the load cell. Horizontal LVDTs are set up on the sides of the horizontal plates to measure strain in the horizontal direction. A vertical dial gage is set up outside of the triaxial cell to measure vertical strain. The top cap and base have filter stones and drainage lines to measure volume change or pore pressure. A Lucite cell is placed around the setup and six rods hold the bottom plate, Lucite cell and top plate together. Figure 2.2.7. shows the schematic of the stress control system. With this system, the b-value can be held constant during shearing.

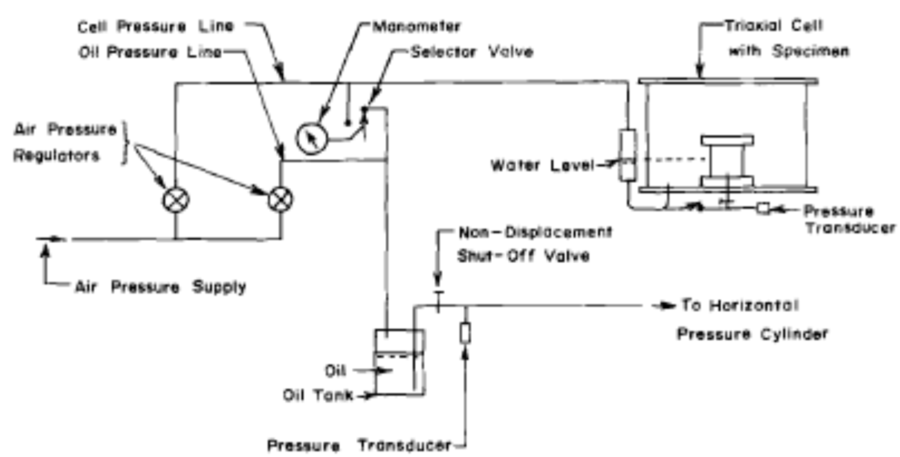

Figure 2.2.7. Schematic diagram of stress control system (after Lade 1978).

2.3. Torsion Shear Devices

Broms and Casbarian (1965) conducted the first study of principal stress rotation effects on the strength of kaolinite clay using a hollow cylinder apparatus. They showed that the continuous rotation of the principal stress axes increases the rate of pore water pressure generation and at the same time, reduces the undrained strength of cohesive soil. In 1975, Lade designed and presented the main features of a torsion shear apparatus in order to study the shear-dilatancy effect on the stress-strain characteristics of cohesionless soil. Lade also discussed in detail the torsion shear apparatus used for his soil testing in 1981. In 1983, Hight et al. discussed in detail the development of a new hollow cylinder apparatus, as well as the principles of its operation. In 1988, Shibuya developed a servo system for the traditional Imperial College hollow cylinder apparatus. Table 2.3.1, taken from Hight et al. (1983), lists certain torsion shear apparatus and explains the tests that were performed. A more complete and recent list taken from Tastan (2009) can be found in Appendix E.

Table 2.3.1. Summary of earlier hollow cylinder apparatuses (after Hight et al. 1983).

	Reference	Sample dimensions: mm			Loading capabilities			Subject of investigation
		i.d.	o.d.	H	p_o/p_i	W	M_T	
Without rotation of principal stress directions	1 Kirkpatrick (1957)	63	102	152	√			Influence of σ_2 on failure of sand
	2 Whitman & Luscher (1962)	25	38/51/76	76/127	√			Strength characteristics of hollow cylinders of sand
	3 Broms & Ratnam (1963)	76	152	114	√	√		Effects of anisotropic consolidation on deformation and strength of clay
	4 Wu *et al.* (1963)	76	102	152	√	√		Failure envelope in sand and clay
	5 Broms & Jamal (1965)	76	152	305	√	√		Analysis of the triaxial test on sand
	6 Esrig & Bemben (1965)	76	102	203	√	√		Failure conditions in sand
	7 Suklje & Drnovesk (1965)	40	64	80	√			Tensile deformation of clays
	8 Barden & Proctor (1971)	38	102	152	√	√		Drained strength of granular material
	9 Jamal (1971)	25/51/76	102	203	$p_o = p_i$	√		Shear strength of sand in extension
	10 Jamal (1972)	35	60	60	√	√		Analysis of the triaxial test on clay
	11 Dusseault (1981)	51	102	200/240	√	√		Tunnelling and pressuremeter testing in sand
With rotation of principal stress directions	12 Broms & Casbarian (1965)	76	127	254	√	√	√	Effect of principal stress direction and magnitude of σ_2 on shear strength of clay
	13 Saada & Baah (1967) (Saada, 1968)	51	71	151	√	√	√	Anisotropy in the deformation and strength of clay (Saada & Zamani, 1969; Saada & Ou, 1973; Saada & Bianchini, 1975) ($p_o = p_i$, α = constant during shear)
	14 Lomise *et al.* (1969)	250	310	180	√	√	√	No data presented
	15 Ishibashi & Sherif (1974)	51	102	13–25	√	√	√	Effect of K_o on liquefaction of sand
	16 Ishihara & Yasuda (1975)	60	100	70	√	√	√	Liquefaction of sand under irregular cyclic loading
	17 Lade (1975)	180	220	50	$p_o = p_i$	√	√	Influence of stress reorientation on stress–strain behaviour of sand
	18 Ishihara *et al.* (1980)	60	100	106	√	√	√	Effect of principal stress rotation on liquefaction of sand
	19 Muramatsu & Tatsuoka (1981)	60	100	100	$p_o = p_i$	√	√	Cyclic undrained stress–strain behaviour of sand

The biggest advantage of the torsion shear test compared to other geotechnical testing apparatuses is that it allows for the inclination of the major principal stress in any direction while complimentary shear stresses are applied to the specimen. The angle between the major principal stress and vertical, α, is tied to the intermediate principal stress parameter b, where

$$b = \frac{\sigma_2 - \sigma_3}{\sigma_1 - \sigma_3} \qquad \text{Eq. 2.3.1}$$

b indicates the relative magnitude of the intermediate principal stress σ_2. σ_1 and σ_3 are the major and minor principal stresses, respectively. For the same inner and outer pressures on the hollow cylinder specimens, the relationship between b and α can be denoted by Eq. 2.3.2.

$$b = \sin^2 \alpha \qquad \text{Eq. 2.3.2}$$

where α is the inclination of major principal stress (Lade et al. 2008).

When the inside and outside pressures are the same in a torsion shear test, the hollow specimen experiences a plane stress state. To get to this state, it is necessary to have the stresses and strains distributed uniformly throughout the specimen. This uniformity can be achieved by having appropriate dimensions for the specimen. Much advancement has been made to the torsion shear apparatus. However, the principles and overall design to date has remained the same.

Principles and Design of Torsion Shear Apparatuses

In principle, the magnitude and direction of the major and minor principal stresses, as well as the intermediate principal stress can be controlled in a torsion shear apparatus. These are controlled under combined axial load, torque, and internal and external radial pressures. Under stress-controlled conditions, this apparatus enables controlled rotation of the principal stress directions on a surface to be attained.

A torsion shear apparatus is made up of basically four major units: 1) a specimen pressure cell, 2) a torque loading unit, 3) an axial loading unit, and 4) a data collection and control unit. Different apparatuses have variations on these basic units, but they all operate on the same principles and basic design.

Principles on Stresses and Strains in Torsion Shear

In the laboratory, it is very difficult to reproduce controlled changes in direction and magnitude of the principal stresses. In most laboratory testing equipment, the principal stresses are fixed. One can only switch and interchange the directions. However, with the torsion shear apparatus, principal stresses can rotate and the specimens can be subjected to axial load (W) and torque (M_t) about a central vertical axis. They can also be subjected to external (p_o) and internal (p_i) radial pressures.

The torque applied to the specimen creates shear stresses ($\tau_{\theta z}$) and ($\tau_{z\theta}$). When the internal and external pressures are different, a gradient of radial stress (σ_r) is established across the cylinder wall. The principal stress rotation on a three dimensional element and on a hollow cylindrical specimen as well as the stresses that act on the specimen during loading can also be seen in the Figures 2.3.1 and 2.3.2.

When performing experiments on hollow cylindrical specimens, (p_o) and (p_i) should act through flexible membranes. This ensures that there are no shear stresses acting on the vertical boundaries. If end restrained is neglected (there are several ways to make sure that end restraint does not interfere with the sample, which will be discussed in a later section), no shear stresses exist on circumferential surfaces through the membrane walls. The shear stress due to torque produces reorientation of the principal stress directions as well as a stress state with three unequal principal stresses. If shear stresses are not applied to the specimen, the confining radial pressure, σ_r, becomes the minor principal stress σ_3 in a compression test, or the major principal stress σ_1 in an extension test. In this case, σ_r is always a principal stress. With torsion shear stresses, σ_r becomes the intermediate principal stress, σ_2. In order to determine the remaining principal stresses, it is possible to resolve the other stresses and shear stresses, (σ_θ), (σ_Z), ($\tau_{\theta Z}$) and ($\tau_{Z\theta}$). The magnitudes of the three principal stresses are determined by the forces that are applied, as well as the internal and external pressures and the geometry of the specimen being tested.

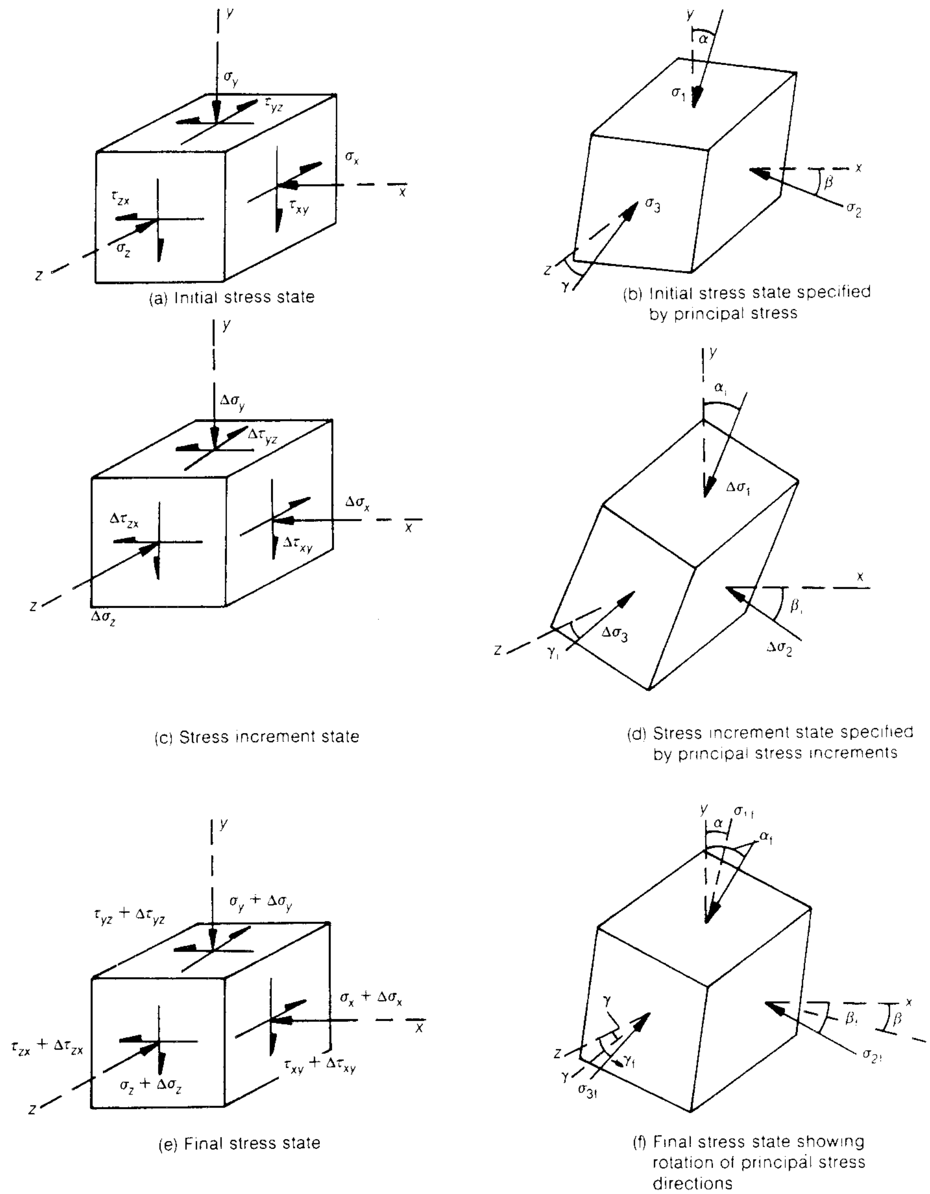

Figure 2.3.1. Principal stress rotation on an element (after Hight et al. 1983).

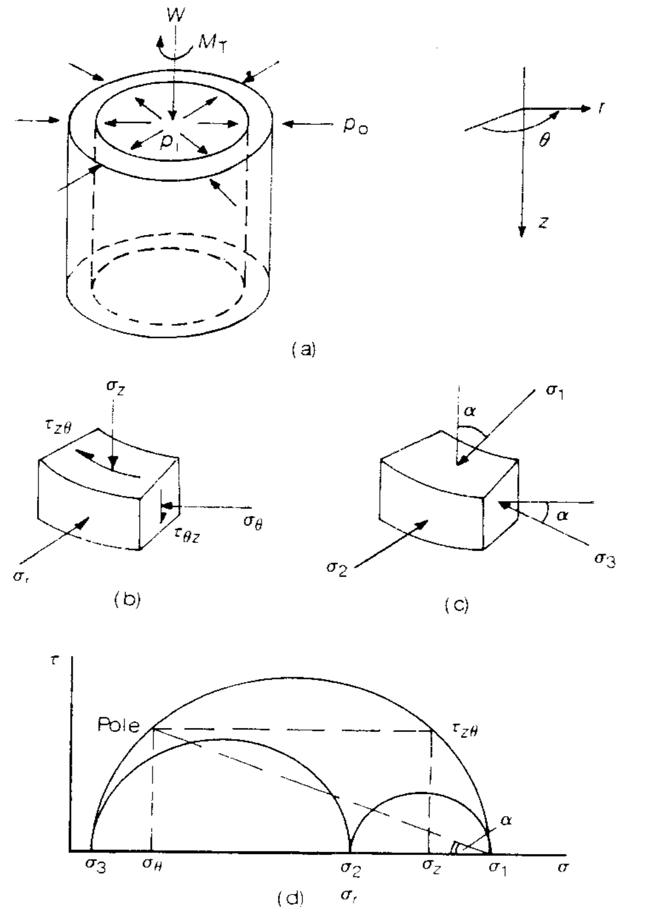

Figure 2.3.2. Idealized stress conditions in a hollow cylindrical element subject to axial load, W, torque, Mt, internal pressure, p_i and external pressure, p_o. (a) Hollow cylinder sample; (b) stresses on an element in the wall; (c) principal stresses on an element in the wall; (d) Mohr circle representation of stress in the wall (after Hight et al. 1983).

In general, the stresses along the specimen wall will not all be uniform. Therefore, it is necessary to work in terms of average stresses. These are represented by: $(\sigma_\theta)_{avg}$, $(\sigma_z)_{avg}$, $(\sigma_r)_{avg}$, and $(\tau_{\theta z})_{avg}$. The following equations for average stresses and strains (taken from Hight et al., 1983) are shown below in Table 2.3.2. It is important to note that Hight et al.

(1983) along with many other researchers have used these equations. The average stress values,$(\sigma_\theta)_{avg}$ and $(\sigma_z)_{avg}$ are based on force equilibrium conditions. However, the average strain values $(\varepsilon_{\theta z})_{avg}$ and $(\gamma_z)_{avg}$ are based on strain compatibility only. These equations do not take into account the constitutive law of the material. The equation for $(\sigma_r)_{avg}$ is based on linear elastic stress distribution. For $(\varepsilon_r)_{avg}$ and $(\varepsilon_\theta)_{avg}$, a linear variation of radial displacements across the wall is assumed. For $(\tau_{z\theta})_{avg}$, a uniform stress distribution is assumed.

Table 2.3.2. Definitions of average stresses and strains (after Hight et al. 1983).

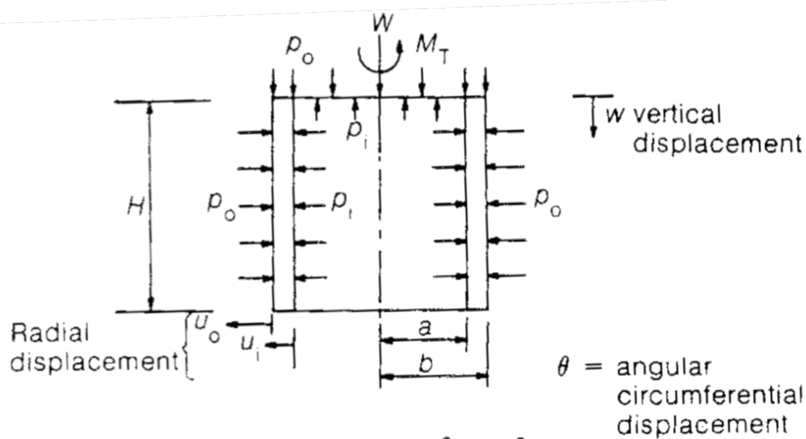

Average vertical stress $$\bar{\sigma}_z = \frac{W}{\pi(b^2 - a^2)} + \frac{(p_o b^2 - p_i a^2)}{(b^2 - a^2)} \quad (1)$$

Average radial stress $$\bar{\sigma}_r = \frac{(p_o b + p_i a)}{(b + a)} \quad (2)$$

Average circumferential stress $$\bar{\sigma}_\theta = \frac{(p_o b - p_i a)}{(b - a)} \quad (3)$$

Average shear stress $$\bar{\tau}_{\theta z} = \frac{3M_T}{2\pi(b^3 - a^3)} \quad (4)$$

Average axial strain $$\bar{\varepsilon}_z = \frac{w}{H} \quad (5)$$

Average radial strain $$\bar{\varepsilon}_r = -\frac{(u_o - u_i)}{(b - a)} \quad (6)$$

Average circumferential strain $$\bar{\varepsilon}_\theta = -\frac{(u_o + u_i)}{(b + a)} \quad (7)$$

Average shear strain $$\bar{\gamma}_{\theta z} = \frac{2\theta(b^3 - a^3)}{3H(b^2 - a^2)} \quad (8)$$

As stated, because normal and shear stresses vary along the thickness of a specimen's wall, average values of (σ_θ) and (σ_z) are calculated. However, since a thick cylinder (where thickness/radius > 0.1) specimen is subjected to deformation, looking at equilibrium alone is not enough. It is necessary also to know the constitutive law of the material to analyze deformations.

Using linearly elastic behavior, (σ_θ) and (σ_r) can be calculated (see Table 2.3.3). (σ_z) can be calculated in a straight forward manner by using the vertical load across the cross section of the specimen. Corrections for membrane stiffness, piston friction and weight of the soil are also part of the calculation for (σ_z).

Sayao and Vaid (1991) considered the specimen as a single element deforming as a right cylinder. They developed expressions that considered stress components assuming a linear elastic isotropic material. However, (σ_z) is not dependent on the material's constitutive law. Wijewickreme (1990) found that considerations of nonlinearity in soil behavior do not affect the average stresses reached when using a linear elastic assumption. In order to get (σ_r), (σ_θ)$_{avg}$ and ($\tau_{z\theta}$), it is necessary to average over the entire volume of the specimen. Sayao and Vaid (1991) compared the equations of both Hight et al. (1983) and Miura el al. (1986). Hight et al. (1983) and Miura et al. (1986) had averaged across the specimen wall instead of taking into account the volume of the specimen. Averaging across the volume takes into account the curvature of the wall. Hight et al. (1983) and Miura et al. (1986) also assumed a plastic constitutive law when calculating ($\tau_{z\theta}$). They found that the differences were minor, usually less than 2%. However, they stated that for consistency, it is necessary to assume one constitutive law when analyzing stresses and strains and not elastic for certain stresses and plastic for others as done as Hight et al. (1983). The strains were analyzed assuming a linear variation of displacement across the specimen wall, just like Hight et al. (1983).

Table 2.3.3. Stresses on a thick cylinder subject to internal and external pressure (a) cross section, (b) element of unit length, (c) derived stresses using linear elastic behavior (after Morshedian (1992).

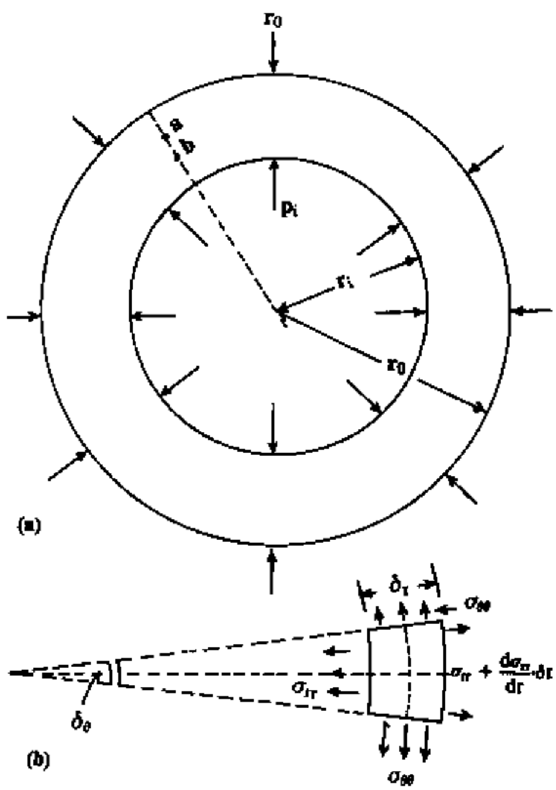

(c)

$$\sigma_{rr} = \frac{p_i r_i^2 - p_0 r_0^2}{r_0^2 - r_i^2} - \frac{(p_i - p_0)\, r_0^2 r_i^2}{r^2\,(r_0^2 - r_i^2)}$$

$$\sigma_{\theta\theta} = \frac{p_i r_i^2 - p_0 r_0^2}{r_0^2 - r_i^2} + \frac{(p_i - p_0)\, r_0^2 r_i^2}{r^2\,(r_0^2 - r_i^2)}$$

The equations they developed are shown in Table 2.3.4. The Lamé equations for calculating mean values of the non-zero stress components that are induced across a specimen wall thickness were derived using equilibrium considerations assuming an isotropic, linear-elastic response.

In the case where the internal and external pressure are equal ($p_i = p_o = p$), one can assume that $(\sigma_\theta)_{avg}$ and $(\sigma_r)_{avg}$ are equal to p if the hollow cylinder specimen is sufficiently tall. Any changes that occur to $(\sigma_\theta)_{avg}$, $(\sigma_z)_{avg}$, $(\sigma_r)_{avg}$, and $(\tau_{\theta z})_{avg}$ create changes in the magnitude and orientation of $(\sigma_1)_{avg}$ and $(\sigma_3)_{avg}$. They create simultaneous changes in $(\sigma_2)_{avg}$, in relation to $(\sigma_1)_{avg}$ and $(\sigma_3)_{avg}$. This relationship can be seen through the following equation for b, the parameter that indicates the relative magnitude of intermediate principal stress.

$$b = \left(\frac{\sigma_{2avg} - \sigma_{3avg}}{\sigma_{1avg} - \sigma_{3avg}} \right) \qquad \text{Eq. 2.3.3}$$

Table 2.3.4. Expressions used for calculating average stresses and strains developed by Sayao and Vaid (1991).

$$\sigma_z = \frac{F_z + \pi (P_e R_e^2 - P_i R_i^2)}{\pi (R_e^2 - R_i^2)}$$

$$\begin{matrix}\sigma_r \\ \sigma_\theta\end{matrix} = \frac{P_e R_e^2 - P_i R_i^2}{R_e^2 - R_i^2} \mp \frac{2(P_e - P_i) R_e^2 R_i^2 \ln (R_e/R_i)}{(R_e^2 - R_i^2)}$$

$$\tau_{z\theta} = \frac{4 T_h (R_e^3 - R_i^3)}{3\pi (R_e^4 - R_i^4)(R_e^2 - R_i^2)}$$

$$\varepsilon_z = \frac{-\Delta H}{H}$$

$$\varepsilon_r = \frac{-(\Delta R_e - \Delta R_i)}{R_e - R_i}$$

$$\varepsilon_\theta = \frac{-(\Delta R_e + \Delta R_i)}{R_e + R_i}$$

$$\gamma_{z\theta} = \frac{2 \Delta\theta (R_e^3 - R_i^3)}{3 H (R_e^2 - R_i^2)}$$

As stated previously in Equation 2.3.2, the b stress parameter can also be described with relation to (α), which is the orientation of the major principal stress (σ_1) to the vertical by the equation, $b = \sin^2(\alpha)$ when both internal and external pressures are the same. When the internal and external pressures are not equal, then both b and α can be independently controlled. The three stresses (σ_1), (σ_2) and (σ_3), along with (α), can all be independently controlled.

Other stress-related parameters, besides b, can be determined from the four stress components induced by the specimen (σ_θ), (σ_z), (σ_r), and ($\tau_{\theta z}$). These are:

$$p = \frac{\sigma_1 + \sigma_2 + \sigma_3}{3} \qquad \text{Eq. 2.3.4}$$

$$q = (\sigma_1 - \sigma_3) \qquad \text{Eq. 2.3.5}$$

$$\alpha = \frac{1}{2}\tan^{-1}\left(\frac{2\tau_{z\theta}}{\sigma_z - \sigma_\theta}\right) \qquad \text{Eq. 2.3.6}$$

where p is the mean normal stress, q is the deviator stress and as mentioned before, α is the angle between the major principal stress direction and vertical. The effects of α on material behavior are direct results of cross-anisotropy, which will be discussed in detail in chapters.

Design of a Torsion Shear Apparatus

A torsion shear apparatus can be used to study the behavior of soils while rotating the principal stress directions. This apparatus allows for the individual control of vertical normal stress, cell pressure, and the applied shear stress. When designing the specimen height, careful attention must be paid to ensure that shear bands can fully develop and that the end restraint does not cause effects on the specimen behavior.

Through the use of cap and base rings, the vertical normal stress and shear stress are transferred to the specimen. The loading system and other components can be located under the loading table or elsewhere so as not to interfere with the specimen when being prepared and tested.

Careful attention should be paid to ensure that the apparatus is capable of accommodating large normal and shear strains so that once the specimen reaches failure, there is a minimal amount of induced non-uniformity in the stress and strain distributions. When transferring the shear stresses to the specimen, no slippage can occur between the specimen and the stress application mechanisms.

Key parts of the torsion shear apparatus include cap and base rings (with full friction surfaces to transfer shear stresses), a membrane, forming jackets, and draining lines (which allow for measurement of the volume change of the specimen). The loading system and torque loading system can differ from apparatus to apparatus. This is a design choice and can vary. Torque and a vertical load (which can be in some cases supplied by an oil-filled pressure cylinder) can be transferred through the center shaft to the base plate of the apparatus. In Lade's (1981) design, there were four pressure cylinders that allowed for torsion shear stresses in both clockwise and counterclockwise directions. A schematic of Lade's design, as well as Broms and Casabrian's design that used a turntable to shear the specimen are shown in the Figures 2.3.3 and 2.3.4.

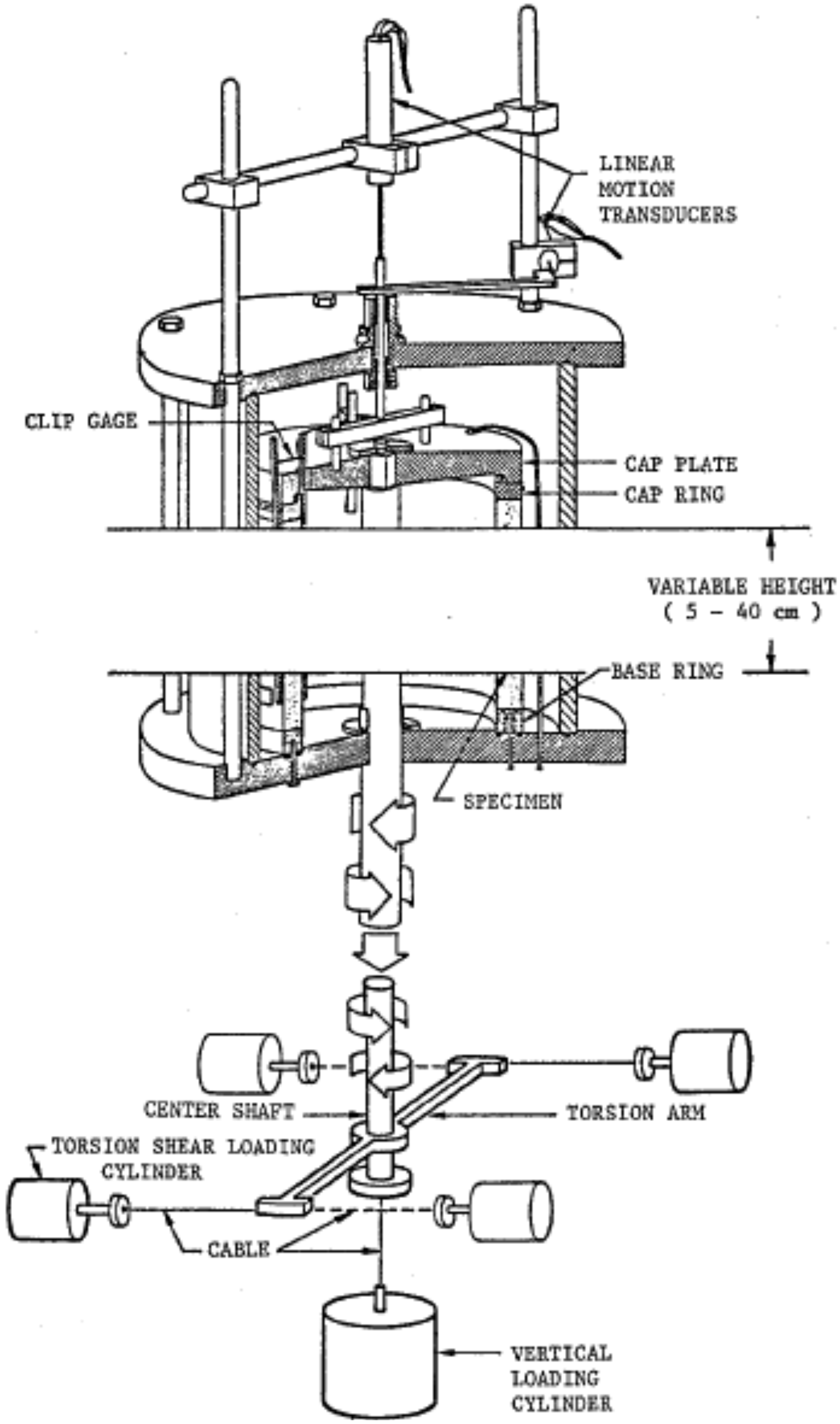

Figure 2.3.3. Torsion Shear Apparatus (after Lade 1981).

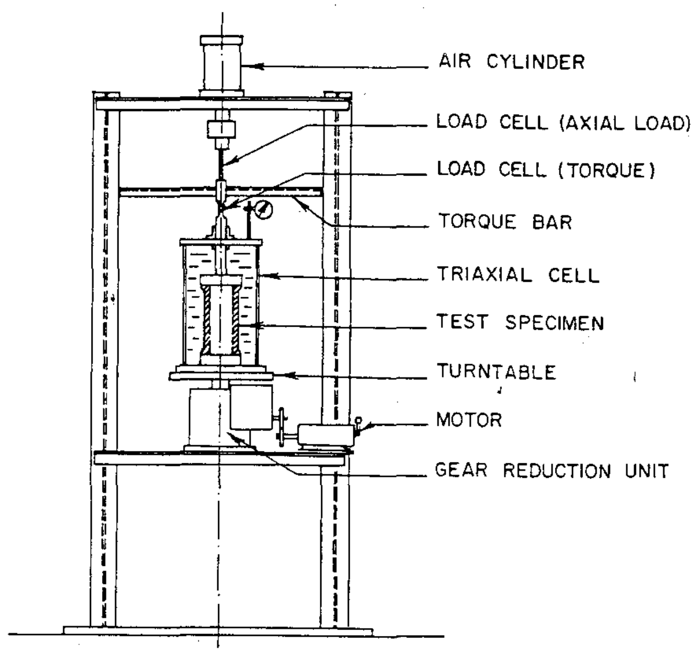

Figure 2.3.4. Test arrangement (after Broms and Casabrian 1965).

In order to measure the vertical and shear deformations, linear motion transducers can be placed outside the cell as shown in Figure 2.3.3. The coil of a vertical linear motion transducer can be set up to measure vertical deformations. Mounted on another rod above the cell, a shear deformation transducer can be placed.

A grid of vertical and horizontal lines can be drawn on the outside surface of the hollow cylinder specimen to allow observations of shear strains. Horizontal deformations can be measured with clip gages and/or LVDTs. Figure 2.3.5 shows another example of a torsion shear apparatus built at the University College Dublin.

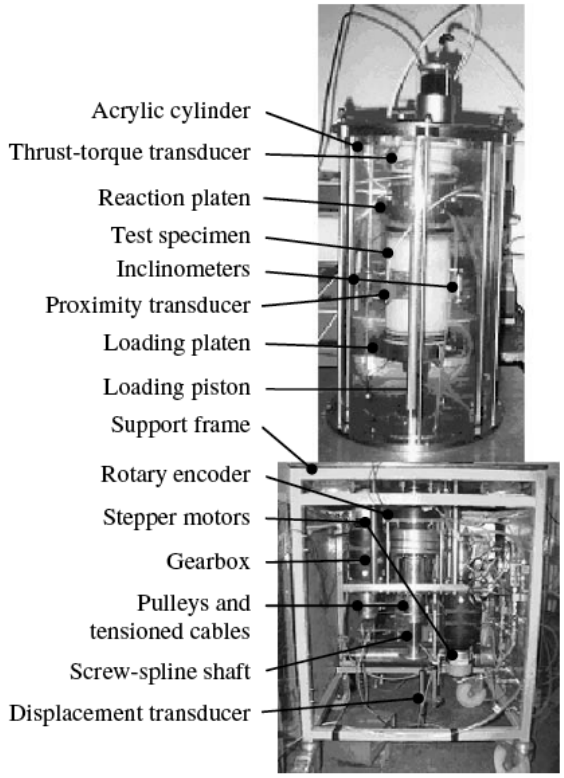

Figure 2.3.5. UCD hollow cylinder torsional apparatus (after O'Kelly and Naughton 2005).

A negative aspect of the torsion shear apparatus is that the tangential, horizontal normal stress in the cylinder wall (σ_θ) cannot be measured. However, during isotropic compression, (σ_θ) can be assumed to be the same as the cell pressure.

In summary, the torsion shear apparatus allows for the ability to control and change applied vertical normal stresses, cell pressures, and shear stresses. The behavior of soils can be examined by applying certain techniques with this apparatus, which produces reasonable uniform stress states. Although designs may be different, they all work on the same principles as well as with the basic components described above.

Influence of Specimen Geometry

Torsion shear equipment offers the benefit that no shear stresses are produced on the vertical surfaces of the specimen, while complimentary shear stresses, $\tau_{\theta z}$ are automatically generated in the specimen, and large and fairly uniform shear strains can be produced. Separate control of the vertical normal stress, the confining pressure, and the shear stress makes it possible to create various initial states of stress before the specimen is sheared. However, there are also limitations. Non-uniformity of stress and strain distributions may develop, especially in specimens with inappropriate dimensions.

Non-uniformity for a given stress state depends on the specimen's dimensions. Wall thickness, diameter and height are components of hollow cylinders. With regards to wall thickness, stress non-uniformity increases with wall thickness for a given average specimen radius where

$$r_{avg} = \frac{(r_i - r_o)}{2} \qquad \text{Eq. 2.3.7}$$

where r_i is the inner radius and r_o is the outer radius.

Figure 2.3.6 (taken from Sayao and Vaid 1991) shows the effect of wall thickness on non-uniformity coefficients for b=0, α=45° at r=2 and 3.

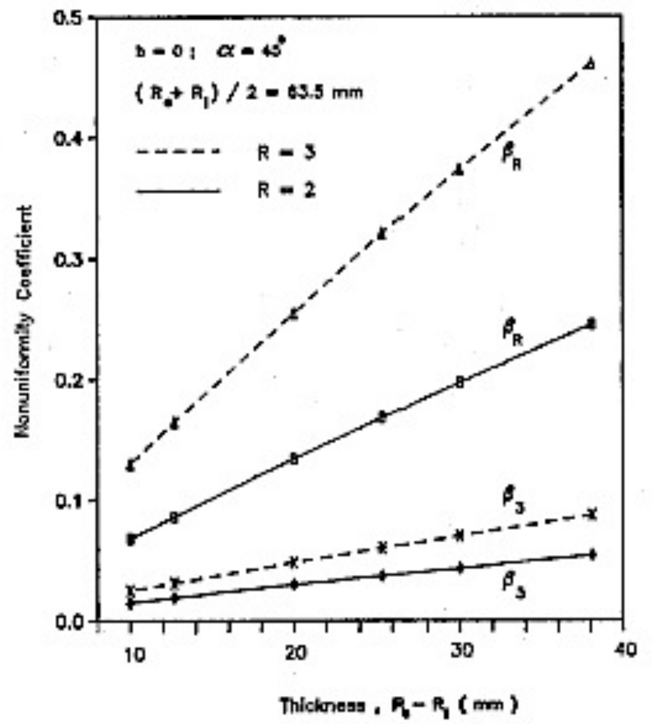

Figure 2.3.6. Effect of wall thickness non-uniformity coefficients (after Sayao and Vaid 1991).

There is a minimum thickness that specimens should have to minimize non-uniformities. Hight et al. (1983) stated two considerations. First, consideration to include a large enough number of sand grains across the wall in order to ensure a uniform sand density must be made. Second, it is important to consider the need to minimize the relative significance of potential volume change corrections due to membrane penetration. In practice, a wall thickness of 20 to 26 mm is considered to be applicable for medium and fine sands. When considering the radii dimensions, a very large inner radius may not be practical in terms of stress path control.

Sayao and Vaid (1991) recommended a r_i/r_e within 0.65 and 0.82 for specimens with a wall thickness within the range of 20-26mm. Specimen height must also be considered when looking at specimen geometry. Radial frictional restraint at the boundaries of the specimen causes stress non-uniformities as well as specimen curvature in the vertical direction. If the height, H to diameter, 2R ratio is within 1.8 to 2.2, then these non-uniformities are considered to be minimal. Any additional techniques to reduce friction on the end platens will help reduce radial friction. Lade (1981) recommends the specimen to have a height of 40 cm and an average diameter of 20 cm, with a wall thickness of 2 cm. Many experiments conducted on this size specimen have been successful and have shown that this size can provide high quality.

Table 2.3.5 shows a list of torsion shear apparatuses up until 1988. Figure 2.3.7 shows the specimen geometry for the apparatuses listed in Table 2.3.4. The boxed-in devices are those that are within the recommended dimensions for specimens (wall thickness: r_o-r_i= 20-26mm, inner radius: $0.65 \leq r_i/r_o \leq 0.82$, and height: $1.8\leq (H/2)*r_o \leq 2.2$).

The topic of stress non-uniformities has been an important consideration by many researchers when dealing with torsion shear apparatuses. Similar to other apparatuses used in geotechnical testing, stress non-uniformities can develop near specimen ends due to the frictional restraint of stiffness at the ends. In tests where torque is applied or where the internal and external pressures are different, the wall curvature also plays a role in producing stress non-uniformities. Sayao and Vaid (1991) and Wijewickreme and Vaid (1991) showed that the stress non-uniformities that occur are related to specimen size, and they decrease as the wall thickness is decreased and as the inner radius is increased.

Naughton and O'Kelly (2007) studied stress non-uniformities in hollow torsion shear specimens, keeping the mean principal stress, b-value and alpha constant. The hollow cylinder specimen size had an inner radius of 35.5mm, an outer radius of 50.0mm and a height of 200mm. They increased the stress ratio and computed the corresponding stress non-uniformities. They found that for triaxial compression and triaxial extension, the stress distributions were completely uniform. However, for (b-value, α)=(1, 0°) and (0, 90°), there were significant stress non-uniformities. For all conditions with α=45°, there were significant stress non-uniformities. These locations would be where the ratio of inner to outer pressures is the maximum (for b=1, α=0°) or minimum (for b=0, α=90°). The circumferential stress (due to the applied torque) is at its maximum value for α=45° values. Figure 2.3.8 shows the regions where serious stress non-uniformities can develop.

Table 2.3.5. Stress path devices using hollow cylinder specimens (after Sayao and Vaid 1991).

No.	Reference		Institution		Specimen Dimensions (mm) H	R_e	R_i	Soil Type	Control Restrictions	Applications
1	Cooling & Smith	1936	Building Research Station	(ENG)	19-38	50.8	41.3	Clay	$F_s=P_e=P_i=0$	Undrained shear strength
2	Norton	1938	M.I.T.	(USA)	50.8	11.1	7.9	Clay	$F_s=P_e=P_i=0$	Torsional deformability ceramic clays
3	Geuze & Kie	1953	S.M. Laboratory, Delft	(HOL)	80.0	19.0	13.0	Clay	$F_s=P_e=P_i=0$	Underained creep
4	Kirkpatrick	1957	University of Glasgow	(SCOT)	152.4	50.8	31.8	Sand	$F_s=T_h=0$	σ_2 effect on failure condition
5	Haythornthwaite	1960	Brown University	(USA)	?	?	?	Silt	$P_e=P_i$	σ_2 effect on failure condition
6	Whitman & Luscher	1962	M.I.T.	(USA)	76 or 127	25 or 19	12.7	Sand	$T_h=0$; $\varepsilon_s=0$	Soil-structure interaction at failure
7	Wu et al.	1963	Michigan State University	(USA)	127.0	50.8	38.1	C&S	$T_h=0$	σ_2 effect on failure condition
8	Broms & Ratnam	1963	Cornell University	(USA)	114.3	76.2	38.1	Clay	$T_h=0$	3-D consol. effects on strength
9	Broms & Casbarian	1965	Cornell University	(USA)	254.0	63.5	38.1	Clay	—	σ_2 and α effects on strength
10	Broms & Jamal	1965	Cornell University	(USA)	304.8	76.2	38.1	Sand	$T_h=0$	Validity of $\sigma_r=\sigma_\theta$ assumption
11	Esrig & Bemben	1965	Cornell University	(USA)	203.2	50.8	38.1	Sand	$T_h=0$	σ_2 and ε_2 effects on strength
12	Suklje & Drnovsek	1965	University of Ljubljana	(YUG)	80.0	32.0	20.0	Clay	$T_h=0$; $\sigma_s=0$	Deformability under plane stress
13	Jamal	1966	Cornell University	(USA)	203.2	50.8	13-38	Sand	$T_h=0$; $P_e=P_i$	Wall thickness effect on strength
14	Saada & Baah	1967	Case W.R. University	(USA)	151.1	35.1	25.4	Clay	$P_e=P_i$	Influence of anisotropy
15	Proctor	1967	University of Manchester	(ENG)	152.4	50.8	19.1	Sand	$T_h=0$	Drained shear strength
16	Lomize et al.	1969	Civil Engineering Institute	(USSR)	180.0	155.0	125.0	Clay	$P_e=P_i$	Drained creep under 3-D stress state
17	Frydman et al.	1971	Israel Institute of Tech.	(ISRL)	203.2	50.8	25.4	Sand	$T_h=0$	End restraint ; membrane penetration
18	Drnevich	1972	University of Kentucky	(USA)	100.0	25.0	20.0	Sand	$P_e=P_i$	Torsional resonant column tests
19	Arnold & Mitchell	1973	University of Adelaide	(AUS)	142.0	76.0	51.0	Sand	$T_h=0$	3-D stress effect on strength
20	Ishibashi & Sherif	1974	University of Washington	(USA)	13 to 25	50.8	25.4	Sand	$P_e=P_i$	Liquefaction characteristics
21	Tong	1975	University of Waterloo	(CAN)	203.2	50.8	31.8	Sand	—	Yield and failure criteria
22	Lade	1975	U.C.L.A.	(USA)	50.0	110.0	90.0	Sand	$P_e=P_i$	α effect on stress-strain
23	Iwasaki et al.	1978	Inst. Ind. Science	(JAP)	100.0	50.0	30.0	Sand	$P_e=P_i$	Stress-strain for $\gamma>10^{-2}\%$
24	Lade	1981	U.C.L.A.	(USA)	400.0	110.0	90.0	Sand	$P_e=P_i$	Influence of specimen's height
25	Dusseault	1981	University of Alberta	(CAN)	200-240	50.8	25.4	Sand	$T_h=0$	Tunelling and pressuremeter paths
26	Fukushima & Tatsuoka	1982	Inst. Ind. Science	(JAP)	200.0	50.0	30.0	Sand	$P_e=P_i$	Deformation & strength behaviour
27	Symes et al.	1982	Imperial College	(ENG)	254.0	127.5	101.5	Sand	—	b and α effects on strain response
28	Ishihara & Towhata	1982	University of Tokyo	(JAP)	104.0	50.0	30.0	Sand	$P_e=P_i$	α effects ; liquef. characteristics
29	Ishibashi et al.	1985	Cornell University	(USA)	142.0	35.5	25.4	Sand	$P_e=P_i$	Liquefaction characteristics
30	Miura et al.	1986	Hokkaido University	(JAP)	200.0	50.0	30.0	Sand	—	α effect on stress-strain & strength
31	Alarcon et al.	1986	Purdue University	(USA)	203.0	35.5	19.0	Sand	$P_e=P_i$	Stress-strain for $\gamma>10^{-2}\%$
32	Anderson et al.	1988	University of sheffield	(ENG)	150.0	75.0	12.5	Clay	$T_h=0$	Pressuremeter paths ; undrained creep
33	Chen et al.	1988	Cornell University	(USA)	193.0	51.0	35.5	Sand	$P_e=P_i$	Dynamic shear mod. of glass spheres
34	Sayao & Vaid	1988	University of B.C.	(CAN)	304.8	76.2	50.8	Sand	—	Effects of α, R, b & σ_m' on strain resp.

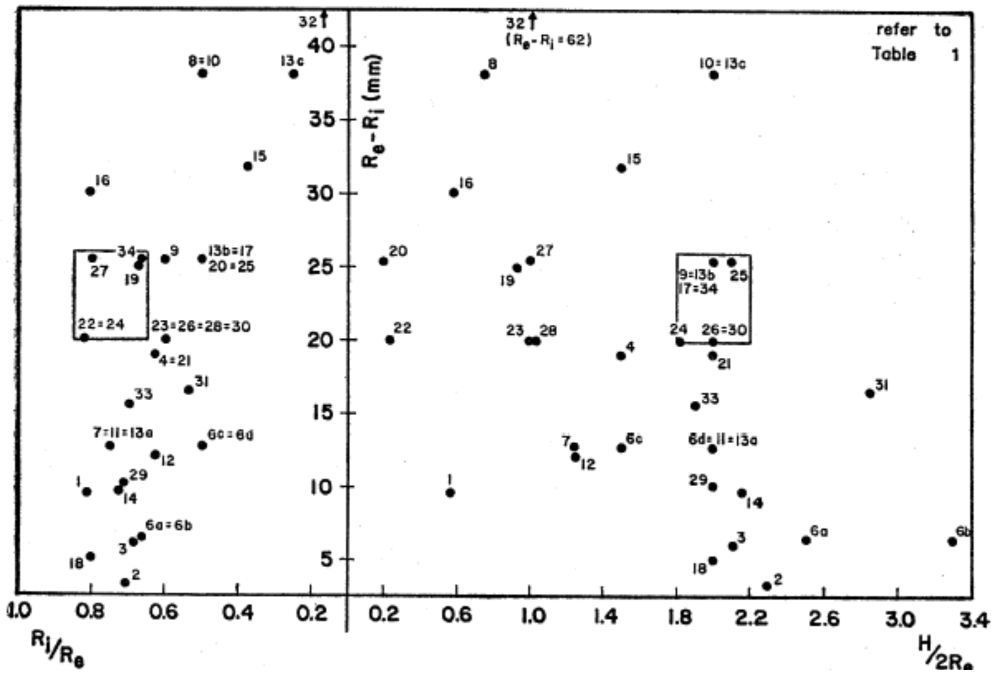

Figure 2.3.7. Specimen geometry of reported holly cylinder devices (after Sayao and Vaid 1991).

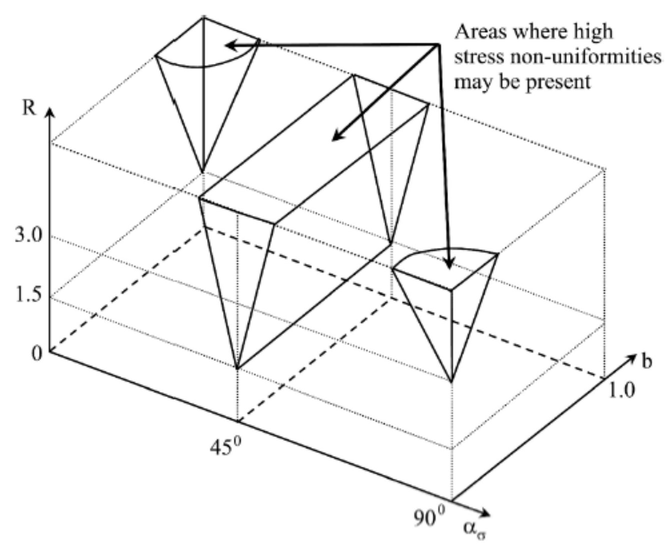

Figure 2.3.8 Areas where serious stress non-uniformities may arise (after Naughton and O'Kelly 2007).

2.4. Cross-Anisotropy

Introduction to Anisotropy

Anisotropy in granular materials can be caused by certain reasons. The arrangement of particles and the directions of the grains major axes on the bedding plane can cause anisotropy. Anisotropy can be inherent and be caused by spatial distribution of contacts and contact forces. Anisotropy can also be induced by using carefully designed stress paths and by controlling the testing procedure. Doing so, the influence of the stress path on the strength and deformability of the soil can be explained.

When properties are the same in all directions within the horizontal plane, yet different from those in the vertical direction (the direction of deposition), soil behavior can be referred to as cross-anisotropic. When natural sand is deposited under gravity, the material structure results in a cross-anisotropic fabric. Two types of anisotropy have been defined for soils. The first type is called inherent anisotropy. This refers to the initial fabric or particle composition when the soil is in its virgin state, before loading happens. The second type of anisotropy is induced by loading and plastic deformation of an originally isotropic soil. This is caused by the non-reversible strain increments placed on a specimen when following a stress path. Any change in inherent condition would be part of this second type of anisotropy.

Lade and Abelev (2003) studied the characteristic state of dense Santa Monica Beach sand. The characteristic line is defined at the point where the volumetric strain, ε_v is equal to zero. At this line, the volumetric behavior of a material alters from contractive to dilative. This line can be shown as a straight line in the q-p' plane and it passes the origin with a slope, ϕ_{CL}. That being stated, Lade and Abelev found that the uniqueness of a characteristic line may not be preserved for an inherently cross-anisotropic material. The location of the characteristic line for an inherently cross-anisotropic material is dependent on two factors, the relative orientation between the direction of loading and the material symmetric axis, as well as the degree of anisotropy.

When analyzing cross-anisotropy in clays, certain mechanical properties (e.g. permeability, stress-strain behavior, and strength) are related to the orientation of the plate-shaped clay particles as well as their depositional environment and preconsolidation history. Studies of clay structures have shown that clay particles tend to become oriented perpendicularly to the major principal stress direction during one-dimensional consolidation. Under these conditions, the normal to the plane is an axis of radial symmetry and the material is considered cross-anisotropic. Properties that are associated with any plane can change with the angle between the plane being looked at and the plane on which the major principal stress acted when the clay was being consolidated. When analyzing clays, the engineering behavior of clay is determined by what the structure is at the time the behavior is studied. This final structure depends on what happened to the initial structure due to additional consolidation or shearing under vertical and/or inclined loading situations.

Inherent versus Induced Anisotropy

Inherent Anisotropy:

In 1944, Casagrande and Carillo studied strength anisotropy in soils. They classified anisotropy into two groups: inherent and induced. Inherent anisotropy implied that anisotropic characteristics were present in the soil before any strains were induced in the soil. Inherent anisotropy was therefore defined as “a physical characteristic inherent in the material and entirely independent of strains.” They defined induced anisotropy as “a physical characteristic due exclusively to the strain associated with an applied stress.” In the 1960’s, several experiments were conducted to further study inherent anisotropy in soils. Below is Table 2.4.1, which summarizes some of the early experiments performed.

Table 2.4.1. Summary of early experiments performed to study anisotropy.

1965	Johansson	Conducted a thorough literature review and found evidence of geometrical anisotropy occurring in soils in situ. Concluded that particle shape and depositional mode affected the particle orientation.
1967	Weindieck	Used a 2D soil model of different sized coins to show a greater number of contacts normal to the vertical direction of sample pouring than parallel to it.
1967	Phillips and May	Constructed a shear box and changed the sample pouring direction with respect to the failure plane. Dry dense samples of Leighton Buzzard sand poured in air through a side or end of the shear box gave max stress ratios 24% higher than for samples poured through the top of the box. There was a difference of ϕ' of 5°.
1968	Parkin et al.	Hydrostatic compression tests on triaxial samples (medium sand) deposited in air showed that the radial strain of the sample was always much greater than the vertical strain. Found that the long dimension of the grains were aligned in the horizontal plane and were symmetrically disposed about the vertical axis.
1972	Arthur and Menzies	Took radiographs showing plan and elevation views of cubical samples of glass ballotini and aluminum discs poured through water. They also did the same with Ham River gravel, poured both through air and water. (see Figure 2.4.1a and b).

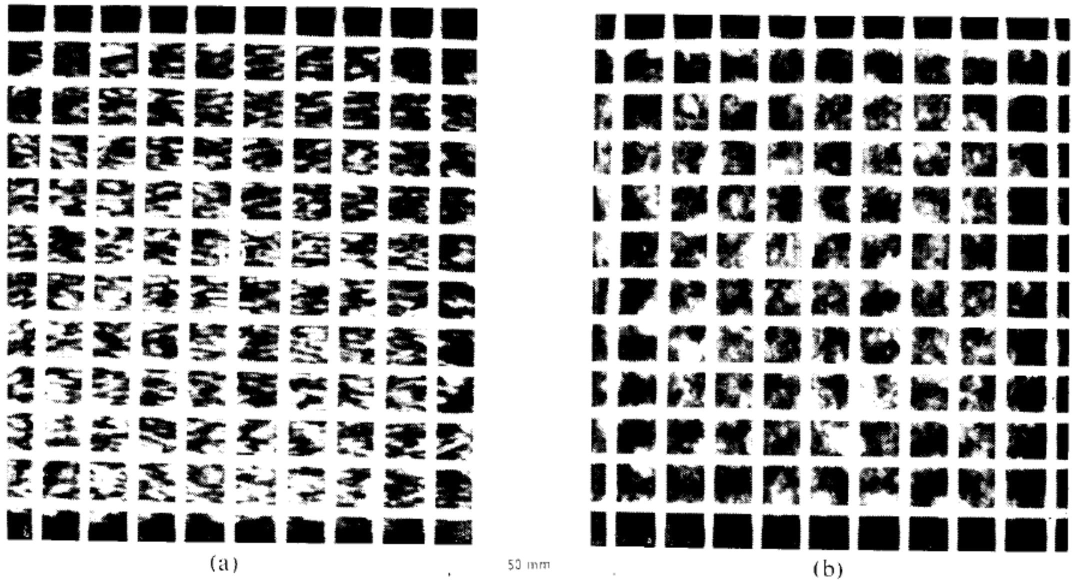

Figure 2.4.1. Radiographs of a cube deposited aluminum discs (a) elevation (b) plan (after Arthur and Menzies 1972).

Early studies were performed with specially built shear boxes both by Phillips and May (1967) and by Duncan and Dunlop (1969). In these tests, inherent anisotropy of sand was studied by pouring sand in different directions with respect to the horizontal failure plane. The tests showed that the shear strength of sand is dependent on the inclination of the bedding planes. Phillips and May (1967) found that for dry dense samples of Leighton Buzzard sand poured through the side or end of the shear box constructed, a stress ratio of 24% higher was attained than when compared to the specimens poured through the top of the box. This corresponded to a variation of friction angle of 5 degrees.

In order to further study inherent anisotropy and not be limited by the shortcomings of the shear box used by Phillips and May (1967), Arthur and Menzies (1972) developed an apparatus that would allow for the deposition of sand in any direction relative to the applied principal stress directions. They created a prism shaped sample and used a true triaxial stress system that worked for a range of stress paths. The cubical samples were prepared while the molds were tilted at various angles to the direction of pouring. Figure 2.4.2 shows the preparation of the specimens.

Samples were prepared with the same porosity and were deposited at angles of tilt, θ of 0°, 20°, 30°, 40° and 90°. They were tested to failure in drained triaxial compression. Figure 2.4.3 shows the strength results. As can be seen from the figure, there is a strength anisotropy of 10% in the maximum principal stress ratio corresponding to over 2° in ϕ'. This occurs between $\theta = 0°$ and $\theta = 90°$. In the region where $20° < \theta < 40°$, there is a discontinuity (which corresponds to the orientation plane of maximum stress obliquity, $45°-\phi'/2$ of approximately 26°).

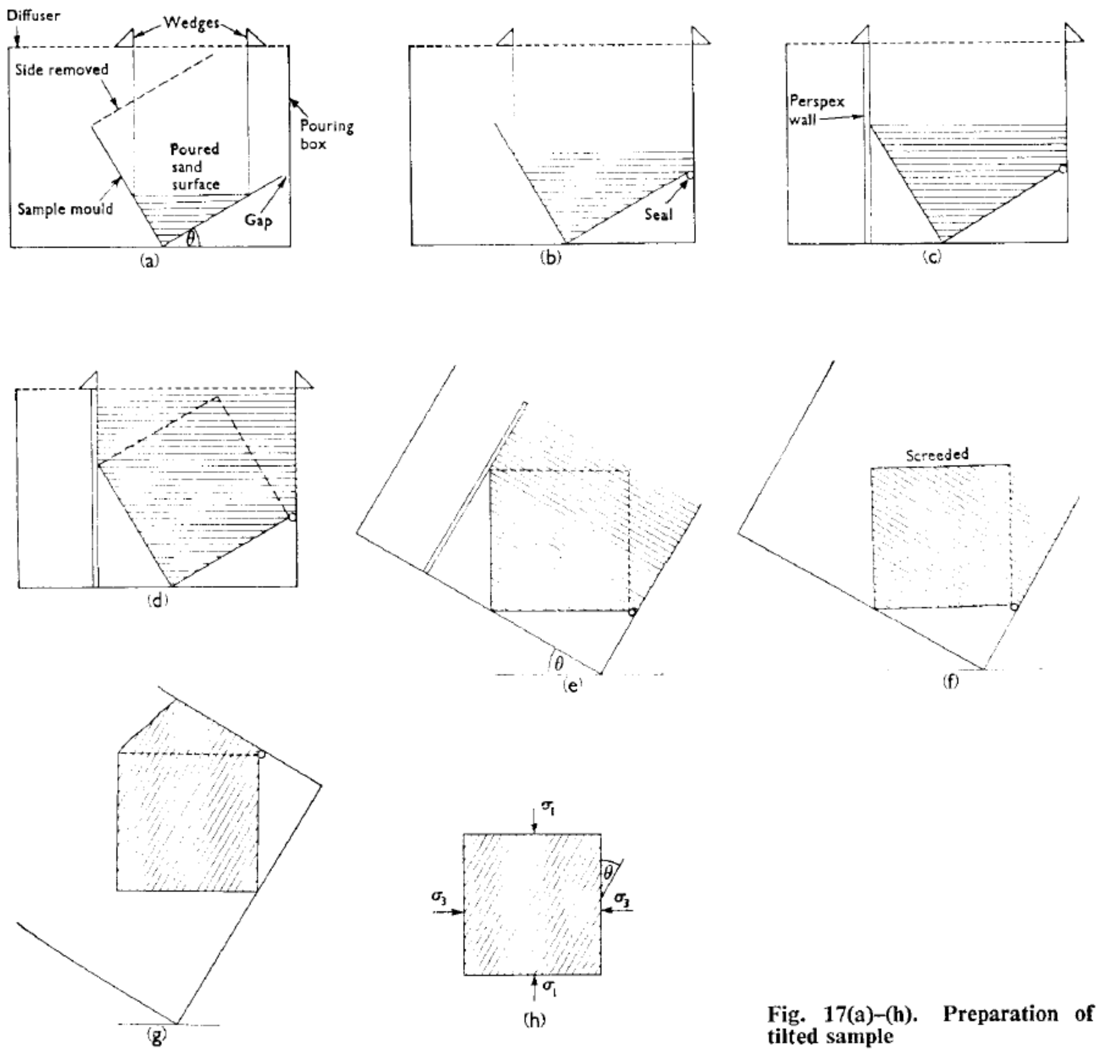

Figure 2.4.2. Preparation of tilted sample (after Arthur and Menzies 1972).

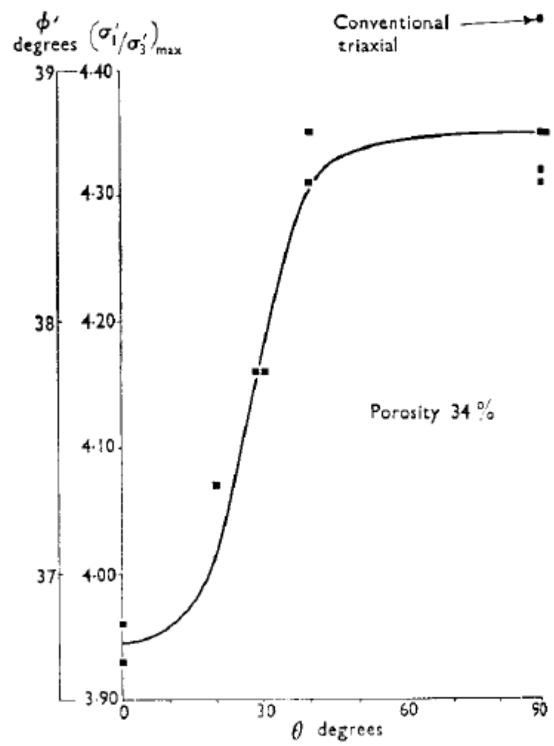

Figure 2.4.3. Variation in drained strength with angle of tilt (after Arthur and Menzies 1972).

Figures 2.4.4a and 2.4.4b show that the magnitudes of the lateral (intermediate) principal strains are different even though they are tied with the same magnitude of the principal stress ($\sigma'_2=\sigma'_3$). As can be seen in the figures, the lateral strain in the direction of layering, ε_2 is in every case lower than the other lateral principal strain, ε_3.

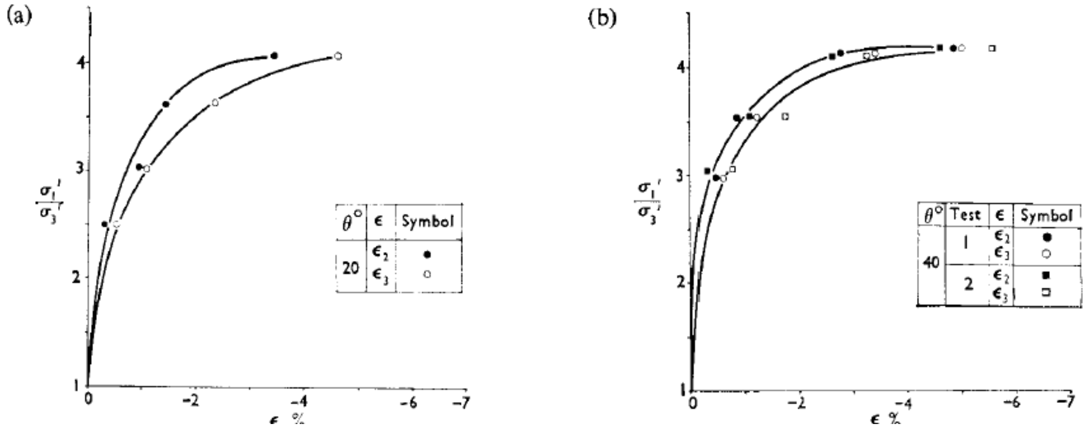

Figures 2.4.4. (a) and (b) Stress ratios-lateral principal strains, (after Arthur and Menzies 1972).

Arthur and Menzies (1972) concluded that in their experiments, the anisotropic behavior of the sand was caused by deposition alone. They stated that the deposition history as well as the stress history was needed to model stress-strain behavior of granular materials. They also noted that the variation in strength was associated with the changes in relative magnitude of the intermediate principal stress.

Arthur and Phillips (1975) found that changing the relation of the plane of deposition to the major principal stress showed inherent anisotropy. They tested homogenous, layered and multilayered samples. For the homogeneous samples, although testing two different sands (Leighton Buzzard and Ham River), they saw that both sands had a rapid change in stress ratio for a small change in principal stress direction. They speculated that the ratio jump might be due to the difference in particle shape or surface texture. They concluded that inherent strength anisotropy could differ considerably among different granular materials.

Induced Anisotropy:

As defined in the previous section by Casagrande and Carillo (1944), induced anisotropy could be defined as “a physical characteristic due exclusively to the strain associated with an applied stress.” Therefore, induced anisotropy is an integral part of the straining process of a soil. However, it is difficult to study induced anisotropy due to the need to have controlled rotation of principal stress directions during shear.

In 1977, Arthur et al. created an apparatus (see Figures 2.4.5a. and 2.4.5b.) to study the controlled changes of principal stress directions in dense sand samples undergoing plane strain. With the new apparatus they were able to create a single sudden rotation of principal stress directions (from 0° to 90°) to each sample of sand. To get rid of any inherent anisotropy, so that only induced anisotropy could be studied, the samples were deposited in the direction of the subsequently applied intermediate principal stress ($\Delta\varepsilon_2$=0). Their tests showed that induced anisotropy caused a large effect on the magnitude of strain increments. It also caused a quick and small reduction in the deviation of the principal axes of stress and strain increments.

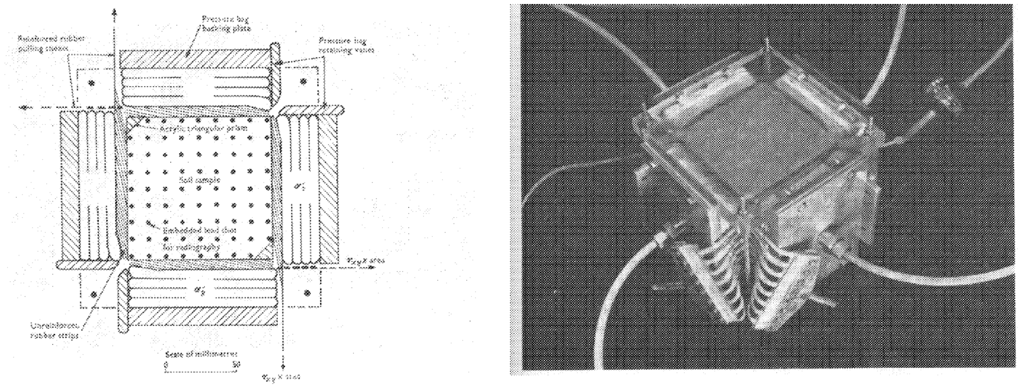

Figure 2.4.5. (a) Application of both normal and shear stresses to the sample. (b) Pulling sheets in place around sample under load (after Arthur et al. 1977).

There was a significant increase in major principal strain with reloading after a principal stress direction with a rotation of θ. A significant amount of strain occurs before reaching the stress ratio of two once θ passes 50°. The major principal strains up until the stress ratio reaches 6 during the reloading path have been plotted against θ in Figure 2.4.6. The peak seen on this graph shows the strain when the rotation is at 75°. At this particular rotation, one no-extension direction of the reloading coincides with one no-extension direction of the first loading. These no-extension directions appear to be the axes of induced anisotropy that define the two directions where the major principal stress would have the minimum amount of stiffness.

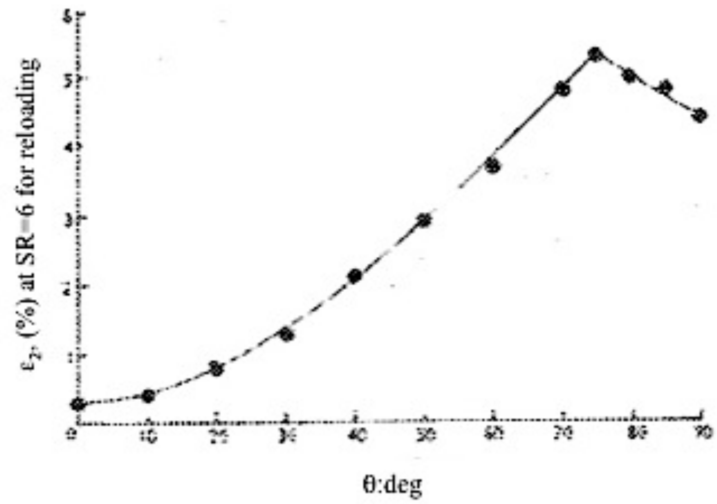

Figure 2.4.6. Major principal strain to achieve a stress ratio of 6 on reloading plotting against rotation of principal stress direction (after Arthur et al. 1977).

Arthur et al. (1977) concluded that there would be three axes of induced anisotropy, two of which were minima and one of which would be a maximum. The maximum would be in the direction of the previously applied principal stress. They found that induced anisotropy did not greatly impact the angle of shearing resistance, φ'. However as seen above, induced anisotropy can have a great influence on the strain needed to attain a certain stress ratio, as well as it can affect the secant modulus when reloading after a rotation of the principal stress direction.

Further studying anisotropy, Lade and Wasif (1988) performed tests on Cambria sand with height to diameter (H/D) ratios of 1.0 and 2.5. The specimens were prepared in a specially designed mold, which was tilted at certain angles (see Figure 2.4.7). The sand grains were poured and shaken in different layers and then frozen. When ready, they were thawed and sheared. Since the specimens were tilted, the major principal stress could be applied at different angles in relation to the bedding planes. Figure 2.4.8 shows the coordinate system for indication of the initial bedding plane inclination of the cross-anisotropic specimens prepared.

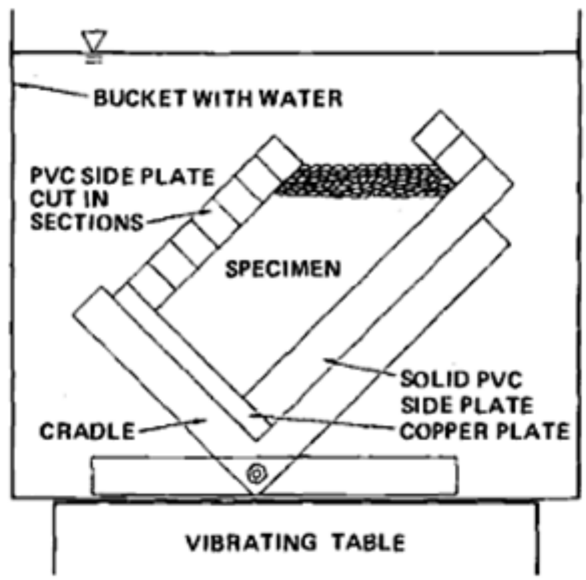

Figure 2.4.7. Mold for Preparation of specimens with inclined bedding planes (after Lade and Wasif, 1988).

Clear effects of cross-anisotropy were seen in tests that were inclined and that had vertical bedding planes. The stress strain curves of the tests performed are shown in Figure 2.4.9. As can be seen, tests with H/D ratio of 1.0 varied very little in strength with varying inclinations. However, a 5.5 degree difference in friction angle was seen in tests with a H/D ratio of 2.5. This can be seen clearly in Figure 2.4.10.

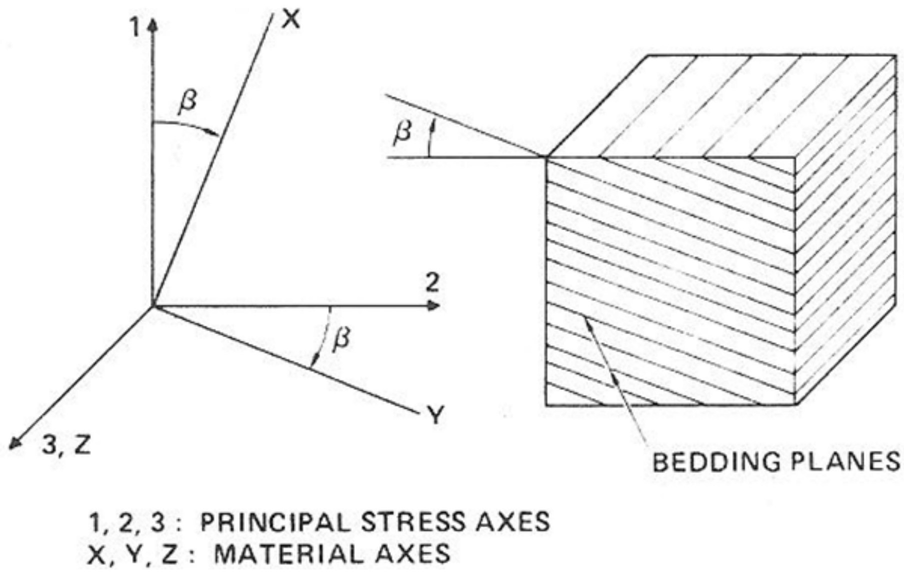

Figure 2.4.8. Coordinate system for the indication of initial bedding plane inclination of cross-anisotropic specimens (after Lade and Wasif, 1988).

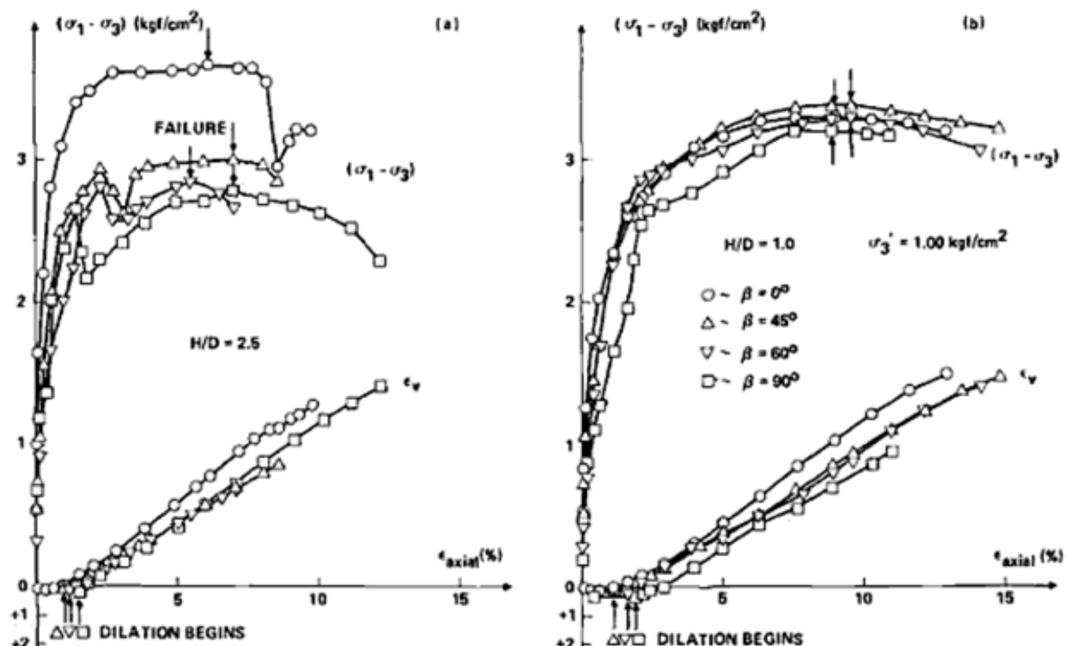

Figure 2.4.9. Stress-strain and volume change characteristics obtained in triaxial compression tests on Cambria sand with cross-anisotropic fabric (after Lade and Wasif, 1988).

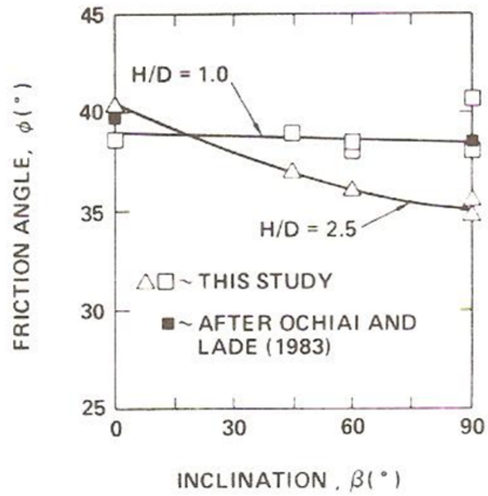

Figure 2.4.10. Variation of friction angles with bedding plane inclination in triaxial compression tests on Cambria Sand with cross-anisotropic fabric (after Lade and Wasif, 1988).

Cross-Anisotropy Results using a true triaxial apparatus

Yamada and Ishihara (1979) used a cubical triaxial apparatus to study a wide range of one-directional loading conditions to further study the effects of anisotropic deformability of sand. Two specimens were sheared by increasing the major principal stress while decreasing the two minor principal stresses simultaneously. Although the stress conditions were identical in the tests, there were differences in deformation characteristics. The strain component in the direction of the major principal stress was larger in the second test than in the first. This showed that the specimen was less compressible in the direction of deposition than perpendicular to the direction of deposition. After looking at similar results from other samples, they concluded that a specimen prepared by vertical deposition of sand generally exhibited anisotropic deformation characteristics in such a way that the specimen is more resistant when compressed in the vertical direction than in the horizontal direction. Two causes can be used to explain these deformation characteristics. Firstly, gravitational force may have an effect and compress the specimen to some extent, making the sand slightly more resistant to vertical deformation. Secondly, inherent anisotropy may have developed when the specimen was prepared underwater. They concluded that the effects were due to inherent anisotropy that formed in the specimen when the sand was deposited under water in horizontal layers.

When looking at volumetric strain, if the sand specimen was isotropic, then all the curves in Figure 2.4.11 would coincide, since the same stress conditions were applied. However, the difference in the volume contraction can be attributed to the difference in the mode of each straining occurring in different directions; a direct result of the inherent anisotropy of the specimens.

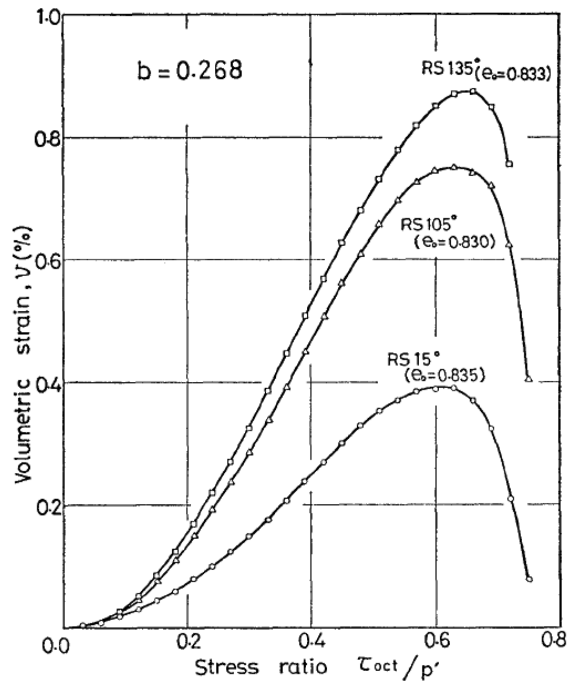

Figure 2.4.11. Volumetric strain versus stress ratio of RS 15°, RS 105° and RS 135° tests (after Yamada and Ishihara 1979).

The anisotropic behavior of specimen can be interpreted using the representation of the strain increment vector plotted in the principal stress space (see Figure 2.4.12). If the sand specimen were to be isotropic, then the strain vectors shown should be oriented symmetrically with respect to XE- and YC- directions. When looking closely at Figure 2.4.12, one can see that the strain increment vectors are oriented more in the clockwise direction. This shows that the shear strain of the specimen is anisotropic in nature. As the stress ratio became large enough to produce maximum volume contraction and failure, the effects of inherent anisotropy present in the sand specimens seemed to disappear. This can be seen in the plane strain increment vectors in Figure 2.4.12. As seen on the strain increment vectors at failure for the XE and YC directions, the vectors are symmetrically oriented. This shows that the inherent anisotropic characteristics cannot be seen at large stress ratios causing failure in the specimen.

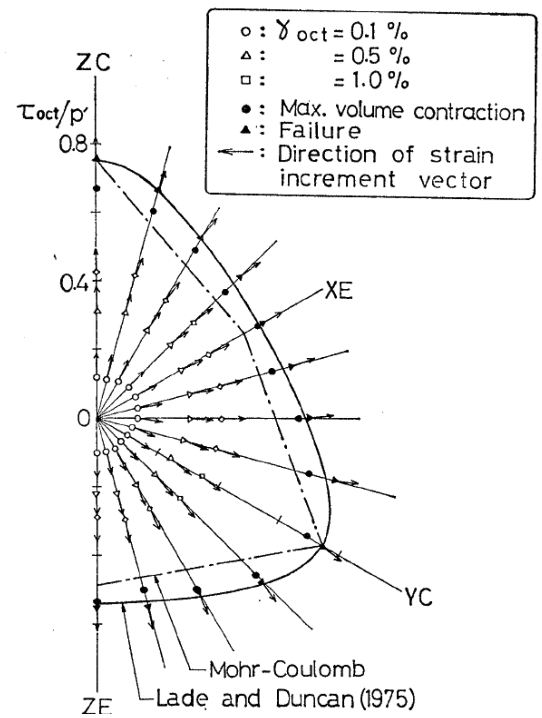

Figure 2.4.12. Representation of measured strains on the octahedral plane (after Yamada and Ishihara 1979).

Cross-Anisotropy Results using a torsion shear apparatus

Miura et al. (1986) studied the drained deformation characteristics of sand that had an anisotropic fabric, which was formed during deposition. This occurs due to the parallel alignments of particles during the deposition process. The specimens were exposed to a continuous rotation of the principal stress axes with the three principal stresses kept constant. By keeping them constant, it is possible to see the deformation characteristics due only to the rotation of the principal stress axes. Tests revealed that the shear deformation characteristics and volume change due to this rotation are not as small as those that happen with irrotational shear. Depending on whether or not directional change of the principal stress occurred, the effects of the anisotropic fabric were different. This difference can be explained due to the predominant sliding on the bedding plane having the lower resistance value against shear stress. The schematic explanation of this is depicted in Figure 2.4.13.

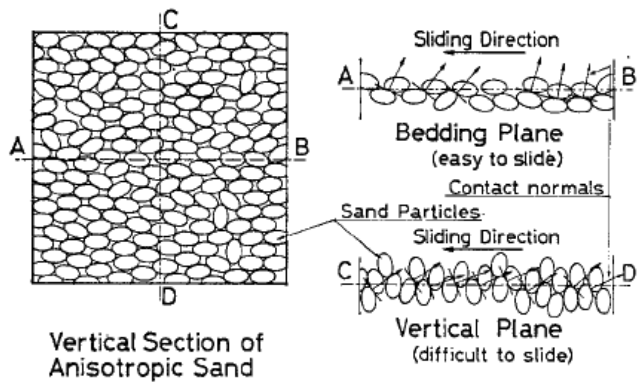

Figure 2.4.13. Schematic explanation for the lowest resistance against sliding on bedding plane (after Miura et al. 1986).

Research done by Oda et al. (1978) showed that the shear plane nearly parallel to the bedding plane appeared when failure strength was at a minimum. Due to this, it can be presumed that the shear stress resistance along the bedding planes is at a minimum. The interlockings between elongated sand particles with their long axes laid horizontally are the poorest on the bedding plane. Because contact planes between particles are parallel to the bedding plane, the largest sliding displacement occurs on the bedding plane. Deformation behavior of anisotropic sand can be predicted by the largest displacements on potential sliding planes.

This can be predicted even under the most general stress conditions involving principal stress rotation.

Miura et al. (1986) also concluded that despite having values of the three principal stresses kept constant, specimens tended to contract accumulatively because of the rotation of principal stress axes, even though they expand due to the increase in shear stress involving no rotation of principal stress axes within the same stress domain. When rotating the principal stress axes, the direction of the principal strain increment axes is located between the principal stress and principal stress direction. It approaches the principal stress axes with increase in the shear strain increment. The magnitude of the strain increment becomes larger at $2\alpha_{de}=\pm 90°$. The direction of the strain increment axes changes to this same direction as well as under the irrotational stress condition.

Three Dimensional Failure Criterion for Cross-Anisotropic Soils

Abelev and Lade (2004) also used true triaxial tests to study the effects of cross-anisotropy on Santa Monica Beach sand. They performed a total of 37 drained, true triaxial tests on cubical specimens. The specimens were oriented in a way so that tests with b-values in all sections of the octahedral plane (Figure 2.4.14) could be performed. When comparing the results from the results of previous studies done on a different type of sand (Cambria Sand), more pronounced effects due to cross-anisotropy of the Santa Monica Beach sand were seen. The major principal stress was always perpendicular or parallel to the bedding planes. Experiments in all three sectors of the octahedral plane showed that air pluviated sand with horizontal bedding planes showed cross-anisotropy with lower strength in the horizontal direction than in the vertical direction. The failure surface was symmetric along the vertical principal stress axis on the octahedral plane.

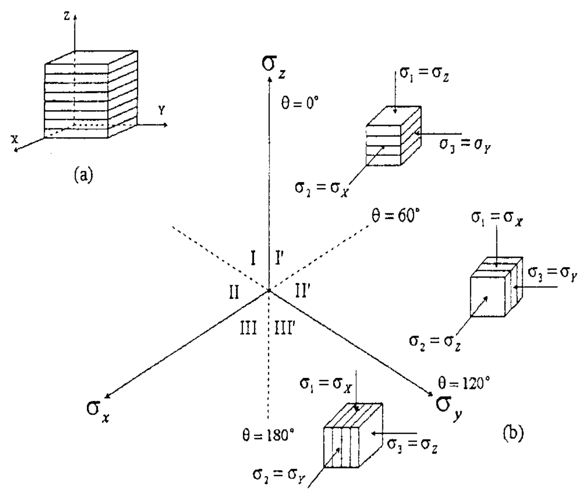

Figure 2.4.14. Specimen orientation (a) in Cartesian coordinate system and (b) as installed in cubical triaxial apparatus (after Abelev and Lade 2004).

In order to create a failure criterion to take into account cross-anisotropy, Abelev and Lade (2004) used the isotropic 3D failure criterion, where

$$\left(\frac{I_1^3}{I_3} - 27\right)\left(\frac{I_1}{p_a}\right)^m = \eta_1 \qquad \text{Eq. 2.4.1}$$

in which I_1, the first stress invariant is calculated by:

$$I_1 = \sigma_1 + \sigma_2 + \sigma_3 \qquad \text{Eq 2.4.2}$$

and where I_3, the third stress invariant is calculated by:

$$I_3 = \sigma_1 * \sigma_2 * \sigma_3$$

Eq. 2.4.3

and p_a is the atmospheric pressure. η_1 and m are constant dimensionless parameters. They created a pseudo isotropic failure surface where the hydrostatic axis was shifted by an angle, α around the stress origin in the vertical triaxial plane. This can be seen in Figure 2.4.15.

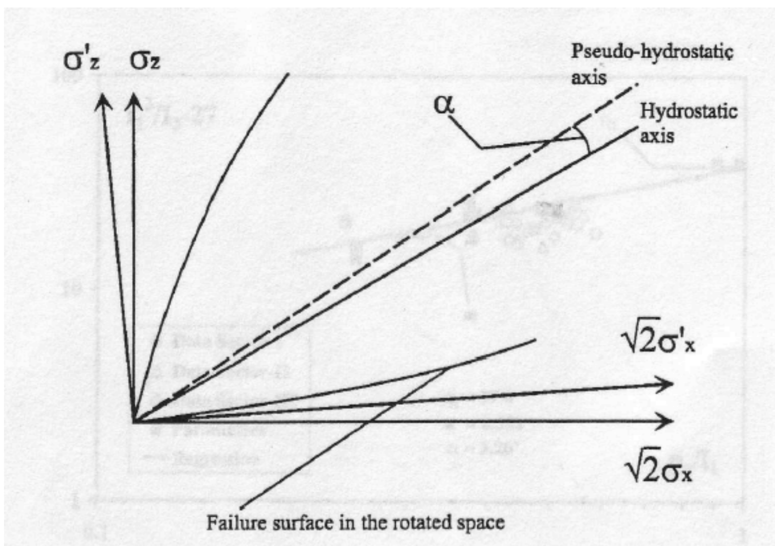

Figure 2.4.15. Rotation of principal stress space around stress origin in vertical triaxial plane to capture cross-anisotropic strength observed in cubical triaxial tests (after Abelev and Lade 2004).

Once new parameters η_1, m and α were chosen, the new cross-anisotropic failure criterion could be plotted on the octahedral plane. See Figure 2.4.16.

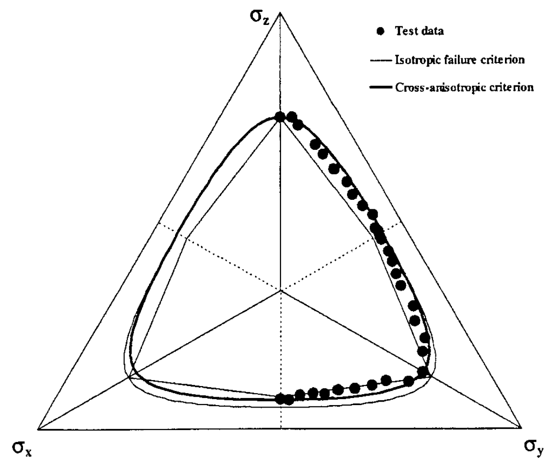

Figure 2.4.16. Octahedral plane with comparison of test data for cross-anisotropic Santa Monica Beach sand and isotropic as well as cross-anisotropic failure criteria (after Abelev and Lade 2004).

As can be seen, the cross-anisotropic failure surface keeps all the properties of the isotropic criterion, except that it has a center axis of α degrees from the hydrostatic axis. Also, where shear banding would occur, failure can occur in the hardening regime. Test data from other tests performed on San Francisco Bay Mud and Toyoura sand were also plotted on the octahedral plane with the cross-anisotropic failure surface. These plots can be seen in Figures 2.4.17a and 2.4.17b.

Further analysis (presented in Lade and Abelev 2004) showed that the variation of maximum dilation illustrated the effects of cross-anisotropy in the specimen due to the initial direction of deposition. They found that the characteristic line of sand in the principal stress space may not be a unique feature in sands with very high degrees of structural cross-anisotropy.

Besides the degree of anisotropy, the location of the characteristic line is dependent on the orientation between the direction of loading and the material symmetry axis.

(a)

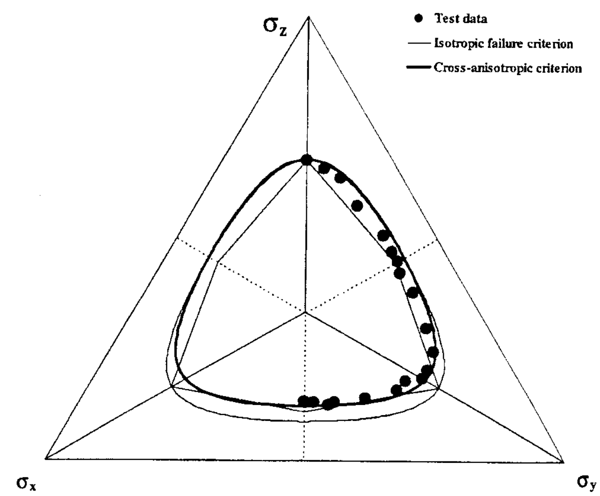

(b)

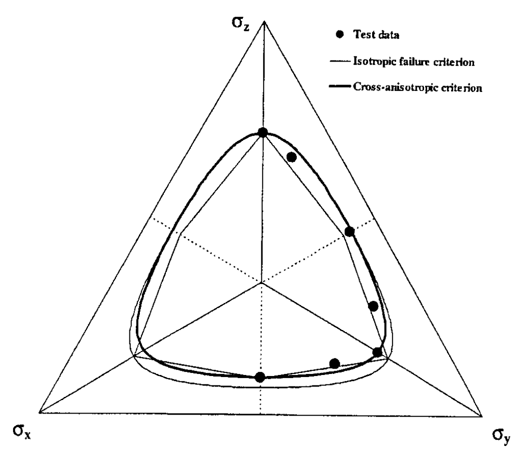

Figure 2.4.17. (a) Octahedral plane with comparison of test data or cross-anisotropic San Francisco Bay Mud and isotropic as well as cross-anisotropic failure criteria; (b) Octahedral plane with comparison of test data for air-pluviated dense Toyoura sand and isotropic as well as cross-anisotropic failure criteria (after Abelev and Lade 2004).

A shortcoming of the previously described failure criterion for cross-anisotropic soils is that it cannot take into account stress rotation. In 2007, Lade modeled the behavior of failure in cross-anisotropic frictional materials, taking into account rotation of the principal stresses. Lade (2007, 2008) developed a newer model that took into account the effects of stress rotation in cross-anisotropic soil, which the previous model by Abelev and Lade (2004) could not account for. This model incorporates the direction of loading relative to the microstructure directions of the material. Lade (2008) combined the isotropic failure criterion (Lade and Duncan, 1975, Lade 1977) with an expression including rotation by Pietruszack and Mroz (2000, 2001) as follows:

$$f = \left(\frac{I_1^3}{I_3} - 27\right)\left(\frac{I_1}{p_a}\right)^m = \eta_0\left[1 + \Omega_1(1 - 3l_2^2)\right] \qquad \text{Eq. 2.4.4}$$

where I_1 and I_3 are the first and third invariants of the stress tensor, p_a is the atmospheric pressure, and m is a constant determined for specific soils. η_0 describes the three dimensional variation of a scalar over a sphere and Ω describes the deviation in three dimensions from the sphere. l_2 is the loading direction which can be defined for cross-anisotropic materials tested in 3D laboratory experiments as:

$$l_2 = \sqrt{\frac{\sigma_y^2 \sin^2\beta + \sigma_z^2 \cos^2\beta}{\sigma_x^2 + \sigma_y^2 + \sigma_z^2}} \qquad \text{Eq. 2.4.5}$$

where σ_1, σ_2, σ_3 are the principal stresses and β is the major principal stress direction with the vertical.

Three material parameters were determined from three conventional triaxial compression tests on vertical specimens and either two triaxial compression tests on horizontal specimens or two conventional triaxial extension tests on vertical specimens. The shear strengths obtained from these experiments in the mid ranges of b-values can represent shear banding and therefore, show a break in the homogeneous deformation of cross-anisotropic soils. Because of this break in the range of middle b-values, the data obtained from the test and used for parameter determination should be gathered at b=0 and/or b=1. The failure criterion established using data from Santa Monica Beach sand can be seen in Figure 2.4.18 and 2.4.19.

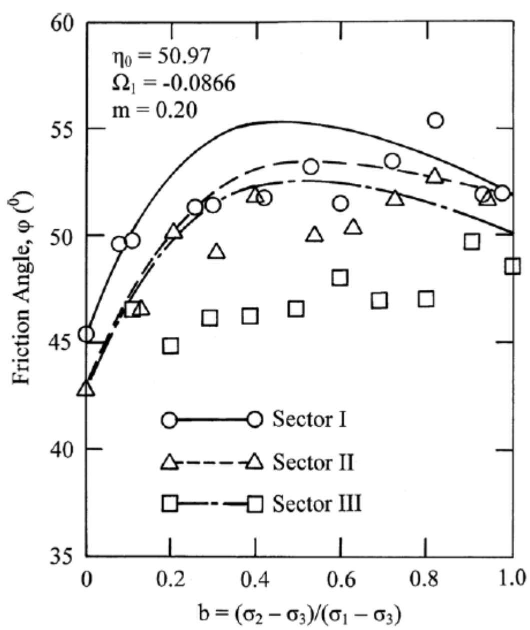

Figure 2.4.18. Comparison of failure criterion with true triaxial test data for cross-anisotropic, dense Santa Monica Beach sand tested in all three sectors of the octahedral plane (after Lade 2007).

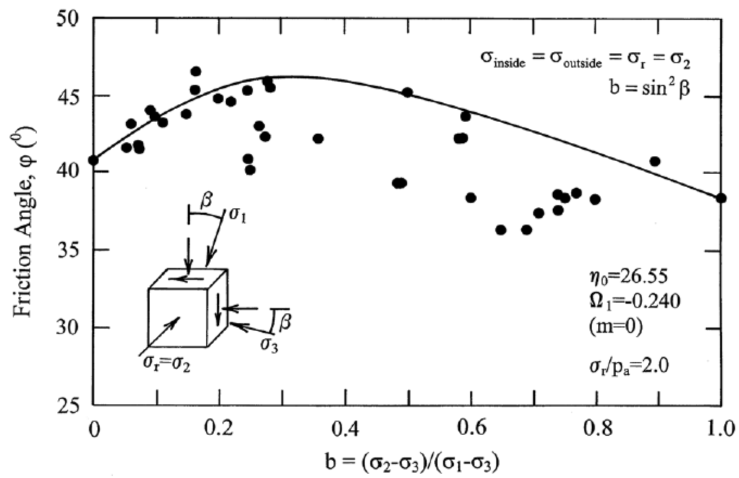

Figure 2.4.19. Comparison of failure criterion with torsion shear test data for medium dense, cross-anisotropic Santa Monica Beach sand. Shear band in the hardening regime reduces friction angles in mid-ranges of b-values (after Lade 2007).

However, not all sets of data can be represented with the proposed failure criterion for cross-anisotropic frictional materials that takes into account stress rotation because special distinctive aspects of the material can control the measured behavior of the material. In particular, sea ice and San Francisco Bay mud could not be modeled using this failure criterion, even though anisotropy was clearly present in their soil fabric. The particular structures of their micro fabrics caused the materials to behave in ways that were not in accordance with the failure criterion and this model could not be applied.

Conclusion

Many experimental tests have been performed to determine and study cross-anisotropy in soils. As previously discussed, anisotropy can be both inherent and induced. In order to study both inherent and induced anisotropy, several experiments including the rotation of principal stresses have been performed. Induced anisotropy can have a great influence on the strain needed to attain a certain stress ratio, and it can affect the secant modulus when reloading after a rotation of the principal stress direction. Several experimental data has been presented in this paper to show how true triaxial shear boxes as well as torsion shear apparatuses have been used to see the effects that anisotropy has on the behavior of soils when reaching failure. A newly developed cross-anisotropic failure criterion for soils has also been discussed to show the difference between isotropic and cross-anisotropic failure surfaces.

2.5. Shear Bands

Introduction to Shear Bands

Localization occurs when the specimen deformation divides from a homogeneous mode to a mode localized where one or more groups of grains form. This coalescence can be referred to as a dominant shear band. Figure 2.5.1 was taken from Saada et al. (1999). Digitized grids at various increments during the test clearly show the formation of shear bands and localization. Shear bands are referred to as “bands” because of the thickness of the zones when they form as well as their change in size with the deformation of the specimen. Localization is said to start at the point where a dominant shear band will grow. If there is no boundary to inhibit it from stopping (as sometimes is the case with certain testing equipment as will be discussed later), the shear band will continue to travel around the specimen. This is usually seen in hollow cylindrical specimens. Complete localization occurs around the peak stress as the critical state is approached. Beyond this point, any further deformation occurring can be referred to as rigid body motion of one part of the specimen compared to the other part of the specimen. Depending on whether sand particles move into or out of the shear band, the band can grow or shrink in thickness. During stress relaxation, the moving blocks of specimen can experience elastic rebound. This can occur while the shear bands are deformed. Due to this motion, the lines that are within shear bands can be considered lines of zero extension. The direction of the shear bands can be identified as directions of propagation of the shear bands.

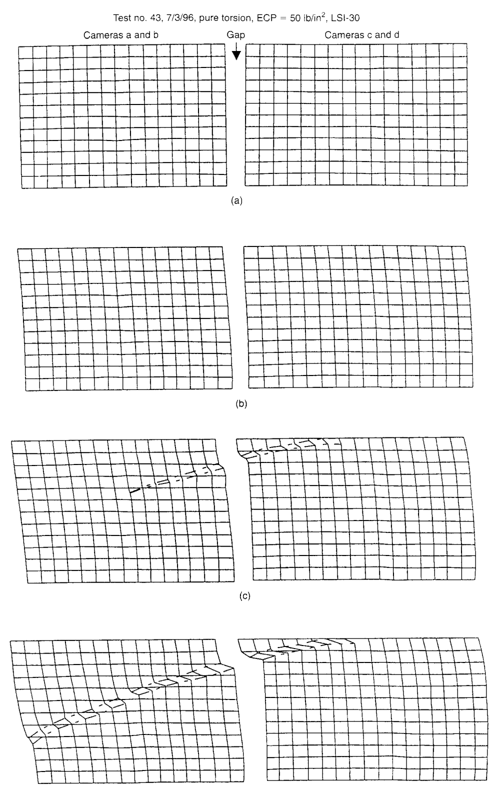

Figure 2.5.1. Digitized grids at various time increments, (a)t=0s, (b)t=1000s, (c)t=2000s, (d)t=3000s (after Saada et al 1999).

Orientation of Shear Bands/Theory of Strain Localization

Strain-localization theory can be used to specify the conditions in which shear bands can emerge within materials that are uniformly stressed and strained. This theory also helps determine the orientation of shear bands when they emerge within a specimen. The theory considers a homogeneously strained material that is able to sustain a uniform Cauchy stress, (σ). The velocity field, (v^0) has a homogeneous spatial gradient, L^0. D^0 is the homogeneous rate of deformation. $\mathbf{W}^0$ denotes the initial spin tensor.

The strain localizes at the point where a velocity field (v) different from (v^0) forms in a planar shear band. The velocity gradient outside the shear band remains equal to L^0. However, the velocity gradient inside becomes $L^0 + \mathbf{gn}$. ($\mathbf{n}$) is the unit vector that is normal to the shear band and ($\mathbf{g}$) is a vector function of the distance across a planar band that vanishes outside the band. The rate of deformation (D) and spin tensor ($\mathbf{W}$) inside the band can be quantified with the following equations:

$$D = D^0 + \tfrac{1}{2}(\mathbf{gn} + \mathbf{ng}) \qquad \text{Eq. 2.5.1}$$

$$\mathbf{W} = \mathbf{W}^0 + \tfrac{1}{2}(\mathbf{gn} - \mathbf{ng}) \qquad \text{Eq. 2.5.2}$$

There are certain major limitations to the strain-localization theory. Although it can predict the emergence of shear bands, it cannot analyze the actual development of the shear bands. It also cannot guarantee that a shear band will form. Because there is no length dimension involved in the theory, it also does not predict the thickness of the shear band.

Besides these shortcomings, the theory of strain localization can be applied to the elastoplastic Mohr-Coulomb model. Doing so, the orientation of shear bands in sands can be predicted. Bardet (1991) showed that the Mohr-Coulomb model overestimates the inclination (θ) of shear bands in granular materials. An extended Mohr-Coulomb model may be used in order to predict more accurate values of (θ). The extended model that was developed uses an additional plastic mechanism to soften the transverse modulus. Because its mathematical structure is simple, an analytical expression can be derived for the plastic modulus and shear-band orientation at the beginning of strain localization.

Different Approaches developed to determine Orientation Angle

Zitouni (1988) stated that the orientation of a dominant shear band can be obtained by using an approach that involves a state of stress (statics) or by using a state of deformation (kinematics). Traditionally, the approach based on statics assumes the Coulomb plasticity criterion. This criterion states that the bands will develop in a direction making an angle (α_C) with the major principal stress where:

$$\alpha_c = 45 + \left(\frac{\phi}{2}\right) \qquad \text{Eq.2.5.3}$$

The value of α is obtained on the basis of conditions for force equilibrium. It is assumed that the intermediate principal stress has no influence on the plastic behavior of the material. Figure 2.5.2 (taken from Saada et al. 1999) depicts Mohr's circle used in this approach. The point on (a) labeled "M" represents the magnitude of the normal and shearing stresses on planes that are found along the shear band. Although the intermediate principal stress (σ_2) is ignored, that does not necessarily mean that plane stress or a plane strain behavior is achieved.

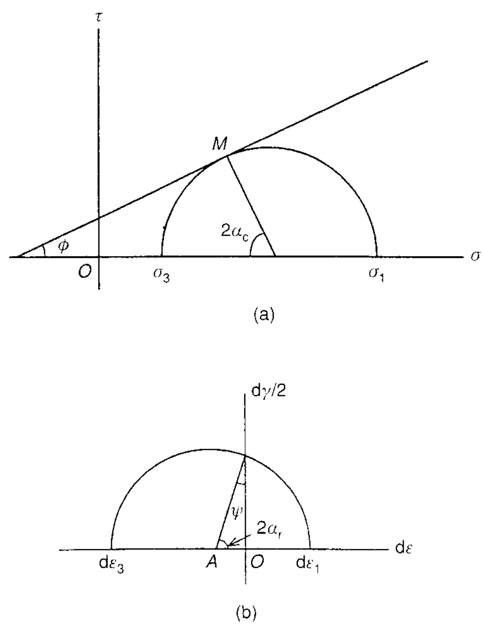

Figure 2.5.2. Mohr circles (a) stress; (b) strain increments (after Saada et. al. 1999).

A second approach based on kinematics was developed by Roscoe in 1970. This approach considers that the shear bands along a principal plane are located along lines where the rate of extension is equal to zero. From Mohr's circle, the direction of zero extension is represented by the angle, α_R. The shear bands develop in a direction making an angle with that of the major principal strain increment by the following equation:

$$\alpha_R = 45 + \frac{\psi}{2} \qquad \text{Eq. 2.5.4}$$

where (Ψ) is referred to as the angle of dilation.

This angle is used to describe the orientation of the shear band in the plane $d\varepsilon_1$, $d\varepsilon_3$. However, this name (angle of dilation), which implies that there is a volume change occurring, can only be justified under plane strain conditions. The value of (Ψ) is acquired when the initiation of the dominant shear band is first seen. (Ψ) is also attained at the peak of the strength curve once the band has completely surrounded the specimen. The peak happens at the point of inflexion of the curve, giving the volume change compared to ε_1.

The angle (Ψ) can be calculated by the method used by Zitouni (1988). This method is based on the formula:

$$\sin\psi = -\frac{1 + (\Delta\varepsilon_3 / \Delta\varepsilon_1)}{1 - (\Delta\varepsilon_3 / \Delta\varepsilon_1)} = -\frac{1 - \tan\theta}{1 + \tan\theta} = \tan\left(\theta - \frac{\pi}{4}\right) \qquad \text{Eq 2.5.5}$$

(θ) is given by the slope of the line AB in a plot of ε_1 versus ε_3. This slope can be seen in the Figure 2.5.3 (taken from Saada et al. 1999). Localization is said to occur where the linear part of the curve stops.

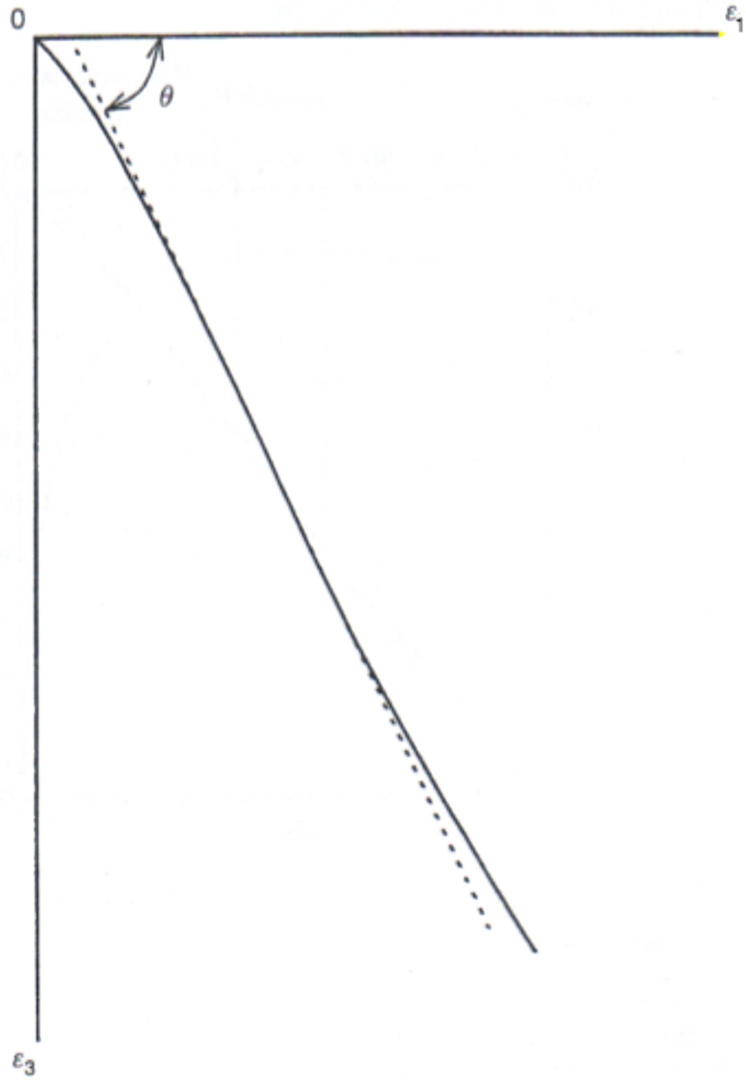

Figure 2.5.3. Zitouni's method for obtaining Ψ (after Saada et al. 1999).

Another method was developed based on direct shear tests by Arthur et al. (1977) and Arthur and Dunstan (1982). They found that the orientation of shear bands was inclined between the Coulomb and the Roscoe directions. They suggested that the average of these two angles should be used to define the direction of shear bands. The equation for the Arthur et al. angle can be seen below and is referred to as "half angle":

$$\alpha_R = 45 - \left(\frac{\phi + \psi}{4}\right) \qquad \text{Eq 2.5.6}$$

Vardoulakis (1980) supported this suggestion through his experimental findings. Later in 1990, Koenders suggested that the inclination of shear bands (α) depended on the average grain size. Figure 2.5.4 shows the relation of Roscoe, Arthur's (half angle) and Coulombs inclination angles versus the average grain size. Further experiments showed that coarse sands created shear bands in the direction of zero extension (as proposed by Roscoe) and fine sands produced shear bands in the direction proposed by Coulomb. Medium sands, with grain sizes in a relatively narrow range produced shear bands that were inclined at Arthur's half angle.

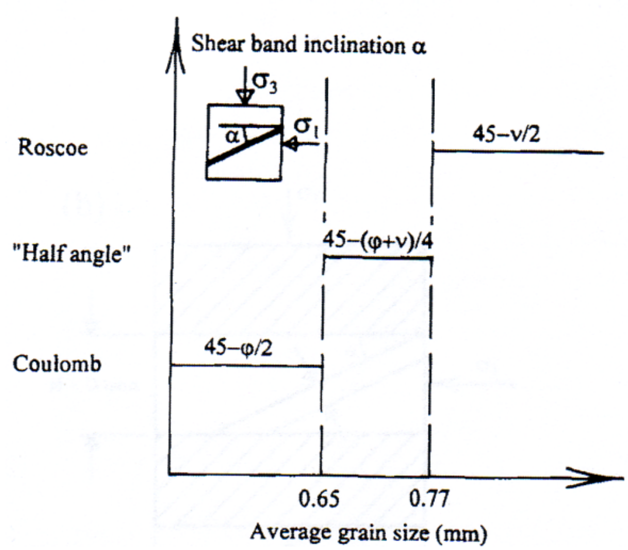

Figure 2.5.4. Proposed Shear band inclination as a function of average grain size (after Lade et al. 1996).

Scarpelli and Wood (1982) conducted simple shear tests on sand, from which they suggested that shear band inclination was affected by the degree on constraint felt by the sand. This was cased by the boundary conditions on the testing apparatus being used.

Vermeer (1990) proposed a theoretical analysis to obtain the shear band inclination. He suggested that in plane-strain tests, the orientation of the shear band would be between Coulomb's and Roscoe's angle. He also said that the boundary conditions (i.e. the membrane which surrounds the sample) could affect the shear band direction. When dealing with fine sands, the membrane plays a minor role. In fine sands, a shear band is usually very thin, about 10-20 times the average grain diameter. In this situation, the Coulomb angle is the most critical inclination for the development of shear bands. However, when dealing with coarse sands, the shear bands emerge thicker. Since they are thicker, they take up a larger proportion of the specimen and in this case, boundary conditions prove to be more important. With shear band development in coarse sands, incorrect stresses at the end of the shear bands can be formed due to the flexible rubber membranes used around specimens. Therefore, the Roscoe angle orientation is obtained in tests with coarse sands. As previously stated, when dealing with medium sands, shear bands develop between these two conditions. Vermeer's conclusions imply that the apparatus used for testing and the boundary conditions set, can influence the results. There exists the possibility that if a specimen is large enough and the boundary conditions do not play an important role, Coulomb's inclination angles can be used.

Figure 2.5.5a shows the development of a shear band in triaxial compression tests with a short specimen (where H=D) and a tall specimen (where H>D). The shear plane transcends a length of D*tan(45 + ϕ/2) for Figure 2.5.5b. The shear band can be seen to fully develop in the taller specimen.

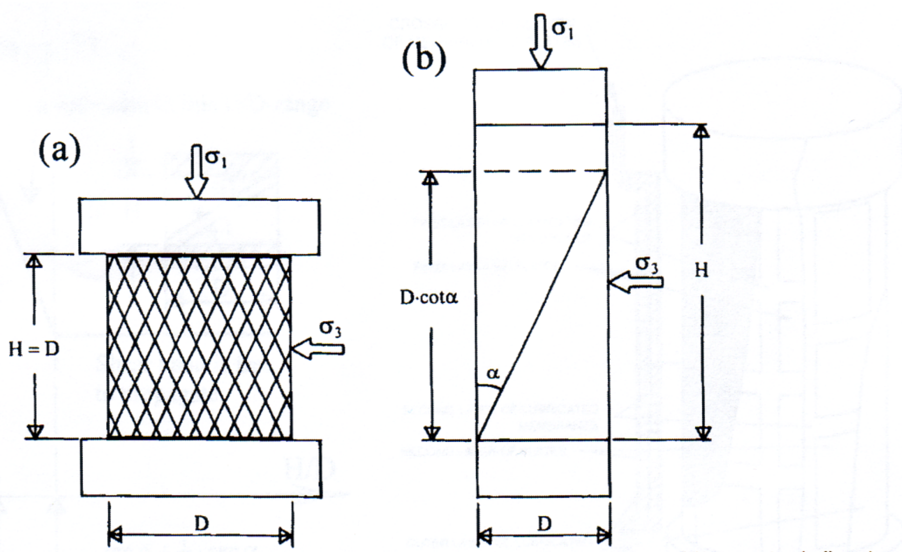

Figure 2.5.5. Testing techniques employed in triaxial compression tests (a) short specimen where H=D with lubricated ends and (b) conventional tall specimen (after Lade et al. 1996).

In Figure 2.5.6, one can see the effect that the specimen boundaries have on the development of shear bands and the inclination angle on different sized specimens. Figure 2.5.7 shows the effect that lubricated ends have on the development of shear bands.

Han and Drescher (1993) conducted plane-strain biaxial compression tests on dry coarse sand at various confining pressures. Figure 2.5.8 shows a schematic of the biaxial

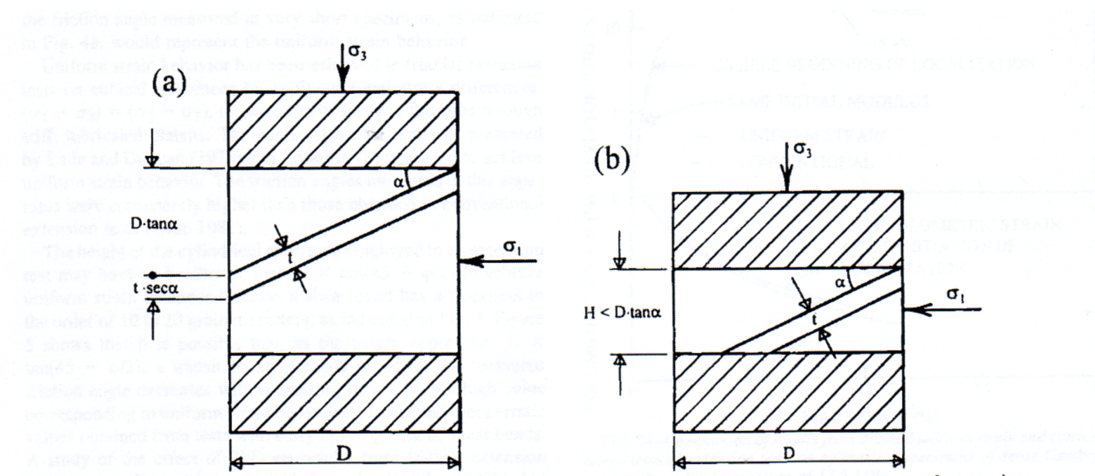

Figure 2.5.6. Shear band inclination and interception in (a) conventional extension tests and (b) extension tests on very short specimens (after Lade et al. 1996).

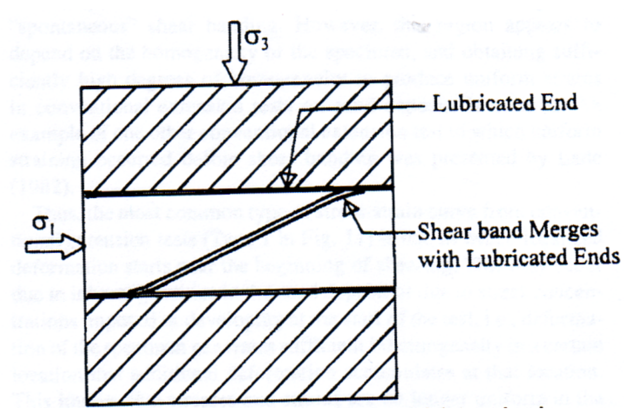

Figure 2.5.7. Merging of shear bands with lubricated ends (after Lade et al. 1996).

apparatus used and the incremental deformation that exists inside a shear band. These tests investigated the state of shear band formation, shear band orientation and shear band growth. Their objective was to research the state of shear band formation in poorly graded course sands. There was also an aim to compare the results from the experiments with predictions provided by the equilibrium bifurcation theory for a number of local incremental constitutive equations. Finally, they wanted to investigate the progressive growth of shear bands.

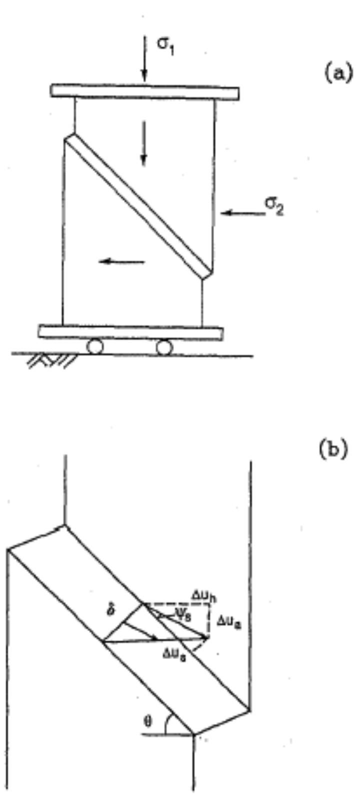

Figure 2.5.8. Biaxial apparatus (a) schematic, (b) incremental deformation in a shear band (after Han and Drescher 1993).

As stated in the previous section, equilibrium bifurcation theory helps explain the formation of shear bands. This theory gives a reason for why shear bands form in tests on specimens despite "ideal" boundary conditions. For a material described by an incremental constitutive equation, the development of shear bands is identified with the presence of a non-uniform deformation field that occurs even under ideal loading conditions. Bifurcation theory gives information on strains at the time of shear banding, shear band orientation and the thickness of shear bands.

In the Han and Drescher study, all of the experimental tests were conducted with displacement controlled axial loading at the displacement rate of 0.2 mm/min. The specimens were subjected to constant confining pressures of 50, 100, 200, or 400 kPa. Constitutive models were set up to make predictions of the experiments. As seen in Figure 2.5.9, the biaxial experiments showed that both the shear strain at shear banding and the shear band orientation in dry, poorly-graded coarse sand are dependent on the magnitude of the confining pressure. When the confining pressure increases, the shear strain increases. The shear band inclination angle measured (with respect to the direction of the major principal stress) decreased as the confining pressure increased.

The shear band orientation was much lower than calculated when using the Coulomb formula (as seen in Figure 2.5.10). When lower confining pressures were applied, the orientation was about 2 degrees higher. At higher confining pressures, the angle was equal to that predicted by the Roscoe formula.

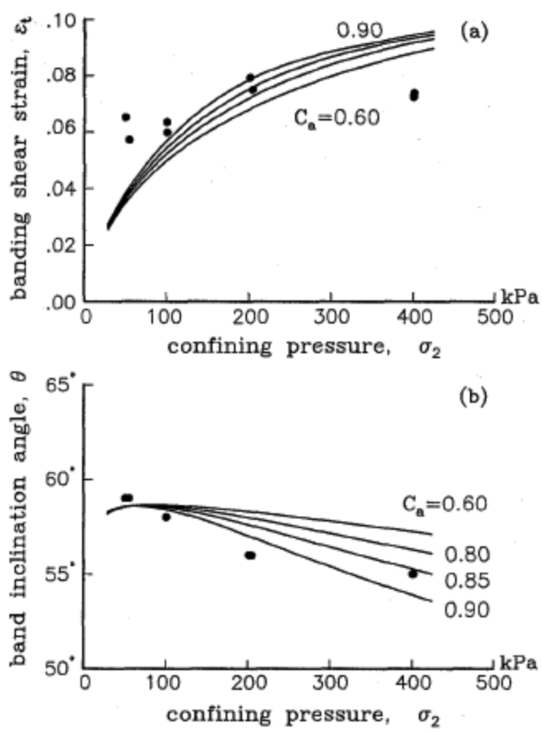

Figure 2.5.9. Test results and predictions; (a) shear strain at shear banding vs. confining pressure; (b) shear band inclination angle vs. confining pressure (after Han and Drescher 1993).

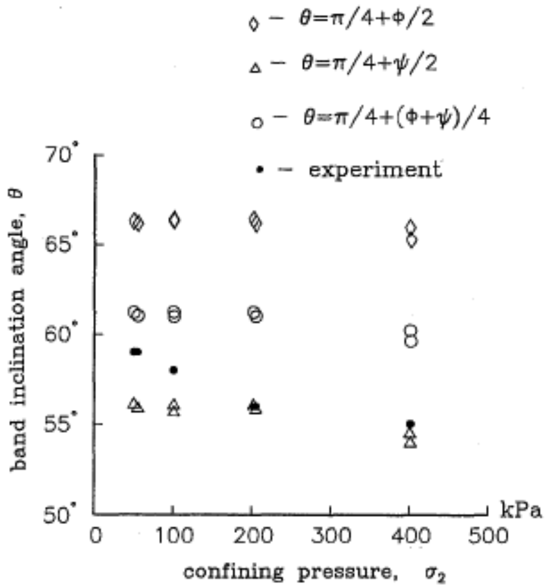

Figure 2.5.10. Test results and classical predictions for the shear band inclination angle (after Han and Drescher 1993).

When comparing the bifurcation analysis for local incremental constitutive equations and Mohr-Coulomb type yield condition to the results, the predictions from these equations gave much smaller shear strains at shear banding than what was shown by the experimental data. The theory does not adequately describe the orientation angle at higher confining pressure or the experimentally observed trend in shear band orientation in relation to the magnitude of confining pressure. It was unknown if using other local constitutive equations and not modifying the yield conditions would get rid of these discrepancies. Shear band growth analysis shows that a non-local constitutive equation and flow theory provide a shear band thickness (seen in Figure 2.5.11) at localization very near what the experimental data showed in the results. The thickness that was seen can be explained by taking into account material dilation and abrasion, which formed parallel shear bands. That implied periodicity is a phenomenon that can be observed in tests on water-saturated sands.

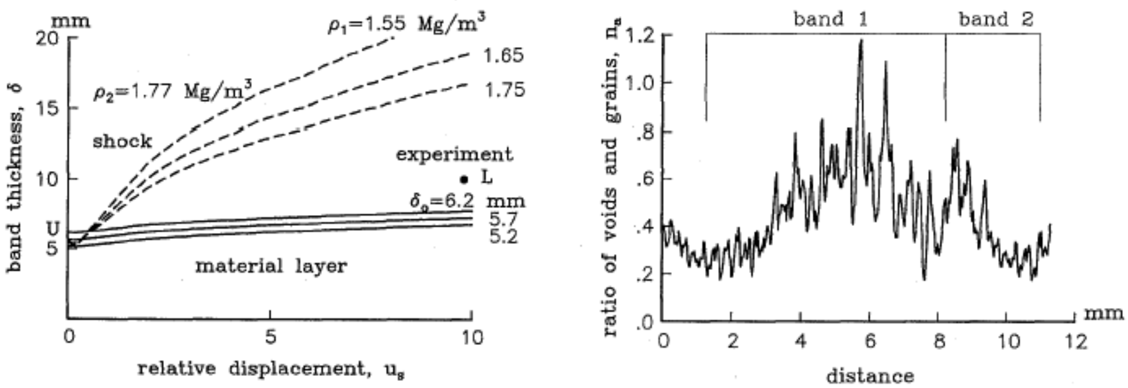

Figure 2.5.11. (a) Shear band thickness vs. shear band relative displacement; (b) Variation of ratio of voids and grains across shear band (after Han and Drescher 1993).

Figure 2.5.12 shows contours and vectors of incremental Digital Image Correlation (DIC) displacements during a biaxial compression test on dense masonry sand performed by Rechenmacher (2005). The image locations are indicated at certain points along the stress-strain curve. Over 10,000 displacement data points across the area being analyzed were produced using DIC analyses for this biaxial test. The images captured over 80% of the specimen height and width. Membrane discoloration and shadowing didn't allow for the entire 100% to be captured. About 3% of the subset displacement vectors are shown for clarity. The scale bar and tick marks on the axes in the figure shown below indicate 20-mm distances horizontally and vertically across the specimen face.

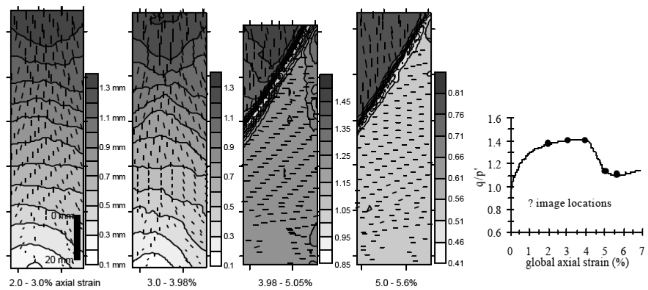

Figure 2.5.12. Local DIC-Derived displacements during biaxial compression test on Mason sand (after Rechenmacher 2005).

From the image taken, shear banding naturally tends to initiate along conjugate planes. When images were compared between biaxial and triaxial tests, the patterns in shear band formation were partly due to the different boundary conditions. When the boundary conditions do not create constraints on the specimen nor do they affect the way that it behaves, as seen in the biaxial apparatus, one dominant, nearly linear shear band is formed. A possible reason for a slower, less abrupt shear band formation in triaxial testing compared to biaxial testing can be explained due to the deformational constraints created from a laterally fixed, non-lubricated top and bottom soil base and cap. The images of the triaxial test that was performed can be seen in Figure 2.5.13.

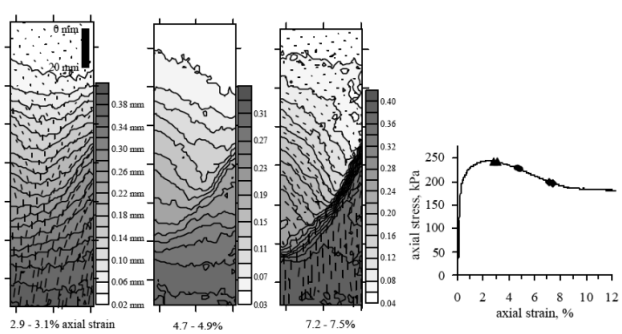

Figure 2.5.13. Local displacements and global behavior during triaxial test on levering sand (after Rechenmacher 2005).

Results from Triaxial Testing Shear Banding and Strain Softening Correlations:

Suzuki and Yamada (2006) conducted a series of experiments in triaxial equipment to study shear behavior of sand from a macromechanical point of view. They also wanted to discuss a possible mechanism of shear behavior. The drained triaxial tests were conducted on Toyoura sand and samples with two distinct void ratios (e = 0.65 and e = 0.80) were prepared. Figure 2.5.14 shows the typical stress-strain curves for two initial void ratios and two types of stress paths. The specimens were all 5 cm in diameter and 10 cm in height. The samples were isotropically consolidated to three values of initial confining stresses.

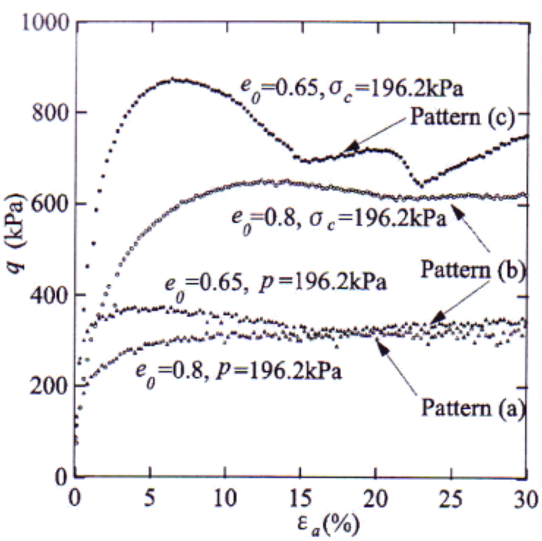

Figure 2.5.14. Typical stress-strain curves for two initial void ratios and two types of stress paths (after Suzuki and Yamada 2006).

In the experiments that were conducted, three typical failure shape patterns were seen for axial strains of up to 30%. These consisted of 1) weakly developed shear bands, 2) fully developed shear bands, and 3) fully developed shear bands that cross diagonally. These are represented in Figure 2.5.15. The results from the stress-strain curves could also be classified into three groups: a) no strain softening, b) strain stiffening after strain softening, and c) two intervals of strain softening (sometimes referred to as double strain softening).

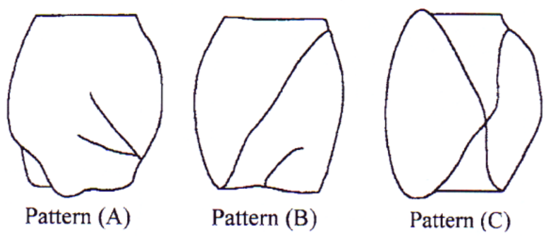

Figure 2.5.15. Failure shape patters: (a) weakly developed shear band, (b) fully developed shear band, (c) diagonally crossing shear bands (after Suzuki and Yamada 2006).

Comparing the data showed that when strain localization was relatively faint, (occurring in weakly developed shear bands), the stress-strain curve exhibits no strain softening. However, when strain localization is strong (occurring in a fully developed shear band), the stress-strain curve exhibits strain softening and subsequent stiffening. It can be stated that the failure shape pattern can be an indicator of the ultimate condition of strain localization. The pattern of the stress-strain curve is strongly related to the failure shape pattern.

This set of data also showed that the stress-strain curve exhibits strain softening when the extent of strain localization is relatively large. Also, strain softening becomes greater as the maximum dilatancy index defines the extent of strain localization. The dilatancy index determines not only the ratio of the volumetric strain increment to the axial strain increment, but also the condition of the strain localization.

Once the peak strength is reached, the dilatancy index gradually decreases. This causes the dilative volumetric strain increment rate to begin to decrease, while the volumetric strain increment is still dilative. An important qualitative change occurs around the peak strength. Due to this behavior, it can be seen that strain softening is strongly correlated to the appearance of a shear band. One possibility is that the peak strength occurs when a shear band begins to form. Two different regimes for the dilatancy index exist, before and after the peak strength is reached. Before the peak strength is reached, the dilatancy index can be produced without dominant strain localization. Beyond the peak strength, the dilatancy index is influenced by the extent of sliding within the shear band. Figure 2.5.16 shows the typical progressive failure of sands in drained triaxial tests. At different points along the curve, the development of shear bands can be seen.

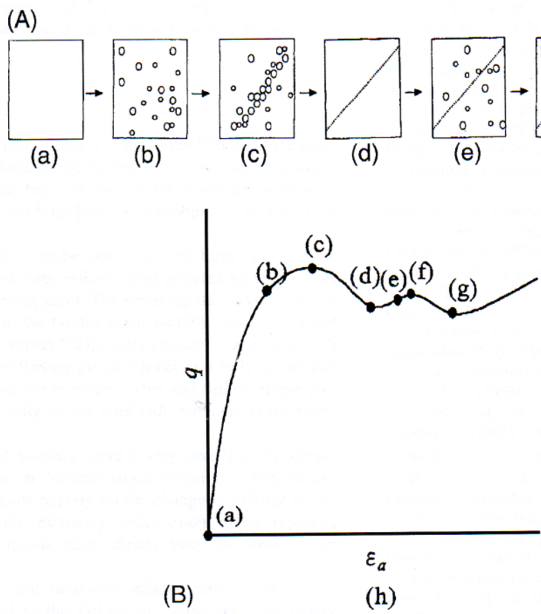

Figure 2.5.16. Illustration of progressive failure of sands in drained triaxial tests (a) initial condition, (b) occurrence of dilative strain areas, (c) continuous linking of dilative strain areas, (d) fully developed shear band, (e) further occurrence of dilative strain areas, (f) continuous link of dilative strain areas, (g) "diagonally crossing shear bands, (h) q vs ea (after Suzuki and Yamada 2006).

The failure process can be summarized by following the points on the curve. At point (a), the initial condition of stress and strain is assumed to be the same throughout the entire specimen. Then at point (b), small compressive and dilative strain areas occur at various locations throughout the soil sample. The dilative strain begins to link continuously at point (c), and the development of a shear band starts to occur. The beginning of the shear band formation coincides with the peak strength. At this point, part of the specimen starts to slide along the developing shear band. When the shear band slides, most of the deformation is absorbed and the dilative strain increment areas of the sample decrease as the shear band develops further. The dilatancy becomes smaller. At point (d), the volumetric strain increment becomes zero, even at points within the shear band. At this point, the dilatancy becomes zero as well and a new equilibrium is reached. At point (e), a new shear band can occur and dilative strain areas develop in the soil sample once again, but only a small stress ratio increment is now needed. Point (f) shows the dilative strain area beginning to link continuously to create a shear band that is more developed. Diagonally crossing shear bands can sometimes develop at this point. Point (g) shows the point where the dilatancy index becomes zero once again, and equilibrium is reached once again.

Results from Triaxial Extension Tests

For materials that dilate under conditions of triaxial compression, plastic strain localization in granular materials leads to the development of shear bands in the post peak softening regime. For materials that do not dilate, meaning that they compress under triaxial compression, the development of shear bands has not been observed. For plane strain conditions in materials that dilate, shear bands develop very close to the point of peak failure. In this situation, the developing shear band negligibly affects the peak friction angle.

When performing triaxial extension tests with uniform stress conditions, the orientation of the shear band occurs at an angle of $45 - \phi/2$ to the planes of the cap and base. If the soil specimen is taller than $D*\tan(45 + \phi/2)$, then shear bands can occur in extension. If $H < D*\tan(45 + \phi/2)$, then it is possible to stop the development of shear bands in a normal triaxial extension test. The friction angle that is measured for short specimens would represent uniform strain behavior. If the specimen is taller, it is possible for shear bands to occur in extension tests. To achieve uniform stress behavior when performing triaxial extension tests on cubical specimens, one must apply equal stress differences. Therefore, (σ_1-σ_3) must equal (σ_2-σ_3). Since the height of the cylindrical specimen is important, it may have to be shorter than D*tan(45 + ϕ/2) to achieve uniform strain behavior. This is because shear bands usually have a thickness of about 10 to 20 grain size diameters.

Figure 2.5.17 shows that a transition zone exists in which the friction angle decreases as the height approaches D*tan(45 + ϕ/2). There is a drop in value as the sample goes from uniform strain behavior to lower, more erratic values that were seen during early development of shear bands.

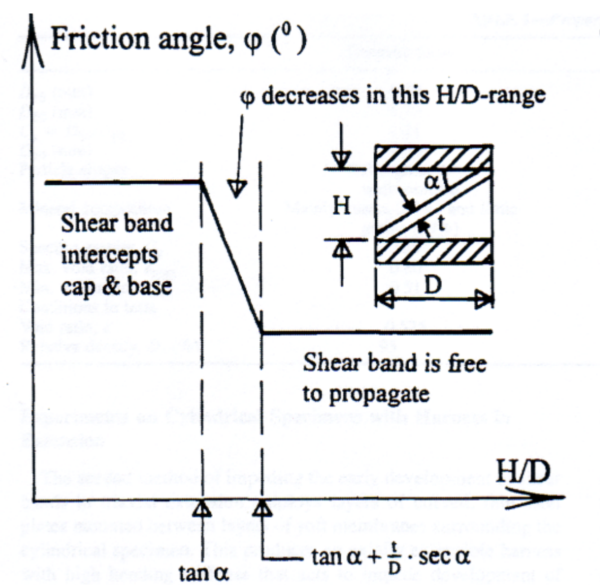

Figure 2.5.17. Expected variation of friction angle with H/D ratio in extension tests (after Lade et al. 1996).

The stress-strain and volume change for two cylindrical specimens under triaxial extension are shown in Figure 2.5.18. Both specimens, one under uniform strain, the other under conventional strain, show volumetric compression. Because necking occurred in one specimen, this caused a lower strength compared to the second specimen. The second specimen had membranes that were reinforced with small curved plates to slow down the development of necking. Since necking was prevented in this test, the strength was higher. In triaxial extension tests, if necking and/or shear bands that occur after necking but form before peak failure are present, then premature peak failure can be seen.

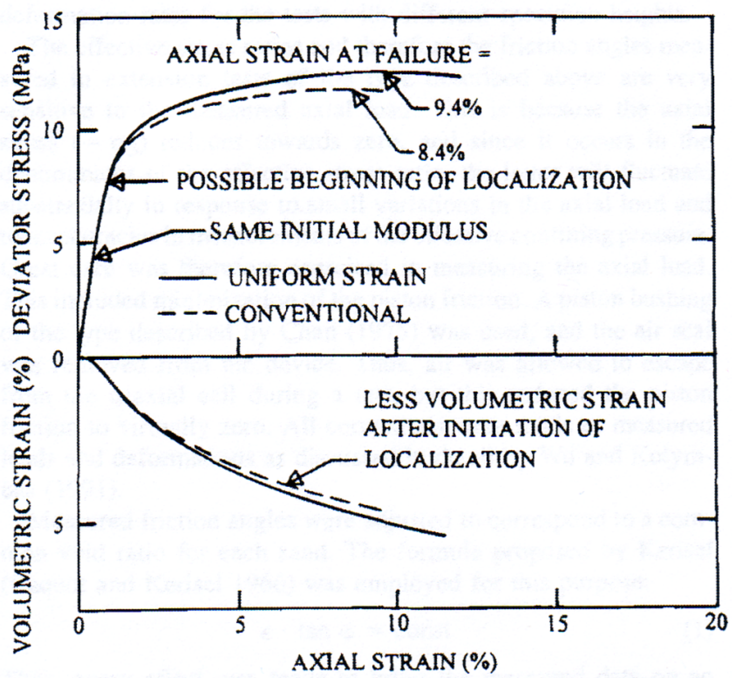

Figure 2.5.18. Comparison of results from drain uniform strain and conventional triaxial extension tests on cylindrical specimens of dense Cambria sand with confining pressure of 17.5MPa (after Lade et al. 1996).

Tests on Cambria sand, medium silica sand and fine silica sand were presented by Lade et al. (1996). The Figures 2.5.19(a)-(c) show the relation of shear band inclination (in degrees) with the height/diameter ratio of the specimens tested in extension tests. All three cases are closer to the Coulomb orientation angle. A possible explanation for the deviation from previous speculation, which states that coarse sand should be closer to Roscoe's number and the medium silica sand to the half angle value could be explained by the anisotropy of the soil. When specimens are formed using the dry pluviation technique, cross-anisotropic samples are formed. The way that the grain axes line up (forming horizontal directions while the grain contact points are vertical), tend to form shear bands that appear more horizontal under triaxial extension loading.

Results of Shear Banding in True Triaxial Tests

When conducting true triaxial tests, the stress-strain relationship obtained from experimental results often show a continuously decreasing strain to failure with increasing b-value. There is a more rapid strength reduction and a pointed peak for b-values ($b=(\sigma_2-\sigma_3)/(\sigma_1-\sigma_3)$) near and larger than the value at plane strain. Due to this, shear bands that form before failure are prevalent over a range of b-values. When stresses are in this range, failure may result due to the shear band that has formed under these stress conditions. Thus, the peak strength may be dependent on the critical condition at which shear banding forms. With true triaxial equipment one can produce uniform stresses and strains over the full range of the intermediate principal stress. Therefore, one can study the influence that the formations of shear bands have on the stress-strain behavior of granular materials.

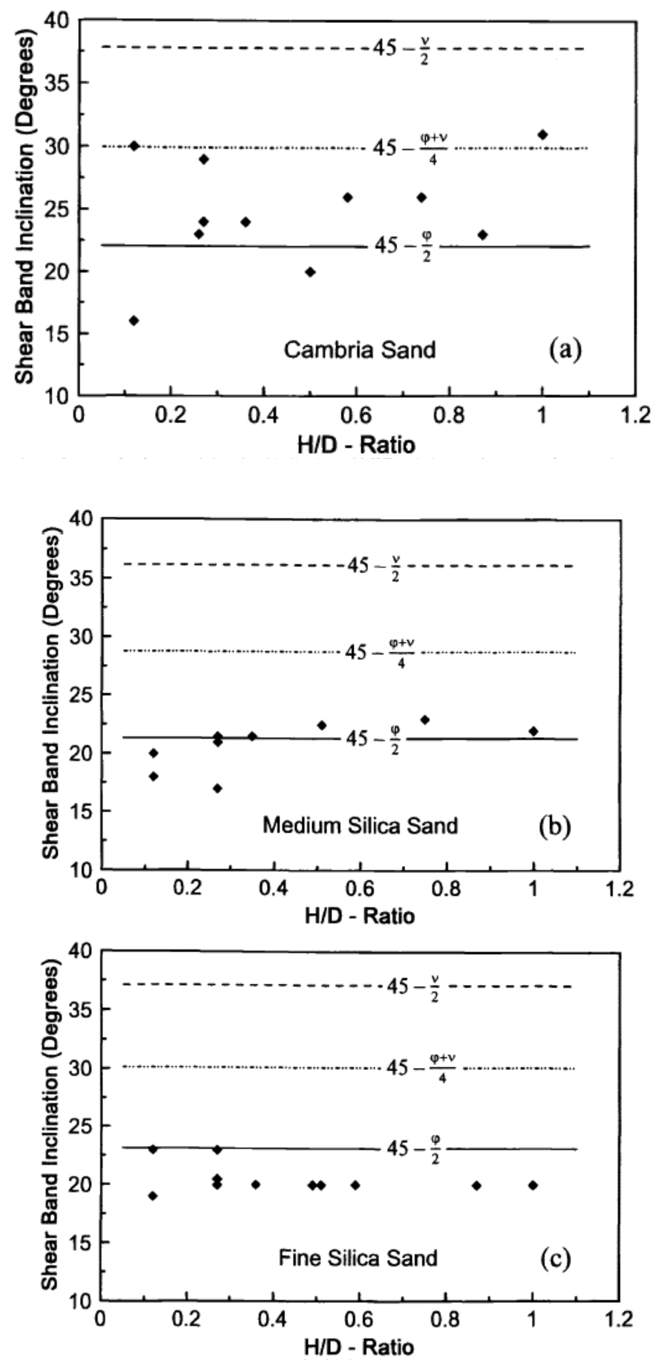

FIG. 13—*Continued*

Figure 2.5.19. Figure 2.5.19. (a) Comparison of measured and proposed shear band inclinations with H/D ratio in extension test on dense specimens of (a)Cambria sand of (b) medium silica sand and (c) fine silica sand (after Lade et al. 1996).

Bifurcation marks the initiation of the formation of a shear band in a sand that dilates. This is a result of continued shearing under uniform stress and strain. At a certain point in this process of continued stress and strain being imposed on to the soil specimen, the stress and strain states allow a localized displacement in order to satisfy equilibrium, compatibility, boundary conditions and constitutive relations. In order to investigate shear banding under 3D conditions, this occurrence has been applied to study existing constitutive models that predict the formation of shear bands, as well as to study the conditions that are present in shear band formation.

When performing bifurcation analysis for 3D stress and strain states, a set of critical hardening moduli, H_c, is normalized with Young's modulus of elasticity, E, as seen in Figure 2.5.20. The values vary with changing values of b.

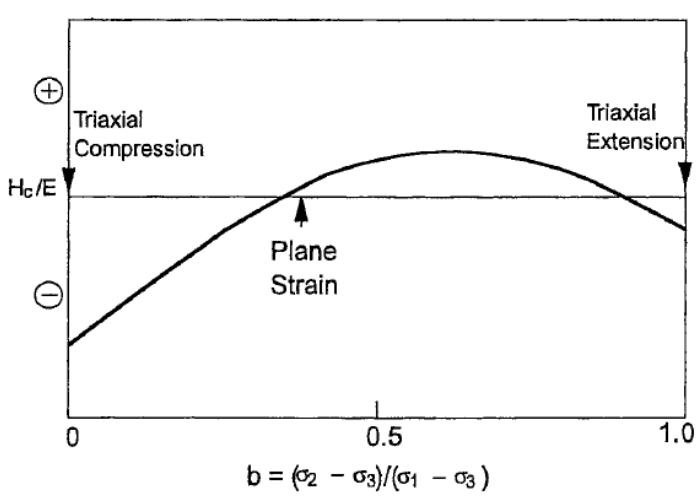

Figure 2.5.20. Schematic diagram of variation of normalized, critical hardening modulus with b according to Rudnicki and Rice (1975) and Rice (1976) (after Lade and Wang 2001).

In 1975, Rudnicki and Rice proposed that shear banding could occur over a range of stress states where the hardening modulus is positive. The means that shear banding can occur during increasing loading before smooth peak failure. The normalized critical hardening modulus can be calculated for true triaxial tests at the point where shear banding starts. In Figure 2.5.21, one can see the variation of the normalized critical hardening moduli for true triaxial tests on dense, medium dense and loose Santa Monica beach sand.

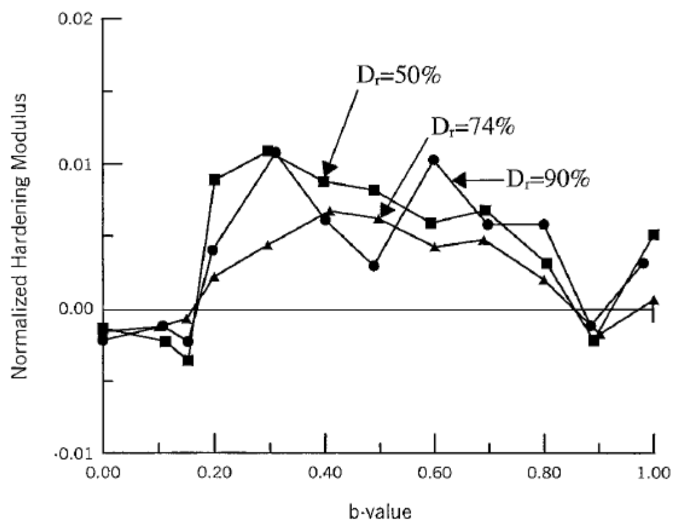

Figure 2.5.21. Variation of Normalized, Critical Hardening Modulus, Hc/E, with b for True Triaxial Tests on Prismatic specimens of Dense, Medium Dense and Loose Santa Monica Beach Sand with σ'_3=49 kPa (after Lade and Wang 2001).

For tests conducted on tall rectangular prismatic specimens with a height to diameter ratio H/D = 2.47, shear bands developed without interference with the lubricated cap and base. For tests with b=1, failure occurred in the horizontal direction due to cross-anisotropy of the specimen and the corresponding pattern can be seen in Figure 2.5.22. The angles of shear band inclination with respect to the direction of the minor principal stress were determined. In most cases, the inclinations angles were between 60˚ and 70˚. They were not necessarily affected by b-values but did increase a little with increasing density.

After analyzing the experimental results, the stress-strain curves and failure surfaces showed shear banding in the hardening regime on the peak strength of the material in the midrange of b-values. Shear banding was seen to start in the hardening regime when b-values reached a range of 0.18 to 0.85. In this region, failure does not occur due to peak failure, but does however occur due to the formation of shear bands.

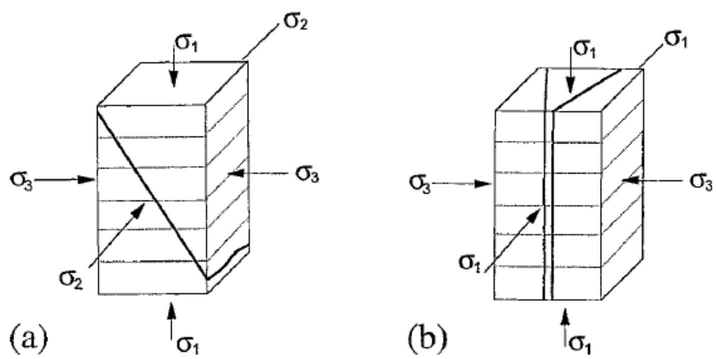

Figure 2.5.22. Modes of Shear banding observed in prismatic specimens of Santa Monica beach sand (a) failure in vertical direction for tests with 0≤b≤1; (b) failure in horizontal direction for tests with b=1 (after Lade and Wang 2001).

In order to make sure that this was the reason, the shear band formation analysis proposed by Rudnicki and Rice in 1975 was used for each test. The hardening modulus prior to the formation of shear banding was calculated. For b-values in the ranges from 0-0.18, and also from 0.85-1, negative hardening moduli were found. This meant that conditions for shear banding were fulfilled in the softening regime. Failure in these regions occurs due to smooth peak failure. In the range of b-values from 0.18 to 0.85, positive values of the hardening modulus were obtained. This occurred immediately before shear bands formed. This indicated that the condition for shear banding is fulfilled on the hardening portion of the stress-strain curve. Peak failure, in this middle range of b-values, is caused by shear banding. Because this occurs, a smooth, continuous 3D failure surface is therefore generally not achieved for soils. Figure 2.5.23 shows the Mohr-Coulomb failure surface as well as the Lade failure surface. The results have higher friction angles than predicted by Mohr-Coulomb. However, Lade's failure surface is quite accurate until the middle range of b-values is reached. In this middle b-value range, shear banding occurs in the hardening regime. Figure 2.5.24 shows the same tests but on the octahedral plane.

Experimental shear band orientations are compared in Figure 2.5.25 with the three theoretical values explained previously. The measured shear band inclinations are between the Coulomb and the Arthur inclinations. With denser sand, the shear bands fit better with the Coulomb inclination. For dense Santa Monica Beach sand, the inclinations are almost equal to the Coulomb inclination angle. In loose sand, there is considerable scatter. This scatter can be explained by the boundary conditions that have an effect on the shear band directions.

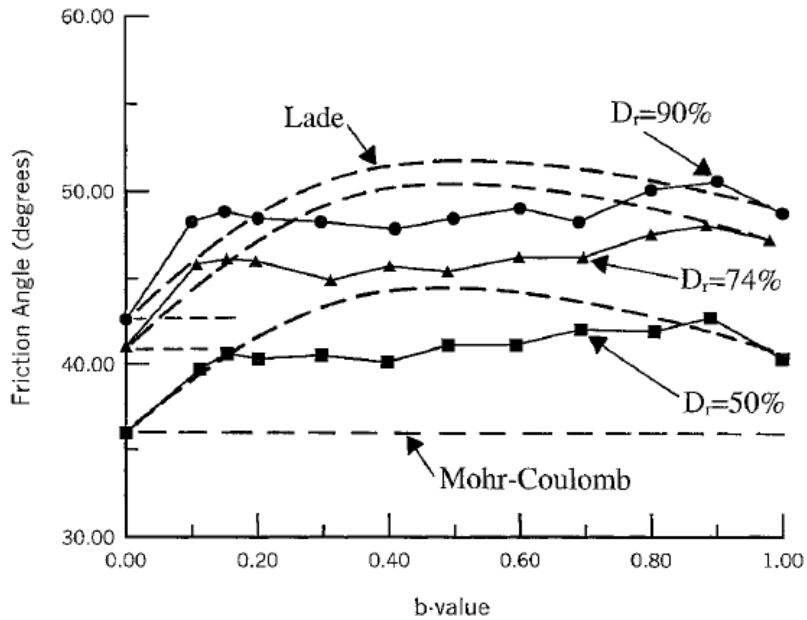

Figure 2.5.23. Comparison of Mohr-Coulomb failure surface and Lade's failure surface with measured friction angles for true triaxial tests on prismatic specimens of dense, medium dense and loose santa monica beach sand with σ'$_3$=49 kPa (effect of shear banding indicated in mid-ranges of b-values) (after Lade and Wang 2001).

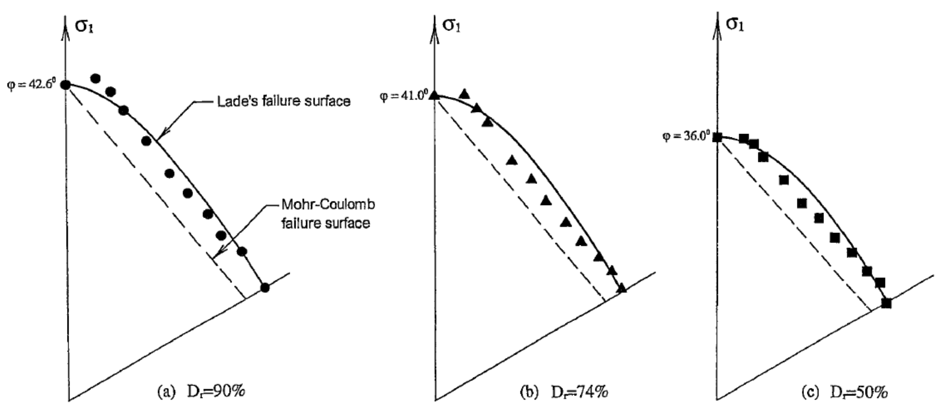

Figure 2.5.24. Experimental failure surfaces for true triaxial tests with σ'$_3$=49 kPa compared with Mohr-Coulomb failure surface and Lade's failure surface in octahedral plane on prismatic specimens of Santa Monica Beach Sand (a) dense, (b)medium dense, (c) loose (after Lade and Wang 2001).

Results from Torsion Shear Testing

Lade et al. (2008) conducted 34 drained torsion shear tests with rotation of principal stress directions in order to study shear banding in Santa Monica beach sand. All the tests were conducted with the same constant internal and external confining pressures. Therefore, the b-value and the inclination angle of the major principal stress were connected. Shear bands were able to develop freely without noticeable restraint from the rubber membranes. Strain localization and shear banding was noticed in the hollow cylindrical specimens.

In the torsion shear tests conducted, the stress-strain curves did not show an abrupt drop off in load carrying capacity at the formation of shear bands, as was observed in the corresponding three triaxial tests. Most stress-strain curves continued with small changes in strength. There was also very little change in the stress-strain curve and the volume change patterns once the shear band was observed to develop. After studying the specimens more closely, it was noticed that some stress-strain curves had a slight upwards rise following the shear band formation. The sliding of one part of the soil specimen on top of the other part ended in one of the parts being restrained at the end rings. Due to this, the specimen picked up some more load. This created a slight increase in stresses. As this occurred after the shear banding, it is not part of the uniform deformation pattern.

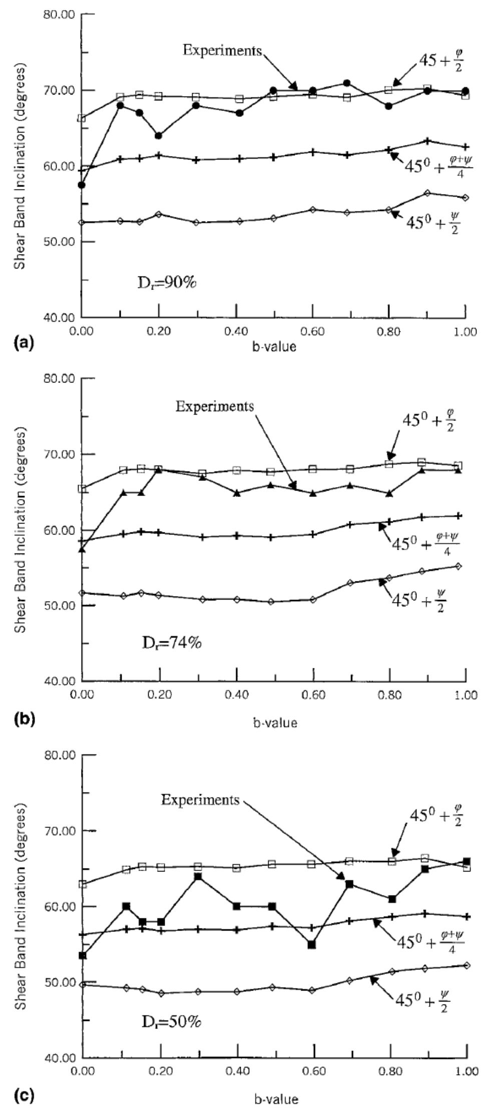

Figure 2.5.25. Experimental shear band directions compared with three theoretical values for Santa Monica Beach Sand (a)dense, (b) medium, (c) loose (after Lade and Wang 2001).

Shear bands that developed in torsion shear testing can be seen in Figures 2.5.26a and 2.5.26b. The shear band lines were drawn on the rubber membrane where kinks were formed. The shear band inclination angle was measured directly on the specimen and then recorded with photographic evidence.

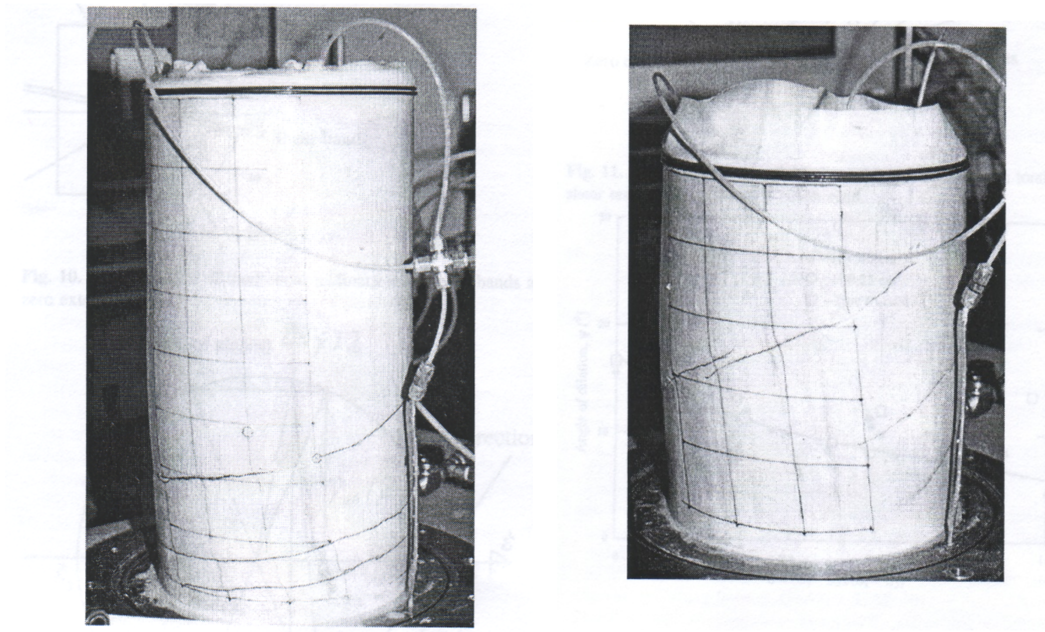

Figure 2.5.26. (a) Picture of 40cm tall torsion shear specimen after failure, (b) picture of 25cm tall torsion shear specimen after failure (after Lade et al. 2008).

After the shear band inclination angle relative to the σ_1- plane was measured on the specimen, this angle, (ω) is added to the angle (β) of σ_1 that is obtained from the equation, $b=\sin^2\beta$. Therefore, as seen in Figure 2.5.27, the angle of the shear band with relation to the σ_1 plane is $\beta+\omega$.

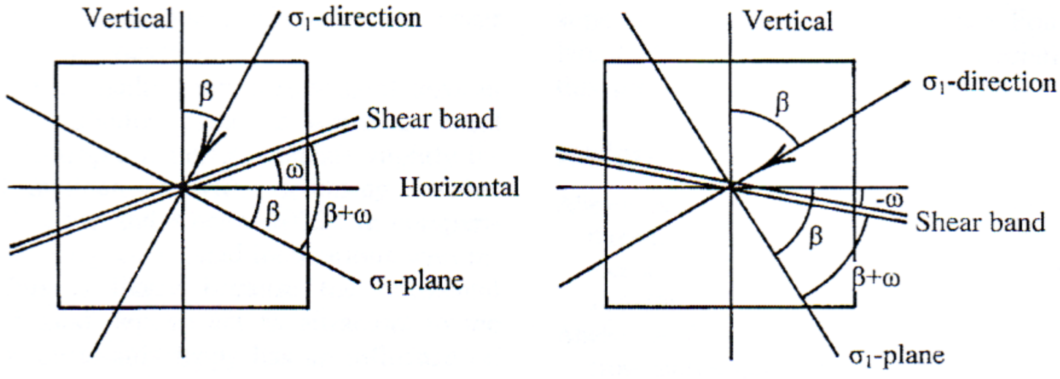

Figure 2.5.27. Inclination of shear bands relative to plane of major principal stress in torsion shear tests (after Lade et al. 2008).

The shear band inclination angles that were measured were compared to the inclination angles of Coulomb, Roscoe and Arthur's orientations. These results can be seen in Figure 2.5.28. This figure shows decreasing shear band inclinations with increasing b-values. This is probably due to the horizontal bedding planes that influence the shear bands. As previously discussed, the anisotropy of the specimen influences the direction of shear bands in torsion shear tests as well as in triaxial tests.

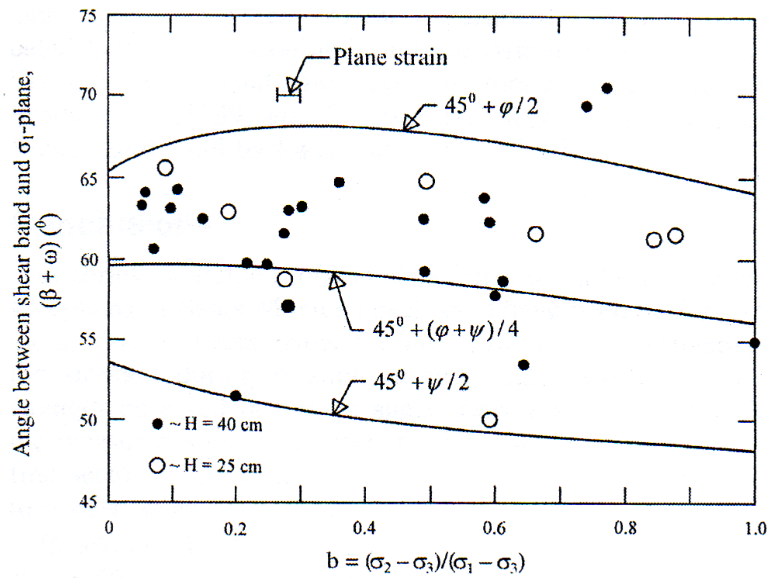

Figure 2.5.28. Comparison of experimental shear band inclinations with theoretical values (after Lade et al. 2008).

2.6. Yield and Failure Surfaces

Introduction:

Yield surfaces of sands can be established from stress-strain data. It is also possible to determine the effects of certain factors such as density, consolidation stresses, anisotropy, material fabric, etc. on yielding behavior. To do so is not an easy task. In order to construct yield surfaces, tests that produce data under complex and unconventional stress paths are performed on the soil. Sometimes, these yield points have to be approximated. Oftentimes, loading the soil causes changes in properties making it difficult to get different yield points along the same yield locus. For materials such as clays, ellipses have often been used to draw the shapes of the yield surfaces. For sands, a wide range of shapes have been used, as it is often more difficult to characterize the yield shapes due to the difficulties just stated. This section will explain the basis and history in the development of yield surfaces and their determination, as well as report experimental research that has been presented in the literature that has helped expand the current knowledge on yield surfaces for sands and clays.

Yielding of Soils

Hvorslev in 1937 showed that the peak shear stress at failure, τ_f of remolded saturated cohesive soils is a "function of the effective normal stress, σ'_f, *on* and of the voids ratio, e_f *in, the plane of failure at the moment of failure*". This function is independent of the sample's stress history. Using Hvorslev's approach, it was only possible to predict the strength at failure when knowing the values of the normal stress and the void ratio at failure. In 1953, Roscoe designed an apparatus for the purpose of imposing uniform shear strains on soil samples. When uniform strains were applied to the samples using this apparatus, it was possible to find out the void ratios at all times during the test by measuring the average void ratio of the entire sample. This strain-controlled apparatus allowed for the measurement of strains beyond failure. They used this simple shear apparatus to study the yielding of cohesionless media and the critical void ratios of those media. Yielding in this case meant what is now referred to as failure.

Hvorslev's failure surface was based upon results of fully drained tests on saturated clays in shear boxes. Refinements to this criterion were introduced by Roscoe et al. (1958) after they performed different tests. The shear tests that were performed by Hvorslev were stress controlled. Therefore, any further study of the conditions of the sample after the peak shear stress could not be studied. Figure 2.6.1 shows Hvorslev's surface.

Critical Voids Ratio and the Ultimate State Surface

Continuous yielding of a specimen can happen when a loading path gets to the yield (failure) surface and then remains on the failure surface. Therefore, it may be difficult to find out if that loading path ends at a specific point. Once the loading path reaches this specific point, it can be said to be at the critical voids ratio state.

The term "critical voids ratio" is usually applied to a particular state of sand. Roscoe et al. (1958) gave two definitions for two states where this term can be applied. The first definition deals with changes of volume in drained tests (per Casagrande 1938). The second deals with changes in effective stress and strength in undrained tests (per Taylor 1948). The critical voids ratio concept is also valid for clays.

In the case of a drained test, the critical voids ratio state is defined by Roscoe as "the ultimate state of a sample at which any arbitrary further increment of shear distortion will not result in any change of the voids ratio". For any series of drained tests that are performed, the critical void ratio points are expected to lie in or near a line of the drained yield surface (failure surface).

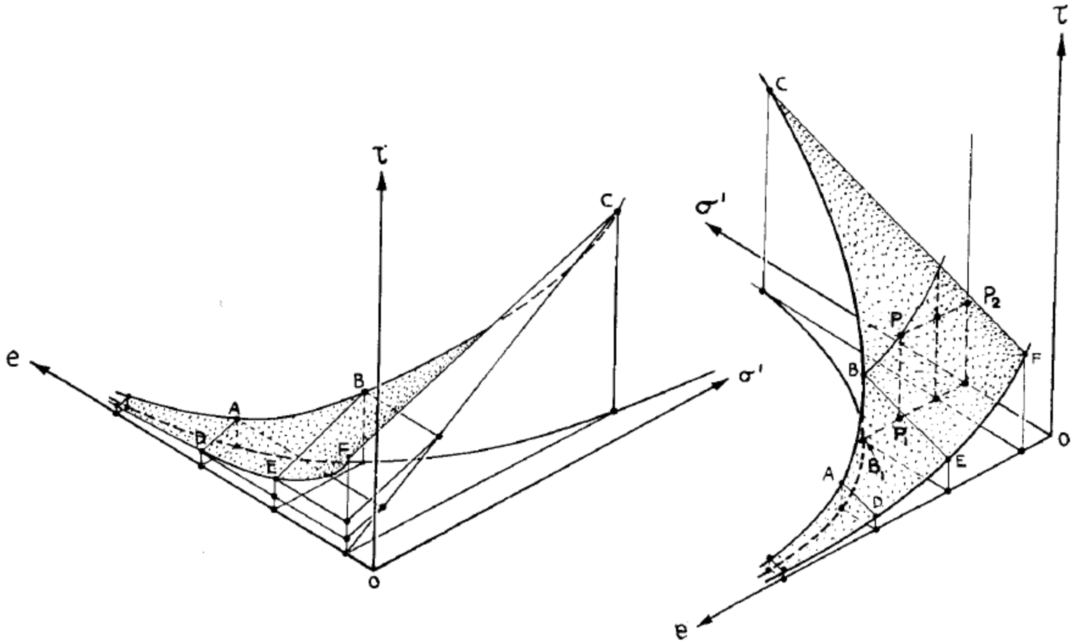

Fig. 1. Two isometric views of the Hvorslev surface for Kleinbelt Ton

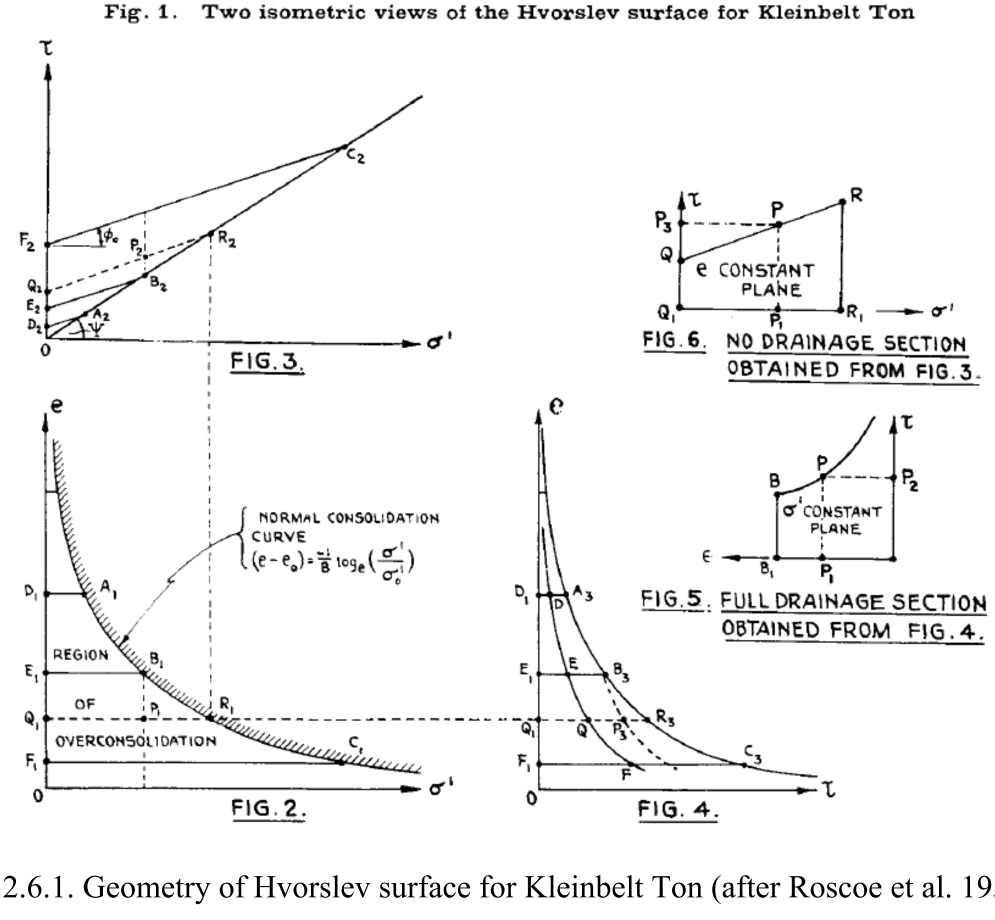

Figure 2.6.1. Geometry of Hvorslev surface for Kleinbelt Ton (after Roscoe et al. 1958).

When dealing with undrained tests, the sample stays at a constant voids ratio. However, the effective stress, p', will change to bring the sample into an ultimate state. This state will be such that the voids ratio remaining during shear becomes the critical voids ratio. For any series of undrained tests, the critical void ratio points are expected to lie in or near the undrained yield surface (failure surface).

When comparing results from drained and undrained tests, if there is a unique line where all of the loading paths converge then that line is called the critical voids ratio line (C.V.R.). The drained and undrained yield (failure) surfaces occur on the same C.V.R. line and may be identical, forming a common yield (failure) surface.

As shown in the previous section, in the beginning stages of discussion of yield/failure surface parameters, the quantities used to represent certain surfaces (like Hvorslev's Surface) were p', q and e. Roscoe et al. (1958) labeled the C.V.R. line discussed in the paragraph above. Later, it was pointed out that the frame of reference that Roscoe used was a state space and the C.V.R. should be called a Critical State Line. When this line is transformed to a three dimensional space, it becomes a surface. This surface is referred to by Poorooshasb (1989) as the "Ultimate State Surface."

The ultimate state surface can be defined as a surface in the state space for which the relation:

$$\frac{\mathrm{dp}}{\mathrm{d}\varepsilon}=\frac{\mathrm{dq}}{\mathrm{d}\varepsilon}=\frac{\mathrm{d}\theta}{\mathrm{d}\varepsilon}=\frac{\mathrm{de}}{\mathrm{d}\varepsilon}=0 \qquad \text{Eq. 2.6.1}$$

The above relation should hold true at every point on this surface in the state space. ε is a shear strain derived from the second invariant of the strain deviator tensor and is a measure of sample distortion.

According to Poorooshasb (1989), once the ultimate state is reached, if a unique relation can be attained between two of the state parameters, a three dimensional space may be used to represent the Ultimate State Surface. For example, if a simple relation exists between the void ratio and the mean normal stress, p', then a space made up of (q,θ,e) could be used. This relationship would be governed by the Casagrande's equation:

$$\mathrm{e_c}=\mathrm{e_0}\lambda\ln\left(\frac{p}{p_0}\right) \qquad \text{Eq. 2.6.2}$$

State Boundary Surface

The state boundary surface was defined by Poorooshasb (1989) as "the surface in the state space enveloping all the possible states a sample of a granular medium may assume." Not all state points enclosed by the state boundary surface can be reached. However, those that are not enclosed are not accessible. Figure 2.6.2 shows the Ultimate State Surface of Sacramento River Sand.

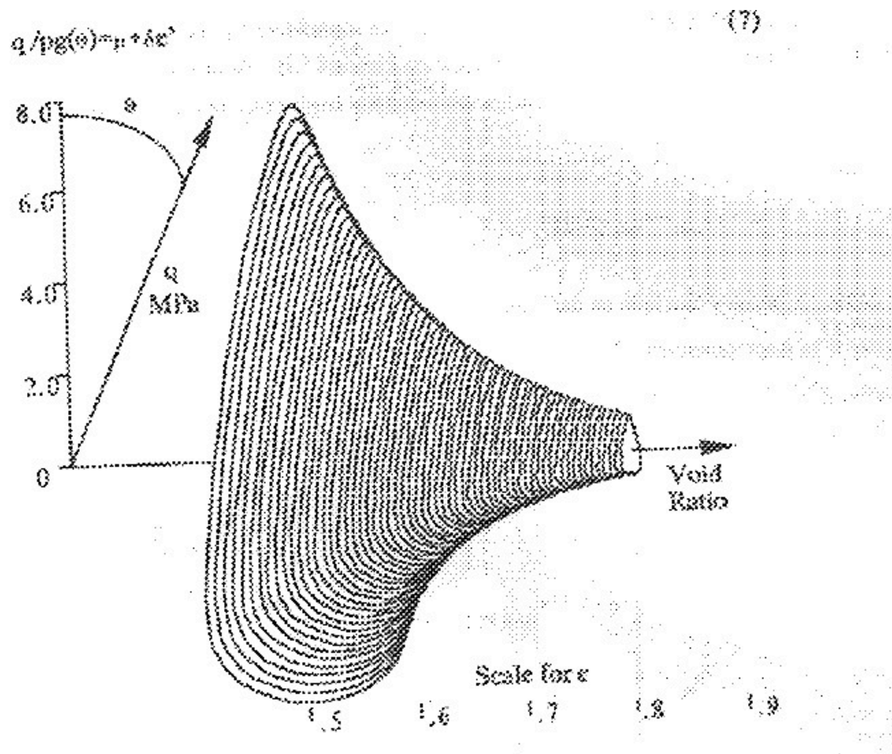

Figure 2.6.2. Isometric View of the Ultimate State Surface for Sacramento River Sand (after Poorooshasb 1989).

Under triaxial compression, the surface assumes the form shown in Figure 2.6.3. The Ultimate State Surface creates only a trace of the State Boundary Surface which lies on the e=0 plane.

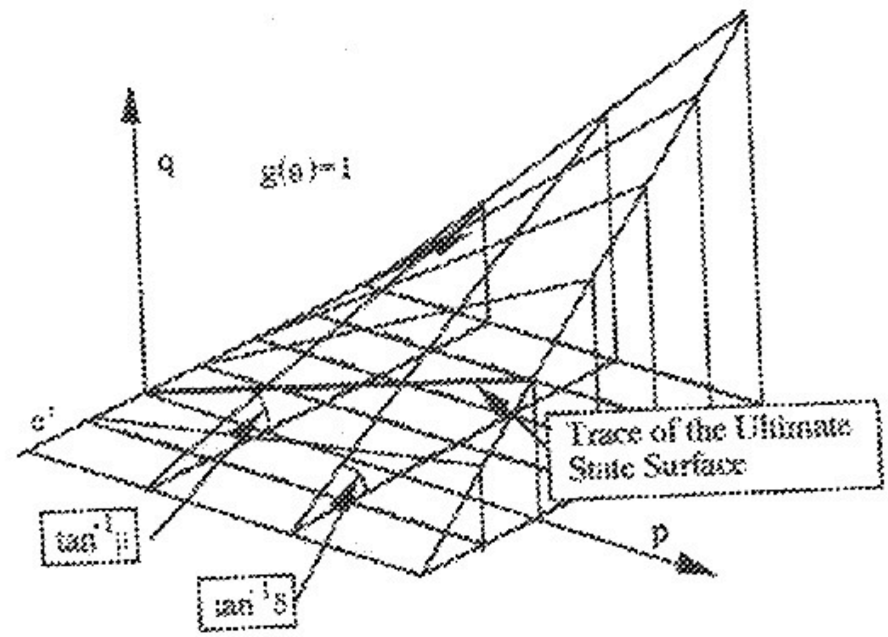

Figure 2.6.3. State Boundary Surface in the (p,q,e') space, g(θ)=1 (after Poorooshasb 1989).

When e is constant, a bullet shaped surface with its apex at the origin of the stress space and its axis along the diagonal is formed. In this situation, the Ultimate State Surface traces a band on the State Boundary Surface, which can be seen in Figure 2.6.4.

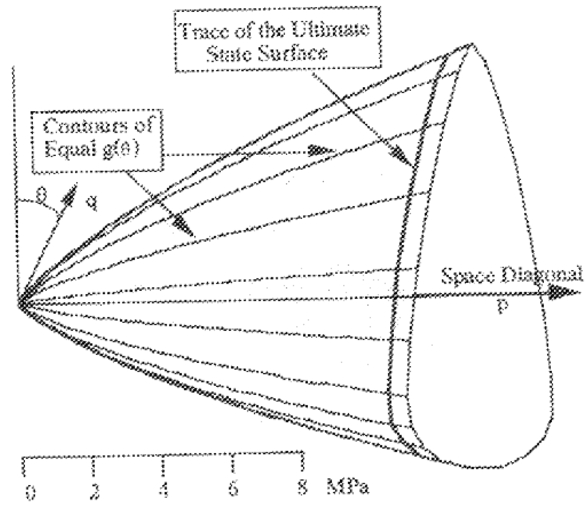

Figure 2.6.4. State Boundary Surface for Sacramento River Sand, e=5 (after Poorooshasb 1989).

Bounding Surface and Yield Surface:

In 1975, Dafalias and Popov introduced the concept of bounding surface. This surface distinguishes between virgin loading and secondary loading. The bounding surface expands and moves during virgin loading as the stress point goes through a certain curve in the stress space. In non-virgin loading, the stress point no longer is touching the bounding surface. The State Boundary Surface encloses the bounding surface and the bounding surface has the same curvature as the state boundary surface. The position of the bounding surface is controlled by the current state of the sample when the loading is in its virgin state, and therefore, will have a similar curvature as the State Boundary Surface. This can be seen in Figure 2.6.5.

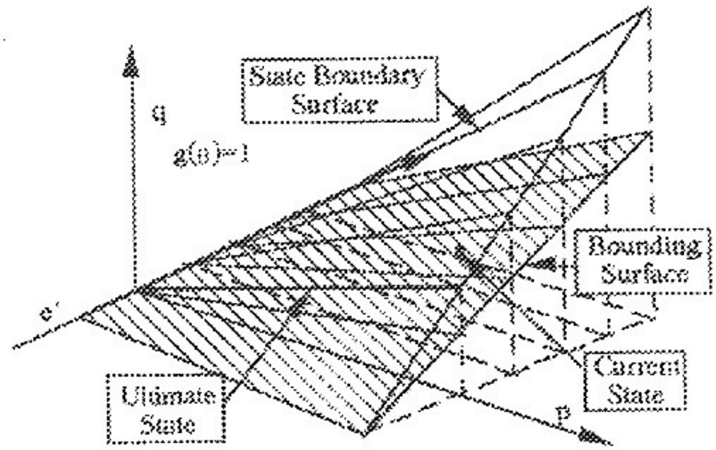

Figure 2.6.5. Bounding Surface and its relation to the state boundary surface in the (p,q,e') space, g(θ)=0 (after Poorooshasb 1989).

When the sample undergoes virgin loading, the yield surface is tangential to the bounding surface and moves with it. The yield surface encloses the set of points in the state space for which the behavior of the sample is elastic/reversible.

Figures 2.6.6 and 2.6.7 show the State Boundary Surface alongside the bounding surface and the yield surface for various states with constant void ratios. The yield surfaces are all curved. All three surfaces start from the origin. During isotropic consolidation, both the bounding surface and the yield surface shrink to a line that is along the space diagonal. Because of this, no yielding takes place and therefore, no plastic deformations can occur. The material response is only elastic. If the sample experienced anisotropic consolidation (for example, the K_o condition), then there would be a large magnitude of irreversible strains. This is because the stress path is passing various yield surfaces as it is loaded.

Poorooshasb (1989) explained three kinematic constraints of the yield surface. They are quoted as follows:

1. The control meridian, the axis of the yield surface and the space diagonal are at all stages coplanar.
2. As the state of stress changes from σ to $\sigma+\delta\sigma$, the axis of the yield surface must move along the guide plane associated with σ.
3. The new yield surface must contain the new stress point representing the state of stress of $\sigma+\delta\sigma$.

Plastic Potential

A material will yield if the stress point that is located on the yield surface moves outside the yield domain. This causes plastic deformation. The global plastic potential may be used to analyze the direction of the principal strain increment vector if the stress point is located on a control meridian. The local plastic potential can be derived from the global plastic potential and is the same along the control meridian. The local plastic potential surface cuts the θ=constant plane along a curve seen in b-b' in the Figure 2.6.8.

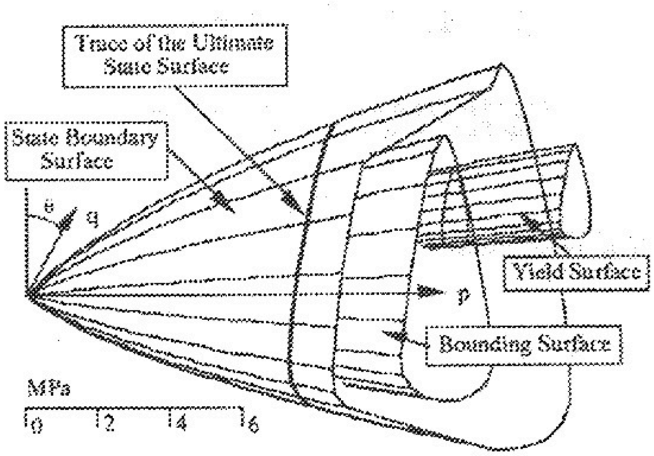

(a)

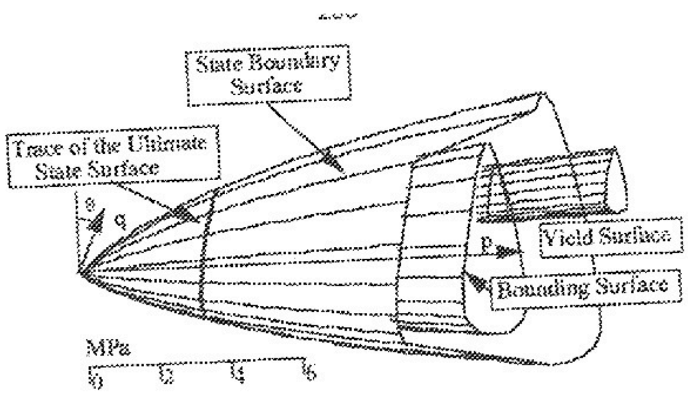

(b)

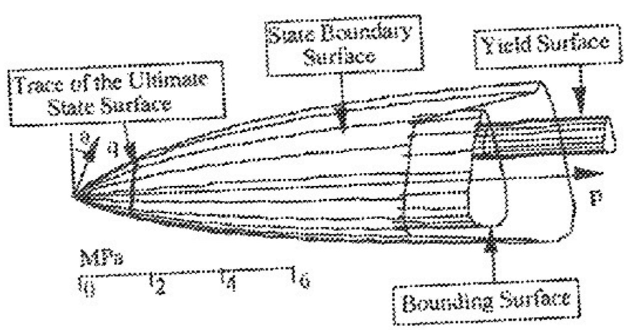

Figure 2.6.6. (a) Yield and Bounding Surfaces for Sacramento River sand, e=0.55 (b) Yield and Bounding Surfaces for Sacramento River Sand, e=0.75 (after Poorooshasb 1989).

(a)
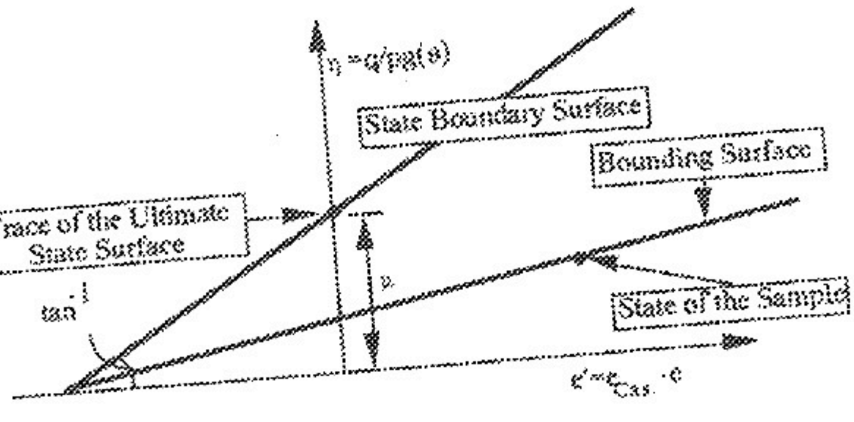

(b)
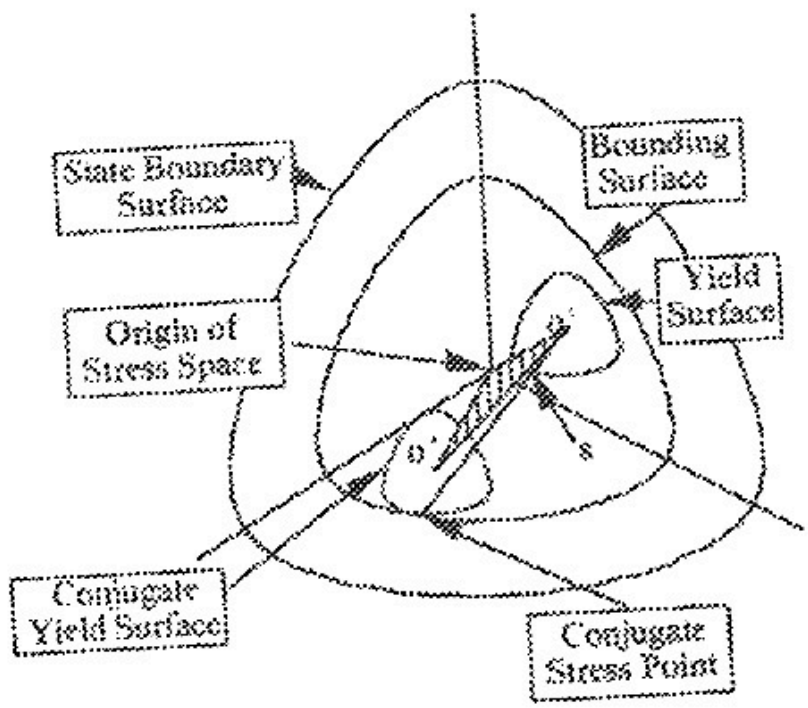

Figure 2.6.7. (a) The two dimensional representation of the state space (b) Yield and conjugate surfaces simplified scheme (after Poorooshasb 1989).

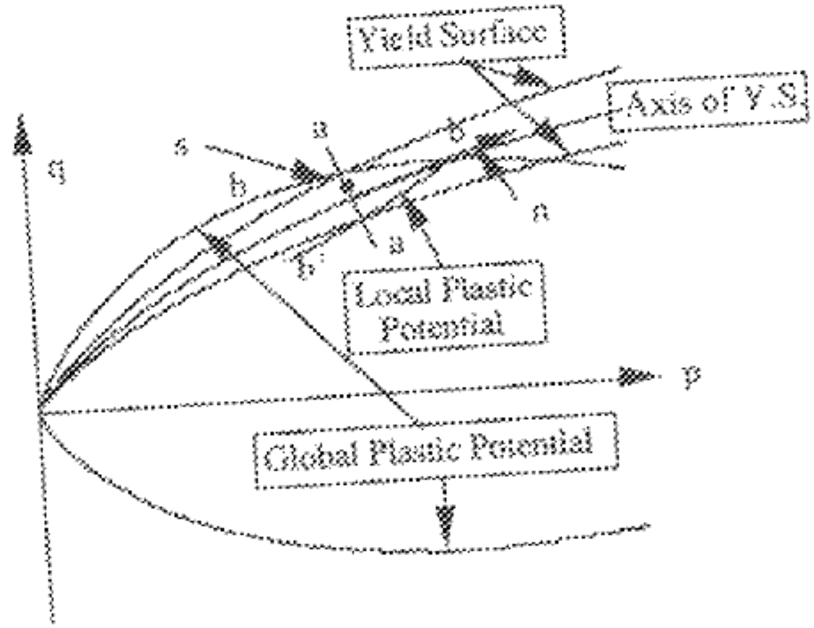

Figure 2.6.8. Global and local plastic potentials on a θ=constant, e=constant plane of the state space (after Poorooshasb 1989).

According to Poorooshasb et al. (1967), "the gradient of the irreversible component of the strain increment vector is independent of the gradient of the stress increment being a function only of the state of the element." Therefore, $d\nu/d\gamma = f(\tau,\sigma,e)$. The plastic potential function, ψ serves to define the components of the strain increment vector. It is given by the following equation:

$$d\varepsilon_{ij}^{\ p} = \frac{d\psi}{d\sigma_{ij}} < d\lambda > \qquad \text{Eq. 2.6.3}$$

The scalar dλ depends on the state of the element and its mode of yielding. Poorooshasb concluded that the plastic potential curves for a given value of e should form a family of geometrically similar curves. This can be seen in Figure 2.6.9.

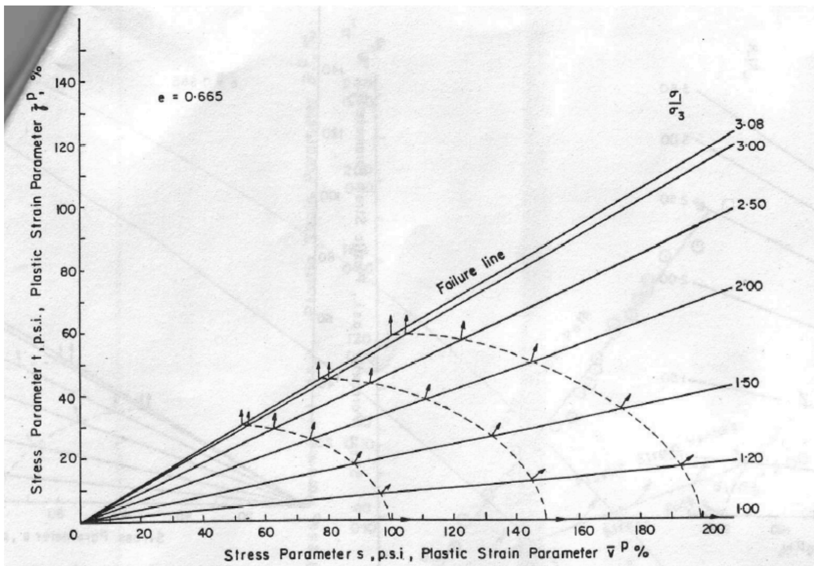

Figure 2.6.9. Establishment of plastic potential curves from the inclination of plastic strain increments, with three values for e (after Poorooshasb 1967).

The flow rule is the relation between the plastic strain increments and the stresses.

$$\Delta\varepsilon_{ij}{}^{p} = \Delta\lambda \frac{dg}{d\sigma_{ij}} \qquad \text{Eq. 2.6.4}$$

Δλ is a constant. This equation shows the strain increments being proportional to the derivatives of the plastic potential, where the plastic potential according to Poorooshasb (1967) is defined by

$$g = (I_1)^3 - \kappa_2 I_3 \qquad \text{Eq. 2.6.5}$$

The value of κ_2 determines the relative magnitudes of the plastic strain increments. $\Delta\lambda$ determines the absolute magnitudes.

Yielding can be defined and explained by taking a look at the state of an element. Poorooshasb et al. (1967) described this state as being represented by a point P in the state space (also called state point). One can consider a sphere, which has a radius, r that contains point P in its center. When something perturbs this sphere, it produces a small change in the state of the element. This change, the state increment vector, can be denoted δ, such that $|\delta| \leq r$. When the cause for this change is removed, a new position of the stress point is reached, P'. There are different categories that the element can be classified, depending on the position of P'. If $|PP'|>r$, then the element is said to be unstable. However, if $|PP'|\neq 0 \leq r$, then it is stable-yielding. Moreover, if $|PP'| = 0$, then it is considered stable-nonyielding. If P has identical elements (identical states who have experienced similar loading histories), then loading of the elements will cause the state points to trace a curve (also referred to as a state path). This path would depend on the loading conditions. Figure 2.6.10 shows these concepts in an illustration.

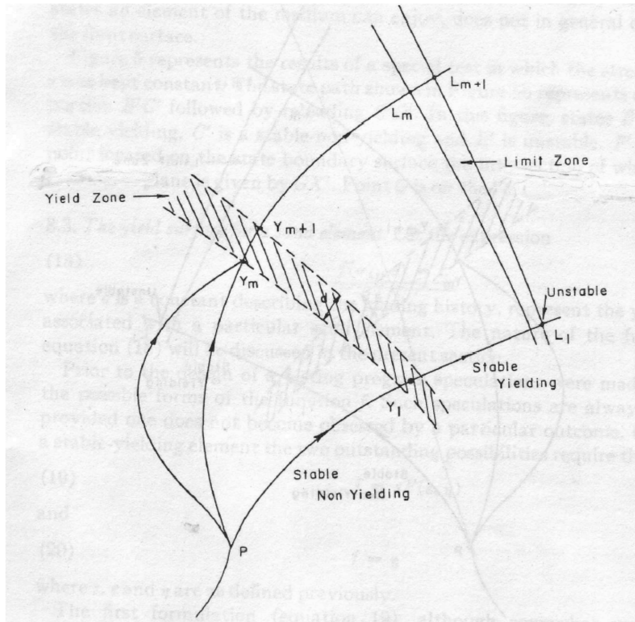

Figure 2.6.10. Illustration of yielding (after Poorooshasb 1967).

The yield surface for a sand element can be written

$$f(\sigma_{ij}, e) = c \qquad \text{Eq. 2.6.7}$$

c is a constant describing the loading history for a particular sand element. Poorooshasb et al. (1967) concluded that a simple formulation of the yield function f, of the form $f = \bar{c}\eta$ ($\bar{c}$ is a function less than but close to 1) was consistent for the behavior of isotropic cohesionless granular materials composed of non-breakable hard particles. Figure 2.6.11 shows a schematic picture of the intersection of a yield surface and of η=constant.

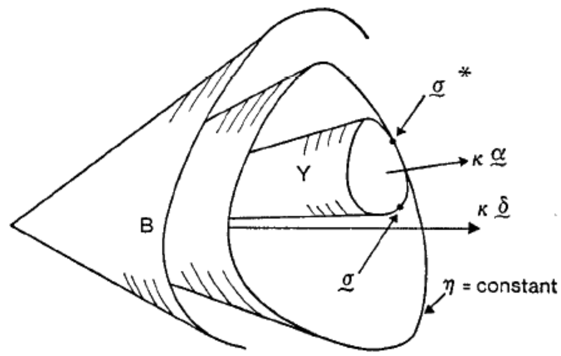

Figure 2.6.11. Intersection of a yield surface and an η=constant surface (after Poorooshasb et al. 1986).

Yielding and Yield Surfaces from Triaxial Tests

Lade and Prabucki (1995) studied the plastic yield surface for soils in the post-peak softening regime. They were interested in the movement of the yield surface due to pre-shearing and wanted to model the soil behavior in the hardening and softening regimes near peak failure. The sand specimens were tested in triaxial compression using certain stress paths where they would be able to establish the yield surface, and then keep searching for another yield surface at another location in the stress space.

As mentioned in the explanation of yield surfaces, the yield surface (expressed in terms of the stress invariants) shows the locus at which the total plastic work is constant. The total plastic work (due to shear strains and volumetric strains) acts as the hardening parameter. It is used to delineate the location and shape of the yield surface. They developed a constitutive model for a single, isotropic yield surface that expressed a contour of constant plastic work, measured from the origin of stress. The isotropic yield surface is shaped as an asymmetric teardrop with a pointed apex at the origin of the principal stress. This can be seen in Figure 2.6.12.

Looking at Figure 2.6.12, one can see that for an isotropic material, the yield surface is perpendicular to the hydrostatic axis, bending towards the origin, and crossing the failure surface at sharp angles. At these points outside the failure line, the stress level is greater than one. Lade and Prabucki also studied the effects of pre-shearing and found that following pre-shearing to peak failure, the yield surface in the region of lower confining pressures moved beyond the failure surface for normally consolidated sand. The sand showed softening beyond the yield surface, which became the failure surface of the region.

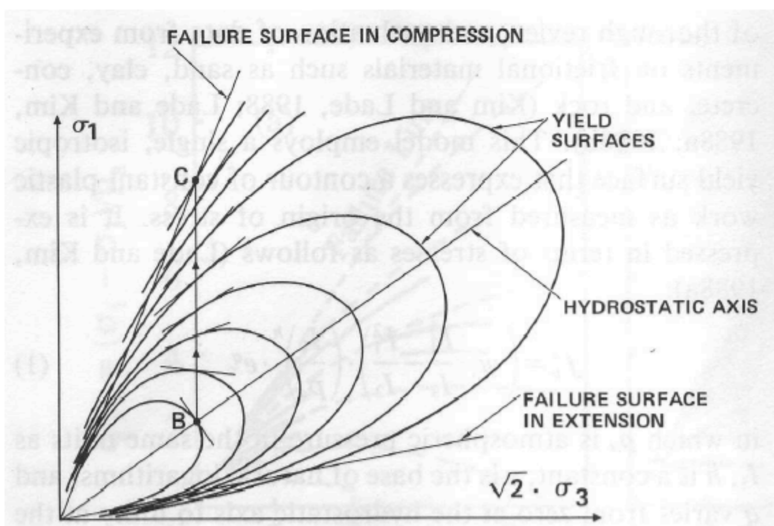

Figure 2.6.12. Pattern of yield surfaces for isotropic granular materials (after Lade and Prabucki 1995).

Yasufuku et al. (1991) also studied the yield characteristics of aniostropically consolidated sand using drained triaxial testing. They tested Aio sand under low and high stresses with different stress paths. They found that the overall shapes of the yield curves under low and high stress levels are similar and by using ellipses that are not symmetrical about the stress path during consolidation, the shapes of the yield surfaces can be drawn. They also found that the relationship between the tangent slopes of the yield curves and stress ratios can be expressed as a unique function of the applied stress ratio, no matter what proportional loading path history was used. They also proposed a yield function for anisotropically consolidated sand. They defined the yield point as the state of stress at a marked change in slope of each stress-strain curve. The yield stress was taken to be the point of maximum curvature, corresponding to the start of fully plastic deformation.

Figure 2.6.13 shows the method that Yasufuku et al. (1991) used which was based on the method used by Poorooshasb et al. (1967) and Miura and Yamamoto (1982). This method involves locating the yield point by an intersection of two simple straight lines. The developed yield curves can be seen on Figure 2.6.14. It is seen that the yield surface shape differ from each other. This difference seems to be related to the dependency of the failure line on the confining pressure. However, the general shape for anisotropically consolidated sand is approximately an elliptical one, which is not symmetrical about the stress path during consolidation.

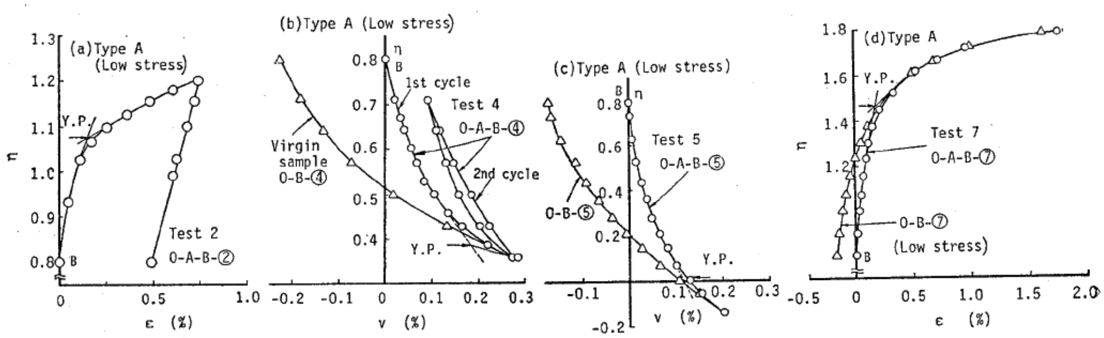

Figure 2.6.13. Typical stress-strain curves for tests of Type A in the low stress level (after Yasufuku et al. 1991).

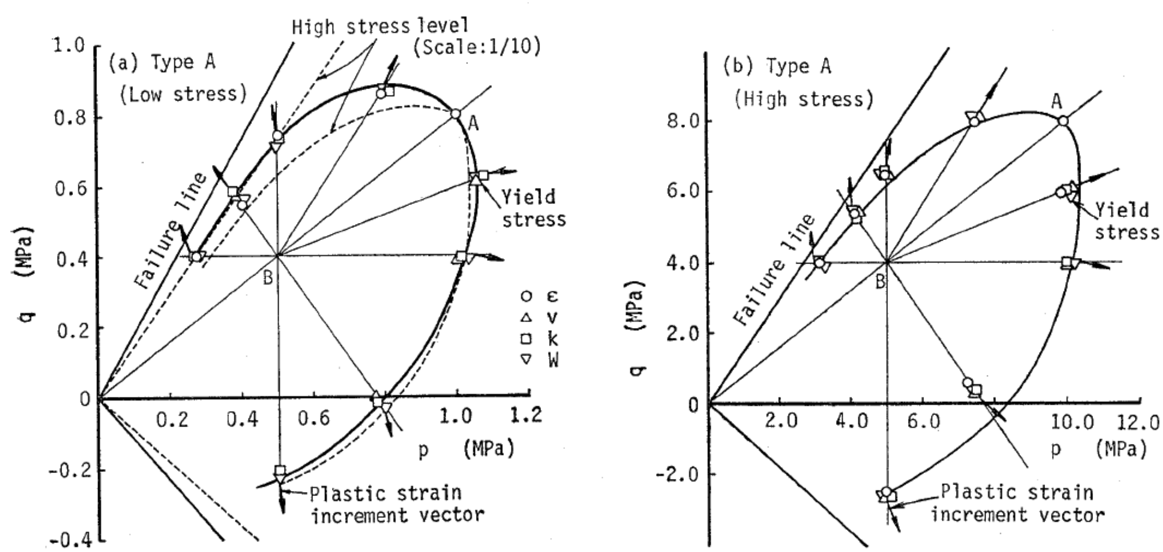

Figure 2.6.14. Experimental yield curves obtained from tests of Type A in the (a) low stress level, (b) high stress level (after Yasufuku et al. 1991).

Yielding and Flow of Sand in Torsion Shear Tests

Pradel et al. (1990) studied the influence of inherent anisotropy on the yielding and plastic flow of loose and dense Toyoura sand with a torsional shear apparatus. The loading path that was followed can be seen in Figure 2.6.15a and 2.6.15b.

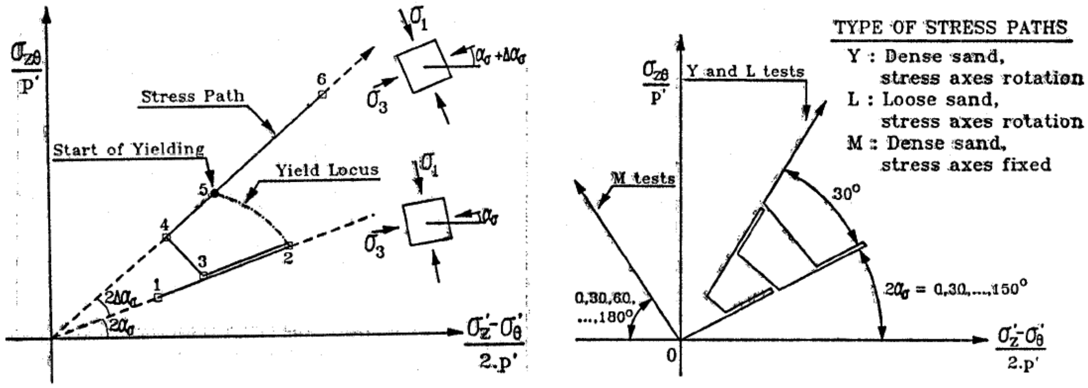

Figure 2.6.15. (a) Loading path for the study of yielding (b) stress paths used for the determination of yield loci (after Pradel et al.1990).

When finding yield points, they experienced that there was not always a sharp change between the elastic and plastic response that was easily observed. Figure 2.6.16 shows the idealized stress-strain behavior during reloading where it is quite easy to get the yield point. However, when the plastic strain in the transition zone is too large, the derivation of the yield point can be subject to some errors and requires assumptions about the stress-strain behavior.

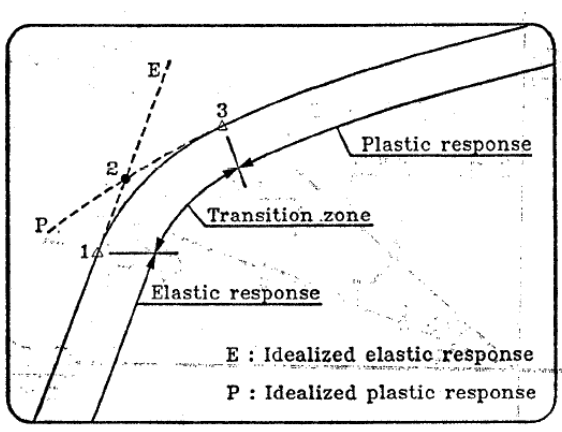

Figure 2.6.16. Idealized stress-strain behavior during reloading (after Pradel et al. 1990).

Pradel et al. (1990) concluded that yielding occurred when stresses reached a particular level of stress for a given direction of principal stresses. The yield loci obtained from different stress-strain curves were not identical, and all the yield loci defined smooth curves of elliptical shape that were independent of density. Pradel et al. (1990) also showed that the direction of principal plastic strain increment in sand during principal stress rotation is very much dependent on the stress increment direction. This response violates the postulate of uniqueness in flow of plasticity theory. Gutierrez et al. (1991) conducted stress probe tests under different states of stress and they found that the plastic strain increment direction depended not only the current state of stress but also on the direction that the stress increment was executed. Based on experimental observations, they saw that the flow of sand is dependent on the stress increment direction as well as on the level of shear stress and then proposed a plastic potential theory (shown in Figure 2.6.17). The new theory proposed to determine the plastic strain increment direction as the normal to the failure surface at the point of intersection of the failure surface and the stress increment vector extended.

Pradel et al. (1990) used a Torsion Shear Apparatus to study the effects of reorienting the major principal stress on the yield behavior of sand. However, they did this only for limited regions of the stress space. Their experimental data showed that there were combined effects of changes in both α_σ and the intermediate principal stress parameter, b.

O'Kelley and Naughton (2009) studied the effects of different orientations of the major principal stress and different magnitudes of the b parameter on the yield behavior of sand separately. The stress paths that they determined used the method of finding yield points and yield loci by Tatsuoka and Ishihara (1974). Figure 2.6.18 shows the process.

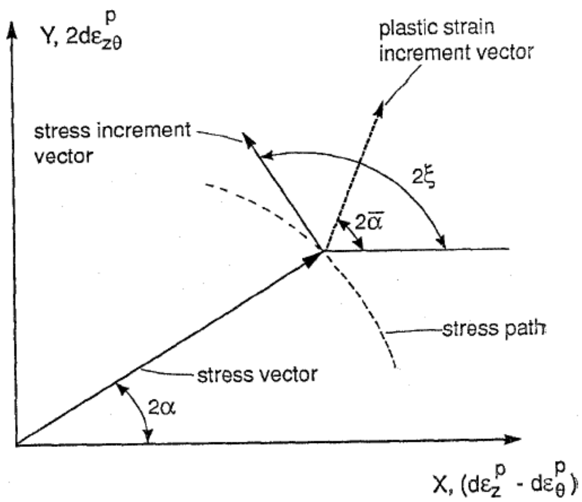

Figure 2.6.17. Stress and plastic strain increment representation in the X-Y stress space (after Gutierrez et al. 1991).

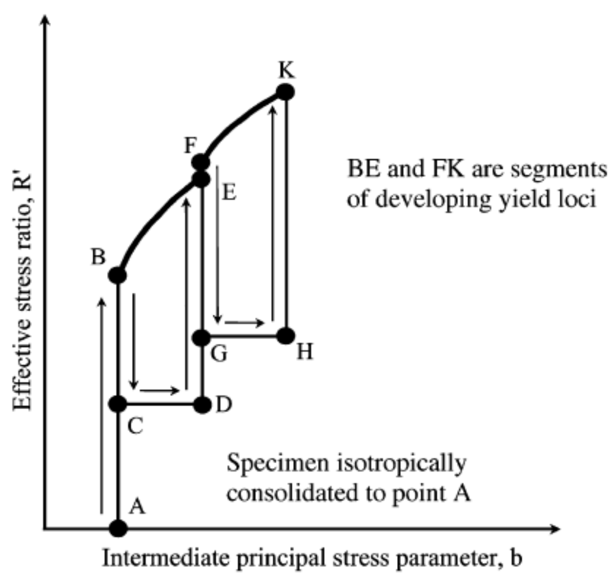

Figure 2.6.18. Stress probing to identify yield loci (after O'Kelly and Naughton, 2009).

Once isotropic consolidation was achieved to the same mean effective confining stress, the sand specimens were anisotropically consolidated to achieve different values of α_σ (α_σ =0°, 30°, 60°, and 90°) and the b parameter (b=0 or increased from b=0 to 0.5). This created a new fabric in the specimen. By increasing the major to minor effective principal stress ratio (σ'_1/σ'_3) until the start of plastic straining, points on the yield surface were found. Once the yield point was established, the principal stress ratio was reduced and the specimen was reconsolidated in order to increase the b parameter by 0.25. Once the b value was reached, the ratio was increased again to search for a second yield point. This allowed a yield locus to be established between the two points. This procedure was repeated to establish segments of the yield loci for different stress states for different specimens. By using this method, it was possible to study the effects of reorienting the major principal axis as well as changes in the magnitude of b separately.

Figure 2.6.19(c) and 2.6.19(d) show the strain responses recorded during the load-unload and reconsolidation stages of the stress path (changes in the R' (principal stress ratio) and the b value). The stress-strain responses seen in Figure 2.6.19(c) were approximately linear-elastic along the unload paths and along the initial phase of the reload paths. The strains during the reconsolidation stages were negligible. This shows that the soil fabric induced in the specimens by the end of anisotropic consolidation (after the second stage) would have remained largely intact for the remainder of the stress path. Near a yield point, the stress-strain response became increasingly non-linear. Due to Pradel et al.'s (1990) suggestion that the yield points derived from the intersection of best fit lines to the initial pseudo-elastic and post-yield slopes provided better approximations of the yield loci for the Matsuoka-Nakai and Lade yield criterion, the yield points were identified by curve fitting. A part of the yield locus was drawn by joining the yield point established for higher values of the b parameter back to the initial yield point.

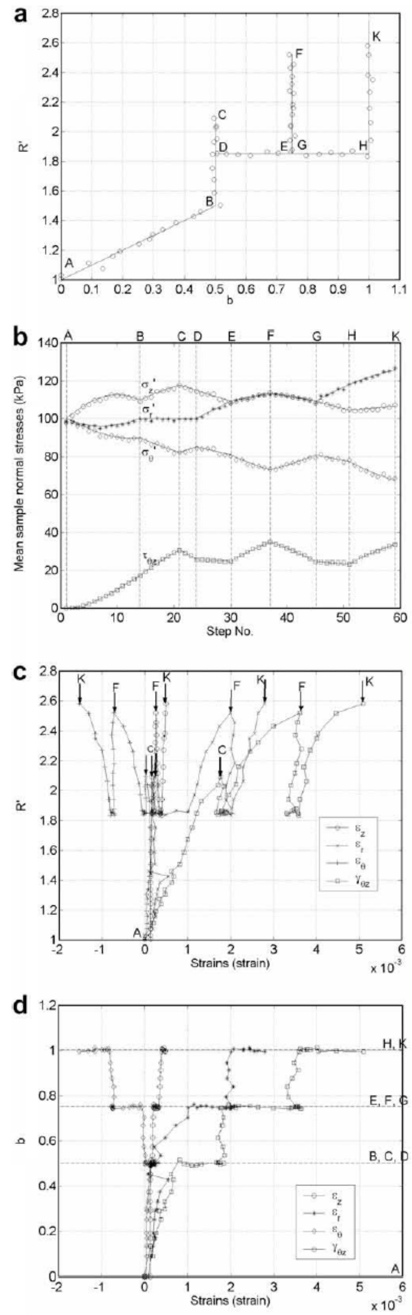

Figure 2.6.19. Stress probing to determine yield points (after O'Kelly and Naughton 2009).

Figure 2.6.20 shows the experimental yield data found plotted on a three dimensional plot with the axes representing, α, b, and the deviator stress, q, where

$$q = \sqrt{(\sigma'_1 - \sigma'_3)^2 + (\sigma'_1 - \sigma'_2)^2 + (\sigma'_2 - \sigma'_3)^2} \qquad \text{Eq. 2.6.7}$$

The data shows that the magnitude of the deviator stress corresponds to the yield loci in a continuous manner. The deviator stress was dependent of the initial value of the b parameter but was independent of α, the rotation that happened during the anisotropic consolidation stage of the stress path. When looking at the b parameter, two trends can be seen. The first observation is for the stress paths that had re-oriented the major principal stress and had the intermediate principal stress parameter initially set at b=0. For this situation, the deviator stress at yield decreased by about 15-20% because of the increase from b=0 to b=0.5. For the stress paths that reoriented the major principal stress and had the b originally set at 0.5, the magnitude of the deviator stress at yield either remained constant or increased slightly due to the increase from b=0.5 to b=1.0.

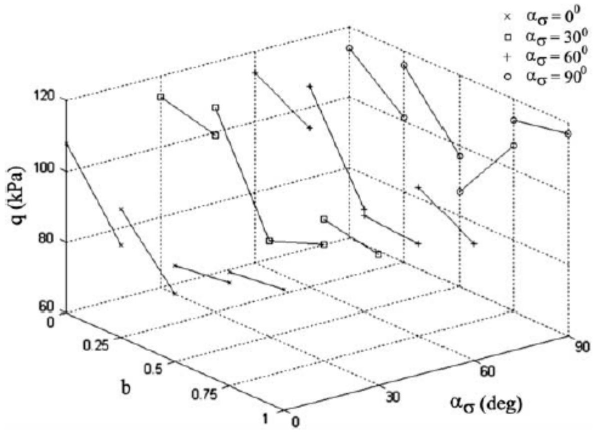

Figure 2.6.20. Variation of deviator stress on yield loci (after O'Kelly and Naughton 2009).

The yield loci were normalized and compared to the Matsuoka-Nakai and Lade criteria. The yield criterion was a bit less for the onset of b values (0>b>0.5) and slightly over for (0.5>b>1.0). Taking account the scatter in the results, they concluded that both criterion were satisfactory for the results (see Figure 2.6.21).

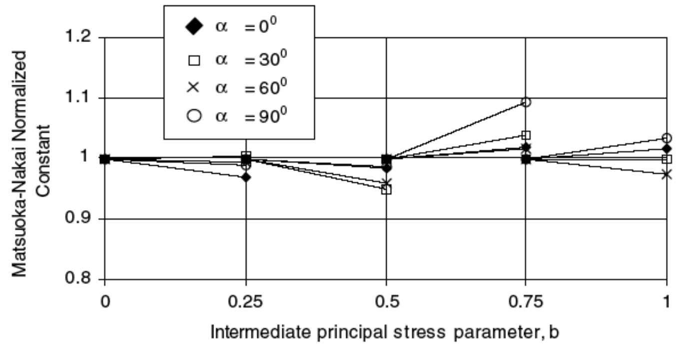

(a) Matsuoka-Nakai criterion.

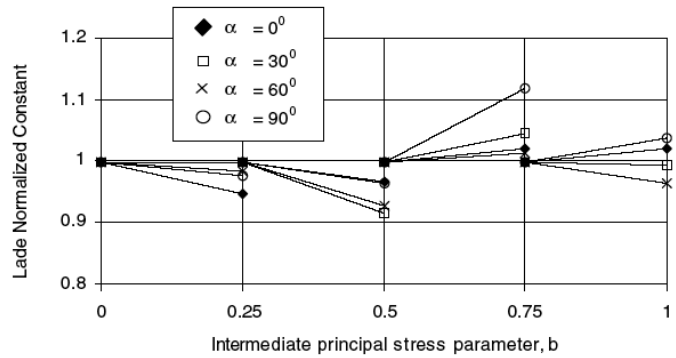

(b) Lade criterion.

Figure 2.6.21. Experimental and theoretical values of points on yield loci (after O'Kelly, and Naughton 2009).

Conclusion on Yield and Failure Surfaces

Research into yield surfaces first began by establishing the failure surface, which in the beginning was referred to as the yield surface. Experiments were performed to determine the critical void ratio and ultimate surface, to find the state boundary surface, then bounding surface and the yield surface. Certain techniques have been developed in order to successfully find the yield surfaces of sands and clays, however, construction of the yield surfaces often requires tests in which unconventional stress paths are created on the soil. In some cases, yield points have to be approximated. Loading of soils often changes the soil properties, making it difficult to reach different yield points belonging to the same yield locus, while the soil retains the same properties (i.e. void ratio, anisotropy). For clays, ellipses have been used as yield surfaces. For sands, more complex yielding behavior has been seen and a wide range of shapes has bee used to show the yielding of sands. Many triaxial tests, alongside fewer torsion shear tests have been performed in order to study yield surfaces. Research still continues on studying the effects of anisotropy and principal stress direction for cross-anisotropic sand deposits.

3. Triaxial Compression and Extension

3.1 Tests Material Used

In this experimental program, all triaxial, true triaxial and torsion shear tests were conducted on Fine Nevada Sand. The sand used is mostly made up of Silica Dioxide, SiO_2, i.e. quartz. X-ray diffraction was performed on the sand and a complete list of the chemical make-up of the sand is presented in Table 3.1.1. The graph format showing the wave intensity is shown in Appendix A.

Table 3.1.1. CUA Vitreous State Laboratory X-Ray Diffraction Analysis on Fine Nevada Sand

Oxide	**wt%**
Al_2O_3	1.67
CaO	0.033
CoO	0.01
Cr_2O3	0.006
CuO	0.003
Fe_2O_3	0.073
K_2O	0.157
MgO	0.058
Na_2O	0.11
P	0.009
S	0.01
Sb_2O_3	0.017
SiO_2	97.73
TeO_2	0.028
TiO_2	0.051
V_2O_5	0.023
ZrO_2	0.006

The specific gravity was also determined in the laboratory through the liquid submersion technique. A detailed description of the procedures can be found in Germaine and Germaine (2009). In order to account for variations associated with temperature, a volumetric flask was calibrated. Distilled water was also used to ensure accuracy in the results. Calculations are provided in Appendix B. The calculated specific gravity for the Fine Nevada Sand used in the experiments was 2.651.

The minimum void ratio was determined by air-pluviating a predetermined amount of sand into a graduated cylinder. This was performed very slowly by dropping a spoonful of sand at a time from a height of 40cm. This ensured that the sand grain structure could reach its densest state. The volume was then measured in order to determine the minimum void ratio. The e_{min} was calculated to be 0.507. The maximum void ratio was determined by sealing the top of the graduated cylinder and slowly turning it upside down and right side up. This was performed several times to ensure that a constant maximum void ratio was achieved. The e_{max} was calculated to be 0.771. The calculations and test data are presented in Appendix C.

The grain size distribution was attained by performing a sieve and hydrometer analysis on the sand. Fine Nevada Sand was sieved through a 0.850 mm opening (Sieve No. 20) to ensure that no larger sand grains or particles were tested for all triaxial, true triaxial and torsion shear tests. The grain size distribution curve is shown in Figure 3.1.1. The sieve and hydrometer data can be found in Appendix D.

It should be noted that the sand used in the triaxial and true triaxial tests was not reused. However, with the torsion shear tests, it was necessary to reuse the sand because over 8800 grams of sand were used in each experiment. As the specimens were sheared under low confining pressures, the sand did not experience any crushing. After each test, the sand was dried in an oven and then separated into containers to ensure that it was not used again until the whole supply had been used up. A sieve analysis on the used sand confirmed that the grain size distribution did not change and that all tests were comparable. Table 3.1.2 summarizes the properties of the Fine Nevada Sand used in the experimental program.

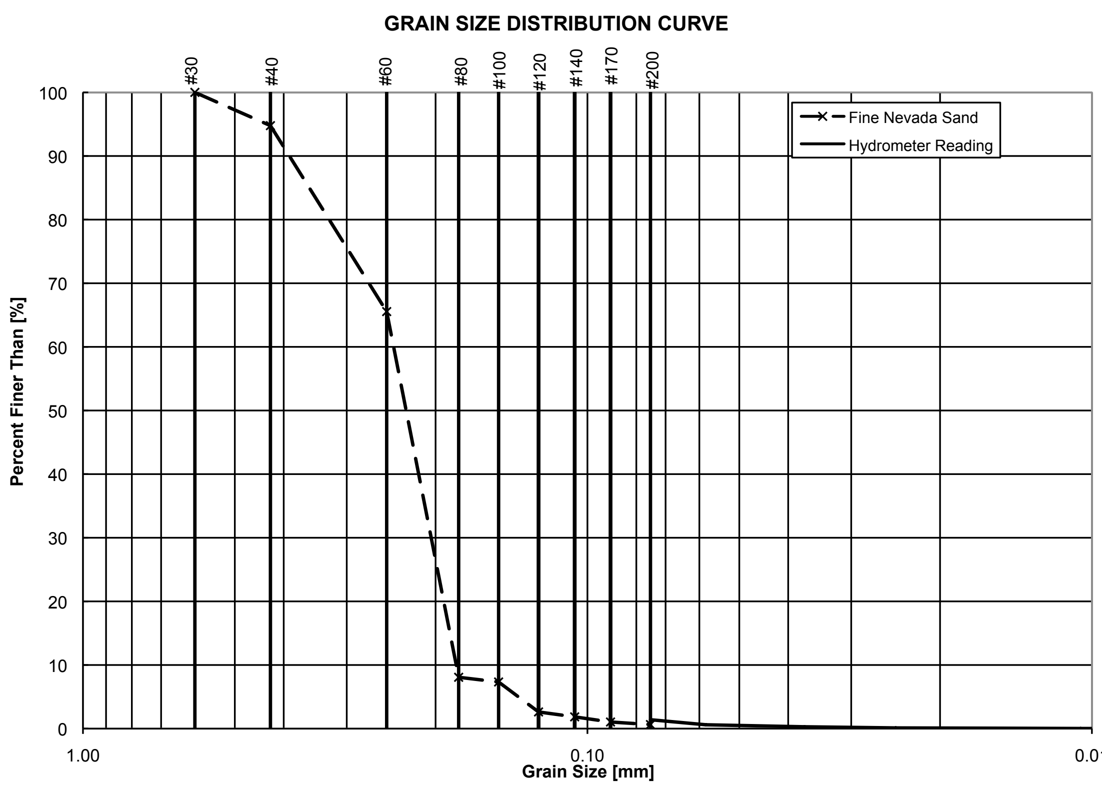

Figure 3.1.1. Grain Size distribution curve including hydrometer analysis on Fine Nevada Sand.

Table 3.1.2. Properties of Fine Nevada Sand.

Specific gravity, G_s	2.651
Min. void ratio, e_{min}	0.507
Max. void ratio, e_{max}	0.771
D_{10} (mm)	0.114
D_{30} (mm)	0.169
D_{60} (mm)	0.238
Coefficient of uniformity, C_u	2.076
Coefficient of curvature, C_c	1.049

3.2 Triaxial Compression and Extension Tests

A total of ten triaxial compression and one conventional extension tests were performed on Fine Nevada sand in order to attain the parameters that are needed and used in Lade's failure criterion (Lade 2008). For these specific tests, the true triaxial apparatus developed by Lade and Duncan (1973) was used. Four tests were performed with horizontal bedding planes, α=0°. An additional six tests were performed on specimens that had vertical bedding planes, α=90°. One conventional extension test was performed as well. The details and results are presented in the sections that follow. As a point of reference, Figure 3.2.1 shows the Mohr's circle for triaxial compression and extension tests.

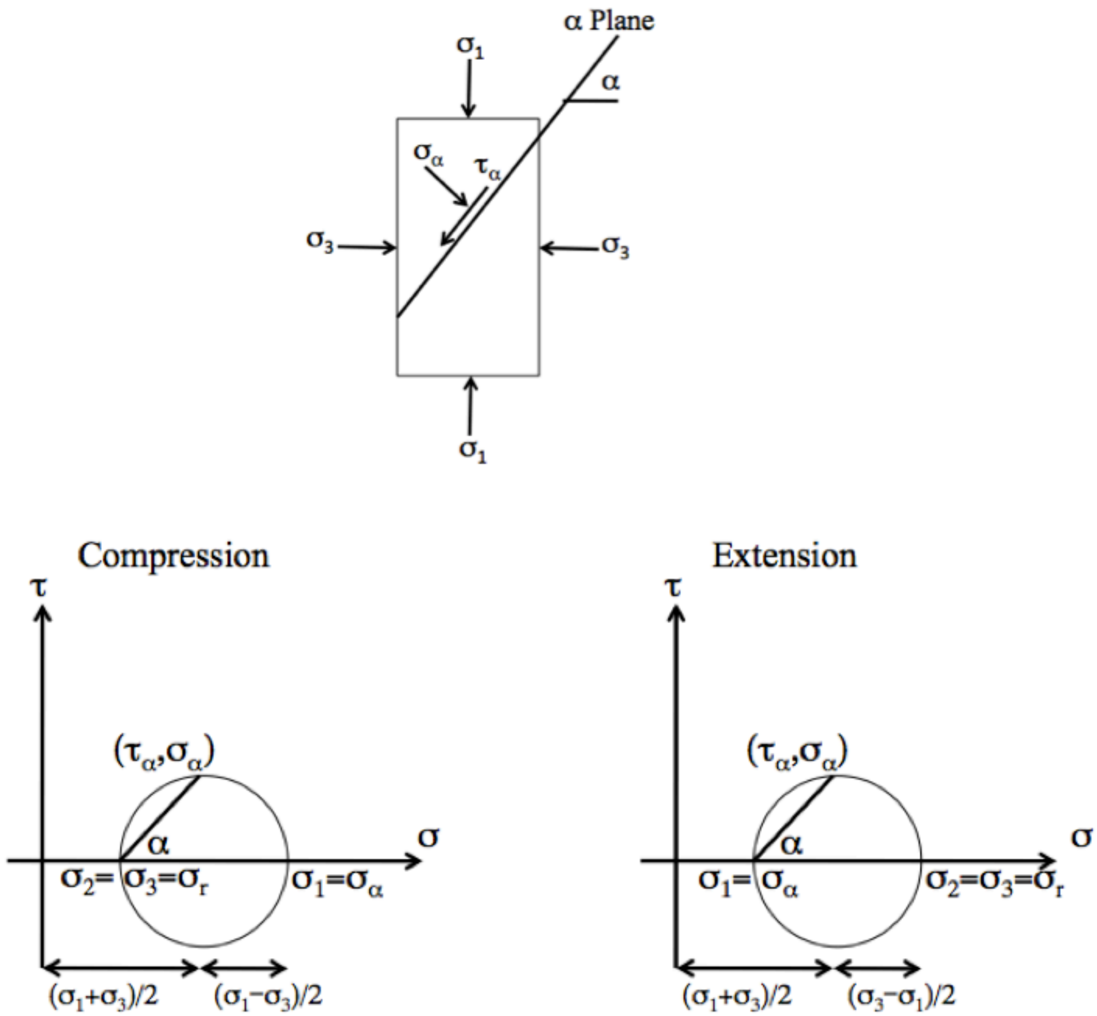

Figure 3.2.1. Mohr's Circle for Triaxial Compression and Extension Tests.

Triaxial Tests Set-up

Lade and Duncan's (1973) true triaxial apparatus (described in Section 2.2) was slightly modified to perform traditional triaxial tests. The horizontal loading system was removed and any openings were plugged to create a conventional set-up. The confining pressure, which acted on all sides of the specimen, was applied by air pressure through a fitting on the base plate and was measured directly from the cell with a pressure transducer. The air pressure inside the chamber created the minor principal stress, σ_3. The vertical load was applied to the specimen through the top cap and base. It was transferred through a stainless steel piston rod that touched a ball placed in a ball socket in the top cap load cell. The flat end of the piston was used to touch the ball, ensuring that the point load was always centered on the ball. The deviator stress from this load with the addition of the confining pressure, σ_3, provided the major principal stress, σ_1. A schematic of the set-up (without the loading plates) can be seen in Figure 3.2.2.

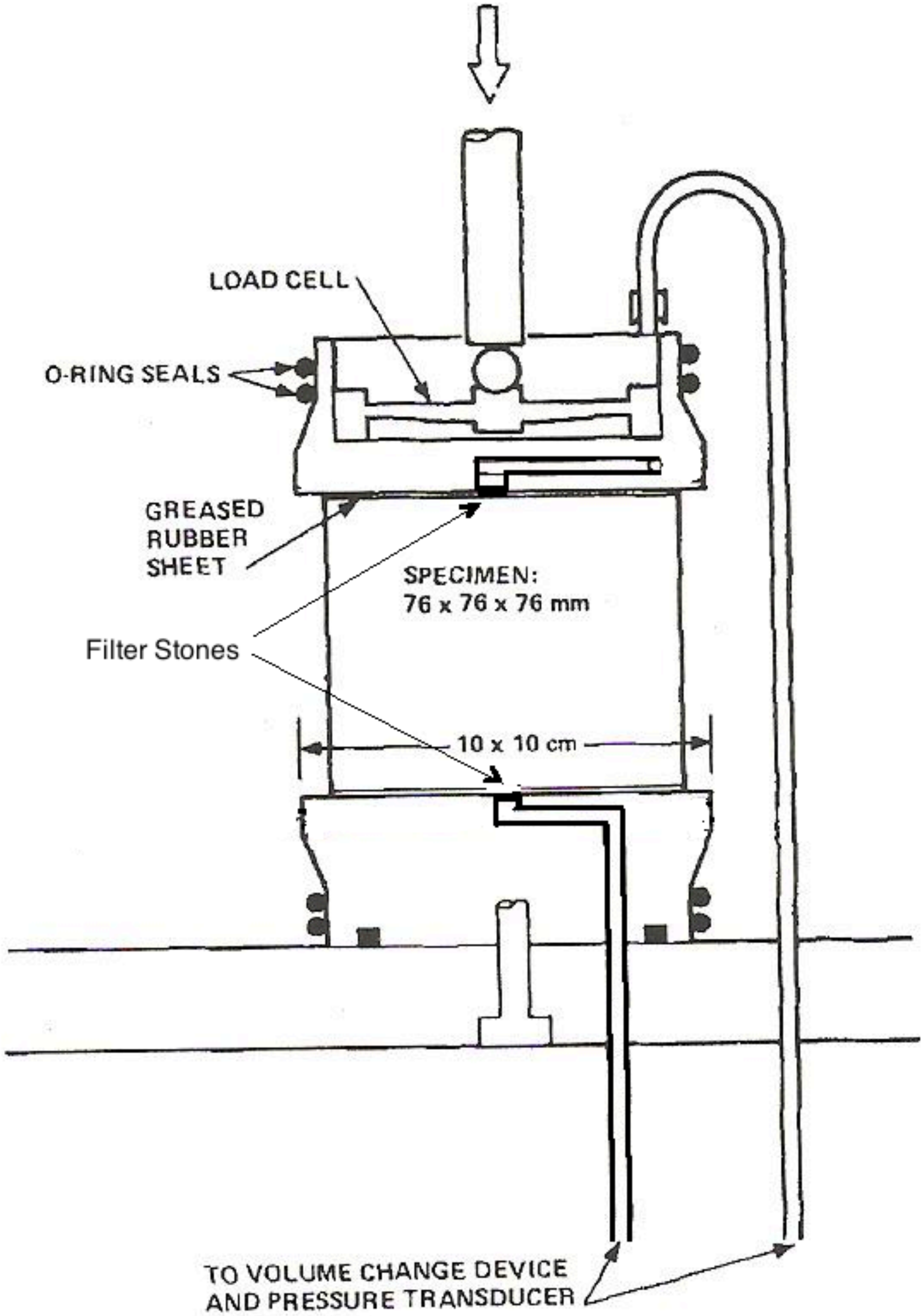

Figure 3.2.2. Triaxial Set up (Modified for Sand) after Lade (1978).

Two load cells were used during conventional triaxial testing. The interior load cell embedded in the top cap was made of beryllium copper. It was supplied with four strain gages glued to the surface and connected in a full bridge. Details can be found in Lade (1978). The cable with the wires connected to the strain gages passed through a sealed opening at the base of the cell and was connected to a Vishay Measurement Group P-3500 Strain Indicator Box. The gage factor was set appropriately and any time that the load cell was taken apart, it was recalibrated. The exterior load cell was a Futek LCF-450 and has a capacity of 226.8kg. The Futek LCF-450 was connected to a Futek IPM500 signal conditioned digital display. Both load cells were calibrated independently of each other and independent measurements were taken during all tests. Measuring the vertical load by two load cells served as a way to confirm that the readings were consistent and correct.

Filter stones and drainage lines on the top and bottom caps allowed for water to flow to the volume change device while the saturated specimen was isotropically consolidated and sheared. In order to measure the saturation of each sample and obtain the Skempton B-Value, the volume change device had a 3-way valve that was connected to a 3447 kPa pressure transducer and a Micro Meters signal conditioned digital display. This 3-way valve made it possible to measure the cell pressure as well as the back pressure on the specimen. A schematic of the volume change device that was used is shown in Figure 3.2.3.

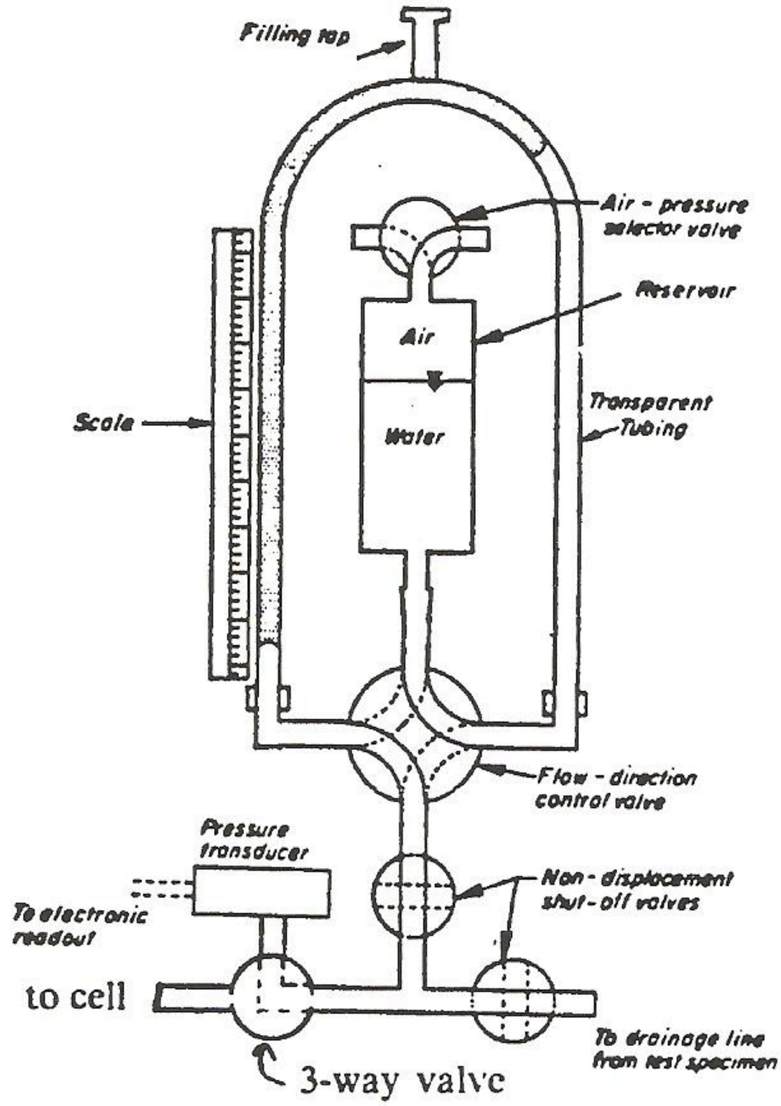

Figure 3.2.3. Schematic of Volume change and Pressure Measuring Device (after Kirkgard 1988).

The triaxial set-up was placed on a Humboldt Master Loader HM-3000. A strain rate of 0.1mm/min was used for the set of tests described in this section.

Specimen Preparation

All specimens were approximately 7.6cm in length, 7.6cm in width and 19cm in height. A void ratio, e, of 0.53 was targeted for each test. This corresponds to 91% relative density. This void ratio and relative density was chosen in order to create a dense specimen to see the effects of shear banding. In general, two factors affect the void ratio when pouring the sand: drop height and rate of sand pouring. In order to ensure the same void ratio for each specimen, the specimen was poured into a funnel with a small tube inside the mouth of the funnel ensuring a constant flow rate of sand. The sand was dropped into a mold that was created of block pieces. These pieces had a thin layer of grease between each piece to ensure that no leaks were created. A bottom copper plate with a hole that was used during the saturation process was also part of the mold. The top face of the mold was left open while the sand was rained in. The funnel was raised as the sand fell to maintain a drop height of 35cm. It was determined empirically that a drop height of 35cm at the flow rate established would create the desired void ratio. As the sand was deposited, the funnel was carefully raised to ensure even bedding planes into the previously assembled mold. A picture of the assembled mold is shown in Figure 3.2.4.

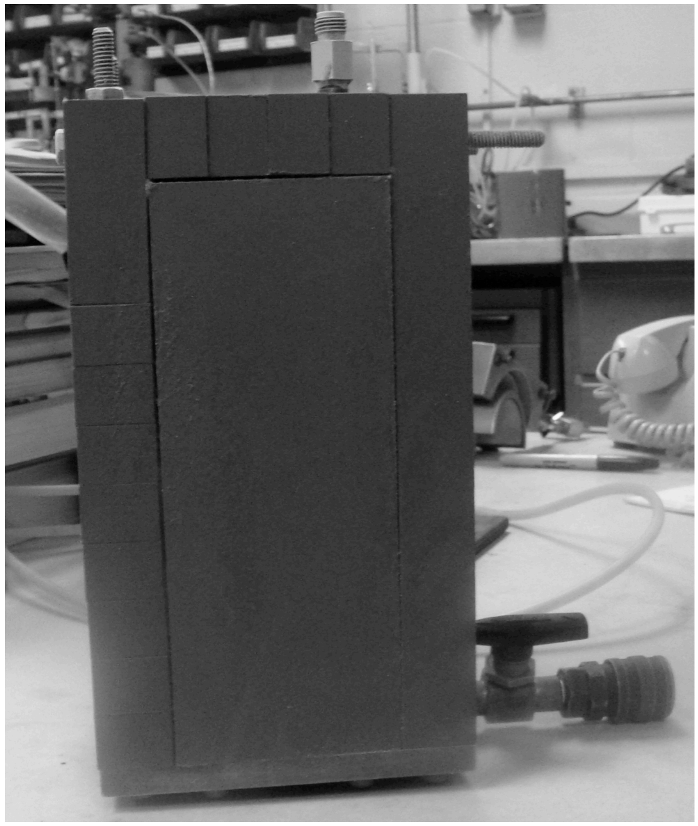

Figure 3.2.4. Picture of mold used to create frozen true triaxial specimens.

For tests with α=0°, the mold would stand vertically and would be open at the top. The mold had a base plate made of copper and its sides were made of plastic pieces (PVC). Rods going through the plastic pieces were fastened and ensured that the mold would not be loose or break apart. The interior of the mold was lightly greased with vacuum grease before depositing the sand in order to easily slide out the specimen. For tests with α=90°, the mold was set on its side and the topside face was left open where the sand could be deposited. Once the sand was deposited, special care was taken to not move the specimen until after it was completely saturated. It was not moved in order to make sure that the bedding planes were not shifted in any way. When the sand was completely deposited, the last and open side of the mold was closed with the plastic pieces and secured with additional rods. On whichever side was facing up, a special piece, which included a fitting, was used. This was done so that any water that expanded during freezing could exit through the fitting and not affect the void ratio of the specimen. After it was closed and sealed, gaseous CO_2 was slowly passed from the bottom up through the specimen, pushing any trapped air out of the fitting in the uppermost plastic plate. Deaired water was then slowly passed through the specimen until it was completely saturated. Any remaining gaseous CO_2 would dissolve in the water, because Henry's coefficient of solubility is about 1.0 vol/vol at room temperature. When the CO_2 saturation process was complete, the specimen was carefully moved to a freezer. The specimen with the copper plate at the bottom was set on an aluminum block inside the freezer to facilitate the freezing process. All specimens were left overnight in the freezer to ensure that they were completely frozen. Any excess water would escape from the fitting located on the top plastic piece of the mold and therefore, the void ratio of the specimen was not changed during the freezing process.

Once the specimen was frozen, it was ready to be set up in the triaxial cell. Special sized membranes that had been formed by dipping a mandrel into fluid latex rubber and molded to the correct dimensions were used for all triaxial and true triaxial tests. All of the membranes were approximately 0.03cm thick. Lubricated ends were placed on the top and bottom caps to ensure that shear stresses between the specimen and end plates did not develop. Two sheets (0.01cm thick) were used. A thin layer of vacuum grease was placed on the aluminum side of the top and bottom cap. Then, one sheet was placed and then another thin layer of vacuum grease was spread between the top and final sheet. Two sheets were found to be adequate in the testing program and allowed for enough lubrication to ensure that the specimens remained as vertical as possible at peak failure. A bulged specimen can affect the direction of the measured shear bands and this is why special care was taken to ensure the lubricated ends worked correctly.

The mold was then carefully disassembled and the frozen specimen was placed on the bottom cap. The membrane was stretched over the specimen and secured with two O-rings at each of the top and bottom cap. The drainage lines connected to a vacuum held at 25 kPa effective confining pressure. The vacuum was applied through a bubble chamber and therefore, any leaks in the membrane would be indicated. Liquid latex rubber was then painted on to the sample to ensure that no holes and leaks existed. Once the liquid latex rubber dried, the Lucite cell wall and the top lid of the triaxial cell were installed and secured to the base plates with six tie rods. The piston was also inserted through the top lid and rested lightly on the ball placed in the ball socket of the interior load cell. The specimen was then left overnight to ensure that all ice had thawed completely.

Once thawed, deaired water was filled into the outer cell and a confining pressure of 25 kPa was applied to the cell while the vacuum was removed. For tests using the inner top cap load cell, only air pressure was used, as the load cell was not water proofed. Deaired water was again introduced into the specimen in order to saturate the drainage lines. Once saturated, the top and bottom drainage lines were hooked up to the volume change device and back pressure was added to the specimen, keeping the effective confining pressure at 25 kPa. A back pressure of 100 kPa helped in saturating the specimen. The saturation was tested after the back pressure was left on the specimen for several hours. The specimen was then isotropically consolidated and sheared.

Calibration of Measurement Devices

Several measuring devices had to be calibrated to ensure accurate readings throughout testing. First, in order to ensure that all pressure gages were reading accurately, the gages were hooked up in parallel to the air supply line. Various pressures were applied and the pressure gages were each connected to ensure that the same readings were displayed. No problems were experienced with the pressure gages. A Mitutoyo digital dial gage was used in order to measure axial deflections. The accuracy of the dial gage was tested with a Mitutoyo digital micrometer. Both readings on the dial gage and micrometer were in unison. The volume change device was also calibrated in order to convert the readings recorded into actual volume. The calibration was done by opening one side of the drainage valve and letting the water drain into a graduated cylinder. By recording the measured water and the readings on the volume change device, a calibration constant was attained.

In order to calibrate both the internal embedded top cap load cell and the external load cell, a proving ring was used. Although the manufacturer of the proving ring provided a calibration sheet, the calibration was double checked in the laboratory prior to the calibration of the load cells. By using a hanger system set-up (shown in Figure 3.2.5), the deflection on the proving ring was measured as weights were added to the hanger. The additional weight of the system was excluded and the deflection and load were calibrated. It was found that the manufacturer's proving ring calibration sheet corresponded to the experimental results.

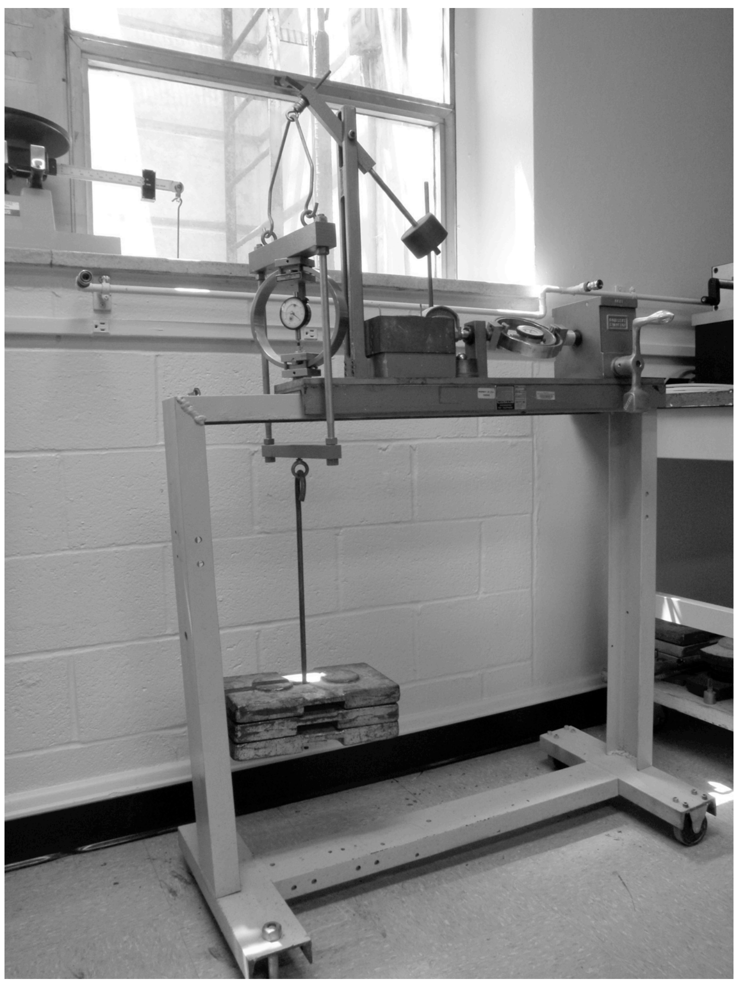

Figure 3.2.5. Calibration of Proving Ring Set-up.

Once the proving ring was confirmed to be accurate, the external load cell was calibrated in compression with the proving ring by setting it up in a loading machine. With the load cell and proving ring in place, the applied load was calculated with the proving ring calibration sheet and the corresponding reading on the external electronic load signal measuring device. With these readings, the calibration curve was attained. A similar procedure was employed for the embedded top cap load cell. However, if at any time, the load cell was unscrewed from the top cap, the calibration was checked and changed as needed. Any changes made to the top cap can affect the calibration of the embedded load cell and therefore, a new calibration was performed. For the one extension test performed, the load cell was also calibrated in extension.

Corrections and Stress-Strain Calculations

The cross sectional area was corrected during consolidation and shearing of the specimen. This correction assumed that the specimen deformed as a right prism. Lubricated ends were placed on the specimen top and base caps to keep the shape of the specimen as a rectangular prism as much as possible, minimizing bulging. The area correction is given by equation 3.2.1.

$$A_c = A_o\left(\frac{1-\varepsilon_v}{1-\varepsilon_1}\right) \qquad \text{Eq. 3.2.1}$$

where A_c is the current area of the specimen, A_o is the initial area of the specimen, ε_v is the volumetric strain and ε_1 is the axial strain.

It is well established that membranes provide resistance to the applied loads during specimen shearing. Therefore, it may be necessary to account for this resistance.

According to Degroff et al. (1988), a Poisson's ratio of 0.5 and a Young's modulus of 1400 kPa can be used for membrane corrections. Assuming the membrane is volumetrically incompressible, the following formula can be used to attain the axial load carried by the membrane:

$$F_m = \frac{E_m \varepsilon_m A_m}{(1-\varepsilon_m)} \qquad \text{Eq. 3.2.2}$$

where F_m is the axial load carried by the membrane, E_m is the elastic modulus which is 1400 kPa, ε_m is the axial strain, and A_m is the initial cross-sectional area of the membrane.

The membranes used for triaxial testing were 0.03cm thick and 10cm in diameter. The difference in friction angle at 5% axial strain was less than .09° and therefore, the correction was found to be negligible.

In the only conventional triaxial extension test performed, the piston was rigidly screwed into the piston top cap. Therefore, the chamber pressure applied to the specimen was absent across the area of the piston that is going out from the top cap. This caused an uplift force and a reduction of axial stress on the specimen. The piston uplift can be calculated by

$$F_p = \sigma_3 A_p = \left(u_b + \sigma'_3\right) A_p \qquad \text{Eq. 3.2.3}$$

where F_p is the piston uplift and σ_3 is the chamber pressure which equals the sum of the back pressure, u_b and the effective confining pressure, σ'_3. The weight of the load cell as well as the weight of the top cap was also included in calculating the vertical forces acting on the specimen during triaxial extension.

With the lubricated ends on top and bottom caps, uniform deformations developed well into the post-peak region. Therefore, the effect of non-uniform deformations did not affect the strength of the sand and no corrections were made. The bushing on the true triaxial machine allowed for the piston to slide easily up and down and therefore, no friction on the piston was accounted for in the calculations.

Membrane penetration effects in flexible membranes can sometimes cause a systematic error in calculations and must be checked. Fine Nevada sand was chosen in order to minimize membrane penetration. For drained tests, membrane penetration affects only the volumetric strain and does not affect the effective stress state of the sand. In general certain aspects affect membrane penetration. Particle size is one of the most important factors. The mean grain size, D_{50} is assumed to be representative of the soil being used. Particle shape and the soil's relative density have a minor affect per Baldi and Nova (1985). The effective lateral stress, σ_3' can play a large role for membrane penetration. Baldi and Nova (1985) derived an equation to measure the effects of volume change due to membrane penetration considering the average diameter grain size, effective confining pressure, diameter of the specimen, Young's Modulus and the thickness of the membrane. The equation is as follows:

$$V_m = \frac{d_g}{D} V_0 \left[\frac{\sigma_3^{'} d_g}{E_m t_m} \right]^{1/3} \qquad \text{Eq. 3.2.4}$$

where V_m is the membrane penetration volume; d_g is the average diameter grain size (taken from D_{50} in a grain size distribution analysis); D is the initial diameter of the specimen; V_0 is the initial volume; σ_3' is the effective confining pressure; E_m is Young's modulus for the membrane and t_m is the thickness of the membrane.

The D_{50} of the Fine Nevada Sand used in the experimental program was calculated to be 0.022cm (see Figure 3.1.1). Since the specimens were square, an equivalent diameter for the area of the specimen was calculated to be 8.56cm. The initial volume was 1097.44 cm^3. The final effective confining pressure for most of the true triaxial tests was 50 kPa. As previously noted, the thickness of the membranes were 0.03cm and Young's modulus was taken as 1400 kPa. With these parameters, the V_m is 0.41cm^3, where $\Delta\sigma_3$'=25 kPa. Depending on the total volume change for different tests, this value varies from 1 to 3% of the total volume change. Thus, membrane penetration effects were considered to be negligible for triaxial and true triaxial tests.

Although all efforts were made to have specimens with the same void ratio, in some cases, it was not possible. Any slight deviation in method during air pluviation can affect the amount of sand that went into the molds during the specimen preparation. Nonetheless, an equation relating friction angles to void ratio allows for all friction angles to be calculated according to a certain void ratio. By using the equation,

$$e \bullet \tan\varphi = \text{constant} \qquad \text{Eq. 3.2.5}$$

where e is the void ratio, φ is the friction angle and c is a constant, corrected friction angles could be attained. All friction angles were corrected to a void ratio of 0.53.

3.3 Triaxial Compression Tests with α=0° and α=90°

Lade (2007) suggests that is preferable to have three triaxial compression tests on vertical specimens and three triaxial compression tests on horizontal specimens in order to be able to determine the parameters needed for Lade's failure criterion for soils (see Equation 2.4.4). These three parameters are: η_0, m, Ω_1. Therefore, drained compression tests were performed at different confining pressures in both the first and third sector, i.e. on vertical and horizontal specimens.

Preliminary tests were run as trial experiments while setting up the triaxial apparatus. These tests experienced serious problems, not producing reliable results and are therefore not presented. However, Tests 1, 2, 3 and 4 are summarized in Table 3.3.1. Test 1 is also Test TT#1 that will be presented in Chapter 5.

Table 3.3.1. Triaxial Compression Tests with α=0°.

Date	Test	α	σ'_3	e	b-value	σ_1/σ_3
3/21/11	1, TT#1	0°	50.00	0.522	0.00	5.28
4/1/11	2	0°	25.00	0.537	0.00	6.29
4/4/11	3	0°	130.00	0.542	0.00	4.57
4/5/11	4	0°	70.00	0.542	0.00	4.84

The stress strain and volume change curves are presented in Figure 3.3.1 and Figure 3.3.2, respectively.

As the confining pressure increases, the friction angle decreases. With lower confining pressure, there is also more total dilation. The rates of dilation are all very similar in the four tests. Tests 1, 2, 3 and 4 had horizontal bedding planes (where α=0°) and are located in the first sector in the octahedral plane.

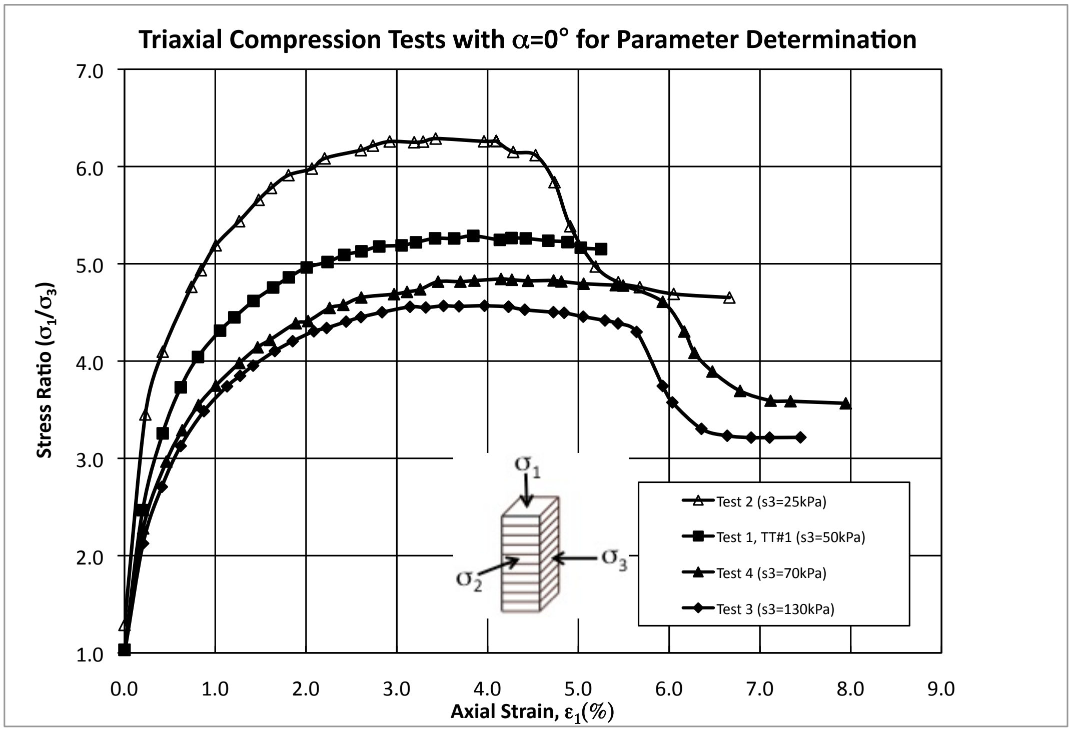

Figure 3.3.1. Triaxial Compression Stress-Strain Curve for $\alpha=0°$ Tests.

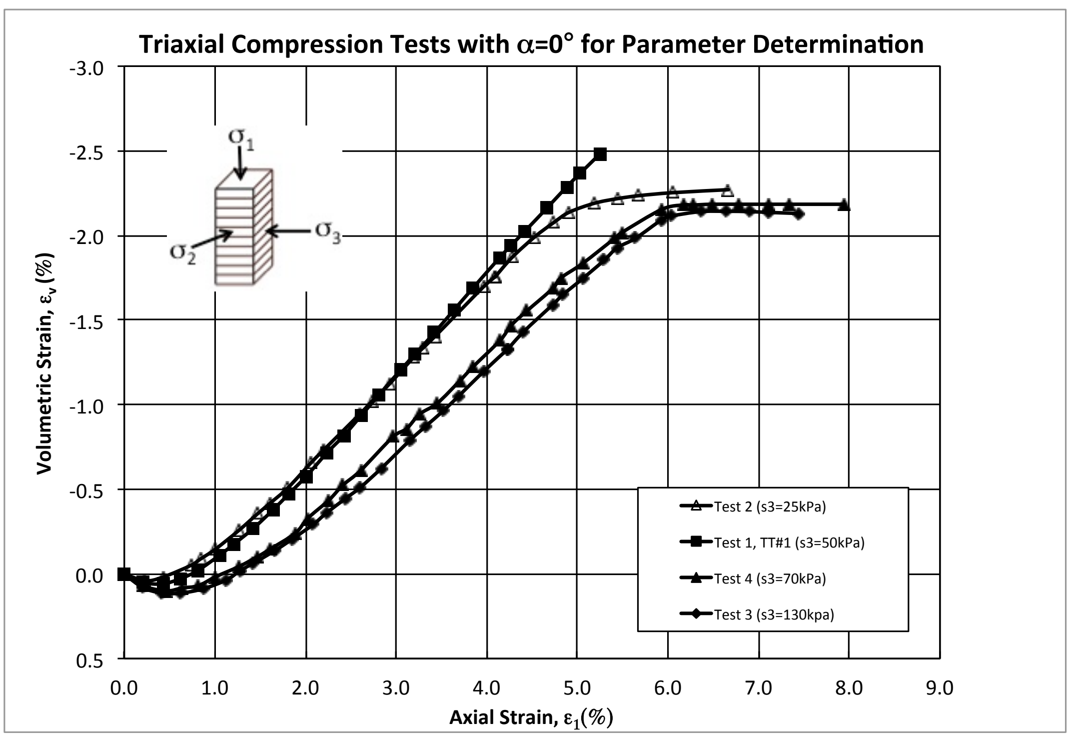

Figure 3.3.2. Triaxial Compression Volumetric Strain for $\alpha=0°$ Tests.

Table 3.3.2. Compression Tests with α=90°.

Date	Test	α	σ'_3(kPa)	e	b-value	σ_1/σ_3
11/19/10	5	90°	25.00	0.533	0.0	4.47
11/24/10	6	90°	75.00	0.538	0.0	4.24
12/4/ 0	7	90°	130.00	0.532	0.0	4.01
2/25/11	8,TT#13	90°	50.00	0.540	0.0	4.13
1/17/11	9, W1	90°	101.00	0.534	0.0	4.15
12/21/10	10, A7	90°	99.00	0.532	0.0	4.06

Six additional tests were performed with vertical bedding planes (where α=90°). Table 3.3.2 summarizes these tests. Test 8 is also presented as Test TT#13 in the True Triaxial Tests in Chapter 5. Tests 9 and 10 are also presented as Tests W1 and A7 in Chapter 4, respectively. Since these tests were typical compression tests with α=90° bedding planes, the data was also used to supplement the other tests in determining the parameters.

The stress strain and volume change curves are presented in Figure 3.3.3 and Figure 3.3.4, respectively.

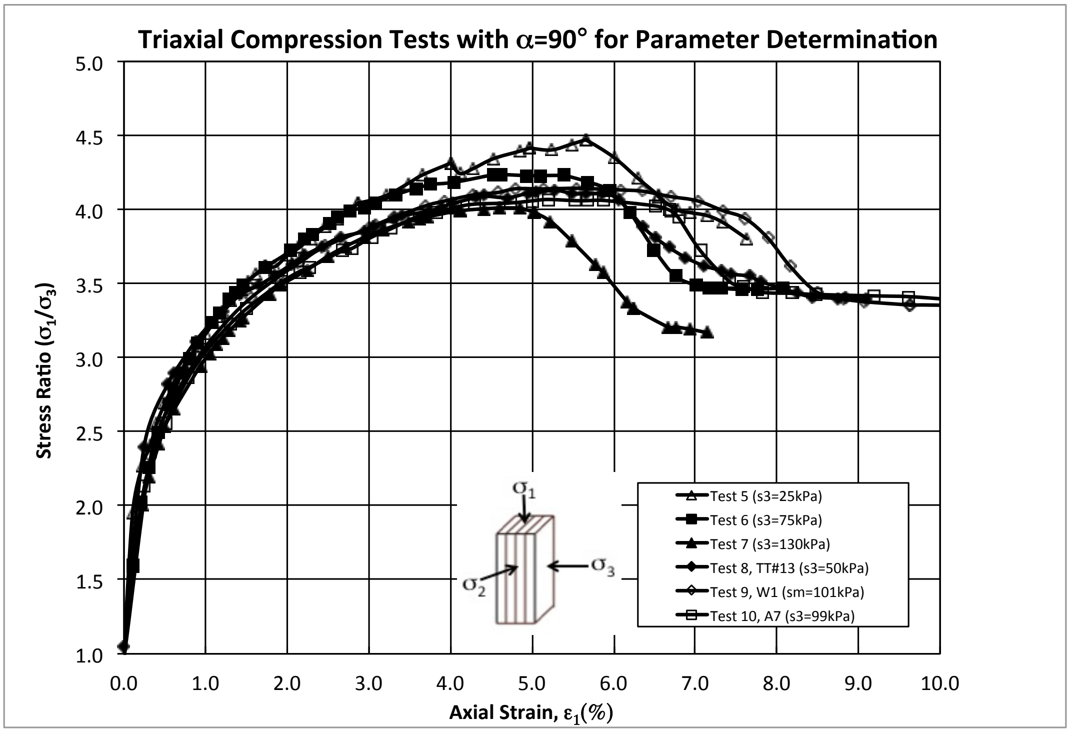

Figure 3.3.3. Triaxial Compression Stress-Strain Curve for α=90°.

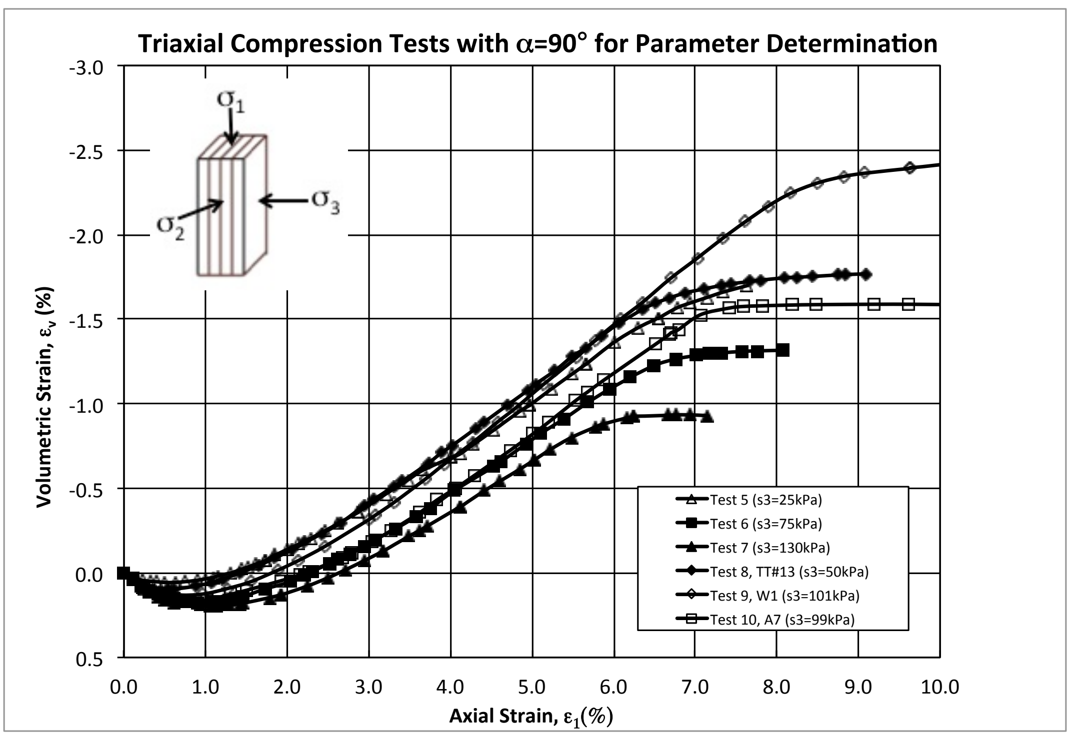

Figure 3.3.4. Triaxial Compression Volumetric Strain for α=90° Tests.

Tests 8(TT#13), Test 6, Test 9(W1) and Test 10(A7) have very similar stress-strain behavior even though they have a difference of up to 50 kPa in effective confining pressure. The same trend is seen in the α=90° tests as in the α=0° tests, i.e. decreasing friction angles with increasing confining pressures. In general, greater dilation is seen with lower confining stress for the α=90° tests. When comparing and analyzing the tests with horizontal versus vertical bedding planes, it was seen that tests with vertical bedding planes (α=90°) have lower stress ratios and friction angles than those with horizontal bedding planes (α=0°). At σ'_3=25 kPa, the friction angles change from 46.6° to 39.4°(horizontal to vertical). At σ'_3=130 kPa, the friction angles change from 39.9° to 36.9°. Thus, the cross-anisotropy is more pronounced at low, rather than high, confining pressures. This shows the cross-anisotropy of the soil and is consistent with results from previous studies that have been presented in Chapter 2.

3.4 Conventional Extension Test

One extension test (Test 11, W5) was performed where the confining pressure was kept constant (at 101 kPa) and the specimen was extended instead of traditionally compressed. This specimen had vertical bedding planes where α=90°. The set-up for this test changed slightly from the previous triaxial compression tests that were performed. In this particular test, a load cell was hung from the triaxial loading machine by a metal rod. Some movement was allowed so that the rod was freely able to rotate to minimize any moment on the specimen. The rod connected to the top of the load cell, was recalibrated for extension. On the bottom side of the load cell, an adaptor piece connected the load cell to the piston. The load cell located in the top cap was removed and a special piece where the piston could be screwed on was fastened into the top cap. The triaxial set up was clamped down at three points to the loading machine to ensure that the cell did not get lifted off the pedestal of the loading machine. The same procedure was performed for the freezing process and set-up of the specimen as was described previously. However, water pressure was used instead of air pressure for the confining cell pressure and a slower strain rate of 0.05 mm/min was used. The stress strain and volume change curves are presented in Figure 3.4.1 and Figure 3.4.2, respectively. Test 11 data is also presented in Chapter 4 as Test W5.

The weight of the load cell, the top cap and the vertical uplift on the piston were considered in calculating the total load acting on the specimen. There was no visible necking at the end of the test and shear bands along the top half of the specimen developed at about 1.3% strain. As can be seen from Figures 3.4.1, failure clearly occurred around 1.3% axial strain and the specimen had a friction angle of 35.9°. Conventional extension tests performed in this manner are notoriously unreliable and inherently unstable due to the concentration of stresses along the weakest part of the specimen. Lade and Wang (2012) describe and explain attempts made to achieve uniform stresses and strains on sand specimens in conventional extension tests.

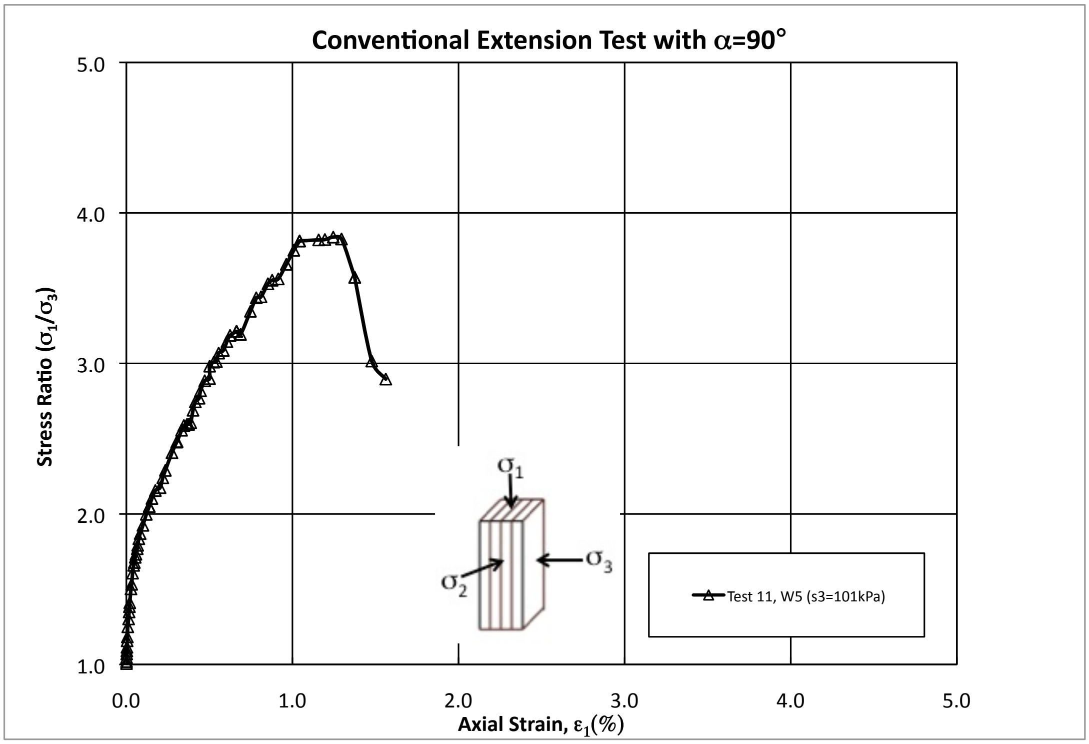

Figure 3.4.1. Triaxial Extension Test 11,W5 Stress-Strain Curve for α=90°.

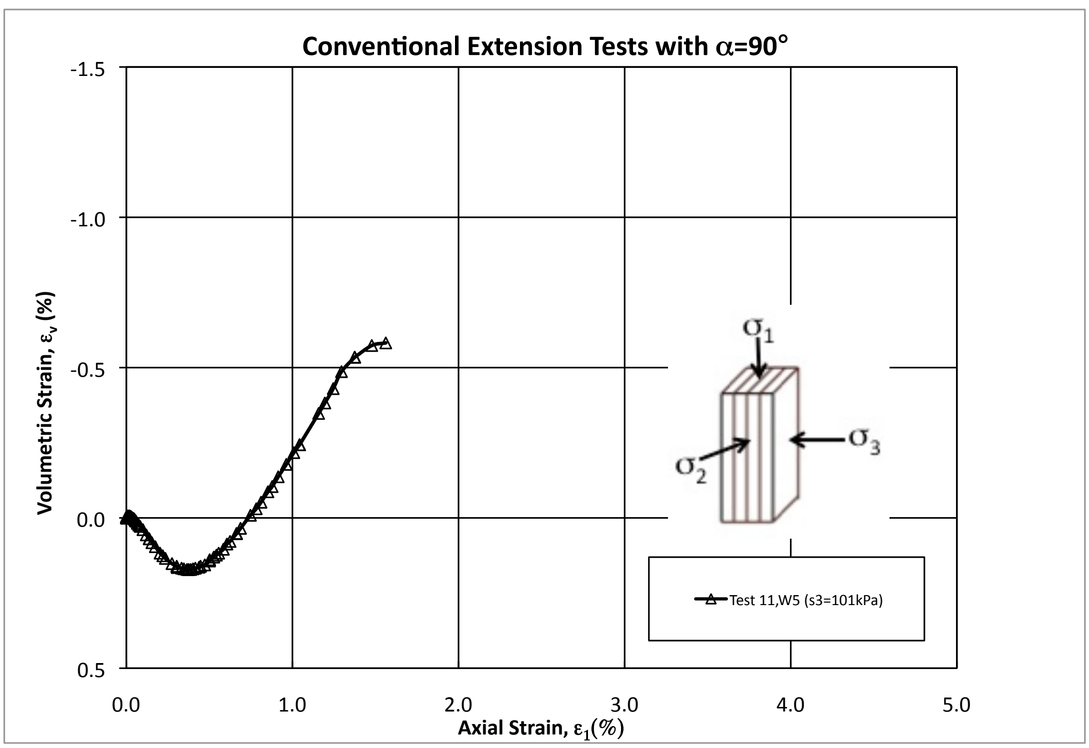

Figure 3.4.2. Triaxial Extension Test 11,W5 Volumetric Strain for α=90°.

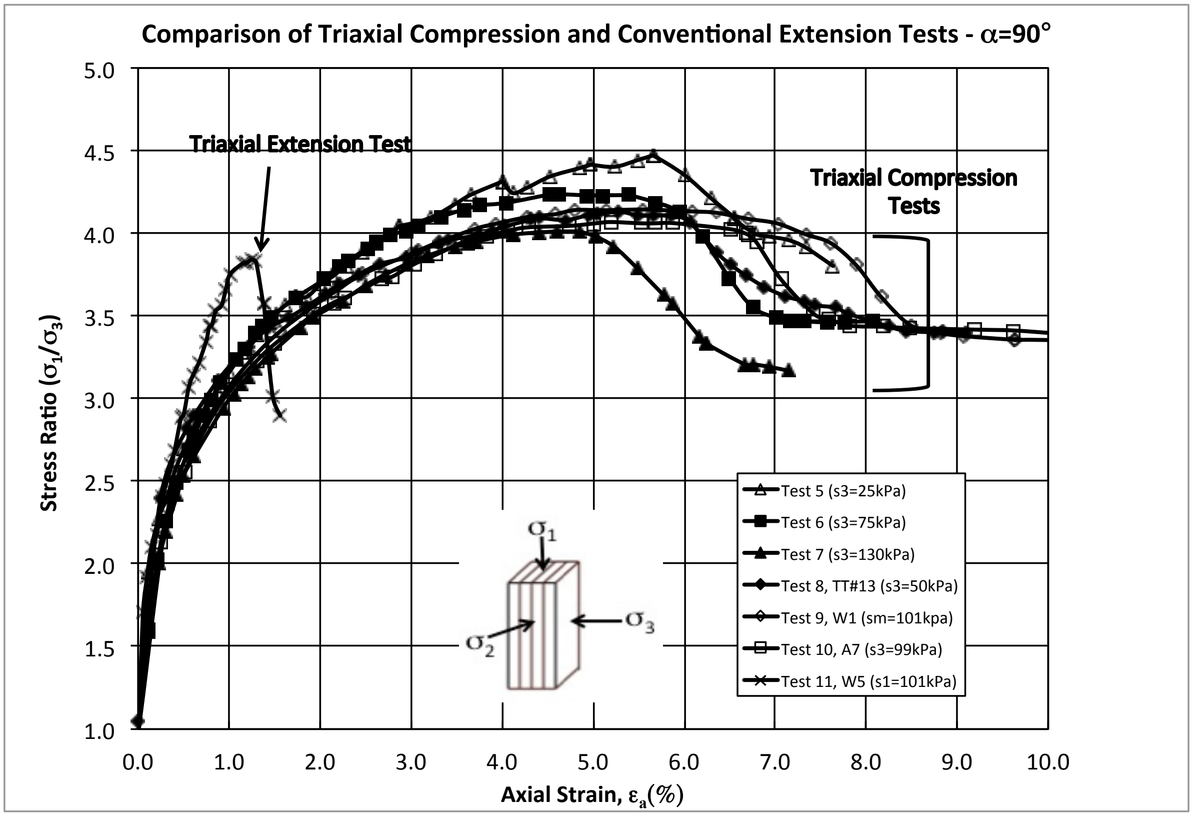

Figure 3.4.3. Triaxial Compression and Extension Stress-Strain Curve for α=90° for Tests 5-11.

Test 11(W5) showed substantially different stress-strain behavior and strength as compared to the previously discussed triaxial compression tests with α=90° (Tests 5-8). Figure 3.4.3 shows that Test 11 has lower effective stress ratio at failure corresponding to lower friction angle than any of the corresponding triaxial compression Tests 5-10. Because of the conclusion from many investigators (such as Roscoe et al. (1963), Yamamuro and Lade (1995), Lade et al. (1996)) in which they explain that conventional triaxial extension tests results cannot be relied upon to produce accurate and high quality results, only Tests 5-8 data will be used to determine the parameters necessary for the cross-anisotropic failure criterion for Fine Nevada Sand.

3.5 A Comment for Specimen B-value and Saturation

When performing triaxial tests, the B-value, which measures the saturation of the specimen, was determined. This was done once the specimen was completely thawed and a back pressure of 100 kPa had been applied for a minimum of two hours. At this point, the cell and specimen pressure readings on the transducer (set up on the volume change device) were recorded. Then, the valve to the volume change device was closed (creating an undrained condition) and the cell pressure was raised by about 5 kPa. The new readings were recorded and then the cell pressure was lowered to the original cell pressure. The drainage valve was re-opened. The B-value was determined using the following equation:

$$B = \frac{\Delta u}{\Delta \sigma_3} \qquad \text{Eq. 3.5.1}$$

where $\Delta\sigma_3$ is the imposed change in all around isotropic cell pressure and Δu is resulting change in pore pressure obtained from undrained conditions.

A B-value of 1.0 shows a fully saturated soil. However, a number of factors strongly affect the value of B and these factors may cause a B lower than 1. In the triaxial compression tests, as well as the tests performed in the true triaxial apparatus, B-values may be lower than unity when calculated. These values measured in the initially frozen specimens ranged from 0.2 to 0.8 for different tests. As described previously, the specimens were saturated fully prior to freezing. When thawed, they were placed under vacuum. During this procedure, it is possible that some small amounts of water could have been sucked out into the bubble chamber that was hooked up to the vacuum. De-aired water was introduced into the sample to get rid of any air that might have been trapped in the specimen, as well as to fully saturate the lines leading to the volume change device. During this procedure an air bubble might have stayed in the specimen and not dissolved under the 100 kPa back pressure. This would definitely affect the calculated B value. In order to determine the degree of saturation of the specimens, a slightly different procedure was performed.

The B-value was calculated in the same manner as was previously described but instead of lowering the cell pressure back down to the original value, the drainage valve was opened and the volume change that occurred was measured. The saturation of the specimen could then be calculated by using the equation:

$$S = \left[1 - \left[\frac{u_2}{n} \left(c_d + \frac{f_m}{V_o} \right) \left(\frac{1+B}{B} \right) \right] - \frac{f_s}{V_o} \right] \qquad \text{Eq. 3.5.2}$$

where u_2 is the pore pressure measured after increasing the cell pressure, n is porosity of the sand, c_d is the volume compressibility of the soil skeleton, V_0 is the initial volume of the specimen, B is the measured B-value (from Eq. 3.6.1) and f_s is the flexibility of the pore pressure measuring system. Tubings, valves, etc. introduce factors that affect f_s. The measured volume change part of Eq. 3.5.2 can be substituted as follows:

$$\left(c_d + \frac{f_m}{V_o}\right) = \frac{\Delta V_{measured}}{V_o \Delta\sigma_3}$$

Eq. 3.5.3

The porosity of Fine Nevada Sand was calculated to be 0.35 and f_s = 5 x 10^-7 cm/kPa was used to determine the saturation of the specimens after attaining the B-value. All specimens had a saturation of over 96%, which shows that the specimens were sufficiently to produce reliable test results.

3.6 Conclusion

In conclusion, ten drained triaxial compression test and one drained triaxial extension tests were performed in order to attain certain parameter data needed for modeling. Through a special preparation, saturation and freezing technique, tests were performed with both vertical and horizontal bedding planes. The triaxial compression tests, performed at increasing confining pressures, all showed typical stress-strain and volumetric change behavior. Triaxial compression tests with α=90° all showed very similar friction angles. One traditional extension test performed where α=90° failed at a very short strain to failure and lower friction angle.

4. Triaxial Compression Tests with Varying Confining Pressure

4.1 Introduction and Background

Section 3.2 and 3.3 described Tests 1-8 on specimens with both horizontal (α=0°) and vertical (α=90°) bedding planes. When studying anisotropy, the difference in friction angle for the specimens with vertical bedding planes under different confining pressures was not that large, only 3.0°compared to a 7.2° difference for tests with horizontal bedding planes.

A possible explanation for the small difference in friction angle may be found in the amount of strain to failure of the specimens. Tests 5, 6 and 7 failed between 5 and 6% axial strain. It was hypothesized that the possible rotation and movement of sand grains during this large amount of strain could have allowed the sand grains to rearrange themselves before failure and therefore, the effects of anisotropy could appear to be less significant. In order to test this hypothesis, tests with varying stress paths and consequent varying strain-to-failure were performed.

In the literature, almost no previous research was found on tests performed with varying stress paths. Only theoretical and numerical results have been presented by Ng (2004, 2005). Ng (2005) studied the behavior of granular material made up of different densities subjected to different stress paths using numerical models. The discrete element method was used to simulate experiments on specimens that were made up of ellipsoid particles.

Different densities were used to show the air pluviation method for a specimen in a rectangular prism and then different stress paths were employed to study the behavior and strength of the specimens.

Ng (2005) found that the axial compression simulation resulted in the lowest shear strength. The plane strain simulation had the highest friction angle for all samples and the difference between the plane strain and axial compression strengths increased with the density of the sample. He also observed that the dilatancy component of shear strength depended on the mean stress at failure. A greater dilatancy component was obtained when there was a large difference between the mean stress at failure and the initial mean stress.

With only this limited numerical research available, an experimental program was designed to study the effects that the stress path may have on the shear strength of soil. In the sections that follow, the experimental program will be described and the results will be presented.

4.2 Experimental Program

With the same triaxial apparatus that was used for the tests described in Chapter 3, a series of 13 tests were performed on tall prismatic specimens with vertical (α=90°) bedding planes. The specimens had the same dimensions as in the previous tests described (7.6cm in length, 7.6cm in width and 19cm in height). The deposition, freezing and set-up of the specimens were also done the same way as previously presented in Section 3.1. The experimental program can be divided into two main categories: 1) 8 tests performed with confining pressure supplied by compressed air and 2) 5 tests performed with confining pressure supplied by water. Stress paths with different directions in the triaxial plane were employed for each test. The stress path employed for each specimen was varied by changing the confining pressure in the triaxial cell.

In order to accurately change the confining pressure in the triaxial cell, the cell pressure (whether air or water) was measured by a pressure transducer, which was hooked up to a digital display. This pressure transducer and display was also used in calculating the saturation of the specimen. A pressure regulator was manually regulated to certain pressures and the corresponding readings on the display were recorded. With these recordings, a calibration curve was attained and the confining pressure could be changed according to the desired stress path.

A program was set up to calculate the real time mean stress on the specimen, taking account of vertical load, axial strain, and volume change. Readings from the vertical deformation gage, the vertical load cell and the volume change device were recorded. With these readings, the current area, resulting deviator stress and major principal stress were calculated. Then, the current mean principal stress was calculated for each step in loading. Depending on what stress path direction was desired, the required confining pressure was calculated. An equation for the change in confining pressure required, $\Delta\sigma_3$, was used for its calculation in terms of the increment in mean confining stress, $\Delta\sigma_m$, and the increment of major principal stress, $\Delta\sigma_1$. The pressure gage was manually adjusted until the digital read-out displayed the correct corresponding pressure. This cycle was performed throughout the entire test as fast as physically possible. The strain rate for all tests varied from 0.01mm/min to 0.05mm/min ensuring a slow enough strain rate to manually input the data and adjust the confining pressure.

4.3 Stress Paths for Tests performed with varying σ_3 with air

The first eight tests had a variety of stress paths along the hydrostatic axis of the triaxial plane. Figure 4.3.1 shows the stress paths that were followed for Tests A1-A8. The order by which they are plotted is by increasing mean principal stress. Tests A5 and A8 overlay each other as they follow the same stress path. This is also true for Tests A1 and A6. These tests were repeated to ensure repeatability in the testing.

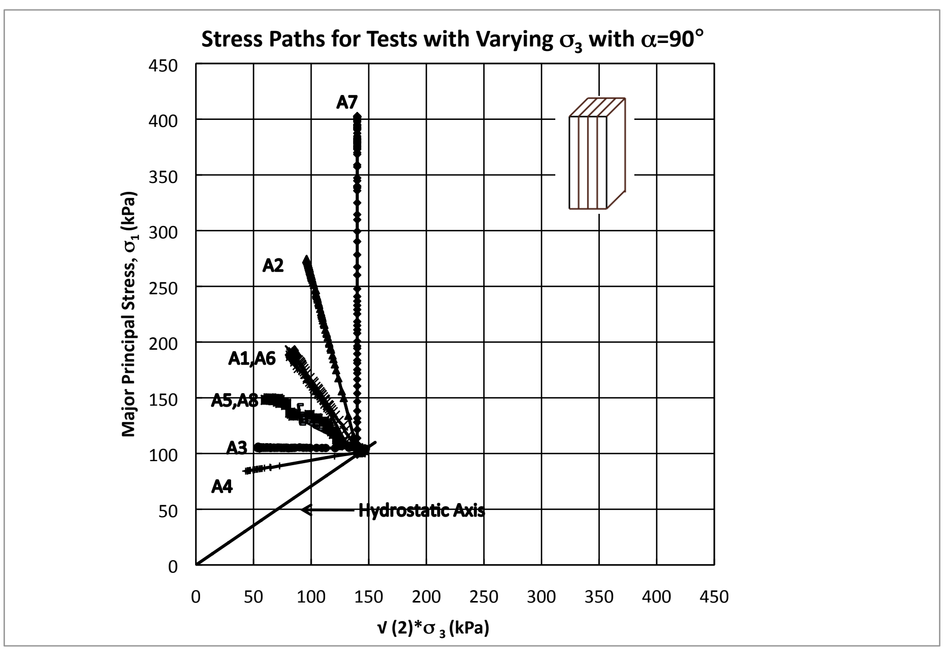

Figure 4.3.1. Stress paths along hydrostatic axis for Tests A1-A8 on Triaxial Plane.

4.4 Stress Paths for Tests performed with varying σ_3 with water

When compared to water pressure, air pressure takes a little bit of time to fully be applied in the cell. There is somewhat of a buffer time between the increase/decrease from the manual regulator and the actual applied pressure inside the cell. In hopes that the testing would be more stable and to get rid of this delay, tests were re-run on certain similar stress paths with water in the triaxial cell. The inside load cell was removed and the cell was completely sealed to be watertight. The line to the transducer was also completely saturated and careful attention was paid to ensure that no air bubbles were present in the line. This was important as any bubbles might affect the displayed pressure transducer reading for the confining pressure and the cell pressure was adjusted in accordance with the displayed reading. The stress paths that were followed for the tests with water in the triaxial cell are presented in Figure 4.4.1.

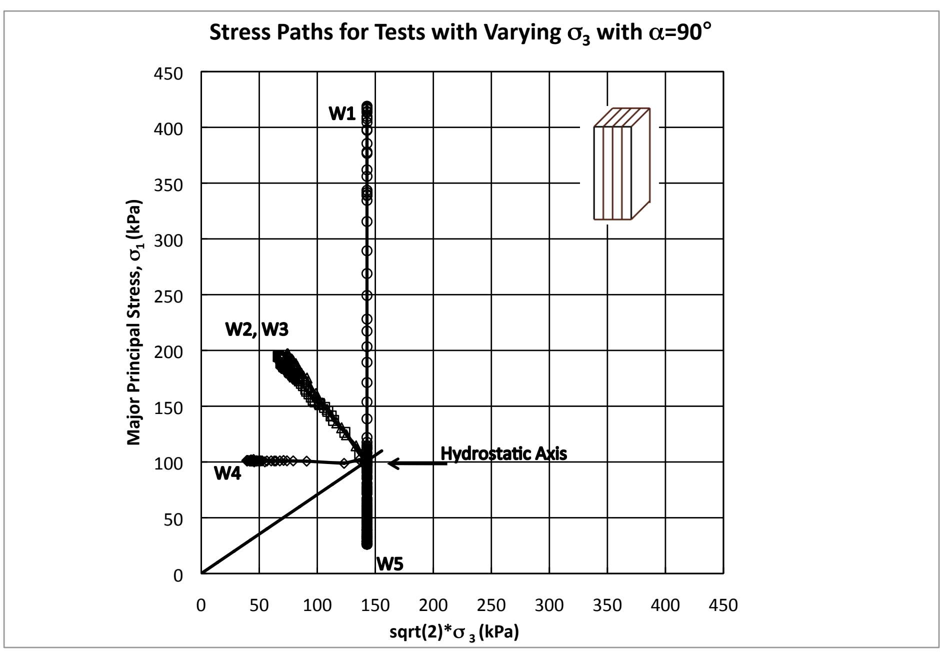

Figure 4.4.1. Stress paths along hydrostatic axis for Tests W1-W5 on Triaxial Plane.

4.5 Instability of Tests with varying σ_3 when approaching Failure

When performing the tests described above, large instabilities were encountered as the specimen approached failure. These instabilities were seen for tests where the confining pressure, σ_3 was varied. Traditional compression and extension tests (tests that maintain σ_3 constant) did not experience this instability. Because of the instability that was seen in the initial trial test, the tests were performed at very slow strain rates, from 0.01mm/min to 0.05mm/min. With a slower strain rate, the resulting incremental deviator stress was in turn less and the confining pressure was adjusted accordingly with smaller incremental changes. As the specimen's strength increased, it behaved very stably with changes in confining pressure that were required to follow the intended stress path. For all of the stress paths described in Section 4.3 and 4.4 (besides the conventional triaxial compression and extension tests), as the deviator stress increased, the confining pressure was lowered. How much the confining pressure was lowered, depended on the stress path being followed. As long as the deviator stress increased and the specimen was able to take additional stress, there were no instabilities experienced. However, as the specimen began to fail, the resulting deviator stress became lower and in order to stay on the same stress path, the confining pressure should be increased. With this increase in confining pressure, the specimen gained strength. As the specimen's new strength was recorded and the calculated σ_3 was known, then the confining pressure once again had to be lowered. Since it was already at/near failure, the specimen would lose strength after experiencing the lower confining pressure and would therefore need a higher confining pressure to stay along stress path. Examples of this behavior are shown in

Figures 4.5.1 and 4.5.2. These figures compare two types of tests, one done with air as confining pressure, the other with water, both of which follow the same stress path.

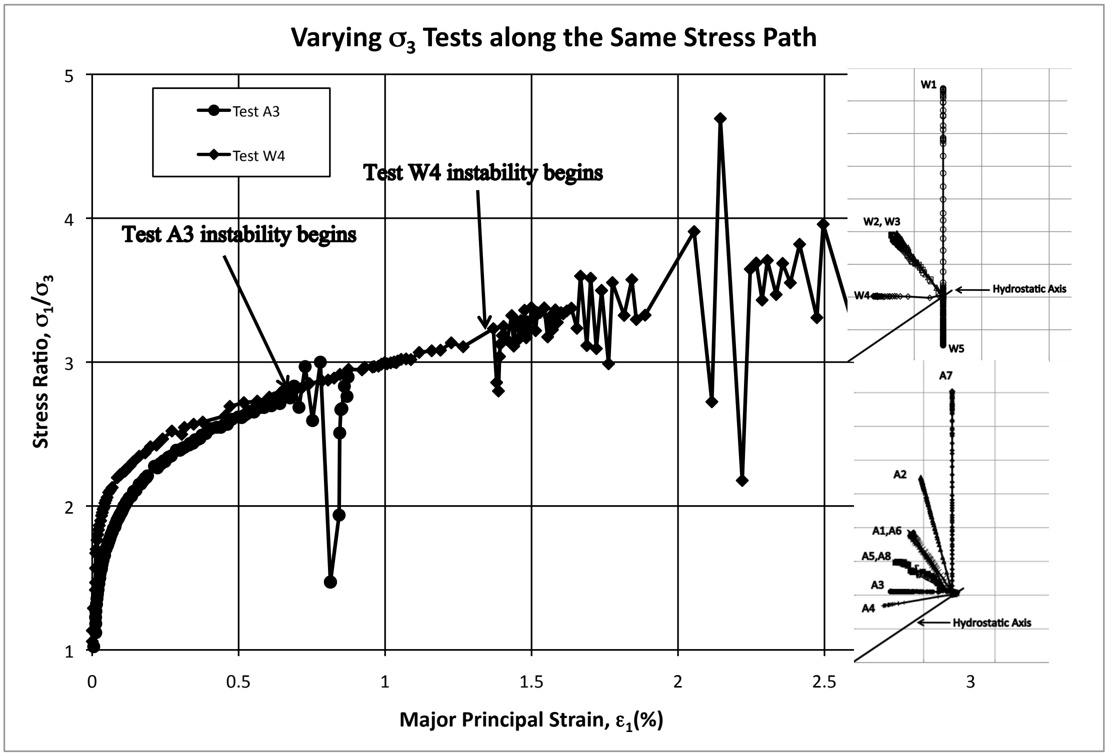

Figure 4.5.1. Stress-strain plot showing initiation of instability of Tests W4 and A3, both of which are along the same stress path.

These cycles occurring for all of the tests, created a zig-zag pattern in the stress-strain and volume change curves. The specimens were strained as far along as possible without experiencing too great a fluctuation in stress ratios. Once it was too difficult to continue along the desired stress path, the test was stopped. The lower the mean principal stress was, the harder it was to control the stress path. No shear bands were seen, as the specimens were not sheared post peak failure. In order to correct for this instability, the average was taken between fluctuating points and the friction angle was calculated from a point were there was little or no instability. An example of the corrected stress-strain curve for Test A3 is shown in Figure 4.5.3. In the sections that follow, only the corrected data is presented.

As can be seen from Figures 4.5.1 and 4.5.2, tests performed with air in the confining cell experienced greater instability than those performed with water. Although they were corrected in the manner described above, the results had too much scatter to be considered in the analysis. Therefore, only test data for tests W1 through W5 is presented in the section that follows.

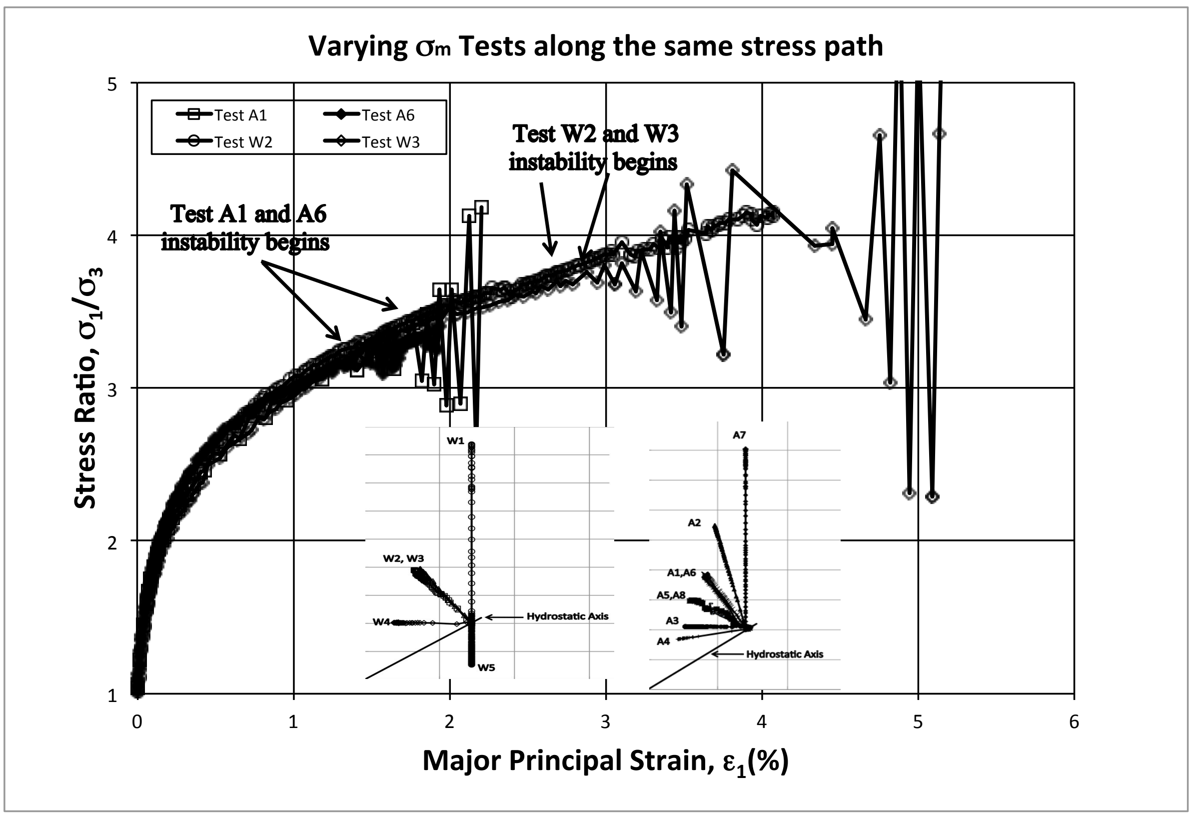

Figure 4.5.2. Stress-strain plot showing initiation of instability of Tests A1, A6, W2 and W3, all of which are along the same stress path.

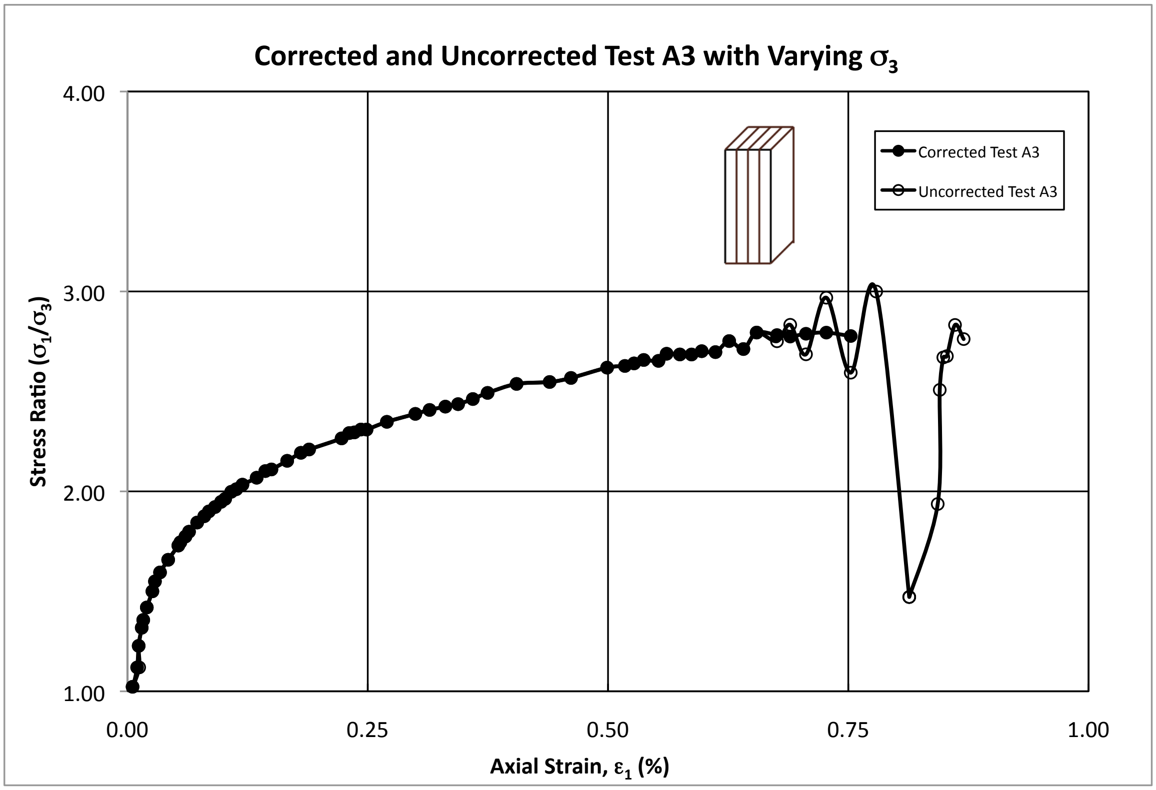

Figure 4.5.3. Stress-Strain Plot of Corrected and Uncorrected Test A3.

4.6 Stress-Strain and Volume Change behavior and of Tests with varying σ_3

The stress-strain and volume change curves for Tests W1 through W5 are presented in Figures 4.6.1 and 4.6.2. Test W2 failed with less axial strain because its confining pressure was varied. Test W1 was a conventional triaxial compression test and therefore, failed at larger strain. Test W1 is omitted from Figures 4.6.3 and 4.6.4 in order to see Tests W2-W5 in more detail. As seen from the figures, W2 through W4 have very similar stress-strain curves. W1 is a traditional compression test and W5 is a conventional extension test that has been described in Chapter 3, Section 3.4.

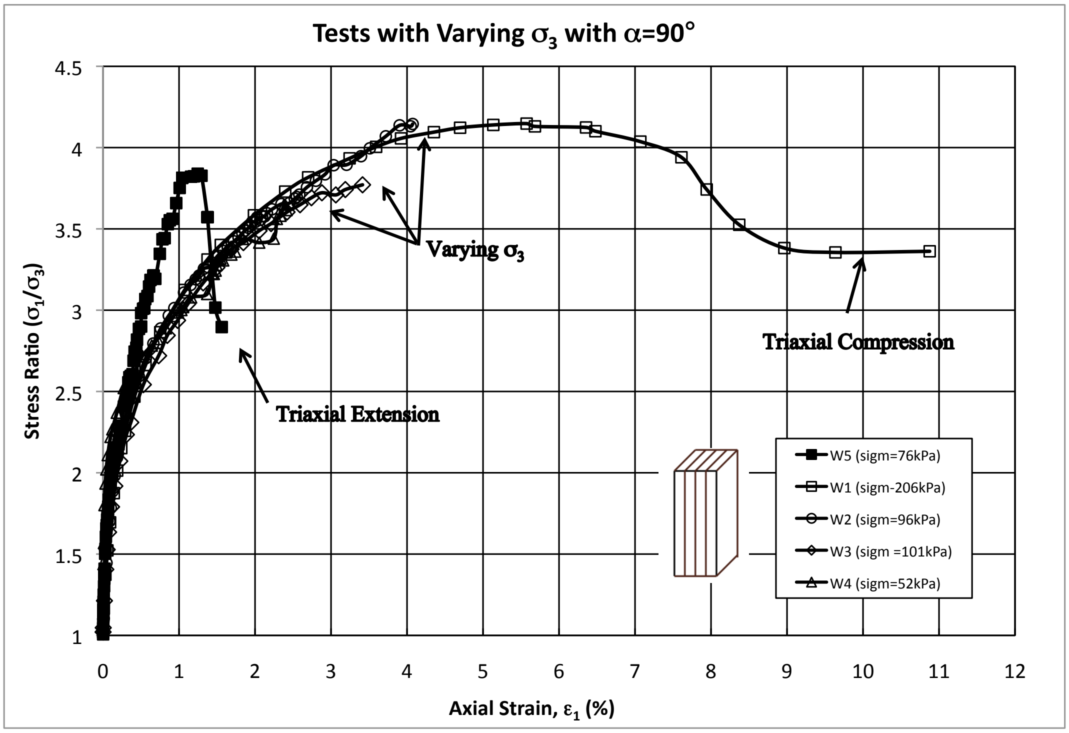

Figure 4.6.1. Stress-Strain Plots for Tests W1-W5 with Varying σ_3.

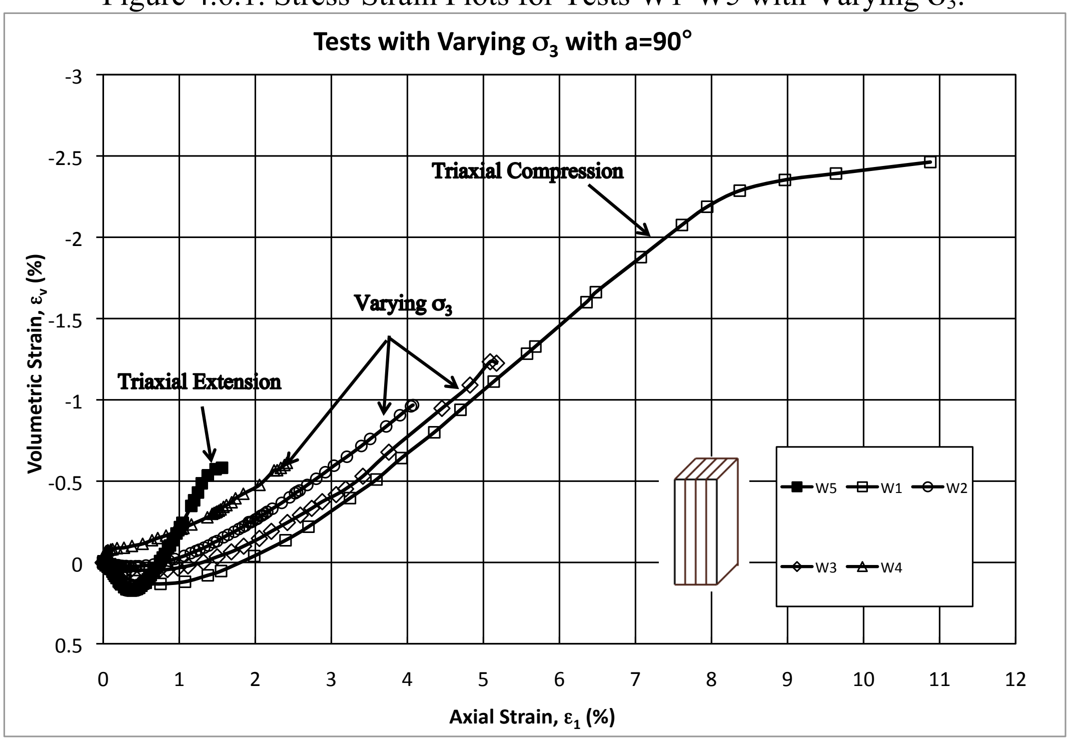

Figure 4.6.2. Volume Change for Tests W1-W5 with Varying σ_3.

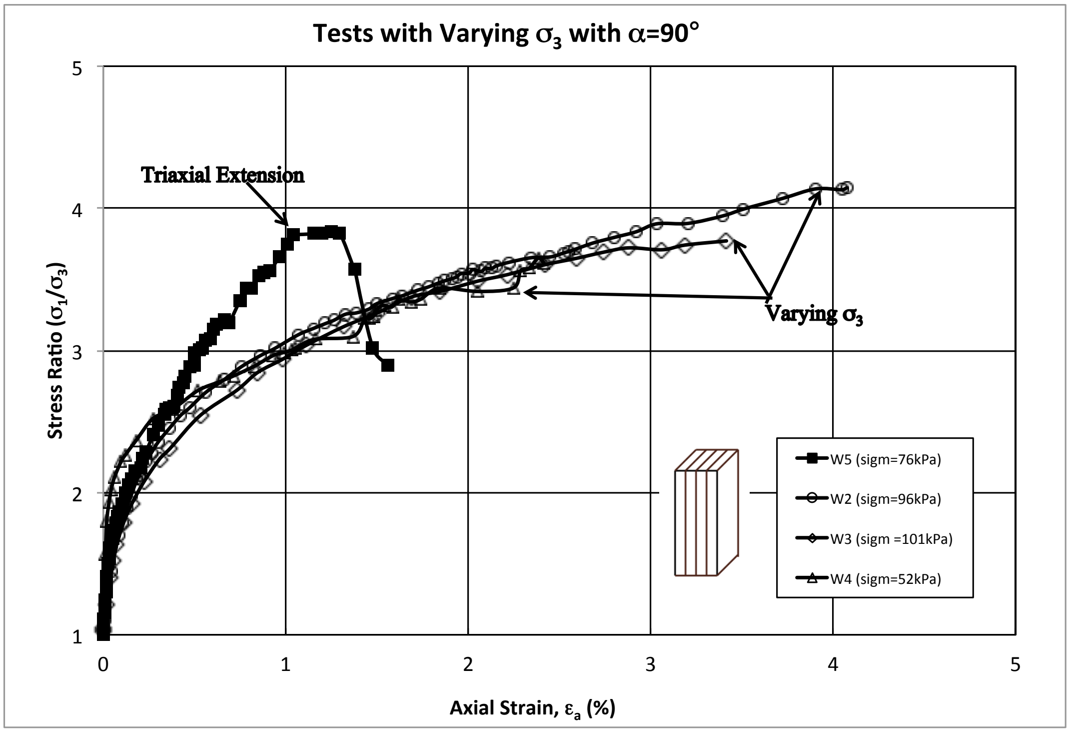

Figure 4.6.3. Stress-Strain Plots for Tests W2-W5 with varying σ_3.

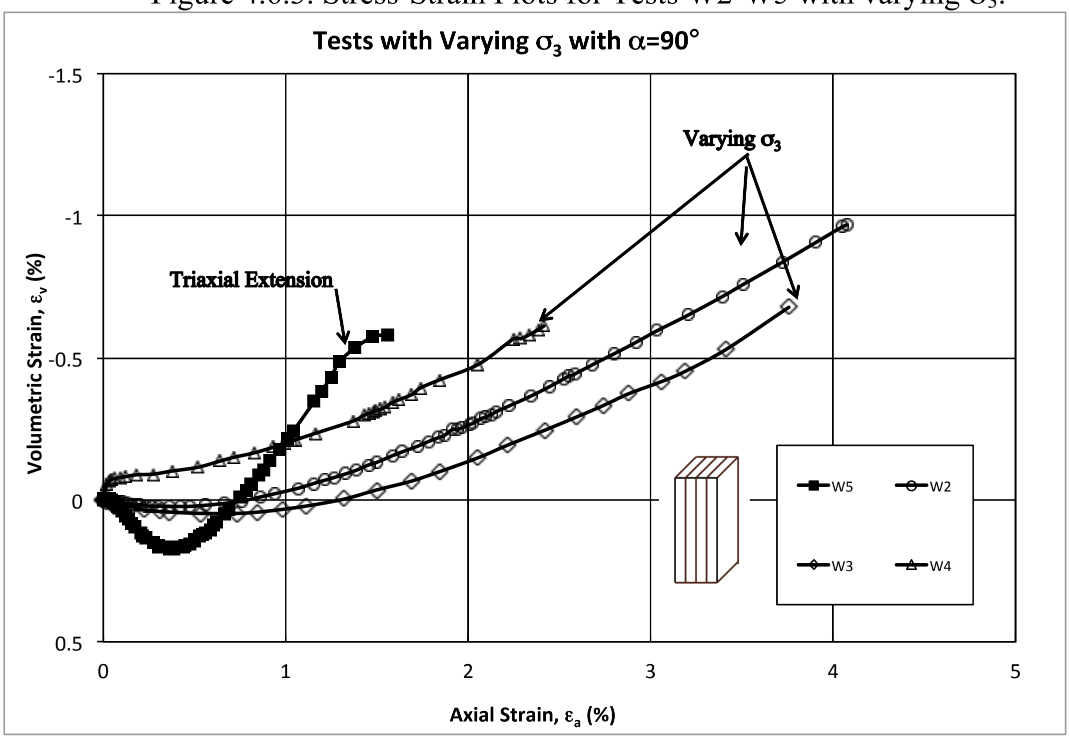

Figure 4.6.4. Volume Change for Tests W2-W5 with varying σ_3.

Tests with varying σ_3 (at σ_m=101 kPa) for α=90°

In order to be able to compare tests results from the true triaxial testing apparatus and the torsion shear apparatus (which will be discussed in great detail in Chapter 6), triaxial compression tests with constant mean normal stress at about 101 kPa were performed. As will be described later, the torsion shear tests were all performed with constant mean normal stress of 101 kPa. Therefore, several tests with stress paths perpendicular to the hydrostatic axis were performed at 101 kPa were performed with the same method described in Section 4.2, by changing the confining pressure in the triaxial cell. Because the tests done with air pressure in the triaxial cell were extremely unstable when reaching failure (as described in Section 4.5), the tests were repeated twice with water in the triaxial cell. The stress-strain curves for the tests are presented in Figure 4.6.5. For comparison and reference, the data for the torsion shear test under triaxial compression at b=0 and α=90° is also presented in Figure 4.6.5. The torsion shear test results are comprehensively analyzed in Chapter 7. The volume change versus axial strain is presented in Figure 4.6.6.

As can be seen from the stress-strain and volumetric strain plots, there is scatter among the three different tests. It must be kept in mind that two different testing apparatuses were used. Test W2 fails at about 0.8% more strain than W3. The torsion shear test fails at the least amount of major principal strain. As seen in Table 4.6.1, friction angle differences of 2.0 and 4.2 degrees are seen between Test W2 and W3 and the torsion shear test.

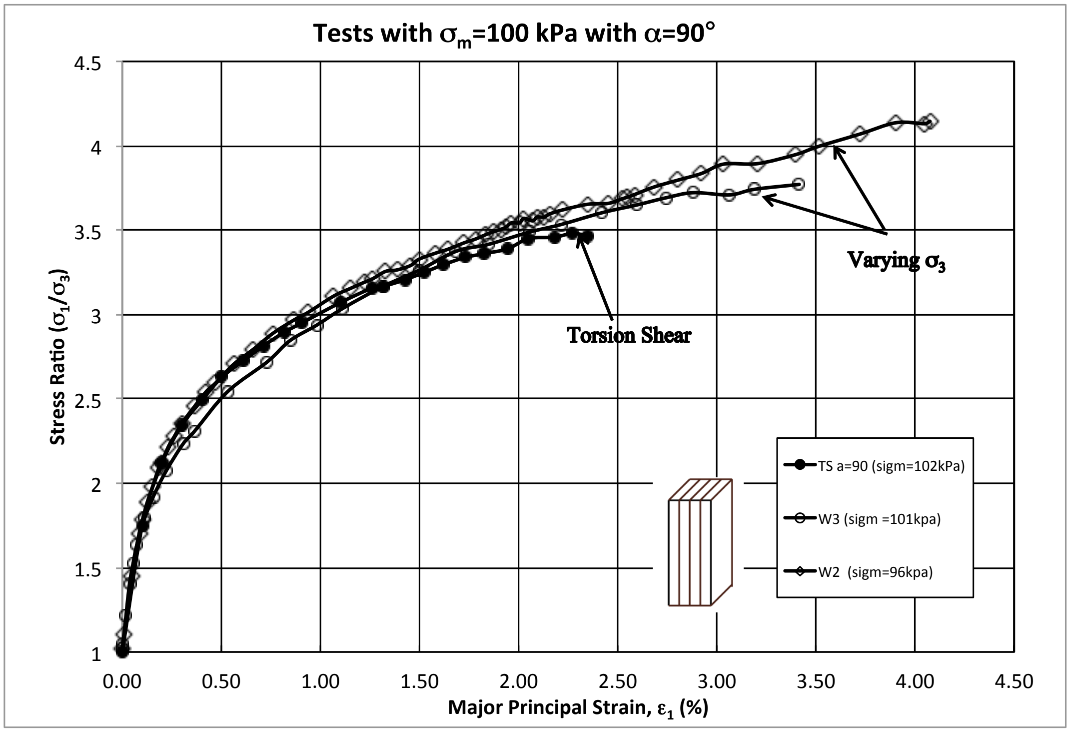

Figure 4.6.5. Stress-Strain curve for Tests with σ'm=101 kPa for α=90°.

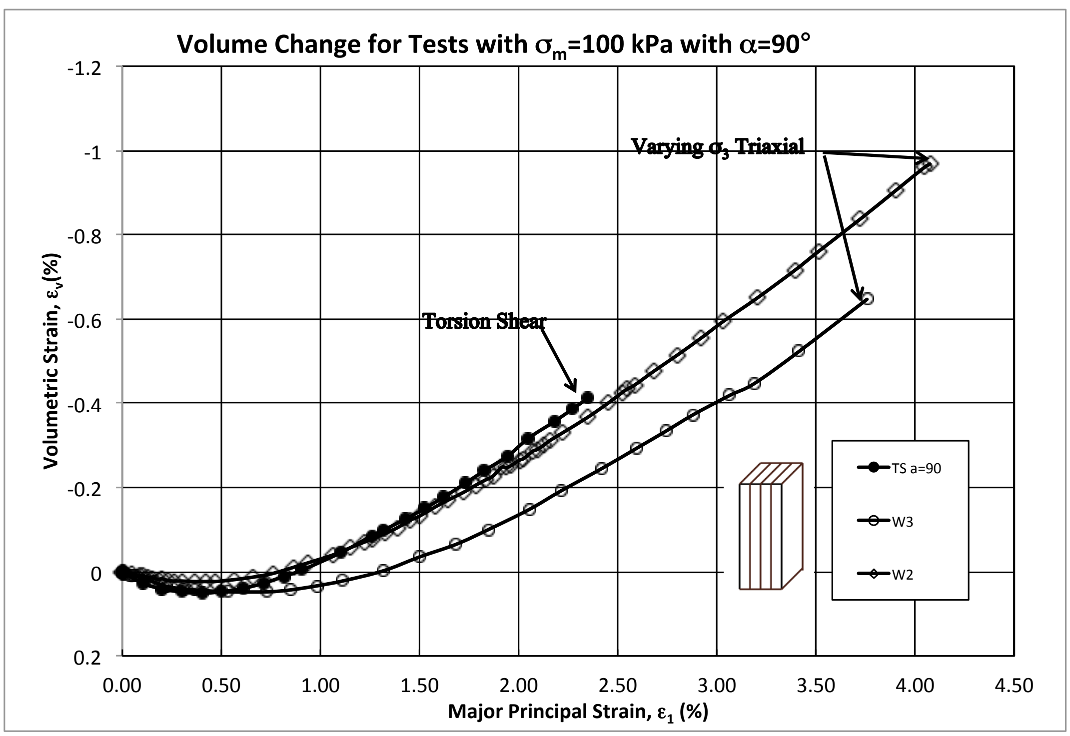

Figure 4.6.6. Volumetric strain curves for Tests with σ'm=101 kPa for α=90°.

Table 4.6.1 Torsion Shear and Triaxial Tests with σ_m=101 kPa for α=90° Tests.

Test No.	φ(deg)	σ_m (kPa)	ε_1 (%)
W3	35.27°	100.77	3.10
W2	37.51°	96.54	3.94
TS 41 (α=90°)	33.27°	100.8	2.27

Stress-Strain behavior of Tests with varying σ_3 at σ_m =101 kPa for α=0°

For further comparison to the torsion shear tests performed, one additional test (Test W6) was performed with horizontal bedding planes (α=0°) in the triaxial apparatus with a mean stress of about 101 kPa. This test was compared to the torsion shear test under normal triaxial compression with b=0 and α=0° conditions. In Figure 4.6.7 and 4.6.8, the stress strain and volumetric change versus axial strain curves are presented. When looking at both curves, it is seen once again that the torsion shear test fails at a much smaller axial strain than the triaxial test on the rectangular prismatic specimen. In this torsion shear test failure occurred with the development of a shear band. However, the friction angles at failure are close to each other with a 1.2° difference. Table 4.6.2 compares these results.

Table 4.6.2 Torsion Shear and Triaxial Tests with σ_m=101 kPa for α=0° Tests.

Test No.	φ(deg)	σ_m (kPa)	ε_1 (%)
W6	39.83	98.35	3.240
TS 23 (α=0)	40.99	101.36	1.542

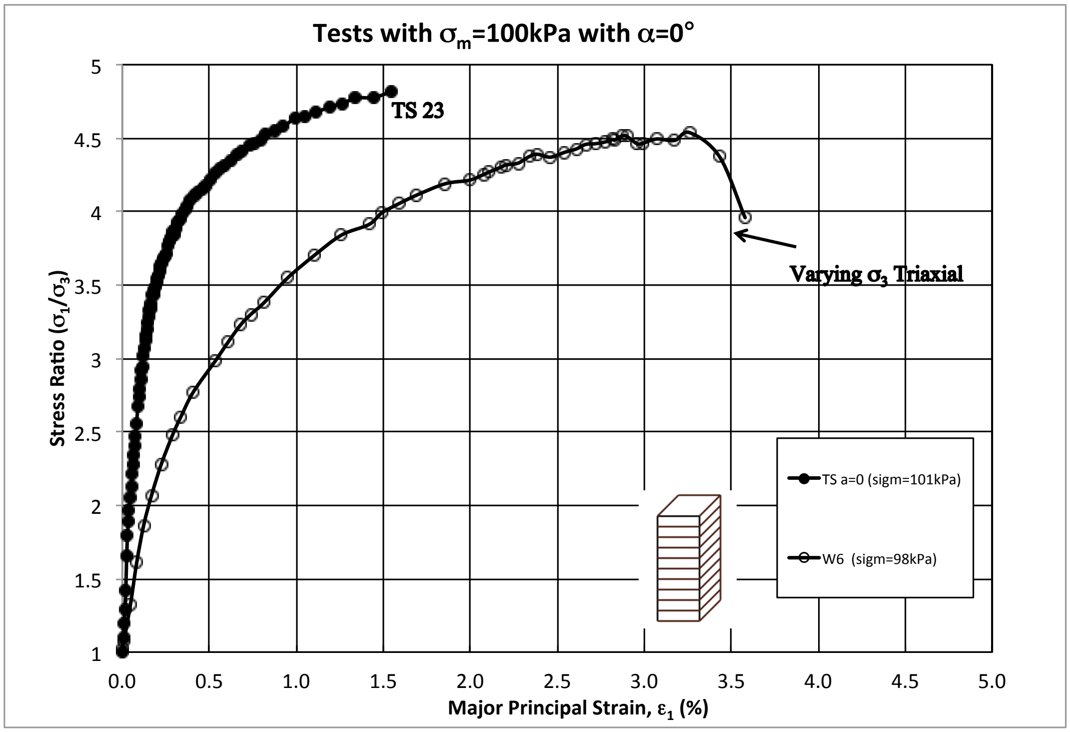

Figure 4.6.7. Stress-Strain curve for Tests with σ’m=101 kPa for α=0°.

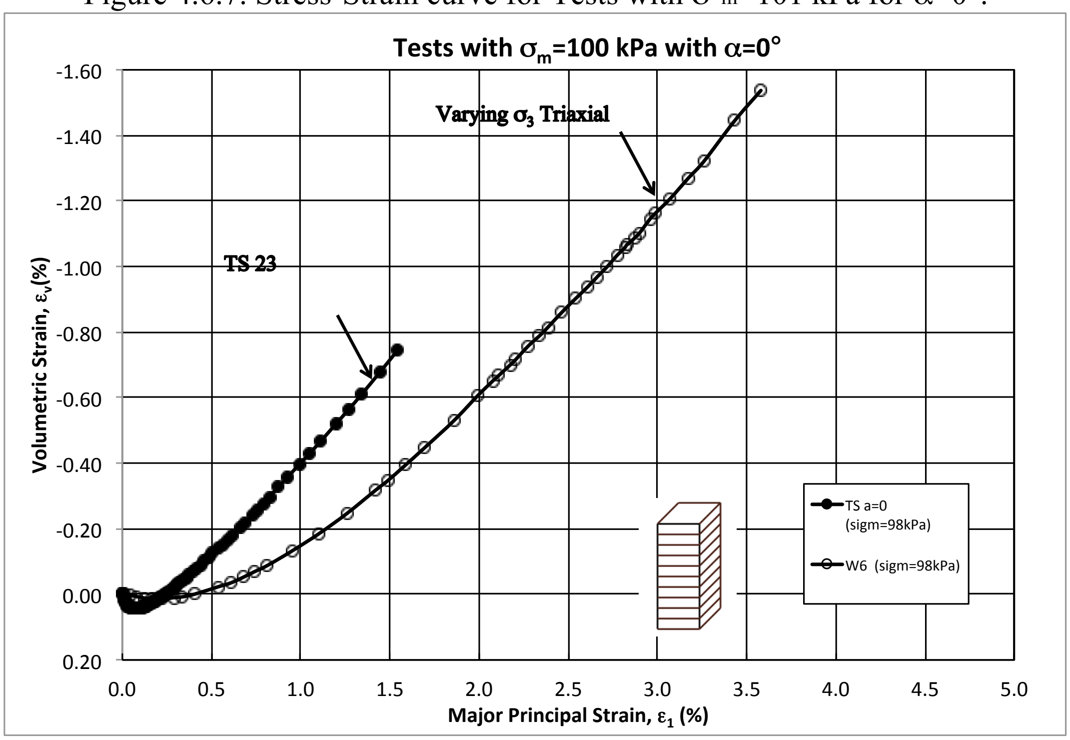

Figure 4.6.8. Volumetric strain curves for Tests with σ’m=101 kPa for α=0°.

4.7 Summary of Friction Angles from Tests W1-W4

Table 4.7.1 summarizes the strength results for all of the tests performed for this study. As can be seen by the void ratio, e column, the tests were all of similar density and therefore, results could easily be compared. As mentioned previously, all tests in this series had vertical bedding planes. The friction angle and stress ratios at failure are summarized, as well as the mean stress at failure. Tests W1 and W2 were very close in friction angle despite the significant difference in mean stress. Test W4's stress path kept σ_1 constant while σ_3 was lowered. Since the strain to failure is lowest for the tests with lowest confining pressure at failure, the fabric has not changed much and the lowest strength is obtained.

Table 4.7.1. Summary of Test Performed with Varying σ_3.

Test No.	α (deg)	e	φ(deg)	σ_1/σ_3	$\sigma_{m(failure)}$ (kPa)	$\varepsilon_{1(failure)}$(%)
W1	90°	0.534	37.904	4.15	206.97	5.50
W2	90°	0.528	37.506	4.13	96.54	3.94
W3	90°	0.530	35.271	3.73	100.77	3.10
W4	90°	0.554	35.935	3.65	52.29	2.50

Figure 4.7.1 shows the variation of friction angle with increasing mean stress for triaxial compression tests with water in the triaxial cell. For Tests W1-W4, it is seen that the friction angle increases with increasing confining pressure at failure, but more importantly, the axial strain-to-failure decreases with decreasing confining pressure at failure. Thus, the tests results tend to confirm the hypothesis that the effect of initial cross-anisotropic fabric affects

the strength. Usually, the highest friction angles are obtained at low confining pressures, but these results show increasing friction angles with increasing confining pressure at failure.

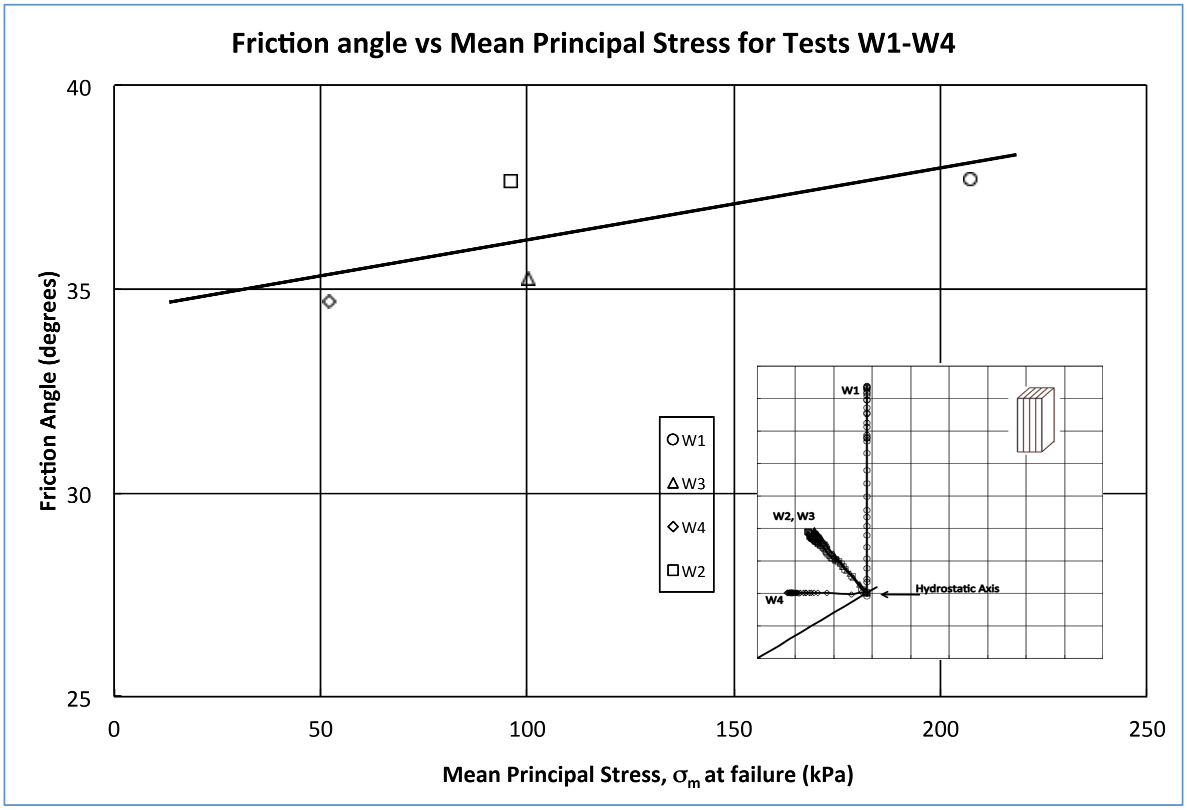

Figure 4.7.1. Variation of Friction Angle with Mean Principal Stress for Tests W1-W5.

4.8 Summary of Dilation Angles from Tests W1-W4

In order to see any effects on friction angle behavior due to dilation angle, an analysis was performed. The angle of dilation,Ψ can be calculated by the following equation:

$$\Psi = \sin\left(\frac{\left(\frac{\Delta\varepsilon_v}{\Delta\varepsilon_1}\right)}{\left(\frac{\Delta\varepsilon_v}{\Delta\varepsilon_1}\right)-2}\right) \qquad \text{Eq. 4.8.1}$$

where $\Delta\varepsilon_v$ is the increment in volume change and $\Delta\varepsilon_1$ is the increment in axial strain.

As can be seen in Table 4.8.1 and Figure 4.8.1, there is little variation in the angle of dilation. Therefore, it can be concluded that the angle of dilation does not change regardless of stress path.

Table 4.8.1. Summary of Tests W1-W4 showing Friction Angle, Mean Principal Stress and Dilation Angle.

Test No.	ϕ(deg)	σ_m(kPa)	Ψ(deg)
W1	37.904	206.97	9.1800
W2	37.506	96.54	9.0100
W3	35.271	100.77	7.6261
W4	35.935	52.29	7.2200

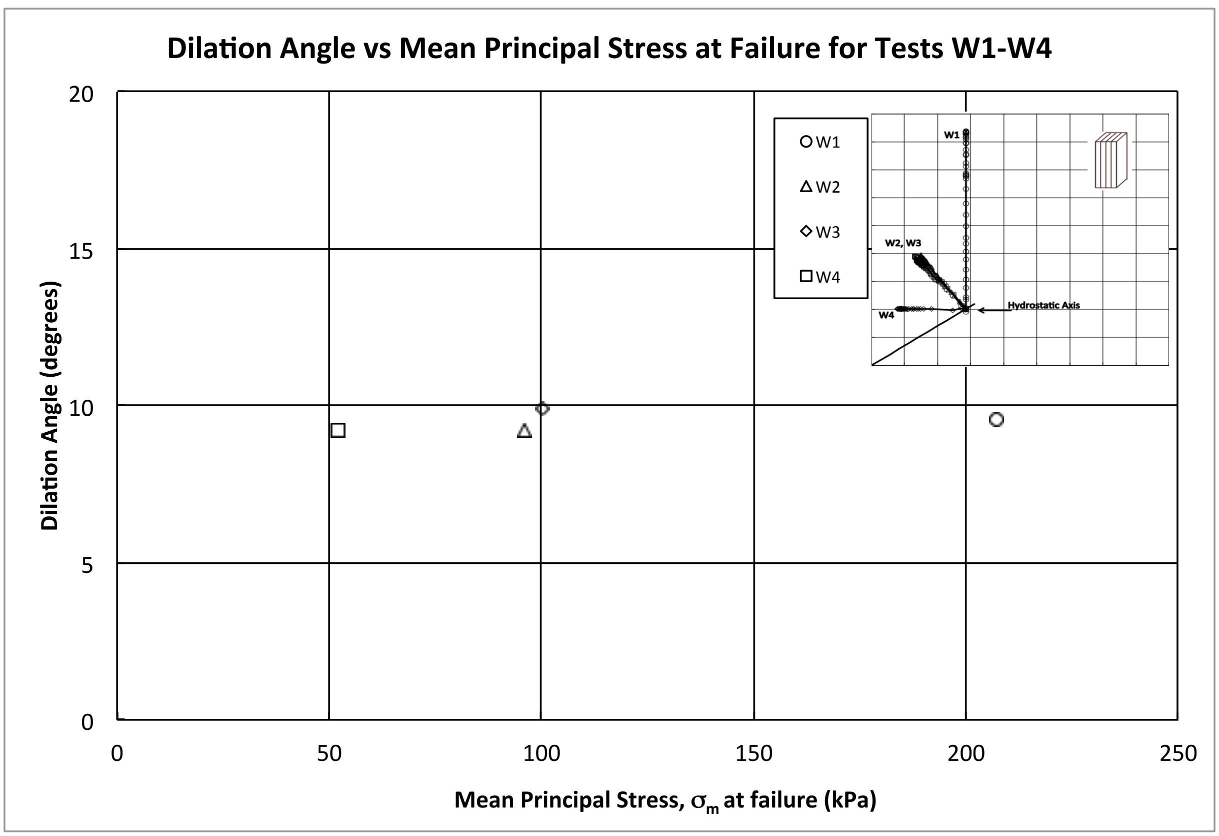

Figure 4.8.1. Variation of Dilation Angle with Mean Principal Stress for Tests W1-W5.

4.9 Conclusion

In conclusion, triaxial compression tests where α=90° were done to study the effects of stress paths on cross-anisotropic specimens. By varying the confining pressure, specimens were strained at different stress paths along the triaxial plane. Experiments were done with first air pressure in the triaxial cell, and then with water. Instabilities were seen at failure. However, once the stress-strain behavior was corrected at failure, results showed that for increasing mean principal stress, increasing friction angles are obtained. Dilation angles stayed constant for all tests.

5. True Triaxial Tests on Tall Specimens

5.1 Introduction

An experimental program was designed to study the effects of cross-anisotropy under three-dimensional conditions on Fine Nevada Sand. Eighteen tests were performed using Lade's (1977) true triaxial apparatus. The stress-strain, strength and failure behavior under various loading conditions on the octahedral plane are presented. The occurrence of shear banding and their influence on the strength behavior of the sand was also studied, but will be described in further detail in Chapter 9. The present chapter will focus on the failure surface attained under different b-values where $b=(\sigma_2-\sigma_3)/(\sigma_1-\sigma_3)$ in the three Sectors of the octahedral plane.

Figure 5.1.1 shows the specimen orientation on the Cartesian coordinates as well as on the octahedral plane. As can be seen from Figure 5.1.1, depending on the orientation of the specimen, the bedding planes are subject to different stresses. Changing b-values allows for a variety of points in each Sector. Tests were performed in about 0.25 increments of b-values ranging from zero to one for each of the three Sectors. All specimens had the same dimensions as described previously in Chapter 3 (7.6 cm width, 7.6cm length and 19cm height, H/D ratio=2.5) and were prepared using the same deposition, freezing and thawing techniques also described in Section 3.1.1.

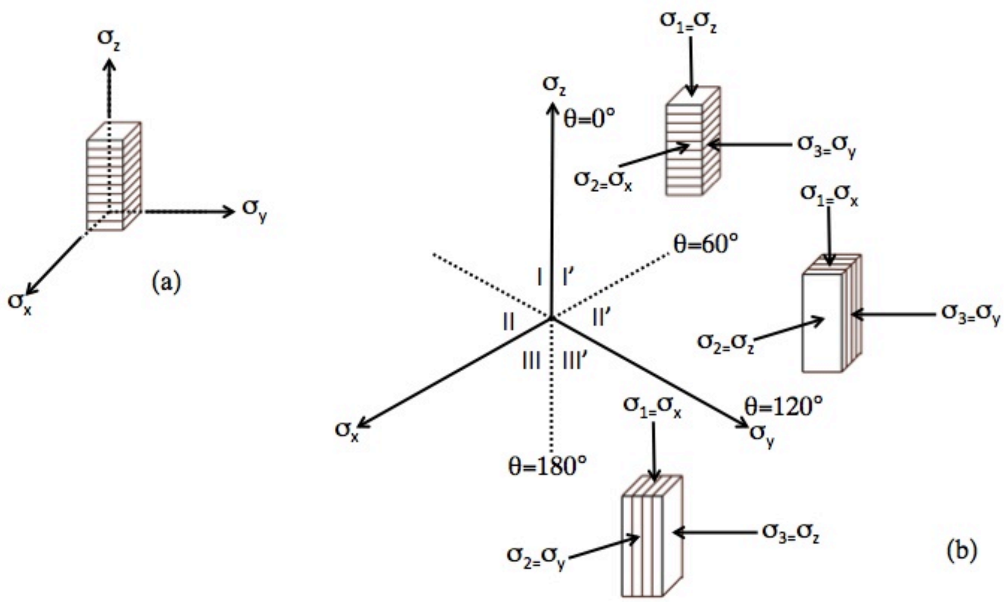

Figure 5.1.1. Specimen orientation in (a) Cartesian coordinate system and (b) on Octahedral plane.

5.2 True Triaxial Apparatus Assembly

The triaxial apparatus described in Section 3.1 was slightly modified in order to be able to produce tests under three-dimensional conditions. However, as described in detail by Lade (1978) a few more parts were added in order to use the horizontal loading device shown in Figure 5.2.1.

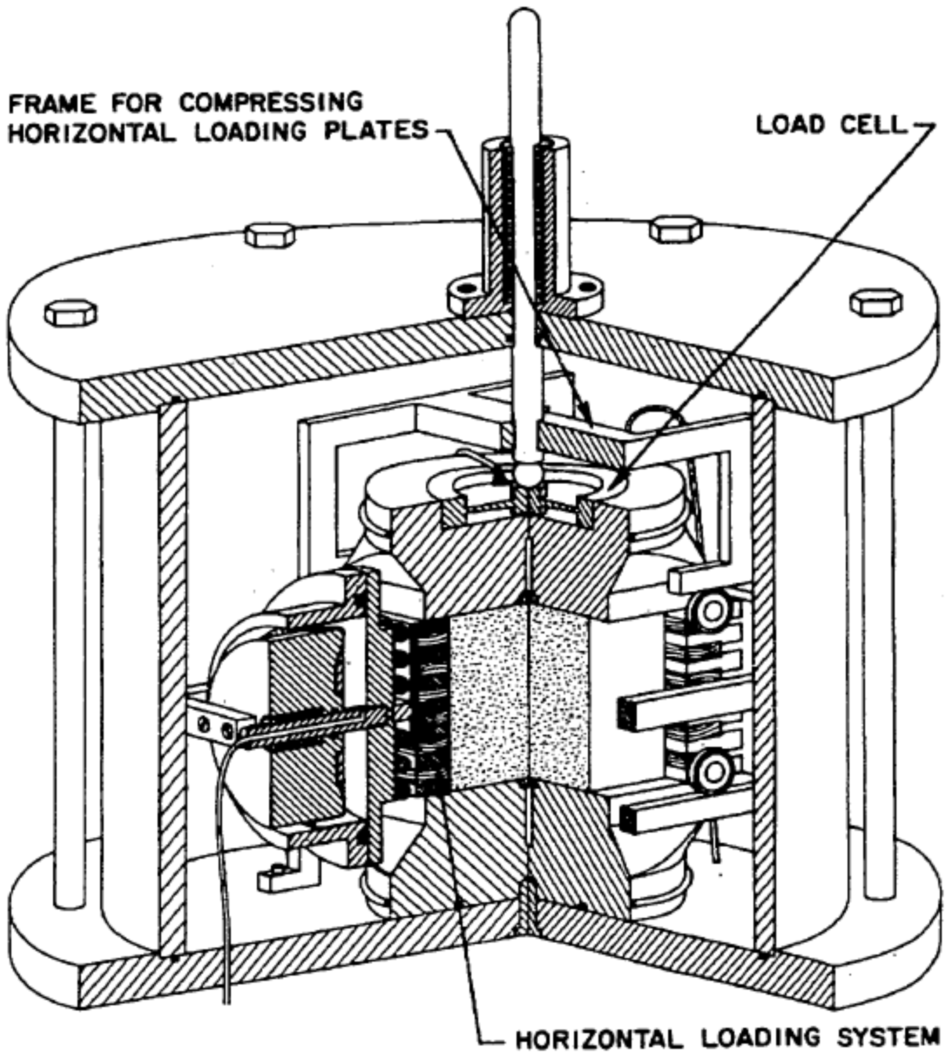

Figure 5.2.1. Schematic view of the cubical device (after Lade 1977).

Once the specimen was set up as described previously in Section 3.1, the horizontal loading system had to be assembled carefully around the specimen. The horizontal loading system sits on two guide rails on opposite sides of the specimen. These guide rails are positioned precisely to allow the horizontal plates to compress without hitting the top and bottom caps and are secured to the bottom plate of the triaxial cell. With these guide rails set in place, the horizontal load is only applied to the specimen. Ball bearings on the bottom and top of the side plates allowed the plates to roll on the guide rails when the plates were being squeezed towards each other. On each of the sides where the horizontal loading system was going to be placed, one sheet of latex rubber membrane was placed on top of a thin layer of vacuum grease covering the entire length and width of the specimen.

The two vertically compressible plates were assembled of alternating pre-stressed and soaked balsa wood and steel laminae. Prior to testing, the balsa wood pieces were compressed three times using a vice and then were soaked in water. This allowed for the strength in the direction perpendicular to the fibers of the balsa wood to be significantly decreased. The same set of balsa wood laminae was used during all true triaxial tests. The balsa wood was also kept soaked at all times between testing. In Figure 5.2.2, the configuration of the balsa wood and steel laminae in relation to the specimen can be seen.

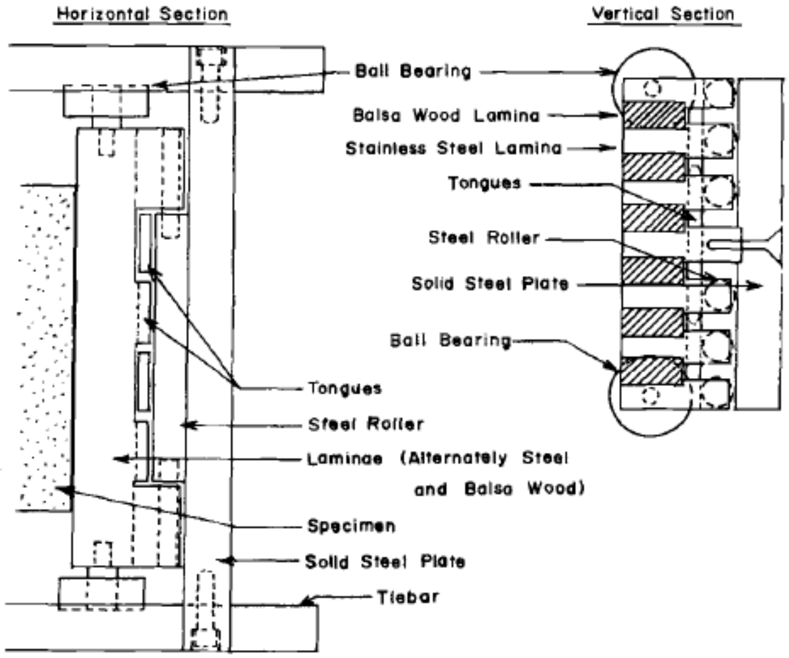

Figure 5.2.2. Horizontal and vertical sections of the horizontal loading plates (after Lade 1978).

Once the balsa and wood laminae were assembled, the two plates were interconnected and secured with screws around the specimen. Once the side plates were placed, horizontal LVDTs were positioned in order to measure horizontal deflections. At this point, the horizontal loading system was slightly squeezed by applying a small amount of pressure to the system to ensure that the plates were lightly touching the specimen. Doing so avoided a false horizontal strain measurement at the beginning of the test. The horizontal load was applied to the specimen by an oil-filled pressure cylinder. A pressure transducer connected to the oil line on the cylinder outside of the triaxial cell was hooked up to a strain gage indicator box and the box provided a digital display of the pressure being applied. A picture of the entire assembly can be seen in Figure 5.2.3.

To complete the entire triaxial assembly, a frame with four legs was attached to the piston by a setscrew. This frame allowed for vertical compression of the side plates. The frame and piston were carefully set while placing the top lid. They were precisely positioned so that the four-legged frame sat on the top ball bearings of the horizontal plates. The flat end of the piston was also positioned to slightly touch the steel ball sitting on the top cap load cell (also described in Section 3.1). With everything in place, the cell was closed and sealed with six tie rods. A digital dial gage was secured on the piston to measure axial deformations. Also, the external load cell (described in Section 3.1) was left in place on the triaxial loading machine in order to compare loads between the external and embedded top cap load cell. A schematic of the horizontal loading system is shown in Figure 5.2.4.

Figure 5.2.3. Picture of True Triaxial Horizontal Loading System with Horizontal LVDTs.

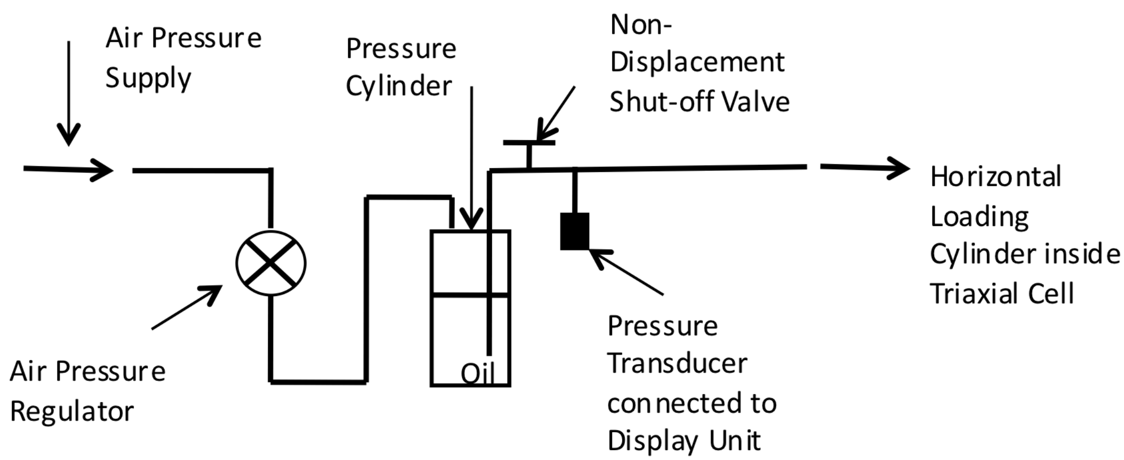

Figure 5.2.4. Schematic of Horizontal Loading System.

5.3 Calibration of Horizontal Loading System

All measurement devices were calibrated to ensure correct measurements. Certain measurement devices such as the volume change, dial gage and the load cells were previously calibrated for the tests described in Chapters 3. However, with the addition of a new system to the assembly, two new devices had to be calibrated: the horizontal loading system and the horizontal LVDTs.

In order to calibrate the horizontal loading system, the horizontal load is calibrated as a function of the pressure transducer readings on the P-3500 strain indicator box. In order to calibrate the pressure transducer readings, a load cell was placed between the two vertical plates. The balsa wood and steel laminae were not assembled for the calibration. The load cell was carefully placed in the middle of the plates in order to minimize any moment effects from any eccentricity. Steel plates were set around the load cell in order to prevent any compression of the plates. Any compression of the plates would provide a false calibration of pressure and load. Once set, pressure was applied to the pressure cylinder and in turn, the plates. Pressure was applied and the reading displayed on the indicator box alongside the load cell reading was recorded for five loading and unloading cycles reaching 200 kPa. The load cell reading was converted to pounds (by a previous calibration described in Section 3.1.3). Using these readings, a calibration curve was determined and applied for the experiments. A picture of the set up for the horizontal loading calibration is shown in Figure 5.3.1. The strain indicator box, pressure cylinder and load cell can be seen.

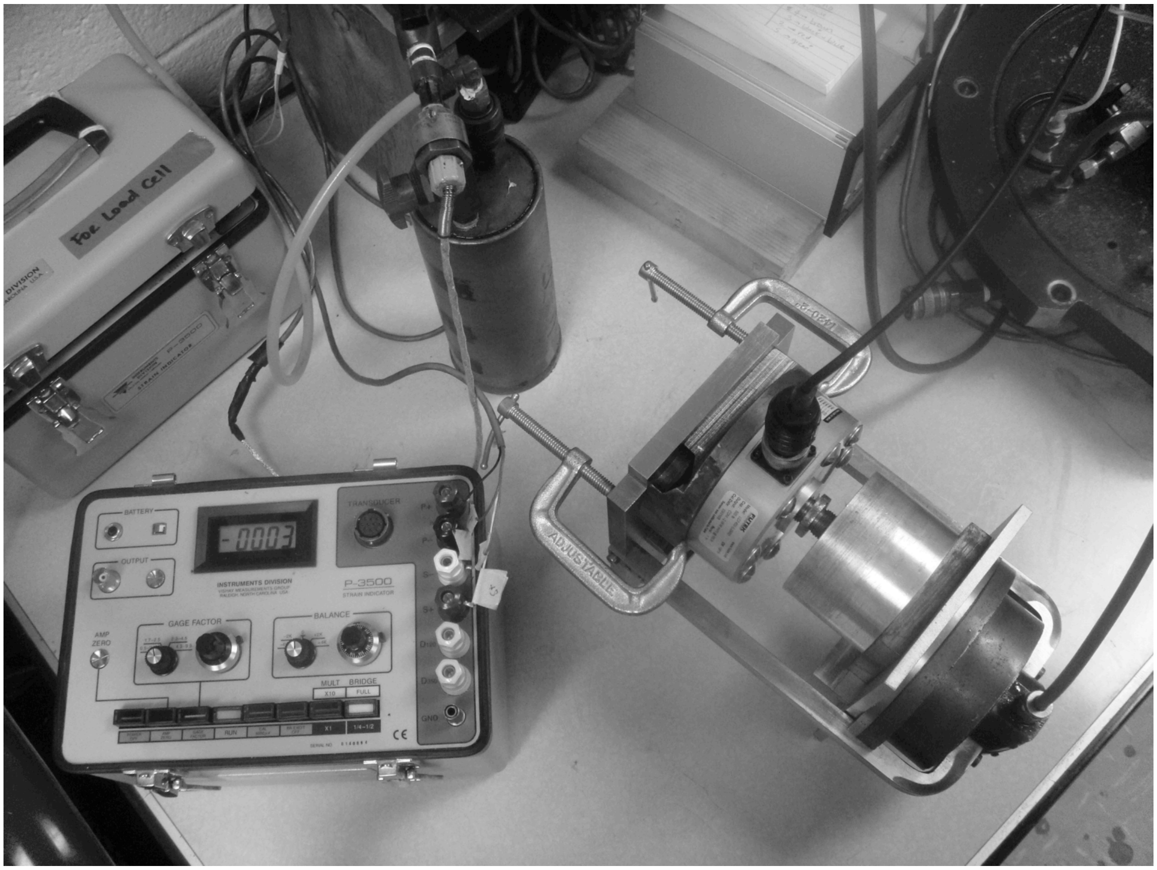

Figure 5.3.1. Picture of set-up for the Horizontal Loading System calibration.

Two horizontal Linear Variable Differential Transformers (LVDTs) were used on each side of the specimen in order to measure horizontal deformations. In order to calibrate the horizontal LVDTs, they were hooked up to an MP2000 signal display unit that displayed real time readings. The LVDTs were secured on stands especially made to calibrate LVDTs, and they were calibrated using Mitutoya Digimac Micrometers. Each horizontal LVDT was calibrated individually and two calibration curves were calculated. A picture of the calibration set up is shown in Figure 5.3.2.

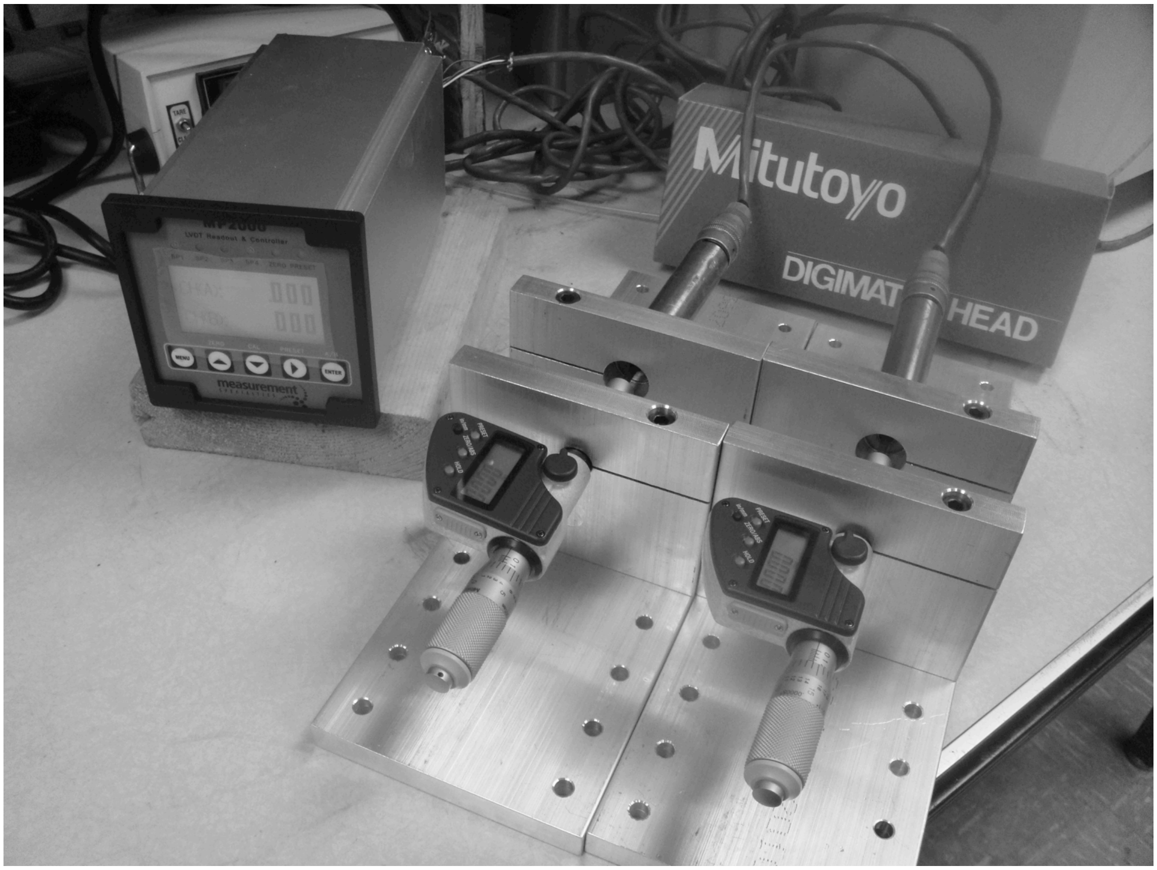

Figure 5.3.2. Picture of set-up for two horizontal LVDTs calibration.

5.4 Experimental Program

As mentioned before, 18 tests were performed on tall rectangular prismatic specimens. The summary of the tests performed according to Sector and b-values is shown in Table 5.4.1. The b-values are not precisely at 0.25 increments for certain tests because of certain calibration and testing conditions that were particular to each test. For these specific cases, details will be explained when analyzing the stress-strain behavior. However, in most of the cases, the b-values were maintained constant as the specimen was sheared.

For the first Sector tests, seven specimens with horizontal bedding planes (α=0°) were prepared. Five specimens in the second Sector and six specimens in the third Sector were prepared with vertical bedding planes (α=90°). The specimens were rotated so that the bedding planes and specimen sides were correctly oriented in accordance with Figure 5.1.1.

Table 5.4.1. Summary of alpha and b-values of True Triaxial Tests in all Three Sectors.

Test No.	α	b-value
Sector I		
TT#1	0	0.00
TT#2	0	0.24
TT#3	0	0.51
TT#4	0	0.75
TT#5	0	0.70
TT#6	0	0.72
TT#7	0	1.00
Sector II		
TT#8	90	0.25
TT#9	90	0.49
TT#10	90	0.70
TT#11	90	0.69
TT#12	90	1.0
Sector III		
TT#13	90	0.00
TT#14	90	0.25
TT#15	90	0.49
TT#16	90	0.72
TT#17	90	0.72
TT#18	90	0.95

All tests were performed with constant confining pressure. A confining pressure of 50 kPa was set for most tests. Tests with b=1.0 were set at a lower confining pressure of 30 kPa.

As confining pressure was applied in the triaxial cell, the horizontal loading bellofram diaphragm was also subject to this cell pressure. In order to keep the piston placed correctly and to prevent any oil from running back into the pressure cylinder, the non-diplacement valve was closed to the pressure cylinder. Once the final total confining pressure was set in the triaxial cell, the amount of pressure required to produce the initial zero reading in the oil pressure cylinder transducer was applied. With higher confining pressures, a greater initial pressure is required to zero the cylinder before the test. The air pressure supply line only reached about 800 kPa, and this pressure is not sufficient to increase the load in the horizontal loading system when running tests with higher b-values where a larger horizontal load was required. Therefore, the confining pressure in the triaxial cell was set to a lower pressure.

A program was set up to maintain a constant b-value throughout the entire test. After isotropic compression, the new area and volume were calculated. With a shearing rate of 0.1mm/min, the specimen was sheared on the loading machine. Readings were taken from the vertical dial gage, two horizontal LVDTs, and both vertical load cells. With these values input to the program, the major principal stress was calculated according to the corrected area of the specimen. The corresponding calibration for the horizontal load that produced the required intermediate principal stress for the desired b-value was calculated. With this known, pressure to the horizontal loading system was added manually with the pressure regulator until the desired reading was reached on the P-3500 strain indicator box. At this point, the appropriate intermediate principal stress was applied. New readings were attained immediately and the cycle was repeated until the specimen was sheared and shear bands were observed.

5.5 Calculation of Horizontal Force required and Corrections to Horizontal Strains

In order to calculate the required horizontal load for any b-value, a relationship between b, the areas and the vertical force was derived. As previously stated, the intermediate principal stress, σ_2 can be expressed by the following equation:

$$b = \frac{(\sigma_2 - \sigma_3)}{(\sigma_1 - \sigma_3)} \rightarrow (\sigma_2 - \sigma_3) = b(\sigma_1 - \sigma_3)$$

Eq. 5.5.1

Since intermediate principal stress is a summation of the confining pressure, σ_3 and the horizontal deviator stress, σ_{2d}, and because stress is a force divided by an area, it can be written that,

$$\sigma_2 = (\sigma_{2D} + \sigma_3) \rightarrow \sigma_{2D} = (\sigma_2 - \sigma_3)$$

where

$$\sigma_{2D} = \frac{F_2}{A_2}$$

Eq. 5.5.2

where F_2 is the horizontal force and A_2 is the area of the sides of the specimen (length times height).

A similar equation can be derived for the major principal stress including the vertical deviator stress such that,

$$\sigma_1 = (\sigma_{1D} + \sigma_3) \rightarrow \sigma_{1D} = (\sigma_1 - \sigma_3)$$
$$where \qquad \text{Eq. 5.5.3}$$
$$\sigma_{1D} = \frac{F_1}{A_1}$$

where F_1 is the vertical force and A_1 is the area of the top of the specimen (length times width).

By combining equations 5.5.1, 5.5.2 and 5.5.3, the following relationship for the horizontal force can be derived where,

$$\frac{F_2}{A_2} = b\left(\frac{F_1}{A_1}\right) \rightarrow F_2 = b\left(\frac{A_2}{A_1}\right)F_1 \qquad \text{Eq. 5.5.4}$$

Using equation 5.5.4, the force required for the horizontal loading system was calculated. By knowing the force required, the reading for the pressure transducer was calculated with the calibration curve previously established. In this manner, adequate pressure was applied to the specimen in order to maintain the b-value for the specific experiment.

As described previously, when setting up the horizontal loading system, a small amount of pressure was applied to the horizontal loading system to move the plates as close to the specimen as possible. The reading on the display was recorded and the non-displacement valve on the pressure cylinder was closed. After the total confining pressure was applied, the new pressure transducer reading was recorded. Since the pressure transducer was located between the non-displacement shut off valve and the horizontal loading cylinder inside the triaxial cell, the transducer could display the new readings with the addition of the cell pressure (see Figure 5.2.4). The valve was then opened and pressure was manually increased so that the pressure in the oil filled cylinder was balanced with the horizontal loading cylinder. This prevented the oil in the bellofram diaphragm from running back into the oil cylinder. With this process completed, the plates of the horizontal loading system were still in the original position as close to the specimen as possible. Since the plates did not touch the specimen, no stress was exerted prior to testing.

At the start of the test, the initial gap between the specimen and the horizontal plates was seen in the movement of the horizontal LVDTs. This created some false deformation measurements. To exclude this initial movement of the plates, the strains in the horizontal ε_2-direction were plotted versus the strains in the axial ε_1-direction. Large strains seen at the beginning of shearing which were obviously due to this initial gap between the plates and specimen were subtracted. This allowed for the true horizontal strain to be analyzed. Figure 5.5.1 shows an example of the correction applied to the ε_2 strain calculations for all of the true triaxial tests.

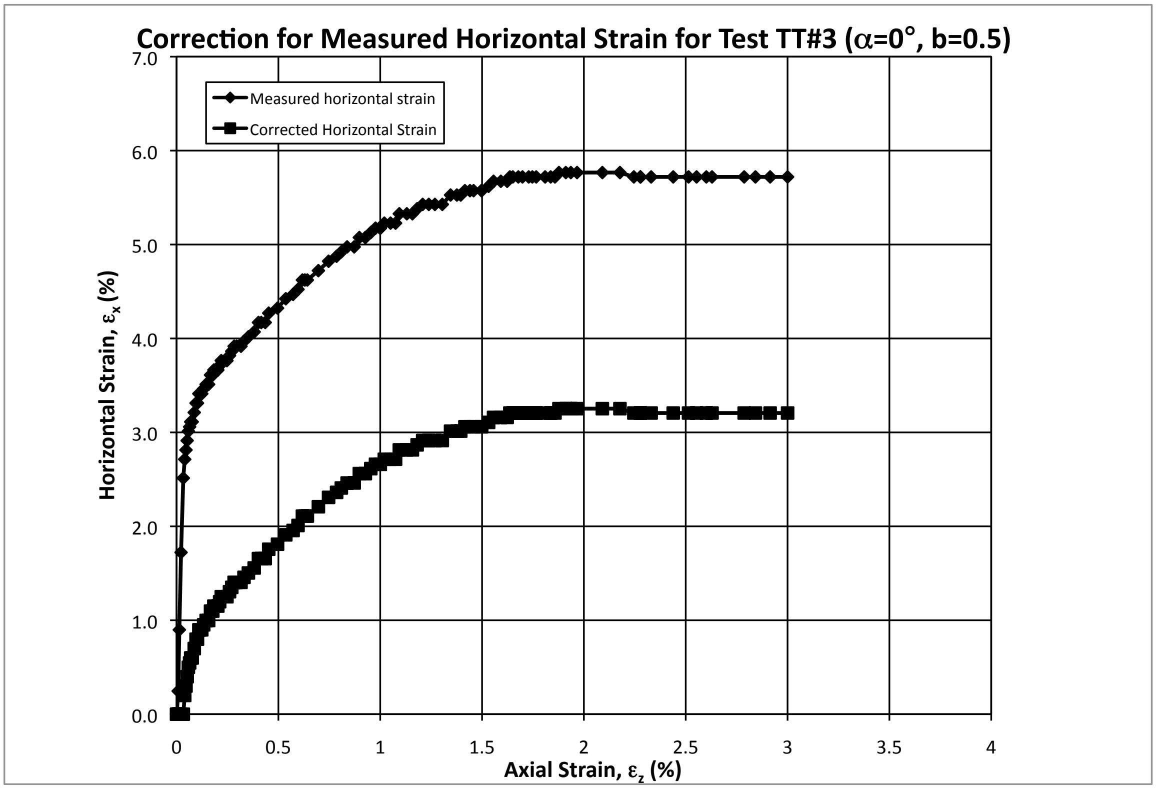

Figure 5.5.1. Example of the correction applied when calculating ε_2 for true triaxial tests.

5.6 Correction to Friction Angle and b-values due to Measurement Errors

In order to account for any measurement errors, an analysis was done for both friction angles and b-values. This analysis used the Least Squares Method to determine the error for true triaxial tests, assuming certain values of error in vertical force, F_v, inner and outer pressures, p_i and p_o, inner and outer radii, r_i and r_o and alpha values. A table with the summary and the effect on friction angle and b-values for different ranges of errors is presented in Table 5.6.1. As is seen, the friction angle varies from 0.2 to 2.5 degrees for the measurement inaccuracies presented. The worst effect occurs for the condition b=1 and α=0°. The major contributor of the error is seen to be the cell pressure. The force and area deviation are seen to play minor roles in the friction angle error. A detailed description of how these values were calculated can be found in Appendix J.

When looking at the error in b-value, the cell pressure does not affect the error analysis. The only terms that are important are the areas in the vertical and horizontal direction on which the forces in the horizontal and vertical directions are applied. The analysis of varying measurement errors on the b-value can be seen in Table 5.6.2. As can be seen, the variation of b-value is very small, ranging from 0.002 to 0.026.

Table 5.6.1. Comparison of measurement Errors in friction angle for different values of ΔFv, ΔFv, ΔAv and ΔAh for four true triaxial tests.

#	**b**	**ϕ (°)**	**F (kg)**	**ΔF**	**A (cm^2) (cm^2)**	**ΔA**	**σ_{cell} (kPa)**	**$\Delta\sigma_{cell}$**	**Δϕ (°)**
1	0	42.97	133.1	0.5	60.92	0.5	50	0.5	**0.226**
7	1	50.36	121.4	0.5	59.22	0.5	30	0.5	**0.300**
13	0	37.6	97.7	0.5	61.24	0.5	50	0.5	**0.236**
18	0.95	46.8	163.2	0.5	59.62	0.5	30	0.5	**0.219**
#	**b**	**ϕ (°)**	**F (kg)**	**ΔF**	**A (cm^2) (cm^2)**	**ΔA**	**σ_{cell} (kPa)**	**$\Delta\sigma_{cell}$**	**Δϕ (°)**
1	0	42.97	133.1	1	60.92	0.5	50	1	**0.383**
7	1	50.36	121.4	1	59.22	0.5	30	1	**0.552**
13	0	37.6	97.7	1	61.24	0.5	50	1	**0.406**
18	0.95	46.8	163.2	1	59.62	0.5	30	1	**0.367**
#	**b**	**ϕ (°)**	**F (kg)**	**ΔF**	**A (cm^2) (cm^2)**	**ΔA**	**σ_{cell} (kPa)**	**$\Delta\sigma_{cell}$**	**Δϕ (°)**
1	0	42.97	133.1	1	60.92	0.5	50	2	**0.639**
7	1	50.36	121.4	1	59.22	0.5	30	2	**1.056**
13	0	37.6	97.7	1	61.24	0.5	50	2	**0.711**
18	0.95	46.8	163.2	1	59.62	0.5	30	2	**0.671**
#	**b**	**ϕ (°)**	**F (kg)**	**ΔF**	**A (cm^2) (cm^2)**	**ΔA**	**σ_{cell} (kPa)**	**$\Delta\sigma_{cell}$**	**Δϕ (°)**
1	0	42.97	133.1	1	60.92	1	50	5	**1.677**
7	1	50.36	121.4	1	59.22	1	30	5	**2.506**
13	0	37.6	97.7	1	61.24	1	50	5	**1.701**
18	0.95	46.8	163.2	1	59.62	1	30	5	**1 631**

Table 5.6.2. Comparison of Measurement Errors in b-values for different values of ΔF_v, ΔA_v and ΔA_h.

Test No.	b	Fv (kg)	ΔFv	Fh (kg)	ΔFh	Av (cm^2)	ΔAv	Ah (cm^2)	ΔAh	Δb-value
1	0	133.1	0.5	0.0	0.5	144.4	0.5	60.92	0.5	**0.002**
7	1	121.4	0.5	304.0	0.5	144.4	0.5	59.22	0.5	**0.013**
13	0	97.7	0.5	0.0	0.5	144.4	0.5	61.24	0.5	**0.002**
18	1	163.2	0.5	406.0	0.5	144.4	0.5	59.62	0.5	**0.014**
Test No.	b	Fv (kg)	ΔFv	Fh (kg)	ΔFh	Av (cm^2)	ΔAv	Ah (cm^2)	ΔAh	Δb-value
1	0	133.1	1	0.0	1	144.4	0.5	60.92	0.5	**0.003**
7	1	121.4	1	304.0	1	144.4	0.5	59.22	0.5	**0.015**
13	0	97.7	1	0.0	1	144.4	0.5	61.24	0.5	**0.004**
18	1	163.2	1	406.0	1	144.4	0.5	59.62	0.5	**0.012**
Test No.	b	Fv (kg)	ΔFv	Fh (kg)	ΔFh	Av (cm^2)	ΔAv	Ah (cm^2)	ΔAh	Δb-value
1	0	133.1	1	0.0	1	144.4	1	60.92	1	**0.003**
7	1	121.4	1	304.0	1	144.4	1	59.22	1	**0.026**
13	0	97.7	1	0.0	1	144.4	1	61.24	1	**0.004**
18	1	163.2	1	406.0	1	144.4	1	59.62	1	**0.025**

After performing the analysis of the importance of measurement errors, errors were assigned to the measured values for all true triaxial tests. These errors were calculated for both friction angles and b-values. The cell pressure error was estimated to be at 0.5 kPa (0.005kg/cm^2). This is about 1% of the total cell pressure applied. The error on the vertical and horizontal forces were both estimated to be 1kg (also about 1% of the applied vertical load) and the area measurement error was estimated at 0.5cm^2 (almost 1% of the horizontal area). Although these errors are provided, the integrity of the tests performed is strong and it is believed that these errors are on the conservative side.

The results from the analysis are shown in Table 5.6.3. The worst case of error in friction angle occurs in Sector II where α=90°, b=1.0. The measurement errors result in only 0.325 degrees. A summary of friction angle errors and b-value errors is presented in Table 5.6.3. To get a better visual understanding of the deviation with respect to b-values, Figures 5.6.1 and 5.6.2 are also presented.

Table 5.6.3. Summary of Friction Angle and b-value Measurement Errors for all Ttrue Triaxial tests.

Test No.	b	α	ϕ (°)	Fv (kg)	ΔFv (kg)	Ah (cm^2)	ΔAh (cm^2)	σ_{cell} (kg/cm^2	$\Delta\sigma_{cell}$ (kg/cm^2)	$\Delta\phi$ **(°)**	Fh (kg)	ΔFh (kg)	Av (cm^2)	ΔAv	D**b-value**
Sector I															
1	0	0	42.97	133.1	1	60.9	0.5	0.510	0.005	**0.252**	0.0	1	142.52	0.5	**0.003**
2	0.2	0	46.42	161.2	1	60	0.5	0.510	0.005	**0.237**	92.8	1	147.03	0.5	**0.004**
3	0.5	0	50.35	203.0	1	59.4	0.5	0.510	0.005	**0.220**	244.2	1	150.39	0.5	**0.006**
4	0.8	0	51.73	221.3	1	59.5	0.5	0.510	0.005	**0.214**	404.5	1	151.98	0.5	**0.009**
5	0.7	0	52.84	236.6	1	59	0.5	0.510	0.005	**0.209**	398.8	1	151.95	0.5	**0.008**
6	0.7	0	52.44	229.6	1	59.9	0.5	0.510	0.005	**0.211**	403.5	1	151.9	0.5	**0.008**
7	1	0	50.36	121.4	1	59.2	0.5	0.306	0.005	**0.320**	297.9	1	154.9	0.5	**0.014**
Sector II															
8	0.2	90	46.29	159.1	1	59.9	0.5	0.510	0.005	**0.238**	93.6	1	148.5	0.5	**0.004**
9	0.5	90	49.13	187.7	1	59.2	0.5	0.510	0.005	**0.226**	217.4	1	150.25	0.5	**0.006**
10	0.7	90	52.47	232.6	1	59.4	0.5	0.510	0.005	**0.210**	383.4	1	152.18	0.5	**0.008**
11	0.7	90	52.45	233.6	1	60	0.5	0.510	0.005	**0.210**	383.7	1	137.12	0.5	**0.009**
12	1	90	50.49	117.3	1	58.7	0.5	0.306	0.005	**0.325**	281.2	1	151.96	0.5	**0.014**
Sector III															
13	0	90	37.6	97.7	1	61.2	0.5	0.510	0.005	**0.281**	0.0	1	140.82	0.5	**0.004**
14	0.3	90	45.21	146.9	1	59.1	0.5	0.510	0.005	**0.245**	90.1	1	145.77	0.5	**0.004**
15	0.5	90	44.3	140.8	1	59.7	0.5	0.510	0.005	**0.248**	165.2	1	148.98	0.5	**0.007**
16	0.7	90	49.57	195.8	1	60.4	0.5	0.510	0.005	**0.222**	331.4	1	152.18	0.5	**0.009**
17	0.7	90	50.07	200.9	1	60.2	0.5	0.510	0.005	**0.222**	347.0	1	151.03	0.5	**0.009**
18	0.9	90	46.8	163.2	1	59.6	0.5	0.510	0.005	**0.236**	370.3	1	153.74	0.5	**0.012**

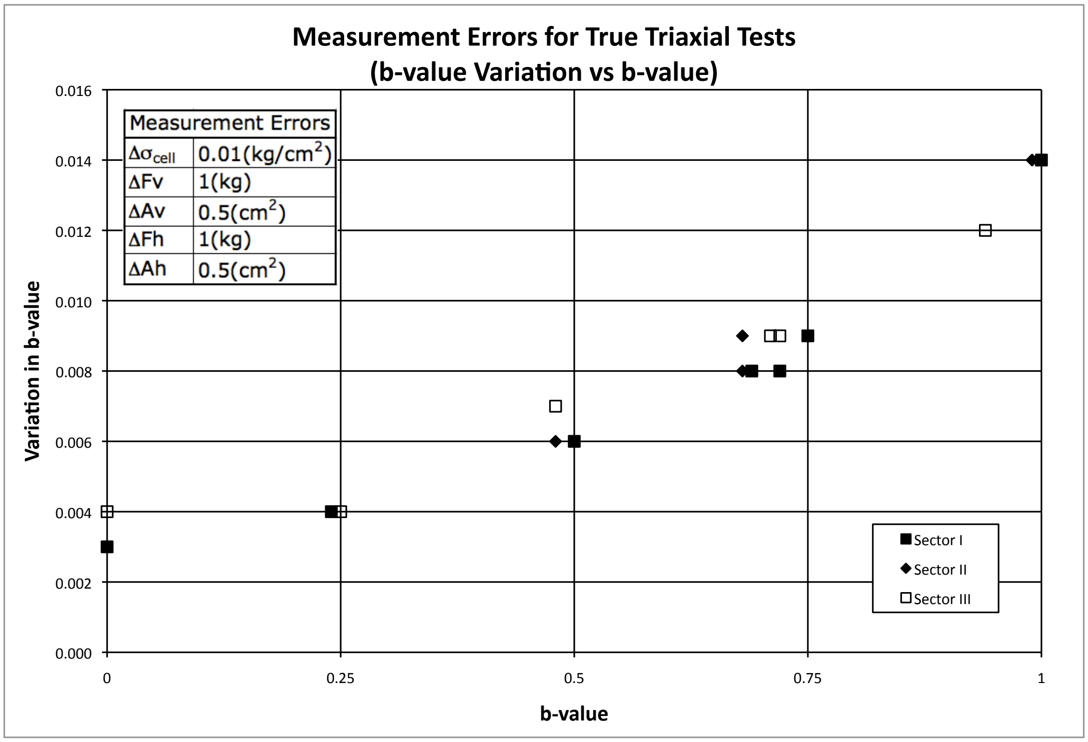

Figure 5.6.1. Summary of b-value Measurement Errors for True Triaxial tests plotted.

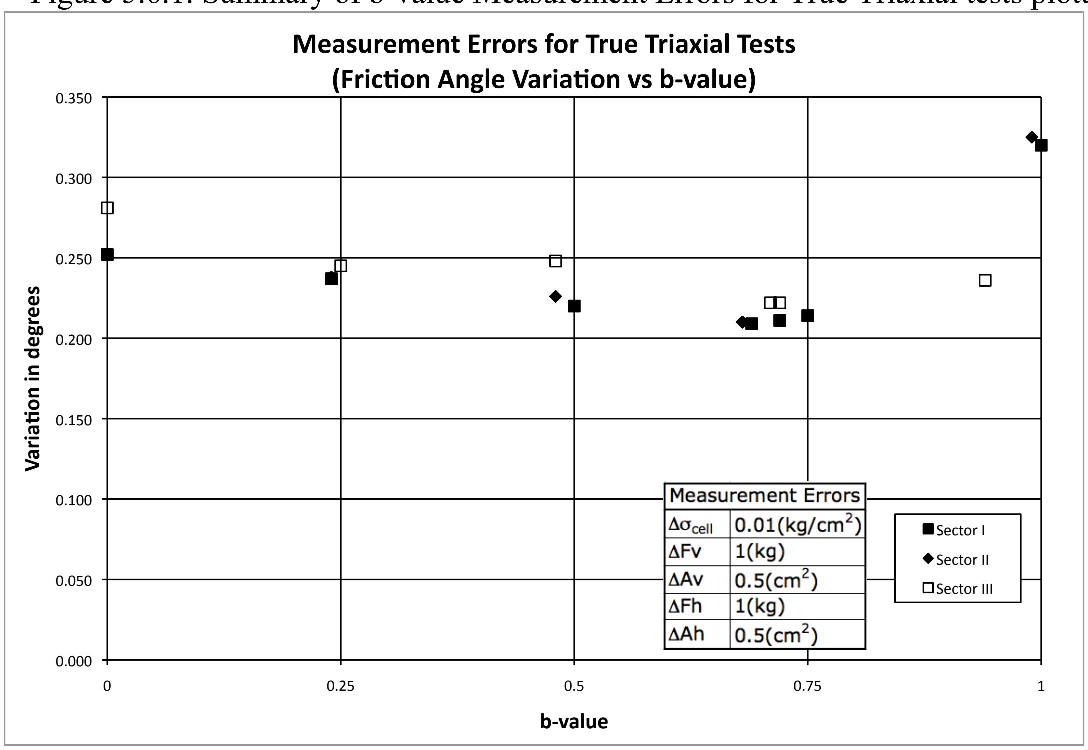

Figure 5.6.2. Summary of Friction Angle Measurement Errors for True Triaxial tests. plotted.

5.7 Translating Failure Points to the Same Octahedral Plane

The octahedral plane is a plane whose normal vector, the hydrostatic axis creates equal angles with each of the principal axes. The octahedral plane can be used to present results of tests with three unequal stresses. The center point of the octahedral plane represents the hydrostatic axis, where $\sigma_1=\sigma_2=\sigma_3$. The three axes (120 degrees apart) represent the projections of the principal stress axes in 3D on the octahedral plane. The axes are located symmetrically such that $\sigma_1=\sigma_2$, $\sigma_2=\sigma_3$, and $\sigma_3=\sigma_1$. A diagram of the octahedral plane and the corresponding stresses in each sector is shown in Figure 5.7.1 and in Figure 5.7.2.

The octahedral plane serves as a good diagram on which to represent the three principal stresses of the true triaxial tests. However, because the tests were not under the same constant mean normal stress at failure, they do not all fall on the same octahedral plane. In order to analyze all data from the true triaxial tests across the same conditions, the failure points were shifted to the same octahedral plane where the mean normal stress is σ'_m=100 kPa corresponding to a value of the first stress invariant of I_1=300 kPa. This plane was chosen because the torsion shear tests to be presented later were all done with I_1=300 kPa and it was the intent to compare the results of the two types of tests. A detailed description of how to project stress points onto the same octahedral plane is provided in Appendix F.

In the sections that follow, all presented stress points for true triaxial tests have been projected onto the I_1=300 kPa octahedral.

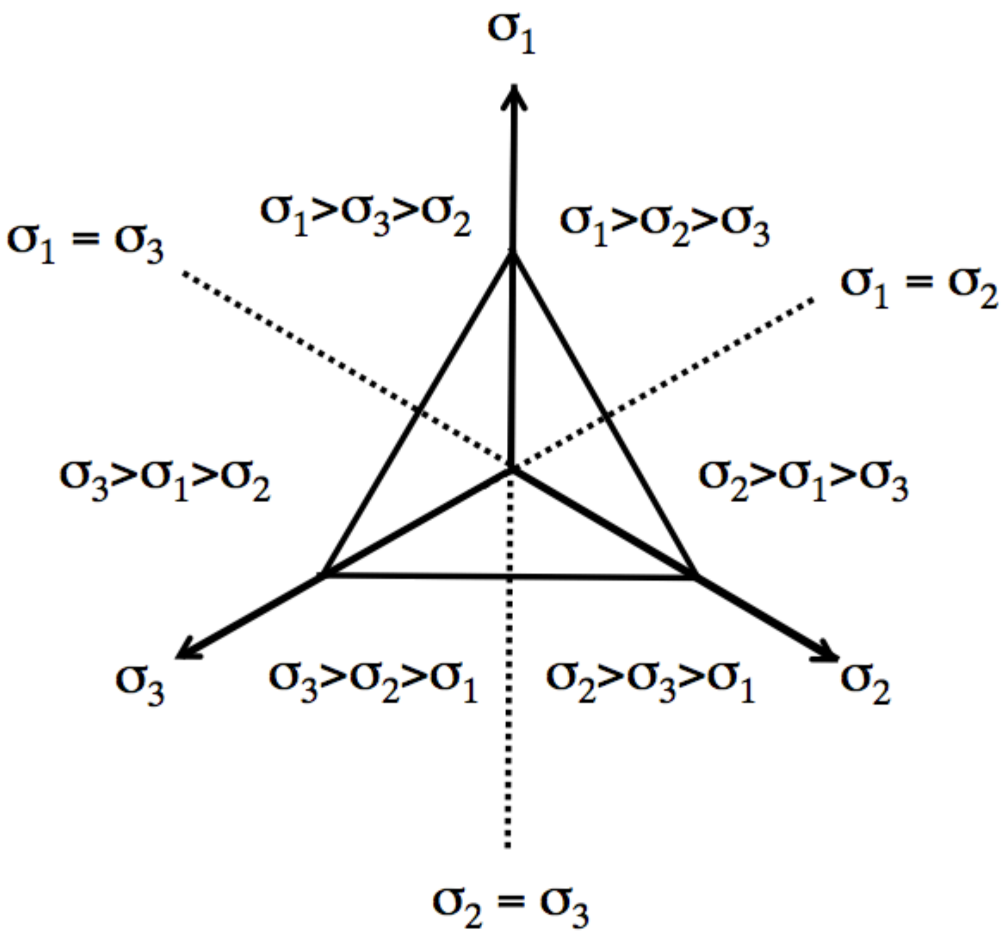

Figure 5.7.1. Octahedral Plane in 2D showing the stress states in each part of the plane.

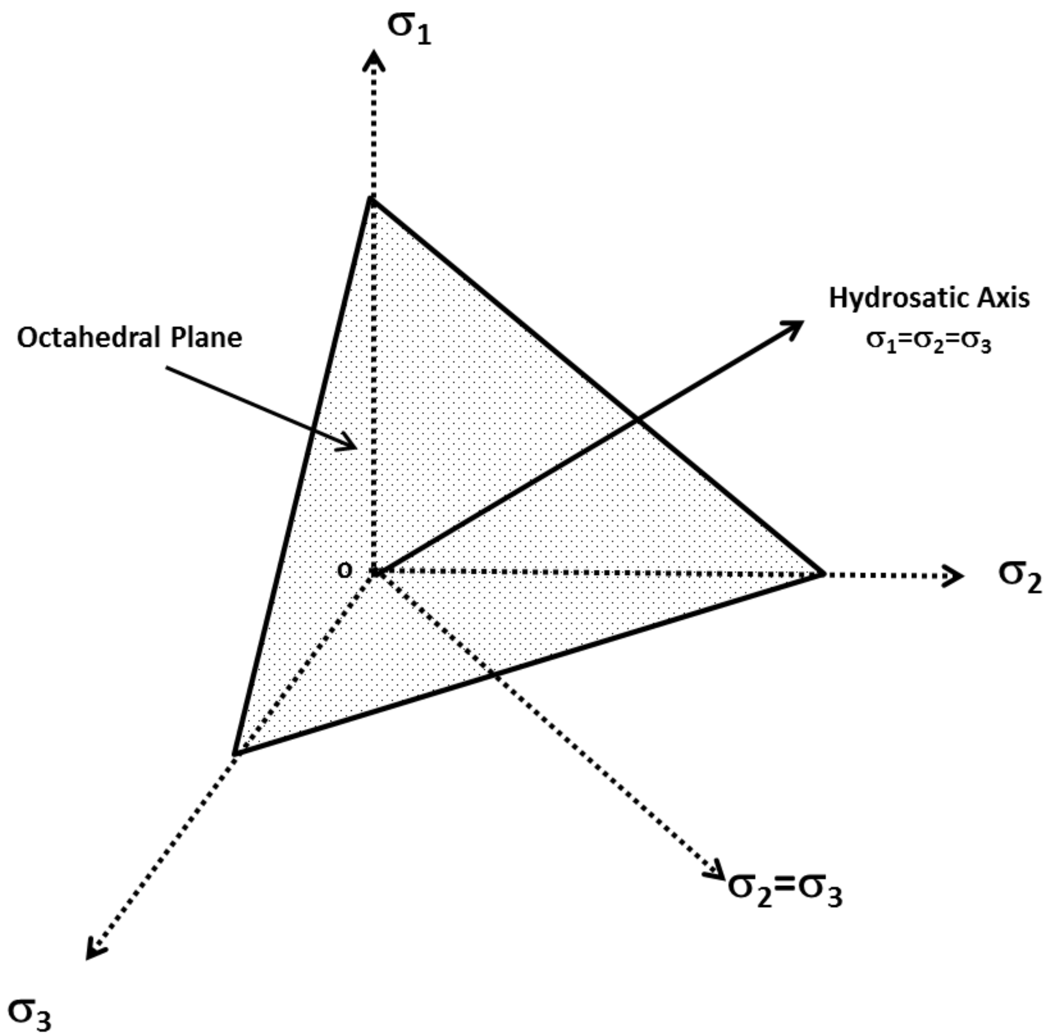

Figure 5.7.2. Principal Stress space in 3D showing Octahedral Plane and Hydrostatic Axis.

5.8 Sector I Tests

Specimens tested in Sector I of the octahedral plane have horizontal bedding planes, where α=0°. In this part of the experimental study, seven specimens were prepared and tested with different b-values. A summary of the tests as well as the stresses at failure is presented in Table 5.8.1 and Figure 5.8.1. The friction angle values have been corrected for void ratio variation (as mentioned in Section 3.2.2) and have all been corrected to a void ratio of 0.53. The stresses have also been shifted to the I_1=300 kPa plane on the Octahedral Plane. For b-values from 0 to 0.69, the friction angle increases. However, the friction angle decreases once it passes about 0.69 and drops by about two degrees as it reaches 1. This trend can be seen in Figure 5.8.6.

Table 5.8.1 Summary of Sector I Tests with stresses at failure.

Test No.	**b-value**	**σ_1/σ_3**	**ϕ (°)***
TT#1	0.00	5.49	43.34
TT#2	0.24	7.16	48.85
TT#3	0.51	9.23	53.41
TT#4	0.75	9.99	54.78
TT#5	0.70	10.59	55.84
TT#6	0.72	10.32	55.42
TT#7	1.00	8.83	52.80
*Friction angles listed in the table have been corrected for void ratio variation and have been shifted to I_1=300 kPa			

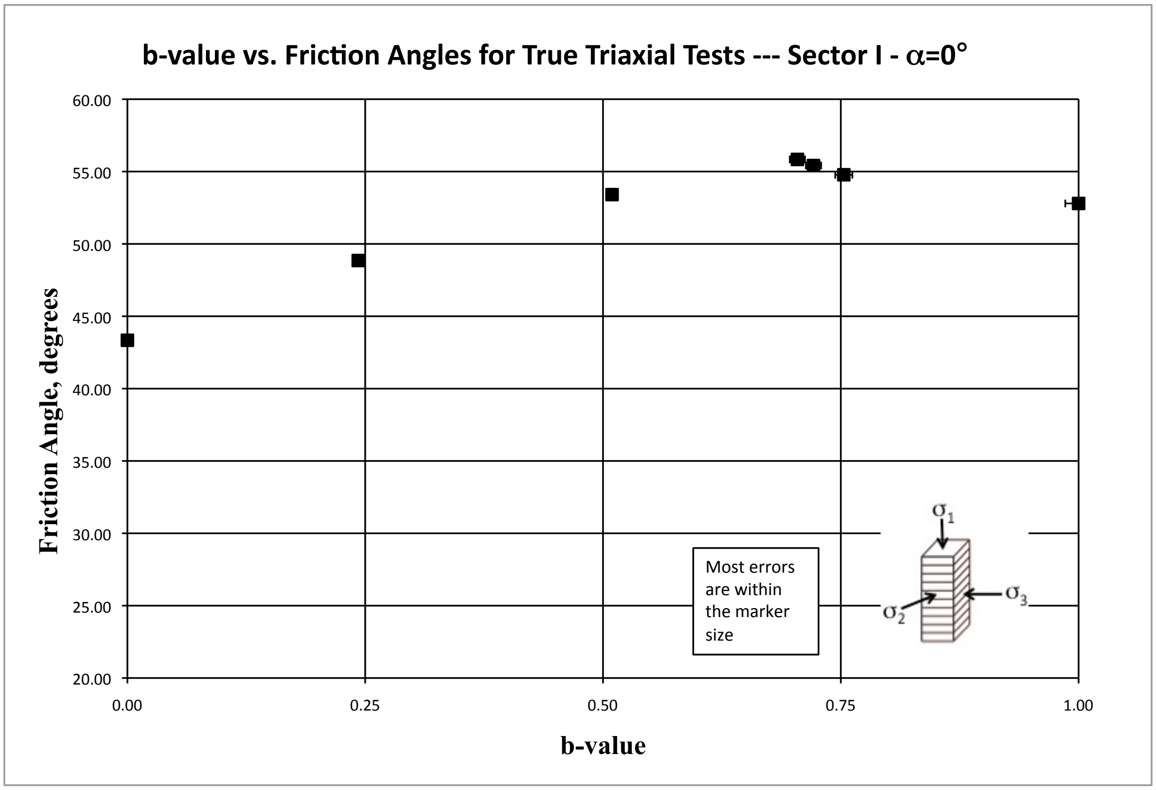

Figure 5.8.1. Varying Friction Angle with b-values for Sector I Tests.

As seen from the table, there are three tests with a b-value near 0.75. Test TT#4 was sheared at a constant b-value of 0.75 for the entire duration of the test. However, as mentioned previously in Section 5.4, for tests with higher b-values the confining pressure had to be lowered. Before knowing this, Tests TT#5 and TT#6 were conducted at b-values of 1.0 until the air pressure supply line was maxed out. Once this occurred, the horizontal stress could not be kept at the corresponding b-value of 1.0 and therefore, dropped as the vertical deviator stress increased. Because of this circumstance, the horizontal stress was kept constant while the specimens were sheared. The b-values listed in Table 5.1.1 are the b-values that were calculated according to the applied horizontal and axial stress at failure. In Test TT#7, the confining pressure was lowered to 30 kPa and the test was able to hold a constant b-value of 1.0 during the entire shearing of the specimen.

Figure 5.8.2 shows the stress paths followed for the different tests in Sector I according to b-value. As is seen, Tests 5 and 6 deviate from the intended b-value and as the horizontal pressure is kept constant and the vertical load is increased, the b-value decreases until failure and stays constant at that value until the softening regime is reached.

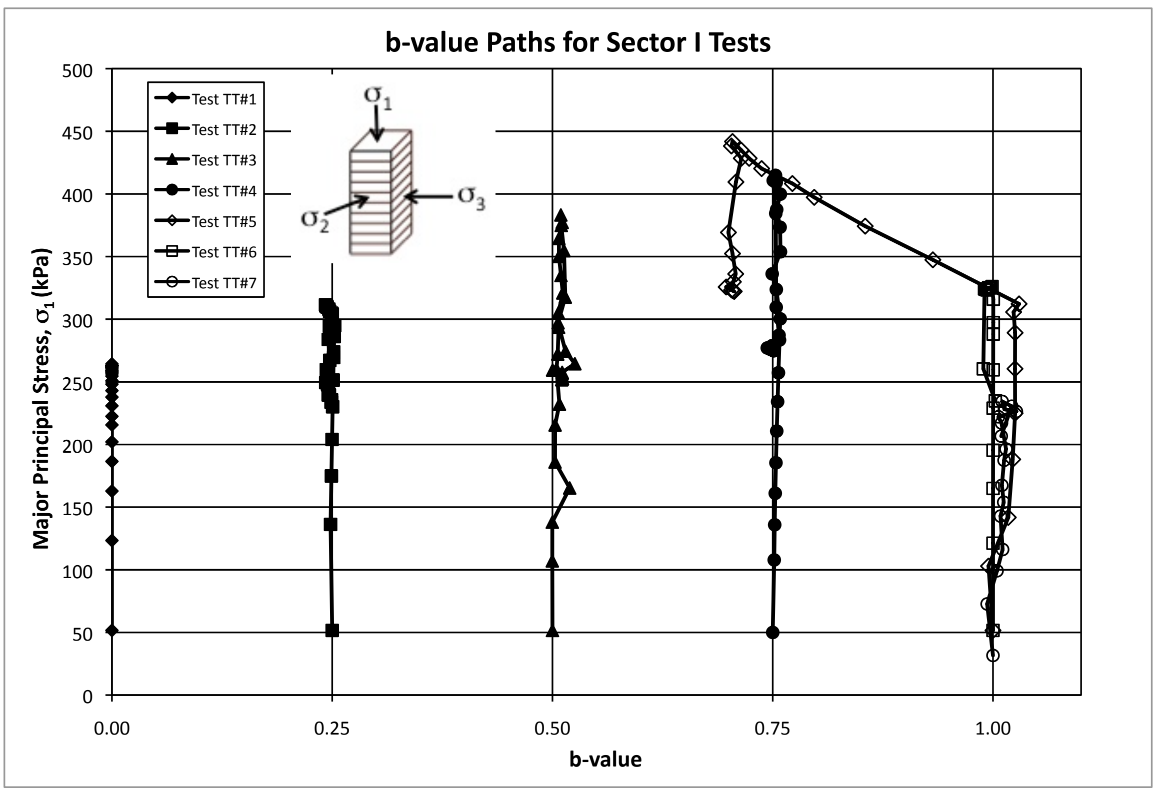

Figure 5.8.2. b-value stress paths for Tests TT#1-TT#7.

Even though the stress paths changed slightly towards the end, it is seen that the friction angles and stress ratios of all tests that failed at a b-value of 0.75 are extremely close to each other. This confirms the repeatability of the results.

The stress-strain and volume change behavior for Tests TT#1 through TT#7 are presented in Figure 5.8.3 and 5.8.4. As the b-value increases, the axial strain at failure also decreases. After peak failure, certain specimens developed shear bands. The beginning of the shear bands can be seen where there is a sudden drop in stress ratio. However, shear banding and its effects will be discussed in detail in Chapter 9. When looking at the volume change behavior, there is also a trend that shows more dilation with increasing b-values. The angle of dilation is presented in Figure 5.8.5. The angles for all tests were plotted. As can be seen from the figure, there is some scatter among the results for b=0.75, particularly at TT#5 and TT#6. This is due to the changes in b-value stress path described earlier. The angle of dilation is constant until about 0.5 and then increases with increasing b-value. Table 5.8.2 lists the angle of dilation for each test in Sector I. The dilation angle was calculated by analyzing the slope of the volume change at failure. The equation for angle of dilation, Ψ is written as

$$\Psi = \sin^{-1}\left(\frac{\frac{\Delta\varepsilon_v}{\Delta\varepsilon_1}}{\frac{\Delta\varepsilon_v}{\Delta\varepsilon_1}-2}\right) \qquad \text{Eq. 5.8.1}$$

where $\Delta\varepsilon_v$ is the incremental volumetric strain and $\Delta\varepsilon_1$ is the incremental axial strain.

The axial strain and horizontal strain was also analyzed. In Figure 5.8.6, it is apparent that as b-value increases, the horizontal strain also increases. This is due to the increase in horizontal deviator stress applied by the horizontal loading system. For tests TT#5 and TT#6 which were originally b=1.0 tests, the horizontal strain overlaps that of test TT#7 where b=1.0. However, as the b-value starts to decrease, the horizontal strain also decreases and follows very closely the strain shown by TT#4 where b=0.75. The horizontal strain for Test TT#7 where b=1.0 (σ_2=σ_1) does not level off towards failure like the other tests. The horizontal strain increases linearly until failure is reached.

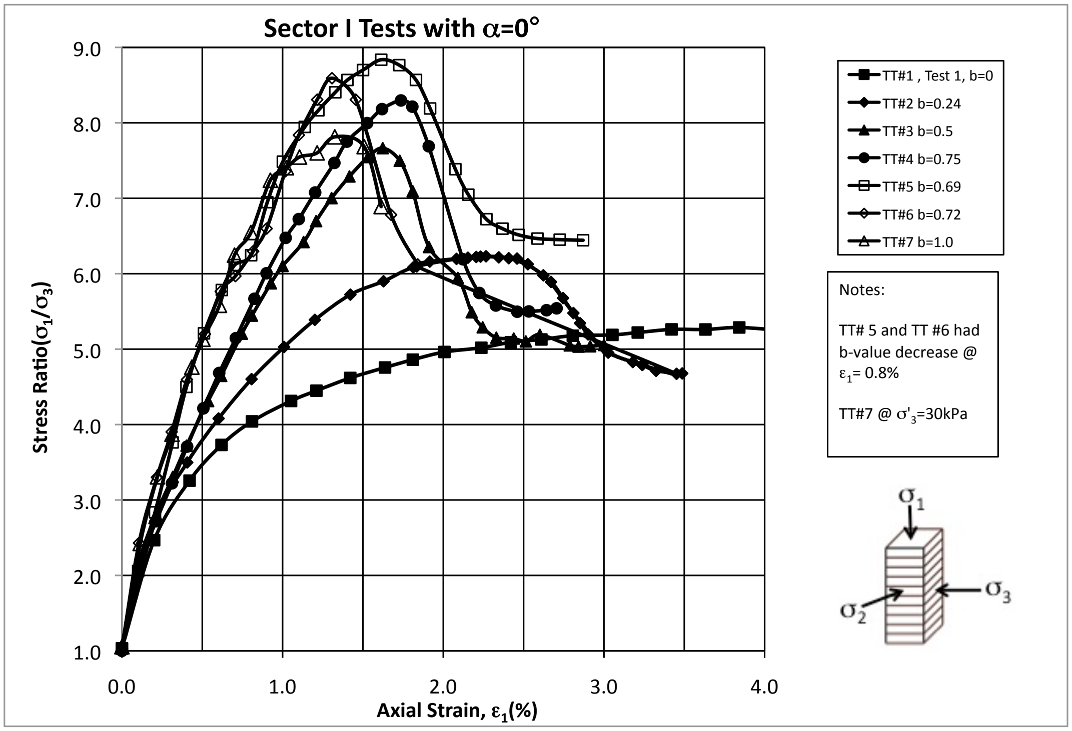

Figure 5.8.3. Stress-strain curves for Tests TT#1-TT#7 in Sector I.

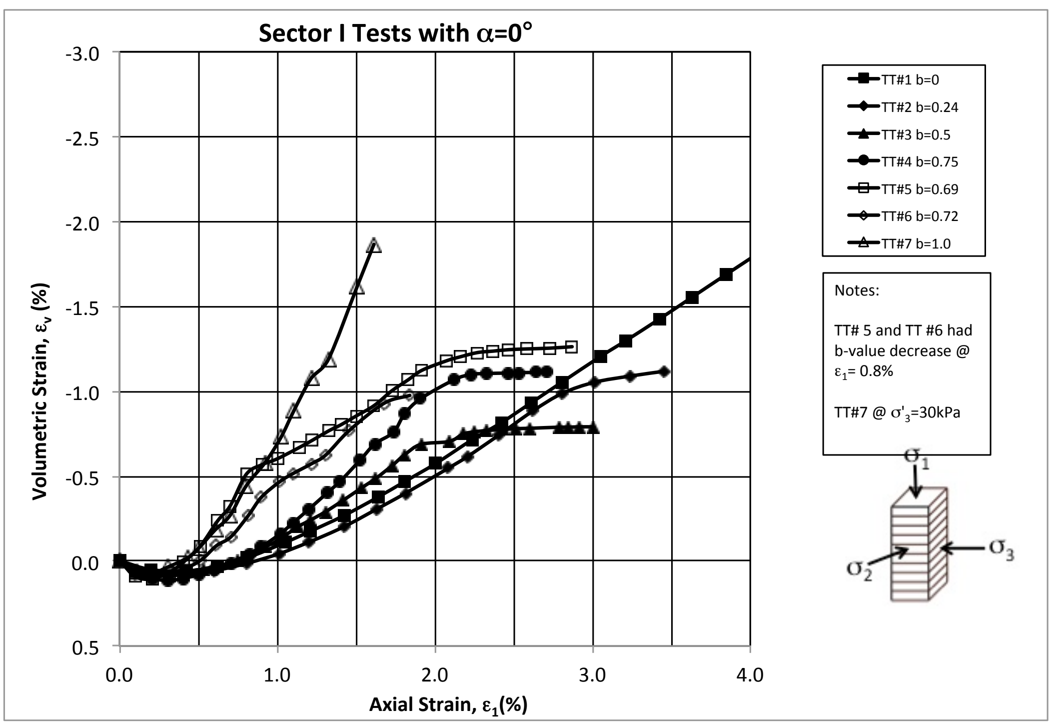

Figure 5.8.4. Volume Change curves for Tests TT#1-TT#7 in Sector I.

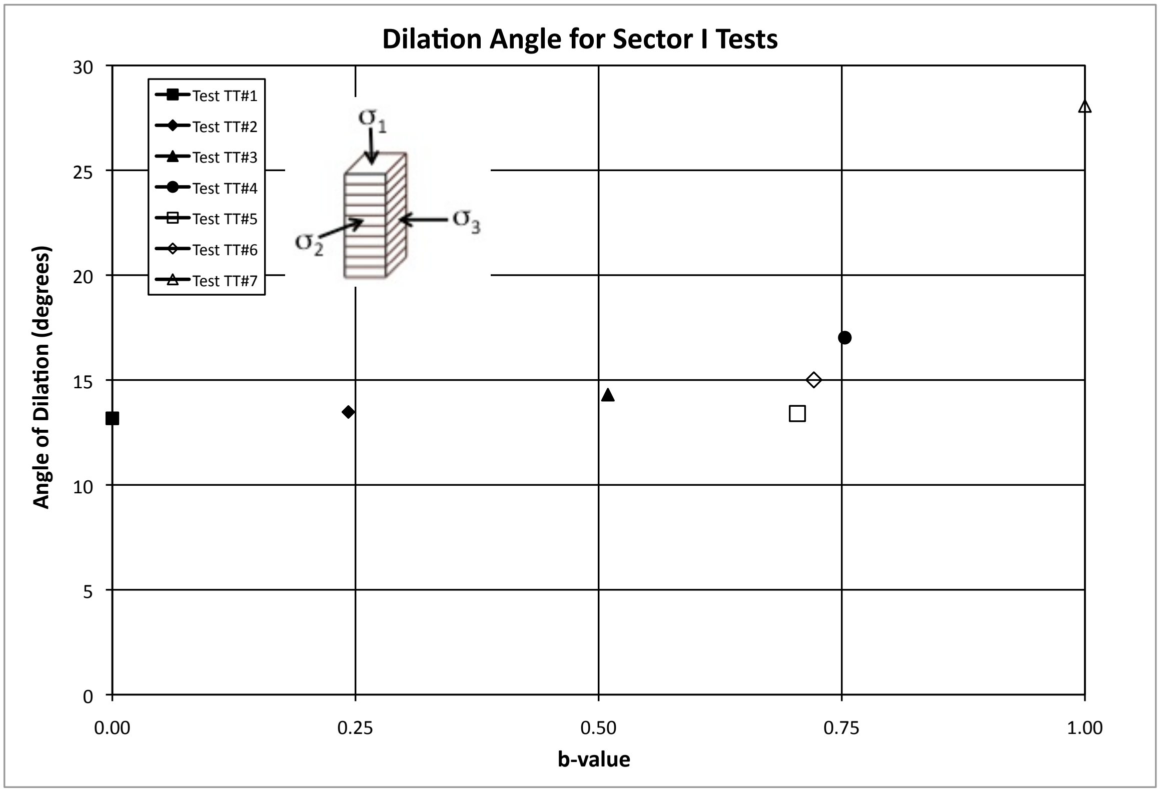

Figure 5.8.5. Angle of Dilation for Sector I Tests.

.

Table 5.8.2. Summary Table of Dilation Angles for Sector I Tests.

Sector 1		
Test No.	**b-value**	**Dilation Angle (°)**
TT#1	0	13.17
TT#2	0.24	13.48
TT#3	0.51	14.30
TT#4	0.75	17.02
TT#5	0.70	13.40
TT#6	0.72	15.01
TT#7	1.00	28.07

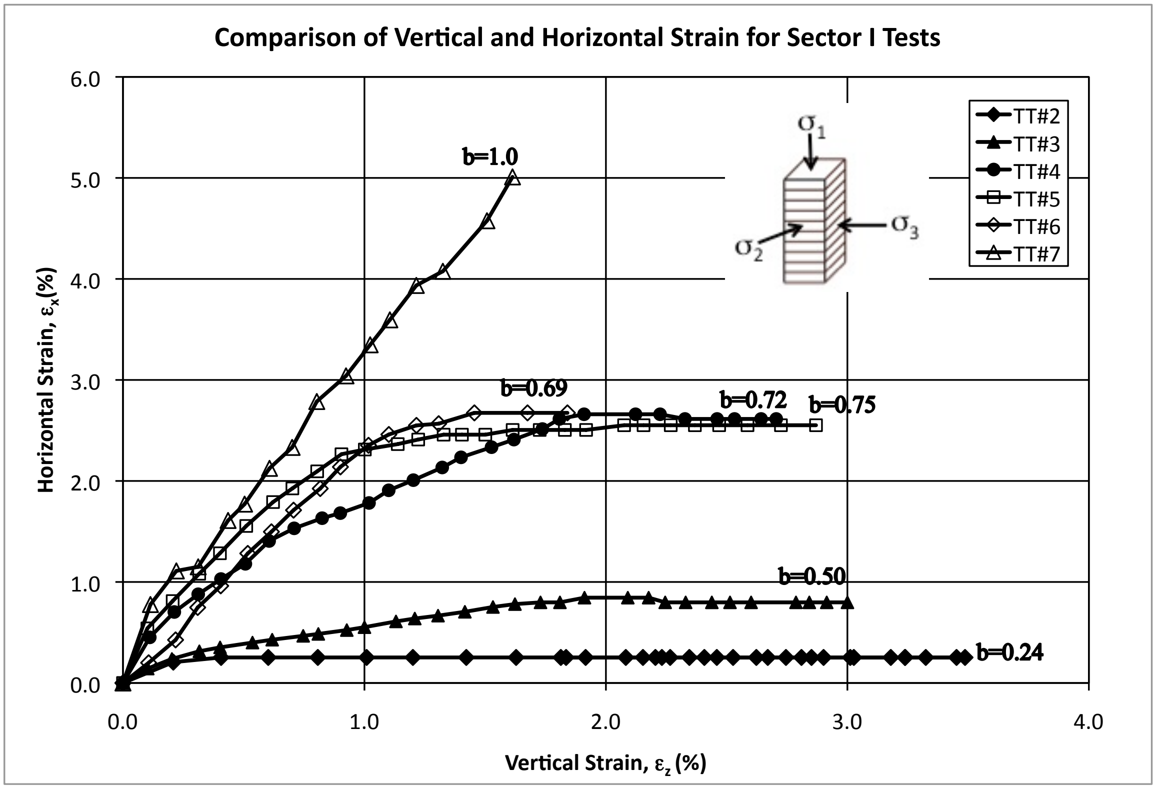

Figure 5.8.6. Comparison of horizontal and vertical strains for Sector I tests.

5.9 Sector II Tests

A total of five specimens were sheared in order to attain test data for Sector II of the octahedral plane. Specimens in this Sector have vertical bedding planes where α=90°. As seen in Figure 5.1.1, the face of the specimen that is perpendicular to the bedding planes is placed in the σ_2 direction. A summary of the tests performed is provided in Table 5.9.1. This summary includes Test TT#13 where b=0 and α=90°. TT#13's test conditions are shared on the octahedral plane between Sector II and III and are therefore presented in both sections. Test TT #7 and TT #12 are also shared and are compared later in Figure 5.9.7.

As described before with TT#5 and TT#6, when running Test TT#11, the pressure in the air supply line reached its maximum. Therefore, instead of being able to fail the specimen at the desired b-value of 1, the horizontal stress was kept constant while the axial stress reached its maximum and sheared the specimen. Therefore, Tests TT #10 and TT#11 both were sheared at almost the same exact b-value at failure. The friction angle difference for both tests is 0.6 degrees, showing once again the repeatability of the results of the tests. In order to shear the specimen at a constant b-value of 1.0, the confining pressure was lowered to 30 kPa. The results of the six tests in Sector II are summarized in Table 5.9.1 and Figure 5.9.1. The stresses presented are stresses at failure. The stress paths with relation to b-value and major principal stress are presented in Figure 5.9.2.

Table 5.9.1. Summary of Sector II Tests with stresses at failure.

Test No.	**b-value**	σ_1/σ_3	**ϕ (°)***
TT#13	0.00	4.16	38.02°
TT#8	0.25	7.15	48.99
TT#9	0.49	8.65	52.44
TT#10	0.70	10.34	55.45
TT#11	0.69	10.36	55.49
TT#12	1.00	8.60	52.34

*Friction angles listed in the table have been corrected for void ratio variation and have been shifted to I_1=300 kPa

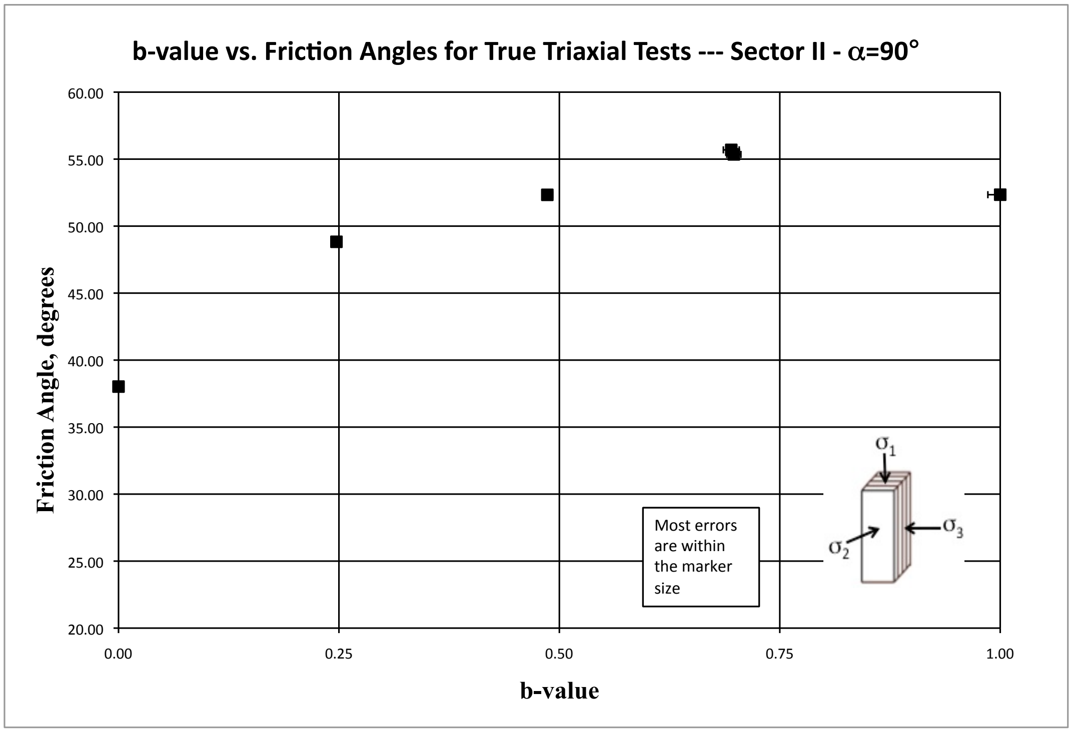

Figure 5.9.1. Varying Friction Angle with b-values for Sector II Tests.

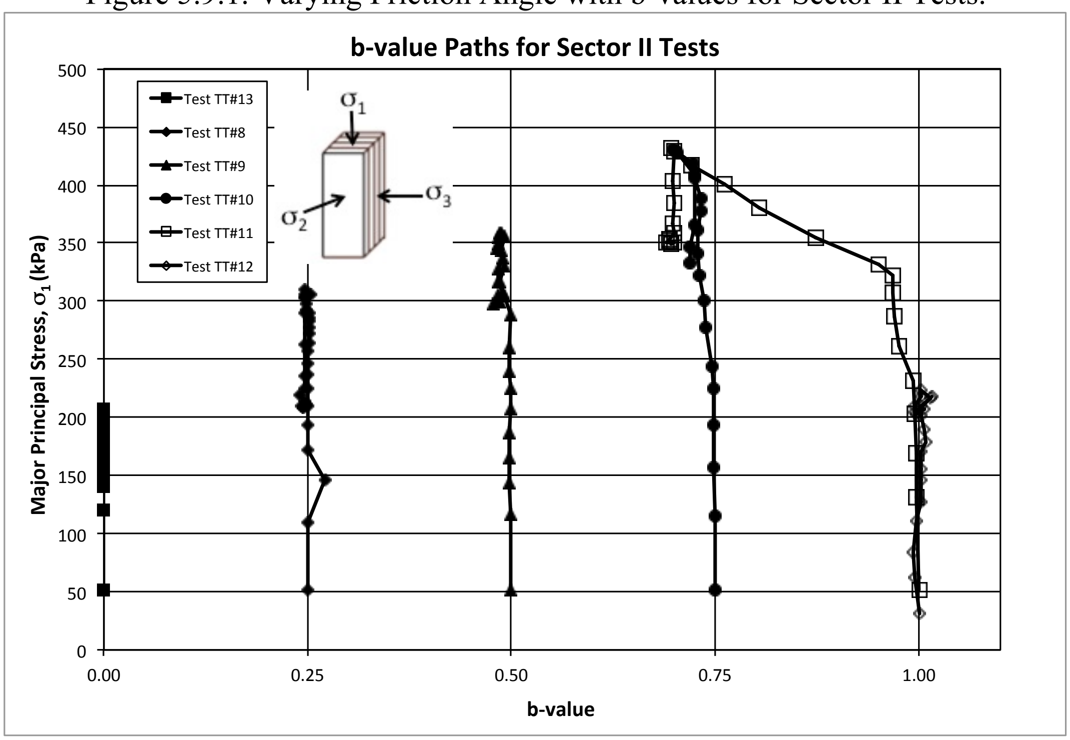

Figure 5.9.2. b-value stress paths for Tests TT#8-TT#13.

The stress-strain and volume change curves for Tests TT#8 through TT#13 are presented in Figures 5.9.3 and 5.9.4. As the b-value increases from 0 to 0.75, the stress ratio also increases. With a b=1.0, the stress value decreases. The axial strain to failure also decreases as the b-value increases. The stress-strain behavior of TT#10 and TT#11 follow the same curve and fail at almost the same stress-ratio and friction angle. TT#11 begins to drop b-value at about 0.5% axial strain. Due to the initial increase in strain under b=1.0 conditions for TT#10, the total volume change begins to show dilation earlier than TT#11. However, once they reach the same b=0.75 value at about 1% axial strain, it can be seen that the curves follow the same exact slopes. Shear banding occurs sooner in TT#11 due to the experienced increase in dilation and change in stress path.

The angles of dilation for Sector II tests are presented in Figure 5.9.5 and a summary of the values is presented in Table 5.9.2. When looking through the scatter for the repeated tests at b=0.75, there is an upward trend as b-increases. This is apparent when looking at the slopes of the volume change shown in Figure 5.9.4.

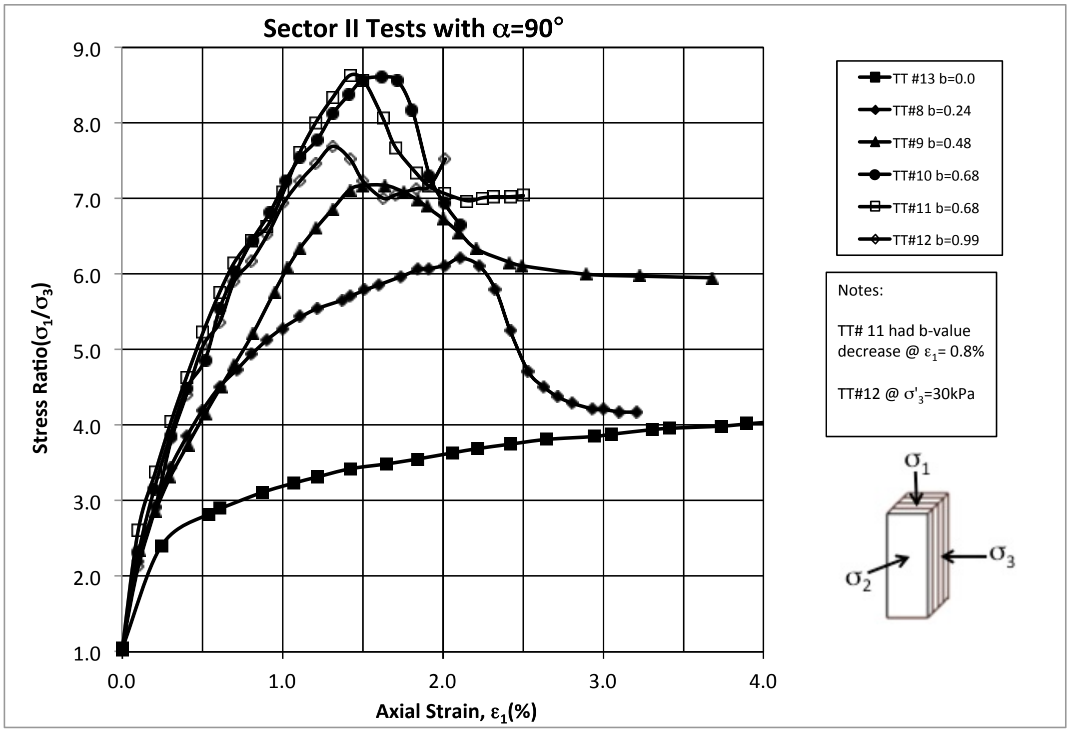

Figure 5.9.3. Stress-strain curves for Tests TT#8-TT#13 in Sector II.

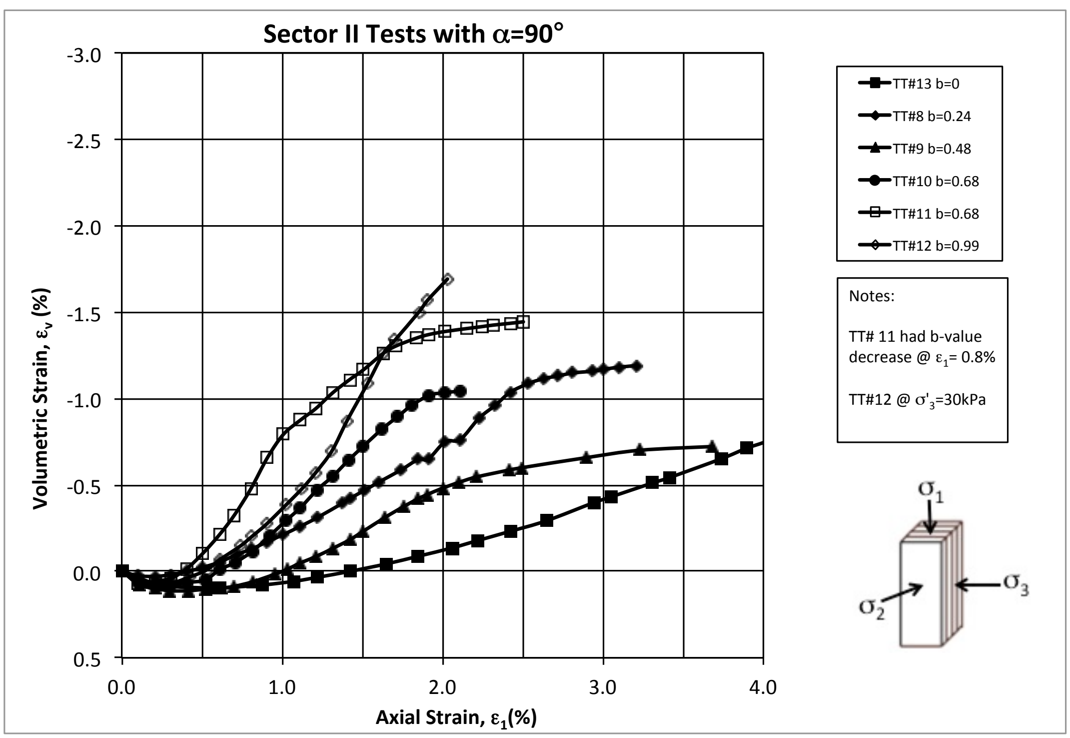

Figure 5.9.4. Volume Change curves for Tests TT#8-TT#13 in Sector II.

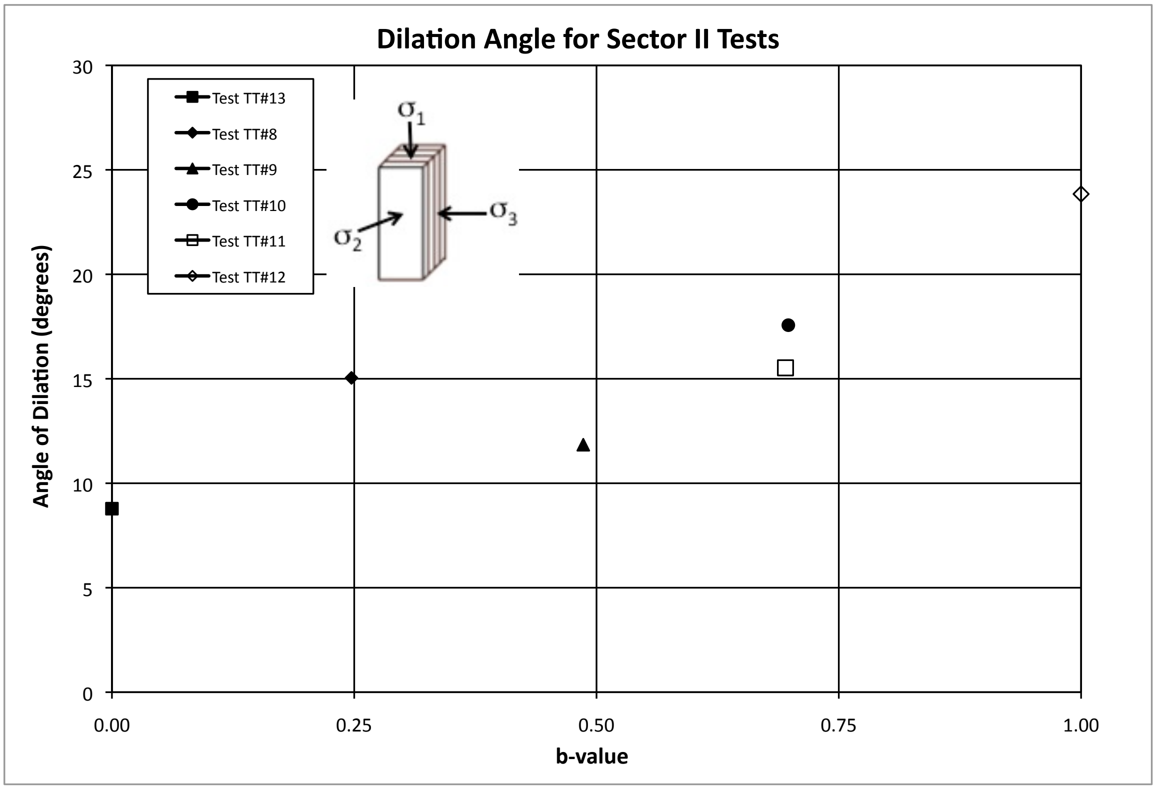

Figure 5.9.5. Angle of Dilation for Sector II Tests.

Table 5.9.2. Summary Table of Dilation Angles for Sector II Tests.

Sector II		
Test No.	**b-value**	**Dilation Angle**
TT#13	0	8.47
TT#8	0.24	15.04
TT#9	0.48	11.84
TT#10	0.68	17.57
TT#11	0.68	15.52
TT#12	0.99	23.84

As shown with Sector I, the axial and horizontal strains were graphed and studied. The horizontal strains are similar to those seen in Sector I. With increasing b-value, the horizontal load is also increased. Therefore, more strain in the horizontal direction will be seen. When comparing Sector I and Sector II, more horizontal strain is seen in Sector II for b=0.25, 0.5 and 1.

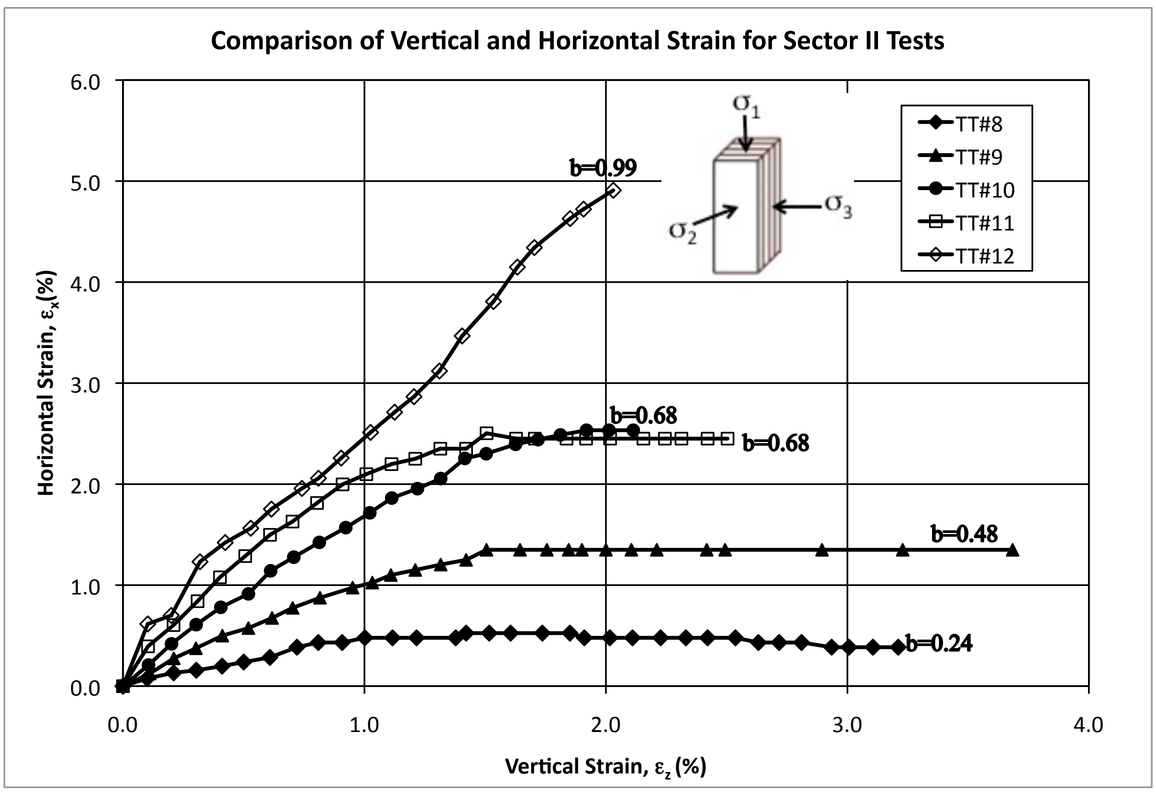

Figure 5.9.6. Comparison of horizontal and vertical strains for Sector II tests.

As a way to double-check the results from Sector I, Specimen TT#12 was sheared at b=1.0. This point is shared on the octahedral plane between Sectors I and II. Looking back at the results from Test TT #7, there is only a slight difference in friction angle of 0.17 degrees. The overlay of the plots is presented in Figures 5.9.7 and 5.9.8. In order to see more details of the graphs, the axial strain on the figures is shown only to 2%. The axial strains to failure for both tests are the same. Also, the peak stress ratios are very near each other. Therefore, the two tests can confirm each other.

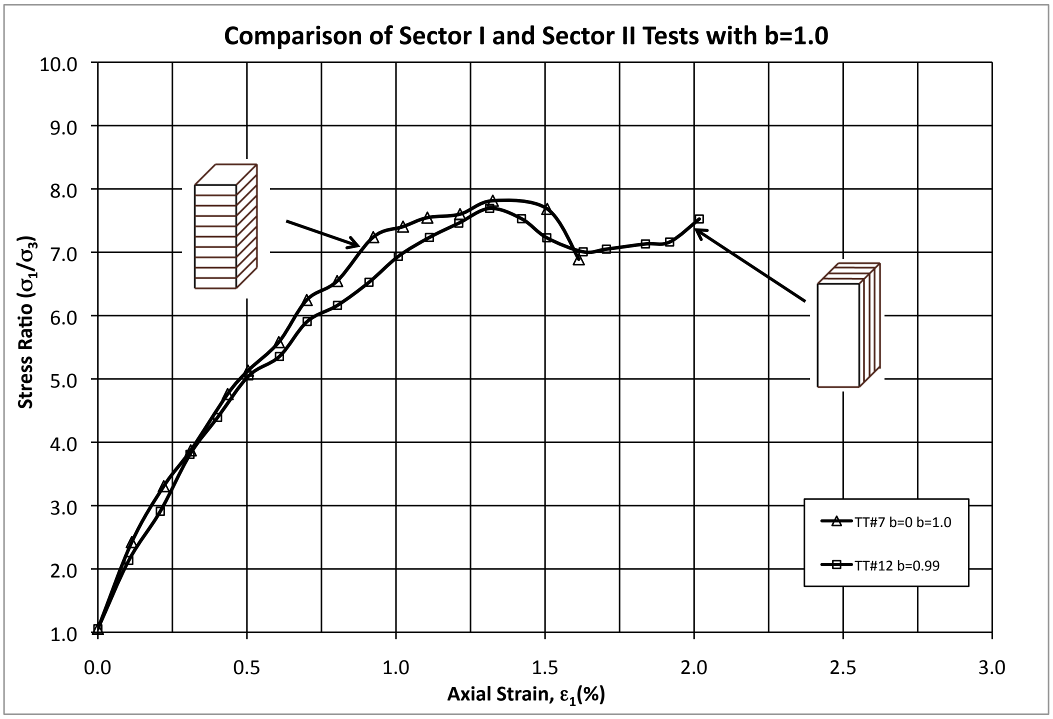

Figure 5.9.7. Stress Ratio Comparison of Sector I and II Tests with b=1.0.

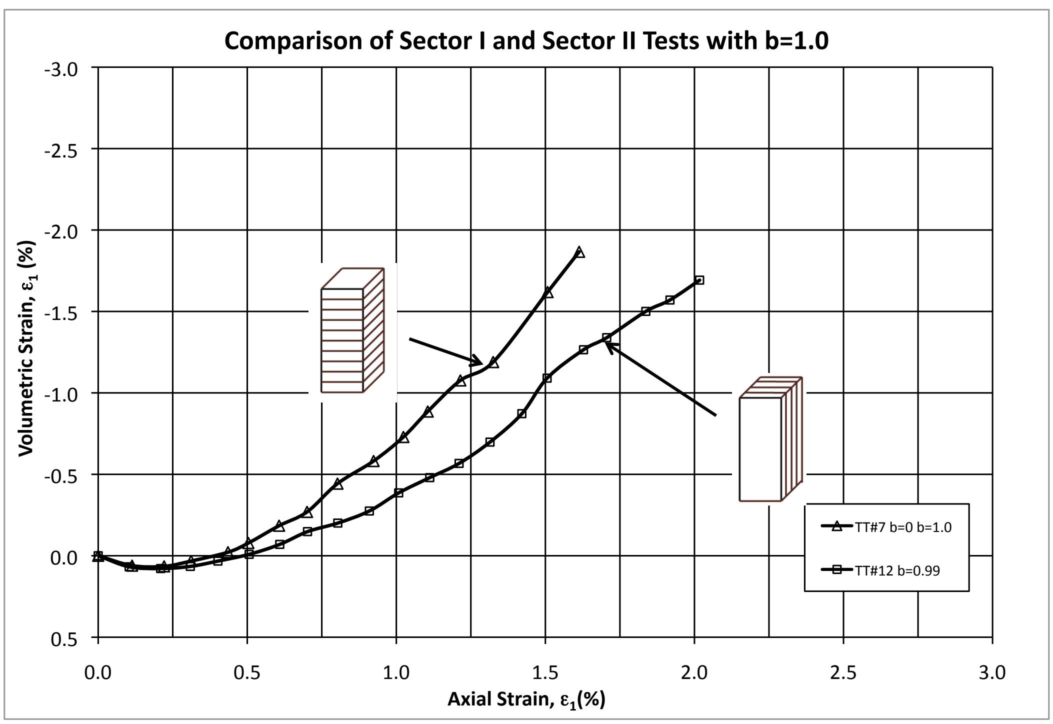

Figure 5.9.8. Volume Change Comparison of Sector I and II Tests with b=1.0.

5.10 Sector III Tests

A total of six specimens were sheared with vertical bedding planes of α=90° that correspond to the third Sector. The intermediate principal stress was applied to the face of the specimen that was parallel to the vertical bedding planes. Therefore, the face perpendicular to the bedding planes was exposed to the confining pressure, σ_3. A summary of Tests TT#13 through TT#18 is presented. Test TT#17 began with a b-value of 1.0 but due to having insufficient air pressure once again, the specimen sheared at a b-value of 0.72. As can be seen in Table 5.10.1 and Figure 5.10.1, a difference of only 0.5 degrees is seen between Tests TT#16 and TT#17. Figure 5.1.2 shows the stress paths followed for the Sector III tests. The test data shows an upward trend until 0.5. At b=0.5, there is a low friction angle which was due to the occurrence of shear banding during the hardening regime. Then as b-value increases from 0.5 to one, the similar trend seen earlier is seen for Sector III.

Table 5.10.1. Summary of Sector III Tests with stresses at failure.

Test No.	**b-value**	σ_1/σ_3	**ϕ (°)***
TT#13	0.00	4.16	38.02
TT#14	0.25	6.74	47.88
TT#15	0.49	6.78	48.15
TT#16	0.72	8.94	53.17
TT#17	0.72	9.18	53.62
TT#18	0.95	7.76	50.29
*Friction angles listed in the table have been corrected for void ratio variation & have been shifted to I_1=300 kPa			

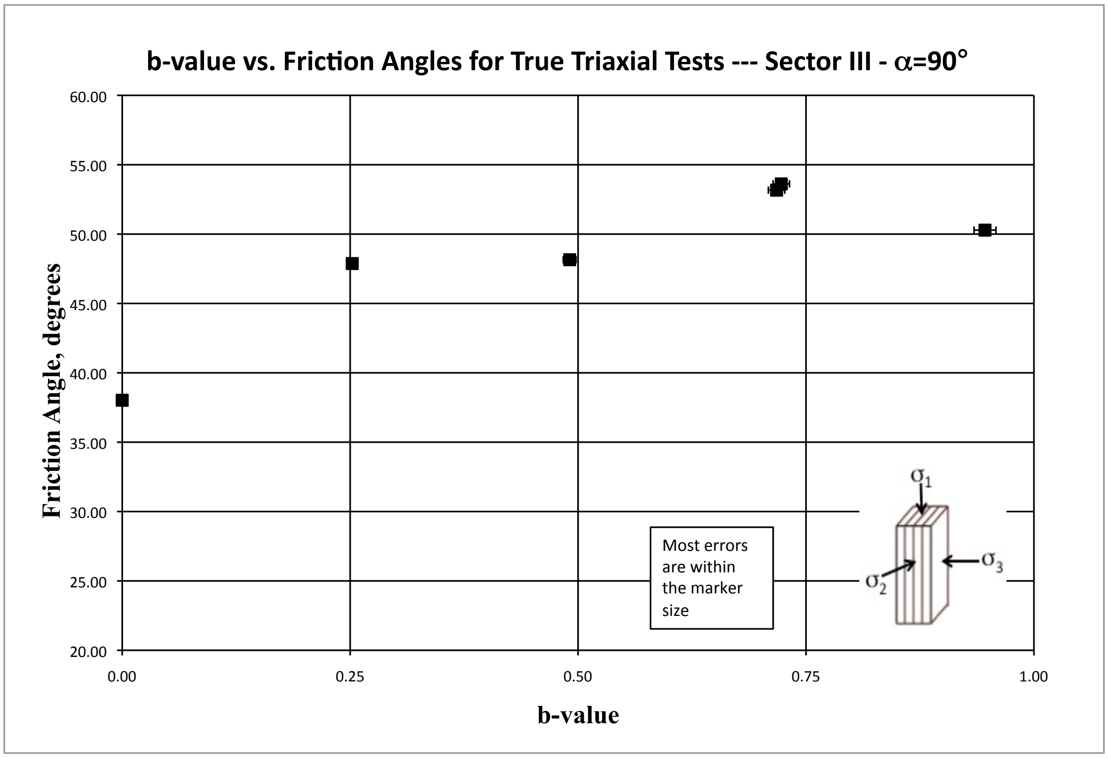

Figure 5.10.1. Varying Friction Angle with b-values for Sector III Tests.

The stress-strain and volumetric change graphs are presented in Figures 5.10.3 and 5.10.4. When looking at the behavior of the stress-strain curves for Tests TT#16 and TT #7, they look very similar. Because the b-value=1.0 for Tests TT#17 during the beginning of the test, the specimen experienced a greater intermediate principal stress compared to TT#16. This caused a faster increase in stress with less axial strain (i.e. a steeper curve in the beginning of the test). Once the b-value started to drop, the specimen behaved similarly to Test #17. Around and after peak failure both curves are almost the same. This behavior is also seen in the volume change graphs.

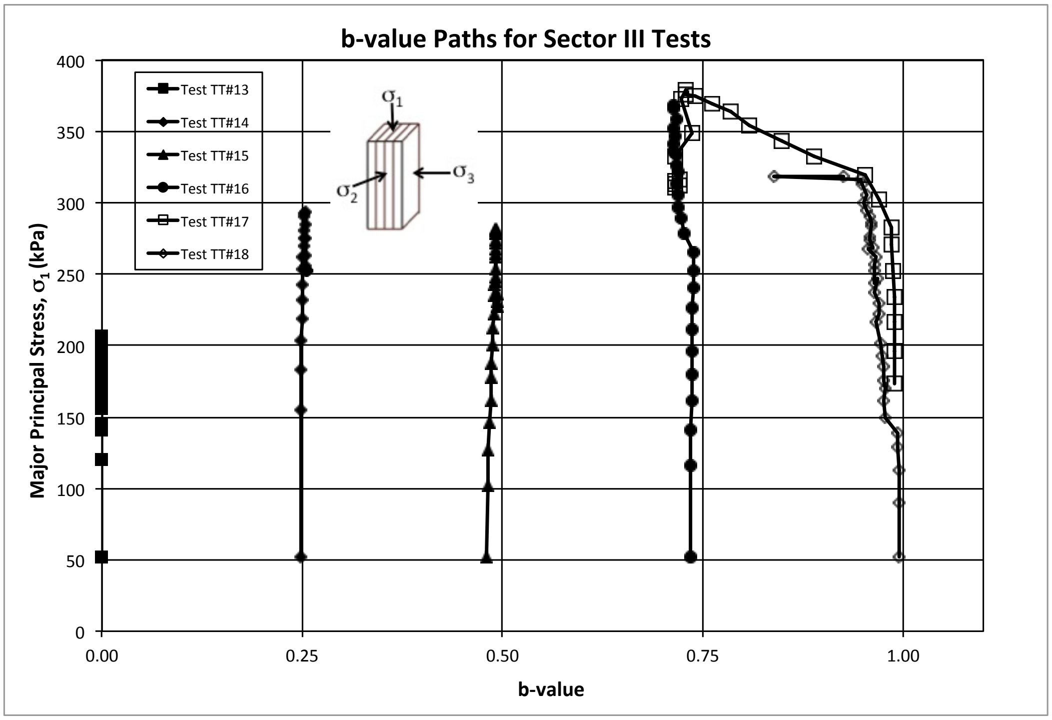

Figure 5.10.2. b-value stress paths for Tests TT#13-TT#18.

Similar to Sectors I and II, the strength increases from b=0 to b=0.25. However, as seen in Lade and Abelev (2003) the strength drops for Test TT#15 due to the occurrence of shear bands. The development of shear bands, causes the specimen to shear prematurely and this is reflected in the peak friction angle at failure. The friction angle increases once again for TT#16 and TT#17 (where b=0.71 and 0.72, respectively) and lowers for TT#18 at b=0.94. The patterns in strength with increasing b-values is similar to those seen in Sectors I and II, with the exception of TT#15. When comparing b=0 and b=1.0, the largest difference in friction angle (9.2°) is seen in Sector III. Sectors I and II had a difference of 7.9° and 6.2°, respectively. An increase in angle of dilation is seen once again with tests in Sector III and is presented in Figure 5.10.5. The summary of the dilation angles is presented in Table 5.10.2.

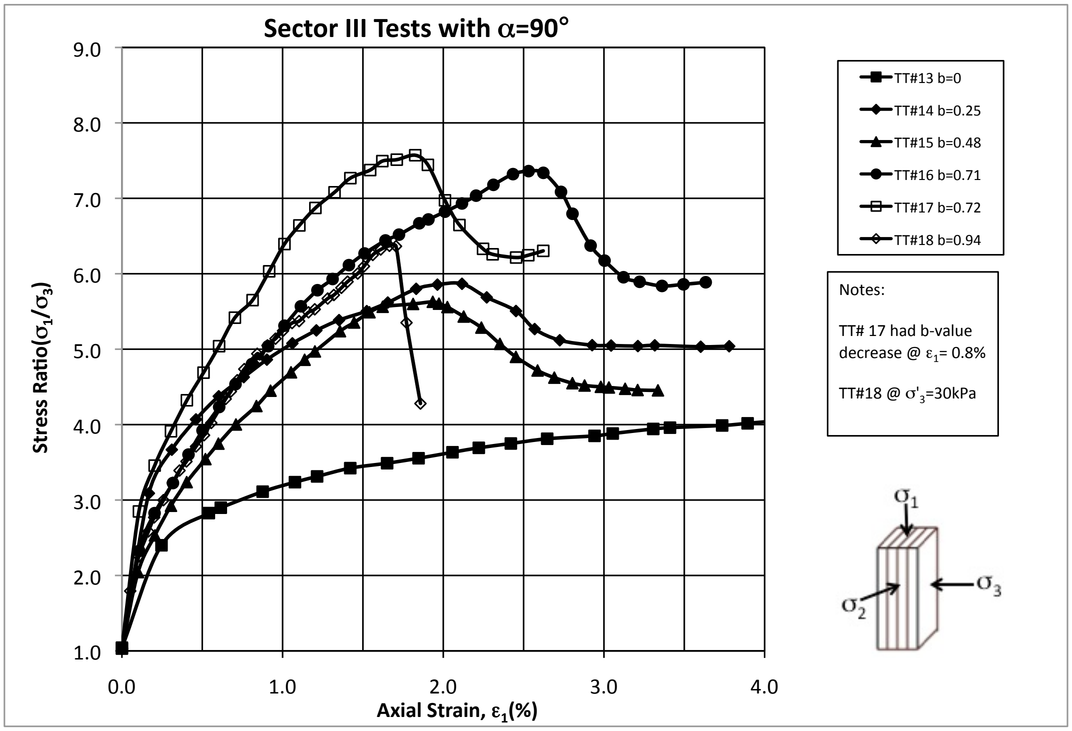

Figure 5.10.3. Stress-strain curves for Tests TT#13-TT#18 in Sector III.

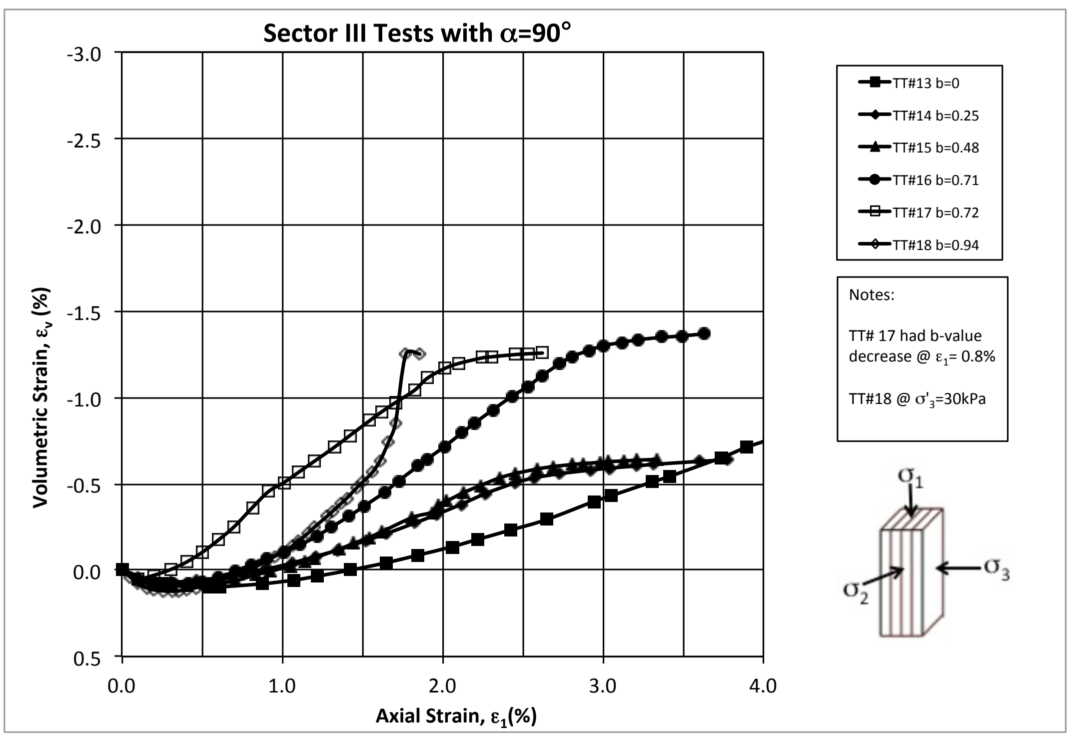

Figure 5.10.4 Volume Change curves for Tests TT#13-TT#18 in Sector III.

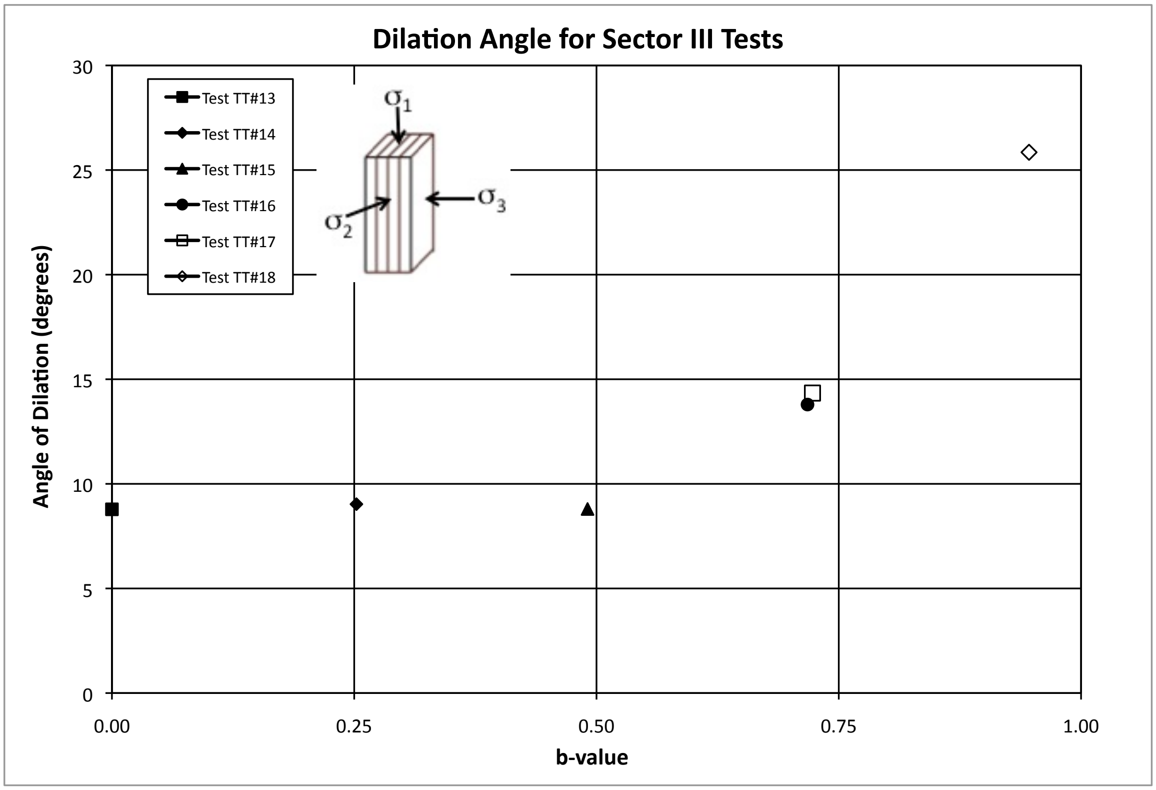

Figure 5.10.5. Angle of Dilation for Sector III Tests.

Table 5.10.2. Summary Table of Dilation Angles for Sector III Tests.

Sector III		
Test No.	**b-value**	**Dilation Angle**
TT#13	0	8.78
TT#14	0.25	9.03
TT#15	0.49	8.80
TT#16	0.72	13.80
TT#17	0.72	14.34
TT#18	0.95	25.85

The comparison of vertical and horizontal strain for Sector III tests is presented in Figure 5.10.6. Once again it is seen that with increasing b-value the horizontal strains also increase. At the points where the horizontal strain levels off, there is less axial strain and greater horizontal strain than in Sector II.

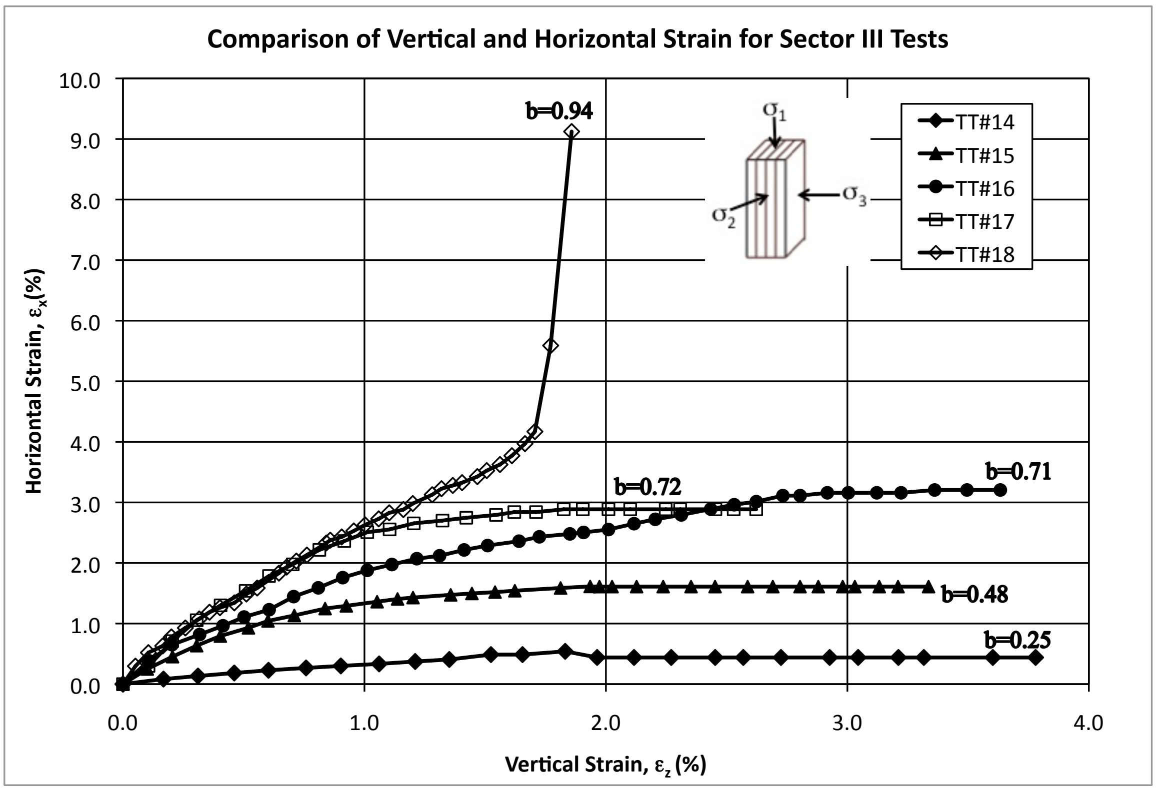

Figure 5.10.6. Comparison of horizontal and vertical strains for Sector II tests.

5.11 Conclusion

In order to study cross-anisotropy and its effect on the strength behavior of Fine Nevada sand, Sectors I, II and III must be analyzed together. Figure 5.11.1 shows the varying strengths according to Sector for various b-values. These results are similar to those by Lade and Abelev (2003) where strength decreases when moving from Sector I to III. Because of the deposition of the sand grains, as explained in Chapter 2, the grains are strongest in the horizontal bedding plane (α=0°) direction where the major principal stress is perpendicular to the long axes of the grains. This is seen in the results from Sector I. They are the weakest in the vertical direction (α=90°) when the major principal stress is parallel to the long axes of the grains (seen in Sector III). Results from Sector II show that the effect of the intermediate principal stress, σ_2, when perpendicular to the bedding planes, (see Figure 5.1.1) is not as pronounced as when σ_2 is parallel to the bedding planes.

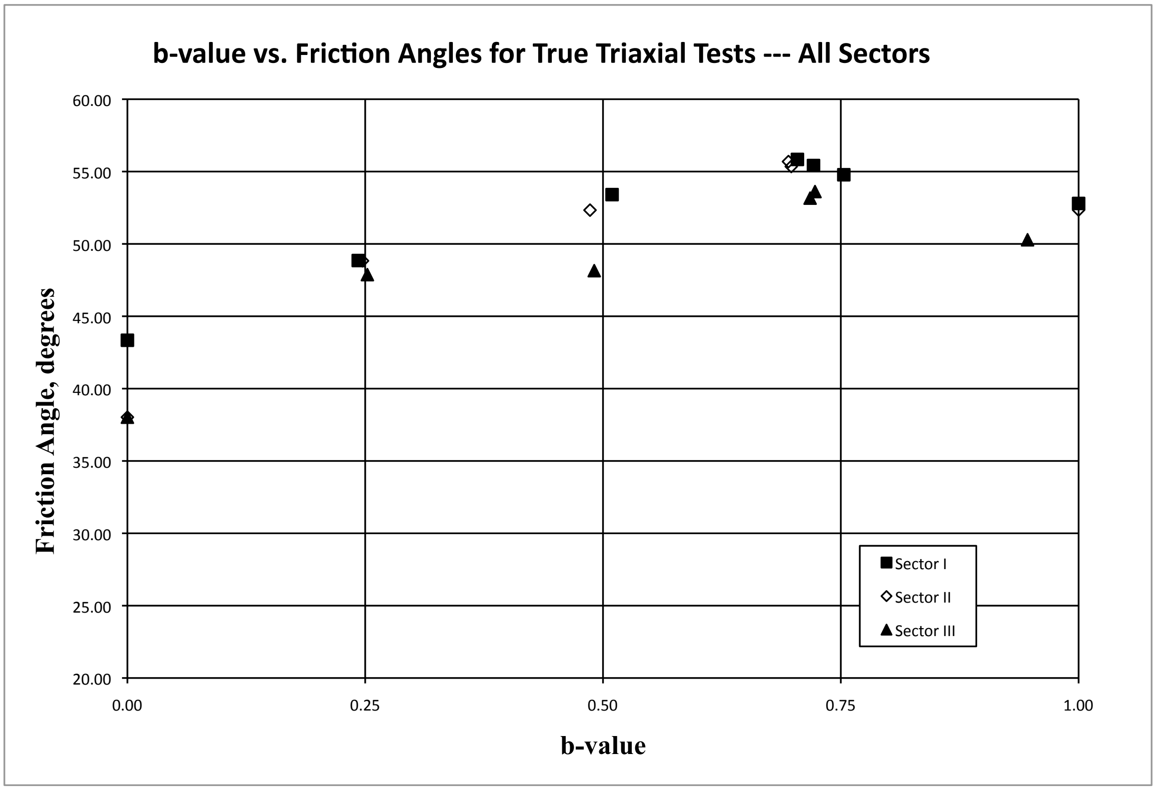

Figure 5.11.1. Summary of friction angle versus b-value for all Sectors.

In order to see the clear difference among the three Sectors, Table 5.11.1 summarizes the friction angle by b-values. The difference presented in the last column of the table is calculated by subtracting each of the friction angles from the largest friction angle for that particular b-value. As can be seen, the largest difference is between tests in Sectors I and III. Friction angles for Sector II are closer to Sector I than Sector III for all b-values.

A summary of the calculated dilation angles for all sectors is presented in Figure 5.11.2. As can be seen, for all sectors, the dilation angle increases with b-value. The increase for lower b-values is less steep from b=0 to b=0.5. However, for tests with b=0.75 and b=1.0, there is a great increase in dilation angle and volumetric change. Tests with varying stress paths have been omitted from this figure as their b-values were not constant and produced some scatter in the dilation angle results. However, they have been previously plotted for their individual sectors.

Table 5.11.1. Summary of Friction angle by b-value for Sectors I, II and III.

	Sector	**b-value**	σ_1/σ_3	ϕ	Δ
b=0					
TT#1	I	0.00	5.49	43.34	0.00
TT#13	III	0.00	4.16	38.02	-5.32
b=0.25					
TT#2	I	0.24	7.16	48.85	-0.14
TT#8	II	0.25	7.15	48.99	0.00
TT#14	III	0.25	6.74	47.88	-1.11
b=0.5					
TT#3	I	0.50	9.23	53.41	0.00
TT#9	II	0.48	8.65	52.44	-0.97
TT#15	III	0.48	6.78	48.15	-5.26
b=0.75					
TT#4	I	0.75	9.99	54.78	-1.06
TT#5	I	0.69	10.59	55.84	0.00
TT#6	I	0.72	10.32	55.42	-0.42
TT#10	II	0.68	10.34	55.45	-0.39
TT#11	II	0.68	10.36	55.49	-0.35
TT#16	III	0.71	8.94	53.17	-2.67
TT#17	III	0.72	9.18	53.62	-2.22
b=1.0					
TT#7	I	1.00	8.83	52.80	0.00
TT#12	II	0.99	8.60	52.34	-0.46
TT#18	III	0.94	7.76	50.29	-2.51

*Friction angles listed in the table have been corrected for void ratio variation and have been shifted to I_3=300 kPa

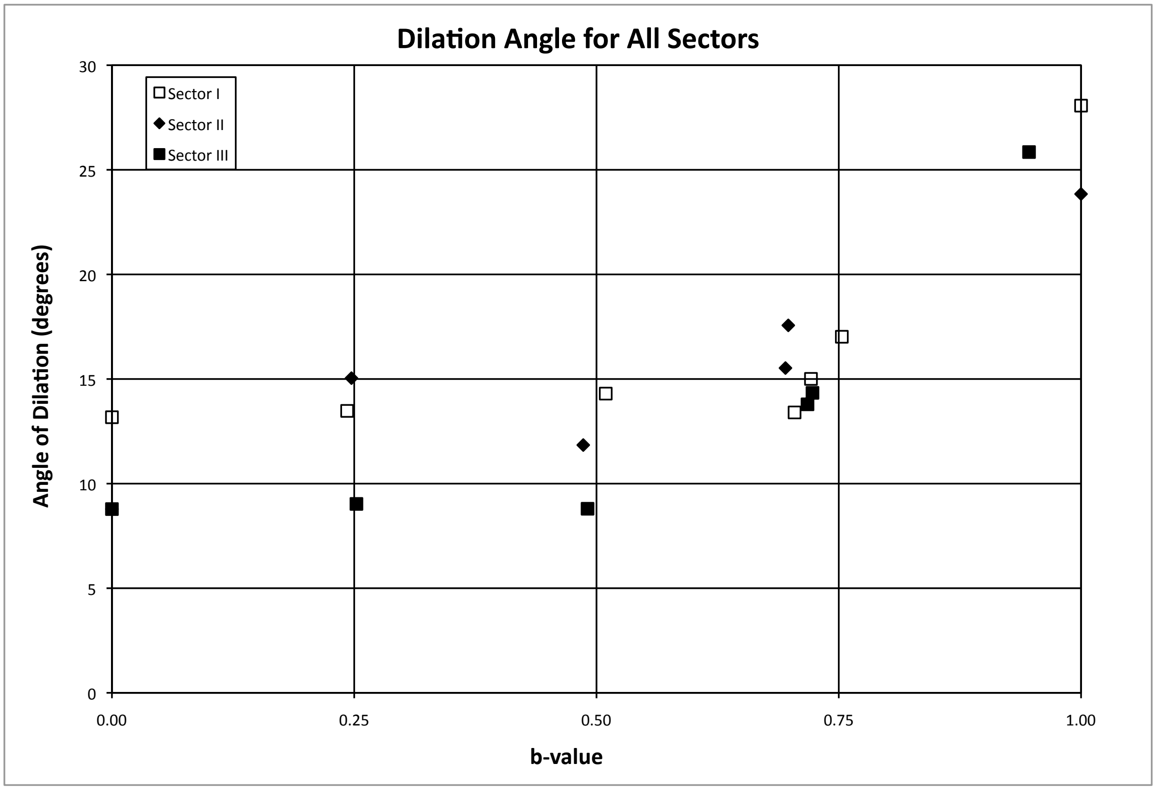

Figure 5.11.2. Summary of Dilation Angle for All Sectors.

In order to plot all of the strength points all in the same octahedral plane, the principal stresses were modified according to the following equation,

$$(\sigma_1^*, \sigma_2^*, \sigma_3^*) = (\sigma_1, \sigma_2, \sigma_3)\left(\frac{\sigma_{oct}}{\frac{1}{3}(\sigma_1 + \sigma_2 + \sigma_3)}\right) \qquad \text{Eq. 5.11.1}$$

where σ_1, σ_2, and σ_3 are the principal stresses at failure, and σ_{oct} is the octahedral normal stress corresponding to the plane where the results will be plotted. Since only the magnitudes of the principal stresses are modified, the stress ratios remain constant and therefore, there is no effect on the friction angle. The results were all plotted on a plane corresponding to I_1=300 kPa. Results from all of the tests performed are plotted on the octahedral plane in Figure 5.11.3.

This value of I_1=300 kPa was within the range in which the torsion shear tests were performed, making it a suitable plane for further comparison of test results. The results are plotted in Figure 5.11.4. It is important to note that although the torsion shear tests were performed at I_1=300 kPa, most of the true triaxial tests fails around I_1=500 kPa. The two planes can be seen in Figure 5.11.5.

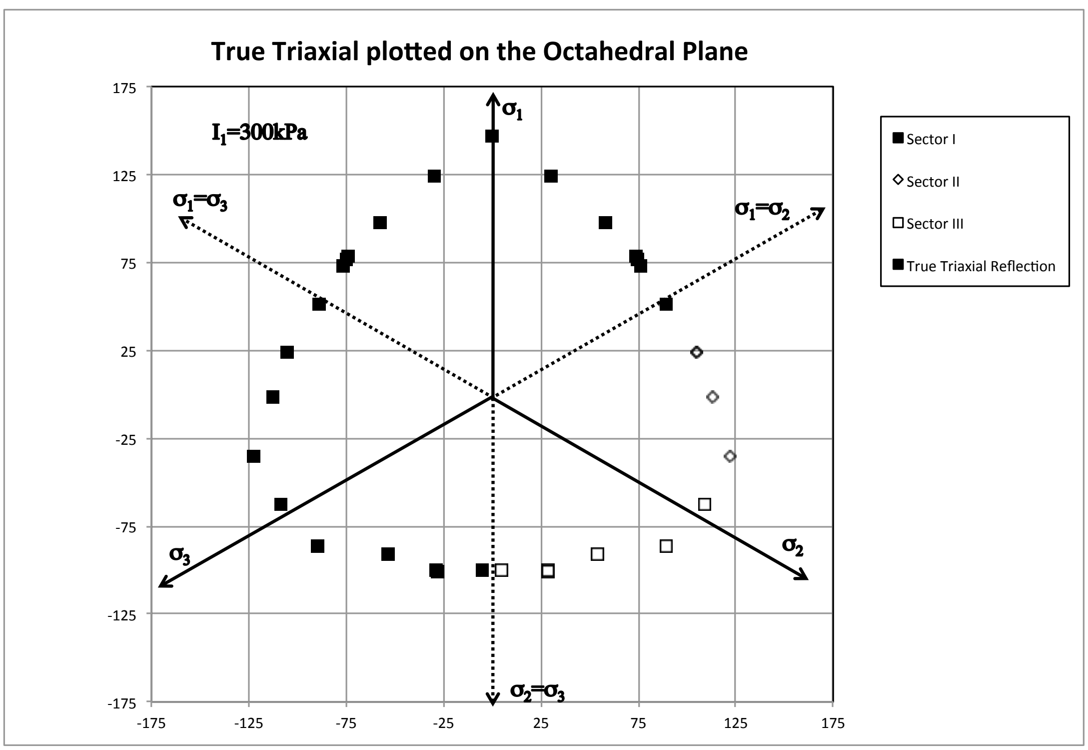

Figure 5.11.3. True Triaxial Test Results plotted on the Octahedral Plane.

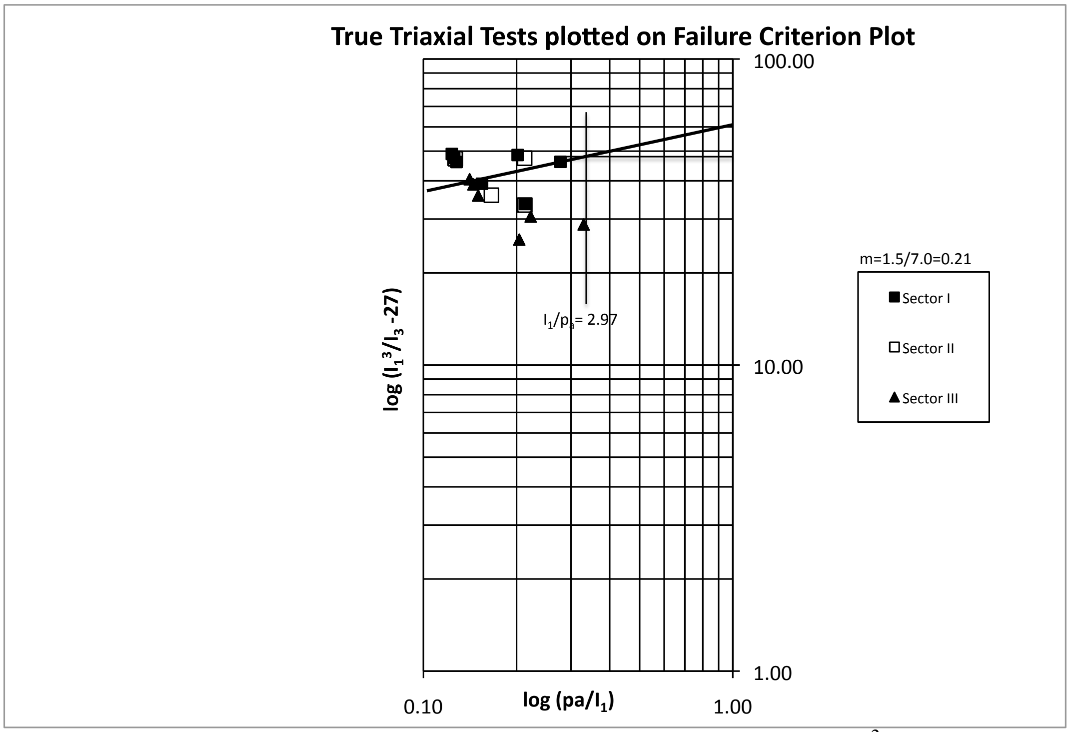

Figure 5.11.4. Plot of true triaxial failure stresses on p_a/I_1 vs $(I_1^3/I_3 - 27)$ diagram.

6. Torsion Shear Experimental Program

6.1 Introduction

Chapter 5 presented tests that were performed in order to fully study the failure surface of Fine Nevada Sand in three dimensions. The true triaxial apparatus allows for application of the three principal stresses, and by the freezing technique implemented, the specimen could be placed in different configurations in order to study its strength at two values of alpha, 0° and 90°. As already described in Chapter 2, a shortcoming of the true triaxial apparatus is the inability to change principal stress direction. It is to say; different values of alpha besides 0° and 90° cannot be applied. However, with a torsion shear apparatus, changes in the principal stress direction can be easily applied.

With the ability to change alpha as well as b-values, torsion shear tests serve as a way to truly study the cross-anisotropic behavior of sand. An experimental program was created consisting of a total of 22 torsion shear tests. These tests are labeled TS 23-44. Each test had a certain alpha and b-value held constant. The mean normal stress was also held constant at 101 kPa. Alpha values ranged from 0° to 90° at 22.5° increments and b-values from 0 to 1 at 0.25 increments.

Test data from 22 previously performed torsion shear tests (Van Dyck 2012) are also included in the experimental results to show the full failure surface of Fine Nevada Sand under all loading conditions. They are labeled as Tests 1-22.

The torsion shear apparatus can be broken down into three main parts: (1) the torsion shear specimen and cell which sits on a rotary turntable, (2) the main panel board which displays inner and outer pressures, measures volume change and applies the back pressure, load and vacuum and (3) the data acquisition system which uses LabView 8.5.1 to change the internal and external pressures and the load for the desired stress path as well as measures and records readings.

6.2 Calibration of measurement devices

All test equipment was calibrated in a similar manner to that described in Section 3.2.3. However, the torsion shear apparatus has several components different from the true triaxial apparatus. The torque right and left load cell, along with the vertical load cell were calibrated with a loading machine and proving ring. The volume change devices for both the inner cell and specimen cell (the volume of the outer cell was not measured) were calibrated also. Using LabVIEW, a reading was recorded at the full height of the volume change device. This represented the maximum amount of volume change for the cylinder. The de-aired water was let out of the volume change cylinder and captured in a graduated cylinder. It was weighed and the volume of water captured was recorded. The reading for the empty volume change cylinder was also recorded. By knowing the full span of the volume change cylinder and the volume it held inside, a calibration was found and the program was adjusted. This procedure was also done for the specimen volume change cylinder.

Inner and outer pressure gage sensors were also calibrated by recording the readings by LabVIEW and comparing them to the readings physically shown on the pressure gages. By adding pressure manually to the gage, different readings were recorded and any offsets in readings were calibrated in the computer program.

Both horizontal and vertical LVDTs were calibrated using a micrometer similar to the method described in Section 3.2.3 for calibration of LVDTs. The entire length of the LVDT cores was calibrated and only the linear portion of the LVDT was used during testing. As a double check on the Horizontal LVDT calibration, a mechanical dial gage was used during testing. Readings were recorded by hand and then were compared to what was recorded during the test. In no instances, were the dial gage and HLVDTs off from each other.

6.3 Corrections to the Recorded Data

In a manner similar to that described in Section 3.2.3, certain corrections had to be looked at in order to determine if they would affect the measured stress-strain behavior of the specimens.

When considering membrane strength effects, unlike the triaxial and true triaxial tests, torsion shear specimens use two membranes. Therefore, the membrane effects of both the inner and outer membrane should be accounted for. Torsional membrane strength effects also should be considered. By using the theory of elasticity and assuming that both the inner and outer membranes stay upright during shearing, the torsional membrane strength effects can be found (Tatsuoka et al. 1986). Taking the previously assumed Poisson's Ratio for rubber as 0.5, the following equations were used to determine membrane strength effects.

$$\Delta\sigma_a = -\frac{4}{3}\frac{E_m t_m}{r_o^2 - r_i^2}[r_o\{2(\varepsilon_{am})_0 + (\varepsilon_{\theta m})_0\} + r_i\{2(\varepsilon_{am})_i + (\varepsilon_{\theta m})_i\}$$

Eq. 6.3.1

$$\Delta\sigma_t = -\frac{2}{3}\frac{E_m t_m}{r_0 - r_i}[\{(\varepsilon_{am})_0 + 2(\varepsilon_{\theta m})_0\} + \{(\varepsilon_{am})_i + 2(\varepsilon_{\theta m})_i\}$$

Eq. 6.3.2

$$\Delta\sigma_r = -\frac{2}{3}\frac{E_m t_m}{r_0 + r_i}[\{(\varepsilon_{am})_0 + 2(\varepsilon_{\theta m})_0\} - \{(\varepsilon_{am})_i + 2(\varepsilon_{\theta m})_i\}$$

Eq. 6.3.3

$$\Delta\tau_{\alpha t} = -2E_m t_m \frac{r_0^3 + r_i^3}{(r_0^3 - r_i^3)(r_0 + r_i)}\gamma_{\alpha t}$$

Eq. 6.3.4

where $\Delta\sigma_a$, $\Delta\sigma_t$, $\Delta\sigma_r$, and $\Delta\tau_{\alpha t}$ are the axial, circumferential, radial and shear membrane strengths, respectively. E_m, t_m, r_o and r_i are the Young's modulus, membrane thickness, outer radius and inner radius, respectively. $\varepsilon_{a\theta}$ and $\varepsilon_{\theta m}$ are the strains in the membrane and they can be calculated by adding the initial membrane strains and the axial and radial strains during isotropic compression and during torsional shear.

The diameters of the inner and outer membranes were 18cm and 22cm, respectively. The thickness of the membrane varied from the top to the bottom of the membrane due to its fabrication process. The average thickness was calculated to be 0.047cm. A Young's modulus of 1400 kPa was used for rubber. The calculated friction angle difference at the maximum strain due to membrane strength effects was 0.005 degrees and therefore, was not included in the calculations.

In tests with changes in effective confining pressure, the volumetric deformation consists of changes in the soil skeleton as well as changes in the volume due to membrane penetration. In cases of hollow cylinder specimens, both inner and outer membranes are used so membrane penetration must be analyzed. Therefore, to accurately measure volume change, the effects of membrane penetration must be analyzed. Per Wong et al. (1975) and Martin et al. (1978), the use of large test specimens will reduce the effects of membrane penetration but will not totally eliminate them. Using Equation 3.2.4, membrane penetration effects were calculated for both the inner and outer membranes. This accounts for about 1% of the total volume change for the torsion shear tests. Therefore, membrane penetration effects are negligible and not considered in corrections.

Because the piston on the torsion shear apparatus is part of the top cap, piston uplift has to be accounted for. As stated in Section 3.2.2, the vertical uplift can be calculated by multiplying the area of the piston by the total pressure in the outer cell. The uplift force is then subtracted from the total force applied to the specimen. For tests under compression the uplift force is subtracted from the total downward force. For extension tests, where the vertical force is already in the upward direction the negative uplift force acts as an additional load and therefore increases the total vertical negative load. A free body diagram of the piston uplift that acts on the top cap is shown in Figure 6.3.1.

In certain tests of the experimental program, the uplift pressure was not included in the calculated and applied forces and pressures while shearing the specimen. Therefore, once this correction was added to the recorded test data, the b-values and alpha values were not the targeted values. Once this uplift was corrected in the computer program before shearing, the applied forces and pressures were on target. For tests that are in increments of 0.25 for b-values from 0 to 1 and increments of 22.5° of alpha from 0° to 90°, the correct uplift pressure was accounted for prior to testing. The tests that are somewhat off these incremental targets have been corrected after shearing. Tests where the uplift was not correctly accounted for before shearing have been designated with a * behind their test number. A list of these tests is presented in Table 6.3.1.

Three tests in particular (7*, 13*, and 16*) exhibited an unexpected major principal stress in the radial direction (where $\sigma_r > \sigma_1$). Due to the uniqueness of this condition, the test results do not exactly fit the same conditions as the rest of the tests. These three tests experienced failure in the σ_z-σ_r plane instead of the σ_z-σ_θ plane, which is where the shear stress was applied. These tests will be discussed in great detail in Chapter 10. For consistency in presenting the test data, they will be excluded from the failure plots and failure surface results.

Table 6.3.1. List of Torsion Shear Tests. Tests designated with * did not have uplift correction prior to shearing.

Test No.	**alpha (°)**	**b-value**	**Test No.**	**alpha(°)**	**b-value**
1 *	0.00	0.00	23	0.00	0.00
2	0.00	0.75	24 *	0.00	0.27
3	22.41	0.00	25 *	0.00	0.55
4 *	23.97	0.27	26	0.00	1.00
5 *	23.53	0.27	27 *	24.04	0.02
6	22.48	0.50	28	23.69	0.23
7 *	*20.13*	*0.87*	29	22.21	0.75
8	22.47	0.99	30 *	22.92	0.85
9	44.98	0.25	31	44.71	0.02
10 *	42.60	0.54	32 *	31.76	0.18
11	44.98	0.75	33	44.99	0.50
12 *	42.26	0.80	34	44.95	1.00
13 *	*33.86*	*0.94*	35 *	69.89	0.16
14	67.33	0.00	36	67.80	0.25
15	67.47	0.50	37 *	69.91	0.55
16 *	*72.06*	*0.96*	38	67.42	0.75
17	68.21	1.00	39 *	70.56	0.79
18	90.00	0.04	40 *	73.08	0.80
19 *	90.00	0.07	41	90.00	0.00
20 *	90.00	0.54	42 *	90.00	0.32
21 *	90.00	0.78	43 *	90.00	0.78
22 *	90.00	0.99	44 *	90.00	0.99

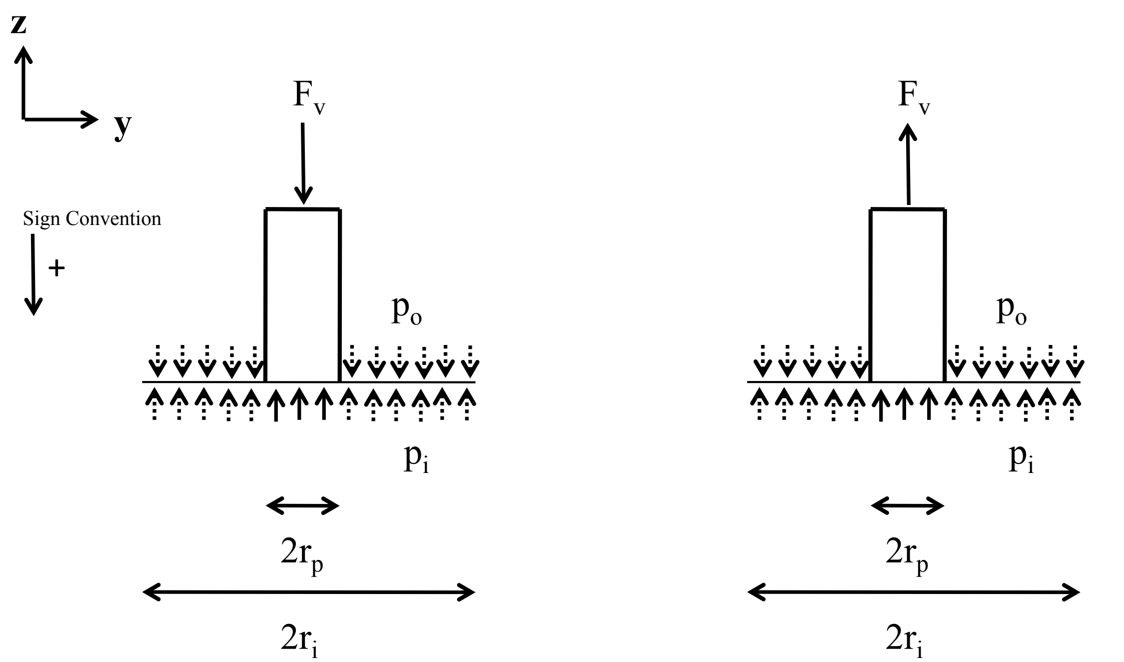

(a) Compression

$\Sigma F_z = 0$

$F_v + p_o(2r_i - 2r_p) - p_i(2r_i) = 0$

(b) Extension

$\Sigma F_z = 0$

$-F_v + p_o(2r_i - 2r_p) - p_i(2r_i) = 0$

Figure 6.3.1. Free body diagram of forces acting in the vertical direction on the top cap of the torsion shear specimen for (a) compression and (b) extension tests.

Since the bushing that housed the piston was not completely frictionless, this friction had to be accounted for as well. By doing a simple friction test which consisted of rotating the torsion shear assembly (without a specimen in place) with the piston in place, it was determined that 9 in-lbs of torque were present in piston friction while rotating the assembly. This load was subtracted from the total torque applied to the specimen during testing. A vertical piston friction of 3 pounds was calculated as well. This friction was also deducted from the vertical load applied to the specimen.

Although all efforts were made to have specimens with the same void ratio, in some cases, it was not possible. Any slight deviation in method during air pluviation can affect the amount of sand that enters into the molds during the specimen preparation. Nonetheless, an equation relating friction angles to void ratio allows for all friction angles to be calculated according to a certain void ratio. By using the equation,

$$e \bullet \tan\varphi = \text{constant} \qquad \text{Eq. 6.3.5}$$

where e is the void ratio, φ is the friction angle and c is a constant, corrected friction angles could be attained. All friction angles were corrected to a void ratio of 0.53.

The stresses were calculated at mid-height of the specimen and therefore, half of the weight of the soil was added to the vertical load. Because the piston, top cap, torque arms and the horizontal bar that attached the torque arms to the specimen weighed a considerable amount, this load was also added to the total applied vertical force.

6.4 Corrections for Measurement Errors

In order to account for any measurement errors, an analysis was done for both friction angles and b-values. This analysis used the Least Squares Method to determine the error for torsion shear tests, assuming certain values of error in vertical force, F_v, inner and outer pressures, pi and p_o, inner and outer radii, r_i and r_o and moment, M values. Details of the equations and methods used to derive the measurement errors are provided in Appendix I.

A table with the summary and the effect on friction angle and b-values is presented in Table 6.4.1. This table summarizes different friction angle variations at the four extremes of the experimental program (α=0°, b=0; α=0°, b=1; α=90°, b=0 and α=90°, b=1). As is seen the friction angle varies from 0.04 to 12.6 degrees for the measurement inaccuracies depending on which measurement errors are assumed. The b-value measurement inaccuracies are very small (see Table 6.4.2). They range from 0 to 0.02. It is important to note that the deviation of inner and outer pressures causes the greatest increase in inaccuracy for friction angle, b-value and alpha. The error assumed for these measurements is therefore, the most important.

Table 6.4.1 Table showing effect of various measurement inaccuracies on friction angle for Torsion Shear Tests.

Test No.	b	ϕ (°)	F (kg)	ΔF	α (°)	$\Delta\alpha$	p_o (kg/cm^2)	Δp_o	p_i (kg/cm^2)	Δp_i	r_o (cm)	Δr_o	r_i (cm)	Δr_i	$\Delta\phi$ (°)
23	0	41	232.3	0.5	0	1	0.446	0.001	0.445	0.001	11.194	0.001	9.121	0.001	**0.040**
26	1	53	84.6	0.5	0	1	1.354	0.001	1.617	0.001	11.115	0.001	9.096	0.001	**0.252**
18	0.1	36	-93.9	0.5	90	1	0.704	0.001	0.423	0.001	10.798	0.001	8.763	0.001	**0.083**
22*	1	36	-130.6	0.5	90	1	1.332	0.001	1.331	0.001	10.945	0.001	8.948	0.001	**0.200**

Test No.	b	ϕ (°)	F (kg)	ΔF	α (°)	$\Delta\alpha$	p_o (kg/cm^2)	Δp_o	p_i (kg/cm^2)	Δp_i	r_o (cm)	Δr_o	r_i (cm)	Δr_i	$\Delta\phi$ (°)
23	0	41	232.3	1	0	1	0.446	0.050	0.445	0.050	11.194	0.050	9.121	0.050	**1.814**
26	1	53	84.6	1	0	1	1.354	0.050	1.617	0.050	11.115	0.050	9.096	0.050	**12.582**
18	0.1	36	-93.9	1	90	1	0.704	0.050	0.423	0.050	10.798	0.050	8.763	0.050	**1.592**
22*	1	36	-130.6	1	90	1	1.332	0.050	1.331	0.050	10.945	0.050	8.948	0.050	**7.218**

Test No.	b	ϕ (°)	F (kg)	ΔF	α (°)	$\Delta\alpha$	p_o (kg/cm^2)	Δp_o	p_i (kg/cm^2)	Δp_i	r_o (cm)	Δr_o	r_i (cm)	Δr_i	$\Delta\phi$ (°)
23	0	41	232.3	1	0	1	0.446	0.010	0.445	0.010	11.194	0.010	9.121	0.010	**0.364**
26	1	53	84.6	1	0	1	1.354	0.010	1.617	0.010	11.115	0.010	9.096	0.010	**2.517**
18	0.1	36	-93.9	1	90	1	0.704	0.010	0.423	0.010	10.798	0.010	8.763	0.010	**0.411**
22*	1	36	-130.6	1	90	1	1.332	0.010	1.331	0.010	10.945	0.010	8.948	0.010	**1.469**

Test No.	b	ϕ (°)	F (kg)	ΔF	α (°)	$\Delta\alpha$	p_o (kg/cm^2)	Δp_o	p_i (kg/cm^2)	Δp_i	r_o (cm)	Δr_o	r_i (cm)	Δr_i	$\Delta\phi$ (°)
23	0	41	232.3	1	0	1	0.446	0.020	0.445	0.020	11.194	0.020	9.121	0.020	**0.726**
26	1	53	84.6	1	0	1	1.354	0.020	1.617	0.020	11.115	0.020	9.096	0.020	**5.033**
18	0.1	36	-93.9	1	90	1	0.704	0.020	0.423	0.020	10.798	0.020	8.763	0.020	**0.652**
22*	1	36	-130.6	1	90	1	1.332	0.020	1.331	0.020	10.945	0.020	8.948	0.020	**2.898**

Table 6.4.2 Table showing effect of various measurement inaccuracies on b-value for Torsion Shear Tests.

Test No.	b	ϕ (°)	F (kg)	ΔF	α (°)	$\Delta\alpha$	p_o (kg/cm^2)	Δp_o	p_i (kg/cm^2)	Δp_i	r_o (cm)	Δr_o	r_i (cm)	Δr_i	Δb-value
23	0	41.4	232.3	0.5	0	1	0.446	0.001	0.445	0.001	11.194	0.001	9.121	0.001	**0.000**
26	1	53.1	84.6	0.5	0	1	1.354	0.001	1.617	0.001	11.115	0.001	9.096	0.001	**0.001**
18	0	36.1	-93.9	0.5	90	1	0.704	0.001	0.423	0.001	10.798	0.001	8.763	0.001	**0.001**
22*	1	36.1	-130.6	0.5	90	1	1.332	0.001	1.331	0.001	10.945	0.001	8.948	0.001	**0.001**

Test No.	b	ϕ (°)	F (kg)	ΔF	α (°)	$\Delta\alpha$	p_o (kg/cm^2)	Δp_o	p_i (kg/cm^2)	Δp_i	r_o (cm)	Δr_o	r_i (cm)	Δr_i	Δb-value
23	0	41.4	232.3	1	0	1	0.446	0.050	0.445	0.050	11.194	0.050	9.121	0.050	**0.011**
26	1	53.1	84.6	1	0	1	1.354	0.050	1.617	0.050	11.115	0.050	9.096	0.050	**0.012**
18	0	36.1	-93.9	1	90	1	0.704	0.050	0.423	0.050	10.798	0.050	8.763	0.050	**0.016**
22*	1	36.1	-130.6	1	90	1	1.332	0.050	1.331	0.050	10.945	0.050	8.948	0.050	**0.030**

Test No.	b	ϕ (°)	F (kg)	ΔF	α (°)	$\Delta\alpha$	p_o (kg/cm^2)	Δp_o	p_i (kg/cm^2)	Δp_i	r_o (cm)	Δr_o	r_i (cm)	Δr_i	Δb-value
23	0	41.4	232.3	1	0	1	0.446	0.010	0.445	0.010	11.194	0.010	9.121	0.010	**0.002**
26	1	53.1	84.6	1	0	1	1.354	0.010	1.617	0.010	11.115	0.010	9.096	0.010	**0.003**
18	0	36.1	-93.9	1	90	1	0.704	0.010	0.423	0.010	10.798	0.010	8.763	0.010	**0.004**
22*	1	36.1	-130.6	1	90	1	1.332	0.010	1.331	0.010	10.945	0.010	8.948	0.010	**0.006**

Test No.	b	ϕ (°)	F (kg)	ΔF	α (°)	$\Delta\alpha$	p_o (kg/cm^2)	Δp_o	p_i (kg/cm^2)	Δp_i	r_o (cm)	Δr_o	r_i (cm)	Δr_i	Δb-value
23	0	41.4	232.3	1	0	1	0.446	0.020	0.445	0.020	11.194	0.020	9.121	0.020	**0.004**
26	1	53.1	84.6	1	0	1	1.354	0.020	1.617	0.020	11.115	0.020	9.096	0.020	**0.005**
18	0	36.1	-93.9	1	90	1	0.704	0.020	0.423	0.020	10.798	0.020	8.763	0.020	**0.007**
22*	1	36.1	-130.6	1	90	1	1.332	0.020	1.331	0.020	10.945	0.020	8.948	0.020	**0.012**

After consideration of the torsion shear apparatus used and the consistency of running the experiments, measurement errors for the tests performed were selected. These are summarized Table 6.4.3. Since each test is different, there is no constant measurement at failure. Therefore, an average of about 0.5% of the measurements taken at failure has been chosen for the measurement errors assumed in this analysis.

Table 6.4.3 Summary of Measurement Errors estimated for Torsion Shear Tests.

Measurement Errors	
ΔF_v (kN)	0.010
ΔM (kN-cm)	0.049
ΔP_o (kPa)	0.490
ΔP_i (kPa)	0.490

The resulting measurement errors for friction angle, b-value and alpha are shown in Table 6.4.4 for each test performed. The friction angle varies from 0.46 to 3.6 degrees. Figures 6.4.1, 6.4.2 and 6.4.3 plot the inaccuracies for all tests. They are separated by alpha values. As can be seen on the figures, the highest friction angle inaccuracy occurs at α=0° at higher b-values. As alpha increases, the inaccuracies decrease. Overall, they tend to stay at around one to two degrees. The b-value error shows an increase in measurement variation as the b-value increases. The alpha measurement errors vary from 0.1 to 0.5 degrees and show a slight increase with higher b-values.

Table 6.4.4. Measurement inaccuracies of friction angle and b-value for all Torsion Shear Tests.

Test No.	b	ϕ (°)	α (°)	F (kN)	ΔF (kN)	M (kN*cm)	ΔM (kN*cm)	p_o (kPa)	Δp_o (kPa)	p_i (kPa)	Δp_i (kPa)	$\Delta\phi$ (°)	Δb-value	$\Delta\alpha$ (°)
23	0.00	41.57	0	2.279	0.01	0.000	0.049	43.752	0.490	43.683	0.490	**1.494**	**0.014**	**0.123**
1*	0.01	37.36	0	1.928	0.01	0.000	0.049	46.583	0.490	46.877	0.490	**1.428**	**0.017**	**0.145**
24*	0.27	45.89	0	1.723	0.01	0.000	0.049	69.081	0.490	77.540	0.490	**2.054**	**0.016**	**0.141**
25*	0.55	53.51	0	1.414	0.01	0.000	0.049	93.763	0.490	110.723	0.490	**3.054**	**0.017**	**0.144**
2	0.75	57.02	0	1.208	0.01	0.000	0.049	116.245	0.490	138.865	0.490	**3.564**	**0.017**	**0.146**
26	1.00	53.27	0	0.828	0.01	0.000	0.049	132.702	0.490	158.569	0.490	**3.488**	**0.020**	**0.172**
3	0.00	39.4	22.38	1.689	0.01	7.753	0.049	48.129	0.490	43.096	0.490	**1.321**	**0.015**	**0.239**
27*	0.02	36.34	24.04	1.428	0.01	7.243	0.049	52.335	0.490	47.853	0.490	**1.278**	**0.017**	**0.279**
28	0.26	44.48	22.97	1.310	0.01	7.497	0.049	73.711	0.490	77.227	0.490	**1.749**	**0.016**	**0.257**
4*	0.27	47.03	23.73	1.282	0.01	7.719	0.049	75.228	0.490	71.780	0.490	**1.233**	**0.017**	**0.292**
5*	0.27	41.39	24.18	1.168	0.01	6.984	0.049	74.124	0.490	77.365	0.490	**1.655**	**0.017**	**0.285**
6	0.51	46.31	22.01	0.993	0.01	6.611	0.049	96.465	0.490	107.360	0.490	**2.126**	**0.017**	**0.276**
29	0.75	46.75	22.77	0.679	0.01	6.131	0.049	116.393	0.490	132.390	0.490	**2.341**	**0.017**	**0.310**
7*	0.83	40.7	24.11	0.215	0.01	4.709	0.049	129.218	0.490	148.663	0.490	**2.374**	**0.026**	**0.438**
30*	0.85	46.18	22.92	0.554	0.01	5.671	0.049	116.737	0.490	133.355	0.490	**2.476**	**0.021**	**0.340**
8	0.97	41.87	22.87	0.416	0.01	5.187	0.049	130.321	0.490	149.559	0.490	**2.211**	**0.023**	**0.361**
31	0.00	36.25	44.91	0.476	0.01	9.458	0.049	59.162	0.490	43.854	0.490	**0.892**	**0.017**	**0.360**
32*	0.18	40.58	31.76	-0.117	0.01	8.385	0.049	63.230	0.490	49.646	0.490	**1.186**	**0.019**	**0.371**
9	0.24	38.85	44.99	0.232	0.01	9.223	0.049	80.675	0.490	73.366	0.490	**1.136**	**0.018**	**0.369**
33	0.50	45.02	44.99	0.008	0.01	9.319	0.049	101.430	0.490	101.292	0.490	**1.559**	**0.018**	**0.366**
10*	0.55	40.55	41.96	-0.161	0.01	7.743	0.049	101.430	0.490	101.292	0.490	**1.330**	**0.021**	**0.435**
11	0.75	40.36	44.98	-0.184	0.01	7.536	0.049	118.323	0.490	124.184	0.490	**1.451**	**0.022**	**0.452**
12*	0.81	41	41.54	-0.348	0.01	7.079	0.049	117.565	0.490	123.219	0.490	**1.527**	**0.023**	**0.475**
13*	0.94	39.2	33.86	-0.486	0.01	6.143	0.049	129.563	0.490	139.354	0.490	**1.518**	**0.026**	**0.543**
34	1.00	35.61	44.95	-0.307	0.01	6.230	0.049	129.356	0.490	139.285	0.490	**1.331**	**0.026**	**0.547**
14	0.00	35.01	67.50	-0.501	0.01	6.266	0.049	65.367	0.490	40.062	0.490	**0.563**	**0.018**	**0.286**
35*	0.16	37.74	69.85	-0.585	0.01	5.544	0.049	68.884	0.490	46.819	0.490	**0.639**	**0.019**	**0.293**
36	0.25	37.57	67.68	-0.705	0.01	6.107	0.049	86.122	0.490	69.091	0.490	**0.734**	**0.019**	**0.298**
15	0.50	39.52	67.40	-0.862	0.01	5.765	0.049	105.636	0.490	96.327	0.490	**0.897**	**0.020**	**0.319**
37*	0.56	38.19	70.03	-0.899	0.01	4.767	0.049	104.878	0.490	96.948	0.490	**0.887**	**0.022**	**0.325**
38	0.75	32.98	67.54	-0.836	0.01	4.501	0.049	119.220	0.490	117.151	0.490	**0.743**	**0.026**	**0.408**
39*	0.79	34.68	70.62	-0.915	0.01	3.877	0.049	117.289	0.490	115.427	0.490	**0.815**	**0.026**	**0.383**
40*	0.80	34.97	73.06	-0.987	0.01	3.558	0.049	127.632	0.490	129.907	0.490	**0.887**	**0.028**	**0.406**
16*	0.80	30.68	74.14	-0.923	0.01	3.081	0.049	125.494	0.490	127.839	0.490	**0.720**	**0.031**	**0.437**
17	1.00	37.11	68.26	-1.028	0.01	4.610	0.049	135.217	0.490	138.389	0.490	**1.012**	**0.025**	**0.396**
41	0.00	34.27	90.00	-0.865	0.01	0.000	0.049	68.532	0.490	39.710	0.490	**0.460**	**0.019**	**0.159**
18	0.06	36.32	90.00	-0.921	0.01	0.000	0.049	69.008	0.490	41.468	0.490	**0.535**	**0.018**	**0.158**
19*	0.08	40.37	90.00	-1.035	0.01	0.000	0.049	66.815	0.490	36.959	0.490	**0.639**	**0.017**	**0.143**
42*	0.32	45.1	90.00	-1.230	0.01	0.000	0.049	87.777	0.490	66.815	0.490	**0.904**	**0.017**	**0.149**
20*	0.52	41.81	90.00	-1.277	0.01	0.000	0.049	108.394	0.490	97.500	0.490	**0.970**	**0.020**	**0.173**
43*	0.78	40.41	90.00	-1.252	0.01	0.000	0.049	120.185	0.490	114.945	0.490	**0.916**	**0.023**	**0.198**
21*	0.78	41.27	90.00	-1.339	0.01	0.000	0.049	121.702	0.490	116.048	0.490	**1.038**	**0.022**	**0.185**
22*	0.99	39.36	90.00	-1.281	0.01	0.000	0.049	137.527	0.490	130.500	0.490	**0.573**	**0.022**	**0.187**
44*	0.99	35.72	90.00	-1.240	0.01	0.000	0.049	129.425	0.490	129.287	0.490	**0.876**	**0.026**	**0.225**

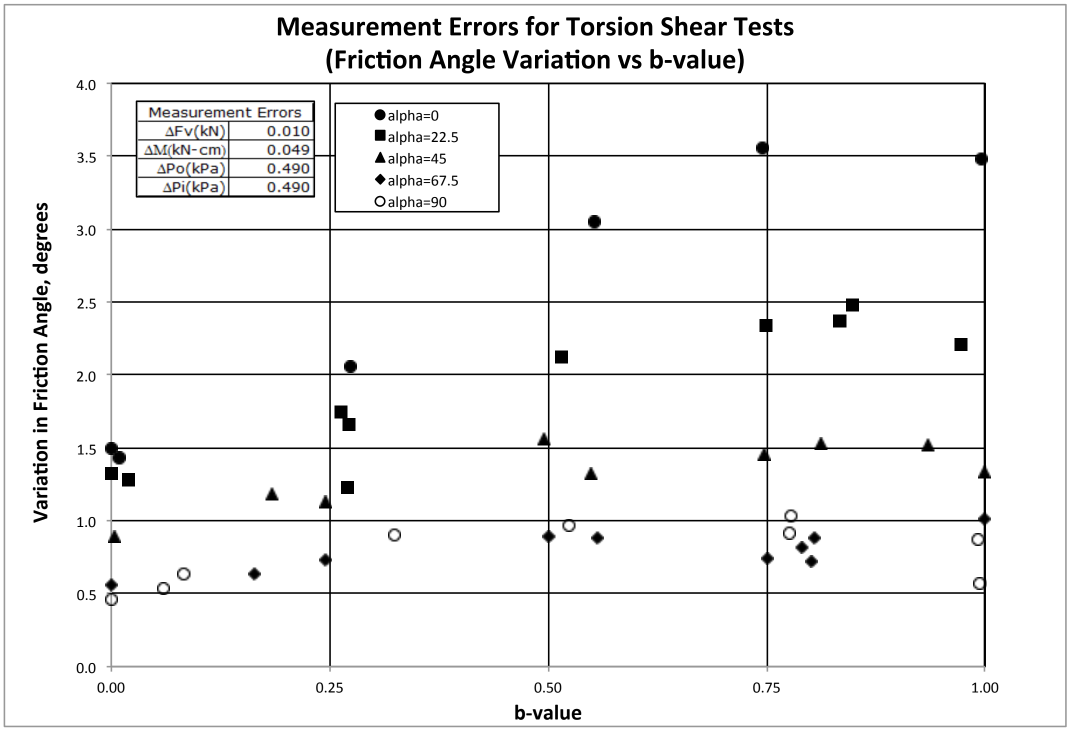

Figure 6.4.1. Torsion Shear measurement inaccuracies in friction angle for all tests.

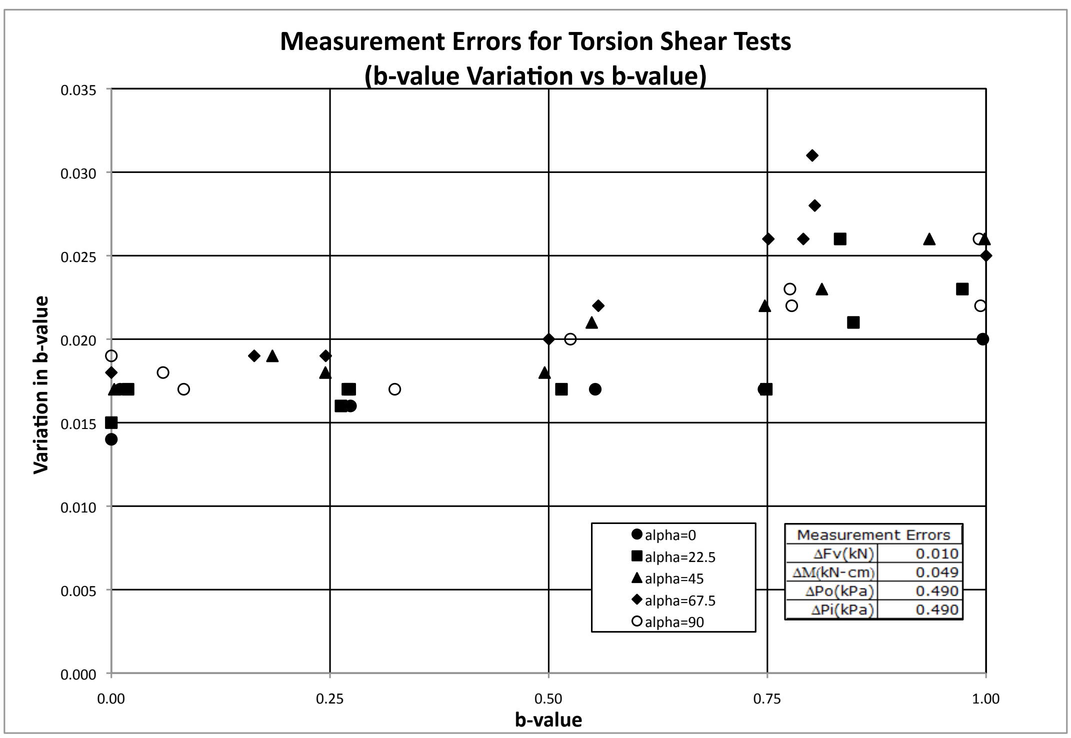

Figure 6.4.2. Torsion Shear measurement inaccuracies in b-value for all tests.

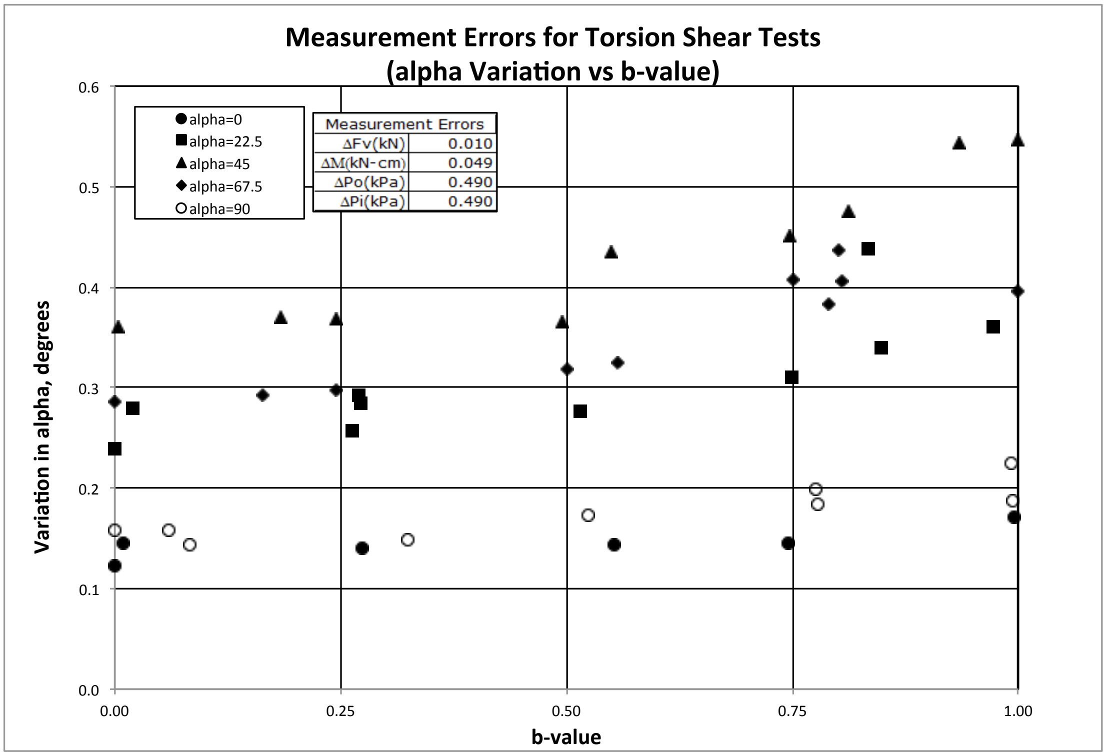

Figure 6.4.3. Torsion Shear measurement inaccuracies in alpha value for all tests.

6.5 Description of Torsion Shear Specimen and Cell

Specimen preparation

In order to attain comparable results, all specimens were made using a prefabricated inner and outer mold, which created a specimen with the same dimensions. The inner and outer radius of the specimens, were 9cm and 11cm, respectively. The specimen height was 40cm. For each test, the inner and outer radius, as well as the height of the specimen, was physically measured in order to calculate the void ratio of the specimen. A list of the tests as well as the void ratio and relative density is provided in Table 6.5.1.

Table 6.5.1. Summary of Torsion Shear Tests at different alphas and b-values.

Test No.	**alpha (°)**	**b-value**	**void ratio**	**relative density (%)**	**Test No.**	**alpha (°)**	**b-value**	**void ratio**	**relative density (%)**
1 *	0.00	0.00	0.510	98.86	23	0.00	0.00	0.531	90.91
2	0.00	0.75	0.530	91.29	24 *	0.00	0.27	0.530	91.29
3	22.41	0.00	0.523	93.94	25 *	0.00	0.55	0.530	91.29
4 *	23.97	0.27	0.548	84.47	26	0.00	1.00	0.532	90.53
5 *	23.53	0.27	0.524	93.56	27 *	24.04	0.02	0.510	98.86
6	22.48	0.50	0.526	92.80	28	23.69	0.23	0.531	90.91
7 *	20.13	0.87	0.552	82.95	29	22.21	0.75	0.531	90.91
8	22.47	0.99	0.541	87.12	30 *	22.92	0.85	0.529	91.67
9	44.98	0.25	0.530	91.29	31	44.71	0.02	0.535	89.39
10 *	42.60	0.54	0.555	81.82	32 *	31.76	0.18	0.560	79.92
11	44.98	0.75	0.540	87.50	33	44.99	0.50	0.528	92.05
12 *	42.26	0.80	0.559	80.30	34	44.95	1.00	0.541	87.12
13 *	33.86	0.94	0.533	90.15	35 *	69.89	0.16	0.531	90.91
14	67.33	0.00	0.538	88.26	36	67.80	0.25	0.533	90.15
15	67.47	0.50	0.525	93.18	37 *	69.91	0.55	0.528	92.05
16 *	72.06	0.96	0.536	89.02	38	67.42	0.75	0.528	92.05
17	68.21	1.00	0.532	90.53	39 *	70.56	0.79	0.531	90.91
18	90.00	0.04	0.538	88.26	40 *	73.08	0.80	0.541	87.12
19 *	90.00	0.07	0.530	91.29	41	90.00	0.00	0.523	93.94
20 *	90.00	0.54	0.530	91.29	42 *	90.00	0.32	0.530	91.29
21 *	90.00	0.78	0.520	95.08	43 *	90.00	0.78	0.520	95.08
22 *	90.00	0.99	0.520	95.08	44 *	90.00	0.99	0.510	98.86

Before building each specimen, dry Fine Nevada sand was sieved through a No. 20 sieve (850μm opening), to ensure that no larger grains or particles were in the specimen. An inner membrane was placed tightly around an inner form, which was secured to the inner radius of the bottom base ring using an O-ring. A thin layer of 2-ton epoxy was spread along the top of the base ring to allow the sand grains that were deposited to interlock with the base ring. The bottom base ring had four drainage paths covered by filter stones. The bottom base ring was screwed into the base turntable where the drainage holes on the turntable were located. This sealed the membrane and drainage lines. The inner membrane fit tight enough around the inner form so that no vacuum was necessary to hold it up. At this point, the radius of the inner membrane form was measured using a Pi Tape and recorded. The outer membrane was then placed over the inner form and secured to the outer radius of the bottom ring with an O-ring. The outer forming jacket was assembled around the outer radius of the base ring. A vacuum was applied to the forming jacket so that the outer membrane was held tightly around the outer form. With the two membranes in place, the measured sand was put into a funnel above the torsion shear apparatus and slowly deposited using the air pluviation method. The sand exited the funnel by a small tube, which was constantly moved around the entire circumference of the specimen walls. Empirical tests showed that a drop height of 35cm created the desired void ratio (e=0.53).

A small 35cm rod at the end of the deposition tube and a flashlight were used to ensure that the drop height was kept constant. The funnel was lifted ensuring that the 35cm rod never touched the surface of the sand. Bedding planes were kept as horizontal as possible by carefully watching the deposition of sand as well as moving the tube and funnel throughout the deposition process. Splashguards were also placed on the inner and outer membrane in order to prevent losing any sand. Once all of the sand was deposited, any grains that might have fallen outside the specimen were vacuumed, weighed and recorded to ensure a proper calculation of the void ratio. The top surface was leveled and a thin layer of 2-ton clear epoxy was placed underneath the top ring before placing it on the specimen. The top ring was pressed down on the upper layer of sand grains, interlocking the top ring to the sand grains. The epoxy was used in order to transfer shear stresses from the top and base rings to the specimen, avoiding slippage at the interfaces. Using two O-rings, the inner and outer membranes were secured to the top cap. Similar to the base ring, the top ring had four drainage paths that were covered by filter stones. Drainage lines, which led to the volume change device, were connected to the top ring. A bubble chamber, which was connected to these drainage lines, was at this time also connected.

A small vacuum of 48 kPa was applied to the specimen and the outer and inner forms were removed. With the bubble chamber attached, any holes in the membranes were indicated once the forms were removed. The specimen inner and outer membranes were painted with rubber latex liquid glue until any holes were plugged. The rubber latex liquid glue was allowed to completely dry before any additional layers were painted on the membranes. Once any leaks were stopped, a grid of horizontal and vertical lines was drawn on the outer front membrane using a felt pen with waterproof ink or a permanent marker. This allowed for a visual check during shearing and as a way to notice shear bands as they developed. A picture of each specimen was taken prior to shearing and the height at three places as well as the outer radius were measured and recorded. Finally, a top cap with four toggles was screwed on to the top ring. The top cap had a greased O-ring that sealed the connection between the top cap and the top ring. The top cap also had a small rod to which the piston would then be attached later. A picture of a prepared specimen standing under a vacuum of 48 kPa with the grid lines drawn can be seen in Figure 6.5.1.

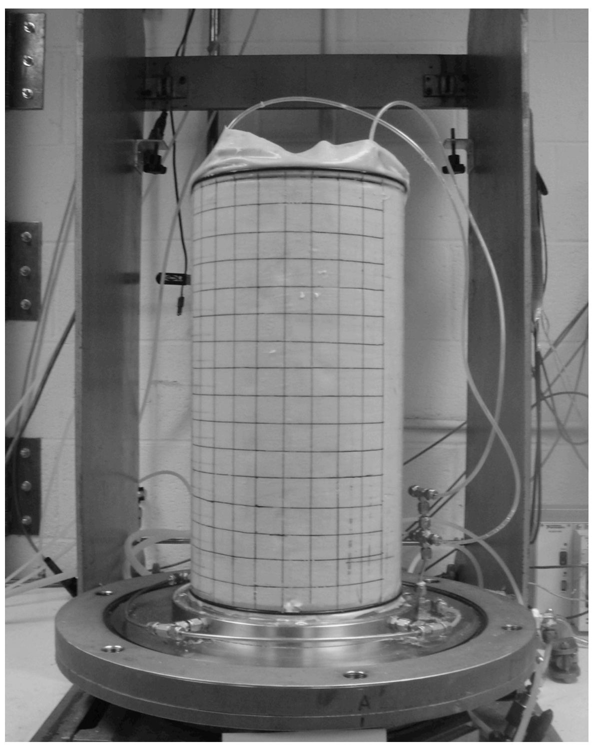

Figure 6.5.1. Picture of a torsion shear specimen prior to saturation.

Specimen saturation

With the specimen ready for the saturation process, gaseous Carbon Dioxide (CO_2) was slowly introduced into the inner cell. The four toggles on the top cap were left open for about 15 minutes to let the CO_2 push any air out of the inner cell. After approximately 15 minutes, de-aired water slowly filled the inner cell. Once the deaired water came out of the top cap toggles, three toggles were closed, the deaired water was stopped and the fourth toggle was then closed. This ensured that water filled the entire inner cell and that no pressure was trapped in the inner cell.

Once the inner cell was completely saturated, the outer cell acrylic cylinder was placed around the specimen. The acrylic cylinder sat over a greased O-ring that was placed in a groove in the outer circumference of the base plate. A top lid was carefully placed on top of the acrylic cylinder. The top lid also had a greased O-ring inside a groove and sat precisely over the acrylic cylinder. It was important to check the O-rings as any slips or discontinuities in the O-rings could cause the outer cell to leak during shearing.

The piston was slightly greased and inserted through the top lid piston sheath and secured with a 17mm bolt so that the piston was attached to the top cap that was resting on the specimen. The greased piston sheath was designed to minimize friction through ball bearings inside the piston sheath. Six vertical tie rods connected the top lid to the base plate. The tie rods were tightened with threaded bolts. It was also important to have these as tight as possible to ensure that no water was able to leak out of the outer cylinder during testing. Any leaks affect the pressures applied during testing and can severely affect the results.

With the entire outside cell sealed, deaired water was slowly introduced to the system. Once full and some water had leaked out of the top cap drainage vents, the water was stopped and the vents were closed. At this point, pressure was applied to the inner and outer cell simultaneously. This could be done manually or using the LabView program. As the pressure was applied, the vacuum on the specimen was lowered. Once 48 kPa was applied to both inner and outer cells, the bubble chamber was disconnected and the backpressure line was directly connected to the main control board, in order to saturate the specimen.

Using the CO_2 method, gaseous CO_2 was slowly passed from the bottom through the specimen and out the top drainage line. A small line with a three-way valve was connected to the drainage lines and led out of the base plate. When flipped in one direction, the three-way valve led to a small pig-tail that was placed in a glass of water in order to see how fast the CO_2 was flowing through the specimen. The specimen was saturated with CO_2 for 15 minutes. Then, deaired water was introduced through the bottom ring, filled the specimen, went out of the top ring, through the drainage lines and into the glass of water. Water was allowed to flow through the specimen for about 15 minutes to ensure full saturation. Then, the three-way valve was flipped to a pressure transducer, which would be used in measuring the saturation of the specimen when performing the B-value test to check the degree of saturation.

A back pressure of 48 kPa was applied to the specimen while the inner and outer cell pressures were simultaneously raised to 98 kPa and left on for a minimum of two hours. In most cases, the specimen was left overnight with the back pressure applied to let the specimen fully saturate. Skempton's B-value saturation test was performed to check the degree of saturation by recording the initial value of the pressure transducer, closing the drainage lines, and increasing both the inner and outer cell pressure simultaneously. The new pressure transducer reading and pressures were recorded and the pressures were brought back down to their values prior to the increase. The drainage lines were again opened, and the B-value was calculated according to the following equation, which was also described in Section 3.5.1.

$$B = \frac{\Delta u}{\Delta \sigma_3} \qquad \text{Eq. 6.5.1}$$

where Δu is the change in back pressure recorded from the pressure transducer and $\Delta \sigma_3$ is the change in both inner and outer pressures.

Once this was recorded, the three-way valve was closed and the preparation for the test was continued. A picture of the torsion shear specimen held under inner and outer pressure of 48 kPa and fully saturated can be seen in Figure 6.5.2.

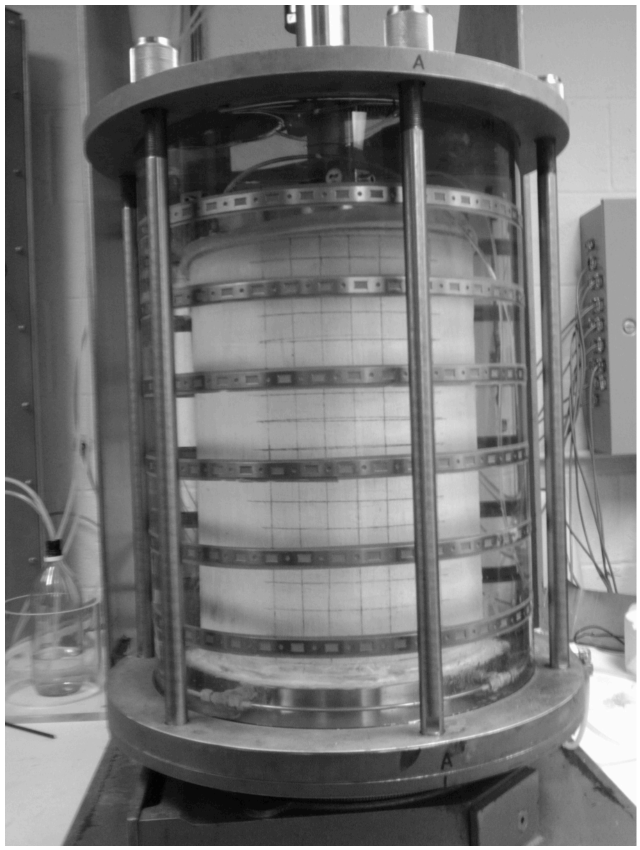

Figure 6.5.2. Picture of Torsion Shear Specimen under 48 kPa water pressure after it has been fully saturated.

6.6 Set-up of Torsion Shear Apparatus

Connection of Instrumentation

With the specimen ready for testing, several more components had to be added before the specimen could be sheared. Measuring devices such as the vertical LVDT, horizontal

LVDT, vertical load cell, torque arms and torque load cells had to be correctly placed on the assembly prior to testing.

Before any of the instrumentation was assembled, a reinforced rigid body frame was moved up and bolted down to the base of where the turntable was fastened. This created an entire rigid body frame, allowing for accurate measurement of loads for both the vertical load and torque load cells.

A vertical LVDT was secured to the piston in order to measure any axial deformations. An extension rod was placed on a top bolt on the top lid in order to set the horizontal LVDT. The horizontal LVDT assembly had several parts. First, a pie shaped plate with a groove along its curved edge was secured on the piston. One end of the core of the horizontal LVDT was connected to the pie with a radio wire cord. The radio wire cord was fastened with a setscrew and ran along the groove of the pie. Once it exited the LVDT core, the other end of the horizontal LVDT core was connected to another piece of radio wire, which had a weight at the end of it. A frictionless wheel set at the end of the assembly allowed the weight to drop down vertically. The assembly was positioned so that a straight line was established from the far edge of the pie shaped plate, through the LVDT core and to the frictionless wheel.

A load cell was placed on a piston adaptor that allowed the load cell to be set between the piston and an air pressure cylinder located at the top of the rigid body frame. If the piston was not precisely in line with the air pressure cylinder collar, the collar was moved so that no additional torque was applied.

In order to measure the shear stresses, a torque arm assembly was placed perpendicular to the piston. The assembly was secured around the piston and two torque arms with load cells were connected to a back plate of the rigid body frame. Springs were placed between the torque load cells and the rigid body frame to allow for compression and extension of the arms. A picture of a typical torsion shear specimen with the instrumentation set up is shown in Figure 6.6.1.

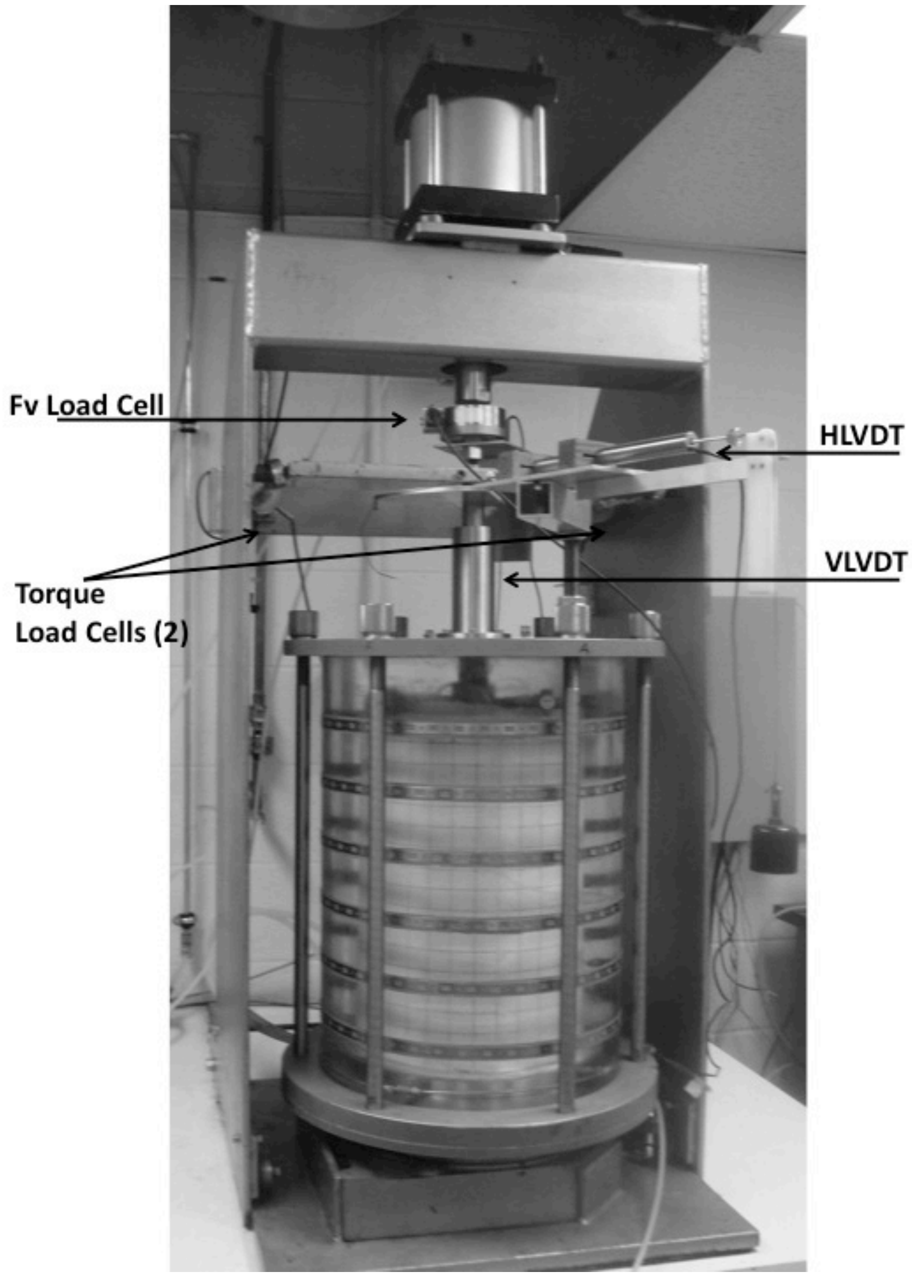

Figure 6.6.1. Picture of typical torsion shear specimen with all of its instrumentation set up (HLVDT, VLVDT, Torque sensors, and Load cell).

Main Panel Board

Section 6.5 described the preparation, assembly and instrumentation devices used for the torsion shear tests that were performed. A main panel board applied pressures and loads, as well as measured the volume change of the specimen during shearing. Two pressure gages displayed the inner and outer pressures applied to the system. This pressure could be applied both manually with a manual regulator and automatically with the computer if the LabView program was turned on. An auto on/off switch valve allowed for the switch between automatic and manual. The back pressure was applied manually to the specimen with a manual regulator and pressure gage. The vertical load could also be applied both manually and automatically to the specimen. Lower and upper air pressure lines were connected to the air pressure cylinder allowing for both compression and extension tests to be performed. Two additional manual regulators were provided to apply vacuum to the specimen and forming jacket during assembly and disassembly. A gage connected to a switch valve between the forming jacket and the specimen displayed the respective applied vacuum.

Two deaired water tanks were also connected to the main panel by lines that led to either the volume change device or the inner and outer pressure lines leading to the torsion shear cell. Pressure sensors on the inner and outer pressure lines allowed for accurate measurements with the computer. A visual check was provided by the previously described inner and outer pressure gages. Although three volume change devices were used for inner, outer and specimen volume change, sensors were only placed to measure volume change for the inner and specimen volume. The outer volume change is not accounted for in any calculations. A picture of the main panel board and entire assembly can be seen in Figure 6.3.2.

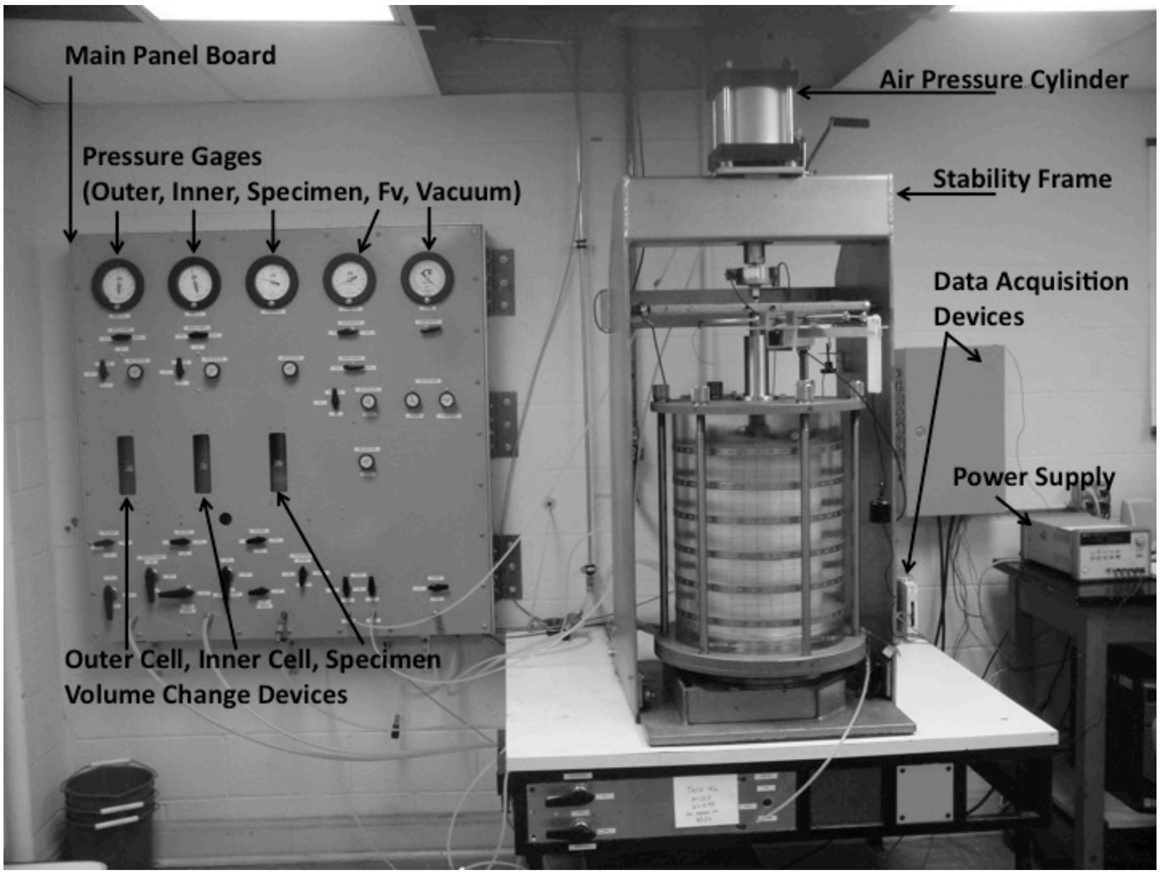

Figure 6.6.2. Typical Picture of a saturated Torsion Shear Specimen before shearing (showing the main panel board, data acquisition devices, air pressure cylinder, stability frame and power supply).

6.7 Equations used for Stress Paths and Strain Calculations

The experimental program designed to study the failure surface of Fine Nevada sand required that a certain b-value, alpha value and mean normal stress were all three held constant during shearing of the specimen. By using the equations presented in Chapter 2, section 2.3.2 and combining them, a set of three equations and three unknowns can be derived and used for the conditions desired for the testing program (i.e. constant alpha, b-values and mean normal stress).

A Mohr circle representation of principal stresses for a hollow cylinder specimen is shown in Figure 6.7.1. A stress block from the hollow cylinder torsion shear specimen is shown in Figure 6.7.2. This stress block shows the main stresses: σ_r, σ_z, σ_θ and $\tau_{z\theta}$.

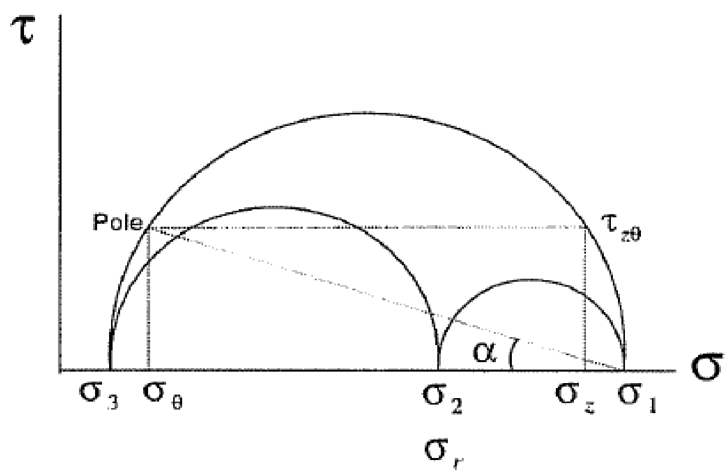

Figure 6.7.1. Mohr Circle Representation of Stress in the Wall of a hollow cylinder specimen (after Hight et al. 1983).

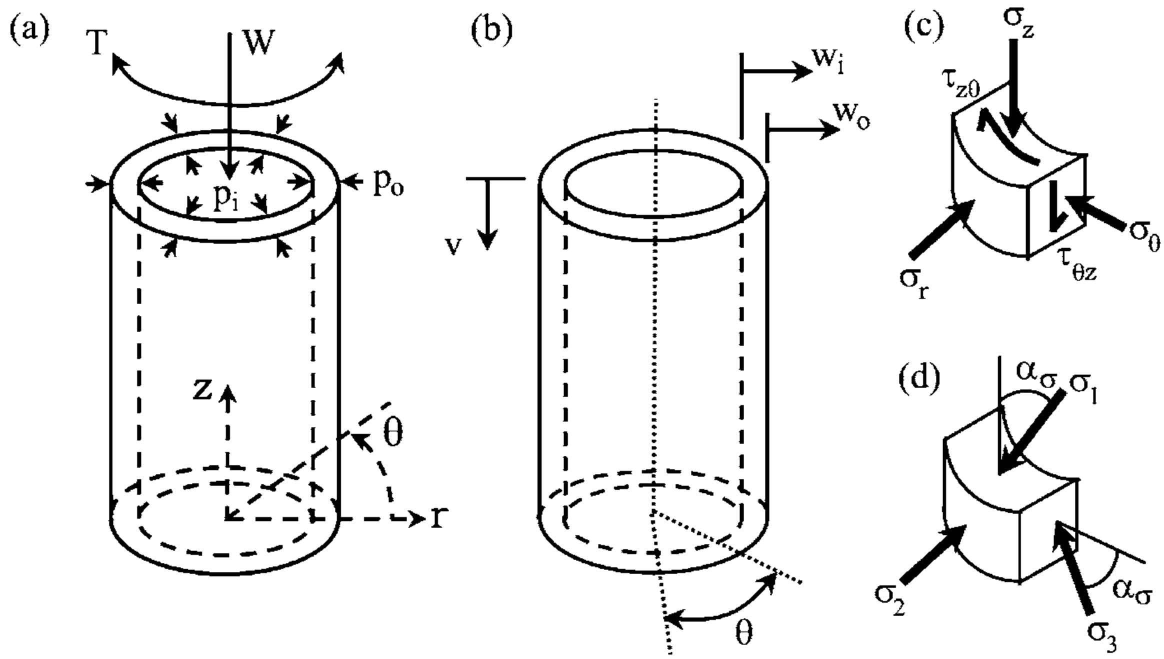

Figure 6.7.2. Stress and deformation states for an hollow cylindrical specimen (a) applied loads and pressures (b) deformations (c) induced stresses and (d) principal.

From Mohr's cicles, the principal stresses can be derived in terms of σ_r, σ_z, σ_θ and α. The equations for the major, intermediate, minor principal stresses and principal stress direction, discussed in Chapter 2, Section 2.3.2 are restated as:

$$\sigma_1 = \frac{\sigma_z + \sigma_\theta}{2} + \sqrt{\left(\frac{\sigma_z - \sigma_\theta}{2}\right)^2 + \tau^2{}_{z\theta}} \qquad \text{Eq. 6.7.1}$$

$$\sigma_2 = \sigma_r \qquad \text{Eq. 6.7.2}$$

$$\sigma_1 = \frac{\sigma_z + \sigma_\theta}{2} - \sqrt{\left(\frac{\sigma_z - \sigma_\theta}{2}\right)^2 + \tau^2{}_{z\theta}} \qquad \text{Eq. 6.7.3}$$

$$\alpha = \frac{1}{2}\tan^{-1}\left(\frac{2\tau_{z\theta}}{\sigma_z - \sigma_{z\theta}}\right)$$ Eq. 6.7.4

The intermediate principal stress ratio can be written as

$$b = \left(\frac{\sigma_2 - \sigma_3}{\sigma_1 - \sigma_3}\right)$$ Eq. 6.7.5

The mean normal stress is calculated as

$$\sigma_m = \frac{1}{3}\left(\sigma_1 + \sigma_2 + \sigma_3\right)$$

Eq. 6.7.6

It is also necessary to know the four basic equations of induced stresses with respect to inner and outer pressures, inner and outer radiuses, vertical load and torque. These equations are based on equilibrium considerations and are independent of the constitutive law of the material being tests (see Section 2.3.2.1). Figure 6.7.3 shows the free body diagram of a cross-section of the specimen.

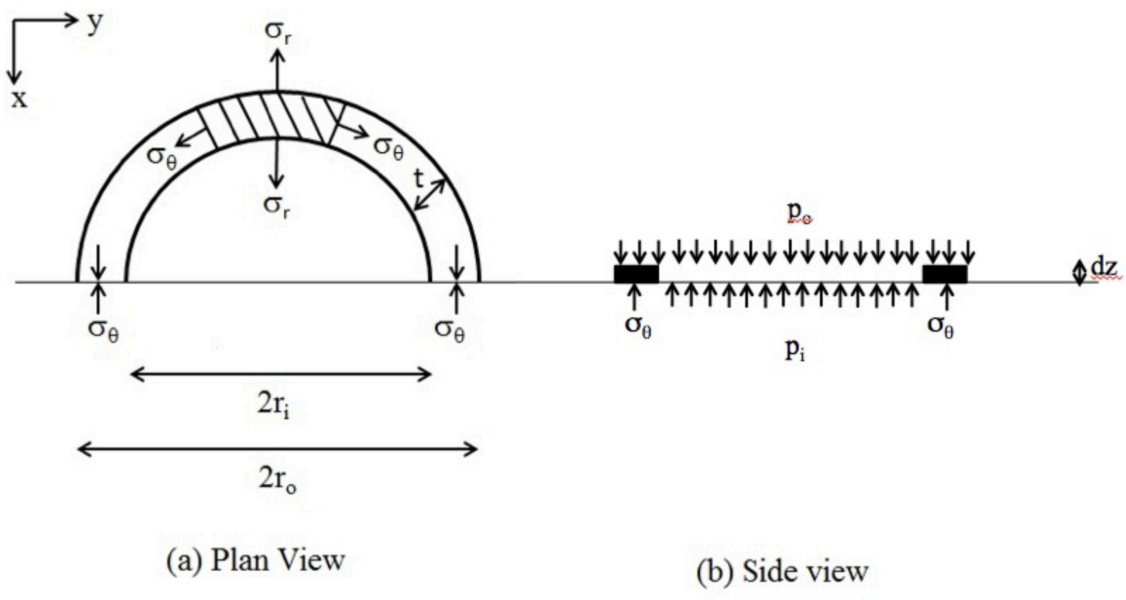

Figure 6.7.3. Torsion Shear Specimen showing Stresses and Pressures (a) Plan View and (b) Side view.

It is seen in that when the sum of the forces in the x direction is set to zero,

$$2\sigma_\theta (t)dz + p_i 2r_i dz - p_o 2r_o dz = 0 \quad \text{Eq. 6.7.7}$$

where $t=r_o-r_i$ and dz=1 yields,

$$\sigma_\theta (r_o - r_i)dz = p_o r_o - p_i r_i \quad \text{Eq. 6.7.8}$$

Solving for σ_θ gives,

$$\sigma_\theta = \frac{p_o r_o - p_i r_i}{r_o - r_i} \quad \text{Eq 6.7.9}$$

When looking at stresses in the vertical direction, it is necessary to look at the free body diagram of the forces acting on the specimen in the z-direction. In this case, the areas of the inner and outer specimen have to be multiplied by the stress imposed by the inner and outer pressures. The stress in the element also has to be multiplied by the area of the element. Vertical force is also added to the calculation. Figure 6.7.4 illustrates the free body diagram.

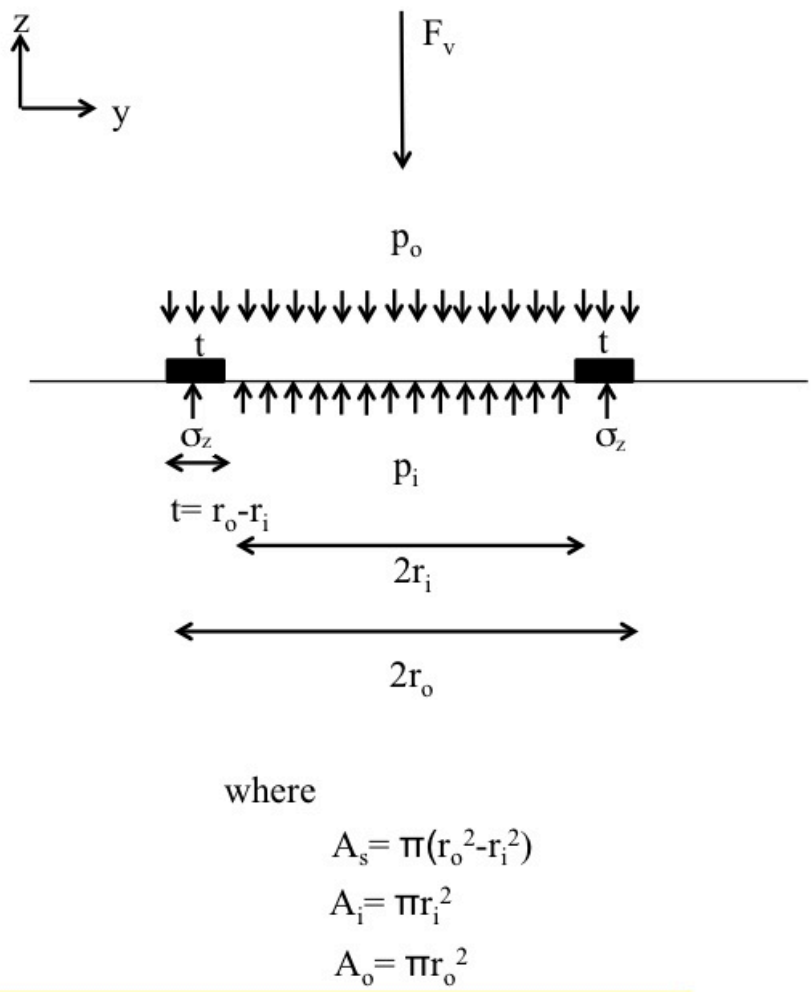

Figure 6.7.4. Vertical forces acting on a Torsion Shear Specimen.

Since force is stress times area, the stresses on the specimen are summed up so that the forces in the z-direction equal zero. It can be said then that,

$$p_o\left(\pi r_o^2\right)+F_v-p_i\left(\pi r_i^2\right)=\sigma_z\left(r_o^2-r_i^2\right) \qquad \text{Eq. 6.7.10}$$

Solving for σ_z gives

$$\sigma_z=\frac{F_v}{\pi\left(r_o^2-r_i^2\right)}+\frac{p_o r_o^2-p_i r_i^2}{\left(r_o^2-r_i^2\right)} \qquad \text{Eq. 6.7.11}$$

In a similar manner, the radial stress can be derived by summing up the stresses in the y-direction. The free body diagram is shown in Figure 6.7.5.

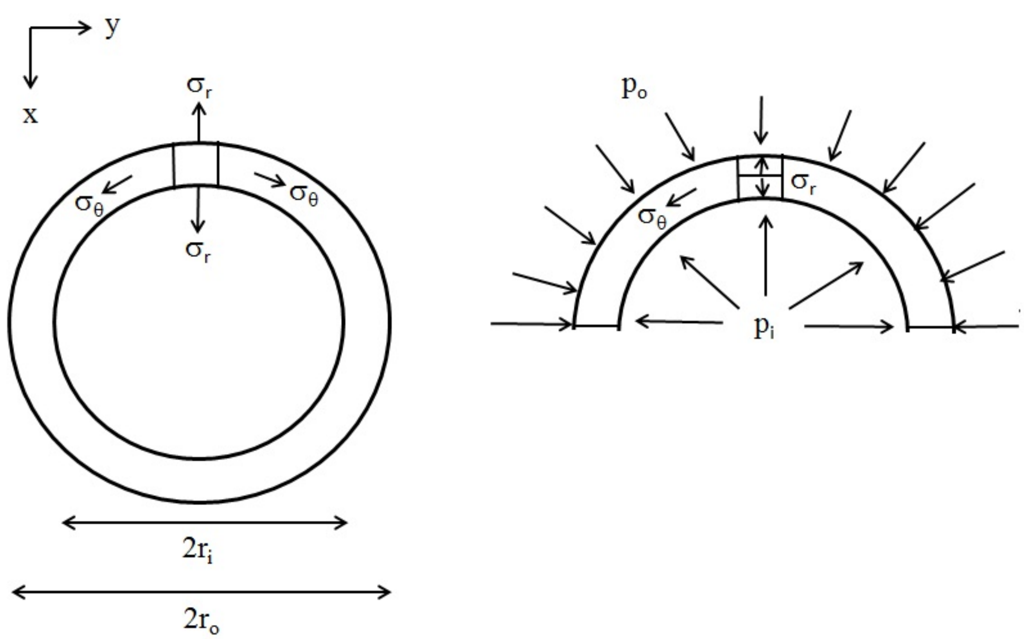

Figure 6.7.5. Radial forces acting on a Torsion Shear Specimen.

$$p_i \frac{2\pi r_i}{2} dz + p_o \frac{2\pi r_o}{2} dz = \sigma_r 2\pi \left(\frac{r_i + r_o}{2} \right) dz \qquad \text{Eq. 6.7.12}$$

When dz=1, then,

$$p_i r_i + p_o r_o = \sigma_r \left(r_i + r_o \right) \qquad \text{Eq. 6.7.13}$$

and σ_r can be written as,

$$\sigma_r = \frac{p_i r_i + p_o r_o}{r_i + r_o} \qquad \text{Eq. 6.7.14}$$

From Logan (1981), the equation for the moment exerted on a hollow circular shaft can be written as,

$$M = \int \tau_{z\theta} \rho dA \qquad \text{Eq. 6.7.15}$$

where A=pr ^{2} , dA=2pdr and r is the thickness of the specimen (r_o-r_i). Integrating over the thickness of the specimen yields

$$M = 2\pi \int \tau \rho^2 d\rho = \frac{2\pi \tau_{z\theta}}{3} (r_o^3 - r_i^3)$$

Therefore,

$$\tau_{z\theta} = \frac{3M}{2\pi (r_o^3 - r_i^3)} \qquad \text{Eq. 6.7.16}$$

By substituting Equations 6.7.9, 6.7.11, 6.7.14 and 6.47.16 into Equations 6.7.4 through 6.7.6, terms can be rearranging so that b, α and σ_m are expressed by only p_i, p_o, r_i, r_o, F_v and M. Since r_i and r_o are measured and known, three equations and unknowns are left. As constants in the tests, b, α and σ_m are also known and therefore, p_i, p_o, and F_v can be calculated. Detailed substitutions of these equations are shown in Appendix H. The equations for p_i, p_o, and F_v are summarized below:

$$p_i = \frac{3(r_o^2 - r_i^2)\sigma_m - \left[\frac{3r_o}{3r_o + r_i} + \frac{3\cos 2\alpha - 2b + 1}{1 - 2b - \cos 2\alpha} * \frac{r_i}{3r_o + r_i}\right]\left(3(r_o^2 - r_{i\,i}^2)\sigma_m - \left(\frac{3(r_o^2 - r_i^2)}{\pi(r_o^3 - r_i^3)}\right)\left(\frac{M}{\tan 2\alpha}\right)\right)}{\frac{3r_i(r_o^2 - r_i^2)}{3r_o + r_i} * \frac{4\cos 2\alpha}{\cos 2\alpha + 2b - 1}}$$

Eq. 6.7.17

$$p_o = \frac{3(r_o^2 - r_i^2)}{r_o(3r_o + r_i)}\sigma_m - \left(\frac{3(r_o^2 - r_i^2)}{\pi(r_o^3 - r_i^3)}\right)\left(\frac{1}{r_o(3r_o + r_i)}\right)\left(\frac{M}{\tan 2\alpha}\right) + \left(\frac{r_i(3r_i + r_o)}{r_o(3r_o + r_i)}\right)p_i$$

Eq. 6.7.18

$$F_v = \frac{3(r_o^2 - r_i^2)}{r_o(3r_o + r_i)}\pi\sigma_m - 3\pi r_o^2 p_o + 3\pi r_i^2 p_i$$

Eq. 6.7.19

The strains in torsion shear were calculated by measuring the horizontal LVDT, vertical LVDT, the volume change of the specimen and the volume change of the inner cell. Average strains were obtained from the assumption that the specimen remained a right cylinder throughout loading. Visual inspection throughout the testing proved this to be true throughout shearing. The following strain equations were used to measure shear strains in torsion shear tests:

$$\varepsilon_z = \frac{\Delta h}{h_o} \qquad \text{Eq. 6.7.20}$$

For a given radius, r, the radial displacement increment, Δu, is assumed to be proportional to the radius through the following relationship (Pradhan et al.,1988) :

$$\Delta u = \frac{\Delta r_o - \Delta r_i}{r_o - r_i}(r - r_i) + \Delta r_i \qquad \text{Eq. 6.7.21}$$

With this relationship, the radial and circumferential strains can be calculated through

$$\varepsilon_r = -\left[\int_{r_i}^{r_o} \frac{\partial \Delta u}{\partial r} r dr \Big/ \int_{r_i}^{r_o} r dr\right] = -\frac{\Delta r_o - \Delta r_i}{r_o - r_i} \qquad \text{Eq. 6.7.22}$$

$$\varepsilon_\theta = -\left[\int_{r_i}^{r_o} \frac{\Delta u}{r} r dr \Big/ \int_{r_i}^{r_o} r dr\right] = -\frac{\Delta r_o + \Delta r_i}{r_o + r_i} \qquad \text{Eq. 6.7.23}$$

$$\Delta r_i = \sqrt{\left(\frac{\pi(r_i^2 h_o) + \Delta I_{vol}}{\pi h}\right)} - r_i \qquad \text{Eq. 6.7.24}$$

$$\Delta r_o = \sqrt{\left(\frac{\pi(r_o^2 h_o) + \Delta I_{vol} + \Delta BP_{vol}}{\pi h}\right)} - r_o \qquad \text{Eq. 6.7.25}$$

$$\left.\begin{aligned}
\varepsilon_{z\theta} &= \frac{1}{\pi(r_o^2 - r_i^2)} \int_{r_i}^{r_o} \int_0^{2\pi} \varepsilon_{z\theta} \cdot (r) \cdot r \cdot d\theta dr \\
\varepsilon_{z\theta} &= \frac{1}{\pi(r_o^2 - r_i^2)} \int_{r_i}^{r_o} \frac{r \cdot \Delta\theta}{2h} 2\pi r \cdot dr \\
\varepsilon_{z\theta} &= \frac{\Delta\theta(r_o^3 - r_i^3)}{3h(r_o^2 - r_i^2)}
\end{aligned}\right\} \qquad \text{Eq. 6.7.26}$$

where Δh is the change in specimen height measured by the vertical LVDT, h_o is the original measured height of the specimen measured prior to testing, h is the current height of the specimen, r_o is the outer radius, Δr_o is the change in outer radius, r_i is the inner radius, Δr_i is the change in inner radius, ΔI_{vol} is the change in inner volume, and ΔBP_{vol} is the change in specimen volume recorded.

$\Delta\theta$ is the angular displacement of the specimen in radians.The angular displacement is calculated by

$$\Delta\theta = \frac{\Delta HLVDT}{r_{meausrementplate}} \qquad \text{` } \qquad \text{Eq. 6.7.26}$$

where $\Delta HLVDT$ is the recorded change in HLVDT reading and $r_{measurement\ plate}$ is the radius of the pie shaped measurement plate to the radio wire cord.

Using Mohr's circle, these strains are converted to major, intermediate and minor principal strains. The total volumetric strain is the summation of these three strains.

6.8 LabView Program

Only three components of the torsion shear test were not automated: the turntable, the B-value saturation test measurement sensor and the back pressure applied to the specimen. As described previously, back pressure was manually applied to the specimen using the manual regulator and pressure gage. A pressure transducer with a display unit was used in measuring the saturation of the specimen. The turntable was rotated with a Maxon gear motor. The voltage to spin the motor was supplied by an external Hewlett Packard triple outlet DC power supply.

However, the internal and external pressure sensors, internal and specimen volume change sensors, load cell, horizontal LVDT, vertical LVDT and the two torque load cells were all connected to a data acquisition unit and displayed in LabView. LabView is a computer program that uses a graphical programming environment in order to develop measurement, test and control systems. It uses graphical icons and wires in the form of a flowchart to allow for easy programming.

The data acquisition system read voltage signals from the measurement devices described in the paragraph above. With this, the program read these signals and through calibrations that were input into the program, the signals were converted to pressures, loads and distances. A graphical front panel allowed the user to input the conditions of the test desired. In this experimental program, b-values, alpha values and a constant mean normal stress were input. The front panel was also used for the initial application of pressures to the inner and outer cells of the specimen as well as for isotropic consolidation.

For tests with rotation, the torque applied from the torque right and left load cells was measured once the table started to rotate. Once a measurement was acquired by the data acquisition system and LabView program, the internal and external pressures and vertical load were changed to ensure the designated b-value and alpha value are applied to the specimen, all while keeping the mean normal stress constant. The applied pressures and load were recorded, as well as the inner volume, specimen volume, horizontal LVDT and vertical LVDT readings. These readings provided the necessary data to study the behavior of the sand under different stress paths.

Tests without rotation, where $\alpha=0°$ and $\alpha=90°$, do not require the torque load cells and the horizontal LVDT, and they are stress controlled tests. For these tests, the vertical load was applied at desired load increments and pressures are changed accordingly to create different b-value conditions with a constant mean normal stress. The desired α and b-values are still set on the front panel so that the correct equations throughout the test are used.

After the specimen reached failure, the rotating table was stopped (for tests with rotation). The backpressure line and the internal and external volume change lines were closed in order to prevent more volume change from occurring. The specimen was then exposed to and held under vacuum. The vertical load, back pressure and internal and external pressures were brought back down to zero and the torsion shear assembly was disassembled. With the specimen held under vacuum, any shear bands were recorded and the sheared specimen was photographed. A typical example of a specimen held under vacuum once it had been sheared is shown in Figure 6.8.1.

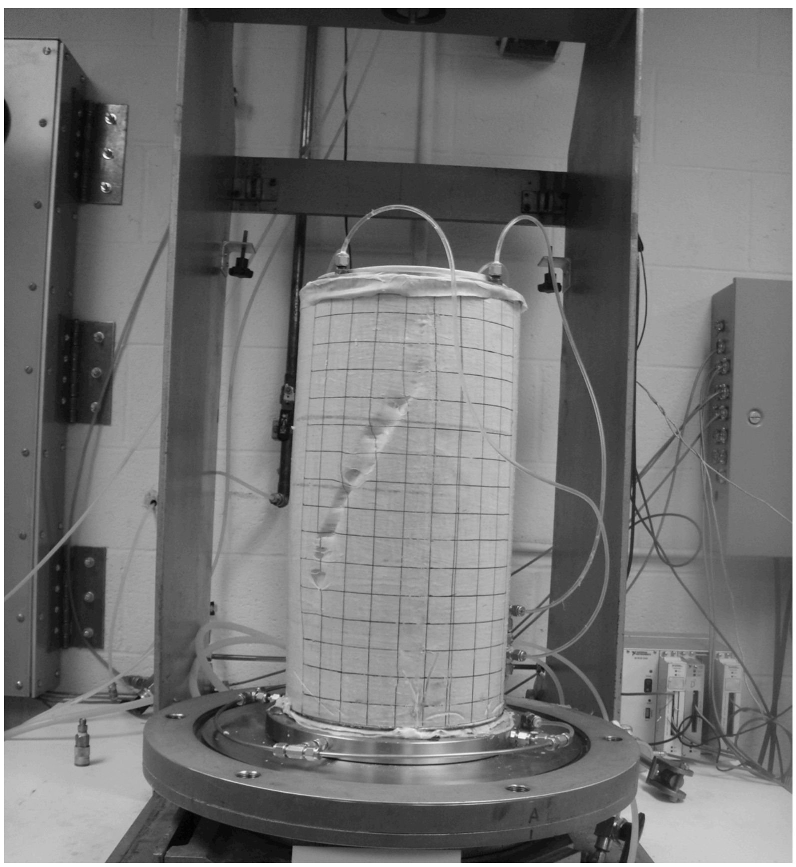

Figure 6.8.1. Typical Picture of Torsion Shear Specimen after failure held up by a vacuum of 48 kPa in order to measure and photograph any developed shear bands.

6.9 Experimental Program

A series of 22 tests were performed in this experimental program in order to study the strength behavior and failure surface of Fine Nevada sand while keeping alpha, b and σ_m constant. As described in details in Sections 6.2 the sand was deposited using the air-pluviation method and saturated using the CO_2 method. Skemptom's B-value for all specimens was found and all specimens showed B-values above 0.94. This saturation number is acceptable for highly dense fine sand. Once ready to begin testing, the specimens underwent isotropic consolidation in 6.9 kPa increments starting at 48.3 kPa to 101 kPa effective confining pressure.

Shearing began for all specimens at initial inner and outer effective confining pressures of 101 kPa. Depending on the stress path indicated for the particular test, the inner and outer confining pressures either increased or decreased. The vertical force also was either in compression or extension. Table 6.9.1 shows the behavior of inner and outer pressures, as well as the vertical force, according to different b-value and alpha configurations. In the p_o and p_i columns, a (-) sign shows a decrease and a (+) sign shows an increase in effective confining pressure throughout shearing. The bolded signs indicate the greater pressure between the two for the condition shown. A (+) sign in the F_v column shows that the specimen was under compression (positive downward force) and a (-) sign shows the specimen was under extension (negative upward force). An (=) sign (seen for b=0.5 and

α=90°) shows constant values (i.e. no changes in original effective confining pressure or vertical load).

Table 6.9.1. Varying Pressures and Vertical Loads for different Torsion Shear Test Configurations.

α(degrees)	b-value	p_i	p_o	F_v
0°	0	-	-	+
0°	0.25	-	-	+
0°	0.5	+	-	+
0°	0.75	+	+	+
0°	1	+	+	+
22.5°	0	-	-	+
22.5°	0.25	-	-	+
22.5°	0.5	+	-	+
22.5°	0.75	+	+	+
22.5°	1	+	+	+
45°	0	-	-	+
45°	0.25	-	-	+
45°	0.5	=	=	=
45°	0.75	+	+	-
45°	1	+	+	-
67.5°	0	-	-	-
67.5°	0.25	-	-	-
67.5°	0.5	-	-	-
67.5°	0.75	+	+	-
67.5°	1	+	+	-
90°	0	-	-	-
90°	0.25	-	-	-
90°	0.5	+	+	-
90°	0.75	+	+	-
90°	1	+	+	-

All efforts were made to stay as close to the targeted alpha and b-values as possible during testing. However, for certain tests due to vertical uplift corrections applied to the data after the test was run, the b-values and alpha values were not exactly on the targeted value. The total stress paths were different for these tests. However, as stress path does not affect failure, the failure points can be presented for all tests. A figure showing the boundary between compression and extension tests while having constant mean stress, b-value and alpha is shown in Figure 6.9.1. Figure 6.9.2 shows the test area where the inner pressure is greater than the outer pressure and vice versa. The arrows show the direction of increasing difference in internal and external pressures for varying b-value and alpha values.

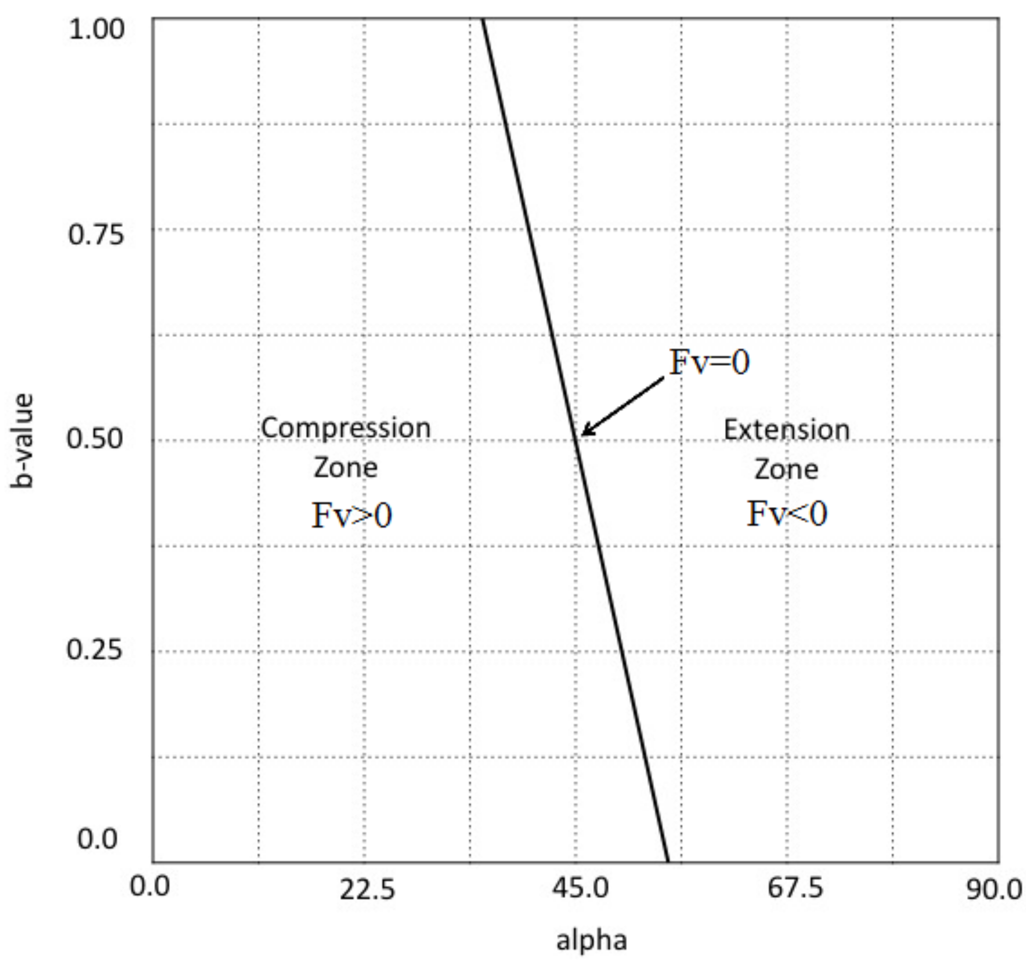

Figure 6.9.1. Boundary area between extension and compression tests for Torsion Shear Tests held at constant alpha, b-value, and mean normal stress.

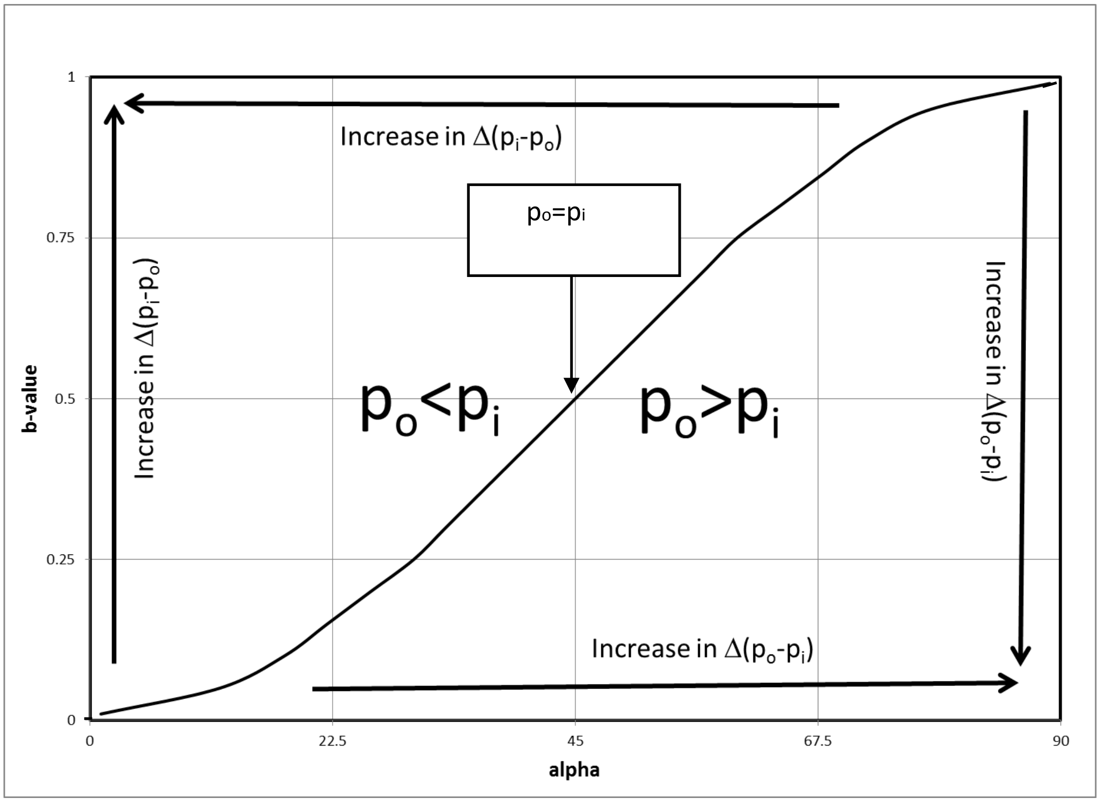

Figure 6.9.2. Boundary area for inner and outer pressure conditions for Torsion Shear Tests held at constant alpha, b-value, and mean normal stress.

7. Torsion Shear Test Results

7.1 Friction Angle Summary and Failure Surface Plots

To provide ease to the reader when presenting the data, the final friction angles will be analyzed both in the b=constant direction and alpha=constant direction. Stress strain and volume change curves for the tests performed as part of this experimental program as well as previous tests in Van Dyck (2012) will be presented at α=constant intervals.

Table 7.1.1 summarizes the tests performed as part of this experimental program and provides the alpha value, b-value, void ratio, and corrected friction angle for each test. The friction angles have been corrected for any changes in void ratio, as well as have been all translated to the same octahedral plane, where I_1=300 kPa. As mentioned in Chapter 6, the data from Tests 1-22 has been included to give an overall and complete picture of the failure surface but these tests were not part of the author's experimental study. Tests designated with a * had the uplift correction applied after shearing and a different stress path was followed than the one originally intended. However, because stress path does not affect failure, they are included in the set of data presented in the following pages.

Tests 7*, 13*, and 16* failed in the radial-vertical plane, a different plane (vertical-circumferential) from the other tests and therefore have been separated out from the test failure results presented in this chapter.

Figures 7.1.1 through 7.1.5 show the failure points plotted versus b-value and Figures 7.1.6 through 7.1.10 show the failure points plotted versus alpha values so that the results can be analyzed through two different variables. Figure 7.1.11 shows the 3D surface plotted with only points chosen at the corresponding intersections at increments of b=0.25 and α=22.5°. As described in Section 6.1.3, the corresponding measurement error bars have been drawn on the failure surface points for Figures 7.6.1 through 7.6.10. Figures 7.1.1 and 7.1.5 also have the true triaxial data results plotted as a reference and comparison.

Table 7.1.1. Summary of Test Results sorted by alpha=constant and b-values.

Test No.	α	b-value	e	φ(°)
23	0.00	0.00	0.531	41.21
1 *	0.00	0.00	0.510	36.78
24 *	0.00	0.27	0.530	45.84
25 *	0.00	0.55	0.530	53.05
2	0.00	0.75	0.529	56.91
26	0.00	1.00	0.532	53.28
3	22.41	0.00	0.523	39.33
27 *	24.04	0.02	0.510	36.31
28	23.69	0.23	0.531	43.4
4 *	23.73	0.27	0.548	47.25
5 *	23.53	0.27	0.524	41.44
6	22.48	0.50	0.526	43.40
29	22.21	0.75	0.531	46.64
30 *	22.92	0.85	0.529	46.15
8	22.47	0.99	0.541	42.92
31	44.71	0.02	0.535	36.20
32 *	31.76	0.18	0.560	40.24
9	44.98	0.25	0.530	38.88
33	44.99	0.50	0.528	45.02
10 *	42.60	0.54	0.555	39.89
11	44.98	0.75	0.540	40.40
12 *	42.26	0.80	0.559	40.26
34	44.95	1.00	0.541	35.64

Test No.	α	b-value	e	φ(°)
14	67.50	0.00	0.538	35.06
35 *	69.89	0.16	0.531	37.64
36	67.80	0.25	0.533	37.64
15	67.40	0.50	0.525	39.46
37 *	69.91	0.55	0.528	38.06
38	67.42	0.75	0.528	31.78
39 *	70.56	0.79	0.531	34.83
40 *	73.08	0.80	0.541	34.90
17	68.21	1.00	0.532	38.33
41	90.00	0.00	0.523	33.24
18	90.00	0.04	0.530	33.88
19 *	90.00	0.07	0.538	38.16
42	90.00	0.32	0.530	45.04
20 *	90.00	0.54	0.530	45.24
43	90.00	0.78	0.520	39.16
21 *	90.00	0.78	0.520	40.35
22 *	90.00	0.99	0.520	36.69
44	90.00	0.99	0.510	36.68

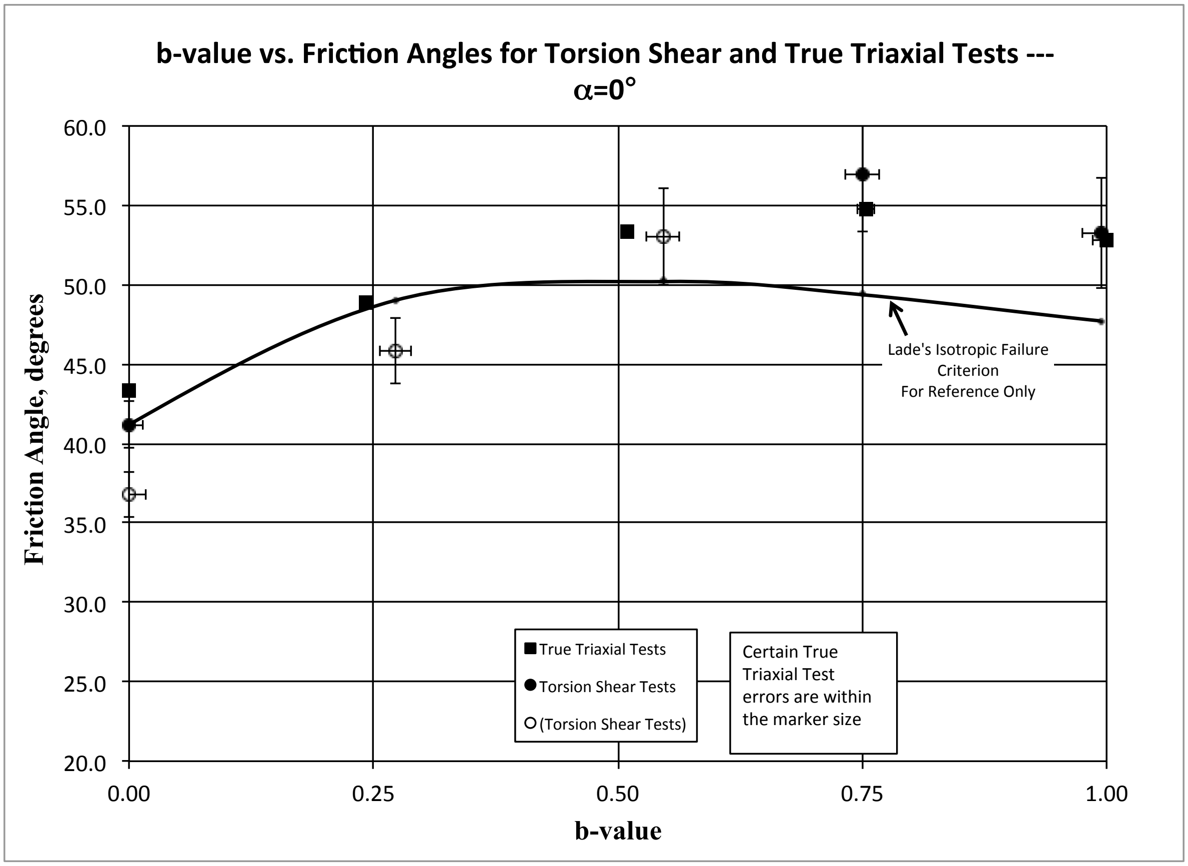

Figure 7.1.1. b-value vs. Friction Angle for α=0° degrees for both Torsion Shear and True Triaxial Tests.

Figure 7.1.1 shows the test results for all α =0° tests. The torsion shear tests have been separated and marked by open and closed circles. The open circles are torsion shear tests that were previously denoted with a (*). These tests did not have the uplift pressure accounted for prior to testing and therefore, followed a different initial stress path than originally desired. Tests with the closed circle were performed after and were performed with all corrections applied prior to and during testing. The true triaxial tests have also been added to the figure to provide a reference and comparison.

As can be seen, the true triaxial and torsion shear tests confirm each other. This shows the validity of the torsion shear apparatus and the test results. Low b-values for torsion shear tests show slightly less friction angles than that of the true triaxial tests but they were well within the scatter. As the b-value increases from zero up to 0.75, there is an increase in friction angle of about 15 degrees. From b=0.75 to b=1.0, the friction angle decreases about 3.5 degrees. This is similar to results from Abelev and Lade (2004). For tests with rotation, other than at 90 degrees, there is no true triaxial test data to compare the torsion shear tests with. Therefore, Figures 7.1.2 through 7.1.4 do not have any additional test data besides that of the torsion shear tests performed.

Figure 7.1.2 shows torsion shear test data for α=22.5° tests. The results follow the same behavior as seen in α=0°, with increasing friction angle as b-value increases. There is also a drop of about 4 degrees from b=0.75 to b=1.0. Overall, the friction angles are lower than α=0° at the same b-values. The increase in friction angle is about 7 degrees from b=0 to b=0.75. This is only half of the increase seen in the α=0° tests.

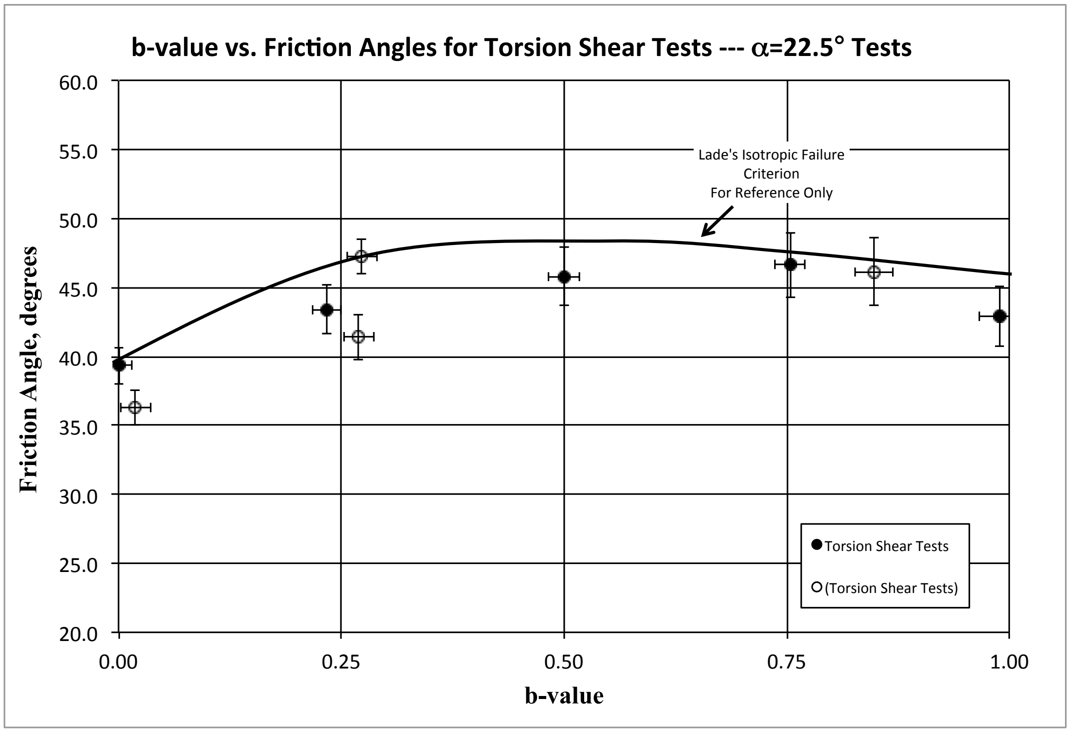

Figure 7.1.2. b-value vs Friction Angle for α=22.5° degrees for Torsion Shear Tests.

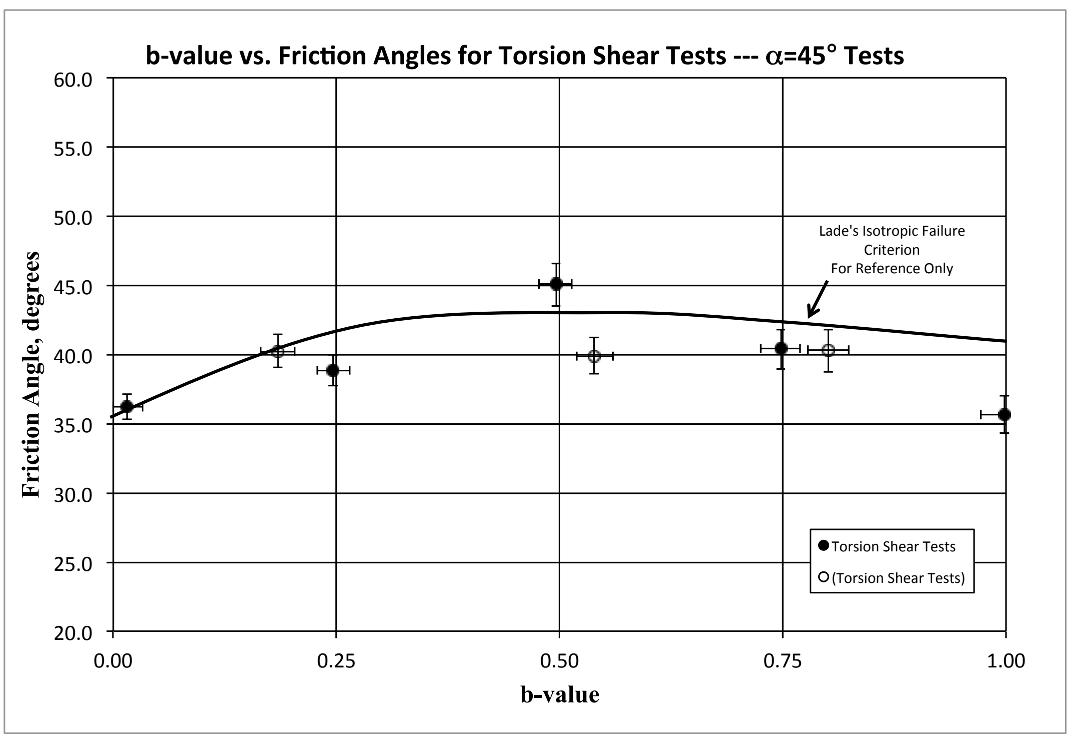

Figure 7.1.3. b-value vs Friction Angle for α=45° degrees for Torsion Shear Tests.

Test data for α=67.5° are presented in Figure 7.1.3. The behavior of the soil under these conditions shows an increase in friction angle from b=0 to b=0.5, unlike α=0° and α=22.5° where there was an increase from b=0 to b=0.75. There is an increase of an average of 8 degrees. At b=0.5 to b=1.0, the strength decreases and the final strength at b=1 is 0.5 lower than that of b=0. Once again, the strength of the soil at α=45° is less than that of corresponding b-values at α=22.5°.

Data for α=67.5° tests (see Figure 7.1.4) showed similar behavior to α=45°. However, a sharp decrease in friction angle is seen at/near b=0.75. It is believed that at this principal stress direction and b-value, the bedding plane direction is close to/equal the principal stress direction. Due to this, strain localization may occur sooner and cause the lower friction angle. It is important to note that three tests conducted at this condition show this same behavior and very similar development of shear bands (as will be discussed further in Chapter 9).

Figure 7.1.5 shows α=90° tests and also shows the true triaxial results for comparison. At low b-values, the tests seem to behave similarly. From b=0.32 to b=1.0, the torsion shear tests begin to lose strength and deviate from the true triaxial test results. The torsion shear tests show significantly less (from 12 to 15 degrees) strength than the true triaxial tests. Lade and Wang (2012) compared triaxial extension tests with flexible versus rigid boundaries. They found that at α=90°, b=1.0, there was an 8.2 degree difference in friction angle between tests performed with rigid long plates to stiffen the soft membrane than in conventional extension tests with flexible membranes. Showing higher strengths, the extension tests with rigid boundaries also showed higher rates of dilations and were more succesful in maintaining uniform strains. Therefore, the strengths obtained from different designs of true triaxial equipment may be affected by the stiffness of the loading plates. It is important to recall that in order to perform α=90° tests in the true triaxial apparatus, the sand was poured and frozen so that the bedding planes could be rotated to create an α=90° condition. However, the major principal stress was still applied in the vertical direction through two rigid boundaries. For torsion shear tests, the bedding planes are always horizontal. Therefore, the major principal stress is rotated and applied in the horizontal direction parallel to the bedding planes to the specimen. This stress acts through the flexible membranes. The difference in strengths seen between the true triaxial and torsion shear test results may be due to this flexible boundary effect in the torsion shear tests.

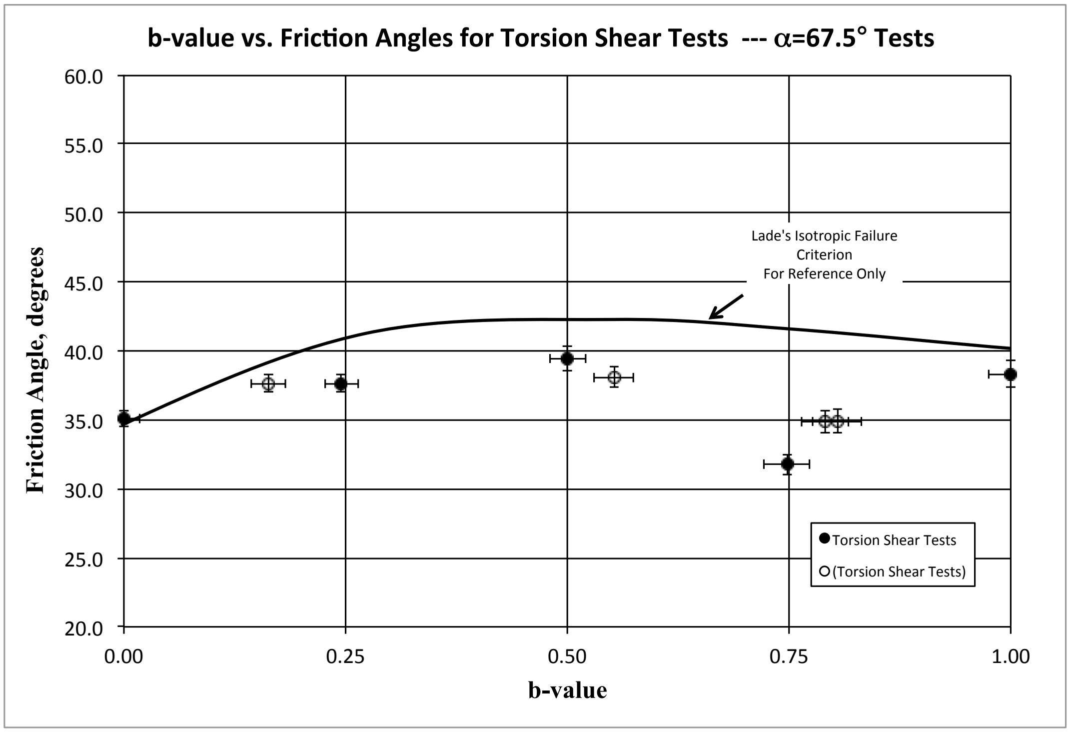

Figure 7.1.4. b-value vs. Friction Angle for α=67.5° degrees for Torsion Shear Tests.

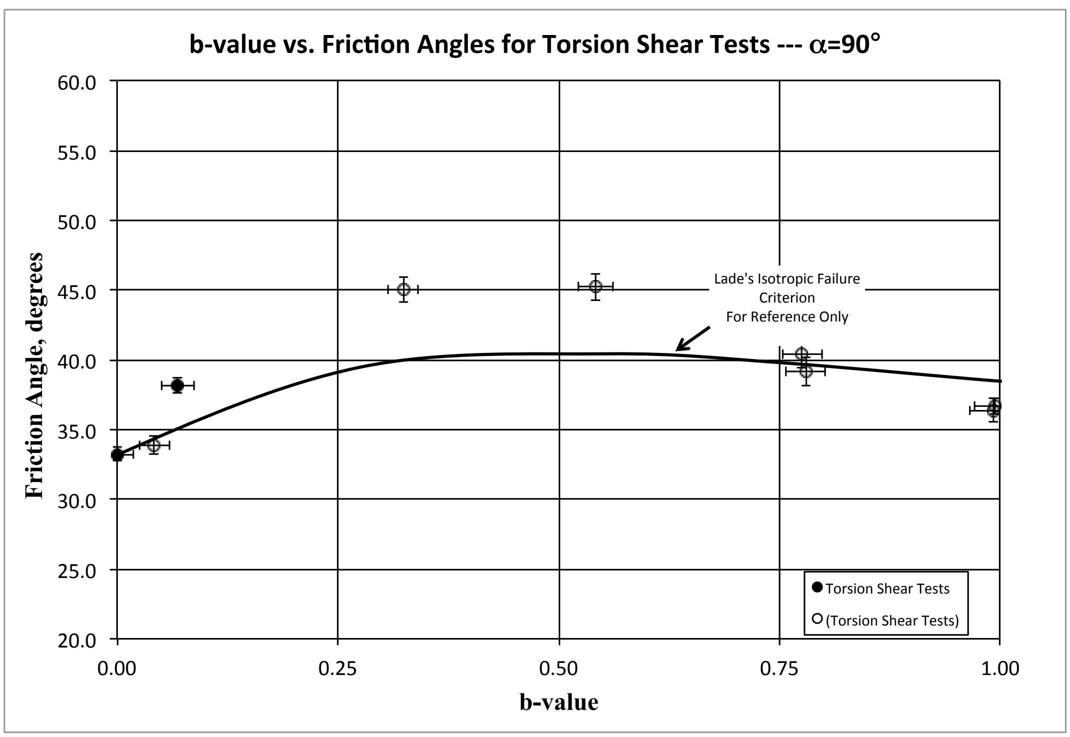

Figure 7.1.5. b-value vs. Friction Angle for α=90° degrees for both Torsion Shear and True Triaxial tests.

To get an understanding of the strength of the soil while the b-value was kept constant, Figures 7.1.6 through 7.1.10 present the results with varying alpha values. Although not all b-values were kept exactly at the corresponding b (especially the tests designated with a *), the test results were grouped and plotted at the nearest b-value.

When looking at the test data with b-value as constant, the tests all show very similar behavior. The strength decreases from α=0° to α=67.5° (where it is the lowest) and then increases to α=90°, ending always at a strength less than that of α=0°. Table 7.1.2 summarizes the tests results and shows the difference in friction angle compared to α=0° for the corresponding b-value.

Table 7.1.2 shows an increase in difference of friction angle for b-values as alpha goes from 0 to 90 degrees. Overall, the drop from α=0° to α=67.5° gets more pronounced as the b-value increases. The greatest drop from α=0° to α=67.5° is seen at b=0.75, where there is an average decrease of 23.7 degrees. An increase in strength seen from α=67.5° to α=90° is the greatest at b=0.25 and b=0.75, increasing an average of 7.5 degrees.

Lade and Wasif (1988) performed tests on specimens of Cambria sand with height/diameter ratios of 1 and 2.5. They prepared the specimens by placing a mold in a bucket of deaired water and then tilting the mold sitting in a cradle to the desired alpha value. The specimen was then placed upright and frozen. When thawed and tested, the major principal stress acted at the angle of the bedding planes. This is a similar procedure as explained previously when preparing true triaxial specimens at α=90°, except with the additional use of a cradle to tilt the mold while pouring the sand into the mold. For tests done at b=0, the tests showed that the friction angle consistently dropped by 5.5 degrees with increasing inclination of the bedding planes. Similarly, as can be seen in Table 7.1.2 and Figure 7.1.6, a drop of 7.6 degrees is seen where α=90° and b=0.

Table 7.1.2. Summary of Torsion Shear test results with the b-value constant.

Test No.		α	b-value	ϕ	$\Delta\phi$
23		0.00	0.00	41.57	0
1	*	0.00	0.01	37.36	-4.21
3		22.38	0.00	39.4	-2.17
27	*	24.04	0.02	36.34	-5.23
31		44.91	0.00	36.25	-5.32
14		67.50	0.00	35.01	-6.56
41		90.00	0.00	34.27	-7.3
18		90.00	0.06	36.32	-5.25
19	*	90.00	0.08	40.37	-1.2
24	*	0.00	0.27	45.89	0
28		22.97	0.26	44.48	-1.41
4	*	23.73	0.27	47.03	1.14
5	*	24.18	0.27	41.39	-4.5
32	*	31.76	0.18	40.58	-5.31
9		44.99	0.24	38.85	-7.04
35	*	69.85	0.16	37.74	-8.15
36		67.68	0.25	37.57	-8.32
42	*	90.00	0.32	45.1	-0.79
25	*	0.00	0.55	53.51	0
6		22.01	0.51	46.31	-7.2
33		44.99	0.50	45.02	-8.49
10	*	41.96	0.55	40.55	-13
15		67.40	0.50	39.52	-14
37	*	70.03	0.56	38.19	-15.3
20	*	90.00	0.52	41.81	-11.7

Test No.		α	b-value	ϕ	$\Delta\phi$
2		0.00	0.75	57.02	0
29		22.77	0.75	46.75	-10.27
30	*	22.92	0.85	46.18	-10.84
11		44.98	0.75	40.36	-16.66
12	*	41.54	0.81	41	-16.02
38		67.54	0.75	32.98	-24.04
39	*	70.62	0.79	34.68	-22.34
40	*	73.06	0.80	34.97	-22.05
43	*	90.00	0.78	40.41	-16.61
21	*	90.00	0.78	41.27	-15.75
26		0.00	1.00	53.27	0
8		22.87	0.97	41.87	-11.4
34		44.95	1.00	35.61	-17.66
17		68.26	1.00	37.11	-16.16
22	*	90.00	0.99	39.36	-13.91
44	*	90.00	0.99	35.72	-17.55

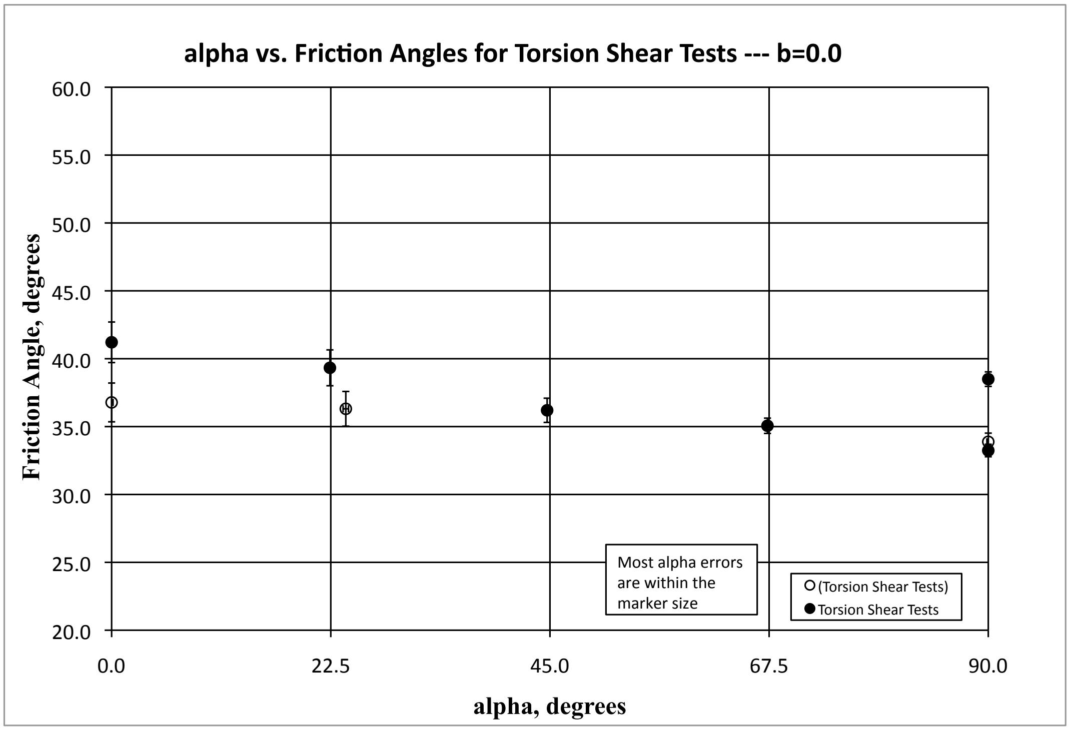

Figure 7.1.6. Alpha vs Friction Angle for b=0 for Torsion Shear Tests.

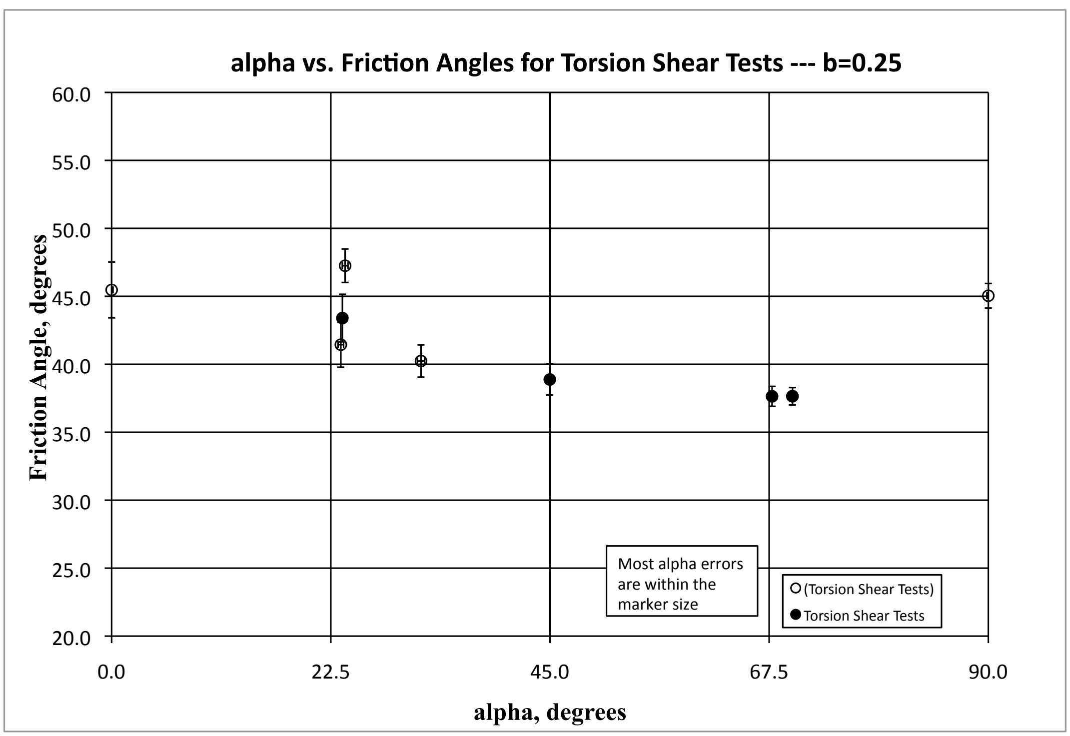

Figure 7.1.7. Alpha vs Friction Angle for b=0.25 for Torsion Shear Tests.

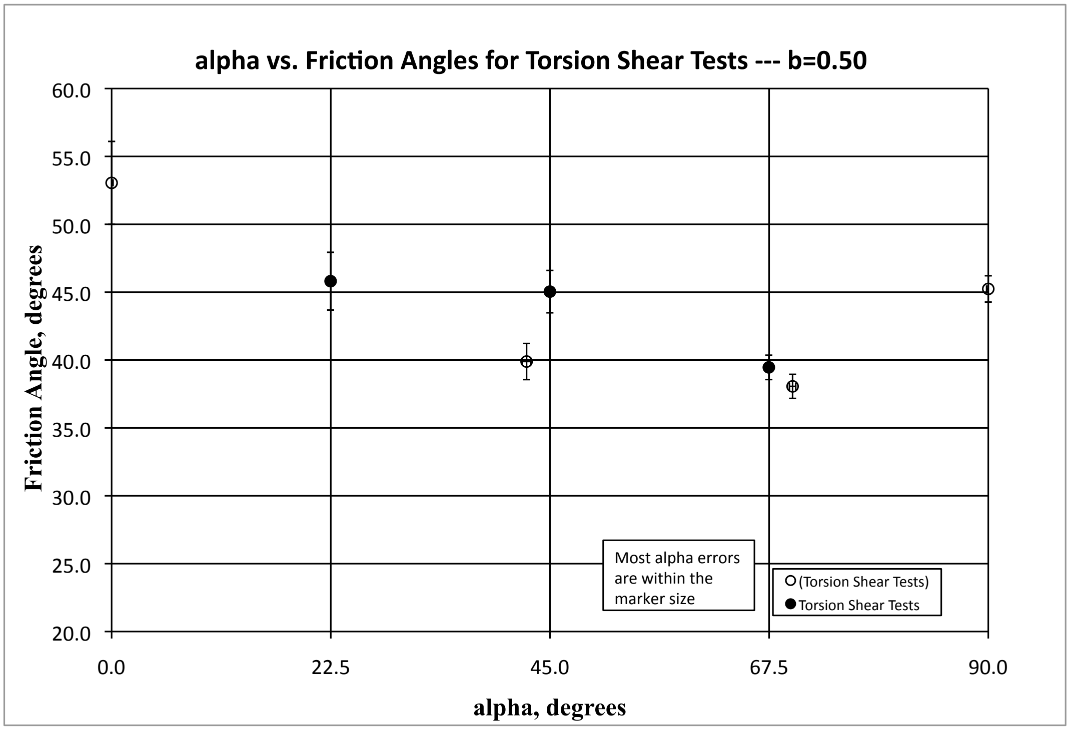

Figure 7.1.8. Alpha vs Friction Angle for b=0.50 for Torsion Shear Tests.

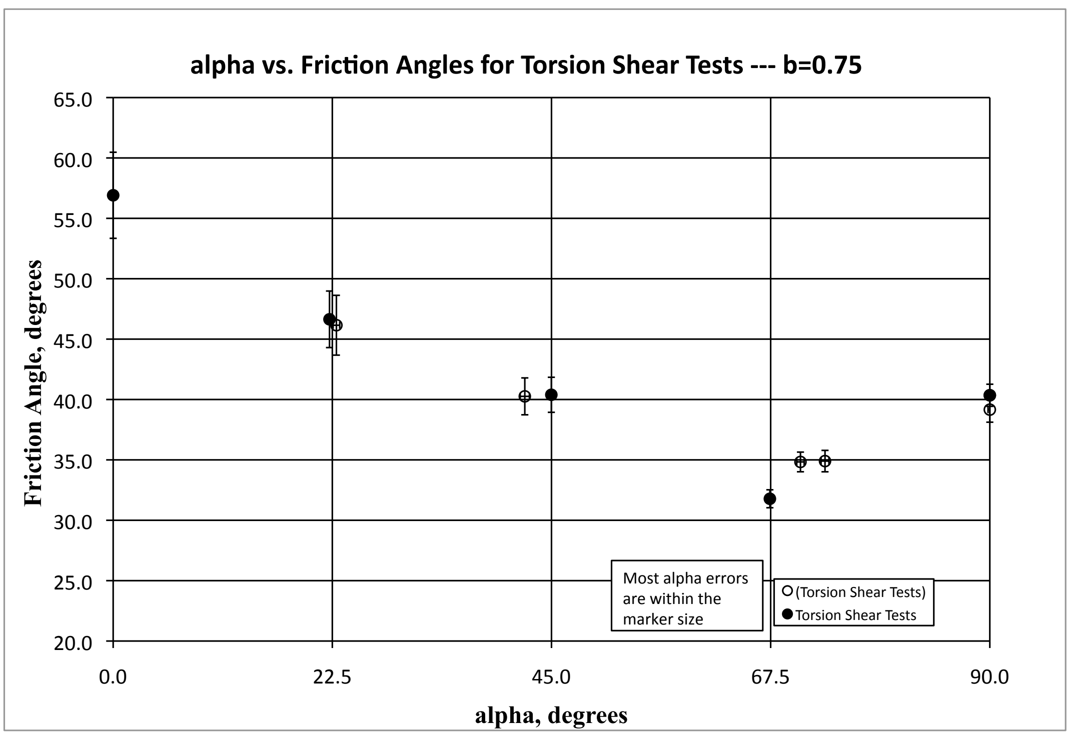

Figure 7.1.9. Alpha vs Friction Angle for b=0.75 for Torsion Shear Tests.

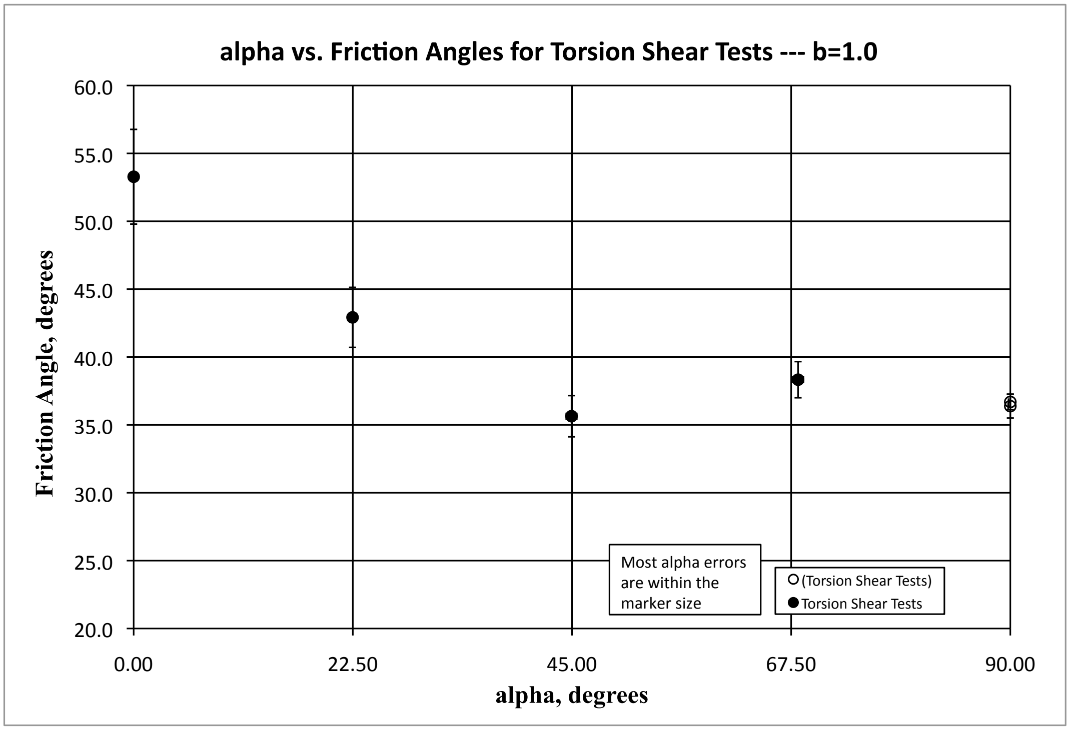

Figure 7.1.10. Alpha vs Friction Angle for b=1.0 for Torsion Shear Tests.

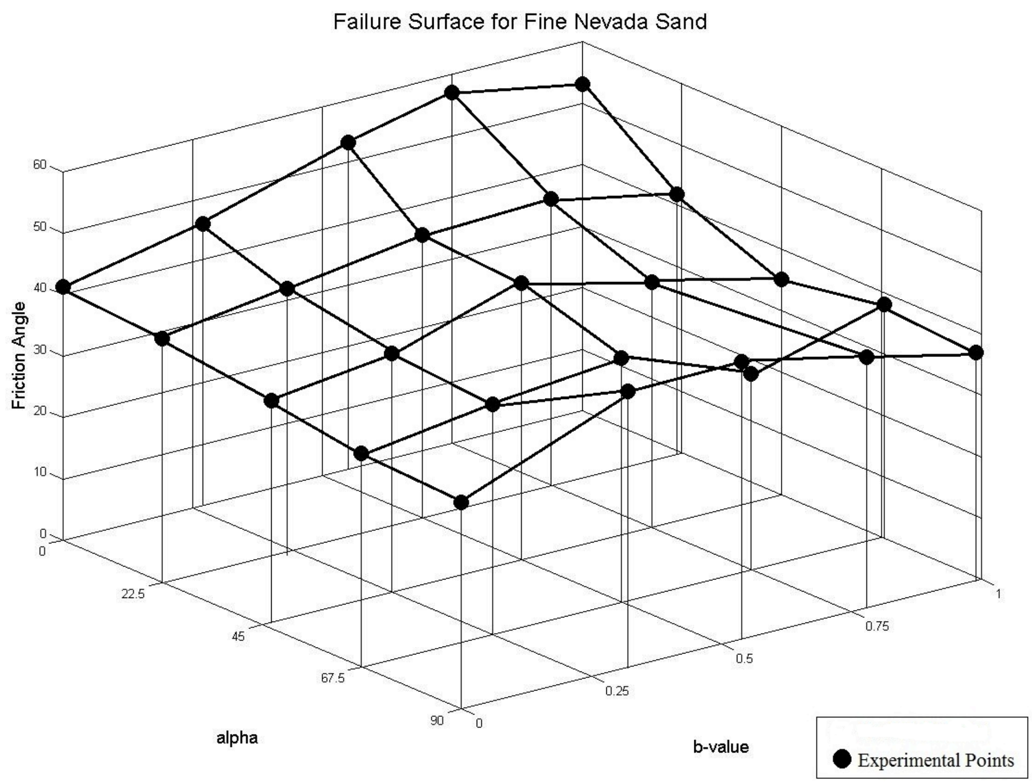

Figure 7.1.11. 3D failure surface plot at increments of 0.25 for b-values and 22.5 degrees for alpha values.

Figure 7.1.11 shows the 3D representation of the test results. Representative points at the intersections of b-value and alpha values have been presented. As was seen in the individual plots (Figures 7.1.1 through 7.1.10), the soil shows the highest strength at α=0° and higher b-values. With increasing alpha values, there is a loss of strength, which at α=90° increases a small amount. The loss in strength at α=67.5° and b=0.75 is seen as a dip in Figure 7.1.11. From the highest to lowest point on the graph, there is a difference of 23.4°. For comparison in 3D, the true triaxial tests have been graphed with the torsion shear tests at α=0° and α=90° in Figure 7.1.12.

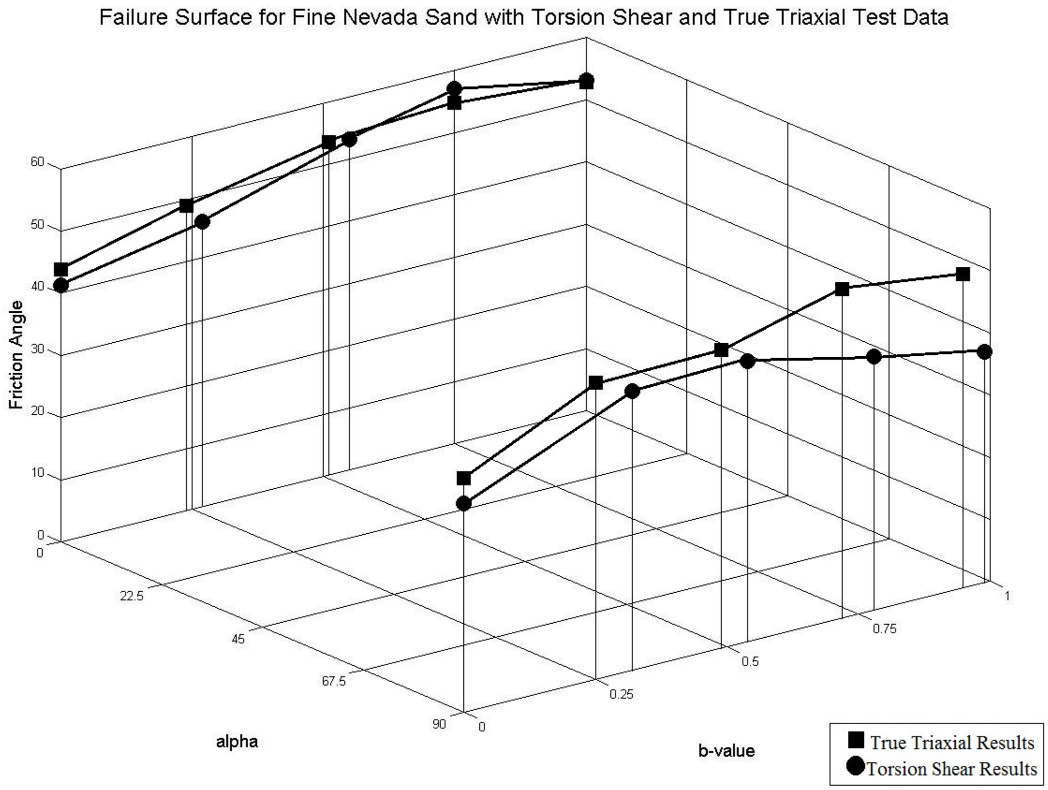

Figure 7.1.12. Comparison of 3D failure surface plot for True Triaxial and Torsion Shear tests.

7.2 Correction to Stress-Strain Curves for Piston Friction

When analyzing the stress strain curves for the test data, certain tests experienced an increase in major principal strain without much, if any increase in stress ratio. This only occurred in tests that had rotation. Tests where α=0° or α=90° did not experience this added strain. This was mainly seen in most of the preliminary set of tests (tests labeled with a *). If the specimen was not perfectly aligned and level with the top lid, a horizontal frictional force was applied to the piston. At the beginning of the test, where the stress level was still very low, this frictional force was picked up by the horizontal LVDT reading. Once the frictional force was overcome, the piston would be free to move and the LVDT readings would be continuous and smooth. In order to verify that this was indeed what was occurring, other dial gages were set up and recorded. The readings of the horizontal LVDT and the dial gages were compared and proven to be the same.

Although it is difficult to quantify the amount of friction in each test, especially with the varying conditions unique to each test, it is believed that the friction did not affect the final strength reached for each specimen. This is confirmed by the true triaxial test results (shown in Chapter 5) for specimens at $\alpha=0°$ and $\alpha=90°$. Failure points for the torsion shear tests performed without rotation fit in within the range of scatter with the true triaxial results. This comparison can be seen in Figure 7.1.1 and 7.1.5.

With this in mind, the set-up of the specimen for the second set of testing (tests labeled without a *) was changed slightly. The procedure deviated from previous tests by ensuring that the bushing was removed before setting the top lid on the acrylic cylinder prior to saturation of the specimen. Without the bushing in place, it was possible to physically see if the specimen, the acrylic cylinder, and the piston were completely centered and aligned with the load cell. Once this was centered, as there was a little bit of tolerance in moving the acrylic cylinder on its O-ring, the top lid was removed to allow the saturation of the inner cell after which the top lid was placed atop the acrylic cylinder again. The bushing was connected and the rest of procedure was completed as described in Section 6.2.

It is believed that this alignment process helped to minimize the effect of piston friction when rotating the specimen. Although every effort was made to create a specimen that was as plum as possible, in certain cases, the horizontal deviation still occurred. Most of the new set of tests did not have this occur. However, four tests (Tests 14, 17, 36, and 38) needed to be corrected. The previous set of tests, as well as these four tests were corrected and an example of the correction is shown in Figures 7.2.1 through 7.2.4. Figures 7.2.1 and 7.2.2 show an example of a correction done to a previous test where there is a pronounced increase in strain. Figures 7.2.3 ad 7.2.4 show an example of a test where a small correction was applied. The stress-strain and volume change plots presented in the sections that follow have all been corrected in this manner if needed.

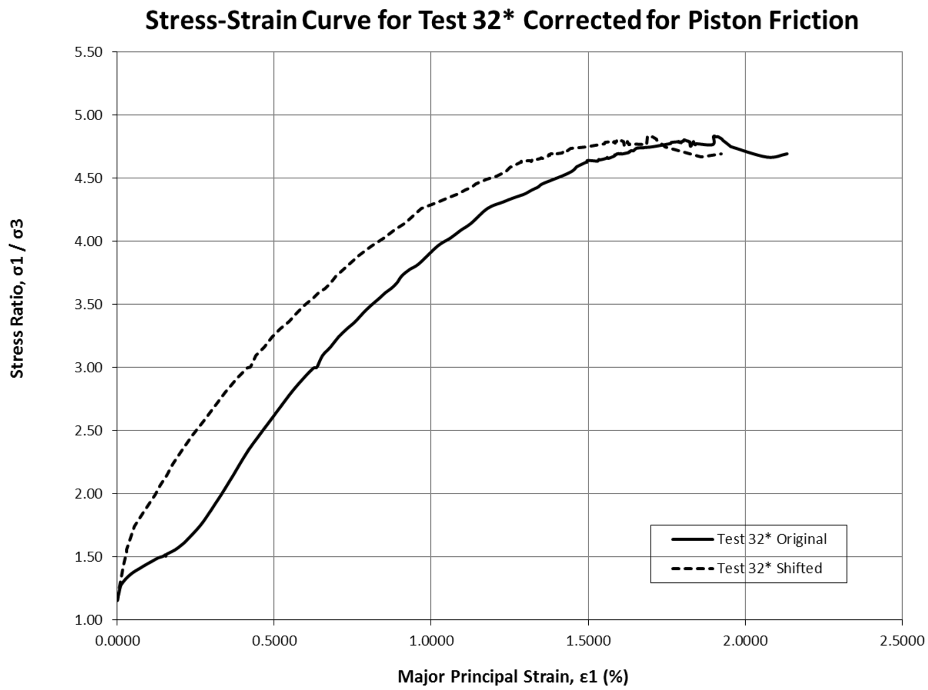

Figure 7.2.1. Stress Strain Curve for Tests 32* showing the correction applied to account for piston friction.

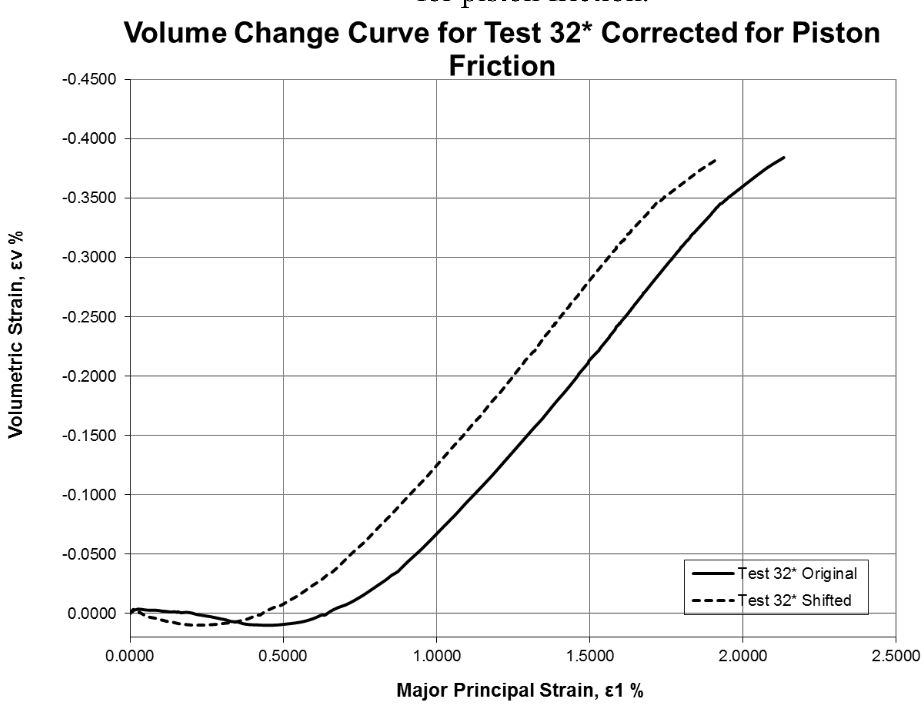

Figure 7.2.2. Volume Change Curve for Tests 32* showing the correction applied to account for piston friction.

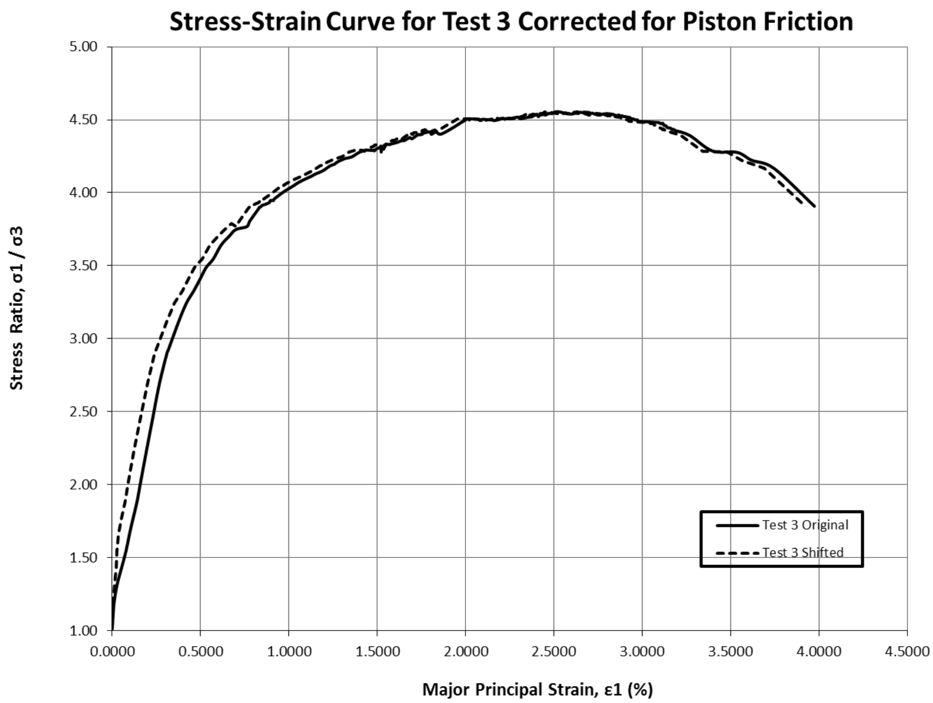

Figure 7.2.3. Stress Strain Curve for Tests 3 showing the correction applied to account for piston friction.

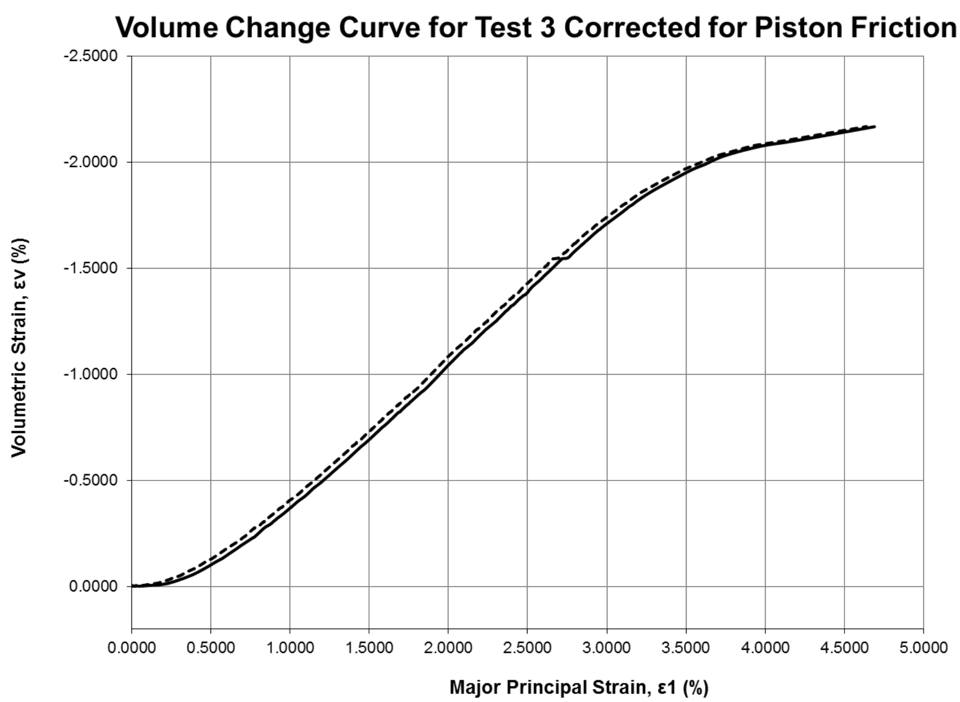

Figure 7.2.4. Volume Change Curve for Tests 3 showing the correction applied to account for piston friction.

7.3 Tests with α=0°

Tests without rotation were performed under stress controlled conditions. In order to change the b-value, internal and external pressures were changed, as well as the vertical load applied. Vertical load was added to the specimen, creating a vertical and principal stress over the area of the specimen. The stress was added until the specimen could no longer hold that stress and shearing occurred. In most instances, shear bands occurred at or near failure. Therefore, a well-pronounced softening regime in the stress-strain curves is not seen.

Isotropic compression was performed on each specimen from 48 kPa to 101 kPa prior to shearing. The isotropic compression charts for α=0° tests can be seen in Figure 7.2.1. All specimens have very similar behavior during isotropic compression in terms of volume change and no obvious leaks or problems can be detected from looking at Figure 7.3.1.

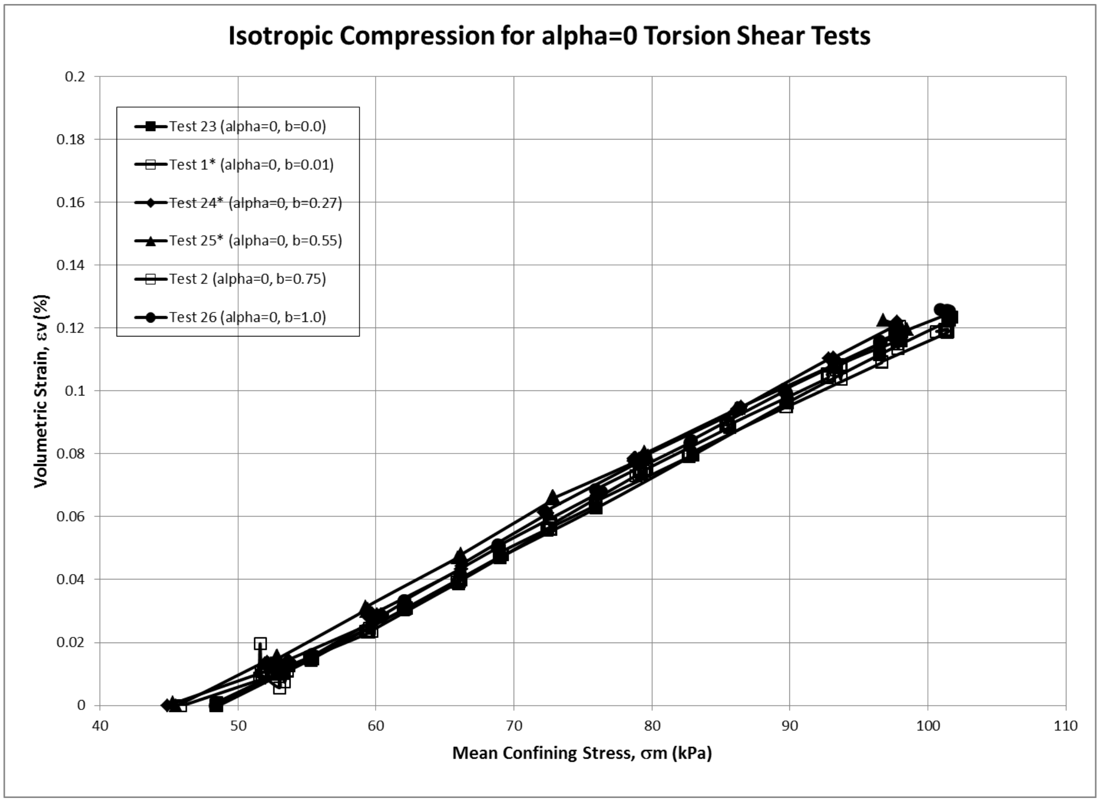

Figure 7.3.1. Isotropic Compression Chart for α=0° Torsion Shear Tests.

The stress-strain plot for these tests is presented in Figure 7.3.2. Since the Tests 25*, 2 and 26 all had very high stress ratios, the entire curve is shown in Figure 7.3.2. The scale on Figure 7.3.3 is cut off at a stress ratio of 7 for consistency and ease when comparing the other tests in Sections 7.4 to 7.7. When looking at Figure 7.3.2 and 7.3.3, a pattern can be seen. As the b-value increases, so does the friction angle. At b=1 however, the friction angle is much lower. This pattern is shown in Figure 7.1.1. The strain to failure also decreases as the b-value is increased. This is typical and was also seen in the true triaxial test results presented in Chapter 5. Section 8.2 explains in detail explanations for why the strain to failure is different between the true triaxial tests and torsion shear tests.

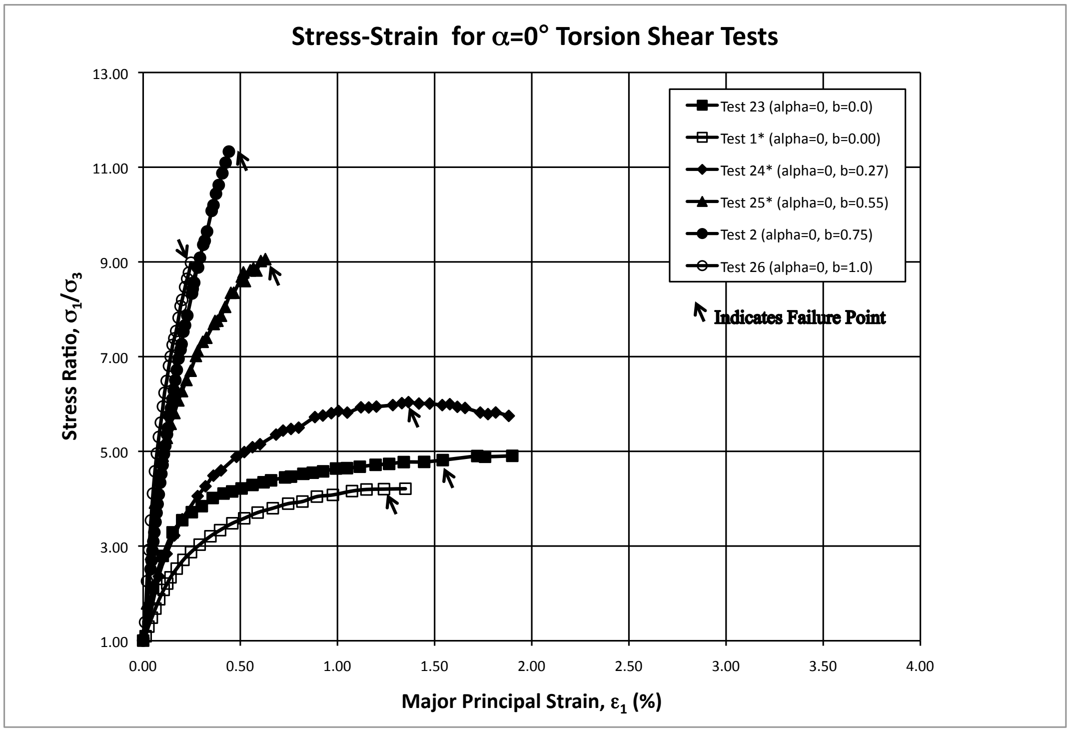

Figure 7.3.2. Stress-Strain Curves for α=0° Torsion Shear Tests.

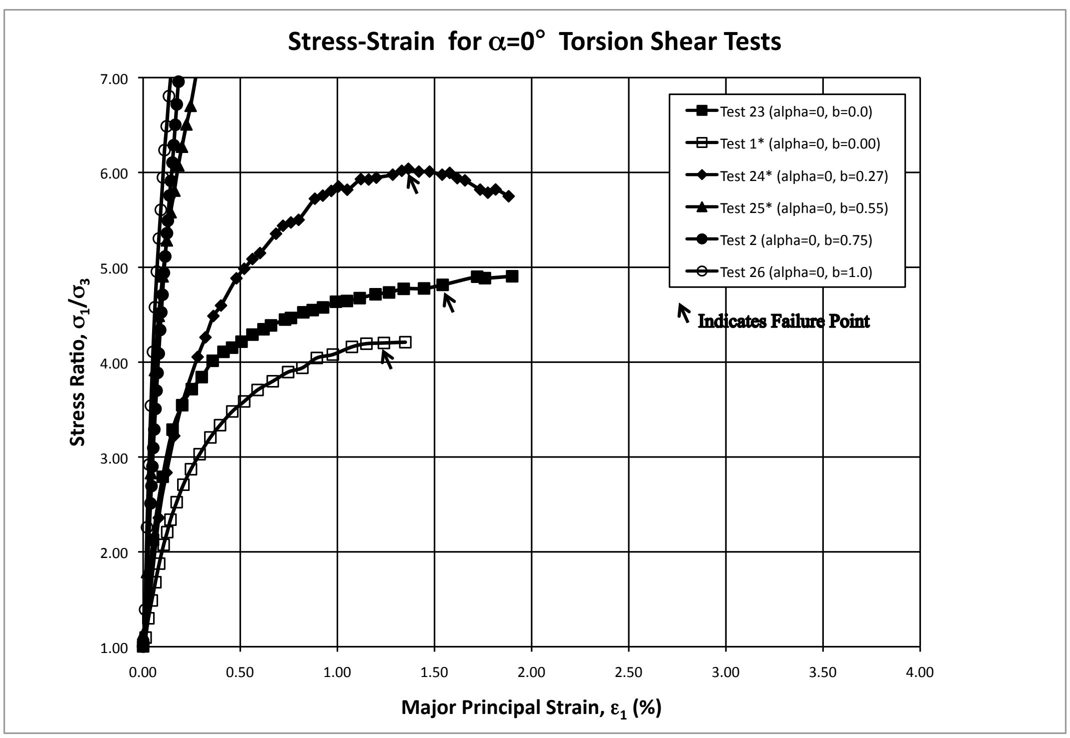

Figure 7.3.3. Stress-Strain Curves for α=0° Torsion Shear Tests only showing up to σ_1/σ_3=7.

The volume change curves for this set of tests are presented in Figure 7.3.4. With increasing b-value, it is thought that there would also be increasing volumetric strain. The volume change does not show such a consistent pattern as did Figure 7.3.3. It is seen here that Tests 24* and Test 25 fall out of the pattern described above. Test 24* shows less volumetric strain than what would be expected. Conversely, Test 25 shows much more dilation than expected. However, the rest of the tests follow the expected pattern. For tests with α=0°, there is a slight increase in dilation angles from b=0.5 to b=1.0 as seen in Figure 7.3.5.

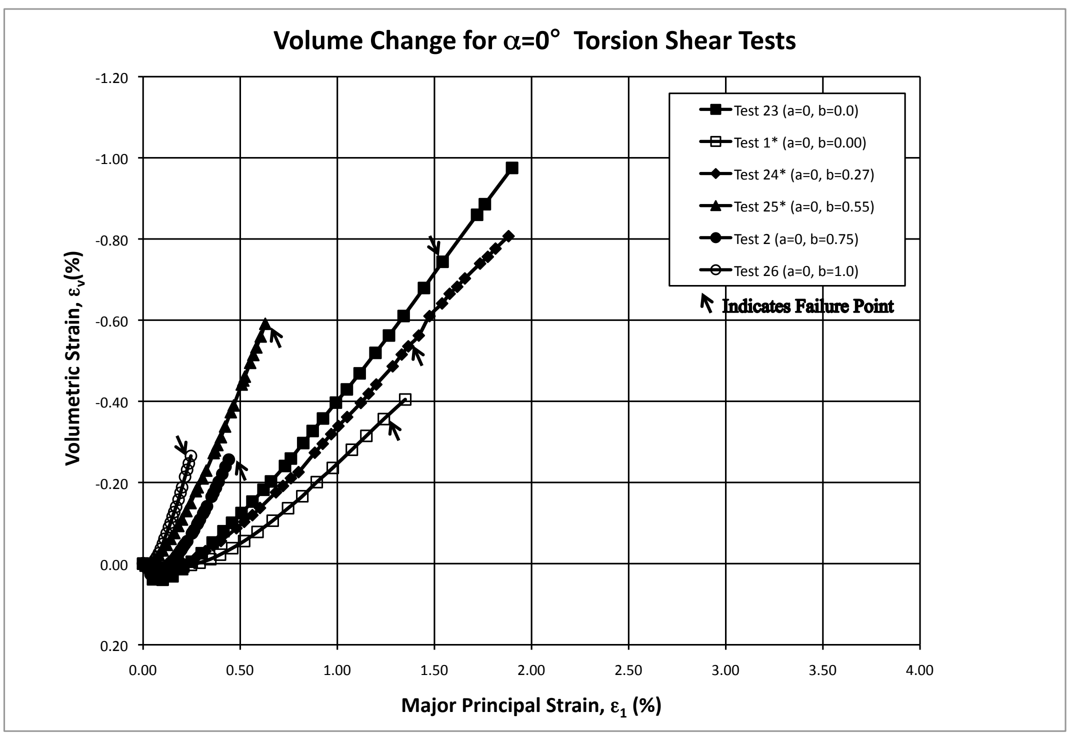

Figure 7.3.4 Volume Curves for α=0° Torsion Shear Tests.

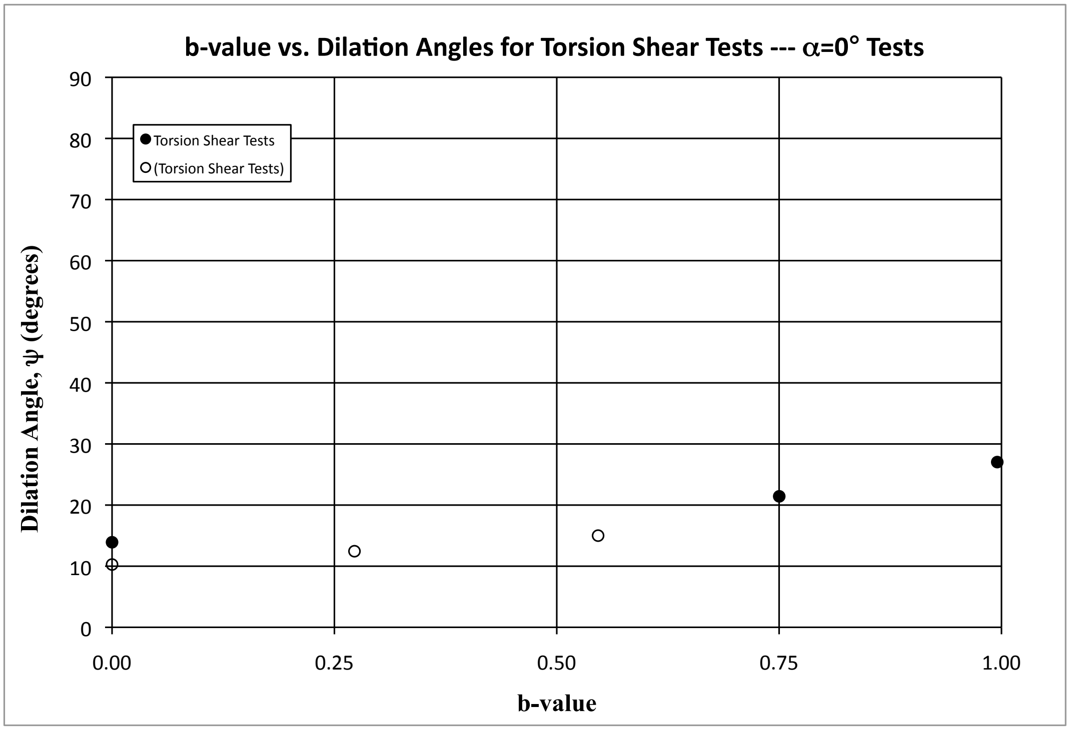

Figure 7.3.5. Dilation angle versus b-value for α=0° Torsion Shear Tests.

7.4 Tests with α=22.5°

The isotropic compression data for tests with rotation at α=22.5° degrees is presented in Figure 7.4.1. All but three tests seem to have a very similar slope and total volumetric strain as the confining pressure was increased. Tests 27* and 28 have quite different slopes and show less total volumetric strain than the rest. Test 27* had a void ratio of 0.51, where the other tests had void ratios near 0.53. The higher relative density of Test 27* can be a reason why there is less volumetric strain. Test 28 has a void ratio of 0.531, which is the targeted void ratio of the tests. However, accidentally, the specimen did not have a total back pressure of 101 kPa before isotropic compression was performed. With only 48 kPa of back pressure, the change in volumetric strain is seen in Figure 7.4.1. Test 29's data was only recorded half way through the isotropic compression and that is why it begins at 81 kPa.

The stress strain, volume change data and dilation angles are presented in Figures 7.4.2, 7.4.3 and 7.4.4. When looking at the stress-strain curves, once again, there is an increase in stress ratio as the b-value increases. Although there is some scatter in the results from repeat tests at similar b-values, the trend is still seen. Just as in the α=0° torsion shear tests, the strength at b-values of 1 dropped significantly. The friction angle can be seen in Figure 7.1.2. There is also decreased strain to failure with increasing b-values.

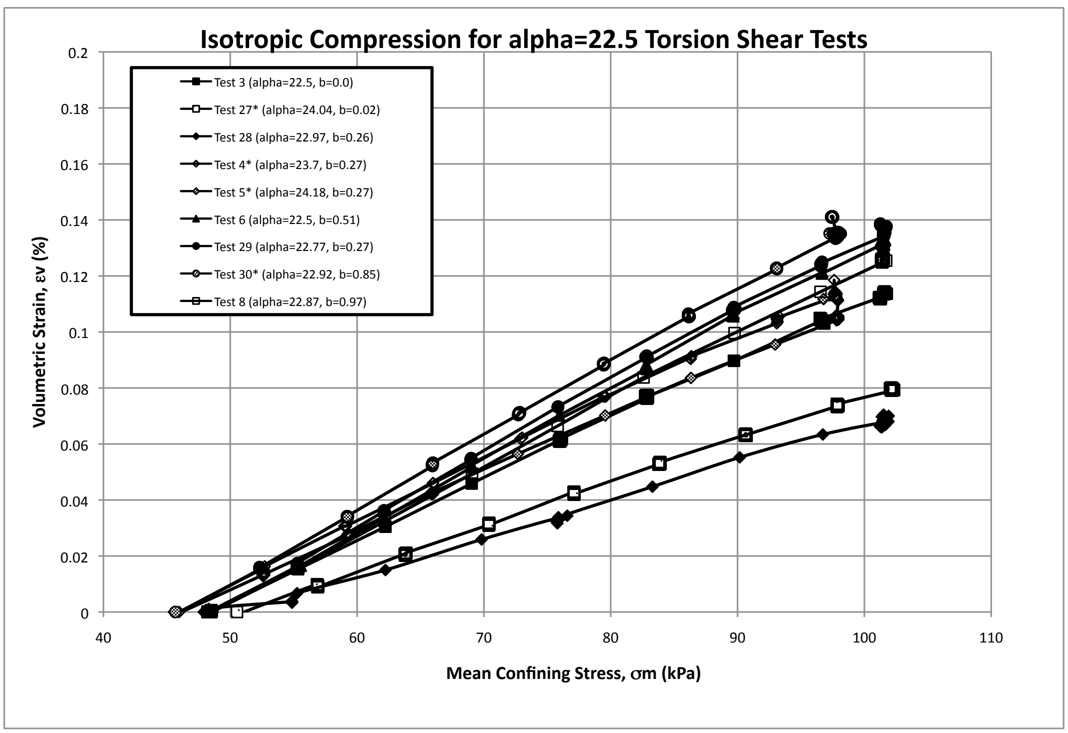

Figure 7.4.1. Isotropic Compression Chart for α=22.5° Torsion Shear Tests.

The volume change curves are presented in Figure 7.4.3. The tests show less total volumetric strain as the b-value increases. Test 5* is the only test that is slightly out of order. There is a little less volumetric strain than tests near b=0. With this exception the rest of the volume change curves correspond to the stress strain behavior seen in Figure 7.4.2.

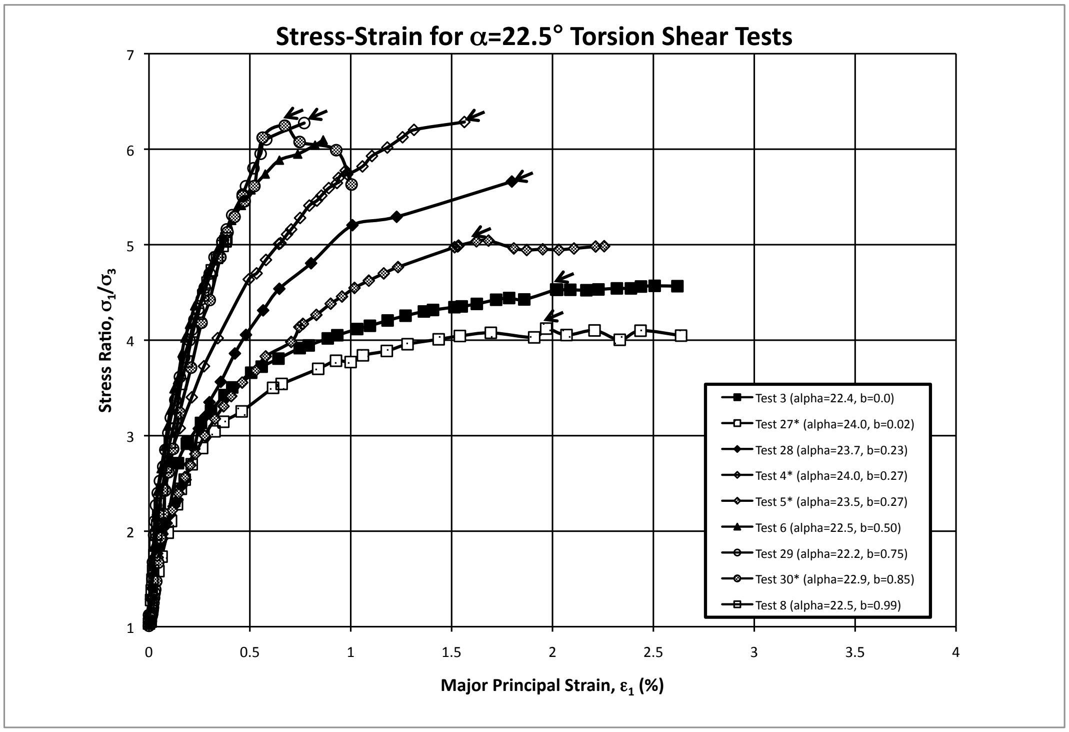

Figure 7.4.2. Stress-Strain Curves for α=22.5° Torsion Shear Tests.

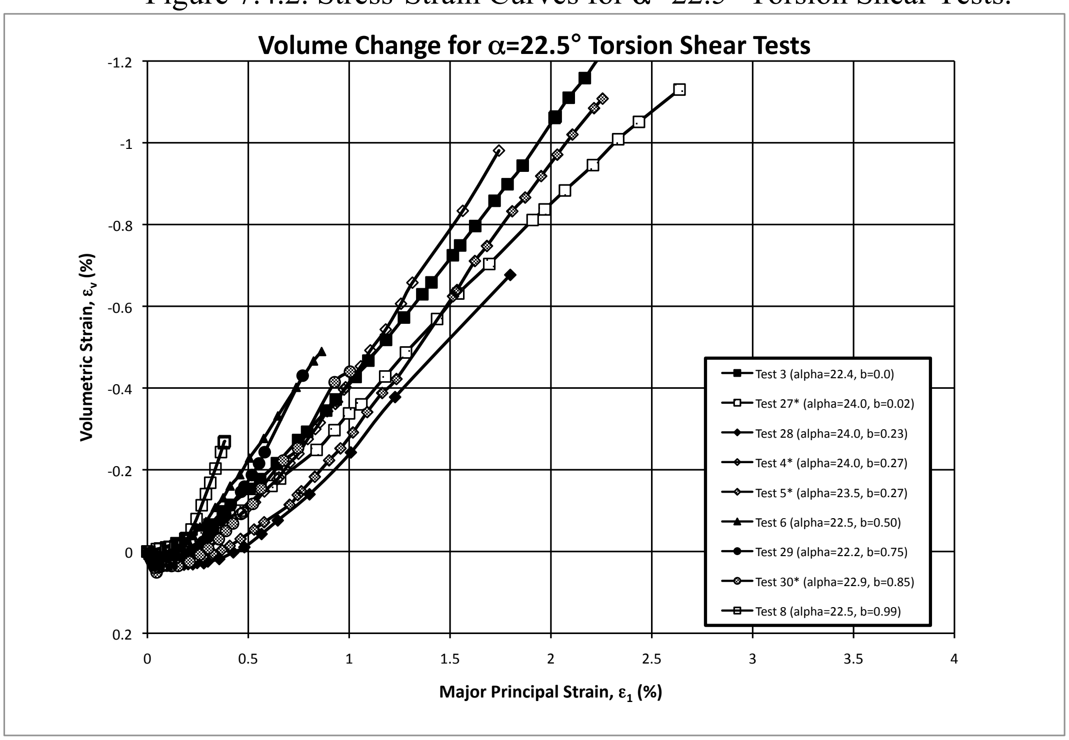

Figure 7.4.3. Volume Change Curves for α=22.5° Torsion Shear Tests.

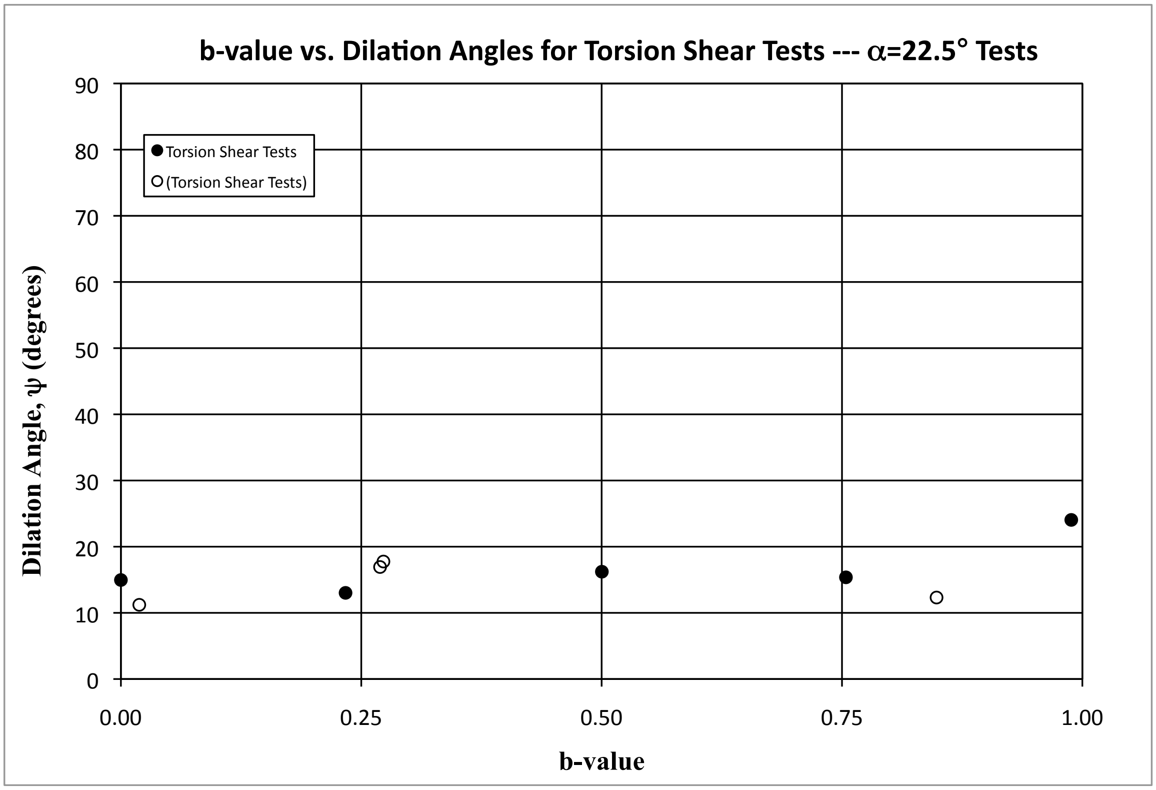

Figure 7.4.4. Dilation angle versus b-value for α=22.5° Torsion Shear Tests.

7.5 Tests with α=45°

Isotropic compression data is shown in Figure 7.5.1. All but Test 12* show similar behavior. Test 12* had a void ratio of 0.56 corresponding to a slightly lower relative density than the rest of the tests. This may be a possible explanation for the increase in volumetric strain with increasing pressure.

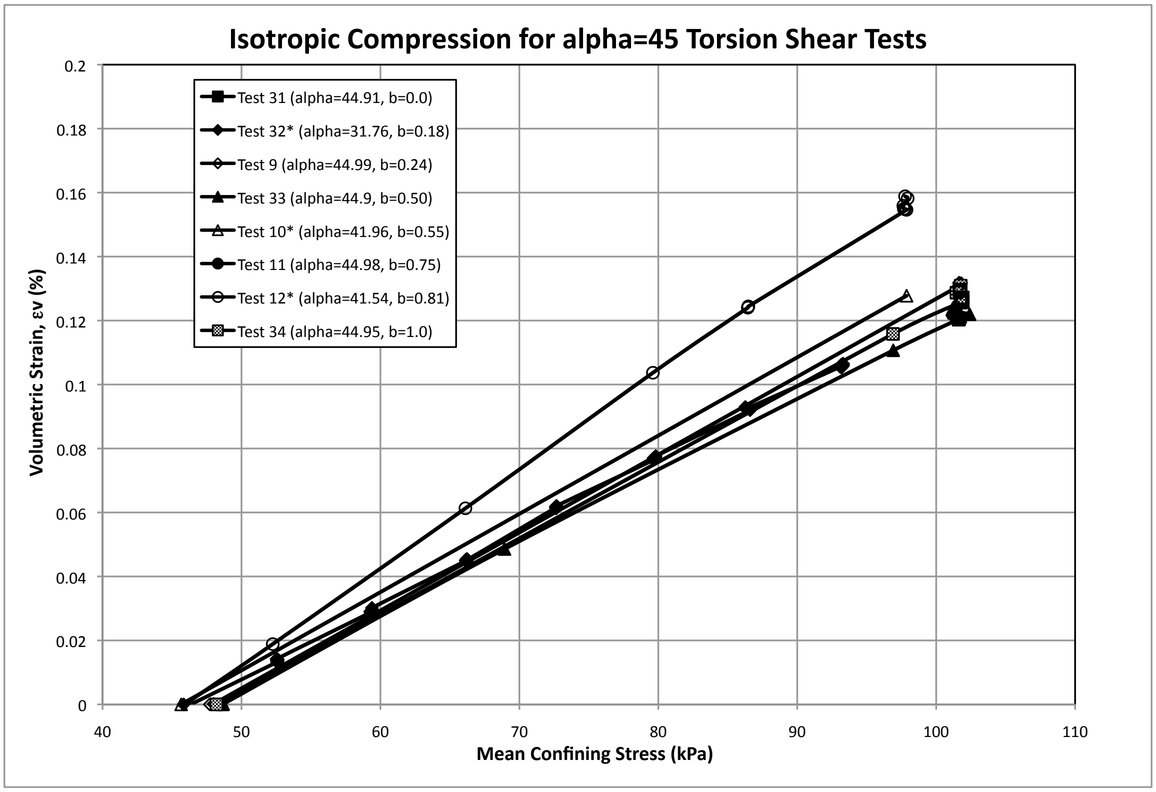

Figure 7.5.1. Isotropic Compression Chart for α=45° Torsion Shear Tests.

In terms of the vertical load in tests at α=45°, it is important to recall Figure 6.6.1, which shows the boundary between compression and extension tests. The α=45° tests at b=0 and b=0.25 are in compression while those at b=0.75 to b=1.0 are in extension. α=45° and b=0.5 is the boundary dividing compression and extension tests. Referring to Figure 7.5.3, there is an increase in strength until b=0.5. For tests with b-values greater than b=0.5, there is a decrease in friction angle. As the b-value increases, the strain to failure decreases. When looking at the volume change, most of the curves are very close to each other, with the exception of Test 31 that had the most strain and therefore, most volumetric strain. Most of the tests have very similar rates of dilation and all show very little total volumetric strain. However, Test 10* and Test 12* show an average of 15 degree increase in angle of dilation above the values for the other tests.

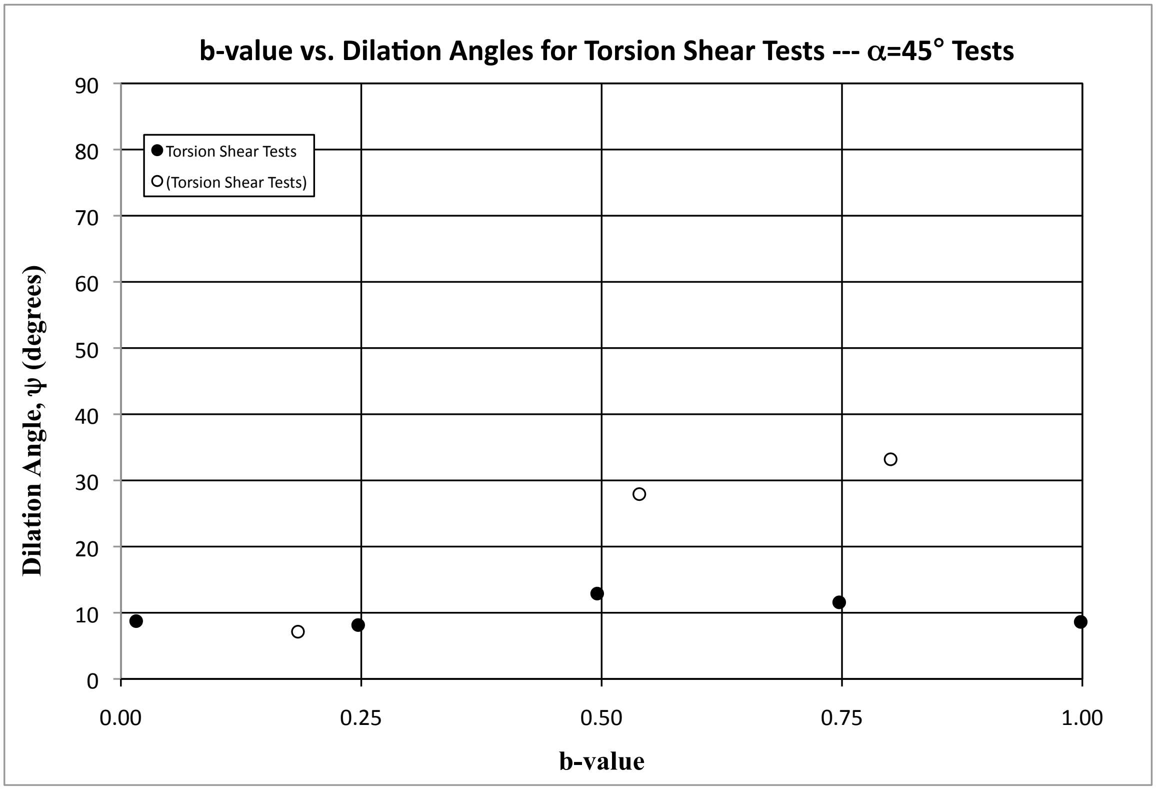

Figure 7.5.2. Dilation Angle versus b-value for α=45° Torsion Shear Tests.

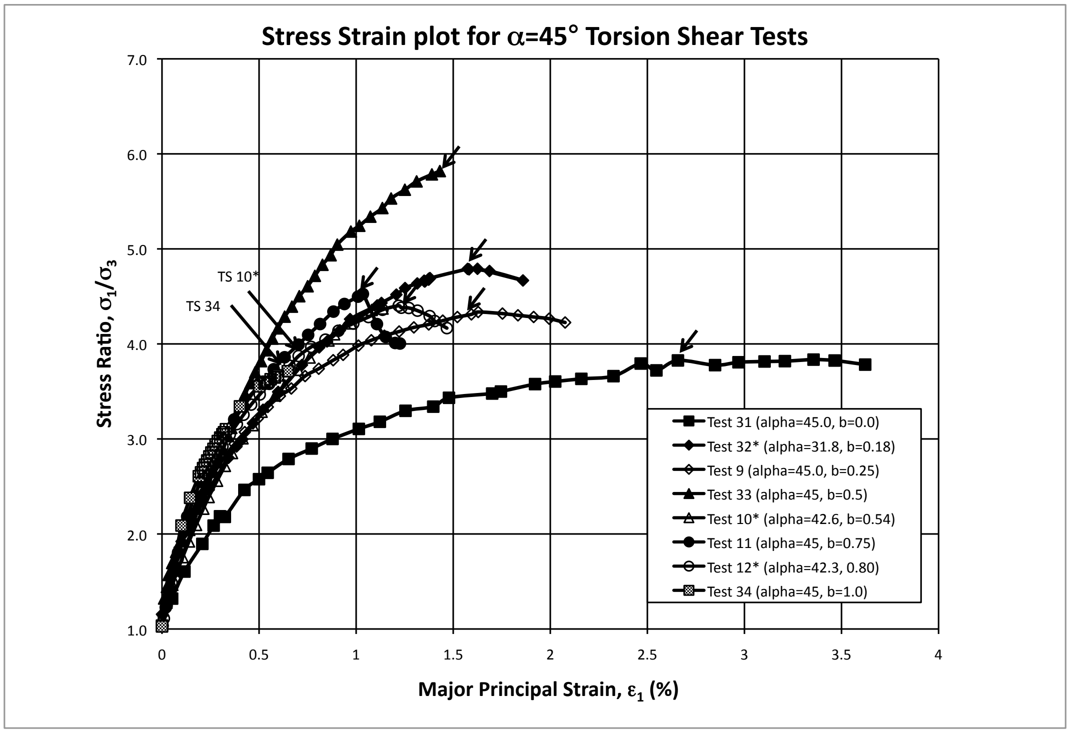

Figure 7.5.3. Stress strain plot for α=45° Torsion Shear Tests.

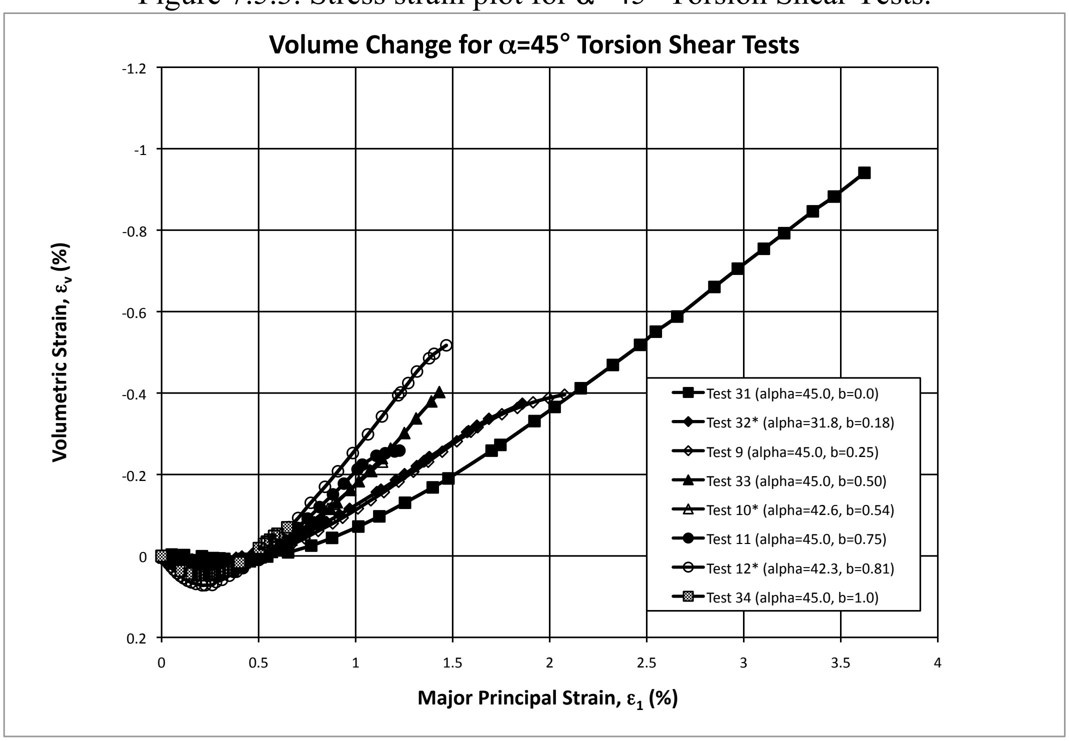

Figure 7.5.4. Volume change plot for α=45° Torsion Shear Tests.

7.6 Tests with α=67.5°

Presented below are the isotropic compression, stress strain and volume change plots for all tests with α=67.5° degrees. All isotropic compression curves have similar slopes and show similar volumetric strain. Prior to isotropic compression, Test 37* did not have the weight of the cross bar and torque arms set up. Therefore, the weight of these pieces was missing in the recorded values of isotropic compression. Without this weight, the specimen was able to show a little bit more volumetric strain. As is seen at the end of isotropic compression for Test 17, a leak was detected after the sample reached 101 kPa confining stress. Although the rate of the leak could be calculated, it is impossible to calibrate it out because the inner and outer pressures for b=1 tests vary throughout shearing. Fortunately, since the b=1 tests have very short total strain to failure, any additional specimen volume change throughout the test was not detrimental to the test results and final strength of the specimen. Because of this leak, the volume change is not presented for Test 17.

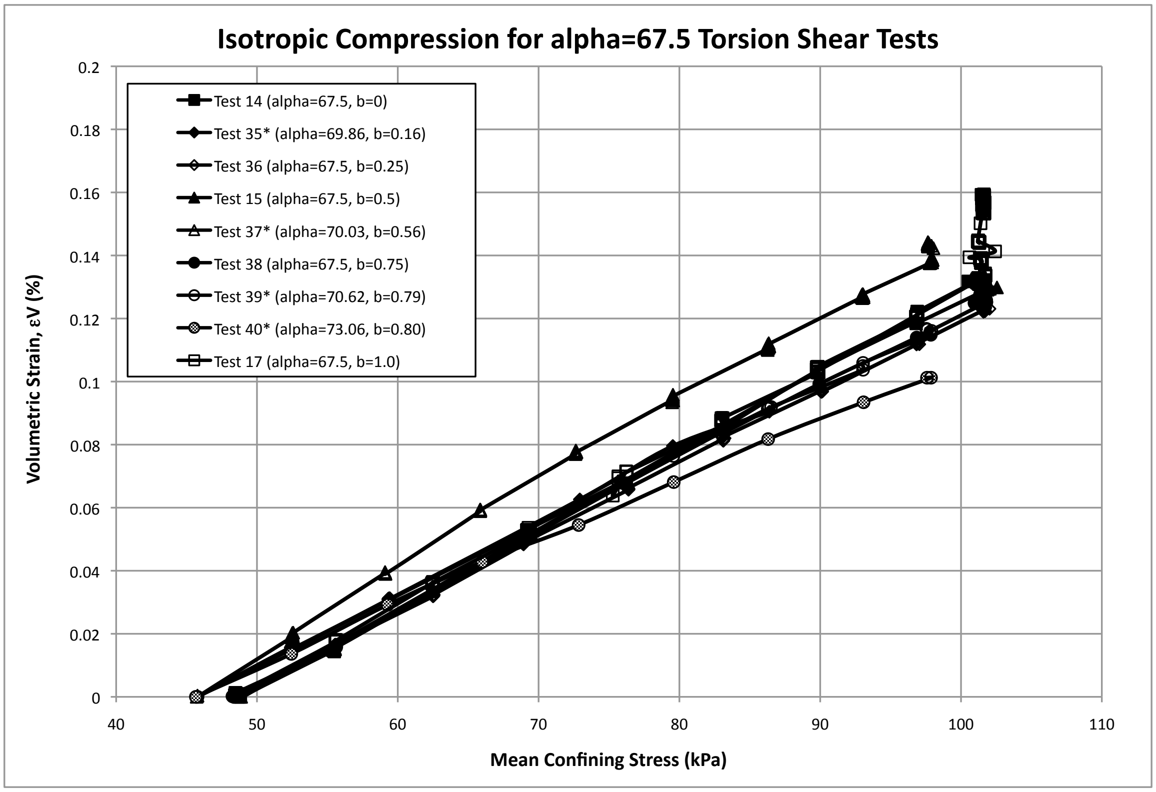

Figure 7.6.1. Isotropic Compression Chart for α=67.5° Torsion Shear Tests.

The stress-strain behavior of tests with their major principal stress at an inclination of 67.5 degrees is presented in Figure 7.6.3. Volumetric strain and dilation angles are presented in Figure 7.6.4 and 7.6.2, respectively. The curves show typical behavior when looking at strain to failure with increasing b-values. The higher the b-value, the less strain to failure. The curves also show increasing strengths from b=0 to b=0.5. At b=0.75, there is a drop in strength and then at b=1.0, the strength increases slightly. The decrease in strength at b=0.75 and α=67.5° was the only location where there is a dip in the strength of the soil. This condition was tested three times and all the test data shows consistency in the results, confirming that this decrease in strength at the condition stated is real. At this condition, for all three tests, large horizontal deep shear bands developed along the top cap. These horizontal shear bands coincide with the shear band angle, when using the Coulomb angle for shear band inclination (Equation 2.5.3).

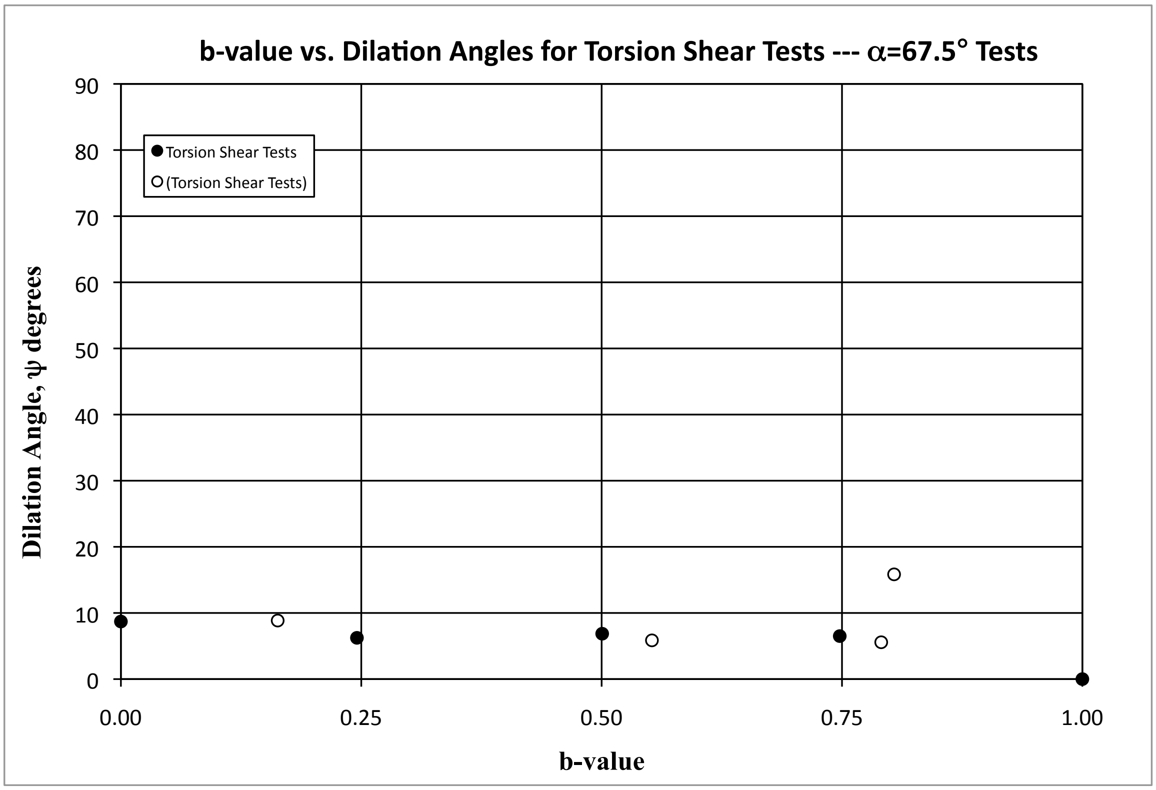

Figure 7.6.2. Dilation Angle versus b-value for α=67.5° Torsion Shear Tests.

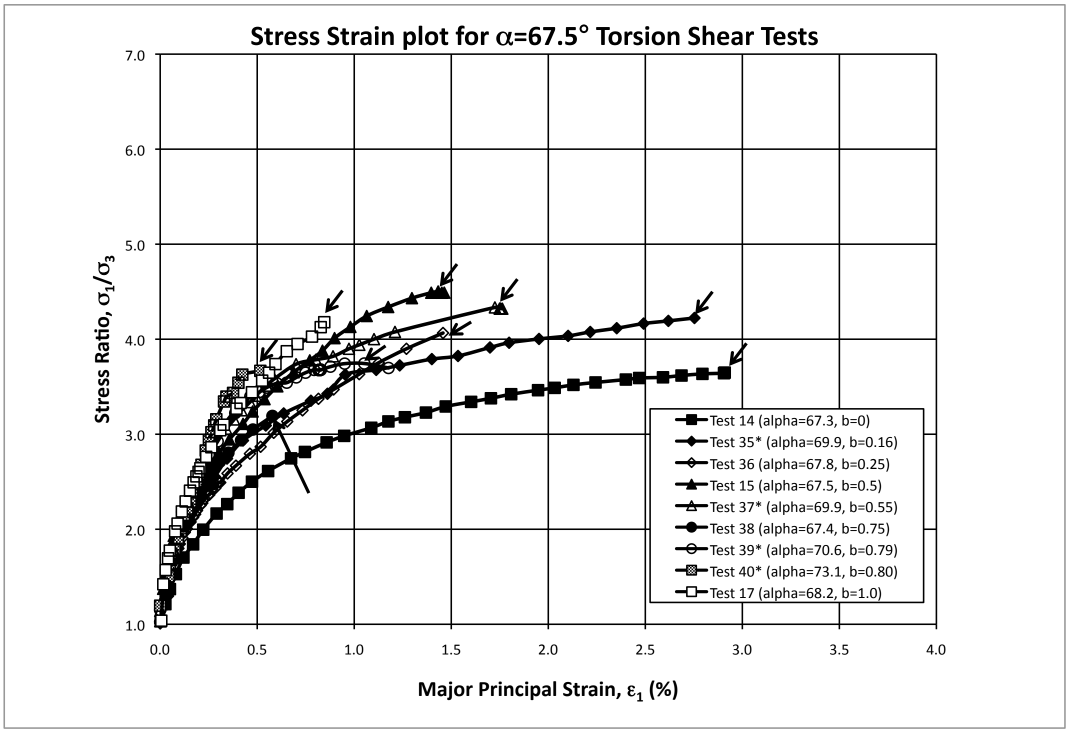

Figure 7.6.3. Stress strain plot for α=67.5° Torsion Shear Tests.

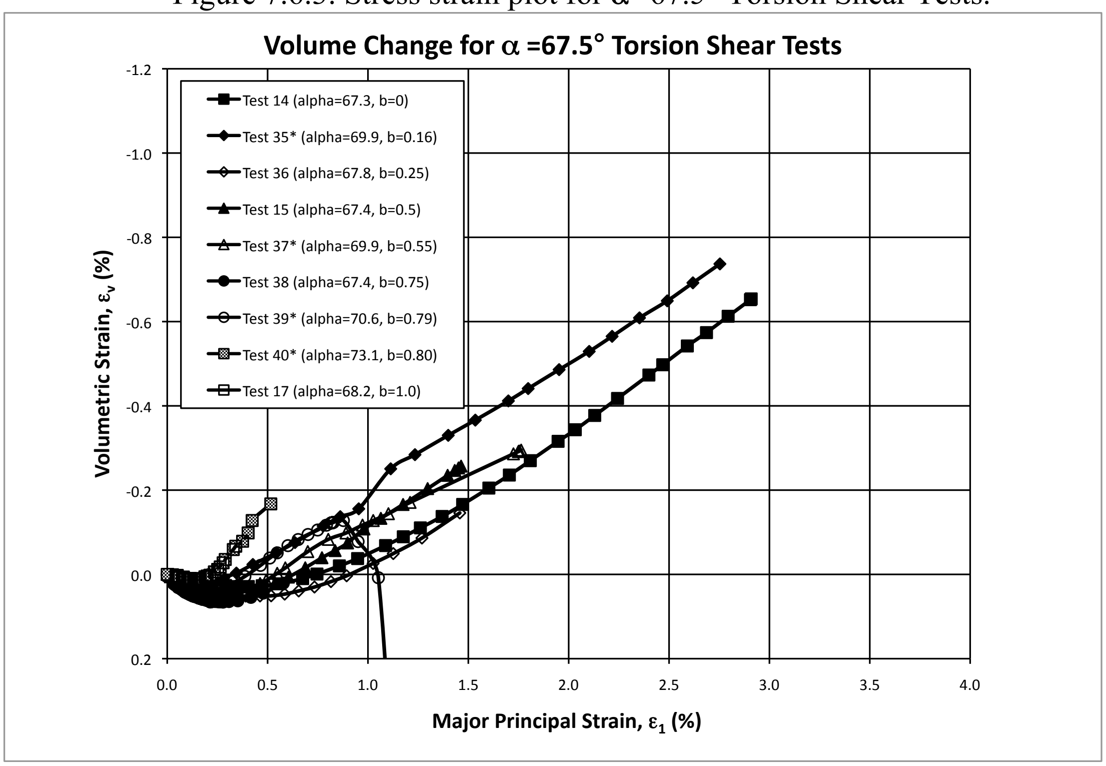

Figure 7.6.4. Volume change plot for α=67.5° Torsion Shear Tests.

7.7 Tests with α=90°

Isotropic compression data, the stress-strain curves and the volumetric strain curves for tests with α=90° are presented in Figures 7.7.1 through 7.7.3, respectively. The pattern for this set of tests is a bit different than what was previously seen for α=0° tests which were also without rotation. The strength increases for b-values from 0 to 0.25. At b=0.5, there is a drop in strength until b=1.0 where the lowest strength is reached. Friction angle failure points can be seen in Figure 7.1.5. As stated when describing Figure 7.1.5, tests done in extension at higher b-values tend to be very unstable. There is quite a deviation in terms of strength when compared to the true triaxial tests done at α=90°. Once again, Lade and Wang (2012) observed a decrease of 8.2 degrees when performing tests with flexible versus stiff boundaries. This is seen when comparing true triaxial results presented in Chapter 5 (with stiff boundaries in the α=90° direction) versus the torsion shear tests (with flexible boundaries in the α=90° direction). A difference of about 10 to 13 degrees is found.

Notably, the two tests that seem to be out of this pattern (Tests 20* and 43*) are also the tests that deviate from the isotropic compression chart shown in Figure 7.7.1. Test 20* shows a greater rate of dilation compared to all the other tests (seen in Figure 7.7.3 and 7.7.4). Test 43* although failing at a similar stress ratio as Test 21, which had similar conditions, shows almost twice the amount of strain to failure as test 21. The stress ratios show a drop in strength after b=0.32.

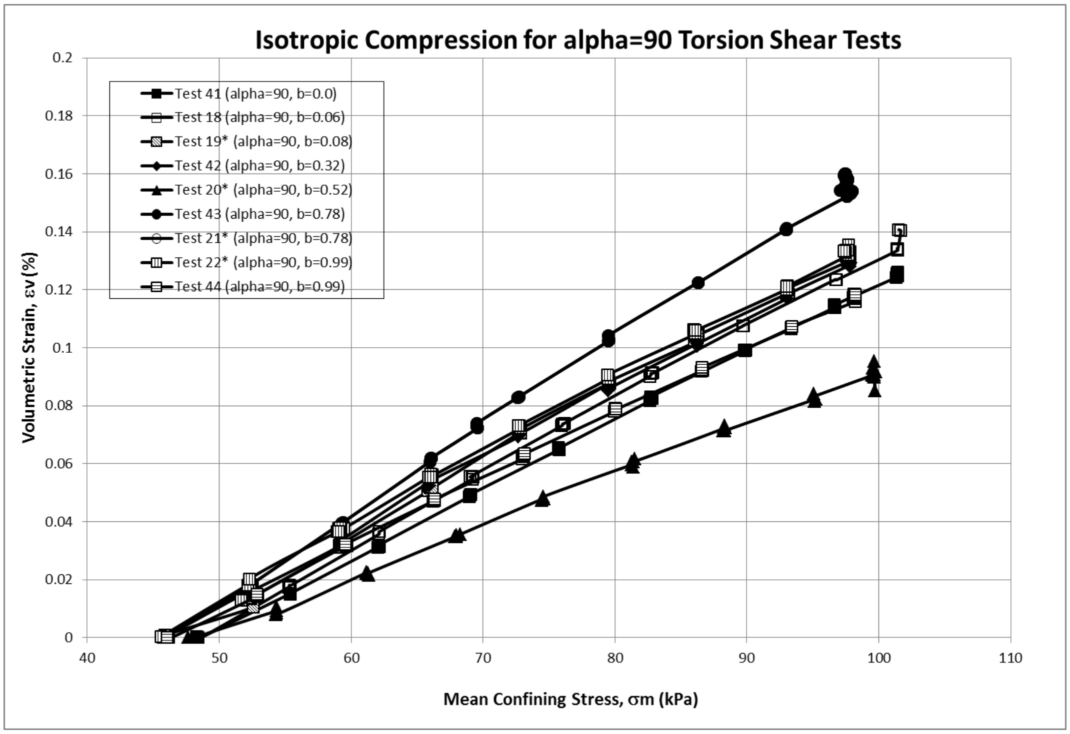

Figure 7.7.1. Isotropic Compression Chart for α=90° Torsion Shear Tests.

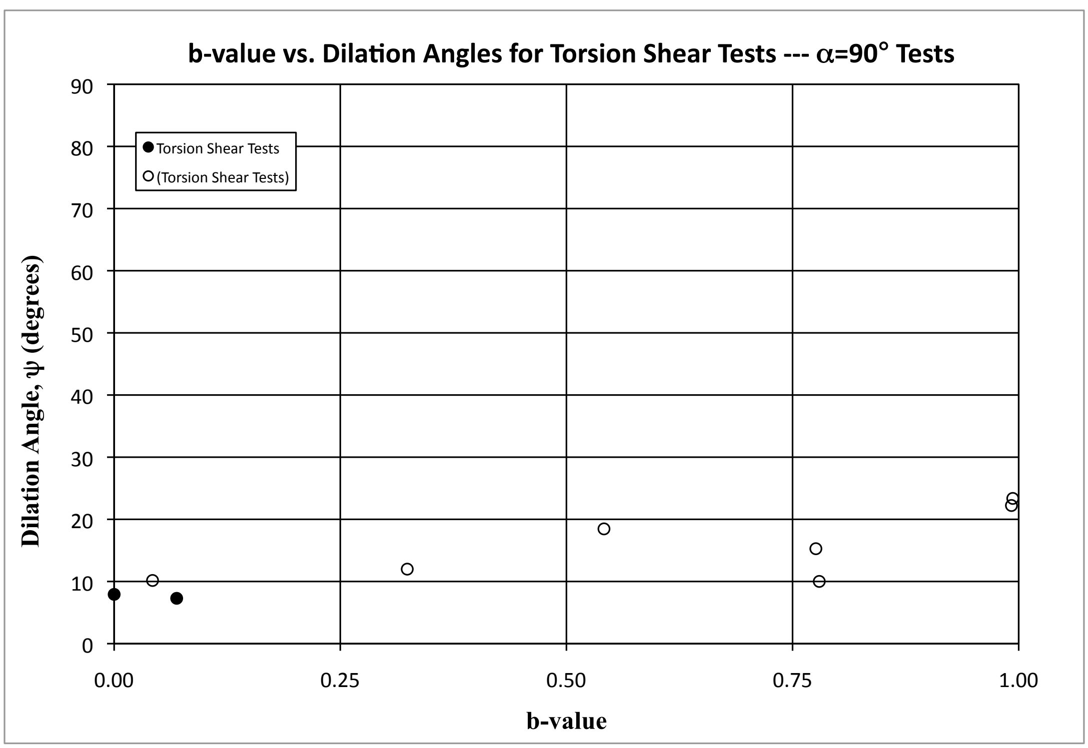

Figure 7.7.2. Dilation Angle versus b-value for α=90° Torsion Shear Tests.

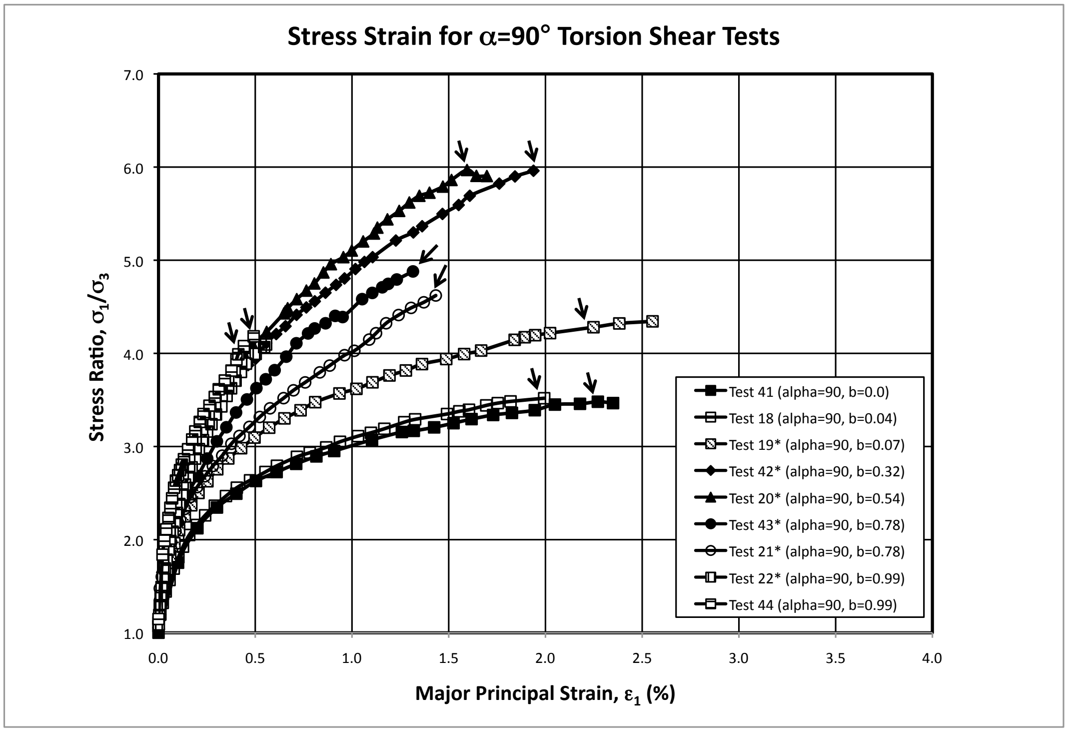

Figure 7.7.3. Stress strain plot for α=90° Torsion Shear Tests.

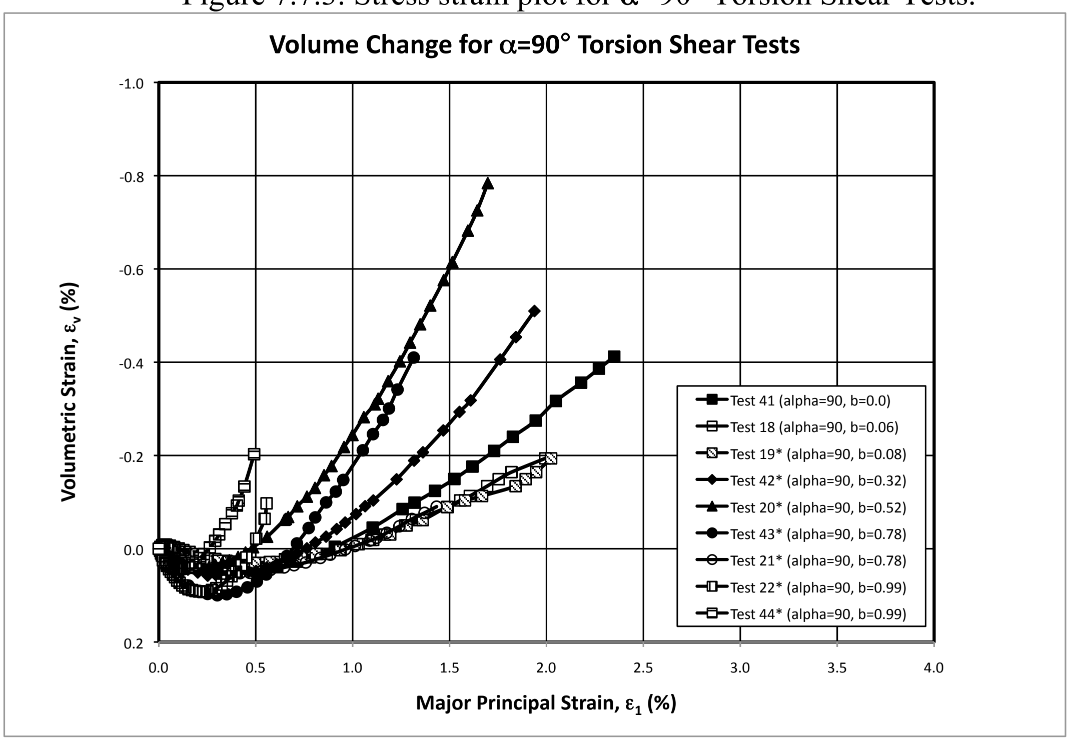

Figure 7.7.4. Volume change plot for α=90° Torsion Shear Tests.

7.8 Conclusion

In summary, torsion shear test results have been provided. Friction angle results for tests in Sector I and III have been compared directly to the true triaxial test results presented in Chapter 5. Tests for α=0° confirmed each other while there was more scatter in the α=90° tests starting at b=0.5 to 1. Torsion shear tests with rotation show that the friction angle decreases as alpha varies from 0° to 90°, showing a dip in friction angle at 67.5°. From b-value=0 to 0.5, there is an increase in friction angle, and then a slight decrease until b=1.0. This occurs for all alpha values besides α=0° and α=22.5°. In these cases, the friction angle continues to increase with increasing b-value until 0.75 and then slightly decreases as it reaches 1.0. Dilation angles tend to stay constant for constant alpha values and changing b-values. As is seen in the stress-strain curves presented, as b-value increases, the stress strain curves become much steeper and fail quickly, with very little strain. Shear bands (discussed in Chapter 9) develop at/near failure, not allowing further progress in the stress-strain curve to develop.

8. Interpretation of Strains in True Triaxial and Torsion Shear Tests

8.1 Introduction

In the previous chapters, stress analysis has been the primary topic when looking at the anisotropic strength and failure surface of Fine Nevada Sand. Although stress analysis is very important, one of the most important aspects when modeling the behavior of frictional materials is the direction of the strain increment vector compared to the direction of principal stress and principal stress increment and the role that anisotropy plays in these directions.

When studying material behavior during stress rotation, it is important to consider the predictions that can be made using both elasticity and plasticity. Stress strain relations are made up of both elastic and plastic strains. Elastic strains are fundamentally very small when compared to plastic strains. However, just because they are small, the elastic strain components cannot be ignored because constitutive models should include elastic strain components, so that the true plastic strain relations can be found.

Fundamentally, incremental elasticity suggests that the increment of elastic strain coincides with the direction of the increment of stress (Figure 8.1.1a). Plasticity theory is based upon the condition that the plastic strain increment coincides with the total stress direction. In 1870, St. Venant (see Figure 8.1.2) suggested the first approach to plastic stress-strain relations. After conducting experiments, he observed that the axes of strain increments coincided with the axes of stress (Figure 8.1.1b). This relationship is also seen in Melan's (1938) equation that is for plastic behavior of isotropic materials.

$$d\varepsilon_{ij}^{p} = d\lambda \frac{\partial g}{\partial \sigma_{ij}} \qquad \text{Eq. 8.1}$$

where dλ is a proportionality constant, and g is the plastic potential function (g=f for associated flow, g≠f for non-associated flow). $\{\partial g/\partial \sigma_{ij}\}$ is normal to the plastic potential surface.

For frictional materials such as soils, elasticity is dominant far away from failure. This occurs at low stress levels near the isotropic state of stress. Elastic strains can also be seen upon unloading and/or reloading. Near higher stress levels and failure, plasticity theory is more adequately applied. When the strain increment vector is perpendicular to the yield surface, then associated flow is obtained. For isotropic materials such as metals, that is correct. However, associated flow can be questioned for frictional materials. From previous data on tests of frictional materials, experimental evidence shows that when using associated flow rules, too large volumetric expansion is predicted. Non-associated flow should be used in constitutive models for frictional materials in order to capture volume change correctly as well as, observed instabilities such as shear banding and liquefaction (Lade et al. 1987, Hong and Lade 1989, Lade et. al 2009). In order to determine associated or non-associated flow, the directions of strain increment vectors relative to yield surfaces are of importance.

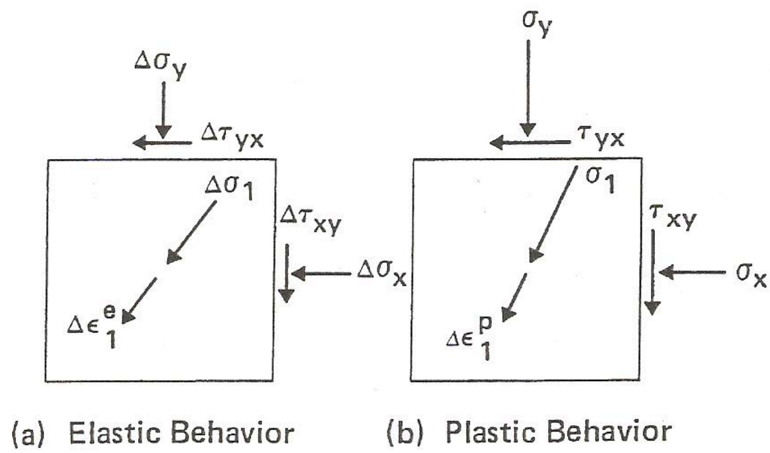

Figure 8.1.1. (a) Elastic, and (b) plastic behavior of soil element during rotation of stress axes (after Lade 2005b).

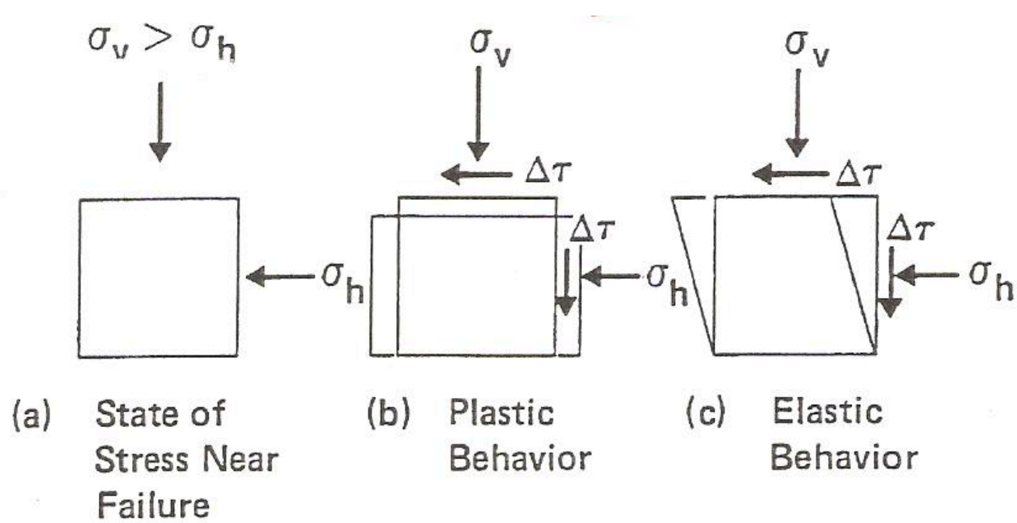

Figure 8.1.2. (a) Stresses on a soil element near failure, its (b) plastic behavior (St. Venant's Principle), and its (c) elastic behavior. (after Lade 2005b)

8.2 Strain Increment Directions in True Triaxial Tests and Torsion Shear in α=0° and α=90°Tests

Lade and Duncan (1973) considered the directions of the strain increments at failure. By definition, the strains at failure are all plastic so there was no need to separate out elastic strains. They found that the normality condition (showing associated flow) was not satisfied. Ko and Scott (1967) also found the same result for tests on Ottowa sand. Although strain increments and the relationship between principal strains in true triaxial tests have been studied before, they will also be analyzed in this thesis.

The intermediate and minor strains plotted versus the major principal strain for each sector of true triaxial tests are presented in Figures 8.2.1 through 8.2.3. For all sectors, the intermediate to major principal strain ratio increases as the b-value increases (seen in part (a) of the graphs). The ratio between minor principal strain and major principal strain increases as b-values increase from 0 to 1. This is seen in part (b) of the graphs.

For b=0 values, there is more strain in the ε_1 direction than in the ε_2 direction for Sector III than in Sector I. The bedding planes for Sector III are vertical (α=90°) and therefore, are in the same direction as the stress, σ_1. When looking at the graphs, it is important to remember that tests at b-values of near 0.25 are very close to the plain strain condition. This causes the intermediate principal strain to be close to or near zero. There is a slight increase when moving through Sector I, II and III. For b=0.25 tests, failure is right around ε_1=2% strain for all three sectors. As the b-value increases, there is an increase in the intermediate principal stain. This increase is also seen when looking from Sector I to II and III. Sector II shows slightly less strain for the same b-value tests than Sector III but they are very close to each other.

It is important to recall that certain stress paths (TT #5, TT #6, TT #11, and TT #17), all started as b=1.0 tests. Since there was not enough pressure in the air supply line to keep this b-value constant up until failure, the horizontal stress was kept constant as the vertical stress increased. These tests failed at around b=0.7. The strain paths are very similar to those of b=1 tests until the drop in stress occurs. This is why there is a break in the slopes of strain for these tests. However, they all end at about the same ε_2 as the b=0.75 tests.

At b=1, in Sector III, the bedding planes are aligned so that the major principal stress and minor principal stress are also in the direction of the bedding planes. This would lead to the expectation that the intermediate and major principal strains would be equal ($\varepsilon_1 = \varepsilon_2$). However, this was not what was seen in Test TT #18. There was almost double the amount of horizontal strain, ε_2 than axial strain, ε_1.

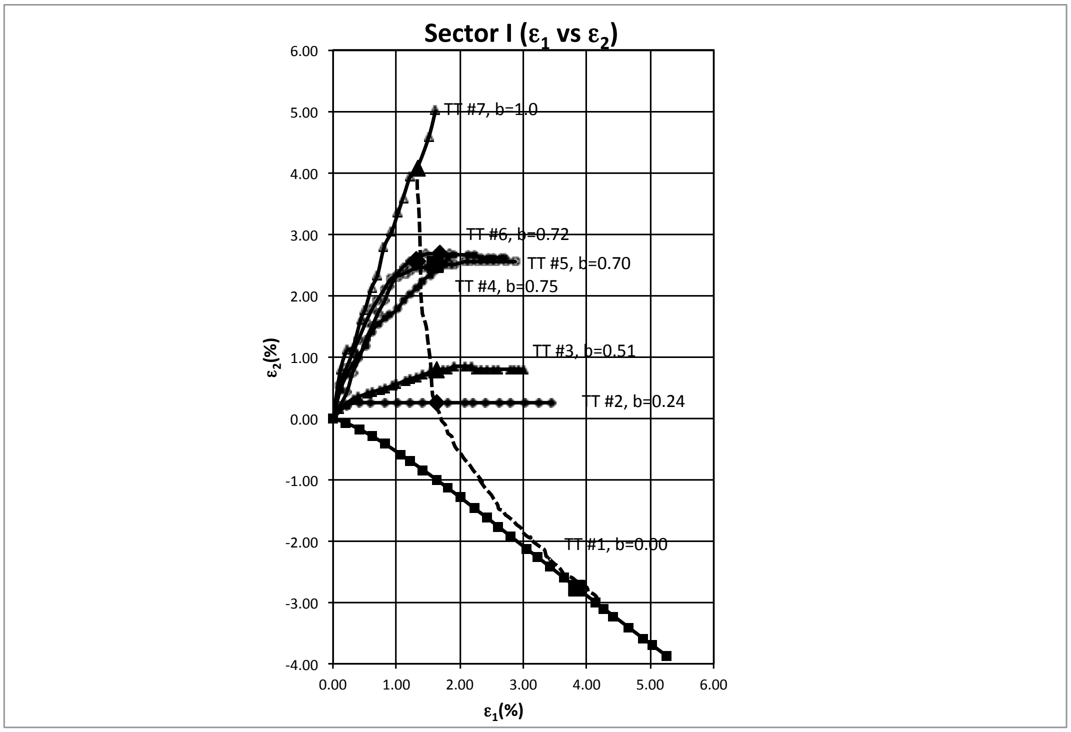

(a)

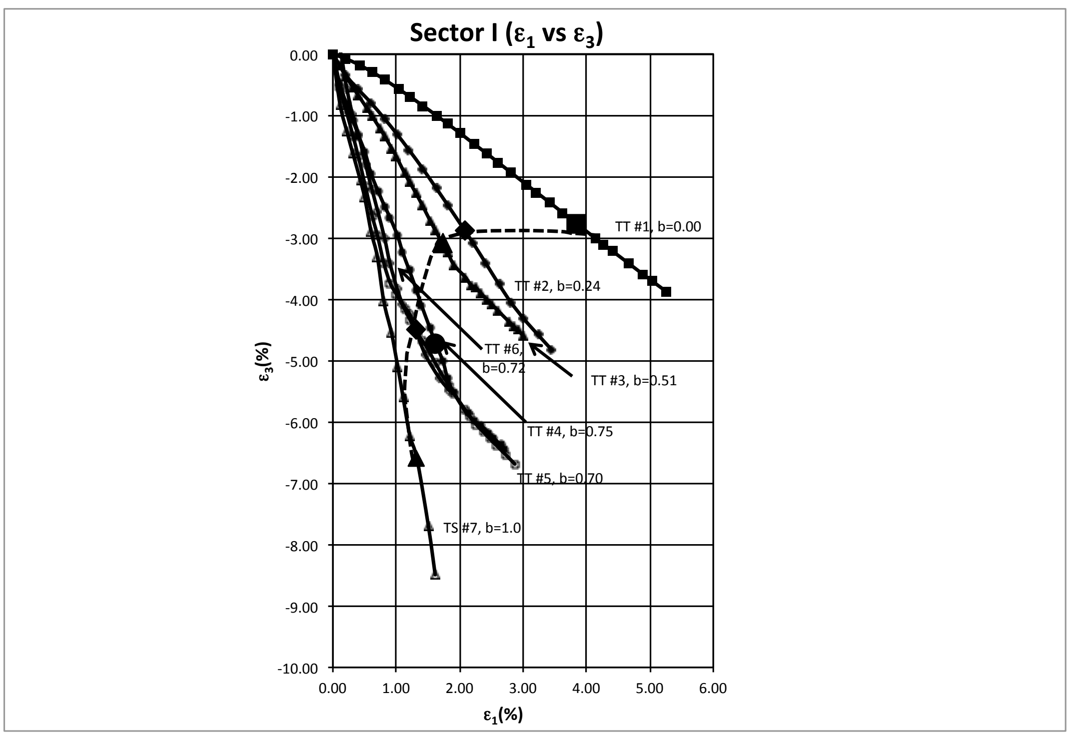

(b)

Figure 8.2.1. Plots of (a) Intermediate versus Major Principal Strain and (b) Minor versus Major Principal Strain True Triaxial Tests in Sector I.

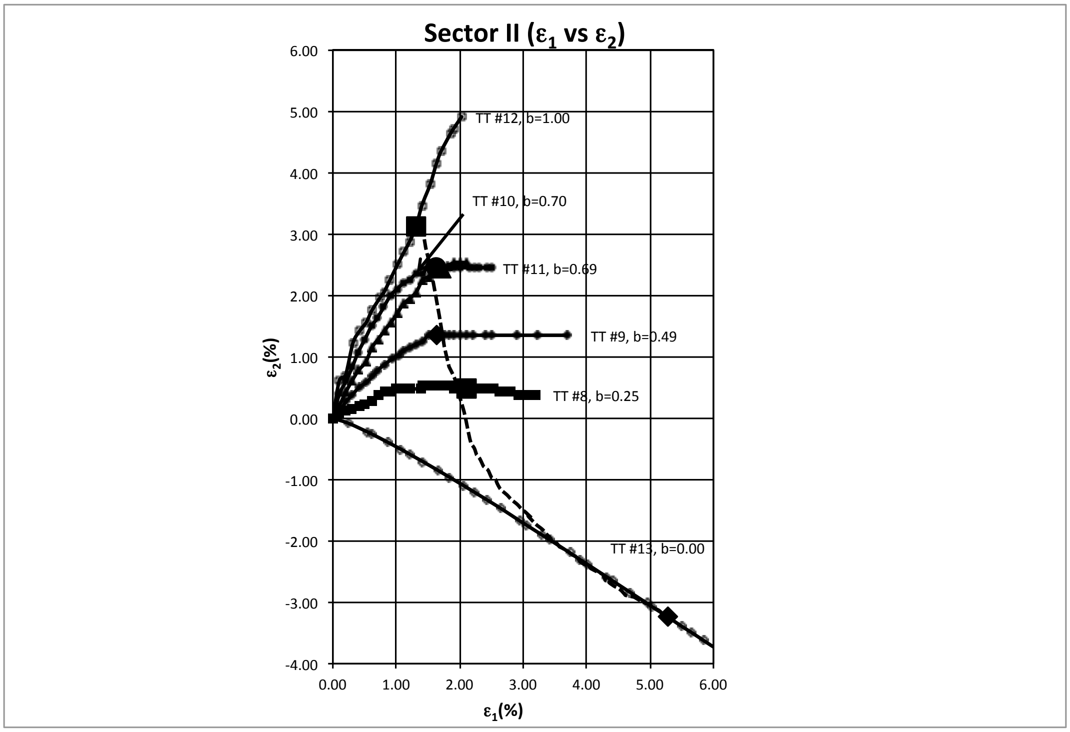

(a)

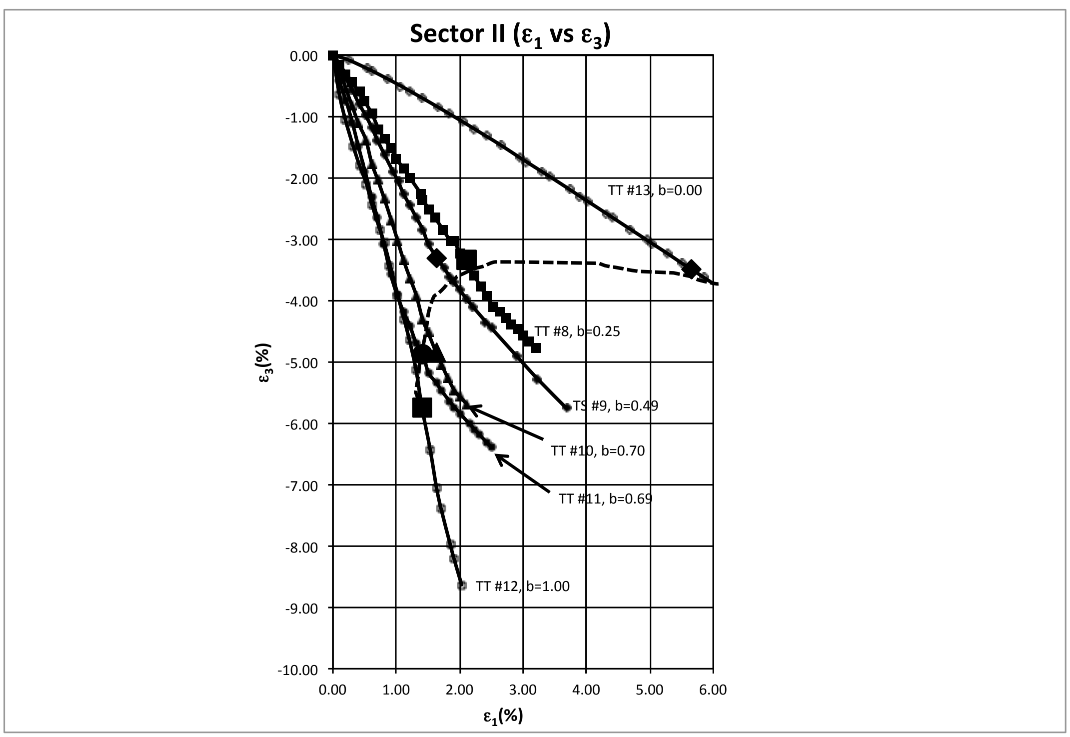

(b)

Figure 8.2.2. Plots of (a) Intermediate versus Major Principal Strain and (b) Minor versus Major Principal Strain True Triaxial Tests in Sector II.

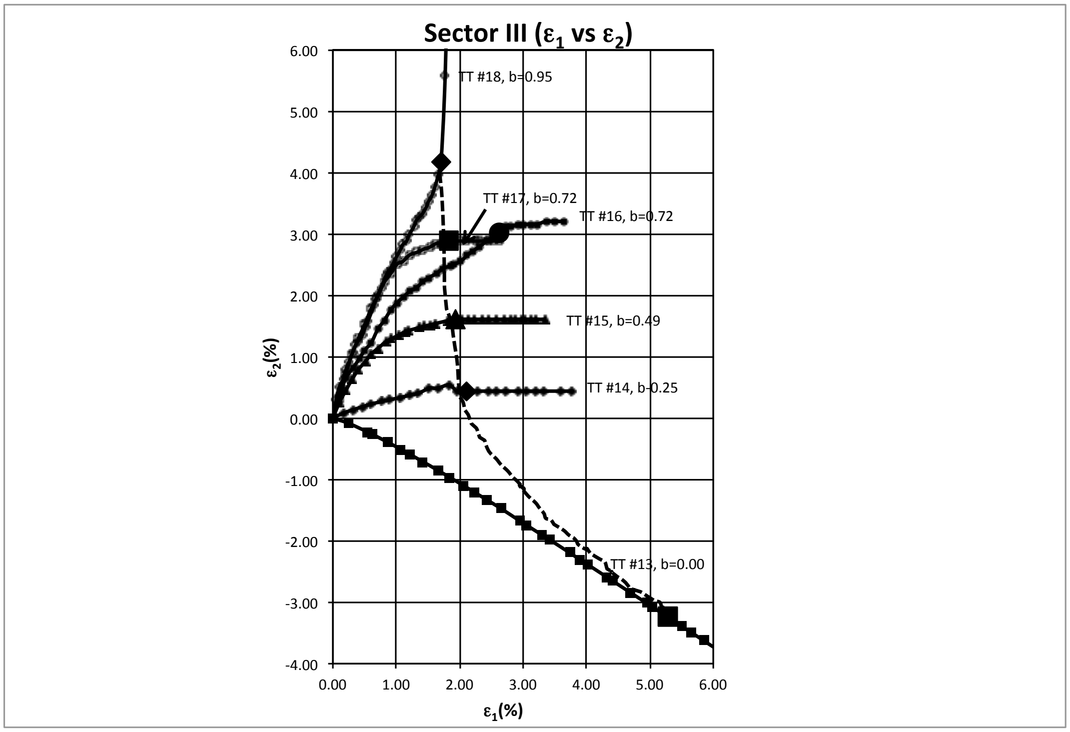

(a)

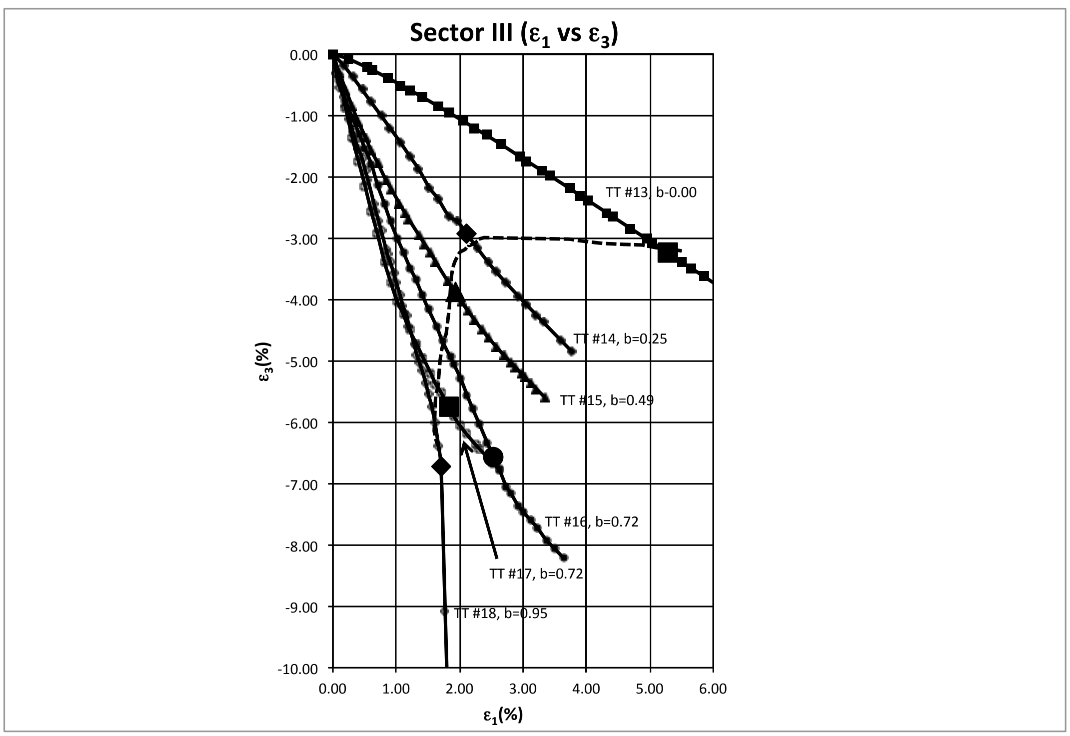

(b)

Figure 8.2.3. Plots of (a) Intermediate versus Major Principal Strain and (b) Minor versus Major Principal Strain True Triaxial Tests in Sector III

In order to plot the strain increment directions on the octahedral plane, the principal strain increments for each test can be considered as a vector, ($\Delta\varepsilon_1$, $\Delta\varepsilon_2$, $\Delta\varepsilon_3$). This vector can be superimposed on the principal stress space. When considering the origin as the starting point of the strain increment vector, the coordinates of the vector will be known ($\Delta\varepsilon_1$,$\Delta\varepsilon_2$,$\Delta\varepsilon_3$). Using a similar procedure as was done to plot stresses on the octahedral plane, the strain increments directions were calculated.

Figure 8.2.4 shows the total stress directions and strain increment directions plotted out on the octahedral plane. The dotted arrows are drawn to go from the origin through the failure point of the different tests. The smaller solid arrows represent the strain increment vectors. In Sector I, the greatest deviation of the strain increment directions from the total stress directions are seen for b=0.25 and b=0.5. At b=0.75 and b=1, the strain increment directions become almost the same as the stress directions. In Sector II, the greatest difference is seen also at b=0.25. Sector III shows overall the most deviation from the strain increment and stress directions coinciding. As was the case in Sector I and Sector II, as b approaches 1, the difference gets smaller until the strain increment coincides with the stress direction.

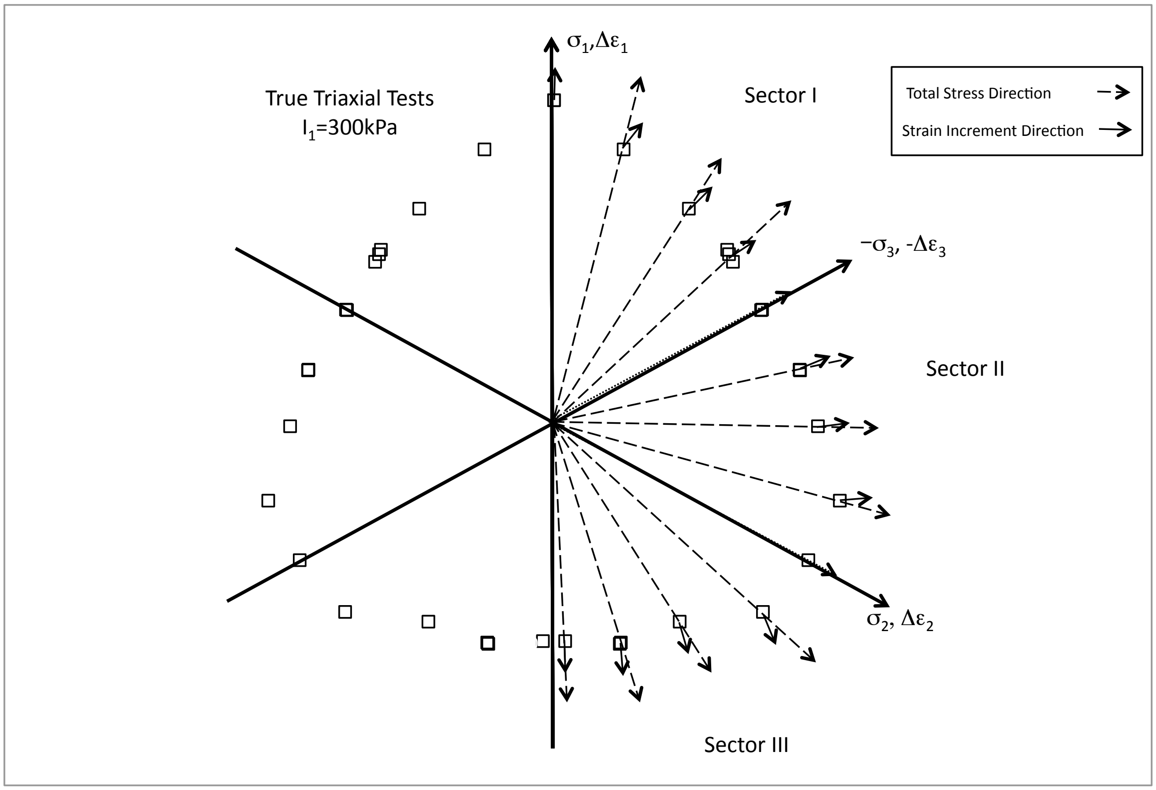

Figure 8.2.4. Octahedral Plane showing Strain Increment Directions and Total Stress Directions for True Triaxial Tests.

The intermediate and minor principal strains for torsion shear tests at α=0° and α=90° were plotted to be compared with the true triaxial results. Figures 8.2.5 and 8.2.6 present the strains for these tests. As is seen, the strains in torsion shear tests are much smaller than those in the true triaxial tests. Chapter 7 presented the friction angle results from both true triaxial and torsion shear tests. The strength results were very similar for α=0° and deviated after b=0.5 for α=90°. Recalling that the stress paths were different for torsion shear tests and true triaxial tests, the stress-strain curves were not superimposed and compared in the previous chapters. Torsion shear tests all had constant mean stress while true triaxial tests had a constant minor principal stress. The true triaxial tests increase the major principal stress while staying with a constant minor principal stress. Test TT #7 was done at a lower confining pressure than TT#1 due to the limitations of the air supply system that has already been discussed in Chapter 5. Torsion shear tests have a different stress path that approaches failure much more quickly. This deviation in stress path when approaching the failure surface is an important factor when looking at the difference in strain to failure for the two types of tests.

Another more subtle difference between the tests is the use of lubricated ends in the true triaxial tests compared to full frictional ends in torsion shear tests. Lade (1982) shows the comparison of stress-strain relations for tests with lubricated caps and bases compared to those with no lubrication, as seen in Figure 8.2.7. Dense specimens with lubrication had almost double the strain to failure than those without lubrication. A similar case is seen in the true triaxial tests (with double lubrication at both top and bottom plates) and the torsion shear tests (with no lubrication; fully frictional end restraints).

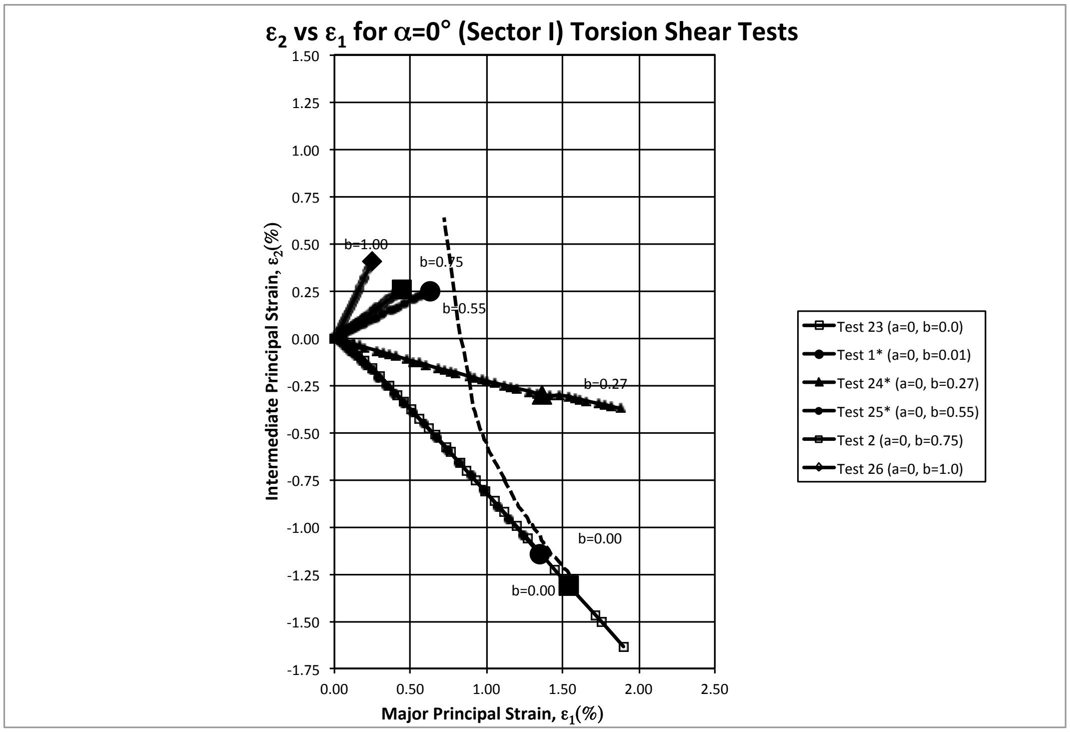

(a)

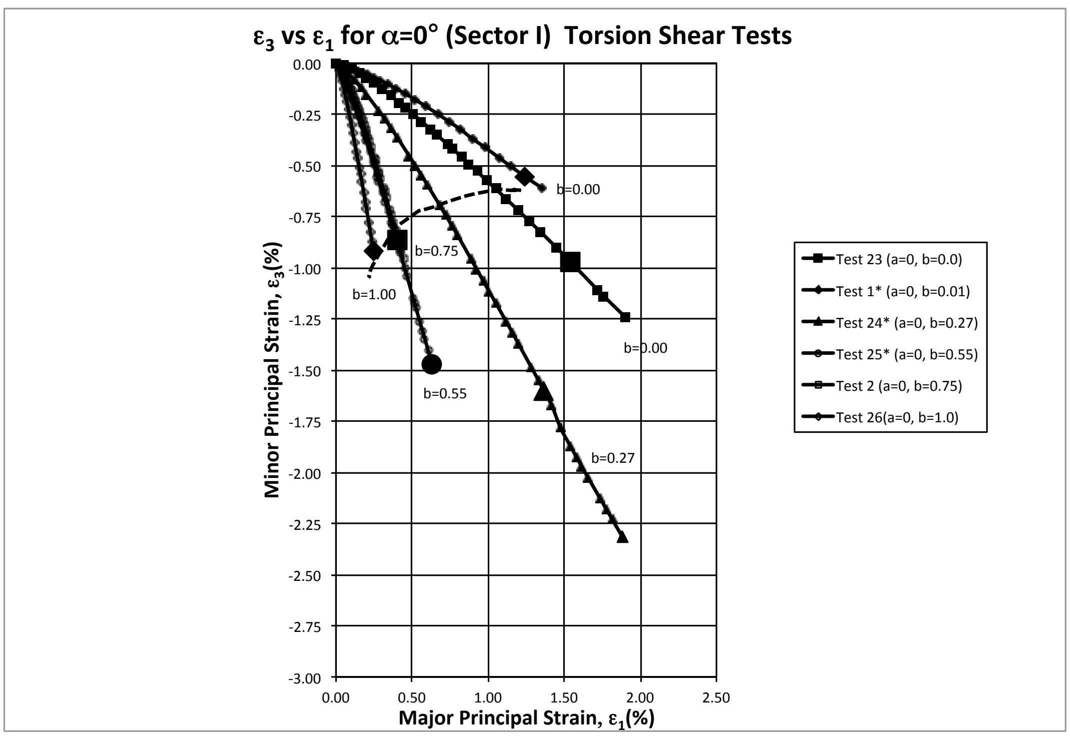

(b)

Figure 8.2.5. Plots of (a) Intermediate versus Major Principal Strain and (b) Minor versus Major Principal Strain Torsion Shear Tests in Sector I.

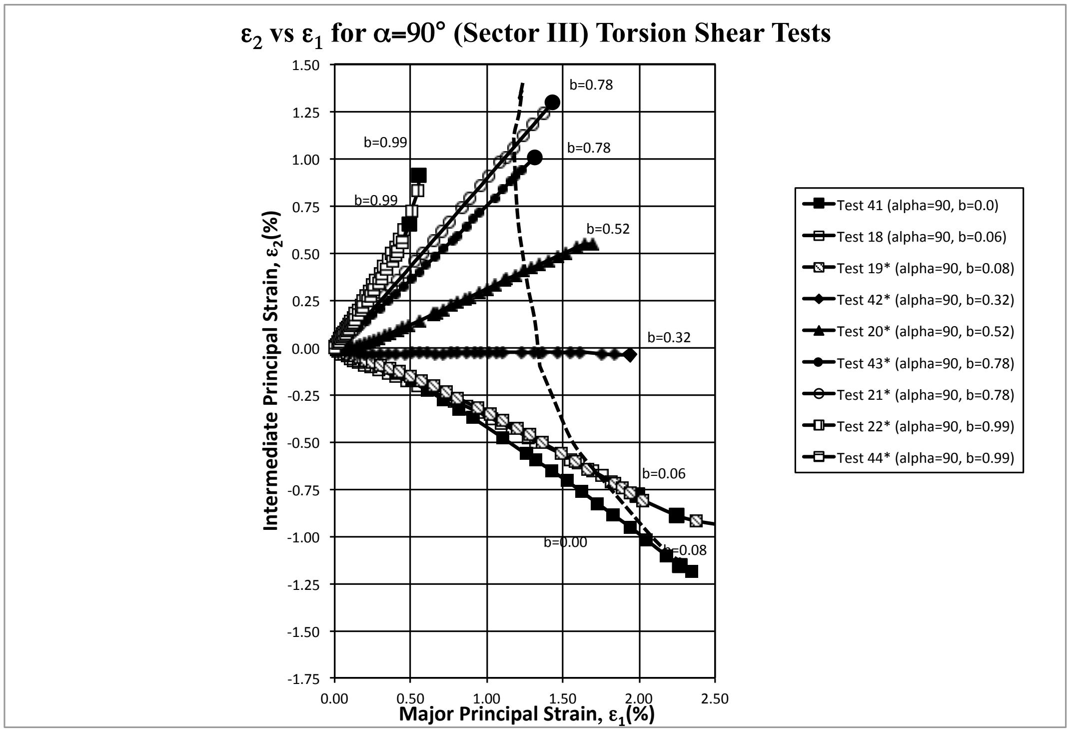

(a)

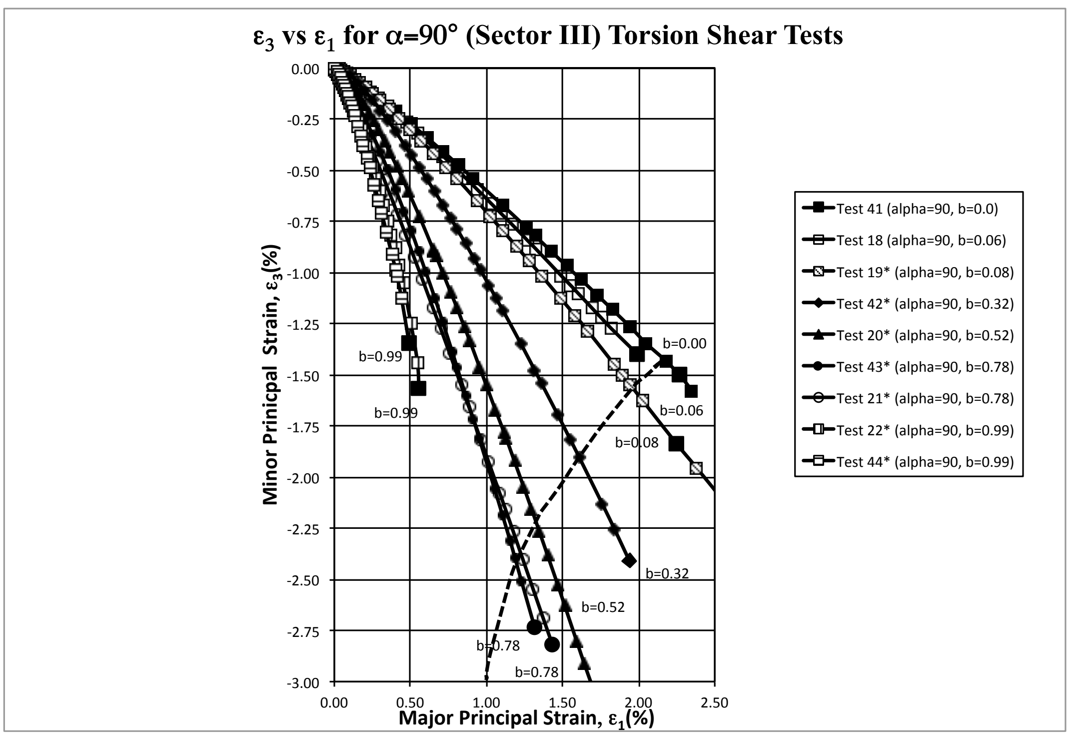

(b)

Figure 8.2.6. Plots of (a) Intermediate versus Major Principal Strain and (b) Minor versus Major Principal Strain Torsion Shear Tests in Sector III.

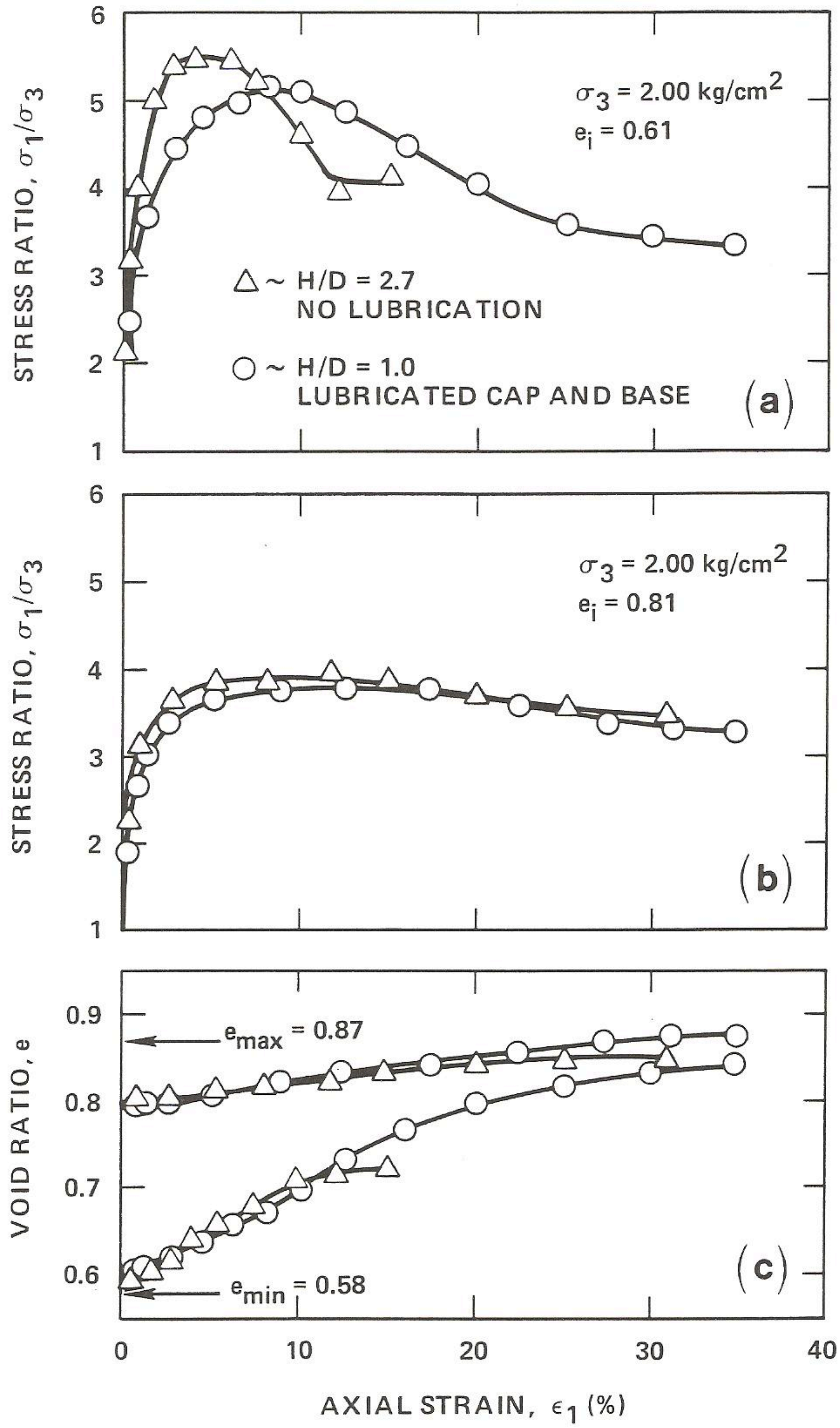

Figure 8.2.7. Comparison of Stress-Strain relations and void ratio changes in triaxial compression tests on specimens with H/D =1.0 and 2.7 for (a) dense and (b) loose Santa Monica Beach Sand (after Lade 1982).

8.3 Strains and Strain Increment vectors in Torsion Shear Tests

Mohr's Circles

Using Mohr's circles, the direction of major principal stress, major principal stress increment and major principal strain increment can be found. Figure 8.3.1 shows the Mohr's circles diagrams used in determining these directions. From these diagrams, relationships can be derived for these angles shown below.

$$\tan(2\psi) = \frac{2\tau_{z\theta}}{\sigma_z - \sigma_\theta} \qquad \text{Eq. 8.3}$$

$$\tan(2\chi) = \frac{2\Delta\tau_{z\theta}}{\Delta\sigma_z - \Delta\sigma_\theta} \qquad \text{Eq. 8.4}$$

$$\tan(2\zeta) = \frac{2\Delta\varepsilon_{z\theta}}{\Delta\varepsilon_z - \Delta\varepsilon_\theta} \qquad \text{Eq. 8.5}$$

where ψ is the angle between σ_1 and vertical, χ is the angle between $\Delta\sigma_1$ and vertical and ζ is the angle between $\Delta\varepsilon_1$ and vertical. Note that the angle labeled ψ in Figure 8.3.1 is indicated by α in this presentation.

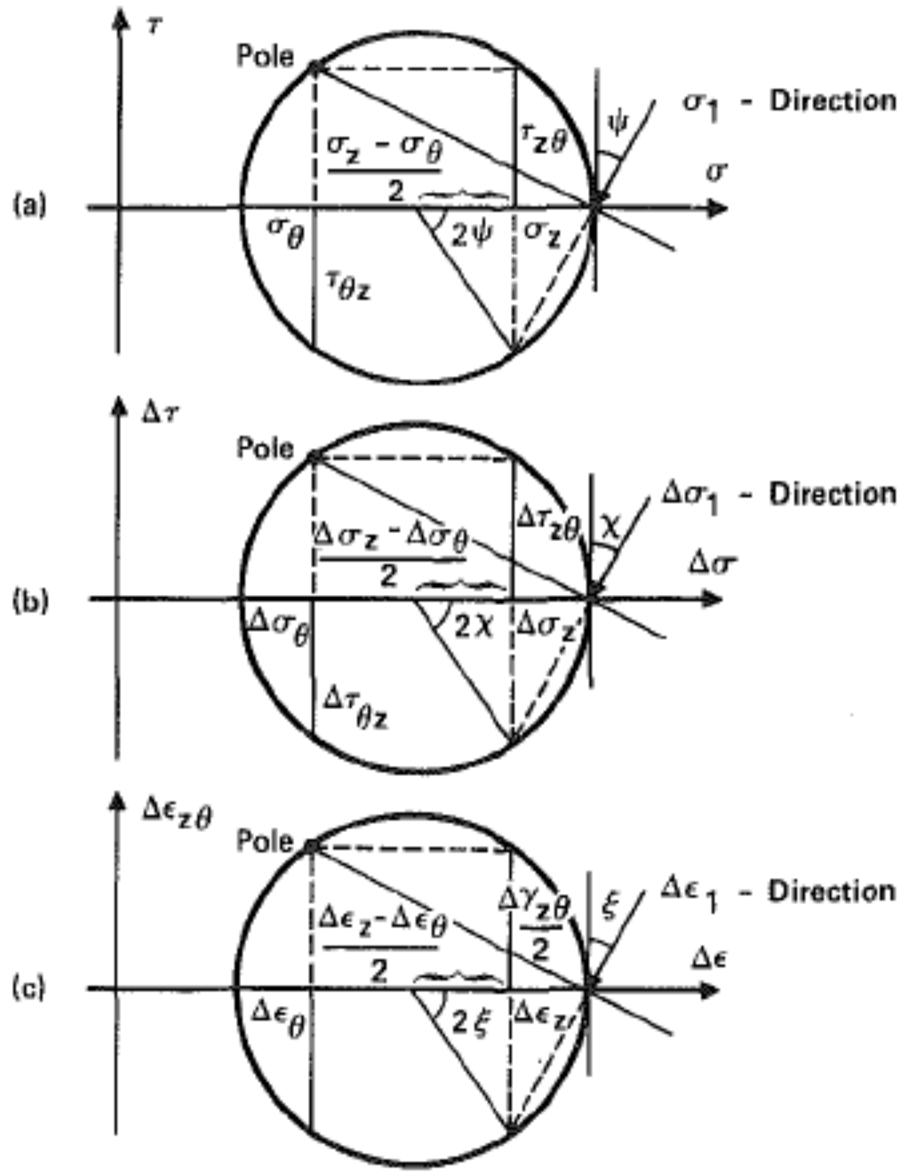

Figure 8.3.1. Directions of Major Principal (a) stress, (b) stress increment and (c) strain increment direction in Torsion Shear Tests (after Hong and Lade, 1989).

Relations between strains

The normal strain differences and shear strains were calculated for torsion shear tests. It is important to state that these are total strains, both elastic and plastic. These have been plotted in Figures 8.3.2 through 8.3.6. The plots are separated by b-value=constant so that the changes with varying alpha directions can be seen. Tests with α=0° and α=90° do not have any shear strain and therefore run along the $\varepsilon_{z\theta}$=0 lines when plotted. By taking the slope of these plots, the strain increment direction can be calculated (Eq. 8.3). Test with α=0° and α=22.5° have a positive strain difference. The other alpha values (α=45°, α=67.5° and α=90°) have negative strain differences. This is because ε_z is less than ε_θ for these tests. As can be seen from looking at the graphs presented below in a series of increasing b-values, the shear strains and normal strain differences get smaller and smaller as the b-value increases. This was also seen when looking at the stress-strain curves presented in Chapter 7.

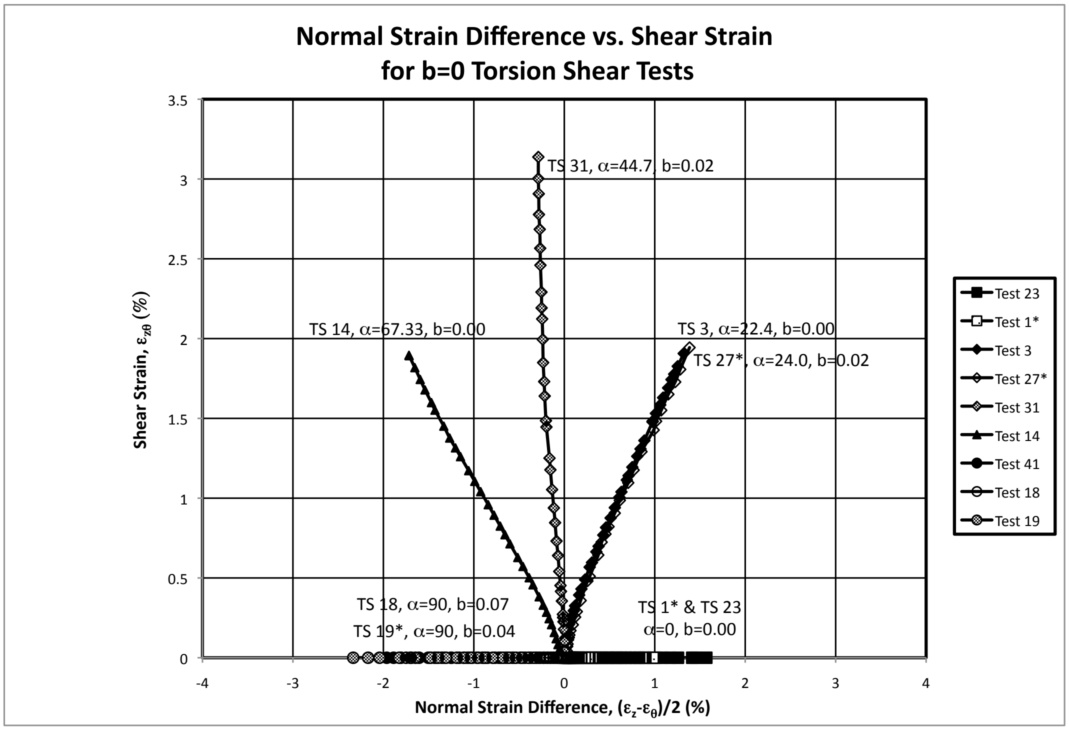

Figure 8.3.2. Normal Strain Differences versus Shear strain for Torsion Shear Tests with b-value=0.0.

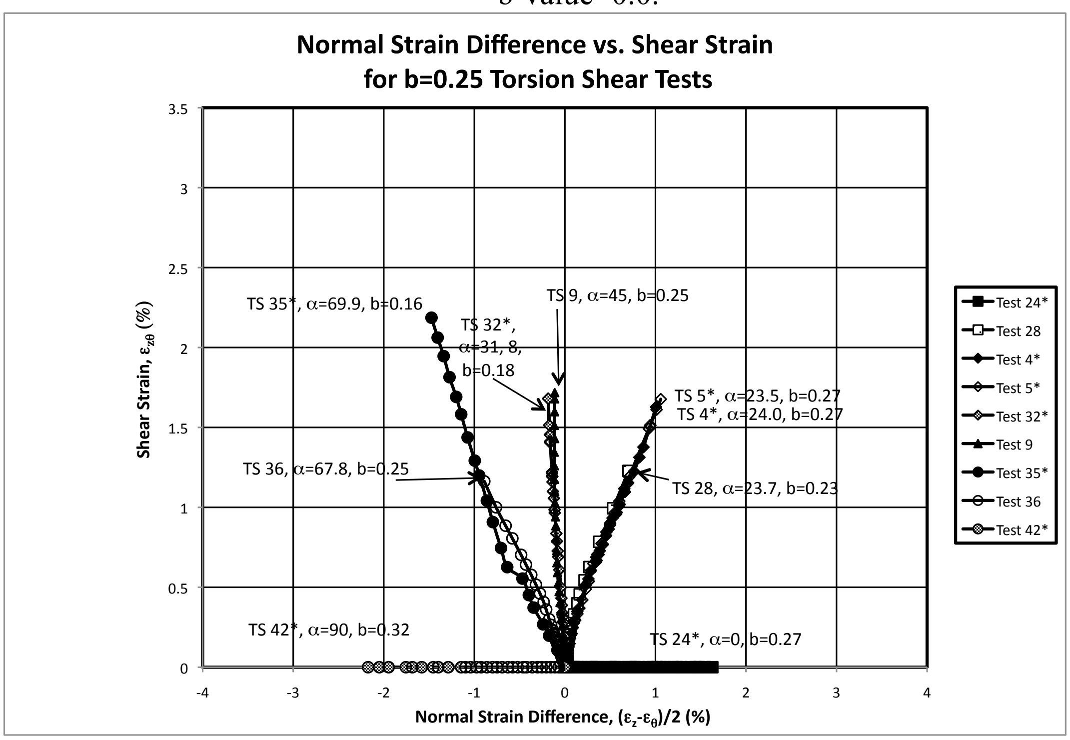

Figure 8.3.3. Normal Strain Differences versus Shear strain for Torsion Shear Tests with b-value=0.25.

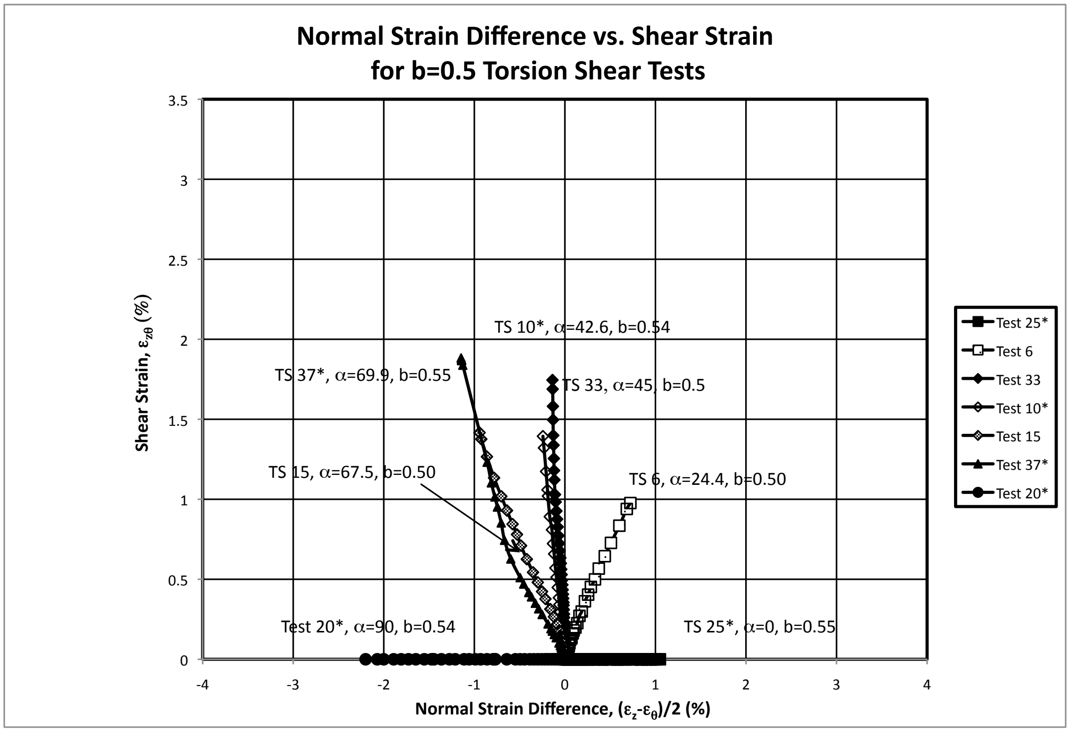

Figure 8.3.4. Normal Strain Differences versus Shear strain for Torsion Shear Tests with b-value=0.50.

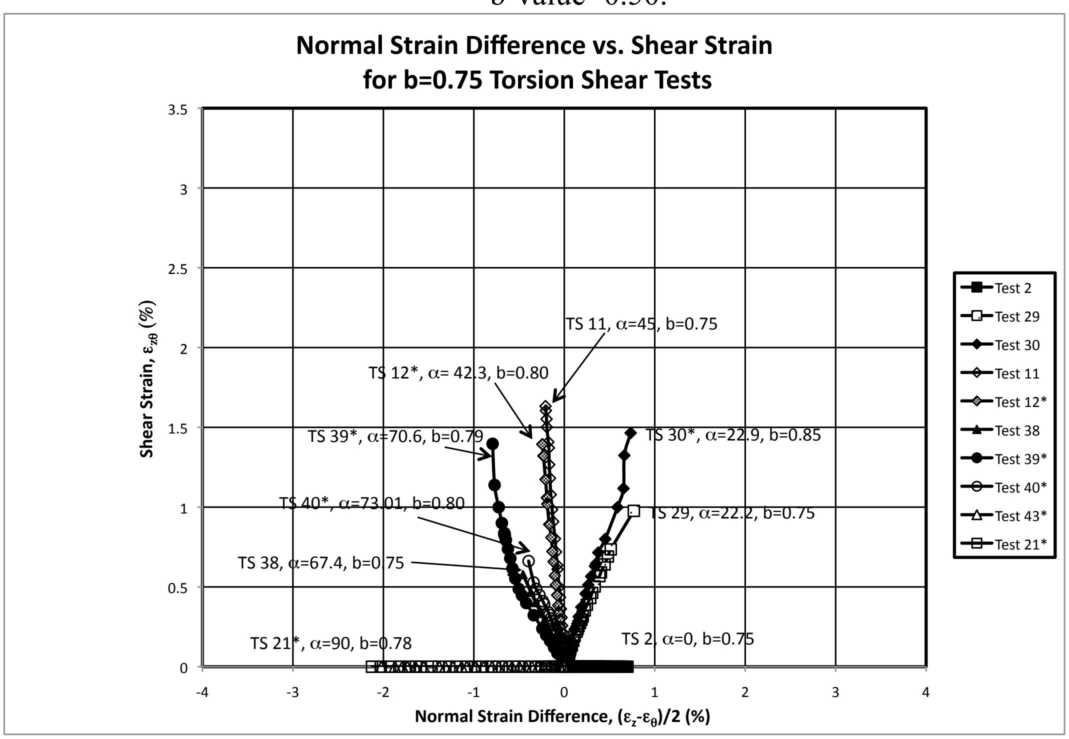

Figure 8.3.5. Normal Strain Differences versus Shear strain for Torsion Shear Tests with b-value=0.75.

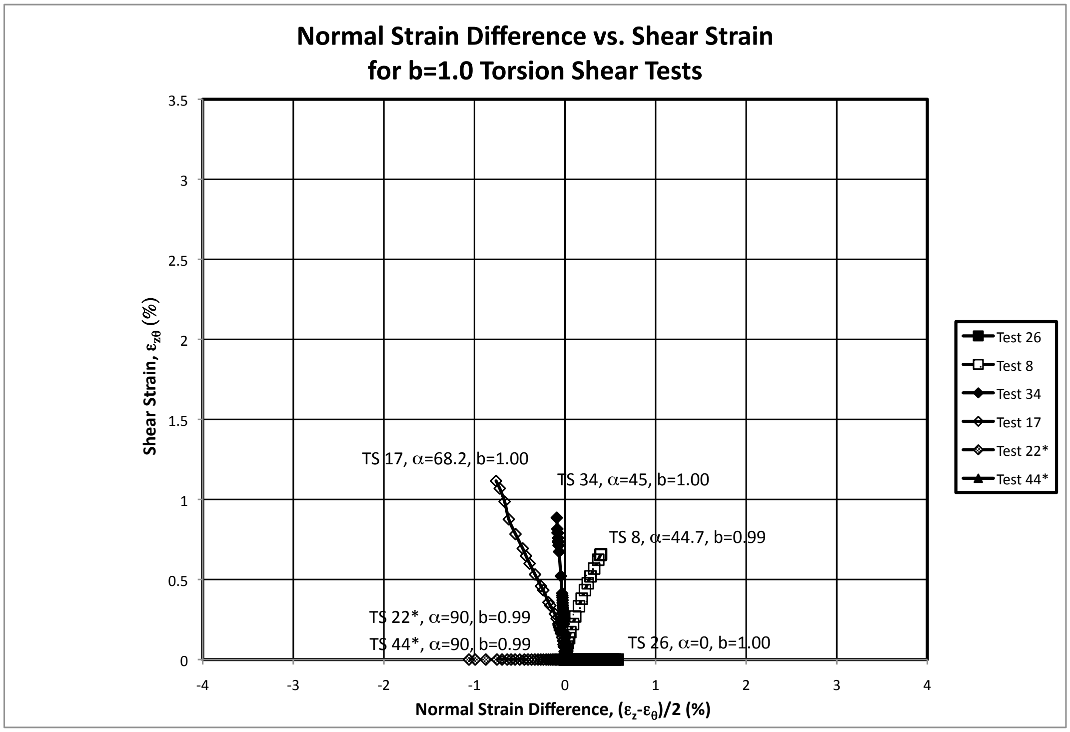

Figure 8.3.6. Normal Strain Differences versus Shear strain for Torsion Shear Tests with b-value=1.0.

When looking at tests with b=0, TS 31 (where α=45°) showed the largest amount of shear strain. TS 3 and 27* (at α=22.4° and α=24°) showed a similar amount of shear strain as TS 14 (α=67.3°). Tests with α=0° have less total strain difference than that of α=90° tests. For b=0.25 tests, shear strains were more scattered. Two or more tests are presented for each direction. The four tests that have less strain (TS 4*, TS 28, TS 32* and TS 36) show a decrease in shear strain as the alpha value increases. Tests TS 5*, TS 9 and TS 35* all fail at approximately the same shear strain of 2.25%. Tests with α=0° have almost the same strain difference as α=90° tests.

Tests with b=0.5 show an increase in shear strain as alpha goes from 22.5° to 45°. TS 37* has a large increase in shear strain in it's last two points as it reaches failure. Without these two points, TS 15 and TS 37* have very similar curves, ending at about 1.5% shear strain. The general trend shows a decrease in shear strain from 45° to 67.5°. This is similar to b=0 strains. Tests with b=0.75 strains a little shorter that b=0.5 strains. The highest strain occurs at α=45°. Once again, there is scatter within the various tests at α=22.5° and α=67.5°, showing tests TS 30* and 39* having more strain than TS 29, TS 40 and TS 38. Lastly, b=1.0 tests showed the least amount of strains (both normal shear difference and shear strain). There is an increase in shear strain as alpha increases.

Strain Increment Vector Directions

When looking at Figures 8.3.2 through 8.3.6, the initial part of most slopes is not linear. This is due to the presence of elastic strains in these plots. The elastic strains were not subtracted from the total strains. As is seen in Figures 8.3.7 through 8.3.11, the elastic strains create an initial deviation of strain increment direction from the major stress direction. As there is more stress applied, and the specimen is in the plastic range of the stress-strain curve, the strain increment direction coincides with the major stress direction. This deviation is mostly seen in α=22.5° conditions. Since there are no shear strains for α=0° and α=90° tests, they are not plotted on Figures 8.3.7 through 8.3.11. Points only until failure are plotted. Strains after failure are not considered as there are great non-uniformities after failure. Only tests that had the correct stress path have been presented in Figure 8.3.7 through 8.3.11. These tests were part of the second set of tests in which the uplift correction was accounted for and the targeted alpha and b-values were reached. Although, the other tests are not wrong, these tests were chosen as representative tests to show the observed patterns.

As seen in the b-value=0 tests, TS 3 starts out having a significantly higher strain increment direction than principal stress direction. As the specimen is sheared, the strain increment direction approaches the principal stress direction. TS 3 levels off near $\gamma_{z\theta}$=1.5% ($\varepsilon_{z\theta}$=0.75%). Looking closely at Figure 8.3.2, the slope of shear strain to normal strain difference begins to become linear near this same point as well. This is where the elastic strains no longer are so large and plastic strains dominate. There is a small deviation also seen in TS 14 up until about $\gamma_{z\theta}$=1.0% ($\varepsilon_{z\theta}$=0.50%). It is important to remember that $\gamma_{z\theta}=2\varepsilon_{z\theta}$. This change of slope is also seen in Figure 8.3.2. There is a slight change of strain increment direction for TS 31 at around $\gamma_{z\theta}$=0.5% ($\varepsilon_{z\theta}$=0.25%). This change is so small that it is not very pronounced in Figure 8.3.2. Although there is a slight deviation from the principal stress direction, it becomes smaller as alpha value increases.

It is interesting to note that the strain increment directions for α=22.5° and α=45° are slightly above the stress direction. For α=67.5°, the strain increment directions are slightly below. This is due to the cross-anisotropic nature of the specimen in correlation with its bedding planes. At α=22.5°, the horizontal bedding planes cause the strain increment direction to become more horizontal and therefore show a slightly higher angle. At α=45°, this also occurs but to a lesser extent. However, at α=67.5°, the strain increment direction becomes less than the principal stress direction. This pattern occurs for all b-values.

Similar to Figure 8.3.7, tests with other b-values show elastic behavior towards the beginning of the test. As strains become more plastic, they tend to line up with the principal stress direction. In a similar pattern, all α=22.5° and α=45° tests show slightly higher strain increment directions and α=67.5° show slightly lower. Although not large, the relative biggest variation occurs at α=22.5°. Tests with α=45° have the closest strain increment directions and principal stress directions throughout the entire straining of the specimen. Tests with b=1 (seen in Figure 8.3.11) show the most variation towards the beginning of the test (in the elastic region). Table 8.3.1 summarizes the deviations of strain increment directions and principal stress directions at failure. Figure 8.3.12 presents a drawing showing the bedding planes of a specimen. The general pattern of what occurred with stress directions and strain increment directions for all b-values is represented in the drawing.

Table 8.3.1. Summary of Strain Increment directions and principal stress directions at failure.

	ξ	α	Δ
b=0			
TS 3	28.3	22.4	5.9
TS 31	48.14	44.95	3.19
TS 14	66.09	67.33	-1.24
b=0.25			
TS 28	30.1	23.7	6.4
TS 9	46.9	45	1.9
TS 36	63.7	67.8	-4.1
b=0.50			
TS 6	26.7	22.5	4.2
TS 33	47.24	45	2.24
TS 15	61.8	67.5	-5.7
b=0.75			
TS 29	25.9	22.2	3.7
TS 11	48.6	45	3.6
TS 38	64.2	67.4	-3.2
b=1.0			
TS 8	29.6	22.6	7
TS 34	47.9	45	2.9
TS 17	68.2	62.2	6

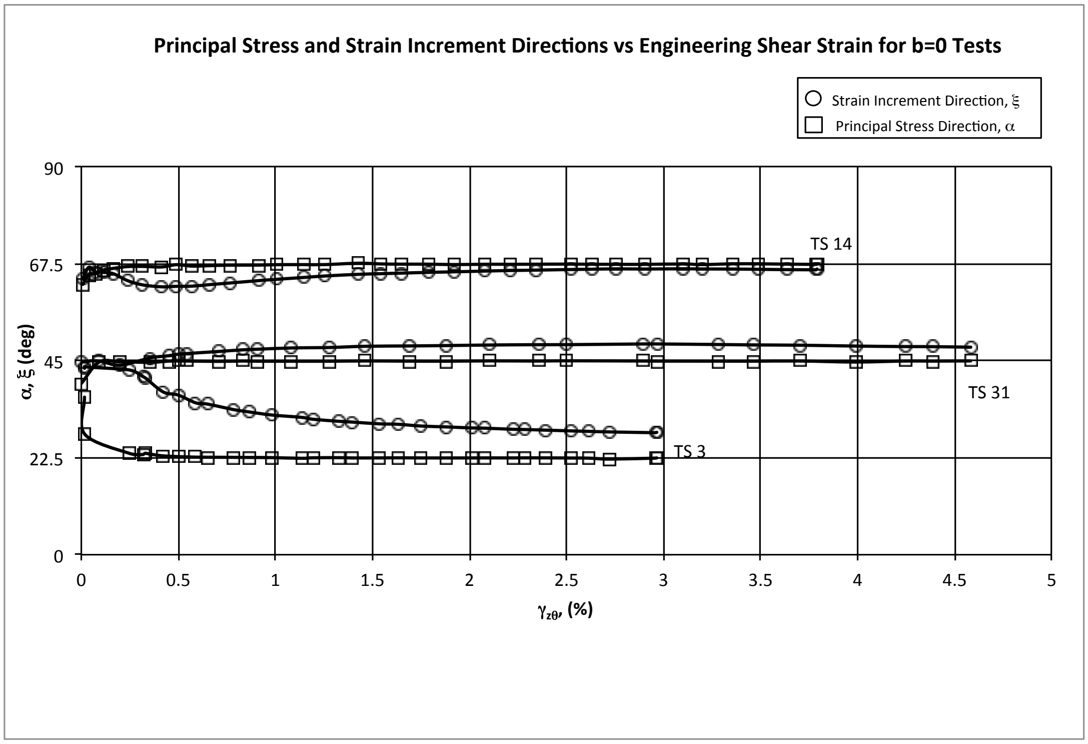

Figure 8.3.7. Principal Stress and Strain Increment Directions versus Engineering Shear Strain for b=0 Torsion Shear Tests.

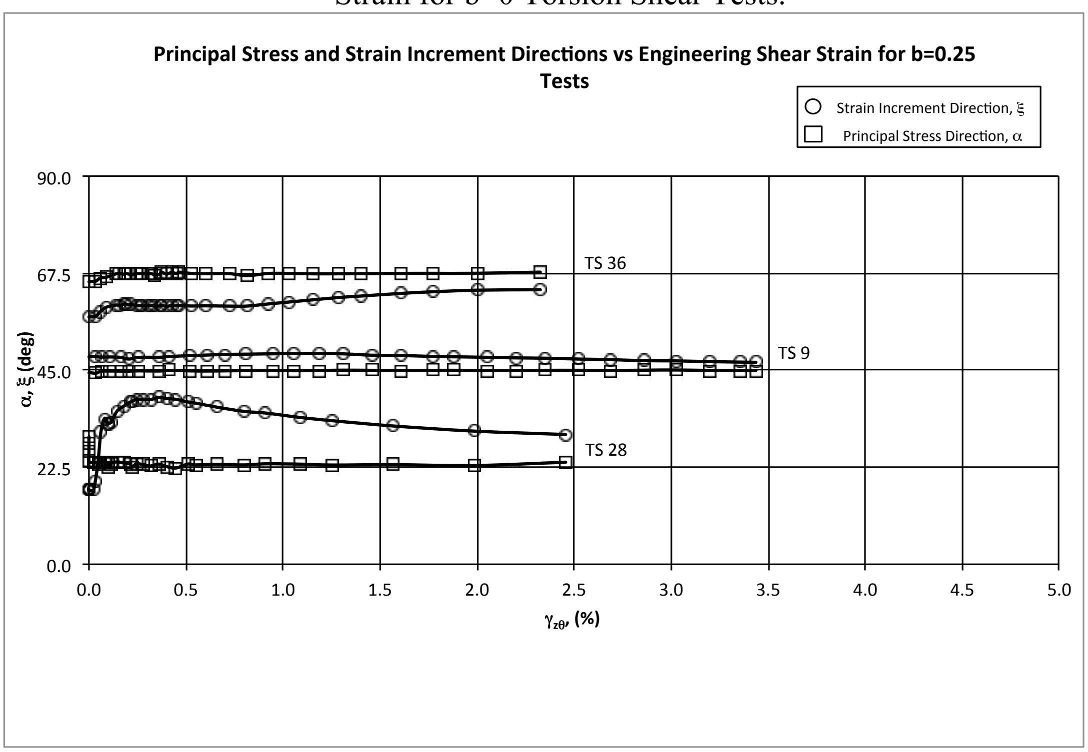

Figure 8.3.8. Principal Stress and Strain Increment Directions versus Engineering Shear Strain for b=0.25 Torsion Shear Tests.

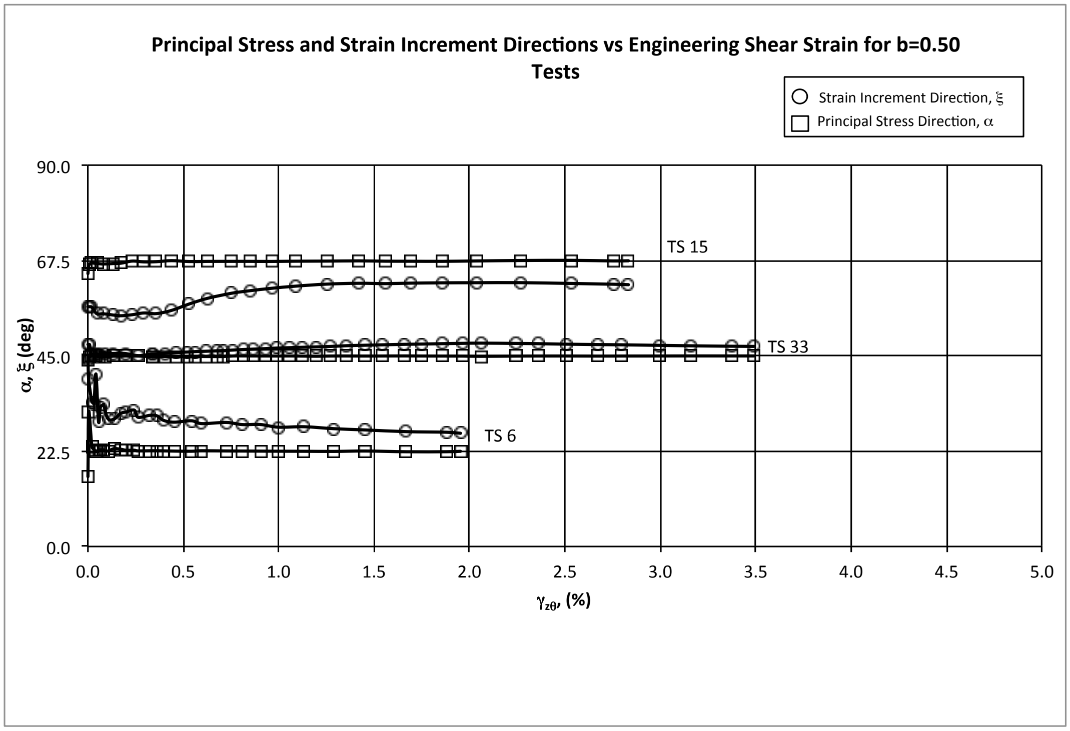

Figure 8.3.9. Principal Stress and Strain Increment Directions versus Engineering Shear Strain for b=0.50 Torsion Shear Tests.

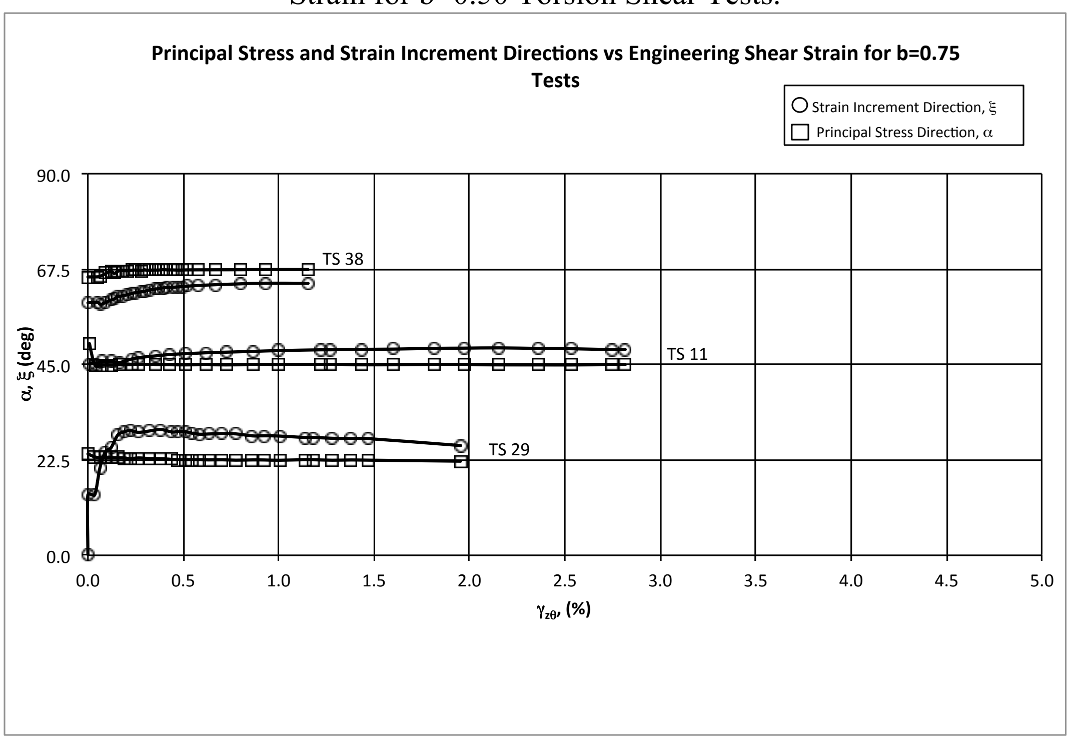

Figure 8.3.10. Principal Stress and Strain Increment Directions versus Engineering Shear Strain for b=0.75 Torsion Shear Tests.

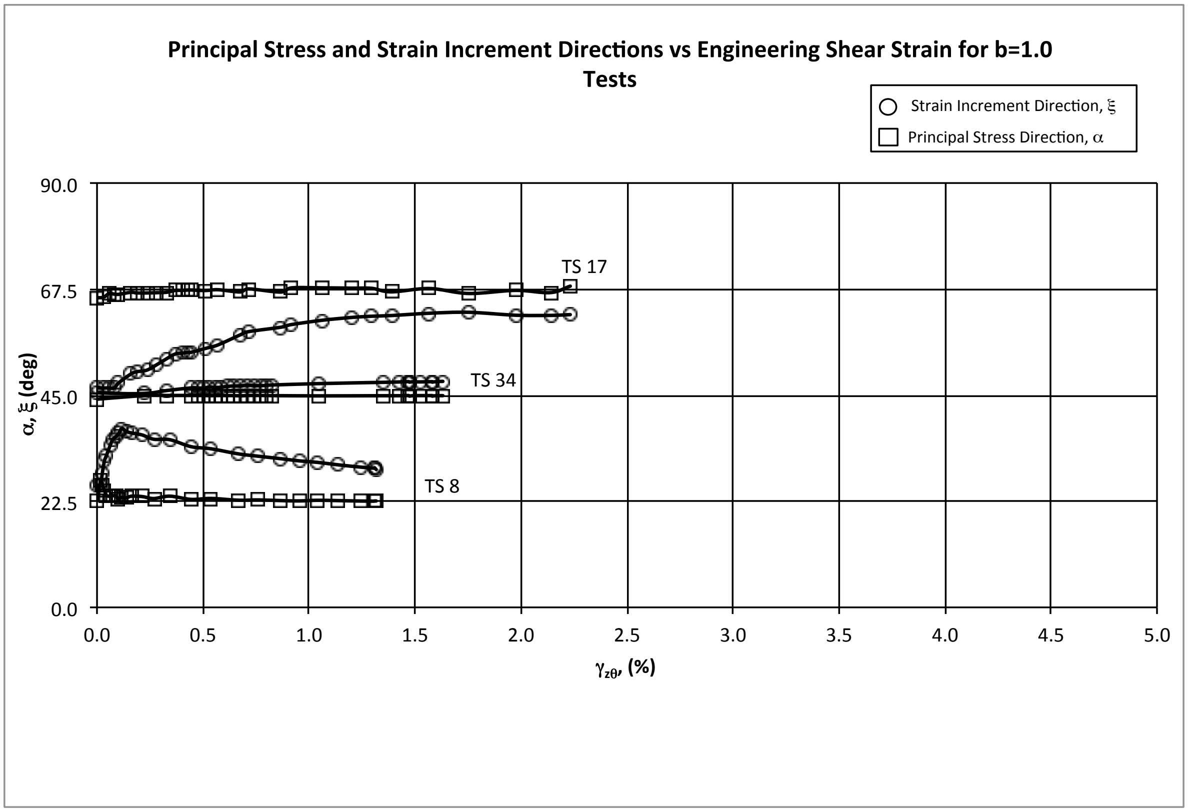

Figure 8.3.11. Principal Stress and Strain Increment Directions versus Engineering Shear Strain for b=1.0 Torsion Shear Tests.

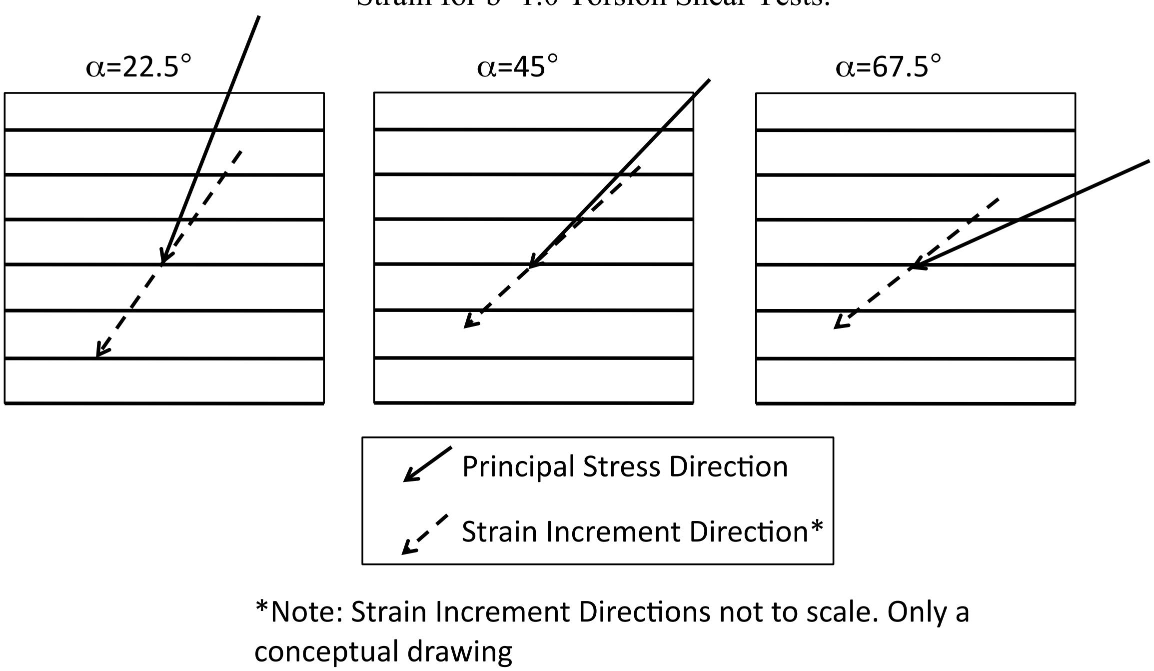

Figure 8.3.12. Patterns of Strain Increment Direction and Principal Stress Directions observed for Torsion Shear Tests.

Looking at the strain increment directions and the stress directions from a different perspective, they can be plotted showing their difference. Figures 8.3.13 though 8.3.17 plot the principal stress directions versus the shear strain. The stress paths are plotted and arrows representing the strain increment directions are overlaid. These arrows show the variation from the stress direction. As can be seen from the graphs, the difference is only slightly noticeable towards the beginning of the tests, as also seen in Figures 8.3.7 through 8.3.11.

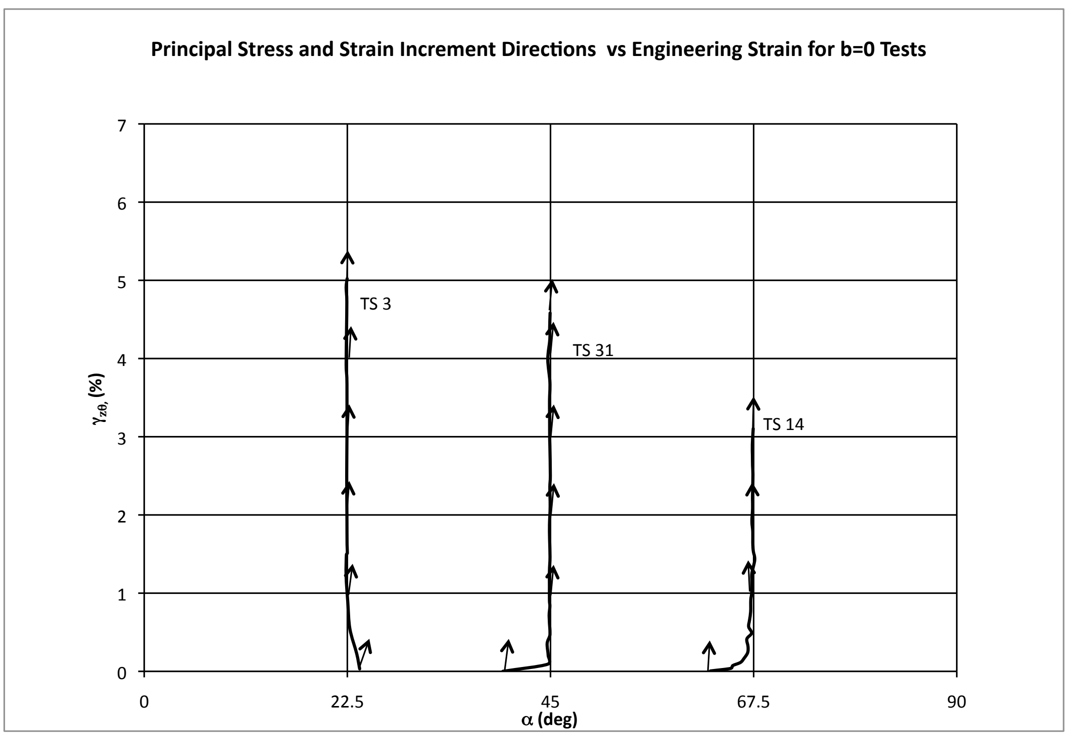

Figure 8.3.13. Principal Stress and Strain Directions versus Engineering Strain for b=0 Torsion Shear Tests.

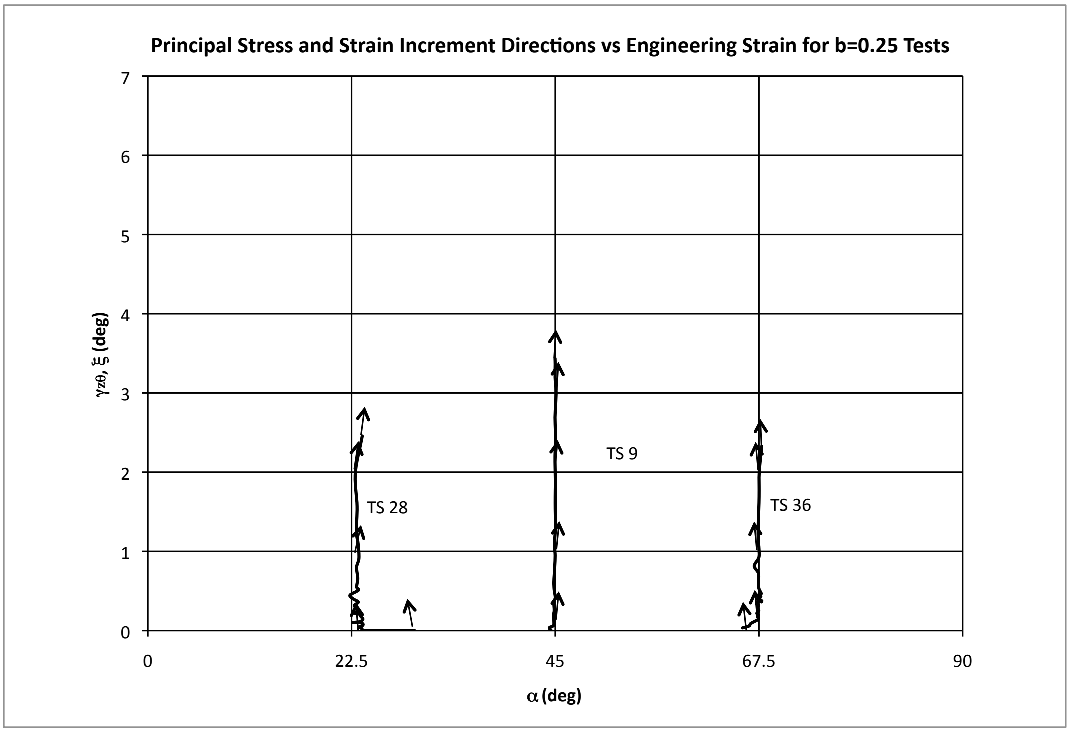

Figure 8.3.14. Principal Stress and Strain Directions versus Engineering Strain for b=0.25 Torsion Shear Tests.

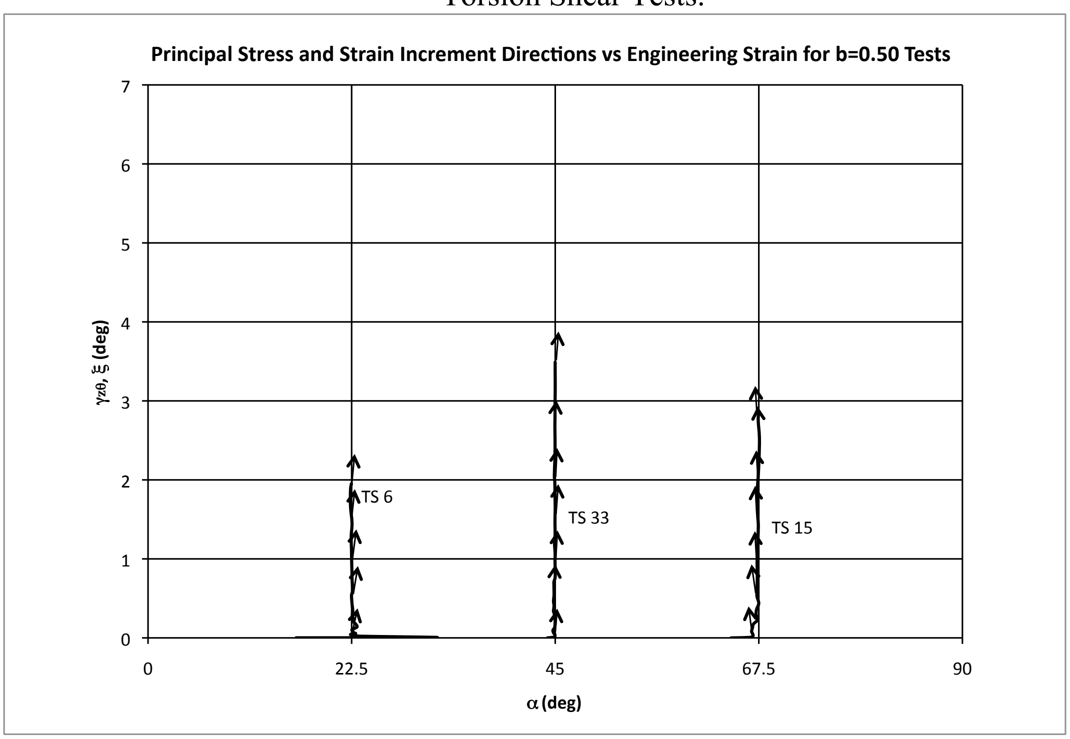

Figure 8.3.15. Principal Stress and Strain Directions versus Engineering Strain for b=0.50.

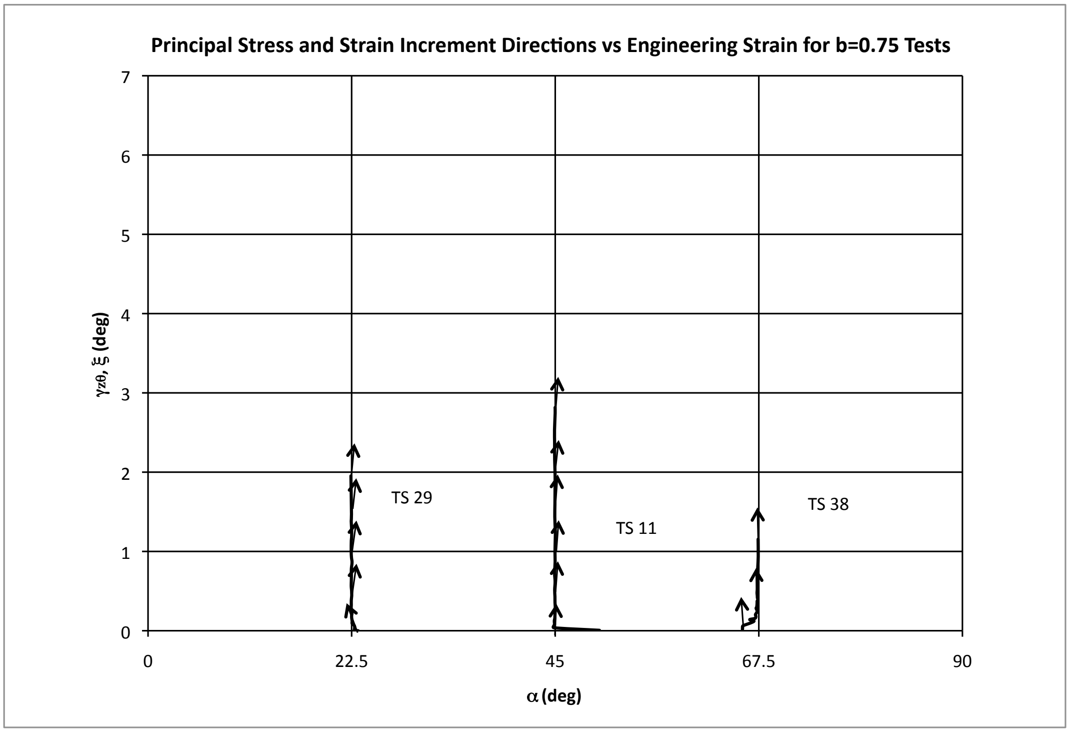

Figure 8.3.16. Principal Stress and Strain Directions versus Engineering Strain for b=0.75 Torsion Shear Tests.

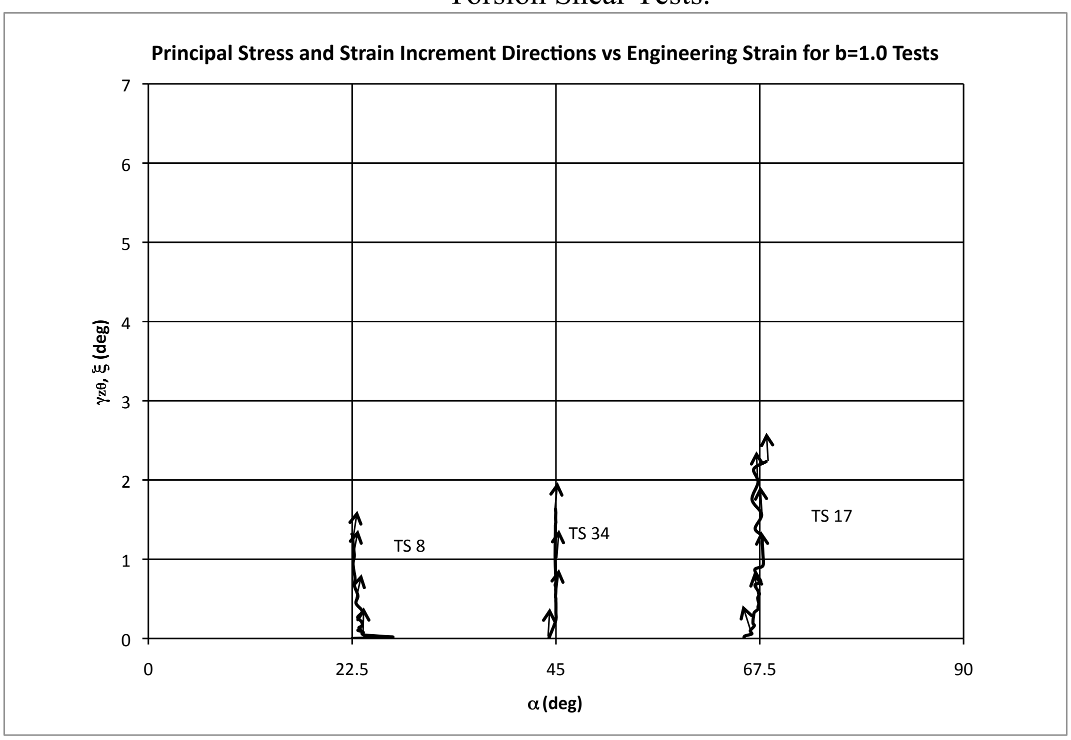

Figure 8.3.17. Principal Stress and Strain Directions versus Engineering Strain for b=1.0 Torsion Shear Tests.

8.4 Conclusion

The preceding pages have summarized and analyzed the strains for both true triaxial and torsion shear tests. For the cases that were possible, where α=0° and α=90° in Sector I and III, torsion shear and true triaxial strains were directly compared. Although the patterns were similar, the total amount of strains was significantly less in the torsion shear tests. Possible explanations are the difference in stress paths for each type of test (constant mean confining stress for torsion shear and constant minor principal stress for true triaxial) and the different end restraints (full frictional surfaces for torsion shear and double lubricated ends for true triaxial tests). Shear strains have been presented for torsion shear tests with rotation. Although no single pattern exists when looking at the various b-values, when looking at the magnitudes of the shear strains as the alpha values increased, the strain increment directions all show non-associated flow in the region of plastic strains and the stress directions become asymptotic to each other but never reached the same directions completely.

9. Shear Band Analysis

Shear bands were observed for a number of triaxial, true triaxial and torsion shear tests. After the specimen had reached failure, it was held under vacuum in order to measure and record any shear bands that had developed. In general, shear bands for triaxial and true triaxial tests were seen after peak failure (in the softening regime). Shear bands in torsion shear tests occurred (with few exceptions) at peak failure. In the sections that follow, the recorded shear band inclination angles will be compared to the existing theories (Coulomb, Roscoe and Arthur), which predict shear band inclination angle. As was stated in Chapter 2, Section 2.6, the Coulomb, Roscoe and Arthur equations are as follows:

$$\alpha_c = 45 + \left(\frac{\phi}{2}\right) \qquad \text{Eq. 9.1}$$

$$\alpha_R = 45 + \frac{\psi}{2} \qquad \text{Eq. 9.2}$$

$$\alpha_A = 45 + \left(\frac{\phi + \psi}{4}\right) \qquad \text{Eq. 9.3}$$

where α_C is the Coulomb angle inclination, α_R is the Roscoe angle inclination and α_A is the Arthur angle inclination. ϕ and ψ are the friction angle and dilation angle, respectively.

As already mentioned, the dilation angle can be calculated by the following equation,

$$\psi = \sin^{-1}\left(\frac{\left(\Delta\varepsilon_v / \Delta\varepsilon_1\right)}{\left(\Delta\varepsilon_v / \Delta\varepsilon_1\right) - 2}\right) \qquad \text{Eq. 9.4}$$

where $\Delta\varepsilon_1$ is the change in major principal strain and $\Delta\varepsilon_v$ is the change in volumetric strain. The slope of the volume change curve is calculated over several points at/near failure.

9.1 Shear Band Analysis for Triaxial Tests

As described in Chapter 3, a series of 10 triaxial compression tests were performed under different confining pressures and bedding plane directions of α=0° and α=90° with the major principal stress to determine the necessary parameters for calibration a constitutive model for cross-anisotropic sand deposits. Shear bands developed and their inclinations were recorded. In most cases for triaxial compression, the shear band plane that was seen was skewed relative to the surface of the specimen. It is possible that the direction of the plane changed by a small amount as it hit the corners of the specimen. Therefore, to calculate the true angles of the shear bands for each plane, vector analysis was performed using the measured heights, widths and directions of the shear bands recorded after failure. An example picture of where the plane developed is shown in Figure 9.1.1. In cases where this occurred, the angle of each plane with respect to the horizontal was calculated. Instead of computing an average between both planes, each plane is plotted in the results. This shows a range and the reader can get a better idea of the variation in shear band inclination angles. In some cases, only one plane developed. Figure 9.1.2 shows an example of this occurrence.

Therefore, vector analysis was not needed for this case since the angle of inclination was directly measured from the horizontal on the specimen after failure.

Table 9.1.1 summarizes the angles of inclination for the 10 triaxial tests. The angle of inclination is measured from the horizontal to the direction of shear band plane. A sketch of the measured shear band angles, α_{sb}, is shown in Figure 9.1.3. For tests where vectors were calculated, the angles were also from the horizontal to the developed shear band planes (seen in Figure 9.1.4).

Figure 9.1.1. Example of sheared specimen with two distinct shear band planes after failure in triaxial testing.

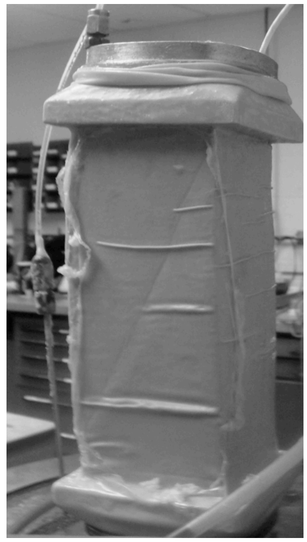

Figure 9.1.2. Example of shear specimen with only one distinct shear band plane after failure in triaxial testing.

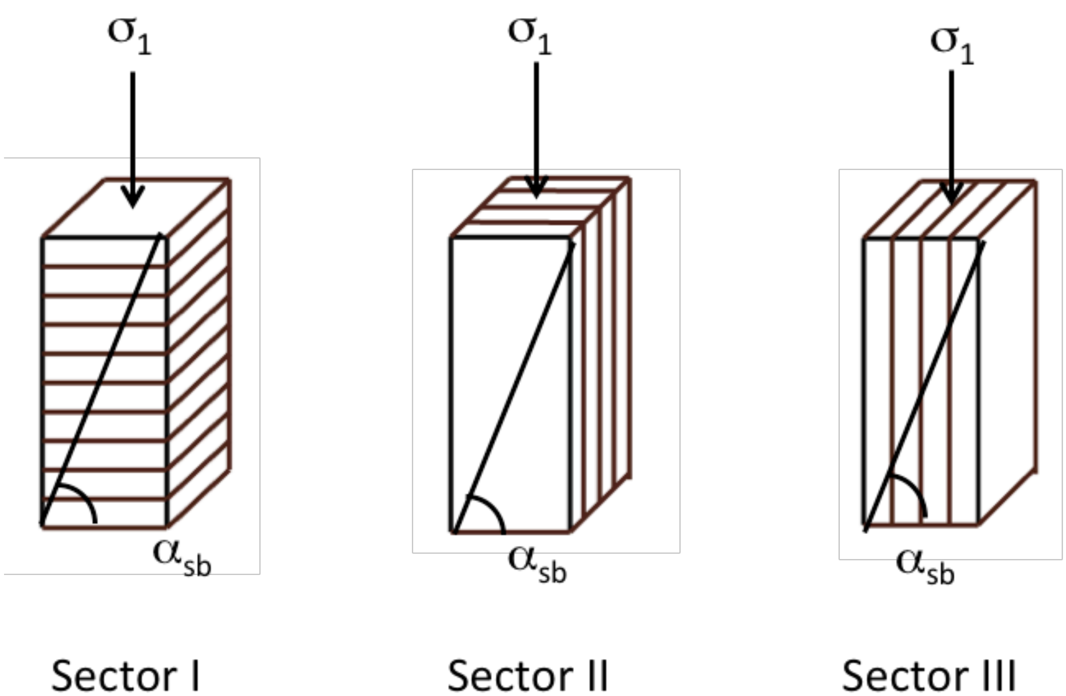

Figure 9.1.3. Sketch of the measured shear band angle for all three sectors in triaxial and true triaxial tests. α_{sb} is measured from the horizontal to the shear plane.

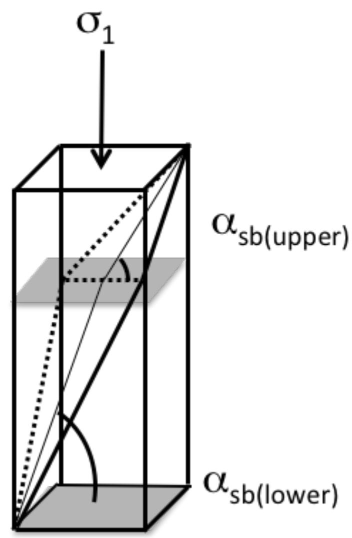

Figure 9.1.4. Schematic showing two planes in a tall prismatic specimen. Shear band inclination angles, $\alpha_{sb\ (upper)}$ and $\alpha_{sb\ (lower)}$ are measured from the horizontal plane to the corresponding shear plane.

In order to calculate the angle between the shear band plane and the horizontal plane for each of the upper and lower shear band planes, the angle between the normal vectors of the horizontal plane and the shear plane was calculated. The normal vector of each horizontal plane is (x,y,z) = (0,0,1). The normal vector, n_{sp}, of the respective shear plane is calculated as the cross product (using the determinant method) of the two measured vectors of the shear plane at the sides of the specimen. The geometric extensions of the visible shear bands for each specimen were measured and put into the following equations to calculate the corresponding vectors, v_1 and v_2.

$$\vec{v}_1 = (x_1, y_1, z_1)$$
$$\vec{v}_2 = (x_2, y_2, z_2) \qquad \text{Eq. 9.1.1}$$

Then, the cross product was calculated using the following equation:

$$n_{sp} = (y_1 z_2 - z_1 y_2)i - (x_1 z_2 - z_1 x_2)j + (x_1 y_2 - y_1 x_2)k$$
$$where$$
$$i = \begin{bmatrix}1\\0\\0\end{bmatrix} \qquad \text{Eq. 9.1.2}$$
$$j = \begin{bmatrix}0\\1\\0\end{bmatrix}$$
$$k = \begin{bmatrix}0\\0\\1\end{bmatrix}$$

Using a reference plane, v_3

$$\vec{v}_3 = (a_1, b_1, c_1)$$
$$\vec{v}_3 = (0,0,1) \qquad \text{Eq. 9.1.3}$$

the shear plane inclination angle can be calculated using

$$\cos\alpha_{sp} = \frac{a_1(y_1 z_2 - z_1 y_2) - b_1(x_1 z_2 - z_1 x_2) + c_1(x_1 y_2 - y_1 x_2)}{\sqrt{(y_1 z_2 - z_1 y_2)^2 + (x_1 z_2 - z_1 x_2)^2 + (x_1 y_2 - y_1 x_2)^2}\sqrt{a_1^{\,2} + b_1^{\,2} + c_1^{\,2}}}$$
$$\cos\alpha_{sp} = \frac{1(x_1 y_2 - y_1 x_2)}{\sqrt{(y_1 z_2 - z_1 y_2)^2 + (x_1 z_2 - z_1 x_2)^2 + (x_1 y_2 - y_1 x_2)^2}} \qquad \text{Eq. 9.1.4}$$

Table 9.1.1. Summary of Triaxial Test Shear Band Inclination Angles.

Test No	**α(deg)**	**α_{sb} (deg)**
1 (TT#1) (lower plane)	0	51.00
1 (TT#1) (upper plane)	0	57.82
2 (lower plane)	0	57.40
2 (upper plane)	0	56.89
3 (lower plane)	0	57.04
3 (upper plane)	0	58.88
4 (lower plane)	0	52.97
4 (upper plane)	0	60.29
5 (one plane)	90	60.00
6 (lower plane)	90	67.13
6 (upper plane)	90	59.54
7 (lower plane)	90	66.86
7 (upper plane)	90	60.56
8 (TT#13) (one plane)	90	63.00
9(W1) (lower plane)	90	58.40
9(W1) (upper plane)	90	59.70
10 (A7) (one plane)	90	60.00

In Figures 9.1.5 and 9.1.6, the measured shear band inclination angles are compared to the predictions of Coulomb, Roscoe and Arthur. As can be seen, for α=0° tests, the inclination angles are between the Arthur and Roscoe shear band inclination predictions. Specimens with vertical bedding planes (α=90°) have slightly higher inclination angles that favor the Coulomb and Arthur predictions. The stress-strain curves have also been presented in Figures 9.1.6 and 9.1.7. The first time that a shear band was seen is indicated with an arrow for each test. For all triaxial tests, the shear bands developed after peak failure well into the softening regime. Therefore, shear bands did not affect the peak strength of the specimens.

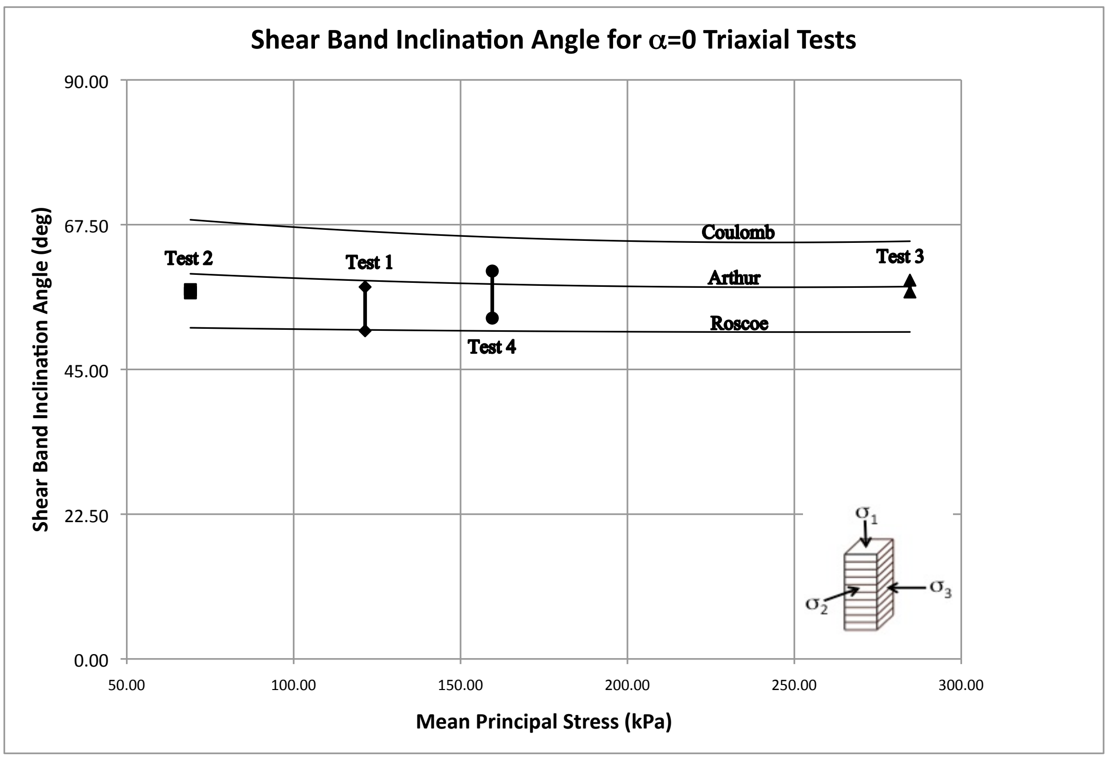

Figure 9.1.5. Shear Band Inclination Angles for Triaxial Compression Tests with horizontal bedding planes (α=0°).

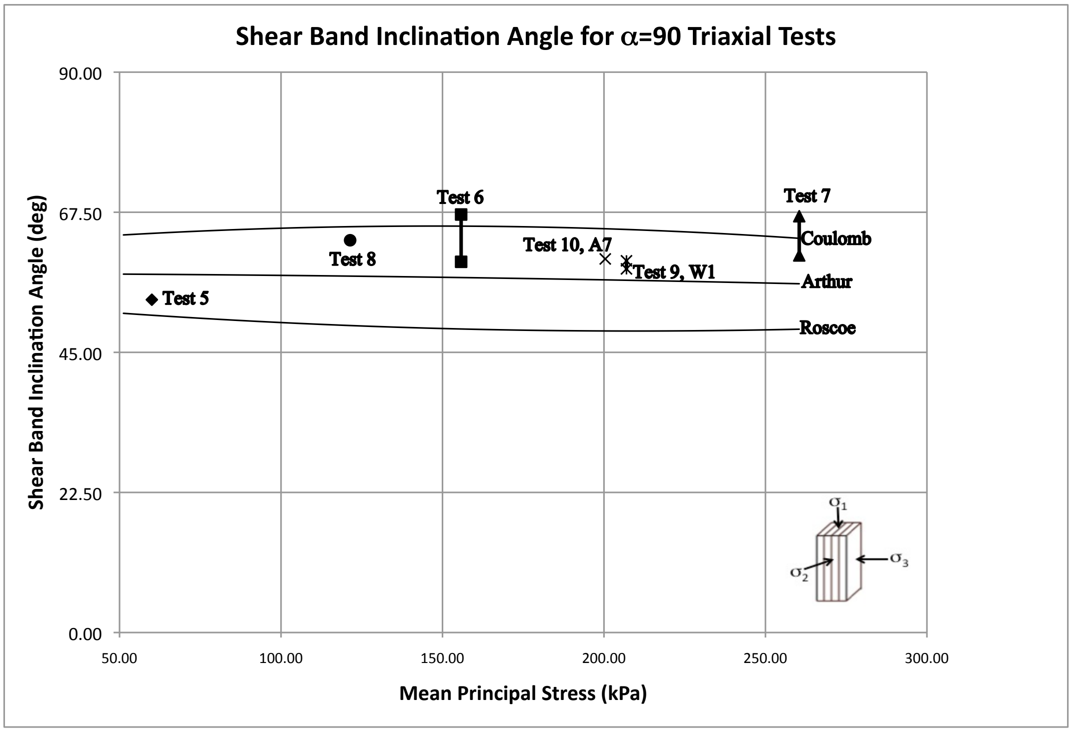

Figure 9.1.5. Shear Band Inclination Angles for Triaxial Compression Tests with vertical bedding planes (α=90°). Test 9 is an extension test with α=90° bedding planes.

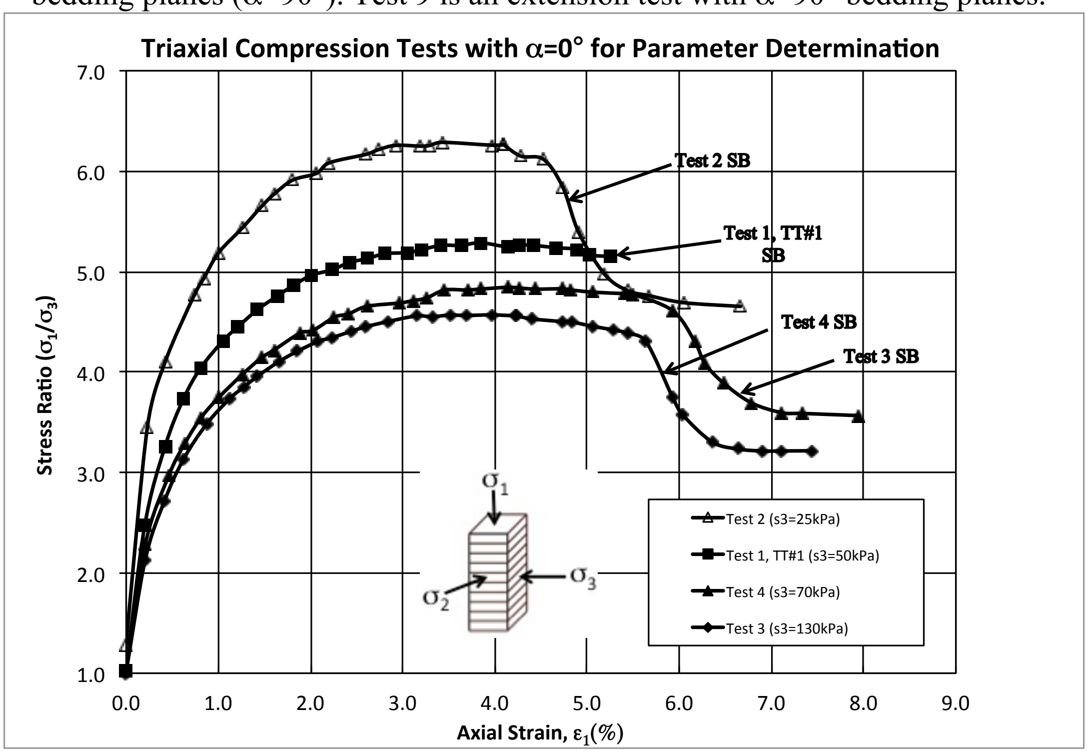

Figure 9.1.6. Stress-Strain curves for Triaxial compression tests indicating Shear Band development for α=0° tests.

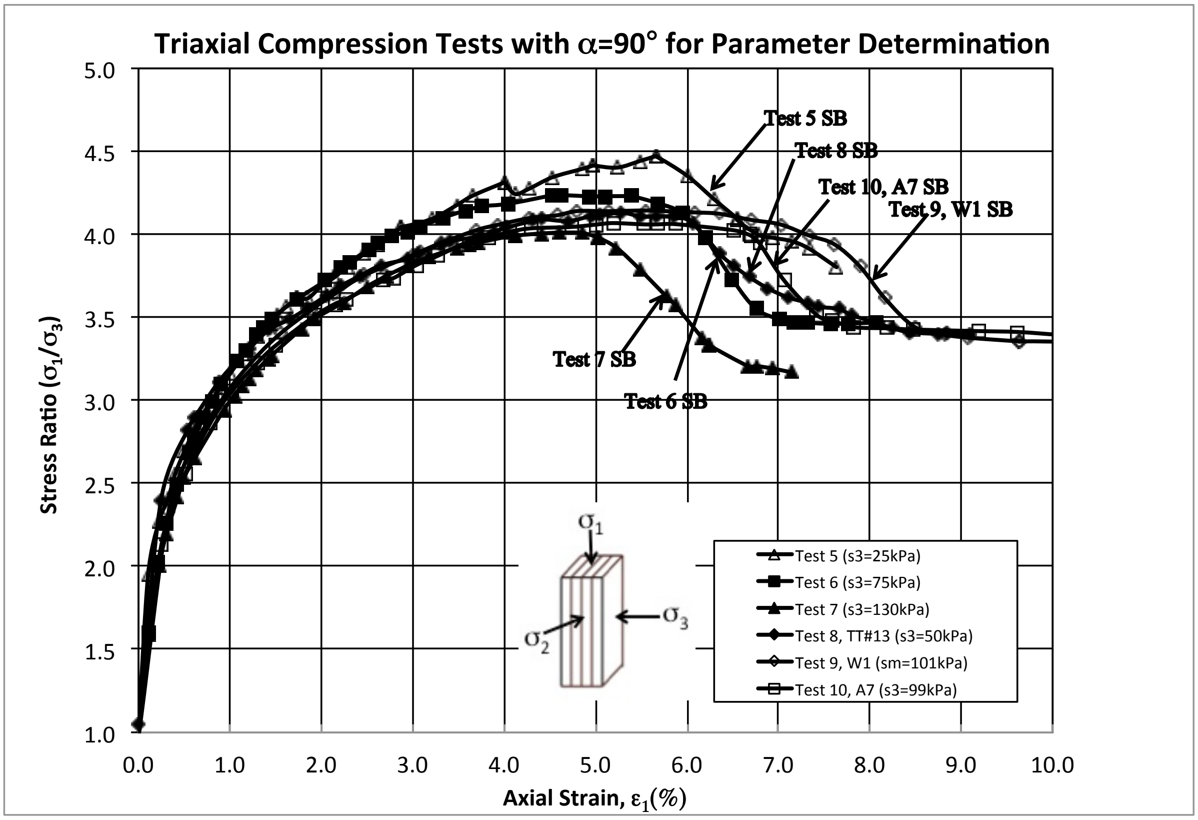

Figure 9.1.7. Stress-Strain curves for Triaxial compression tests indicating Shear Band development for α=90° tests.

9.2 Shear Band Analysis for True Triaxial Tests

Eighteen true triaxial tests were sheared in this experimental program. Shear bands were seen in all but two tests. For Tests TT #16 and TT#18, after the specimen was sheared, a vacuum was inadvertently not applied to the specimen. Therefore, when the horizontal loading plates were removed and the specimen was unloaded, the specimen collapsed. No shear bands could be seen prior to unloading. However, for the other 16 tests, vacuum was applied, and shear bands were recorded. Most failed in one plane as shown in Figure 9.1.3. The normal vector to this failure plane was always in the plane of the major and minor principal stresses. A typical picture of a sheared specimen is shown in Figure 9.2.1. Tests that did not fail along one plane were analyzed using vector analysis (as explained in Section 9.1). This only occurred for Test TT#1. For two tests, Tests TT#7 and TT#12, where b=1, the shear bands developed vertically. It is speculated that this also occurred for Test TT#18 but it is not known for certain since the specimen was not held under vacuum once unloaded. The behavior of Tests TT #7 and TT #12 show both specimens' shearing parallel to the loading direction (Figure 9.2.2). This occurs mid-height of the specimen. Towards the top and bottom of the specimen (towards the end restraints), some shear bands are seen at slightly different angles.

Table 9.2.1 summarizes the shear band inclination angles recorded for true triaxial tests. Figures 9.2.3 through 9.2.4 show the measured shear band inclination angles versus b-value for each of the three sectors. The predicted Coulomb, Arthur and Roscoe inclination angles are also presented. Although there is some scatter in the results, most of the triaxial tests for all three sectors are closest to the Arthur shear band inclination angle prediction. The Arthur prediction takes into account the friction angle and the dilation angle when predicting the shear band inclination. It is important to note, that as seen in Figure 9.2.1, shear bands were free to develop fully across the entire height of the specimen. In cases where the shear band was not restricted by the top and bottom plates, the ends of the shear bands could be seen a couple of centimeters above or below the bottom and top plate. Clear visible shear bands were seen after peak failure in the softening regime of the stress-strain curve for all but b=1 triaxial tests. At b=1, shear bands developed at failure, causing a sharp decrease in strength seen on the stress-strain behavior presented in Chapter 5 (see Figures 9.2.6, 9.2.7, and 9.2.8).

Figure 9.2.1. Typical example of shear band development for most True Triaxial tests.

Specimen TT#7 (α=0°, b=1)

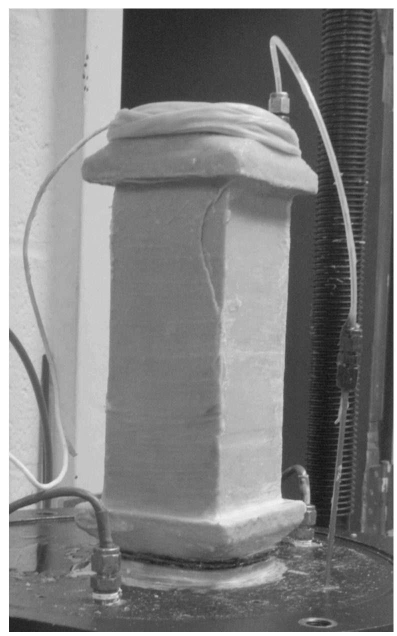

Specimen TT#12 (α=90°, b=1)

Figure 9.2.2. Pictures of Tests TT#7 (Sector I) and TT#12 (Sector II) at b=1 where shear bands developed vertically at failure.

Table 9.2.1. Summary of Shear Band Inclination Angles for True Triaxial Tests.

Sector I	**α(deg)**	**b-value**	**α_{sb} (deg)**
TT#1 (lower)/(upper)	0°	0.00	51.00/57.82
TT#2	0°	0.24	61.50
TT#3	0°	0.51	62.00
TT#4	0°	0.75	64.00
TT#5	0°	0.70	64.50
TT#6	0°	0.72	62.00
TT#7	0°	1.00	90 , 70
Sector II			
TT#8	90°	0.25	64.50
TT#9	90°	0.49	60.00
TT#10	90°	0.70	62.00
TT#11	90°	0.69	62.00
TT#12	90°	1.00	90.00
Sector III			
TT#13	90°	0.00	57.50
TT#14	90°	0.25	59.50
TT#15	90°	0.49	65.00
TT#16	90°	0.72	n/a
TT#17	90°	0.72	63.00
TT#18	90°	0.95	n/a

Looking at Figure 9.2.3, there is a slight positive slope in shear band inclination angle as b-value increases in Sector I. At b=1, the shear band inclination is vertical at 90 degrees. The failure occurs in the horizontal direction. This shows that as the intermediate stress is increased, shear bands tend to develop at steeper angles in the major-minor principal stress plane. Looking at the anisotropy of the bedding planes, the strongest direction for the sand grains to slide in Sector I, would be in the σ_2 and σ_3 directions. The sand grains would tend to slide less in the σ_1 direction for this configuration. At the point where the intermediate and major principal stress directions are the same (b=1.0), the failure direction switches and creates vertical shear bands. Sector II does not show an increased inclination angle as the b-value increases. In Sector II, the σ_2 direction is the direction where the bedding planes create a condition where the sand grains would want to slide less than in the other directions. By changing the intermediate principal stress, there may not be too much of an influence on the shear band inclination angle due to the way the bedding planes are aligned. By switching the bedding planes in Sector III so that the σ_3 direction is the direction where the sand grains have the hardest time sliding, there is once again (as seen in Sector I) an increase in shear band inclination angle as b-value increases, allowing for sliding to occur easily between the sand grains.

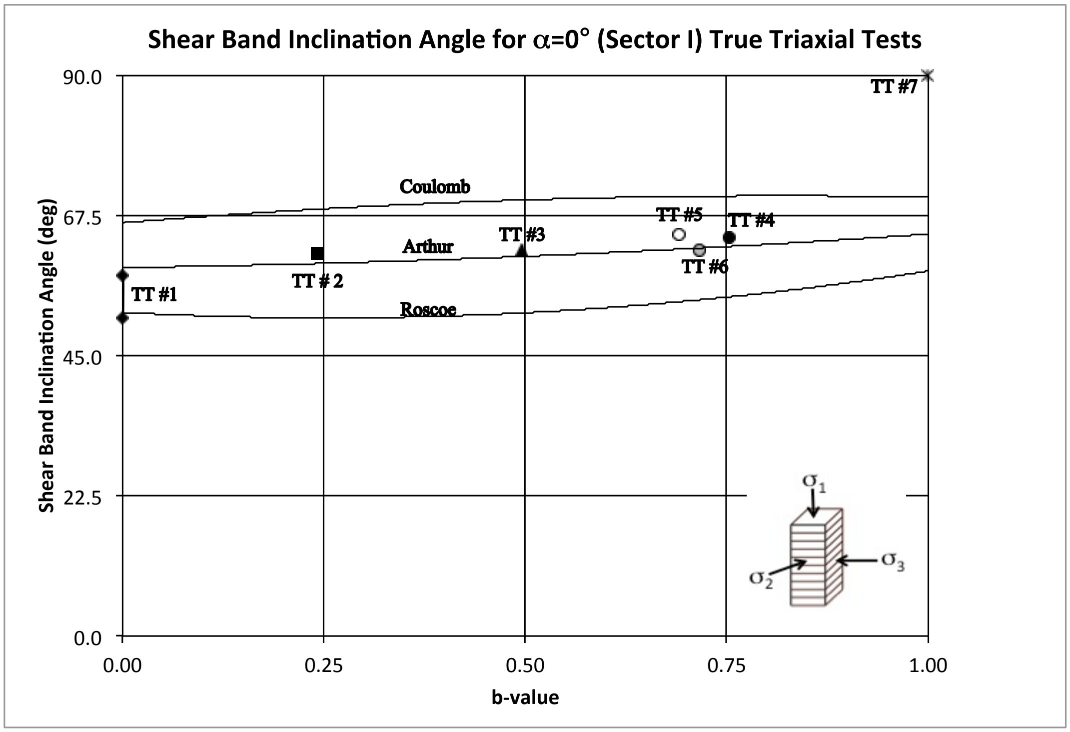

Figure 9.2.3. True Triaxial shear band inclination angles for Sector I tests, including Coulomb, Arthur and Roscoe predictions.

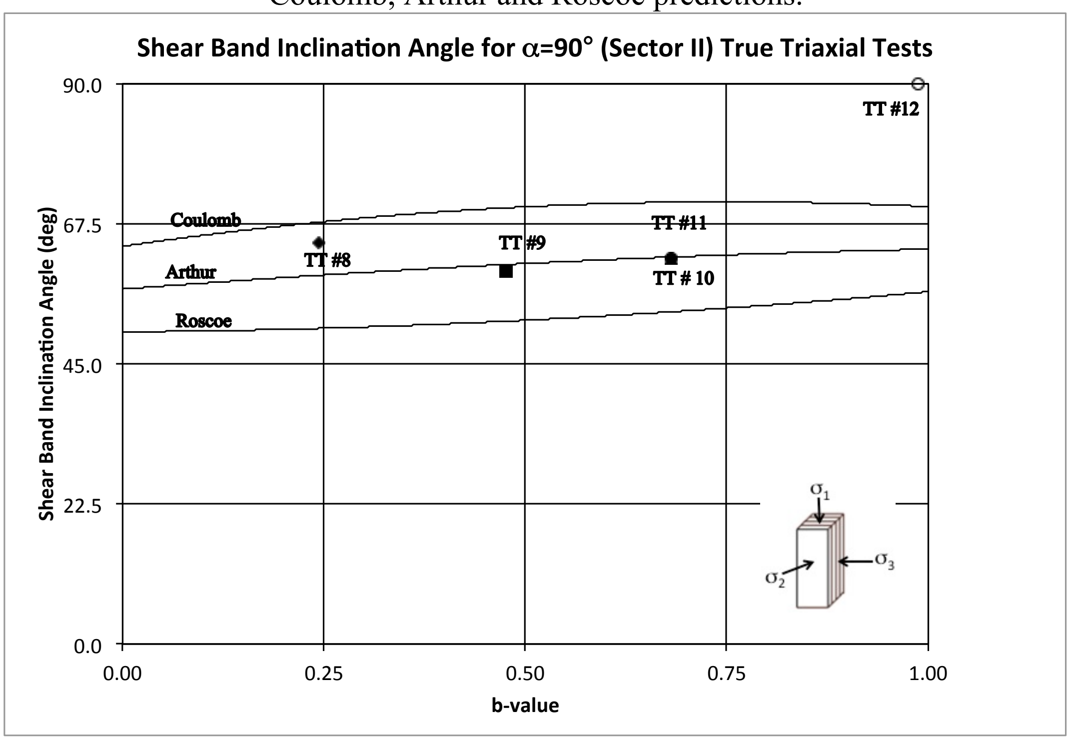

Figure 9.2.4. True Triaxial shear band inclination angles for Sector II tests, including Coulomb, Arthur and Roscoe predictions.

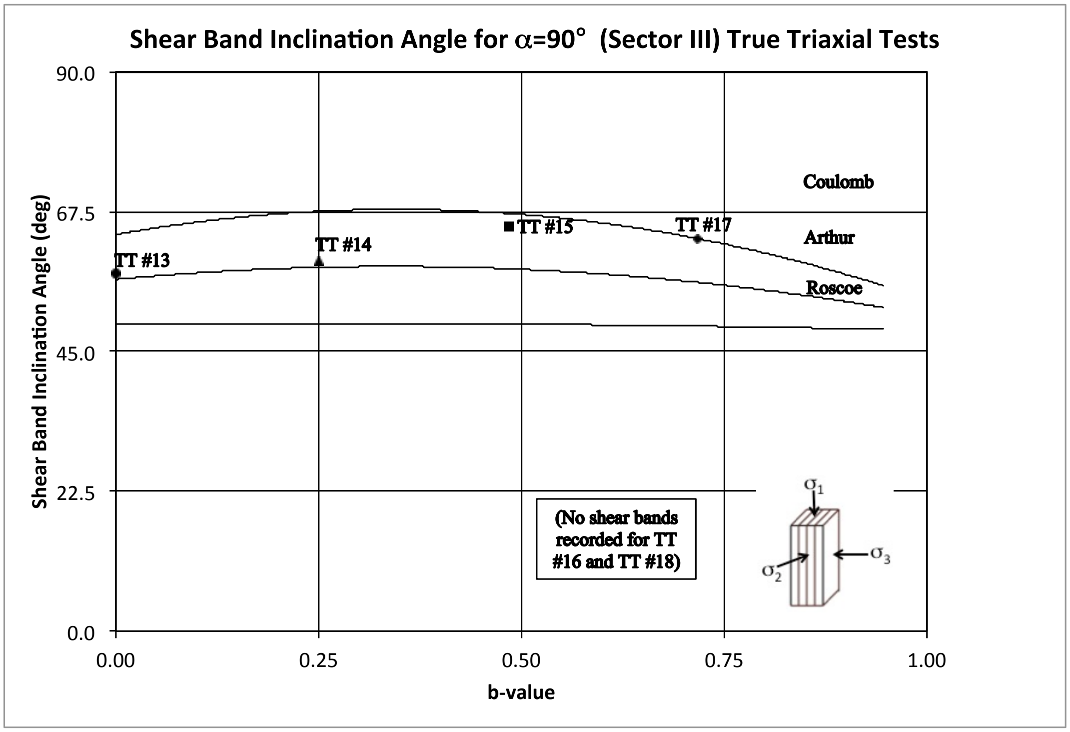

Figure 9.2.5. True Triaxial shear band inclination angles for Sector III tests, including Coulomb, Arthur and Roscoe predictions.

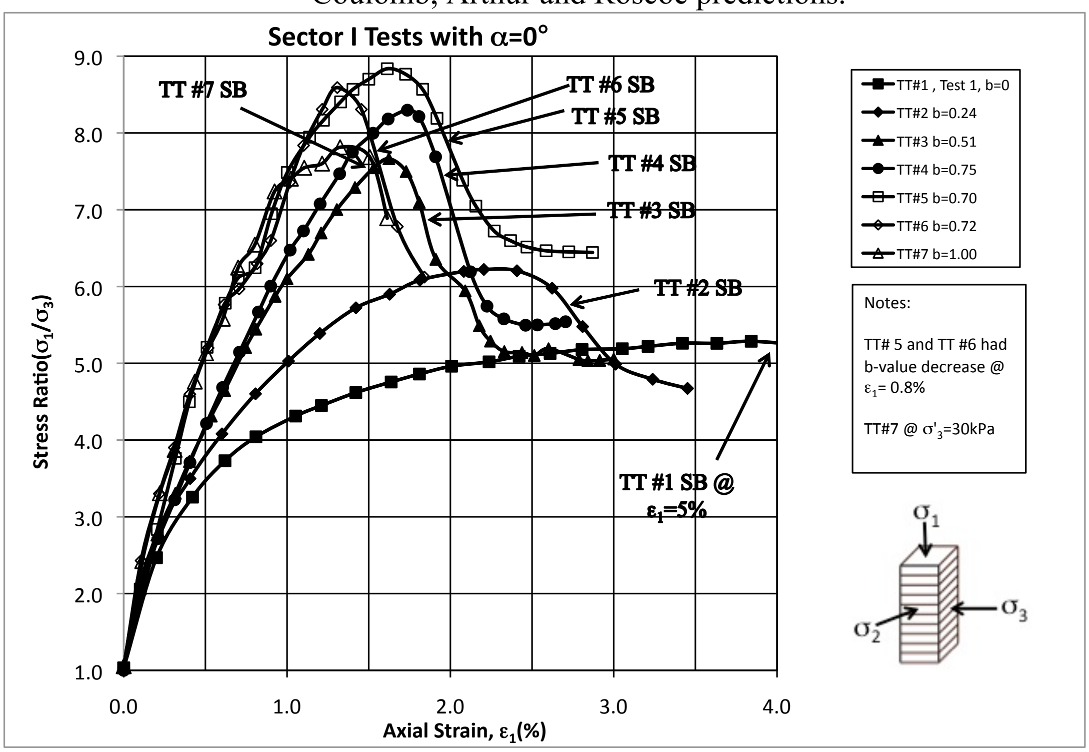

Figure 9.2.6. Stress-strain behavior for Sector I tests (α=0°) with initial point of shear band development is indicated with arrows.

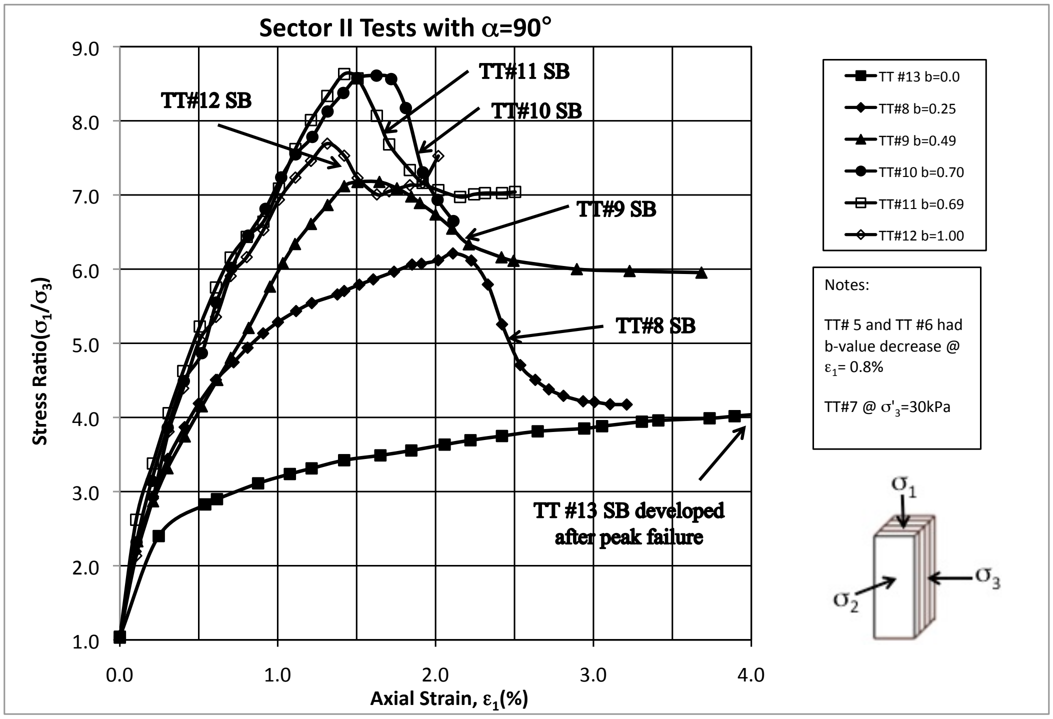

Figure 9.2.7. Stress-strain behavior for Sector II tests (α=90°) with initial point of shear band development is indicated with arrows.

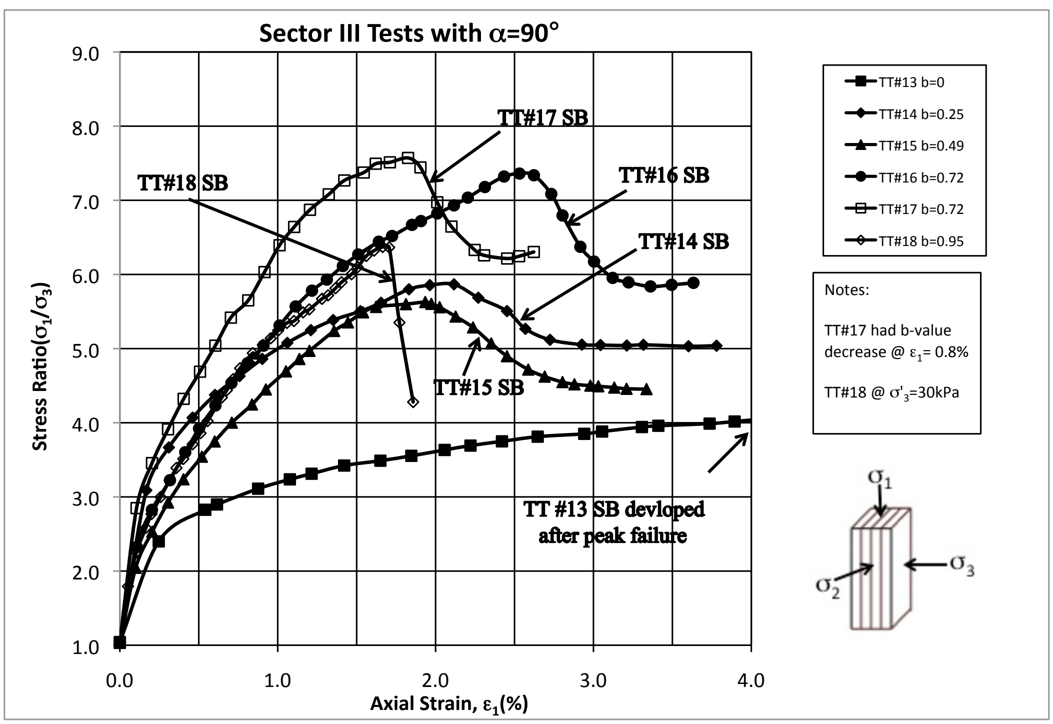

Figure 9.2.8. Stress-strain behavior for Sector III tests (α=90°) with initial point of shear band development is indicated with arrows.

9.3 Shear Band Analysis for Torsion Shear Tests

The true triaxial shear band inclination angles described in Section 9.2 had only one failure plane (all except TT #1 which had two planes). Shear bands that developed in torsion shear specimens were not always in just one direction as was seen in the true triaxial tests. In cases where more than one direction was measured, the span of directions for each test is presented in the results. Out of the 44 torsion shear tests performed, in 41 tests, shear bands were observed. These shear bands are presented in the section that follows. In Test 1*, there were no shear bands observed. For Tests 13* and 34, the top cap seemed to slip during shearing and therefore, no shear bands were seen.

Several shear band patterns developed in the torsion shear specimens. The shear bands were able to develop freely and were not affected by the rubber membranes that are on the specimen's vertical sides. Most shear bands were seen near or right at failure. In some cases (usually for b=0.75 and b=1.0), the shear bands developed right at failure and grew extremely quickly, deforming the specimen. In cases where that did not happen, although peak failure was reached, the specimen was sheared more to develop the shear bands more fully. However, there was no gain in strength after peak failure. By just apparently looking at the stress-strain and volume change curves, it is hard to tell where the shear bands developed. Therefore, the time that they first appeared was recorded manually. There is no sharp drop in stress (as seen in the shear bands that developed for the true triaxial tests) and softening in the stress-strain curves.

Shear bands were measured on the specimen from the horizontal up to the shear band. The grid drawn on the specimen prior to shearing helped in measuring correctly the angles of the shear bands. When the major principal stress was inclined, the major principal stress was added to the shear band angle that was measured (as shown in Figure 9.3.1a). When the shear band was negative of the horizontal, the shear band inclination angle was considered negative and was then found as shown in Figure 9.3.1b. For the sake of plotting all positive numbers, if the shear band was clockwise to the horizontal, it was made positive once the correct inclination had been calculated.

(a)

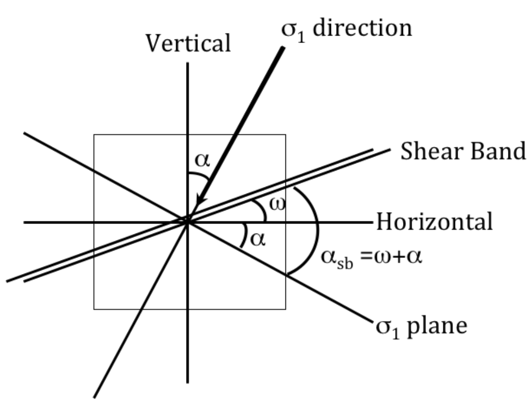

(b)

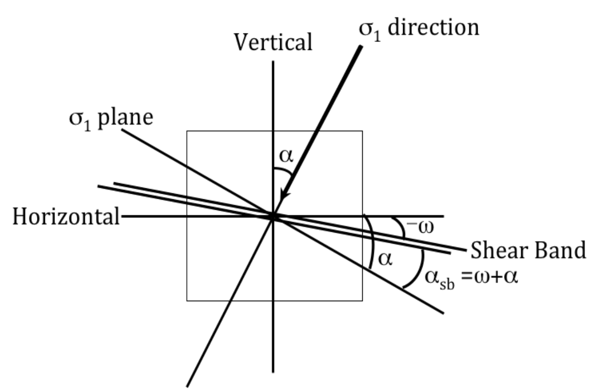

Figure 9.3.1. Inclination of shear bands relative to the major principal stress plane for torsion shear tests (after Lade et al. 2008).

Representative patterns are seen in Table 9.3.1. In many occasions, a torsion shear specimen showed more than just one type of pattern. However, in order to group them, these 6 representative patterns have been named as follows: (a) zig-zag bands, (b) inclined bands, (c) horizontal bands, (d) crossed bands, (e) collapse and (f) r-theta failures. Z-theta failures failed in the z-theta plane and are somewhat similar to when necking occurs. R-theta failures are classified as such because the shear bands failed in the r-theta plane. In all other cases, the shear bands developed in the z-theta plane where the principal stress was applied. The specimen had a sufficient height to diameter ratio to allow the shear bands to develop completely. In cases where the shear bands did not hit the end restraints, they wrapped around the entire specimen.

Table 9.3.1. Different patterns of shear bands seen in Torsion Shear specimens.

	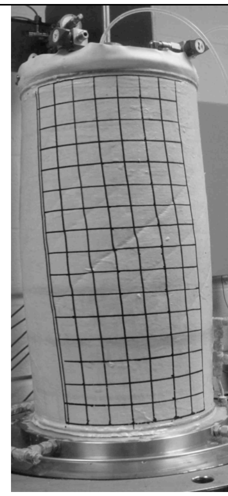	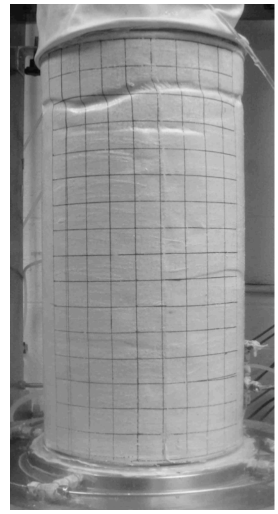
(a) zig-zags bands	(b) inclined bands	(c) horizontal bands (z-theta)
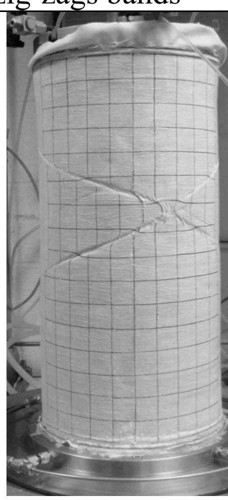	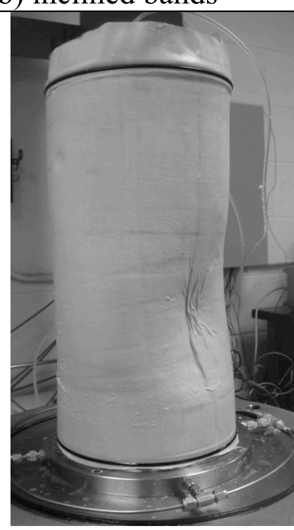	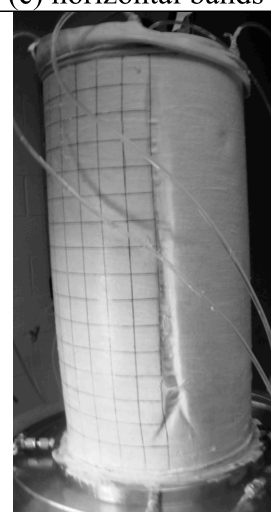
(d) crossed bands	(e) collapse	(f) r-theta

Shear band inclination angles are shown in Figures 9.3.2, 9.3.5, 9.3.8, 9.3.11 and 9.3.14. Tests are separated by alpha=constant values so that the change of shear band inclination angle with b-value can be studied. The summary of shear band inclination angles for all torsion shear tests is presented in Table 9.3.2.

Table 9.3.2. Summary of Shear Band Inclination for Torsion Shear Tests.

Test	**alpha**	**b-value**	$\mathbf{a_{sb}}$	**Patterns**
23	0	0	65-70	inclined, zig-zag (all around)
1*	0	0.01	n/a	none observed
24*	0	0.27	63-71	zig zag (all around)
25*	0	0.55	63-70	zig zag (all around)
2	0	0.75	65-68	zig zag (all around) with r-theta
26	0	1	90	vertical r-theta
3	22.41	0.00	41-45	inclined (wrap around)
27*	24.04	0.02	54	inclined (wrap around)
28	22.97	0.26	64-66	inclined (wrap around)
5*	24.18	0.27	58	inclined (wrap around)
4*	23.73	0.28	64	inclined (wrap around)
6	22.01	0.51	70-72	inclined (wrap around)
29	22.77	0.75	83	inclined r-theta (front)
*7**	*24.11*	*0.83*	*89-91*	inclined *r-theta (front and back)*
30*	22.92	0.85	78-88	inclined r-theta (front)
8	22.87	0.97	90	inclined r-theta (front)
31	44.91	0.00	60	inclined (front)
32*	31.76	0.18	47	inclined (wrap around) (mid&top)
9	44.99	0.24	64-70	inclined (not very deep)
33	44.99	0.50	65	inclined (front bottom)
10*	41.96	0.55	52	inclined (wrap around) (bottom)
11	44.98	0.75	65-70	inclined (wrap around)
12*	41.54	0.81	60-64	inclined (wrap around)
*13**	*33.86*	*0.94*	*n/a*	*under top cap (slip)*
34	44.97	1.00	n/a	under top cap (slip)
14	67.51	0.00	68	sucked in at bottom
35*	69.89	0.16	70	under top cap
36	67.80	0.25	68	under top cap
15	67.45	0.50	72	under top cap and bottom ring
37*	69.91	0.55	60-61	under top cap (deep)
38	67.54	0.75	58-68	under top cap (deep)
39*	70.62	0.79	71	under top cap (deep)
40*	73.06	0.80	60-63	horizontal wrap around r-theta
*16**	*72.06*	*0.96*	*72*	*under top cap (deep)*
17	68.26	1.00	62-63	horizontal wrap around r-theta
41	90	0.00	67-69	collapse inward, crossed
18	90	0.04	65-70	collapse inward, crossed
19*	90	0.07	65	collapse inward, crossed
42*	90	0.32	64-66	crossed all the way around
20*	90	0.54	62-70	crossed all way around, w r-theta
43*	90	0.78	57-58	slanted r-theta all around
21*	90	0.78	64-72	r-theta (almost horizontal), slanted
44*	90	0.99	90	deep r-theta around under top cap
22*	90	0.99	65-70	r-theta around top, crossed

For α=0° tests (Figure 9.3.2), if a trend line would be drawn through all the tests, the shear band inclination angle is almost constant. The spans of shear band angles are slightly higher than the Coulomb prediction at b=0 and then get closer to the Arthur prediction as b=1. Tests 23, 24*, 25*, and 2 all showed a zig-zag pattern wrapping around the middle of the specimen. For TS 2, a vertical "canyon" (r-theta band) developed at the edge of one of the zig-zag patterns. Test 26 had a vertical r-theta band develop at failure. Pictures of these two tests are shown in Figure 9.3.3 (a) and (b), respectively. Since the failure angles are within the specimen wall and are not visible on the outside surface of the specimen, they have not been included in the summary plots that follow. A direct comparison to the prediction angles is not possible for these situations.

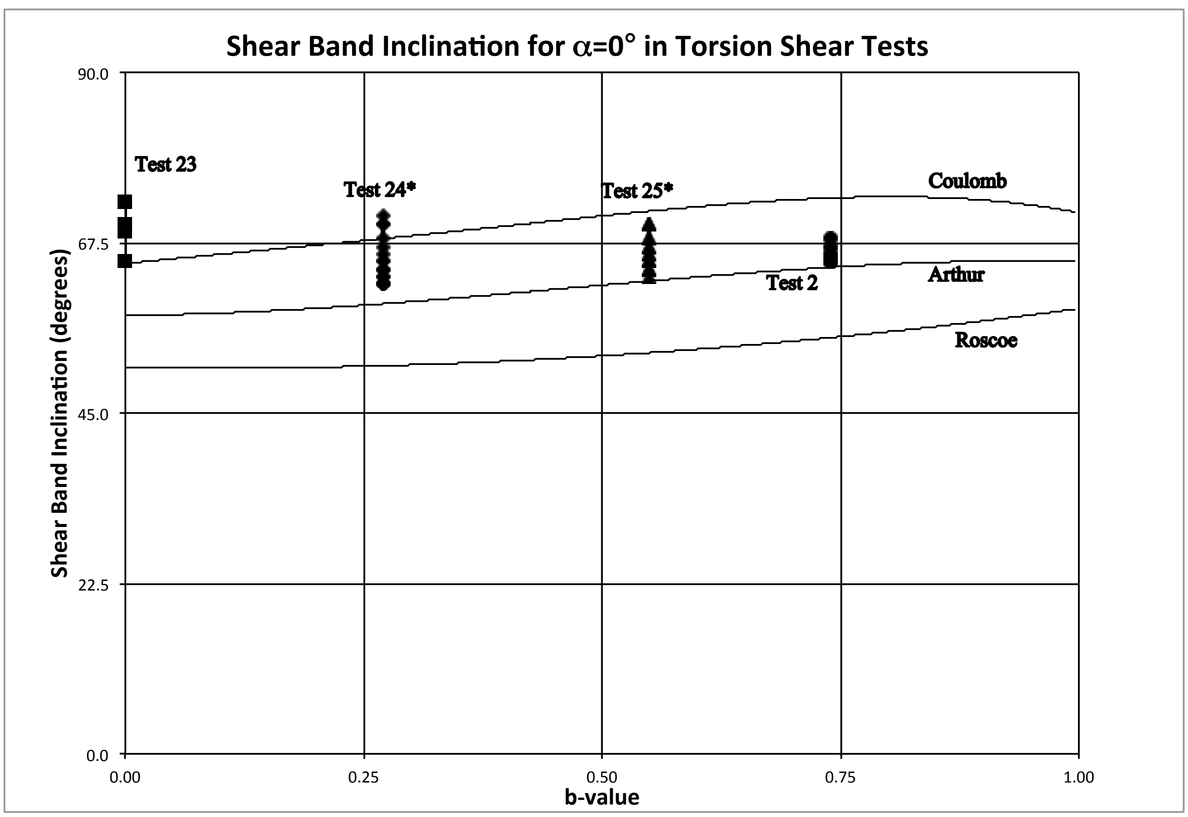

Figure 9.3.2. Shear band inclination angle for α=0° Torsion Shear Tests.

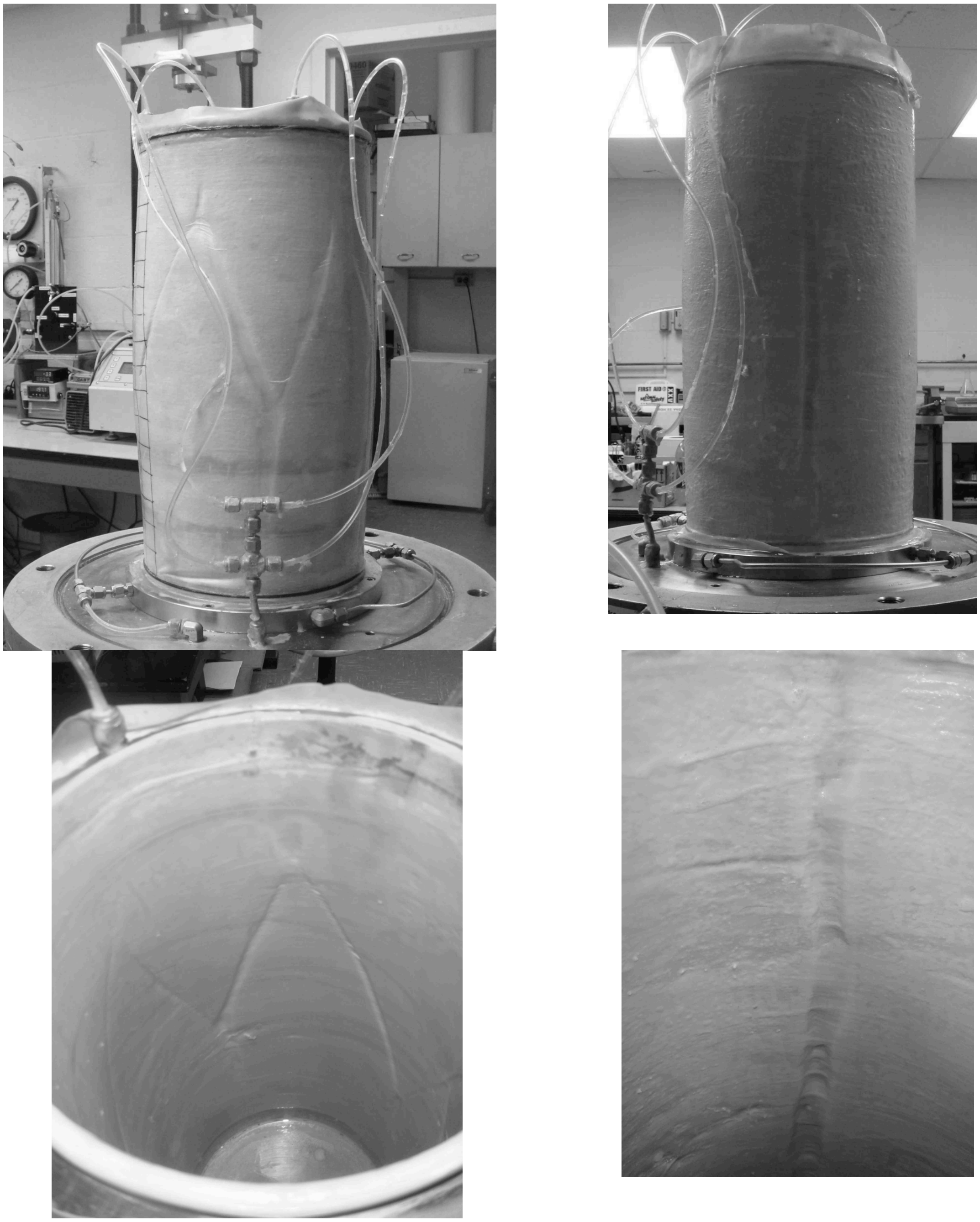

(a) Outside & Inside Shear Bands
(Test 2; (α=0°, b=0.75))

(b) Outside & Inside Shear Bands
(Test 26;(α=0°, b=1))

Figures 9.3.3. Pictures of the outer and inner shear bands that developed for (a) Tests 2 and (b) 26.

The stress-strain curves presented in Section 7.3 has been modified slightly to show the initiation of the shear band development (Figure 9.3.4). For tests with lower b-values of 0 and 0.27 where shear bands were seen, Tests 23 and 24*, respectively, after the shear band was first seen, the test continued to develop the shear band more. However, there was not any significant gain in strength for the specimen. For Test 25*, after the shear band developed there was a significant decrease in strength. Tests 2 and 26* shear bands developed extremely quickly at failure. No shear bands were seen before the last points on the curve. These two tests had large deep “canyons” (r-theta bands) indicating failure in the intermediate stress direction (pictures are shown in Figure 9.3.3). Once these deep r-theta bands developed, the volume change was so large in the inner cell, that the test had to be stopped. However, it was clear that the sample had failed at the point of the shear band developments.

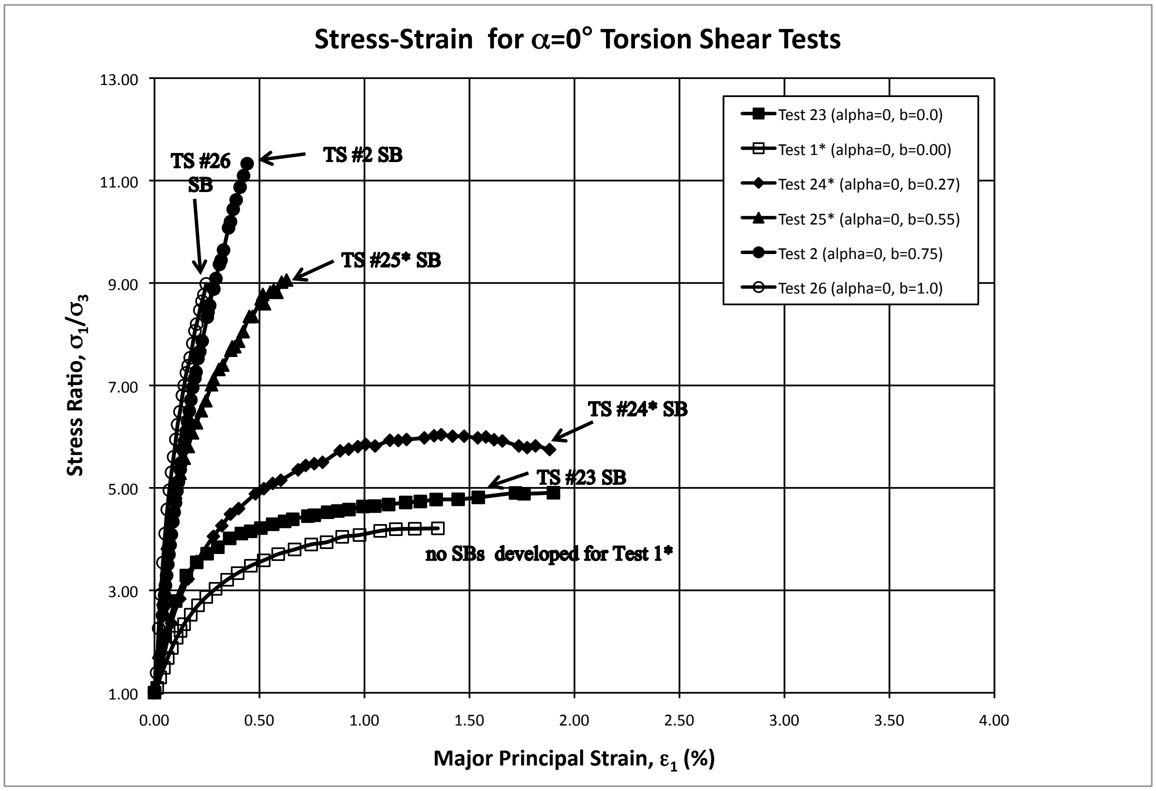

Figure 9.3.4. Stress-strain curves for α=0° Torsion shear tests indicating the onset of Shear band development.

The shear band inclination angles for torsion shear tests with α=22.5° are presented in Figure 9.3.5. The angles clearly increase as the b-value increases but do not follow any one of the three predictions at all. Tests 3 and 27* are below or at the Roscoe inclination angle. Tests 28, 4* and 5* appear to gather around the Arthur angle. Test 6 is near the Coulomb angle. Tests 7*, 8, 29 and 30 are all almost near 90 degrees, far away from the Coulomb angle. These tests developed r-theta shear bands at different angles. They all developed right at failure and are shown in Figure 9.3.6. For these tests, the failure direction was radially, in the intermediate principal stress direction.

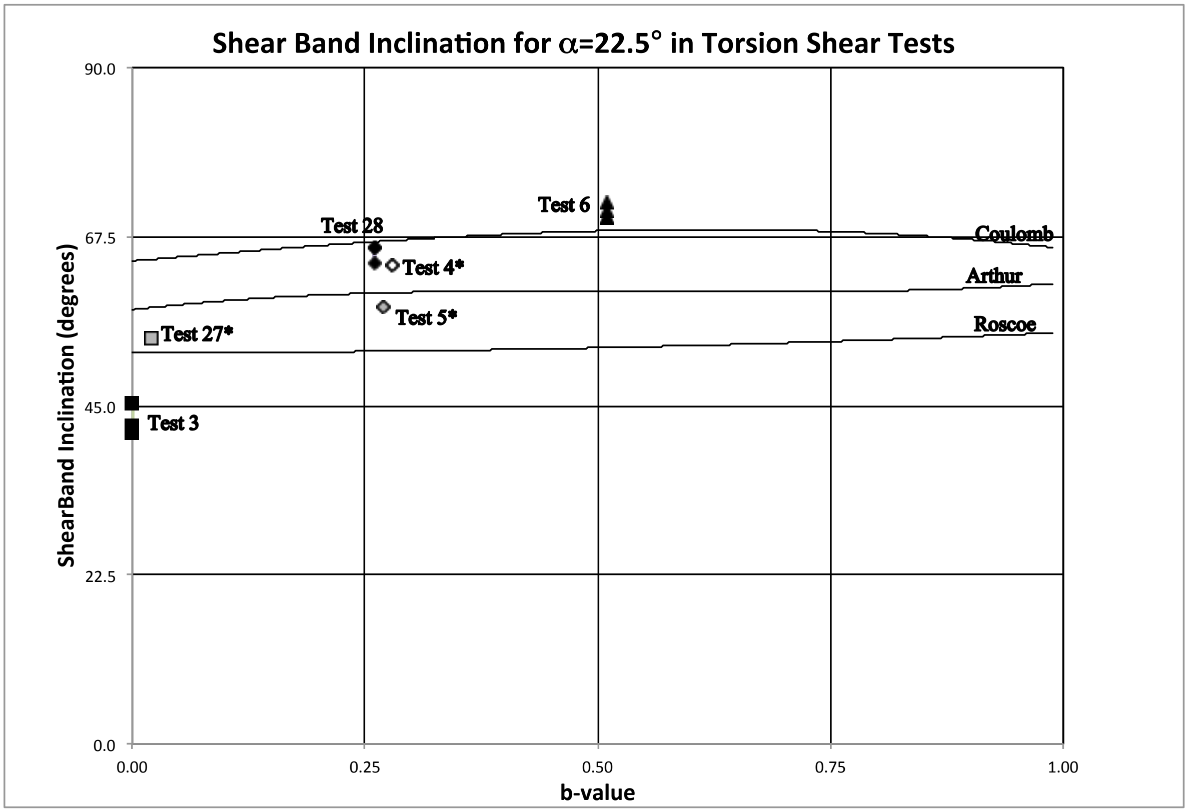

Figure 9.3.5. Shear band inclination angle for α=22.5° Torsion Shear Tests.

The stress-strain curves for α=22.5° are presented in Figure 9.3.7. In this figure, the onset of shear band development is pointed out. Tests where the b-value was less than 0.5 had shear bands that developed past failure. Tests with b=0 shear bands developed shear bands at further strain after failure than the b=0.25 tests. At b=0.5 and b<0.5, the tests show a fast decrease in strength after the shear band is developed. Once the shear band develops at these high b-values, there is no further increase in strength and the strength cannot be kept constant like that of the b=0 tests.

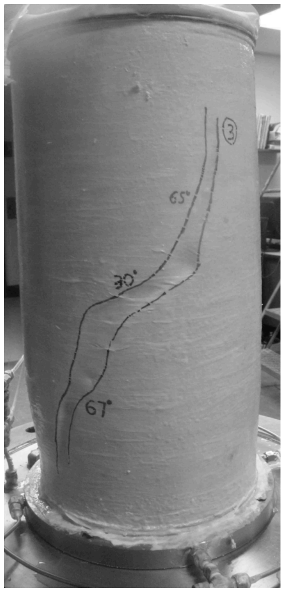

(a) Test 7* (α=24.1°, b=0.83)

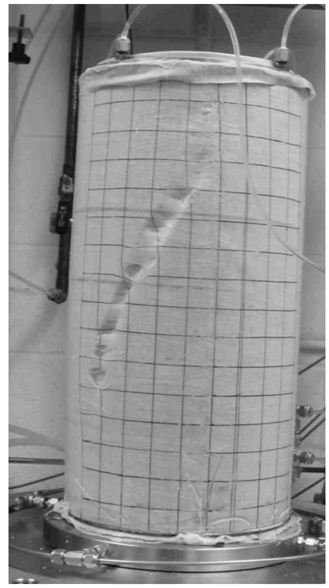
(b) Test 8 (α=22.9°, b=0.97)

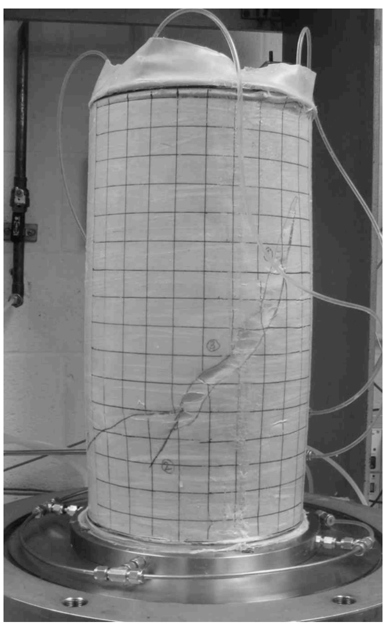
(c) Test 29 (α=22.8°, b=0.75)

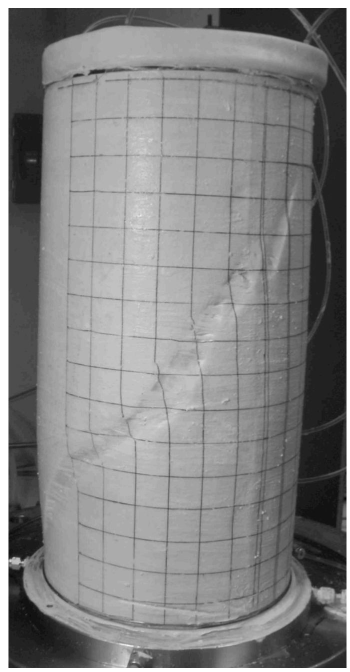
(d) Test 30* (α=22.9°, b=0.85)

Figure 9.3.6. Pictures of Shear band r-theta bands developed for Tests (a) 7*, (b) 8, (c) 29 and (d) 30*.

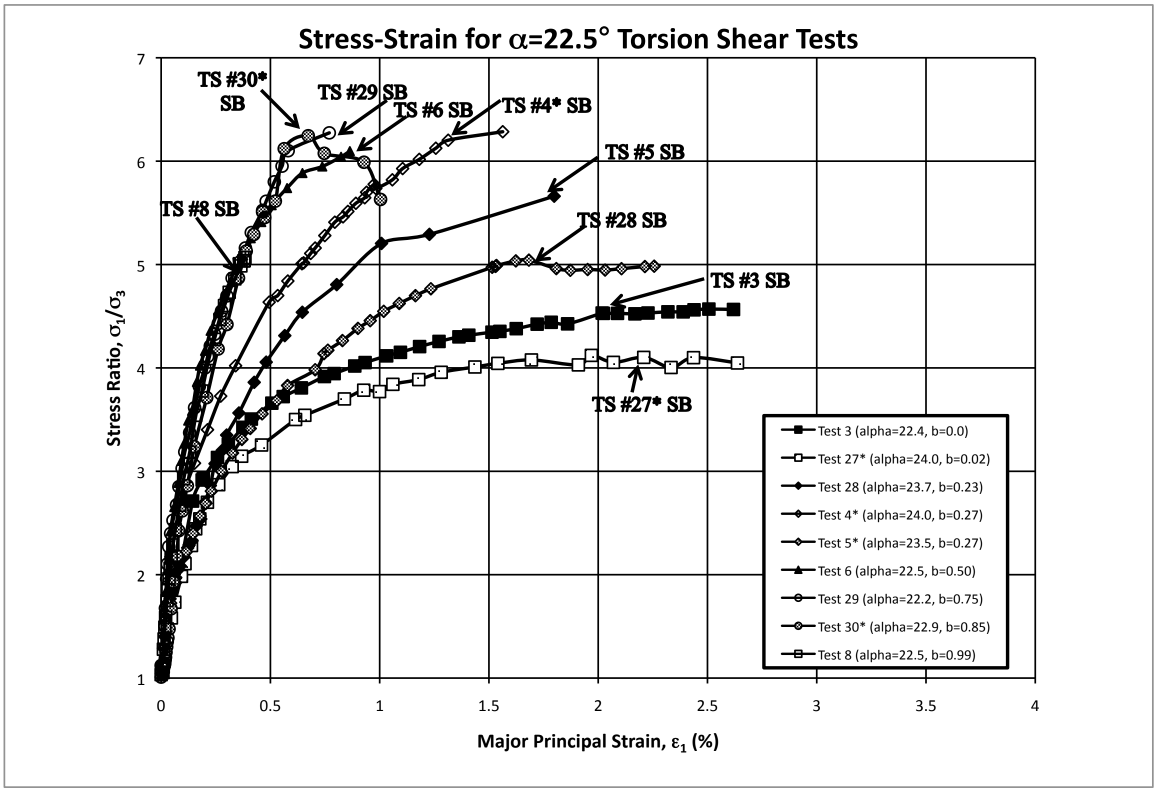

Figure 9.3.7. Stress-strain curves for α=22.5° Torsion shear tests indicating the onset of Shear band development.

Figure 9.3.8 shows the shear band inclination angles for α=45° tests. At α=45°, shear bands were all inclined but they were more horizontal than those at α=0° and α=22.5°. An example is shown in Figure 9.3.9a. With the exception of Test 32* and Test 10*, most of the shear band inclination angles follow the Coulomb prediction. It should be pointed out that Test 32* actually was at α=32° yet it is presented in the α=45° degree tests. Both of these tests had shear bands that wrapped around the entire specimen. The circular band around the specimen that formed was mostly horizontal but with a slight angle. Pictures of Test 32* and 10* are shown in Figure 9.3.9b and 9.3.9c, respectively. As can be seen in the pictures, shear bands also developed right below the top ring. This development also happened in most of the α=67.5° tests that will be described in the next section.

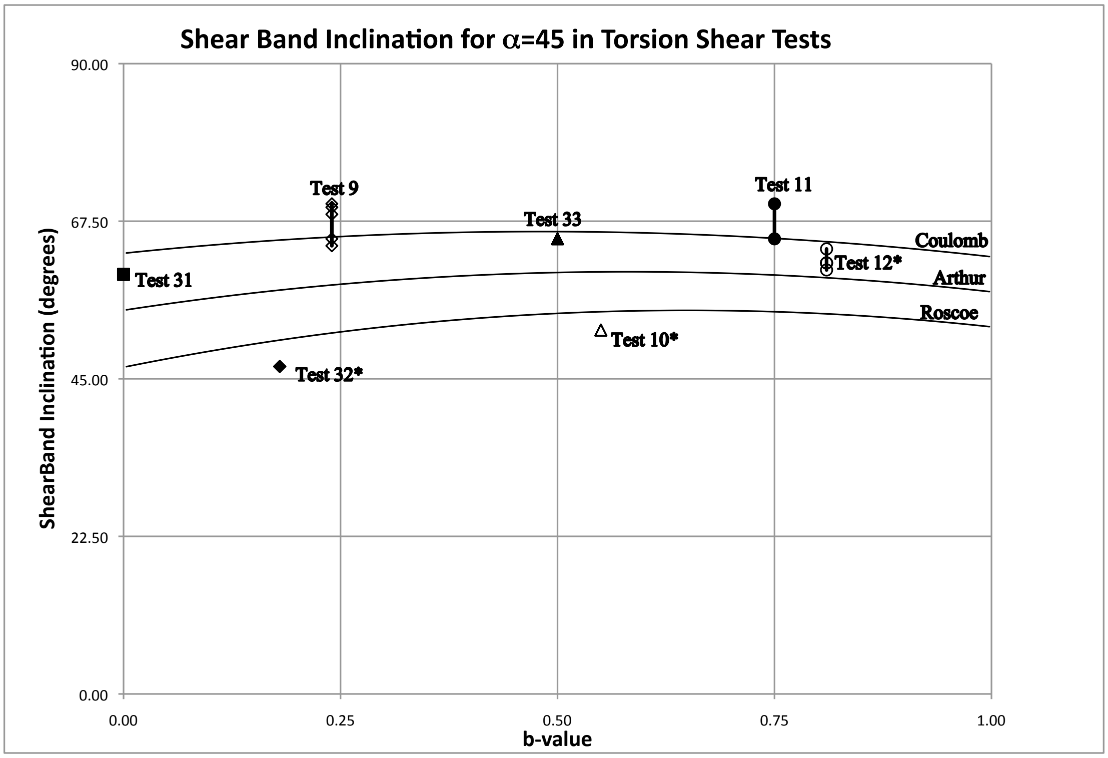

Figure 9.3.8. Shear band inclination angle for α=45° Torsion Shear Tests.

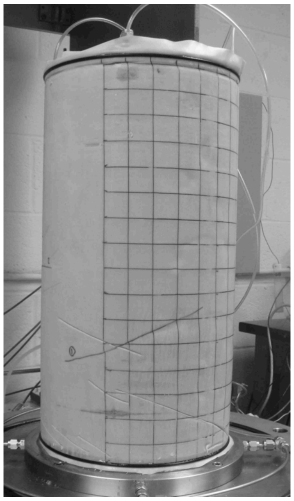

(a)Picture of shear bands of Test 11 (at top ring and body of specimen) (α=45°, b=0.75)

(b) Picture of shear bands of Test 10* (at top ring and body of specimen) (α=41.9°, b=0.55).

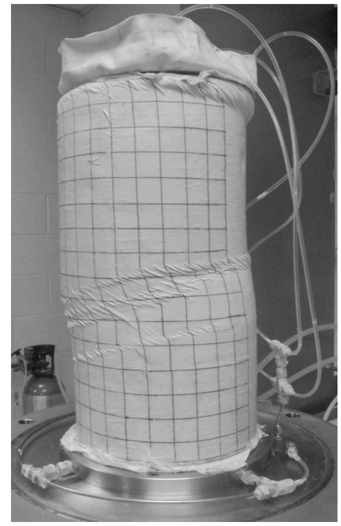

(c) Picture of shear bands of Test 32* (at top ring and body of specimen) (α=31.8°, b=0.18)

Figure 9.3.9. Examples of shear band that occurred at α=45°. (a) Test 11 shear bands are inclined and do not wrap all around specimen, except at top ring; (b) Test 10* and (c) Test 32* shear bands are more horizontal and wrap all around specimen.

The stress-strain curves are presented in Figures 9.3.10a and 9.3.10b. To avoid having too many tests in one graph, they were separated so that the shear band development location could be easily shown. The arrow for Test 31 indicates where the membrane was first seen to have kinks on the previously drawn grid. The kinks began forming well before the specimen failed. During Test 32*, shear bands near the top cap were first noticed and then secondly, parallel shear bands formed in the middle of the specimen (see Figure 9.3.9c). Test 9 had the shear bands develop right at peak failure and then after rotating the specimen more, then a shear band developed underneath the top cap. Test 33 had a shear band develop prior to reaching ultimate peak strength.

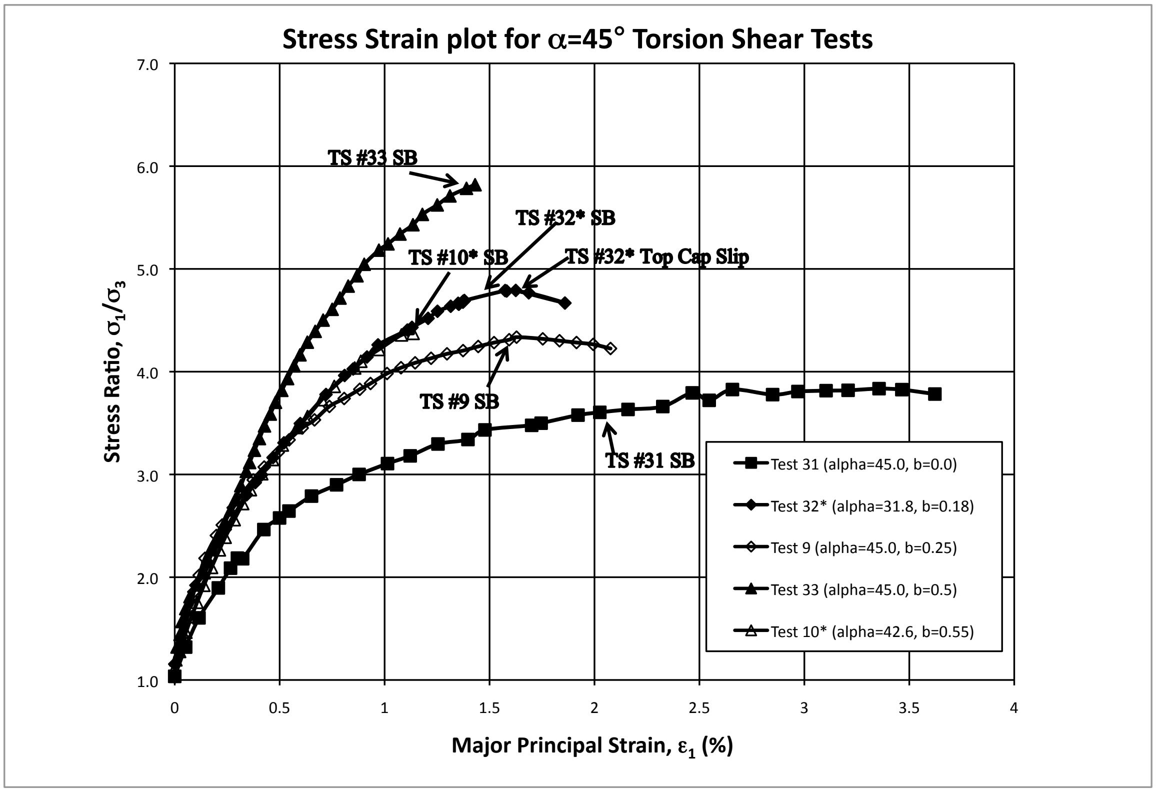

Figure 9.3.10a. Stress-strain curves for α=45° Torsion shear tests indicating the onset of Shear band development. (Tests 31, 32*, 9, 33 and 10*).

In Test 11, a shear band was seen prior to peak failure. The stress ratio dropped a little and then increased to peak failure. At peak failure, the top cap slipped, and there was a drop in strength. This is seen in Figure 9.3.10b. Test 12*'s shear band developed right after the peak stress ratio had been reached. Test 13* and Test 34 had shear bands develop quickly at failure, and were so large that an immediate stress drop was seen.

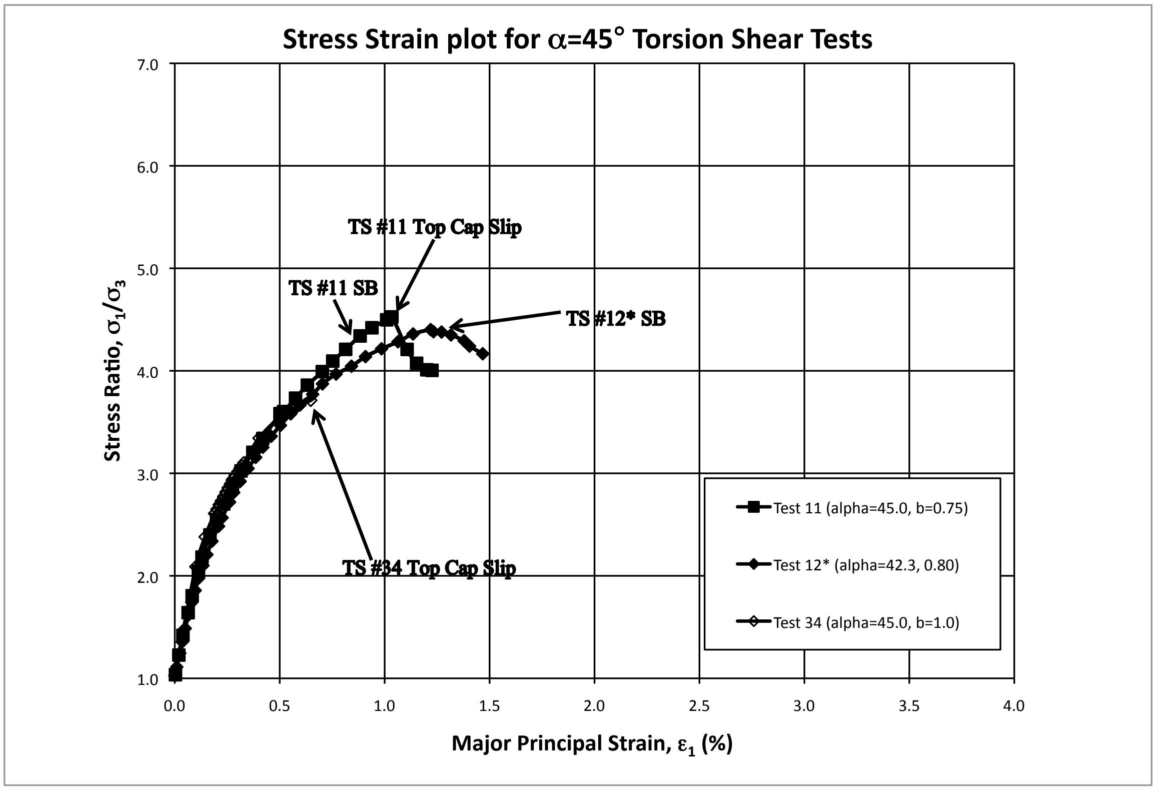

Figure 9.3.10b. Stress-strain curves for α=45° Torsion shear tests indicating the onset of Shear band development. (Tests 11, 12* and 34).

Tests with inclination angles of α=67.5° are presented in Figure 9.3.11. These angles are slightly higher than the Coulomb prediction. For all but three tests (Tests 14, 40* and 17), the shear bands developed right underneath the top cap. The bottom half of Test 14 collapsed inward at failure. This also happened for the α=90° tests at b=0. Tests 35*, 36 and 15 had shear bands develop right underneath the top cap but they were not very thick. It looked as though the top cap had slipped but further inspection showed that it was not the top cap slipping but the shear band forming right at the end restraint. Tests 16*, 37*, 38 and 39* all had deeper and thicker shear bands form underneath the top cap ring. Tests 40* and 17 had thick shear bands wrap all the way around the specimen in the shape of a ring (not underneath the top cap ring). Pictures of these different shear band patterns are shown in Figure 9.3.12.

It is important to remember that at α=67.5° tests, the friction angle/stress ratio of these tests were the lowest (see Figure 7.1.9 and 7.1.11). At 67.5°, the shear band direction is close to the bedding planes. In other words, when ω=0°, $\alpha=\alpha_{sb}$ (see Figure 9.3.1). When these two planes line up exactly, the sand grains are allowed to move easily and therefore, can create less strength in the soil.

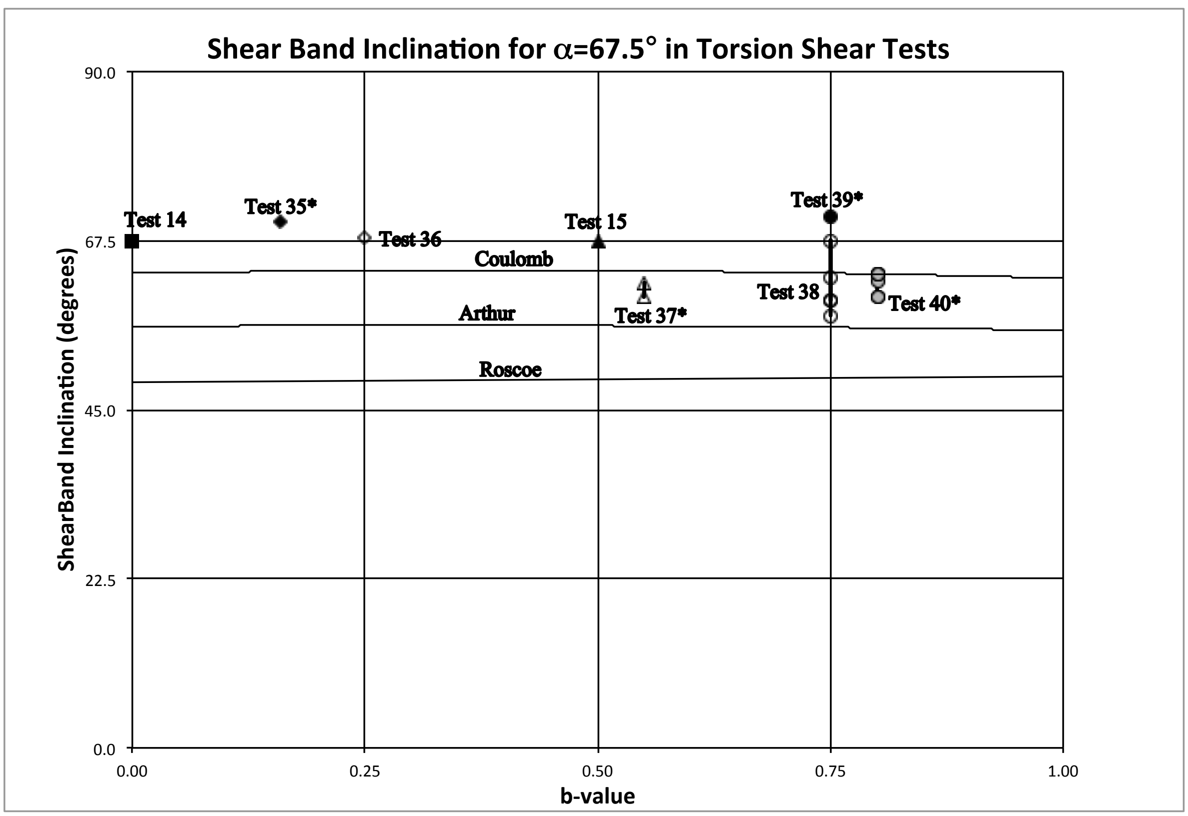

Figure 9.3.11. Shear band inclination angle for α=67.5° Torsion Shear Tests.

(a) Test 14 (α=67.5°, b=0.0)   (b) Test 37* (α=69.9°, b=0.55)   (c) Test 40* (α=73.1°, b=0.80)

Figure 9.3.12. Examples of shear band that occurred at α=67.5° . (a) Test 14 showing inward collapse at failure; (b) Test 37* showing deep top cap shear band and a thin shear band along bottom base and (c) Test 40* showing horizontal deep shear band around the entire specimen.

Figure 9.3.13a shows the stress strain behavior tests from b=0 to b=0.56 for α=67.5° tests. The first time that a shear band was physically seen is indicated as well. For these tests, shear bands occurred at different parts of the stress-strain curves. For example, Test 14’s shear band was visible at about 4% major principal strain. Failure occurred at 2.9%. Test 35* had the top cap shear band visible very near peak failure. Test 36’s shear band was seen right after peak failure, showing a significant decrease in strength once it developed. Test 15 had a top cap shear band develop at less that 1% major principal strain and then another shear band at the base of the specimen near failure. Test 37* also had a top cap shear band develop around 1% major principal strain. However, it kept increasing in strength until it failed at 1.8%.

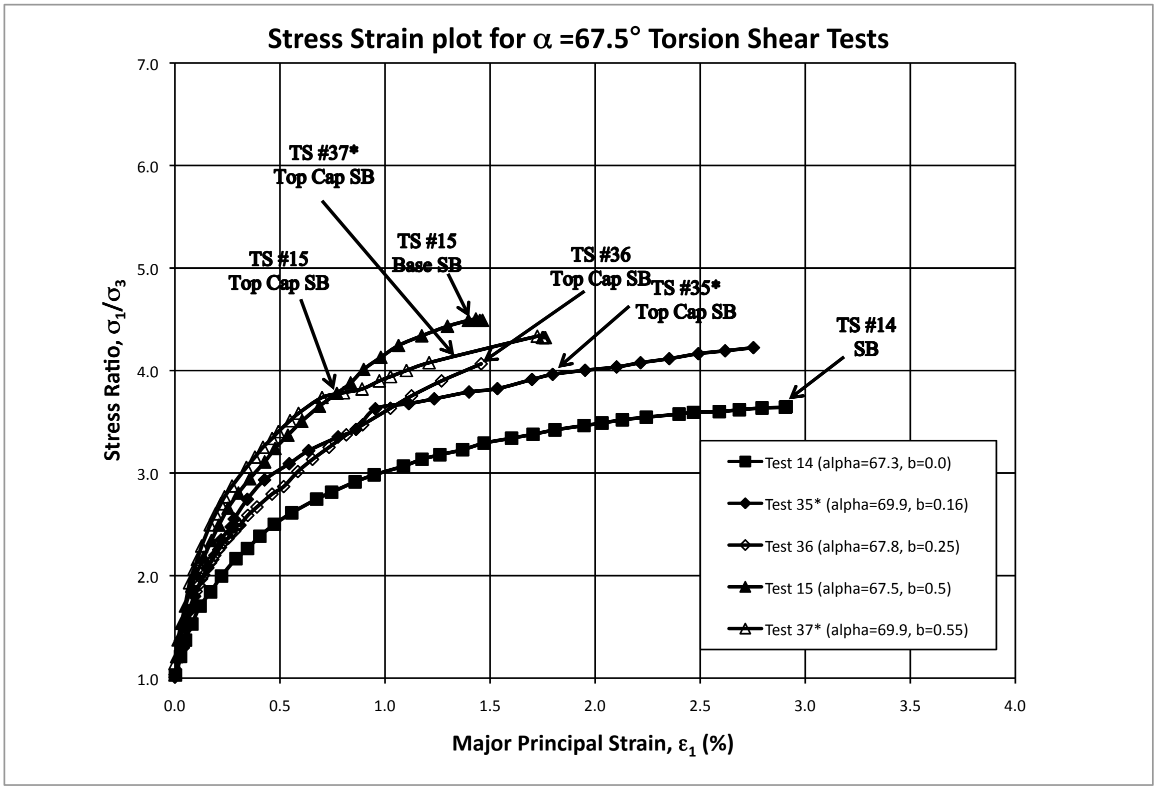

Figure 9.3.13a. Stress-strain curves for α=67.5° Torsion shear tests indicating the onset of Shear band development (Tests 14, 35*, 36, 15, and 37*).

Similarly, as seen in Figure 9.3.13b, Tests 38 and 39* had shear bands develop very close to peak failure. No increase in strength was seen after the shear band developed. Tests 17 and 40* developed right at peak failure. A drop in strength was seen for these two tests right after the shear band developed.

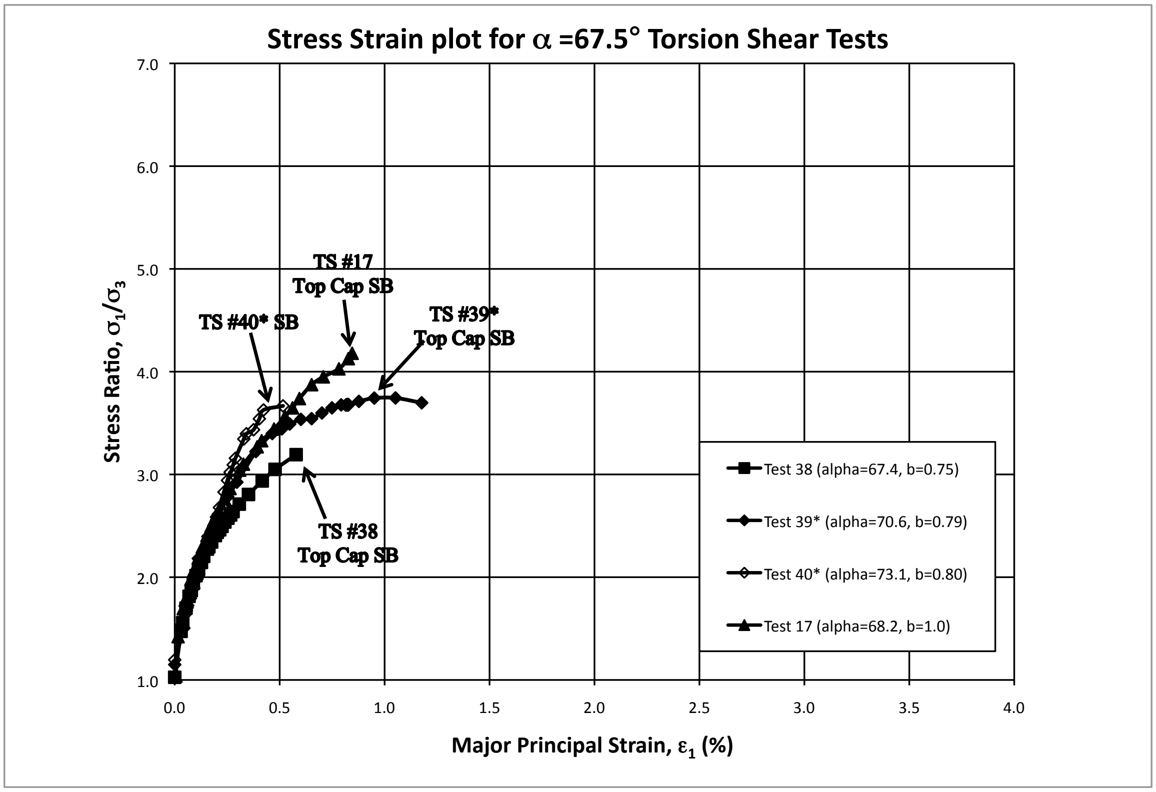

Figure 9.3.13b. Stress-strain curves for α=67.5° Torsion shear tests indicating the onset of Shear band development (Tests 38, 39*, 40, 17).

The last set of tests where α=90° follows the Coulomb prediction as well. The average angle of shear band inclination for these tests is at 67.5 degrees. Tests at α=90° showed crossed shear band patterns. For Tests 18, 19* and 41 (all at or near b=0), the specimen collapsed inward at failure. Crossed shear bands also developed coming out of the collapse (see Figure 9.3.15a). Tests 42* and 20* had shear bands criss-cross each other and wrap all the way around the specimen (see Figure 9.3.15b). Tests 21*, 43*, 44* and 22* all had deep r-theta bands (inclined for b=0.75 and almost horizontal at b=1 tests). Tests 22* and 44* had deep r-theta bands develop right underneath the top ring. For Test 22*, additional crossed shear bands developed coming out of the top cap r-theta band. (see Figure 9.3.16c). Test 21* was similar (having a top cap r-theta band) but the additional shear bands were all around the body of the specimen (Figure 9.3.16a). Test 43* had a deep shear band r-theta band where two shear bands came together (almost crossing) but became horizontal at the meeting point. All shear bands occurred right at peak ultimate strength (Figures 9.3.17a and 9.3.17b).

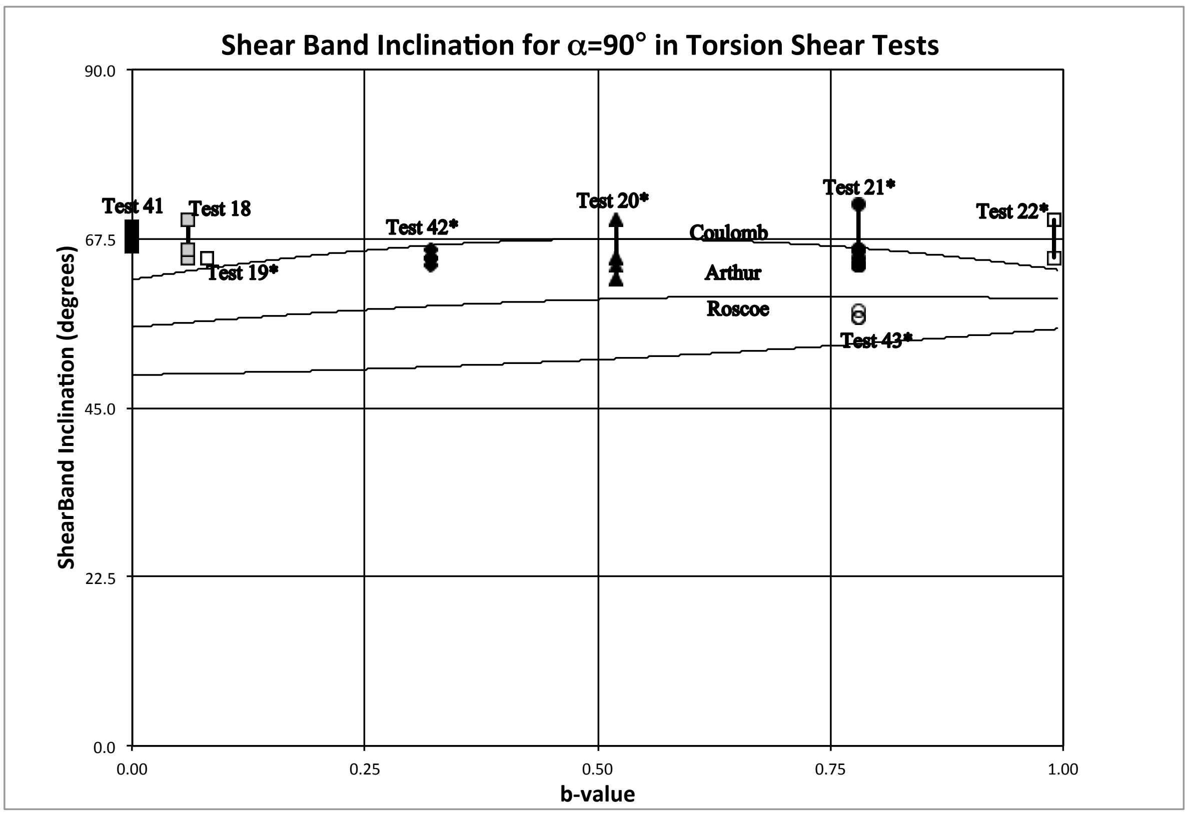

Figure 9.3.14. Shear band inclination angle for α=90° Torsion Shear Tests.

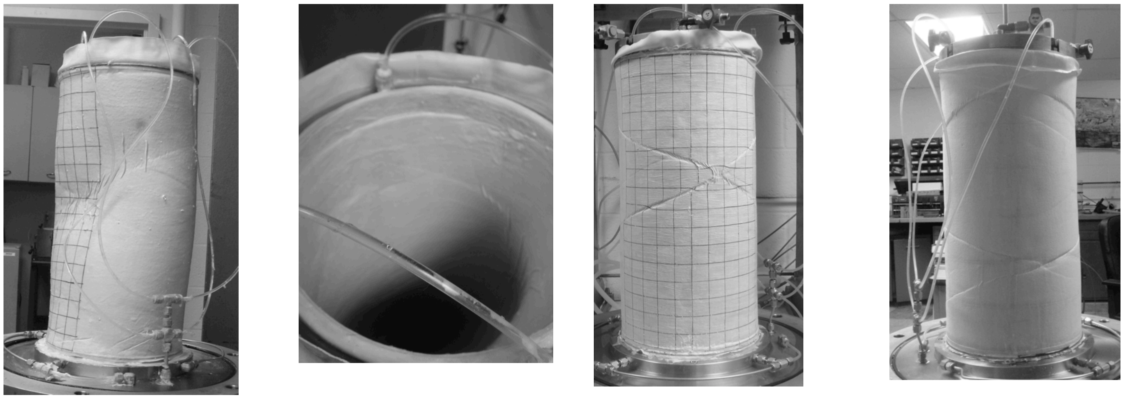

(a) Pictures of Test 18 (outside and inside) (α=90°, b=0.04)

(b) Pictures of Test 42* (front and back) (α=90°, b=0.32)

Figure 9.3.15. Examples of shear band that occurred at α=90 (low b-values). (a) Collapse and two crossing shear bands occurred at failure of Test 18 (b) crossed shear bands at front and back of Test 42*.

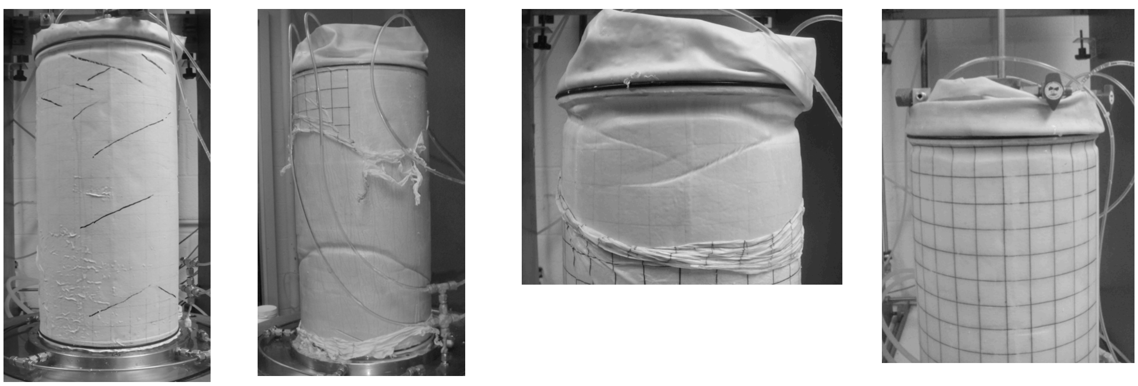

Test 21* (α=90°, b=0.78)

Test 43* (α=90°, b=0.78)

(c) Test 22* (α=90°, b=0.99)

(d) Test 44* (α=90°, b=0.99)

Figure 9.3.16. Examples of shear band that occurred at α=90 (high b-values). (a) Test 21* shows top cap r-theta shear band and smaller crossed bands across the specimen; (b) Tests 43* shows two deep slanted crossed r-theta bands gathering horizontally at front of the specimen; (c) Test 22* shows deep r-theta bands at the top cap with smaller crossed shear bands; (d) Test 44* shows a horizontal deep r-theta band at top cap.

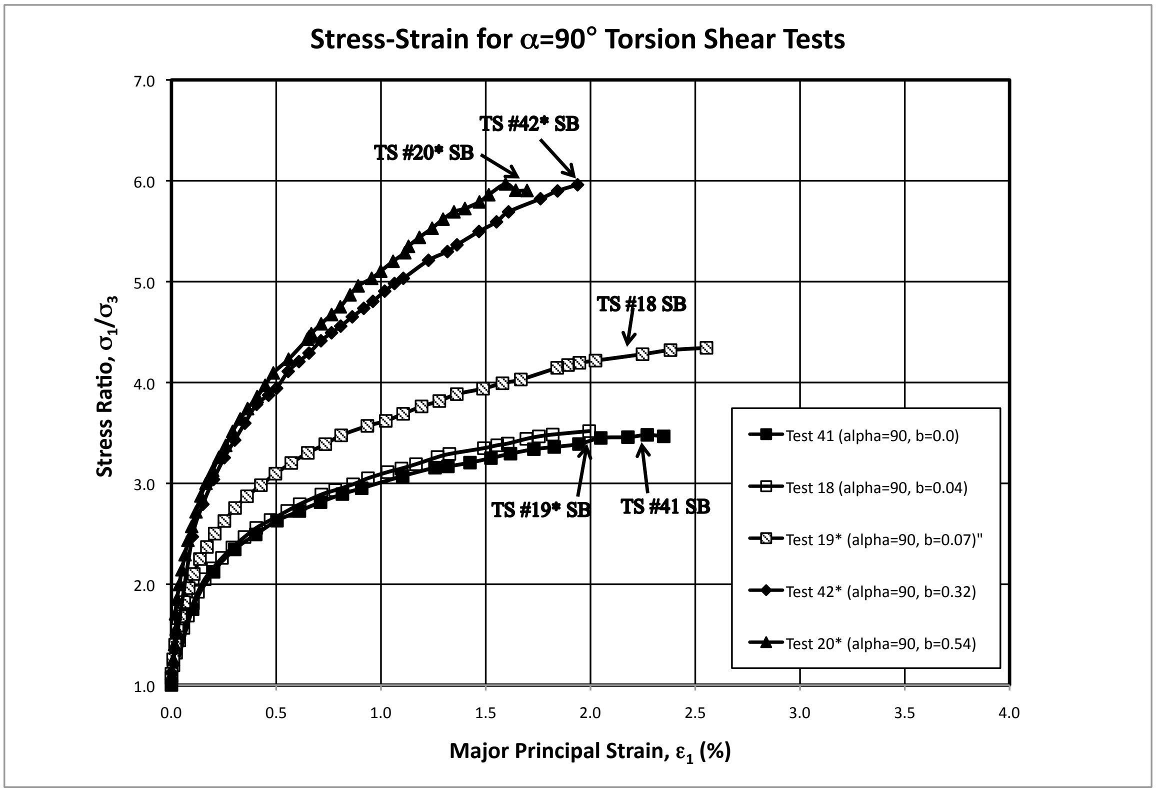

Figure 9.3.17a. Stress-strain curves for α=90° Torsion shear tests indicating the onset of Shear band development (Tests 41, 18, 19*, 42*and 20*).

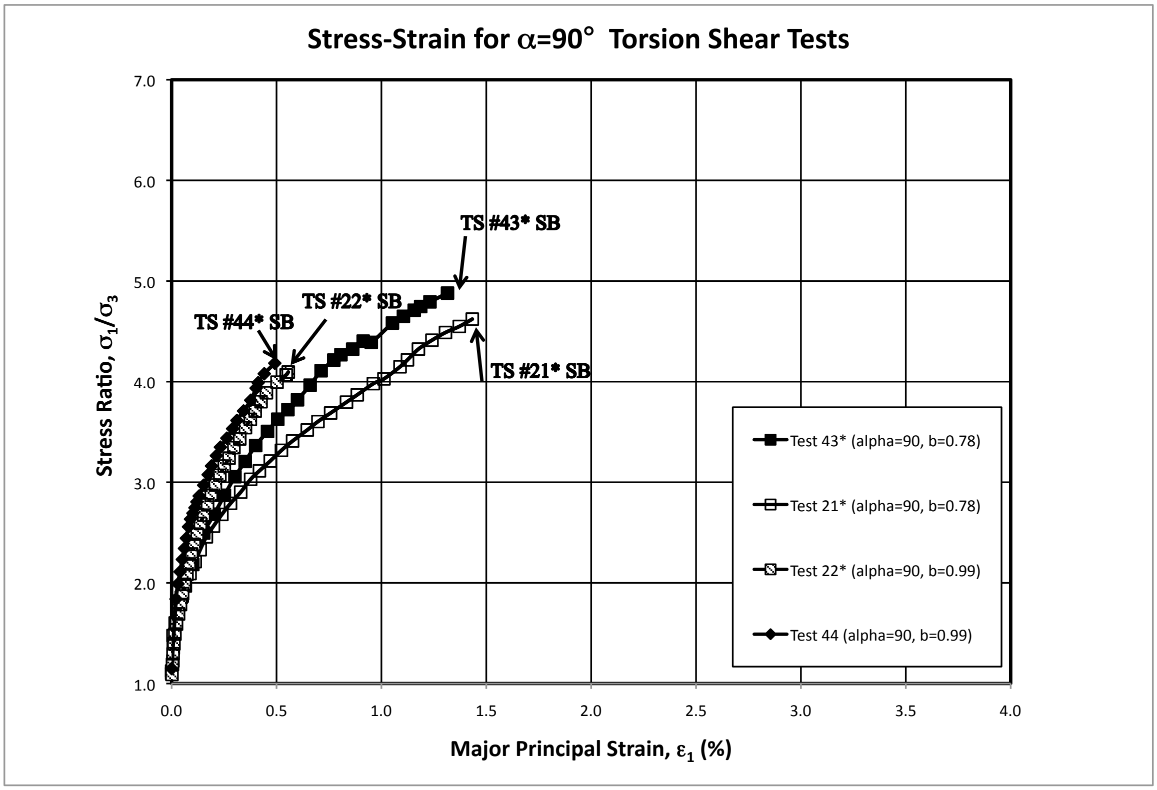

Figure 9.3.17b. Stress-strain curves for α=90° Torsion shear tests indicating the onset of Shear band development (Tests 43, 21*, 22* and 44).

9.4 Discussion of Shear Band Angles

Different shear band patterns and inclination angles have been presented for the various tests done as part of this experimental program. Triaxial and true triaxial shear bands developed well into the softening regime of the stress-strain behavior of the specimens. In triaxial tests, where b=1, shear bands developed right after peak failure showing a very quick drop in strength once developed. The shear band inclination angles for triaxial and true triaxial tests followed the Arthur shear band inclination angle prediction in most cases. Torsion shear tests had more variation in the shear band inclination angle, depending on alpha and b-values. In most cases, shear bands developed and were first seen at or near peak failure. For different alpha values, different patterns of shear band inclinations were seen in torsion shear tests. Although somewhat scattered, α=0° showed angles between Coulomb and Arthur. Alpha=22.5° spanned from Roscoe all the way up to Coulomb as the b-value increased. For α=45°, α=67.5° and α=90°, the shear band inclination angles were all near or above Coulomb's prediction.

Although Fine Nevada sand at the same relative density was tested for all tests in different apparatuses (true triaxial and torsion shear), shear bands at α=0° and α=90° were on average 7 degrees higher in torsion shear tests than in true triaxial. Shear bands were free to develop for the triaxial and true triaxial tests, with a H/D ratio was 2.5. Taking the average diameter of the torsion shear specimen, the H/D ratio was 2. Perhaps a greater H/D ratio allowed the shear bands to develop more freely and at steeper angles. Also, the thickness of the hollow torsion shear specimens was only 2cm. For true triaxial tests, it was 7.6 cm. It is speculated that specimen geometry may affect the development of shear bands. Additionally, the conditions of torsion shear and true triaxial tests were not exactly the same. Torsion shear tests were performed with constant mean stress, and true triaxial tests had constant minor principal stress.

9.5 Conditions where the intermediate stress is not the radial stress

As previously stated in Section 6.7, for torsion shear tests, the radial stress, σ_r, is assumed always to be equal to the intermediate principal stress, σ_2. For most cases in the experimental program, this was the case. However, in the original tests (torsion shear tests marked with a *), the uplift correction was not initially correctly accounted for. Therefore, what was planned to be a b=1.0 test where σ_2 was supposed to be the same as σ_1, the actual uplift pressure that had not been accounted for, created a condition where the radial stress, σ_r, was greater than the largest normal stress in the wall. Since the major principal stress is always the biggest, when this condition occurred, the radial stress (traditionally σ_2) became σ_1. This difference is important because although failure occurred in the z-θ plane, the friction angle is always calculated from the stress ratio, σ_1/σ_3. What was determined to be σ_1 will affect the friction angle.

In order to mathematically prove that there is a case where typically the radial stress can be bigger than σ_1 in the wall, the following equations were derived. It is important to note that these equations are based on the equations used in order to maintain constant b-value, alpha and mean normal stress. These were the conditions of the torsion shear experimental program prepared for this thesis.

Rearranging the intermediate stress ratio where b=1 and setting it to an inequality yields,

$$\begin{aligned}(\sigma_2 - \sigma_3) &> (\sigma_1 - \sigma_3) \\ \sigma_2 &> \sigma_1\end{aligned} \qquad \text{Eq. 9.5.1}$$

In order to see if σ_2 can be in fact be greater than σ_1, it is necessary to use the equations provided in Chapter 6. These derived expressions are in terms of force, inner and outer pressure, inner and outer radii, and moment. Therefore,

$$\frac{p_o r_o + p_i r_i}{r_o + r_i} > \frac{F_v}{2\pi(r_o^2 - r_i^2)} + \frac{2p_o r_o^2 - 2p_i r_i^2 + r_i r_o(p_i - p_o)}{2(r_o^2 - r_i^2)} + \sqrt{\left(\frac{F_v + \pi r_i r_o(p_i - p_o)}{2\pi(r_o^2 - r_i^2)}\right)^2 + \left(\frac{3M}{2\pi(r_o^3 - r_i^3)}\right)^2}$$

Eq. 9.5.2

Through some simplification and solving for force, this equation becomes:

$$F_v < \pi r_i r_o(p_i - p_o) - \frac{\left(\frac{3M(r_o^2 - r_i^2)}{2\pi(r_o^3 - r_i^3)}\right)^2}{8\pi r_i r_o(p_i - p_o)}$$ Eq. 9.5.3

In the case where the applied vertical force is less that the calculated amount with respect to inner and outer pressures, inner and outer radii and moment, the radial stress will become the major principal stress.

9.6 Effects of Radial Stress on Cross-Anisotropic Sand at high b-values

As per the conditions described in Section 9.5, for a given inner and outer pressure and moment, a certain force is needed to keep the balance where the radial and vertical stresses are equal to each other at b=1. In other words, this force is needed to sustain the assumed relationship where ($\sigma_1>\sigma_2=\sigma_r>\sigma_3$). If the vertical force needed for these conditions is less than the vertical force applied, then $\sigma_2=\sigma_r>\sigma_1$ and this may cause out of plane shear bands to occur in the r-θ direction where usually the shear occurs in the z-θ direction. Due to cross-anisotropy of the specimen, under these conditions where b-values are close to unity, shear bands were seen to develop in the r-θ plane. Due to the cross-anisotropic behavior of the specimen with all horizontal directions being weaker, the specimen shear bands may develop as seen in Figure 9.6.1. This condition may develop even if $\sigma_{1wall} > \sigma_{radial}$ due to anisotropy because σ_r is sufficiently large to cause failure in the horizontal r-direction before failure in the wall-plane.

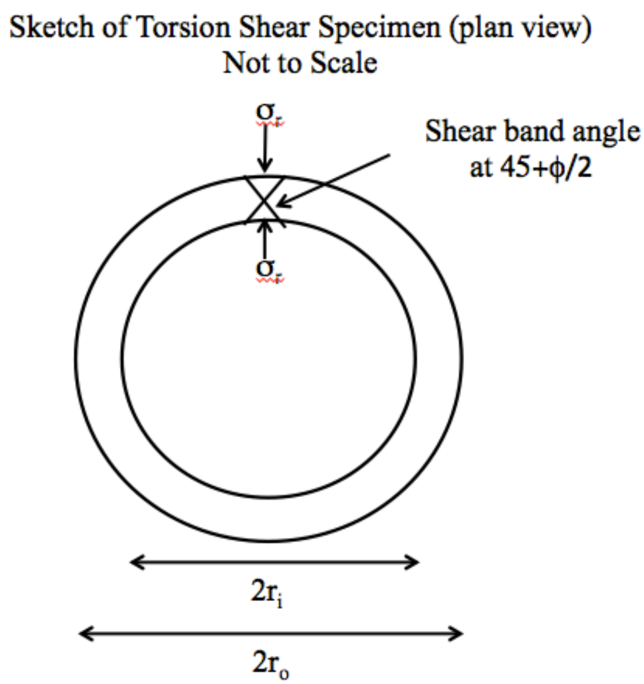

Figure 9.6.1. Schematic of Shear Band Development for high b-value tests where failure occurs in the radial direction.

In tests with b-values approaching unity, the radial stress gets closer and closer to the major principal stress (since at b=1, $\sigma_r=\sigma_2=\sigma_1$). With a cross-anisotropic material, the material will be strongest in the plane normal to the direction of deposition (the vertical plane). Therefore, if the grains are aligned in a manner where the radial stress causes the most strain, as compared to the circumferential stress causing circumferential strain, the specimen will fail in the radial direction. This was seen in some torsion shear tests. Figures 9.6.2 through 9.6.5 show sample test pictures of tests in which this shear banding pattern occurred. Table 9.3.2 lists all the tests that had this condition occur. As can be seen in the table, in all but two cases (where α=67.5° b=0.55 and α=90°, b=0.54), the r-θ shear bands occurred at b-values between 0.75 and 1.0. It is interesting to note that sometimes, more than one shear band developed. Where the shear band was very large and pronounced, usually only one large shear band in the radial direction occurred, affecting a large surface of the specimen. However, in some cases, where shear bands might have been developing before the radial failure, both types are seen, as in Test 20*.

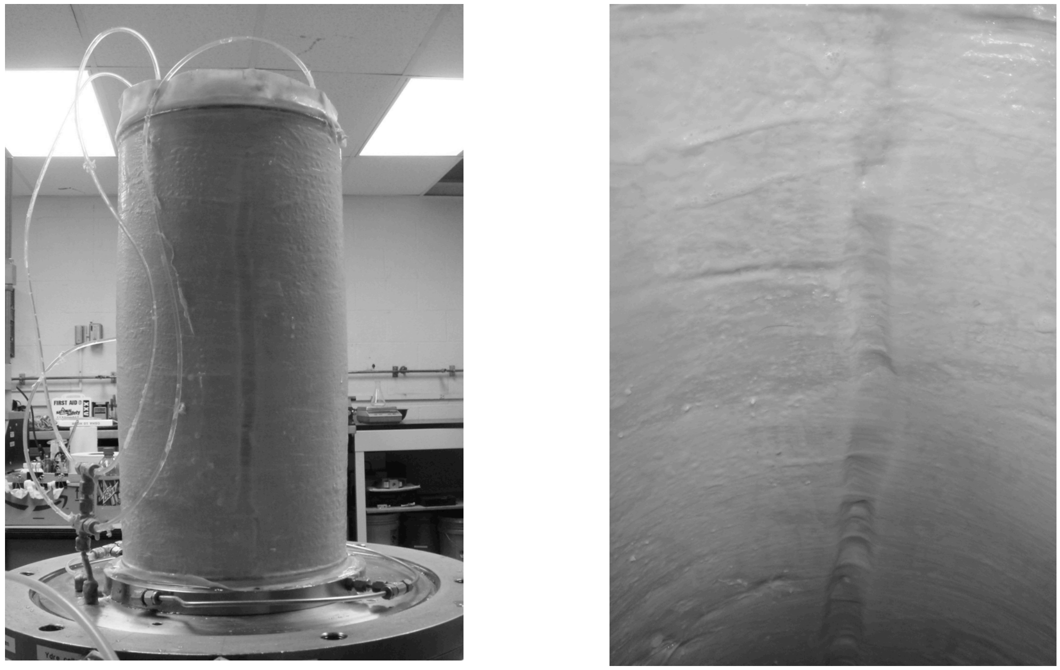

Outside and Inside of Specimen – Test 26 (α=0°, b=1)

Figure 9.6.2. Pictures of tests with Shear bands occurring in the r-θ plane for α=0° Torsion Shear Tests.

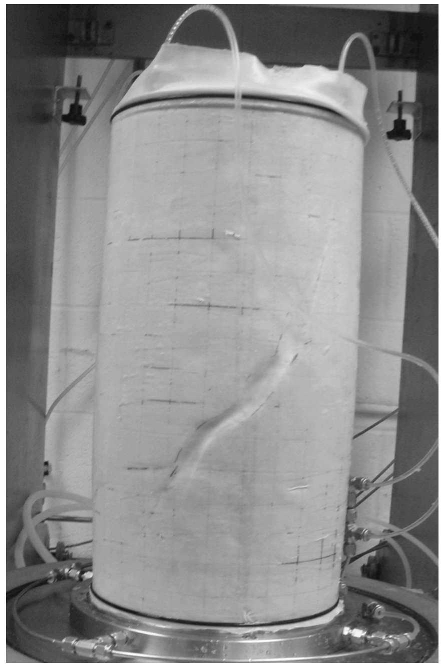

Test 29 (α=22.8°, b=0.75)– Front View

Test 29 (α=22.8°, b=0.75) – Zoomed in Lower Half

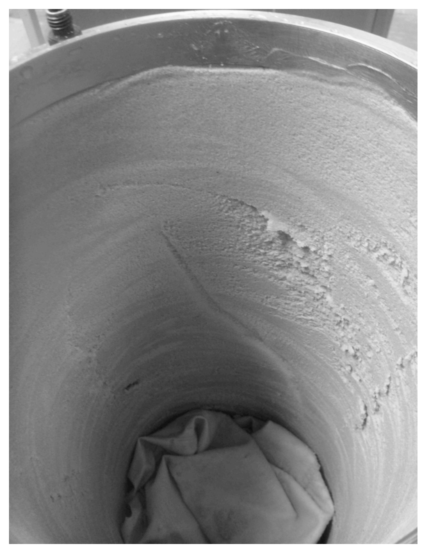

Test 29 (α=22.8°, b=0.75) – Inside w/o Membrane

Figure 9.6.3. Pictures of tests with Shear bands occurring in the r-θ plane for α=22.5° Torsion Shear Tests.

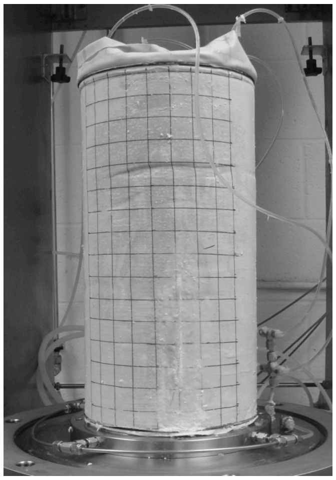

Test 17 (α=68.3°, b=1)
(Front View)

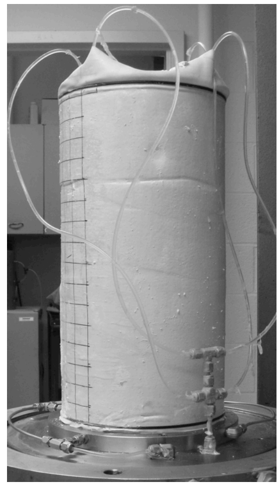

Test 17 (α=68.3°, b=1)
(Right Side View)

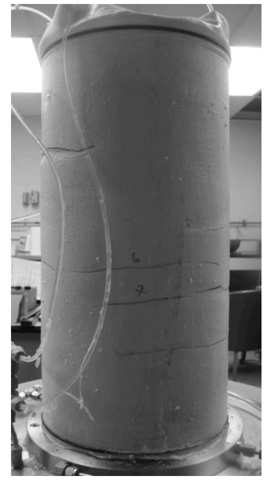

Test 17 (α=68.3°, b=1) (Back View)

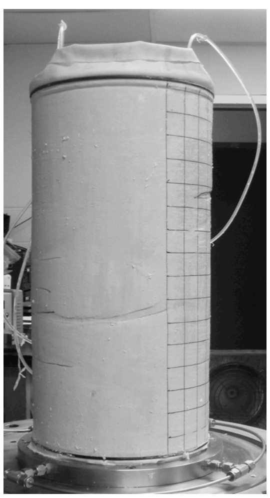

Test 17 (α=68.3°, b=1)
(Left Side View)

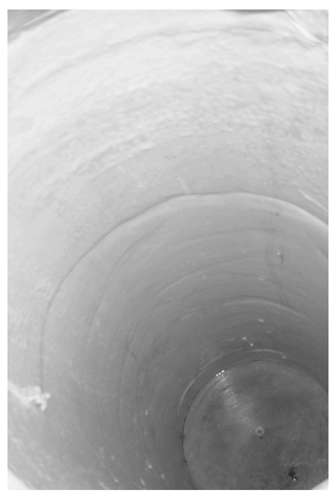

Test 17 (α=68.3°, b=1)
(Inside View)

Figure 9.6.4. Pictures of tests with Shear bands occurring in the r-θ plane for α=67.5° Torsion Shear Tests.

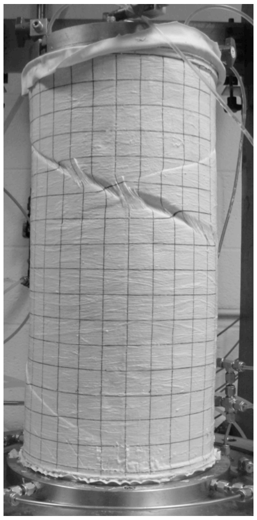

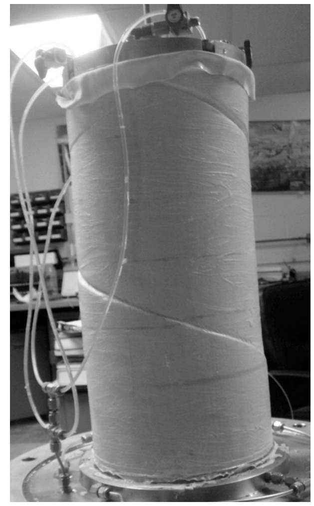

Test 20* (α=90°, b=0.54)
Front View

Test 20*(α=90°, b=0.54)
Right View

Test 20* (α=90°, b=0.54)
Back View

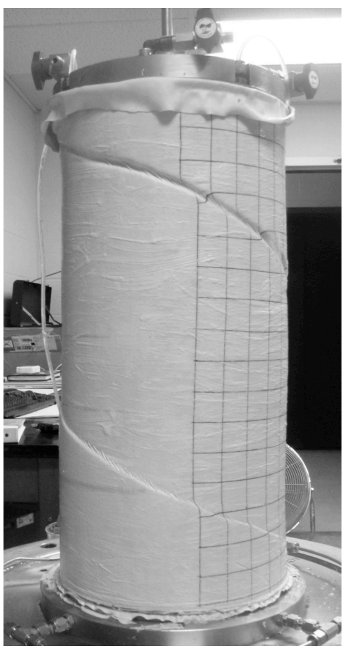

Test 20* (α=90°, b=0.54)
Front View

Test 20*(α=90°, b=0.54)
Front View w/o membrane

Test 20* (α=90°, b=0.54)
Inside view w/o membrane

Figure 9.6.5. Pictures of tests with Shear bands occurring in the r-θ plane for α=90° Torsion Shear Tests

10. Failure Criterion for Cross-Anisotropic Sand Deposits

10.1 Failure Criterion and Parameter Determination

Lade (2007, 2008) presented a general 3D failure criterion for cross-anisotropic soils (Eq. 10.1).

$$f = \left(\frac{I_1^3}{I_3} - 27\right)\left(\frac{I_1}{p_a}\right)^m = \eta_0\left[1 + \Omega_1(1 - 3l_2^2)\right] \qquad \text{Eq. 10.1}$$

where I_1 and I_3 are the first and third stress invariants, respectively and p_a is atmospheric pressure, m indicates the curvature of the failure surface in the meridian planes η_0 is the average value of the opening angle at the stress origin and Ω_1 describes the variation of this opening angle (Lade 2008). l_2 is the loading vector calculated by

$$l_2 = \sqrt{\frac{\left(\sigma_y^2 \sin^2\beta + \sigma_z^2 \cos^2\beta\right)}{\sigma_x^2 + \sigma_y^2 + \sigma_z^2}} \qquad \text{Eq. 10.2}$$

where σ_x, σ_y, and σ_z are the principal stresses.

The loading vector can also be written as a function of stress ratios for true triaxial tests where

For Sector I:

$$l_2^2 = \frac{R^2}{R^2(1+b^2) + 2R(b-b^2) + (2-2b+b^2)} \qquad \text{Eq. 10.3}$$

For Sector II:

$$l_2^2 = \frac{b^2R^2 + 2R(b - b^2) + (1 - 2b + b^2)}{R^2(1 + b^2) + 2R(b - b^2) + (2 - 2b + b^2)} \qquad \text{Eq. 10.4}$$

And for Sector III:

$$l_2^2 = \frac{1}{R^2(1 + b^2) + 2R(b - b^2) + (2 - 2b + b^2)} \qquad \text{Eq. 10.5}$$

where R is the stress ratio and b is the b-value for each test. This criterion is based on a function of stress, which has been previously used in developing a 3D failure criterion for isotropic soils. For a given situation, this function is set to a constant scalar value. This criterion may potentially be used for true triaxial tests and torsion shear tests. Three triaxial compression tests with horizontal bedding planes, and three triaxial compression tests with vertical beddings planes are needed to determine the parameters η_0, m, Ω_1. The tests described in Chapter 3 provide this information and the determined parameters will be determined in the following section. The loading directions are related to the principal directions of the cross-anisotropic microstructure of the soil by l_2 at the right hand side (Eq. 10.1). The expression for l_2^2 can be written in terms of b-values and stress ratios for all three sectors of the octahedral plane as given in Eq. 10.3 through 10.5.

As described in Lade (2007), the first step in determining the value of m, is to plot (I_1^3/I_3-27) versus (p_a/I_1) on log-log scales. Then, the best fitting line can be drawn and m can be calculated as the geometric slope of the best fitting line. The intercept of the line with p_a/I_1=1 is η_{1v}. It is assumed that the curvature for both the horizontal and the vertical specimens are the same and therefore, they both have the same m parameter. Therefore, a parallel line can be drawn through a point for the Sector III tests and η_{1h} can be determined. Table 10.1.1 summarizes the data used from Tests 1-8 (presented in Section 3.3). Figure 10.1.1 shows the points plotted in the log-log diagram. Torsion shear results are also presented in this figure to show a comparison between the two sets of tests. Torsion shear tests were all performed at p_a/I_1=0.33. As can be seen, the torsion shear results are below the true triaxial tests. Since all torsion shear tests had constant mean confining stress, the value of m determined from the true triaxial tests was used for the torsion shear tests.

Table 10.1.1. Data used in determination of parameter, m from Tests 1-8.

Test No.	**α**	**σ_1**	**σ_3**	**I_1**	**I_3**	**(I_1^3/I_3)-27**	**p_a/I_1**
1, TT#1	0	264.21	50.00	364.21	660525.00	46.14	0.28
2	0	157.18	25.00	207.18	98237.50	63.52	0.49
3	0	593.90	130.00	853.90	10036910.00	35.03	0.12
4	0	339.07	70.00	479.07	1661426.24	39.18	0.21
5	90	111.88	25.00	161.82	69886.18	33.63	0.62
6	90	317.88	75.00	467.89	1788126.68	30.28	0.22
7	90	521.37	130.00	781.37	8811153.00	27.14	0.13
8(TT#13)	90	206.51	50.00	306.51	516282.38	28.78	0.33

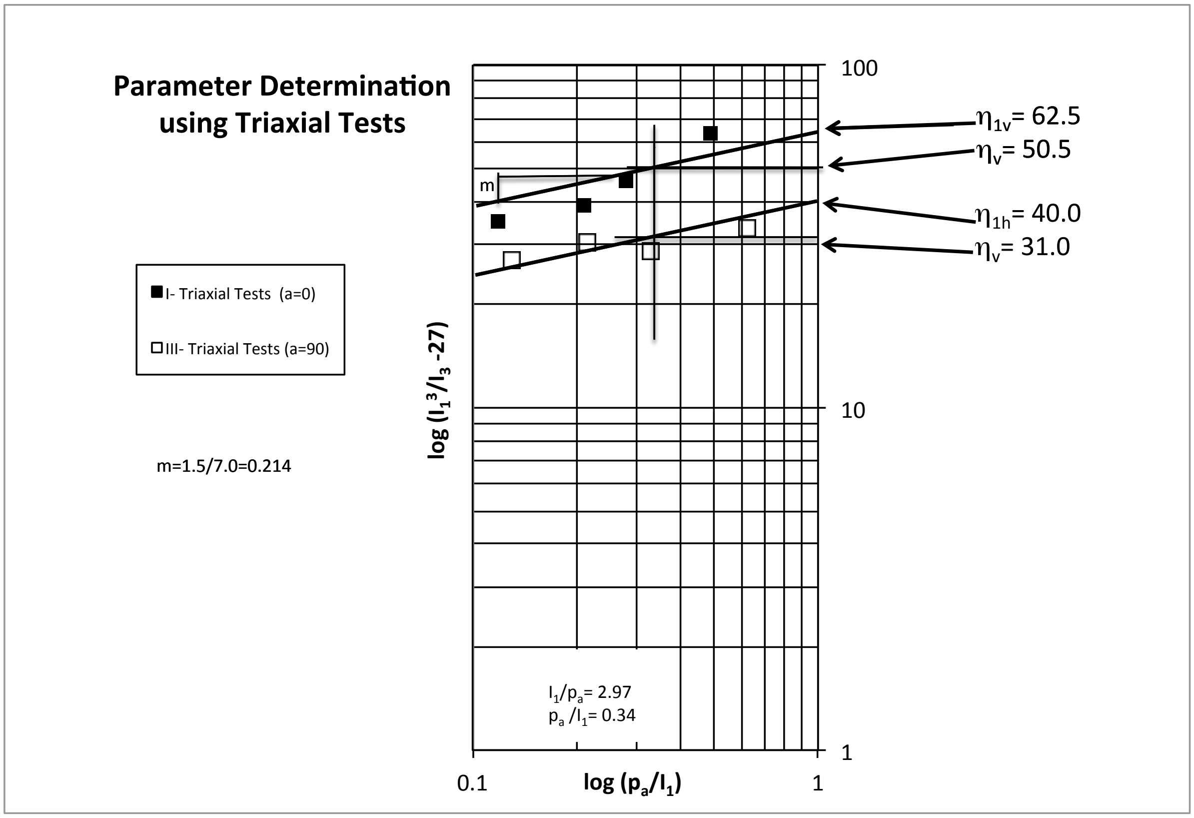

Figure 10.1.1. Log-log plot to determine parameters, m, η_{1v} and η_{1h}.

In order to obtain η_0 and Ω_1 corresponding to the range in which the stresses in the experimental program were performed, parameters were determined at I_1/p_a=2.97 rather than I_1/p_a=1.0. In order to find η_0 and Ω_1, $\eta_{1h,}$ η_h, η_{1v} and η_v need to be found. These numbers are shown on Figure 10.1.1. By solving two linear equations based on the right hand side of Eq. 10.1 and knowing the l_2, which is determined from Eq. 10.3 and 10.5, the parameters can be determined. To solve for l_2 a cubical equation based on the left hand side of Eq. 10.1 is used to determine the stress ratio. This expression is written as follows:

$$\frac{I_1^3}{I_3} - 27 = \frac{(\sigma_1 + 2\sigma_3)^3}{\sigma_1 \cdot \sigma_3^2} - 27 = \frac{(R+2)^3}{R} - 27 = \eta \qquad \text{Eq. 10.6}$$

where I_1 and I_3 are the first and third stress invariants, respectively. σ_1, σ_2 and σ_3 are principal stresses and R is the stress ratio. The values R_v and R_h are obtained from Eq. 10.6 and then substituted into Eq. 10.3 and 10.5. With two equations and two unknowns, the equations can be solved simultaneously so that η_0 and Ω_1 can be determined. η_0 and Ω_1 are found to be 37.229 and -0.196, respectively. At I_1=300 kPa there is a difference of 5.3° in triaxial compression tests on specimens with α=0° and α=90°. Lade and Wasif (1988) observed a 5.5°difference in tests with Cambria sand for α=0° and α=90°.

10.2 Pietrusczack Model based on Torsion Shear Results

Lade's model, which was used in section 10.1, was based on the developments by Pietruszczak and Mroz (2000, 2001). This model was recently expanded by Pietruszack (2011) by using higher order terms and multipliers in the equation. The approach defined the failure criterion in terms of traction components that acted on a physical plane. A spatial distribution of strength parameters and the direction of the physical plane can be solved for by using a constrained optimization technique. This involves searching for the orientation that maximizes the value of the failure function being used. His equations have been slightly modified in order to be consistent with Lade (2007) (see Equation 10.6).

$$\eta_f = \eta_0\left[1 + \Omega_1(1 - 3l_2^2) + a_1\left(\Omega_1(1 - 3l_2^2)\right)^2 + a_2\left(\Omega_1(1 - 3l_2^2)\right)^3 + a_3\left(\Omega_1(1 - 3l_2^2)\right)^4 + \ldots\right] \quad \text{Eq. 10.6}$$

In order to solve for the unknowns, η_0, Ω_1, a_1, a_2, and a_3 (for a fourth order equation), 25 torsion shear test results were used. These parameters were determined using the Least Squares Method (Chapra and Canale 2010) and were performed for different orders of Eq. 11.6. The results are presented in Table 11.2.1. Depending on which order equation is desired, the parameters will change. It is important to do an independent Least Squares based Polynomial Regression (see Appendix K) for each desired order to get the correct parameters. The only parameter needed from the triaxial test results (Figure 10.1.1) is the geometric slope, m. The other terms are determined when solving the optimization problem.

The η_f values that are calculated are shown in Table 10.2.2. As can be seen, there is not much difference in the predicted η_f value when looking at the third and fourth order iteration.

Table 10.2.1. Determined Parameters using 25 Torsion Shear Test results based on Pietrusczack (2011) model.

4^{th} Order Equation	
η_o	30.131
Ω_1	-1.080
a_1	0.186
a_2	-0.680
a_3	0.196
3^{th} Order Equation	
η_o=	29.046
Ω_1=	-0.827
a_1	0.703
a_2	-0.846

2^{th} Order Equation	
η_o	34.792
Ω_1	-0.327
a_1	-0.171
1^{th} Order Equation	
η_o	34.368
Ω_1	-0.321
0^{th} Order Equation	
η_o	35.789

Table 10.2.2. Calculated η_f values for different order equations using 25 Torsion Shear Test results based on Pietrusczack (2011) model.

Order of Equation			0	1	2	3	4
Test	**b-**	**alpha**	η_f	η_f	η_f	η_f	η_f
23	0.00	0.00	35.789	53.838	52.878	38.505	43.782
24*	0.27	0.00	35.789	51.362	50.797	48.365	46.539
25*	0.55	0.00	35.789	47.512	47.436	53.975	50.669
2	0.75	0.00	35.789	43.971	44.207	51.368	50.985
26	1.00	0.00	35.789	39.852	40.287	42.730	45.243
3	0.00	22.41	35.789	49.332	49.044	52.624	49.002
28	0.23	23.69	35.789	47.093	47.061	53.997	50.932
6	0.50	22.48	35.789	44.134	44.358	51.610	51.074
29	0.75	22.21	35.789	40.558	40.971	44.466	46.684
8	0.99	22.47	35.789	37.421	37.890	36.469	39.138
31	0.02	44.71	35.789	38.950	39.404	40.435	43.163
9	0.25	44.98	35.789	37.528	37.997	36.746	39.437
33	0.50	44.99	35.789	35.796	36.253	32.358	34.399
11	0.75	44.98	35.789	33.591	33.988	27.428	27.880
34	1.00	44.95	35.789	31.924	32.242	24.560	23.542
14	0.00	67.33	35.789	29.457	29.604	22.346	19.534
36	0.25	67.80	35.789	28.486	28.550	22.315	19.203
15	0.50	67.47	35.789	27.719	27.709	22.685	19.609
38	0.75	67.42	35.789	27.597	27.574	22.778	19.734
17	1.00	68.21	35.789	26.325	26.165	24.344	22.162
41	0.00	90.00	35.789	25.685	25.450	25.569	24.247
42*	0.32	90.00	35.789	24.129	23.693	29.896	32.174
20*	0.54	90.00	35.789	24.010	23.557	30.313	32.970
43*	0.78	90.00	35.789	24.174	23.744	29.743	31.882
22*	0.99	90.00	35.789	24.315	23.903	29.276	30.999

In order to compare the predictions to the attained experimental results, friction angles were calculated by using Eq. 10.1 and setting the calculated η_f =f in the equation. This equation can be solved in terms of b-value and the various η_0 constants in the following manner:

$$\left.\begin{aligned}
&f = \left(\frac{I_1^3}{I_3} - 27\right)\left(\frac{I_1}{p_a}\right)^m = \eta_f \\
&\left(\frac{I_1^3}{I_3} - 27\right) = \frac{\eta_f}{\left(\frac{I_1}{p_a}\right)^m} \\
&\frac{I_1^3}{I_3} = \frac{\eta_f}{\left(\frac{I_1}{p_a}\right)^m} + 27 = K
\end{aligned}\right\} \qquad \text{Eq. 10.7}$$

This can be written in terms of stresses by:

$$\begin{aligned}
&(\sigma_1 + \sigma_2 + \sigma_3)^3 = K(\sigma_1 * \sigma_2 * \sigma_3) = K\left(\sigma_1 * \left(b(\sigma_1 - \sigma_3) + \sigma_3\right) * \sigma_3\right) \\
&\textit{where} \\
&b = \frac{(\sigma_2 - \sigma_3)}{(\sigma_1 - \sigma_3)}
\end{aligned}$$

The stress ratio can then be determined by:

$$\left.\begin{aligned}
&\frac{\sigma_1}{\sigma_3} = \frac{(\sigma_1 + \sigma_2 + \sigma_3)^3}{\sigma_3^2(b(\sigma_1 - \sigma_3) + \sigma_3) * K} \\
&\frac{\sigma_1}{\sigma_3} = \frac{\left[\sigma_1 + (b(\sigma_1 - \sigma_3) + \sigma_3) + \sigma_3\right]^3}{\sigma_3^2(b(\sigma_1 - \sigma_3) + \sigma_3) * K} \\
&\frac{\sigma_1}{\sigma_3} = \frac{\left[\frac{\sigma_1}{\sigma_3} + \left(b\left(\frac{\sigma_1}{\sigma_3} - 1\right) + 1\right) + 1\right]^3}{\left(b\left(\frac{\sigma_1}{\sigma_3} - 1\right) + 1\right) * K}
\end{aligned}\right\} \qquad \text{Eq. 10.8}$$

This equation can be solved by solving for the cubical equation

$$0 = \left(\frac{\sigma_1}{\sigma_3} + b\left(\frac{\sigma_1}{\sigma_3} - 1\right) + 2\right)^3 - K\left(\frac{\sigma_1}{\sigma_3}\right)\left(b\left(\frac{\sigma_1}{\sigma_3} - 1\right) + 1\right) \qquad \text{Eq. 10.9}$$

With the procedure described above, the following results were attained from the η_f values calculated. In the η_f values presented above, the second order function is far away from the calculated η_f values using Lade's isotropic criterion. The third and fourth order functions are almost exactly the same. It is possible to say that a third order function provides a sufficient simulation. The calculated friction angles for the corresponding order equations and experimental results are presented in Table 10.2.3 and Figures 10.2.1 through 10.2.5. A 3D graph of the experimental and the predicted friction angles is presented in Figure 10.2.6.

Table 10.2.3. Calculated ϕ values for different order equations using 25 Torsion Shear Test results based on Pietrusczack (2011) model.

Test No.	b-value	alpha	ϕ (0thOrder)	ϕ (1thOrder)	ϕ (2thOrder)	ϕ (3thOrder)	ϕ (Results)
23	0.00	0.00	37.430	42.092	41.889	38.269	39.739
24*	0.27	0.00	44.366	49.473	49.318	48.628	48.086
25*	0.55	0.00	45.661	49.698	49.675	51.490	50.605
2	0.75	0.00	44.810	47.764	47.841	49.977	49.871
26	1.00	0.00	42.972	44.534	44.692	45.548	46.377
3	0.00	22.41	37.430	41.101	41.034	41.834	41.024
28	0.23	23.69	43.777	47.636	47.626	49.546	48.732
6	0.50	22.48	45.699	48.691	48.763	50.901	50.754
29	0.75	22.21	44.785	46.582	46.728	47.900	48.595
8	0.99	22.47	43.030	43.677	43.858	43.303	44.329
31	0.02	44.71	37.984	38.979	39.115	39.419	40.186
9	0.25	44.98	43.990	44.660	44.835	44.363	45.360
33	0.50	44.99	45.699	45.702	45.883	44.256	45.131
11	0.75	44.98	44.828	43.918	44.086	41.017	41.250
34	1.00	44.95	42.946	41.291	41.435	37.545	36.950
14	0.00	67.33	37.430	35.201	35.258	32.079	30.587
36	0.25	67.80	43.970	40.764	40.795	37.392	35.366
15	0.50	67.47	45.699	42.045	42.039	39.208	37.180
38	0.75	67.42	44.825	41.101	41.089	38.389	36.399
17	1.00	68.21	42.932	38.512	38.426	37.406	36.093
41	0.00	90.00	37.430	33.645	33.541	33.594	32.994
42*	0.32	90.00	44.954	39.366	39.110	42.390	43.435
20*	0.54	90.00	45.668	39.976	39.708	43.290	44.493
43*	0.78	90.00	44.647	39.045	38.792	41.990	42.986
22*	0.99	90.00	42.988	37.445	37.205	40.086	40.909

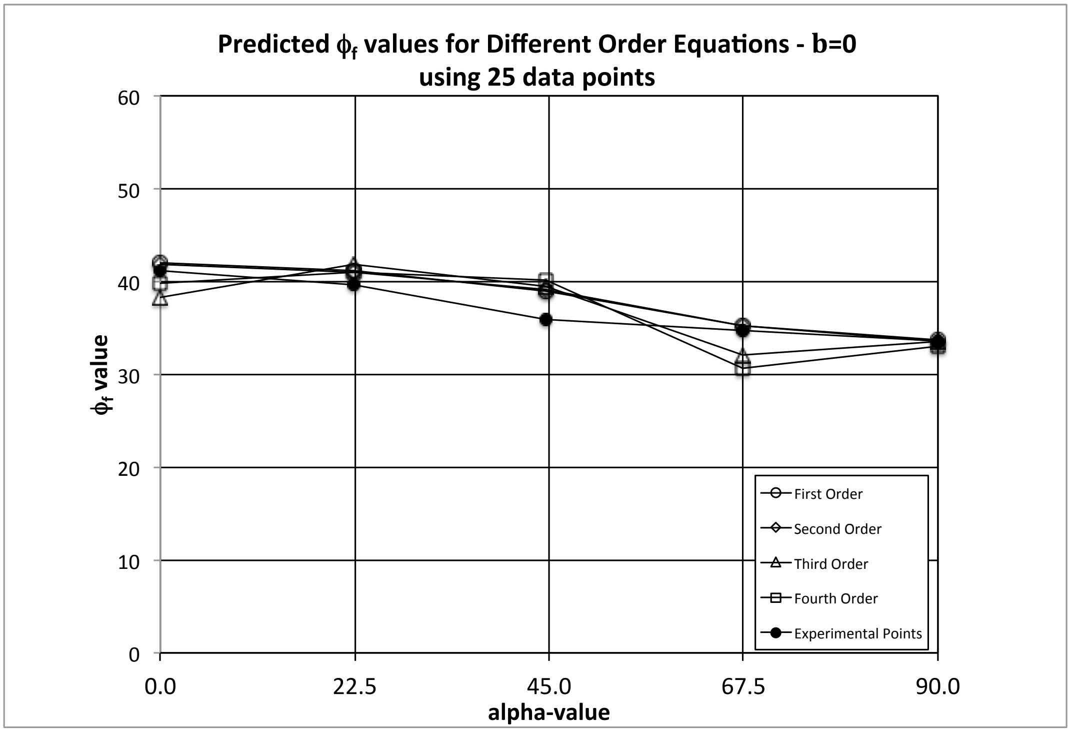

Figure 10.2.1. Predicted friction angle results for different order equations for torsion shear tests at b=0.

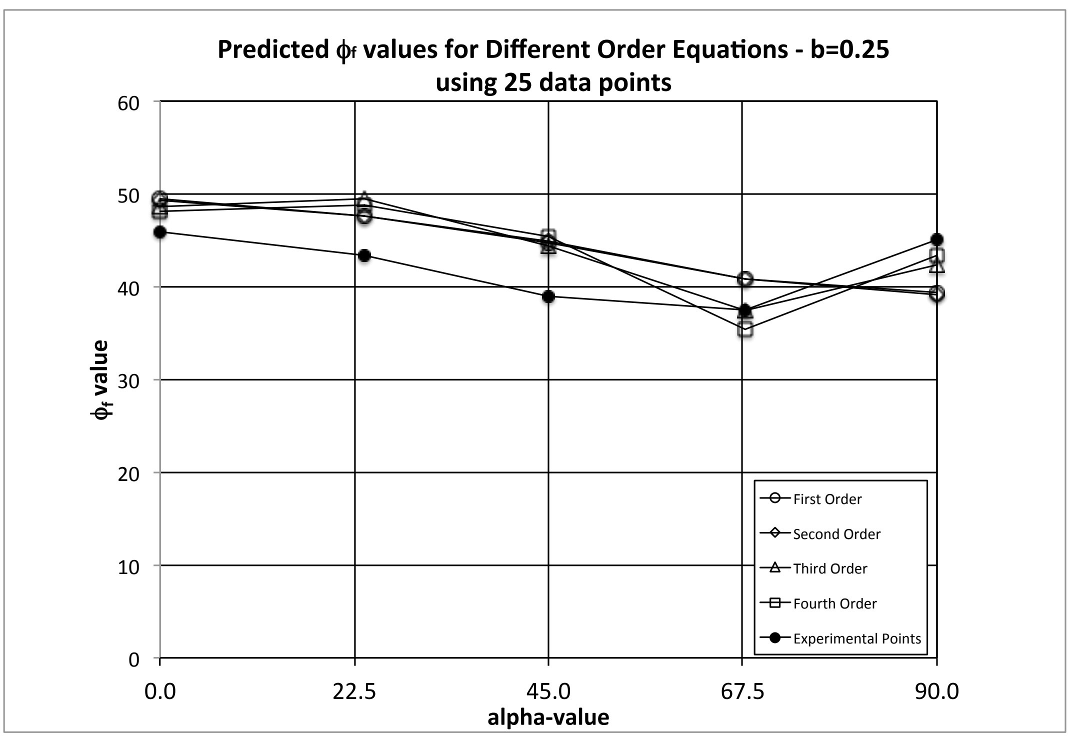

Figure 10.2.2. Predicted friction angle results for different order equations for torsion shear tests at b=0.25.

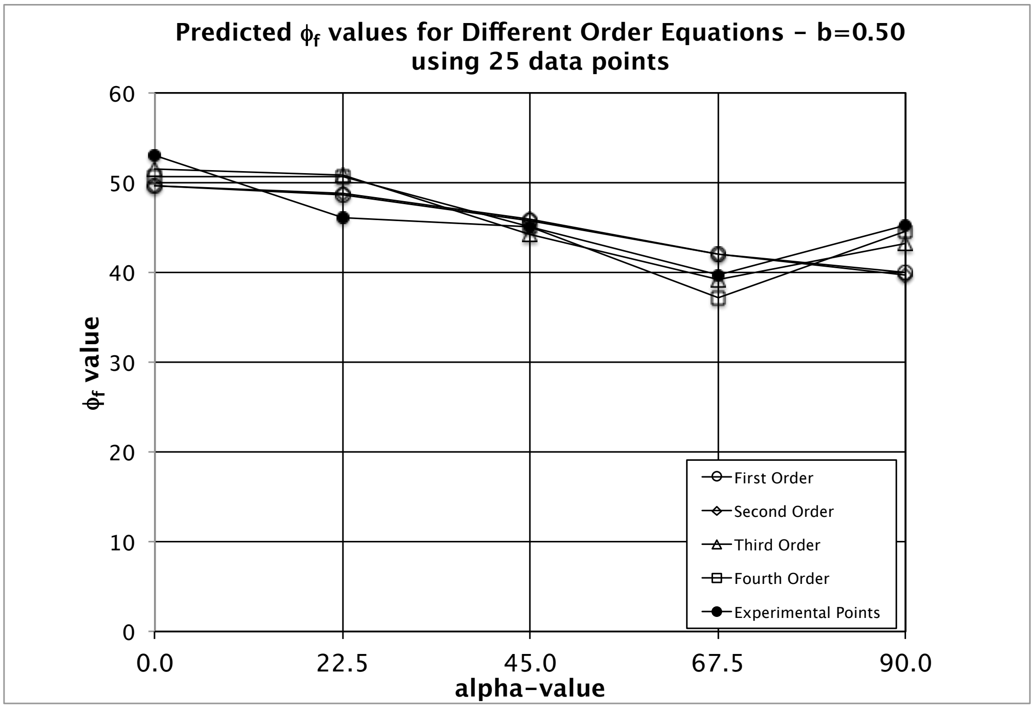

Figure 10.2.3. Predicted friction angle results for different order equations for torsion shear tests at b=0.50.

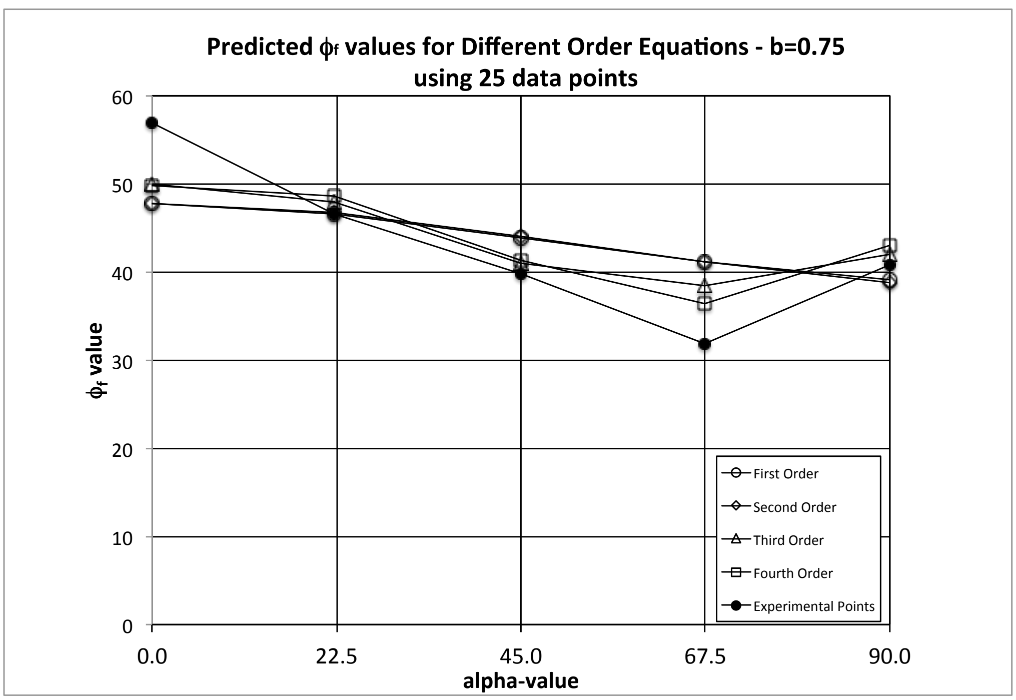

Figure 10.2.4. Predicted friction angle results for different order equations for torsion shear tests at b=0.75.

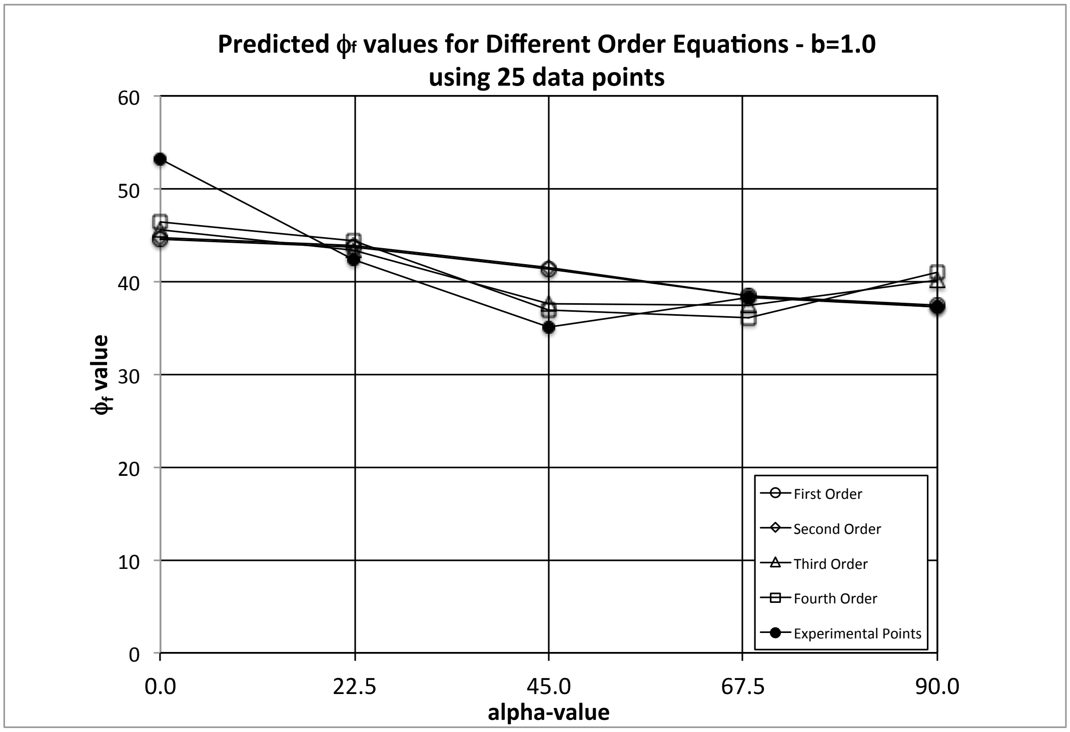

Figure 10.2.5. Predicted friction angle results for different order equations for torsion shear tests at b=1.0.

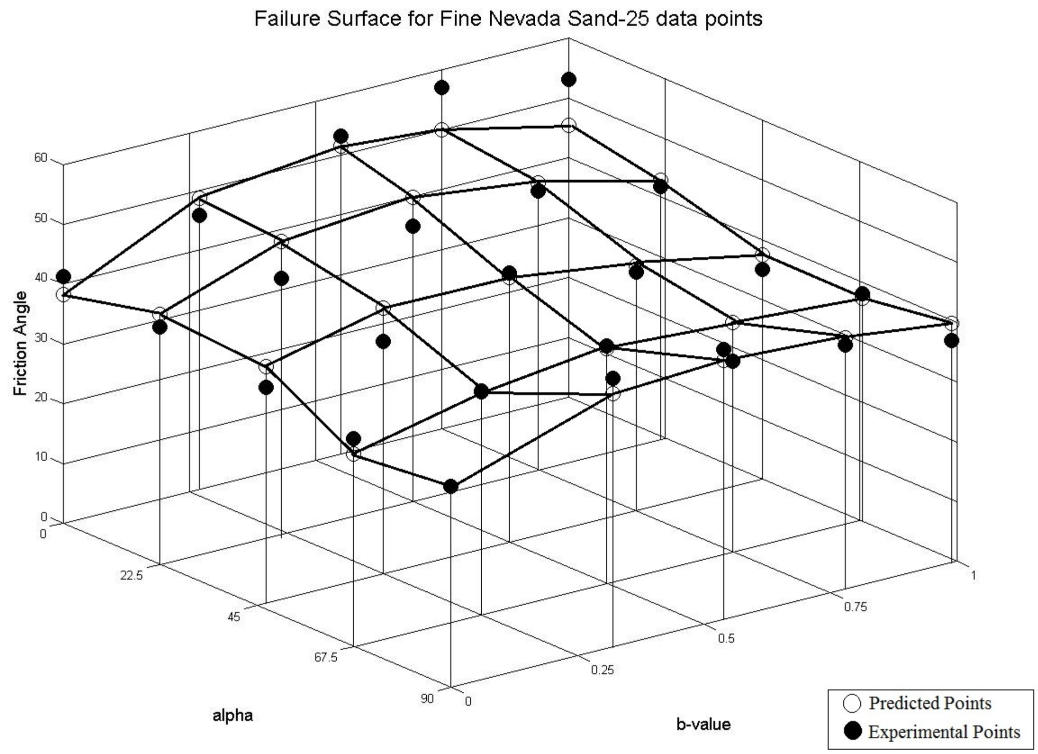

Figure 10.2.6. Failure Surface for Fine Nevada Sand using third order equation with 25 Torsion Shear Data Points.

10.3 Pietrusczack Model based on Modified Torsion Shear Results

Section 10.2 presented the parameters and friction angles that were calculated by using 25 torsion shear points regardless of whether certain friction angles seemed somewhat out of the pattern that was expected. In order to minimize the skewing of parameters by including outlier data, three different versions of data in the paragraphs that follow. The first only uses a total of 20 points were used when calculating the parameters with the regression model. Test 24*(α=0°, b=0.27) was deleted from the data because it was obviously low in the series of α=0° tests. Tests 38 *(α=67.42°, b=0.75), 17 (α=68.21°, b=1.0), 43*(α=90°, b=0.78) and

22*(α=90°, b=0.99) were also deleted because of the effects discussed in Chapter 7 concerning soft boundary effects in that combination of stress path. Using the 20 other points (shown in Table 10.2.3), new parameters were determined so that η_f values and friction angles could be calculated. These new parameters were applied to all 25 data points when determining η_f values and friction angles. Only the third order results are shown in Table 10.3.1 because the third order equation was found to be sufficient and showed only little difference with the fourth order equation in modeling the experimental 3D failure surface. The experimental friction angles are also presented for comparison. A 3D plot using these parameters in the third order equation is presented in Figure 10.3.1.

Table 10.3.1. Parameter determination and calculated η_f and ϕ values for third order equation using 20 Torsion Shear Test results based on Pietrusczack (2011) model.

4th Order Equation	
ηo	29.715
Ω	-1.043
a1	0.307
a2	-0.771
a3	0.217
3th Order Equation	
ηo	29.151
Ω	-0.768
a1	0.934
a2	-1.046
2th Order Equation	
ηo	34.975
Ω	-0.317
a1	0.217
1th Order Equation	
ηo	35.379
Ω	-0.326
0th Order Equation	
ηo=	38.186

Test	b-	alpha	ηf	ϕ	ϕ
23	0.00	0.00	42.703	39.454	41.153
24*	0.27	0.00	51.230	49.437	45.842
25*	0.55	0.00	103.079	55.257	51.817
2	0.75	0.00	51.702	50.069	56.964
26	1.00	0.00	42.557	45.489	53.180
3	0.00	22.41	54.582	42.247	39.708
28	0.23	23.69	55.142	49.837	43.346
6	0.50	22.48	51.977	51.000	46.031
29	0.75	22.21	41.518	44.335	47.858
8	0.99	22.47	36.287	43.230	42.329
31	0.02	44.71	40.233	39.360	35.945
9	0.25	44.98	36.560	44.291	38.882
33	0.50	44.99	32.289	44.225	45.150
11	0.75	44.98	34.543	27.658	41.136
34	1.00	44.95	25.128	37.868	35.087
14	0.00	67.33	23.586	32.684	34.660
36	0.25	67.80	23.875	38.317	37.483
15	0.50	67.47	36.182	24.519	40.303
38	0.75	67.42	24.657	39.503	31.873
17	1.00	68.21	26.725	38.727	38.224
41	0.00	90.00	40.934	28.223	34.714
42*	0.32	90.00	33.266	43.911	45.042
20*	0.54	90.00	33.740	44.824	45.237
43*	0.78	90.00	33.090	43.520	40.887
22*	0.99	90.00	32.556	41.616	37.215

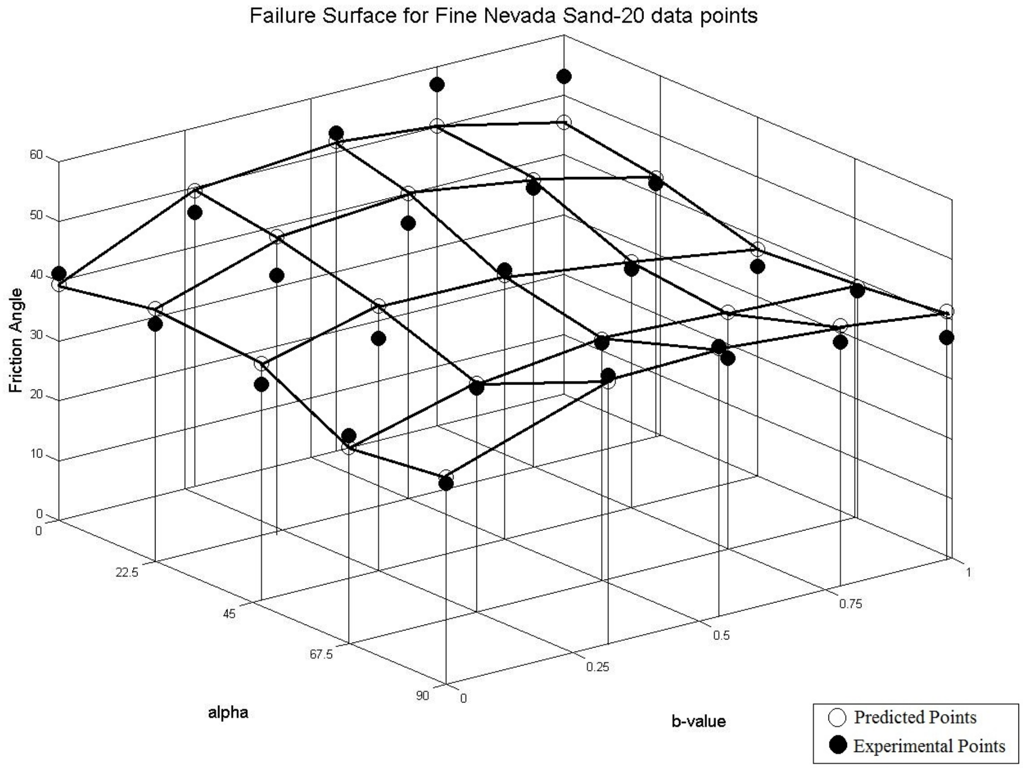

Figure 10.3.1. Failure Surface for Fine Nevada Sand using third order equation with 20 Torsion Shear Data Points.

In a similar fashion, the same iteration using the data presented above was done again. However, the second time, all tests with b-values equal to 0 were given doubled weights in the data used in the regression. This was done in order to add a weighting factor to these tests. These tests are known to be reliable since they were confirmed by both the true triaxial apparatus and the torsion shear apparatus (results were confirmed in Chapter 7). As can be seen by the data, certain friction angles do change based on the new set of parameters. Table 10.3.2 provides a summary of the parameters, η_f values and friction angles compared to the experimental results and Figure 10.3.2 shows the 3D results.

Table 10.3.2. Parameter determination and calculated η_f and ϕ values for third order equation using weighted Torsion Shear Test results based on Pietrusczack (2011) model.

4th Order	
ηo	29.699
Ω	-1.033
a1	0.133
a2	-0.887
a3	0.350
3th Order	
ηo	28.946
Ω	-0.578
a1	1.313
a2	-1.640
2th Order	
ηo	33.197
Ω	-0.292
a1	0.446
1th Order	
ηo	33.883
Ω	-0.316
0th Order	
ηo	37.778

Test	b-value	alpha	ηf	ϕ	ϕ
23	0.00	0.00	47.660	40.708	41.153
24*	0.27	0.00	51.349	49.469	45.842
25*	0.55	0.00	103.891	51.391	50.803
2	0.75	0.00	47.071	48.737	56.964
26	1.00	0.00	39.265	44.319	53.180
3	0.00	22.41	52.121	41.725	39.708
28	0.23	23.69	51.060	48.767	43.346
6	0.50	22.48	47.334	49.683	46.031
29	0.75	22.21	41.388	40.702	46.633
8	0.99	22.47	34.350	42.434	42.329
31	0.02	44.71	37.420	38.508	35.945
9	0.25	44.98	34.560	43.497	38.882
33	0.50	44.99	31.302	43.781	45.150
11	0.75	44.98	33.941	27.835	41.227
34	1.00	44.95	25.964	38.331	35.087
14	0.00	67.33	24.824	33.259	34.660
36	0.25	67.80	25.023	38.964	37.483
15	0.50	67.47	35.533	25.478	40.847
38	0.75	67.42	25.576	40.021	31.873
17	1.00	68.21	27.041	38.894	38.224
41	0.00	90.00	40.788	28.101	34.665
42*	0.32	90.00	31.662	43.207	45.042
20*	0.54	90.00	31.997	44.064	45.237
43*	0.78	90.00	31.539	42.831	40.887
22*	0.99	90.00	31.162	40.984	37.215

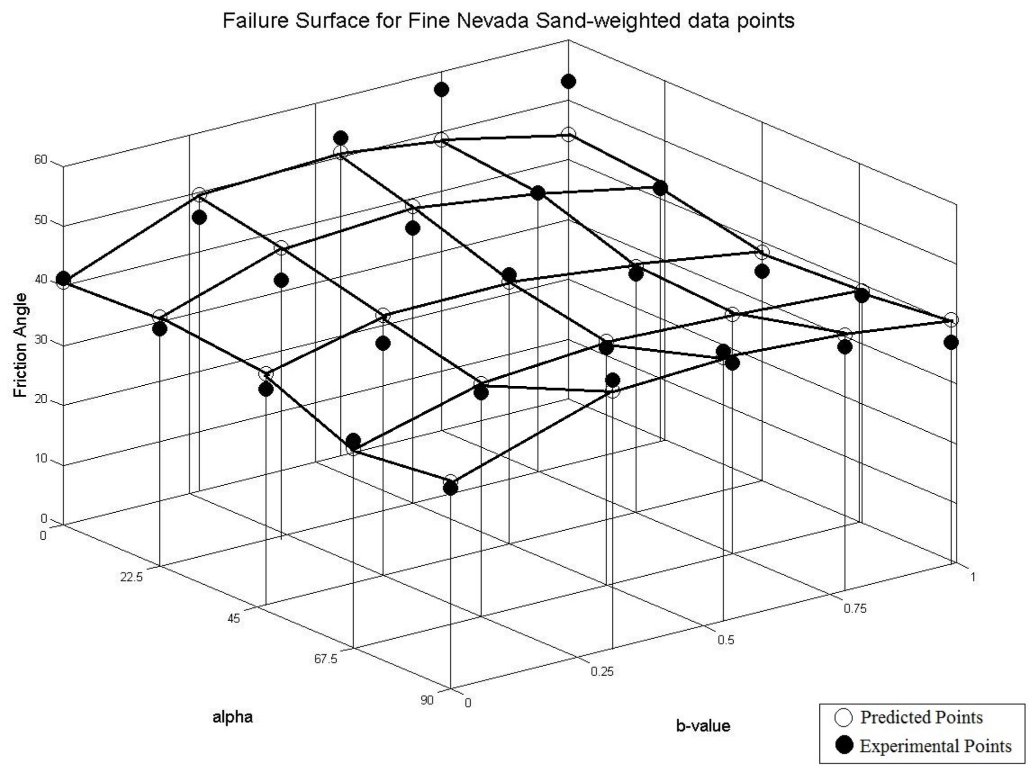

Figure 10.3.2. Failure Surface for Fine Nevada Sand using third order equation with weighted Torsion Shear Data Points.

Realistically, torsion shear and/or true triaxial machines are not easily available. Therefore, without having all of the data from these tests, it is quite difficult to calculate the parameters that have been shown above. However, triaxial tests are very common in most geotechnical laboratories. Therefore, if it is possible to vary the bedding plane inclination, whether when depositing a sand specimen, carving a clay specimen or taking core samples at different inclinations, then this procedure might become more feasible. Therefore, the last parameter determination was performed by only using torsion shear data with b=0 and varying the alpha values. A total of 5 tests were used (Test 23, 3, 31, 14, and 41).

As shown above, the parameters for the different order equations is shown in Table 10.3.3. For the regression model, it is not possible to use a 4^{th} order equation with only 5 points, as explained in Appendix K. Therefore, parameters up until 3^{rd} order were calculated. However, as seen in the previous examples, the third order provides a very close fit.

Table 10.3.3. Parameter determination and calculated η_f and ϕ values for third order equation using five b=0 Torsion Shear Test results based on Pietrusczack (2011) model.

3^{th} Order Equation	
ηo	23.764
Ω	-0.193
a1	4.487
a2	2.080
2^{th} Order Equation	
ηo	23.602
Ω	-0.196
a1	5.022
1^{th} Order Equation	
ηo	25.612
Ω	-0.404
0^{th} Order Equation	
ηo	34.826

Test	b-	alpha	η_f	ϕ	ϕ
23	0.00	0.00	46.096	40.328	41.153
24*	0.27	0.00	41.485	46.460	45.842
25*	0.55	0.00	35.426	45.514	53.054
2	0.75	0.00	30.976	42.736	56.964
26	1.00	0.00	27.059	38.944	53.180
3	0.00	22.41	38.127	38.155	39.708
28	0.23	23.69	34.845	43.401	43.346
6	0.50	22.48	31.158	43.715	46.031
29	0.75	22.21	27.639	41.082	46.587
8	0.99	22.47	25.341	38.071	42.329
31	0.02	44.71	26.372	34.417	35.945
9	0.25	44.98	25.408	39.193	38.882
33	0.50	44.99	24.423	40.248	45.150
11	0.75	44.98	23.461	38.807	39.867
34	1.00	44.95	22.941	36.588	35.087
14	0.00	67.33	22.479	32.145	34.660
36	0.25	67.80	22.395	37.440	37.483
15	0.50	67.47	22.365	39.009	39.727
38	0.75	67.42	22.363	38.132	31.873
17	1.00	68.21	22.393	36.236	38.224
41	0.00	90.00	22.440	32.125	33.589
42*	0.32	90.00	22.641	38.477	45.042
20*	0.54	90.00	22.661	39.163	45.237
43*	0.78	90.00	22.633	38.120	40.887
22*	0.99	90.00	22.610	36.427	37.215

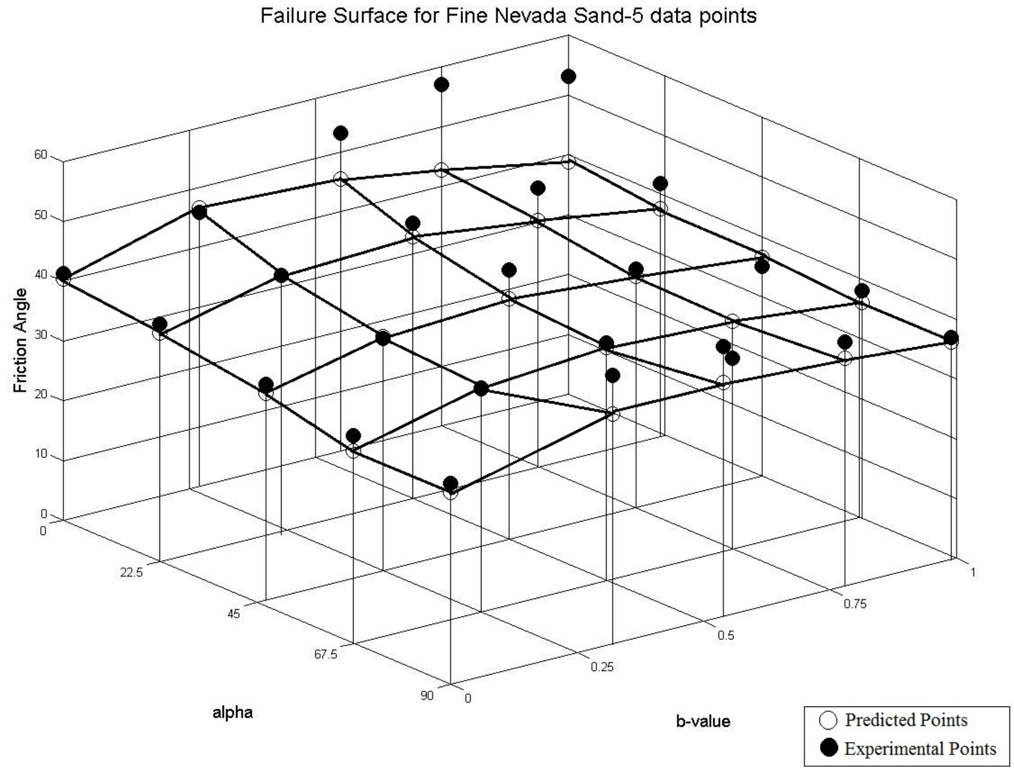

Figure 10.3.4. Failure Surface for Fine Nevada Sand using third order equation with 5 Torsion Shear Data Points.

As can be seen from Figure 10.3.4, only the low b-value are modeled correctly.

The model that produces the best comparison with the experimental results is the weighted model. As a reminder, when calculating the parameters needed, this model omits 5 outlier tests and uses double weights for the front wall test where b=0. A 3D plot showing this model compared to all 44 torsion shear tests results is shown in Figure 10.3.5. One without any test results, just showing the actual surface of the prediction is shown in Figure 10.3.6.

The effect of cross-anisotropy on the failure surface is clearly captured in the model. For comparison, a 3D graph with Lade's isotropic criterion has also been shown in Figure 10.3.7. This criterion is only applicable in the first and third sectors (α=0° and α=90°).

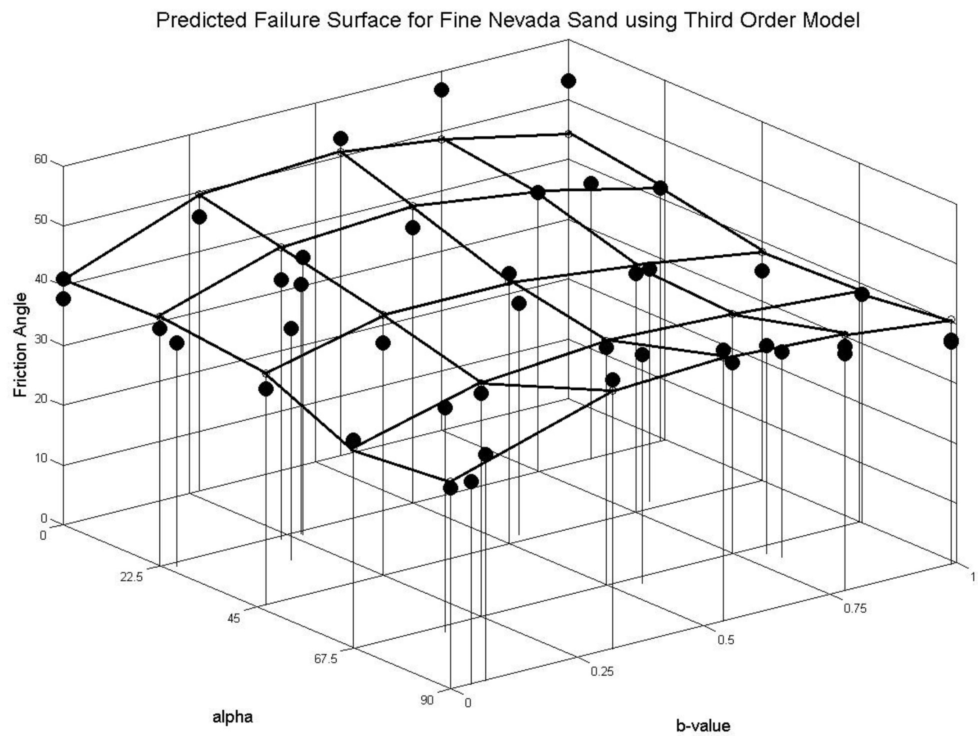

Figure 10.3.5. Failure Surface for Fine Nevada Sand using third order equation with weighted Torsion Shear Data Points and all Torsion Shear Results.

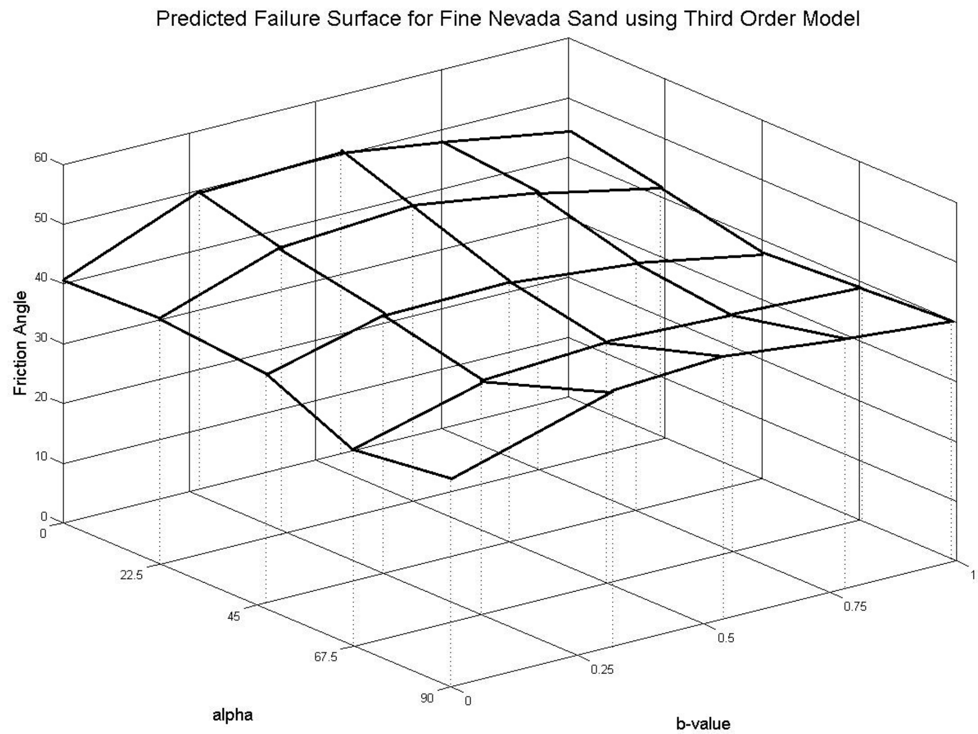

Figure 10.3.6. Failure Surface for Fine Nevada Sand using only the third order equation with weighted Torsion Shear Data Points.

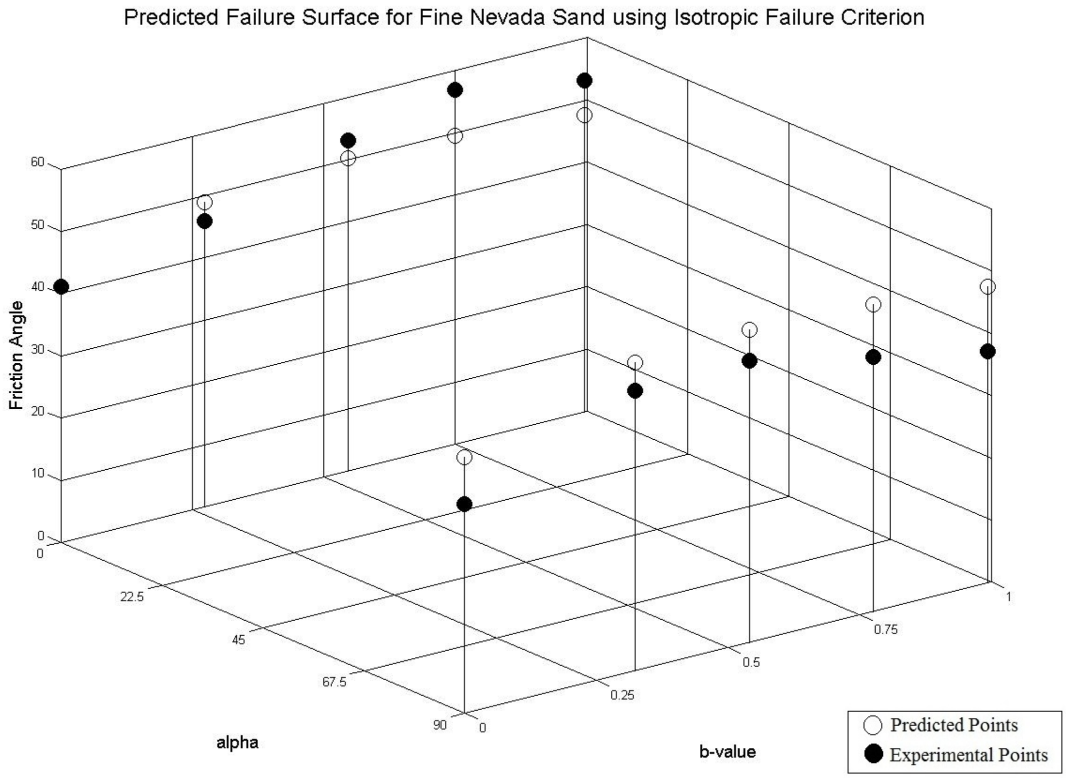

Figure 10.3.7. Failure Surface for Fine Nevada Sand using Lade's Isotropic Failure Criterion with Torsion Shear Data Points.

10.4 Conclusion

A cross-anisotropic criterion has been established from the torsion shear test data. Using the Pietrusczack model (2011), different parameters were established. These parameters were attained by doing a polynomial regression. The corresponding η values were calculated and set to Lade's isotropic criterion in order to determine the friction angle for each point. After several iterations, consisting of using all the points, omitting outliers, weighing the b=0 tests by a factor of two and finally, only using the b=0 tests, the best approximation model was found to be the third order weighted approximation. This model shows the surface and the drops in friction angle closest to the actual experimental points.

11. Conclusion

This thesis consists of the presentation and comprehensive analysis of experimental results attained from a series of systematic drained, triaxial, true triaxial and torsion shear experiments performed on Fine Nevada Sand deposited with cross-anisotropic fabric. These tests were performed in order to be able to attain the needed data and knowledge for the future development of constitutive models that predict the behavior of soil under various conditions that occur in the field, including the rotation of principal stresses.

Triaxial tests were performed as basic tests to give fundamental data about the behavior of sand. Next, true triaxial tests, using a true triaxial apparatus were performed to see the cross-anisotropic behavior of the sand with three different principal stresses, allowing for the variation of b-value in the stress paths chosen. By using a freezing technique, specimens could be rotated so the angle between the bedding planes and the principal stress direction could be changed from 0 to 90 degrees. These tests were then compared to results attained from a new torsion shear machine under similar conditions and stress paths.

As has been presented, the data attained from the true triaixal and torsion shear tests with the use of two independent apparatuses confirm the experimental results and show the reliability of the torsion shear tests performed. The torsion shear tests, all performed with stress paths of constant b-value, mean normal stress and principal stress direction, provide a complete 3D surface for different alpha and b-values.

When looking at this surface, it shows the clear effects of cross-anisotropy on the strength of the sand. When the principal stress direction is at 67.5 degrees, the soil becomes very weak and fails at low friction angles. The soil exhibits it's highest strength at $\alpha=0°$ and b=0.75. Strengths vary over the surface but as α increases the strength decreases as well. Strain analysis also showed similar patterns with the strain to failure becoming increasingly smaller as the alpha values increased at constant b-values.

Torsion shear tests showed that shear bands developed at/near failure. As the b-value increased, shear bands developed quicker and were more pronounced. For certain cases of high b-values, shear bands developed in the non-typical r-θ plane, creating great troughs in the soil. Although it is hard to point to one theory that relates to the prediction of shear bands due to a range of shear band angles measured, the Coulomb theory seems to best model shear band directions for the torsion shear tests.

Finally, an already existing cross-anisotropic failure criterion was adapted and compared to the torsion shear results presented. It was found that Pietruszczak's third order model could be used to model the behavior of Fine Nevada sand under 3D conditions. However, the model proved to predict too low values for where alpha=0 and b=0.75 and 1 when compared to actual test results. In conclusion, the aim of providing the experimental basis for future modeling of cross-anisotropy in the field, shear banding and effects of principal stress rotation on shear strength of soil on frictional materials has been provided via this research.

Appendix A – X-Ray Diffraction Results- CUA Vitreous State Laboratory

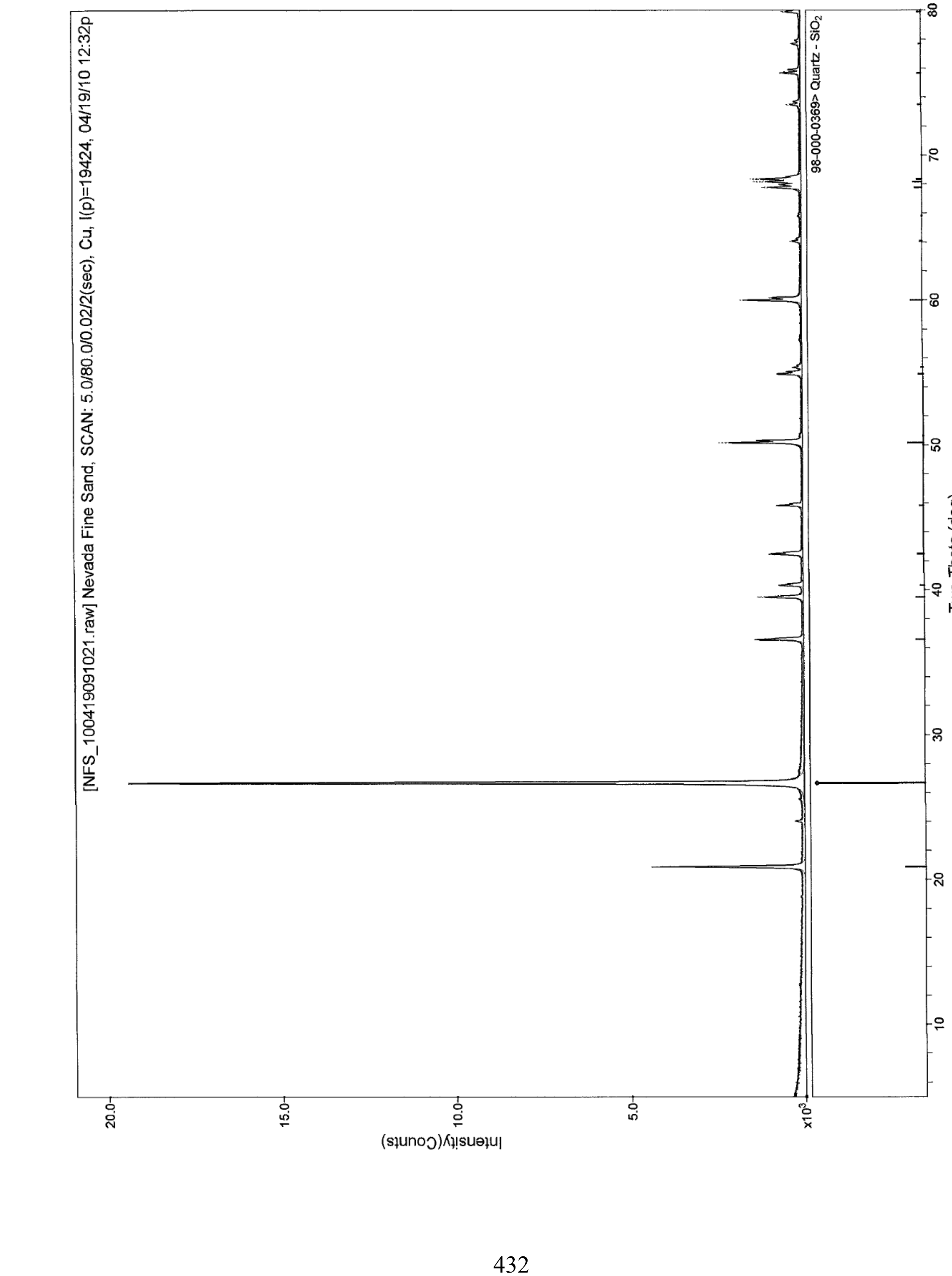
[NFS_100419091021.raw] Nevada Fine Sand, SCAN: 5.0/80.0/0.02/2(sec), Cu, I(p)=19424, 04/19/10 12:32p
Intensity(Counts)
20.0
15.0
10.0
5.0
x10^3
98-000-0369> Quartz - SiO2
10
20
30
40
50
60
70
80
Two-Theta (deg)

PDF#98-000-0369: QM=Calculated; d=Calculated; I=(Unknown)	PDF Card

Quartz

SiO_2

Radiation=CuKa1 Lambda=1.5406 Filter=

Calibration= 2T=20.859-118.310 I/Ic(RIR)=4.22

Ref: Calculated from CSD#369 (MDI-500.csd) by Jade

Hexagonal, $P3_221$ (154) Z=3

CELL: 4.9134 x 4.9134 x 5.4052 <90.0 x 90.0 x 120.0> P.S=

Density(c)=2.648 Density(m)= Mwt= Vol=113.0

Ref: Ibid.

NOTE: J Solid State Chem 36 (1981) 371, Wright A F, Lehmann M S, See also PDF 46-1045. [Quartz.csf]

Strong Lines: 3.34/X 4.26/2 1.82/1 1.54/1 2.46/1 1.37/1 2.28/1 1.38/1

47 Lines, Wavelength to Compute Theta = 1.54059Å(Cu), I%-Type = (Unknown)

#	d(Å)	I(f)	(hkl)	2-Theta	Theta	1/(2d)	#	d(Å)	I(f)	(hkl)	2-Theta	Theta	1/(2d)
1	4.2551	18.8	(100)	20.859	10.430	0.1175	25	1.1802	3.2	(310)	81.491	40.746	0.4237
2	3.3434	100.0	(011)	26.640	13.320	0.1495	26	1.1530	2.2	(131)	83.838	41.919	0.4337
3	2.4567	8.0	(110)	36.546	18.273	0.2035	27	1.1407	0.3	(204)	84.955	42.477	0.4383
4	2.2813	7.7	(102)	39.467	19.734	0.2192	28	1.1145	0.3	(303)	87.446	43.723	0.4486
5	2.2365	3.5	(111)	40.292	20.146	0.2236	29	1.0815	3.4	(132)	90.832	45.416	0.4623
6	2.1276	5.7	(200)	42.453	21.226	0.2350	30	1.0638	0.7	(400)	92.790	46.395	0.4700
7	1.9797	3.4	(201)	45.796	22.898	0.2526	31	1.0478	1.8	(015)	94.646	47.323	0.4772
8	1.8179	14.0	(112)	50.141	25.070	0.2750	32	1.0438	1.2	(401)	95.122	47.561	0.4790
9	1.8017	0.4	(003)	50.622	25.311	0.2775	33	1.0346	2.0	(214)	96.239	48.120	0.4833
10	1.6717	4.2	(022)	54.875	27.438	0.2991	34	1.0149	1.8	(223)	98.746	49.373	0.4926
11	1.6591	1.8	(013)	55.327	27.663	0.3014	35	0.9899	0.4	(042)	102.189	51.095	0.5051
12	1.6083	0.2	(210)	57.234	28.617	0.3109	36	0.9895	1.2	(115)	102.244	51.122	0.5053
13	1.5415	10.5	(121)	59.961	29.980	0.3244	37	0.9872	0.8	(133)	102.568	51.284	0.5065
14	1.4529	2.0	(113)	64.036	32.018	0.3441	38	0.9784	0.4	(034)	103.873	51.936	0.5111
15	1.4184	0.5	(300)	65.787	32.894	0.3525	39	0.9762	0.9	(320)	104.199	52.100	0.5122
16	1.3821	6.7	(122)	67.745	33.872	0.3618	40	0.9607	2.2	(231)	106.613	53.307	0.5205
17	1.3749	7.8	(203)	68.144	34.072	0.3637	41	0.9285	0.2	(410)	112.109	56.055	0.5385
18	1.3719	4.9	(031)	68.315	34.157	0.3645	42	0.9181	0.9	(322)	114.064	57.032	0.5446
19	1.2879	2.6	(104)	73.467	36.733	0.3882	43	0.9160	1.8	(403)	114.471	57.235	0.5458
20	1.2559	3.3	(302)	75.661	37.831	0.3981	44	0.9151	2.1	(411)	114.645	57.322	0.5464
21	1.2284	1.8	(220)	77.672	38.836	0.4070	45	0.9089	0.8	(224)	115.874	57.937	0.5501
22	1.1998	3.3	(213)	79.884	39.942	0.4167	46	0.9009	0.3	(006)	117.533	58.766	0.5550
23	1.1978	1.0	(221)	80.044	40.022	0.4174	47	0.8972	1.7	(125)	118.310	59.155	0.5573
24	1.1840	2.9	(114)	81.171	40.585	0.4223							

Appendix B – Specific Gravity Test for Fine Nevada Sand

Weight of Soil, W_s		206.28 grams
Weight of Bottle, W_b		179.6 grams
Weight of Water, Soil, and Bottle, W_{w+s+b}		806.2 grams
Temperature of Water, $T_{w,\,26^{\circ}}$	26.0	deg. Celsius

Calibration Curve (Mass of Volumetric filled with Water over a range of Temperatures)

Mb+wt (g)	Temp (deg C)	
677.3	28.7	26
677.5	27.2	26
677.9	23.4	26
678.2	20.2	26

$M_{b+wt} = -0.105(T) + 680.34$

$M_{b+wt(26)} = 77.61$ grams

Calculating Specific Gravity at Temperature (26° C)

$$G_{s@26} = \frac{M_s}{(M_{(b+wt)} + M_s) - M_{(b+w+st)}} = \frac{206.28\,grams}{(677.61 + 206.28) - 806.2} = 2.655$$

Calculating Specific Gravity at Room Temperature (20° C)

$\rho_{w26^{\circ}C} = 0.9967870$

$\rho_{w20°C}$= 0.9982063

$$G_{s@20} = G_{s@26} \frac{\rho_{w26°C}}{\rho_{w20°C}} = 2.655 * \frac{0.9967870}{0.9982063} = 2.651$$

$$G_{s@20} = 2.561$$

Appendix C – e_{min} and e_{max} Fine Nevada Sand Test data and Results

Emin

Total weight of sand, W_t	879.8 grams
Volume measured, V_{emin}	500 cm^3

Emax

Total weight of sand, W_t	1413.8 grams
Volume measured, V_{emax}	945 cm^3

Specific Gravity, G_s	2.65
Unit weight of Water, γ_w	1 g/cm^3

$$\gamma_{d\,\max} = \frac{W_t}{V_{e\min}} = \frac{879.8grams}{500cm^3} = 1.759g/cm^3$$

$$e_{\min} = \frac{G_s\gamma_w}{\gamma_{d,\max}} - 1 = \frac{2.65*1g/cm^3}{1.759g/cm^3} - 1 = 0.507$$

$$e_{\min} = 0.507$$

$$\gamma_{d\,\min} = \frac{W_t}{V_{e\max}} = \frac{1413.8grams}{945cm^3} = 1.496g/cm^3$$

$$e_{\max} = \frac{G_s\gamma_w}{\gamma_{d,\min}} - 1 = \frac{2.65*1g/cm^3}{1.496g/cm^3} - 1 = 0.771$$

$$e_{\max} = 0.771$$

Appendix D – Grain Size Distribution Data (Sieve and Hydrometer)

Sieve Analysis for Fine Nevada Sand
Date 14-Sep-10

Shake Time 25 minutes
Sand (g) 600

Sieve No.	Sieve Opening [mm]	Soil+Tare [gr]	Tare [gr]	Soil [gr]		Total weight finer than [gr]	Finer Than [%]
30	0.600						100.00
40	0.425	418.6	387.5	31.10	31.10	563.60	94.77
60	0.250	540.2	366.4	173.80	204.90	389.80	65.55
80	0.180	859.3	517.5	341.80	546.70	48.00	8.07
100	0.150	316.4	312	4.40	551.10	43.60	7.33
120	0.125	406	378	28.00	579.10	15.60	2.62
140	0.106	361	356.4	4.60	583.70	11.00	1.85
170	0.09	352.8	348	4.80	588.50	6.20	1.04
200	0.075	350.9	348.5	2.40	590.90	3.80	0.64
Pan	---------	501.8	498	3.80	594.70	0.00	0.00

D_{10}	0.1144
D_{30}	0.1688
D_{60}	0.2375

C_c	1.0487	coefficient of uniformity
C_u	2.0760	coefficient of curvature

Hydrometer Data	
0.08	1.40
0.06	0.61
0.04	0.29
0.02	0.11
0.02	0.07
0.01	0.02
0.01	0.00
0.00	0.00
0.00	0.00
0.001915378	0.00
0.000850853	0.00

Appendix D – Grain Size Distribution Data (Sieve and Hydrometer)

continued

Hyrdometer Analysis for Fine Neveda Sand

Soil [g]	50
c_m	0.5
μ [mPa-s]$_{24}$	0.916
G_S	2.65
ρ_{w24} [g/cm^3]$_{24}$	0.9972994
g [cm/s^2]	980.67
Hydrometer in water	1000.5
Suspension Volume [liter]	1

h [cm]	14.000
v_h [cm^3]	50.000
A [cm^2]	28.169

Temperature	Elapsed Time [min]	Observed Hydrometer Reading R'_T	Corrected Hydrometer Reading $R_T=R'_T+c_m$	Depth, H [cm]	Grain Size [mm]	Percent Finer [%]
24.00	0.25	1020.00	1020.50	11.54	0.089	62.47
24.00	0.50	1014.00	1014.50	9.95	0.058	43.25
24.00	1.00	1007.00	1007.50	8.10	0.037	20.82
24.00	2.00	1003.00	1003.50	7.04	0.024	8.01
24.00	5.00	1002.00	1002.50	6.77	0.015	4.81
24.00	10.00	1001.00	1001.50	6.51	0.011	1.60
24.00	20.00	1000.50	1001.00	6.38	0.007	0.00
24.00	61.00	1000.50	1001.00	6.38	0.004	0.00
24.00	128.00	1000.50	1001.00	6.38	0.003	0.00
24.00	296.00	1000.50	1001.00	6.38	0.002	0.00
24.00	1500.00	1000.50	1001.00	6.38	0.001	0.00

Calibration Curve

R_T	H_1 [cm]	0.5*(h-v_h/A)	H [cm]
1000.0	0	6.112	6.112
1040.0	10.6	6.112	16.712

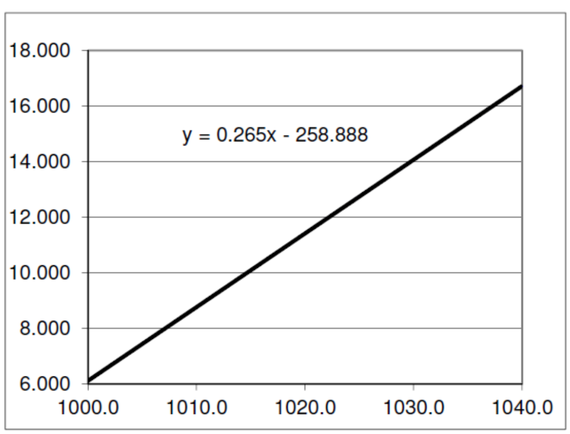

Appendix D – Grain Size Distribution Data (Sieve and Hydrometer) continued

Hydrometery Graph

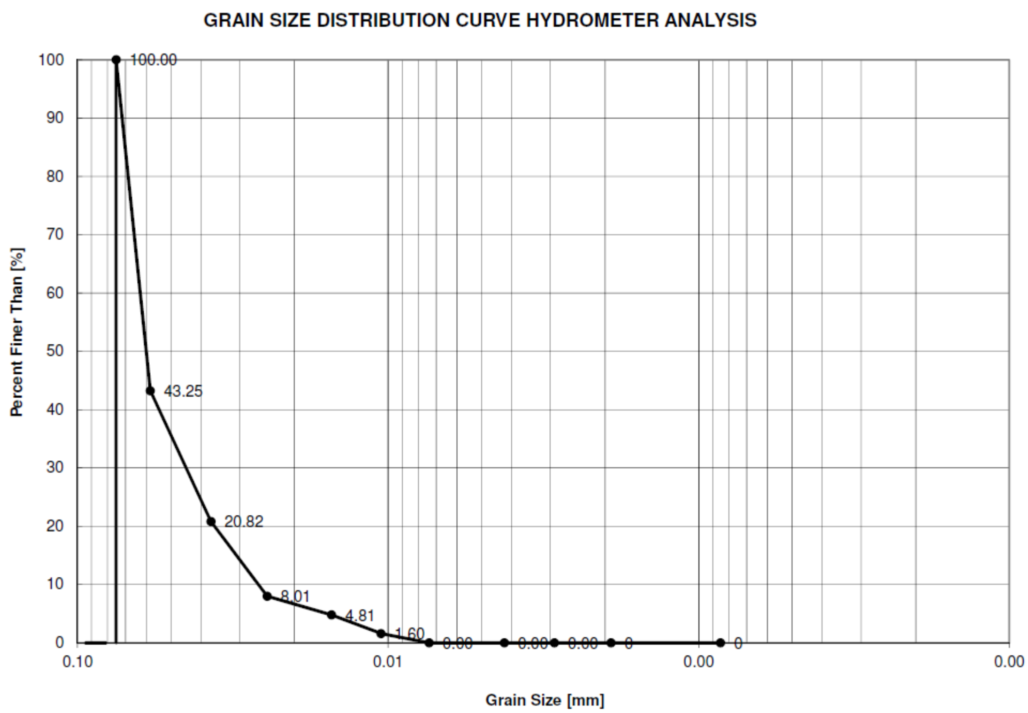

Appendix E - Compiled List of Researchers who worked with Hollow Cylinder Specimens

Table 2.1.Researchers who worked with hollow cylinder (HC) specimens (expanded from Koester 1992)

#	Reference	Year	Specimen Dimensions (mm) H	R_o	R_i	Soil Type	Control Restrictions	Applications	Specimen Preparation Method	Uniformity Check
1	Cooling and Smith	1936	19-38	50.8	41.3	Clay	$F_z = P_o = P_i = 0$	Undrained shear strength	Kneading - remoulded specimens	NO
2	Norton	1938	50.8	11.1	7.9	Clay	$F_z = P_o = P_i = 0$	Torsional deformability of ceramic clays	No info	NO
3	Geuze and Kie	1953	80	19	13	Clay	$F_z = P_o = P_i = 0$	Undrained creep	Kneading - remoulded specimens	NO
4	Kirkpatrick	1957	152.4	50.8	31.8	Sand	$F_z = T_h = 0$	σ_2 effect on failure condition	No info	NO
5	Haythornthwaite	1960	?	?	?	Silt	$P_o = P_i$	σ_2 effect on failure condition	Tamping in 3 layers followed by hydrostatic pressure application	NO
6	Whitman and Luscher	1962	76/127	25/19	12.7	Sand	$T_h = 0; \varepsilon_z = 0$	Soil-structure interaction at failure	No info	NO
7	Wu et al.	1963	127	50.8	38.1	Clay and Sand	$T_h = 0$	σ_2 effect on failure condition	No info	NO
8	Broms and Ratnam	1963	114.3	76.2	38.1	Clay	$T_h = 0$	3-D consolidation effects on strength	Compaction	In terms of water content
9	Broms and Casbarian	1965	254	63.5	38.1	Clay	----	σ_2 and α effects on strength	Compaction	NO
10	Broms and Jamal	1965	304.8	76.2	38.1	Sand	$T_h = 0$	Validity of $\sigma_r = \sigma_\theta$	Low Dr - WP + rodding High Dr - WP + vibration	NO
11	Esrig and Bemben	1965	203.2	50.8	38.1	Sand	$T_h = 0$	σ_2 and ε_2 effects on strength	WP	NO
12	Suklje and Drnovsek	1965	80	32	20	Clay	$T_h = 0; \sigma_z = 0$	Deformability under plane stress	No info	NO
14	Saada and Baah	1967	151.1	35.1	25.4	Clay	$P_o = P_i$	Influence of anisotropy	One-dimensional slurry consolidation	NO
16	Lomise et al.	1969	180	155	125	Clay	$P_o = P_i$	Drained creep under 3-D stress state	No info	NO
17	Jamal	1970	203	51	12.5-38	Sand	$P_o = P_i$	Extension behavior of solid and hollow cylinder specimens	WP + Tamping	NO
18	Barden and Proctor	1971	152.4	50.8	19.1	Sand	$T_h = 0$	Drained shear strength of granular material	No info	NO
19	Bishop et al.	1971	19.1	76.2	50.8	Clay	$\varepsilon_2 = 0$	Residual strength in ring shear torsion	Kneading - remoulded specimens Coring&trimming-undisturbed specimens	NO
20	Frydman et al.	1971	203.2	50.8	25.4	Sand	$T_h = 0$	End restraint; membrane penetration	Low Dr- AP High Dr - WP	NO
21	Drnevich	1972	100	25	20	Sand	$P_o = P_i$	Torsional resonant column test	Low Dr - WP High Dr - AP	NO
22	Arnold and Mitchell	1973	142	76	51	Sand	$T_h = 0$	3-D stress effect on strength	AP + Tamping	NO

Table 2.1. Researchers who worked with hollow cylin der (HC) specimens (expanded from Koester 1992) Contd.

#	Reference	Year	Specimen Dimensions (mm) H	R_0	R_i	Soil Type	Control Restrictions	Applications	Specimen Preparation Method	Uniformity Check
23	Ishibashi and Sherif	1974	13 to 25	50.8	25.4	Sand	$P_o = P_i$	Liquefaction characteristics	WP	NO
24	Tseng	1974	?	72.8	35.7	Sand	$P_o = P_i$	Liquefaction , solid versus hollow specimens	Compaction	NO
25	Ishihara and Yasuda	1975	70	50	30	Sand	$P_o = P_i$; $\varepsilon_2 = 0$	Liquefaction of sands, irregular excitation	AP	NO
26	Lade	1975	50	110	90	Sand	$P_o = P_i$	α effect on stress-strain behavior	No info	NO
27	Al-Hussaini	1981	101.6	76.2	50.8	Clay and Clayey Sand	$\varepsilon'_z = 0$	Tensile properties of compacted soils	Compaction	NO
28	Cheng	1981	76.2	101.6	76.2	Clay	$F_z = P_o = P_i = 0$	Strain rate effects in torsion	One-dimensional slurry consolidation	NO
29	Dusseault	1981	200-240	50.8	25.4	Dense Oil Sand	$T_h = 0$	Tunneling and pressuremeter paths	Trimming and coring	NO
30	Lade	1981	400	110	90	Sand	$P_o = P_i$	Influence of specimen height		NO
31	Saada and Shook	1981	140-152	35.6	25.4	Clay	$P_o = P_i$	Slow cyclic and large shear strain behavior	One-dimensional slurry consolidation	NO
32	Fukushima and Tatsuoka	1982	200	50	30	Sand	$P_o = P_i$	Deformation and strength behavior	AP	NO
33	Symes et al.	1982	254	127.5	101.5	Sand	----	α and b effects on strain response	WP	NO
34	Tatsuoka et al.	1982	100-200	100	60	Sand	$P_o = P_i$, $\varepsilon_z = 0$	Cyclic undrained stress-strain, dense sands	AP & MT & Static moist compaction	NO
35	Donaghe and Gilbert	1983	203.2	50.8	35.6	Sand	$P_o = P_i$	Principal stress rotation; liquefaction	MT	NO
36	Hight et al.	1983	254	127.5	101.5	Sand	----	Specimen dimensions, α and b effects on stress- strain	WP	NO
37	Ishihara and Towhata	1983	104	50	30	Sand	$P_o = P_i$	Wave loading; principal stress rotation; pore pressures	AP	NO
38	Ishihara and Yamazaki	1984	101	50	30	Sand	$P_o = P_i$	Liquefaction in seabed deposits due to wave loads	AP	NO
39	Macky and Saada	1984	108-152	25-35	18-25	Clay	$P_o = P_i$	Dynamics of anisotropic clays, large strains	One-dimensional slurry consolidation	NO
40	Symes et al.	1984	254	127	101.6	Sand	----	Undrained anisotropy and principal stress rotation	WP	NO
41	Tatsuoka et al.	1984	100	50	30	Sand	$P_o = P_i$	Specimen preparation methods, cyclic undrained strength	AP, MT, wet-vibration, WP	NO
42	Ishibashi et al.	1985	142	35.5	25.4	Sand	$P_o = P_i$	Liquefaction characteristics	AP + Tamping	NO

Table 2.1. Researchers who worked with hollow cylinder (HC) specimens (expanded from Koester 1992) Contd.

#	Reference	Year	Specimen Dimensions (mm) H	R_0	R_i	Soil Type	Control Restrictions	Applications	Specimen Preparation Method	Uniformity Check
43	Symes et al.	1985	254	127.5	101.5	Sand	---	Liquefaction under principal stress rotation	WP	NO
44	Ishihara et al.	1985	100	50	30	Sand	$P_o = P_i$	Liquefaction of Ko-consolidated sand under cyclic principal stress rotation and lateral constraint	AP	NO
45	Towhata and Ishihara	1985	100	50	30	Sand	$P_o = P_i$	Undrained strength under cyclic rotation of principal stresses	AP	NO
46	Tatsuoka et al.	1986	100	50	30	Sand	$P_o = P_i$	Sample preparation methods, cyclic undrained strength	AP, MT, wet-vibration, WP	NO
47	Alarcon et al.	1986	203	35.5	19	Sand	$P_o = P_i$	Stress and strain for $\gamma > 10^{-2}$ %	AP	NO
48	Miura et al.	1986	200	50	30	Sand	----	α effect on stress-strain and strength	AP	NO
49	Tatsuoka et al.	1986	200	50	30	Sand	----	Failure and deformation of sand in torsion	AP	NO
50	Anderson et al.	1988	150	75	12.5	Clay	$T_h = 0$	Pressuremeter paths; undrained creep	One-dimensional slurry consolidation	NO
51	Chen	1988	254	127	101.6	Sand	$T_h = 0$	Stress path effects on Monterey No.0/30 sand	AP + Tamping	NO
52	Saada	1988	127-177	35.5	25.5	Sand and Clay	---	Evaluation of the hollow cylinder testing method	Trimming and coring for clays AP for sands	NO
53	Tatsuoka et al.	1989	200	50	30	Sand	$\varepsilon_z = 0$	Simple shear testing using HC	AP	NO
54	Pradel et al.	1990	193	50	30	Sand	----	Yielding and flow under principal stress rotation	AP	NO
55	Talesnick and Frydman	1991	120	35.5	25	Clay	$P_o = P_i$	Comparison against NGI-type direct simple shear	Trimming and coring of undisturbed specimens	NO
56	Dakoulas et al.	1992	203	69.9	50.1	Sand	$P_o = P_i$	Experimental calibration of constitutive model	MT	NO
57	Koester	1992	203	127.0	102	Silty sand	$P_o = P_i$	Cyclic strength, and pore pressure response	AP, MT	NO
58	Yamashita and Toki	1993	100	50.0	30	Sand	$\varepsilon_z = 0$	Effect of fabric anisotropy on cyclic undrained strength	AP through sieves, AP through a funnel and vibration, centrifugal force method	NO
59	Vaid and Sayao	1995	300	75.0	50	Sand	----	Loading behavior under multiaxial stresses	WP	NO
60	Sayao and Vaid	1996	300	75.0	50	Sand	----	Effect of b on deformation response	WP	NO
61	Zdravkovic	1996	203	127.0	102	Silt	----	Anisotropic behavior of silt	SD	NO
62	Zdravkovic&Jardine	1997	254	127.0	101.6	Silt	---	Stiffness characteristics under general stress conditions	SD	NO

Table 2.1. Researchers who worked with hollow cylinder (HC) specimens (expanded from Koester 1992) Contd.

#	Reference	Year	Specimen Dimensions (mm) H	R_0	R_i	Soil Type	Control Restrictions	Applications	Specimen Preparation Method	Uniformity Check
43	Symes et al.	1985	254	127.5	101.5	Sand	---	Liquefaction under principal stress rotation	WP	NO
44	Ishihara et al.	1985	100	50	30	Sand	$P_o = P_i$	Liquefaction of Ko-consolidated sand under cyclic principal stress rotation and lateral constraint	AP	NO
45	Towhata and Ishihara	1985	100	50	30	Sand	$P_o = P_i$	Undrained strength under cyclic rotation of principal stresses	AP	NO
46	Tatsuoka et al.	1986	100	50	30	Sand	$P_o = P_i$	Sample preparation methods, cyclic undrained strength	AP, MT, wet-vibration, WP	NO
47	Alarcon et al.	1986	203	35.5	19	Sand	$P_o = P_i$	Stress and strain for $\gamma > 10^{-2}$ %	AP	NO
48	Miura et al.	1986	200	50	30	Sand	----	α effect on stress-strain and strength	AP	NO
49	Tatsuoka et al.	1986	200	50	30	Sand	----	Failure and deformation of sand in torsion	AP	NO
50	Anderson et al.	1988	150	75	12.5	Clay	$T_h = 0$	Pressuremeter paths; undrained creep	One-dimensional slurry consolidation	NO
51	Chen	1988	254	127	101.6	Sand	$T_h = 0$	Stress path effects on Monterey No.0/30 sand	AP + Tamping	NO
52	Saada	1988	127-177	35.5	25.5	Sand and Clay	---	Evaluation of the hollow cylinder testing method	Trimming and coring for clays AP for sands	NO
53	Tatsuoka et al.	1989	200	50	30	Sand	$\varepsilon_r = 0$	Simple shear testing using HC	AP	NO
54	Pradel et al.	1990	193	50	30	Sand	----	Yielding and flow under principal stress rotation	AP	NO
55	Talesnick and Frydman	1991	120	35.5	25	Clay	$P_o = P_i$	Comparison against NGI-type direct simple shear	Trimming and coring of undisturbed specimens	NO
56	Dakoulas et al.	1992	203	69.9	50.1	Sand	$P_o = P_i$	Experimental calibration of constitutive model	MT	NO
57	Koester	1992	203	127.0	102	Silty sand	$P_o = P_i$	Cyclic strength, and pore pressure response	AP, MT	NO
58	Yamashita and Toki	1993	100	50.0	30	Sand	$\varepsilon_z = 0$	Effect of fabric anisotropy on cyclic undrained strength	AP through sieves, AP through a funnel and vibration, centrifugal force method	NO
59	Vaid and Sayao	1995	300	75.0	50	Sand	----	Loading behavior under multiaxial stresses	WP	NO
60	Sayao and Vaid	1996	300	75.0	50	Sand	----	Effect of b on deformation response	WP	NO
61	Zdravkovic	1996	203	127.0	102	Silt	----	Anisotropic behavior of silt	SD	NO
62	Zdravkovic&Jardine	1997	254	127.0	101.6	Silt	---	Stiffness characteristics under general stress conditions	SD	NO

Table 2.1. Researchers who worked with hollow cylinder (HC) specimens (expanded from Koester 1992) Contd.

#	Reference	Year	Specimen Dimensions (mm)			Soil Type	Control Restrictions	Applications	Specimen Preparation Method	Uniformity Check
			H	R_o	R_i					
63	Nakata et al.	1998	200	50.0	30	Sand	----	Effect of α on undrained behavior	AP	NO
64	Lade and Kirkgard	2000	250	110	90	Clay	$P_o = P_i$	α and b effects on cross-anisotropic behavior	Trimming of undisturbed specimens	NO
65	Toyota et al.	2001	160	40	25	Clay	----	Stress-strain behavior of clays under 3-D stress conditions	One-dimensional slurry consolidation	NO
66	Zdravkovic&Jardine	2001	254	127.0	101.6	Silt	----	Effect of rotating principal stresses during consolidation	SD	NO
67	Lee et al.	2002	230	49	39	Mudstone	$P_o = P_i$	Stress-strain behavior of a mudstone	Drilling	NO
68	Sivathayalan and Vaid	2002	300	76	51	Sand	----	Influence of initial state and α on undrained response	WP	NO
69	Uthayakumar and Vaid	2002	300	76	51	Sand	----	Static liquefaction under multiaxial loading	WP + Vibration	NO
70	Chaudhary et al.	2002	100	50	30	Sand	----	Effect of initial fabric and shearing direction on cyclic deformation	AP, WP, dry rodding	NO
71	Shibuya et al.	2003	254	127.5	101.5	Sand	----	Four-dimensional local boundary surfaces	WP	NO
72	Rolo	2003	254	127	102	Clayey Sand	----	Anisotropic behavior of loose clayey sands	SD	In terms of fines content
73	Chaudhary et al.	2004	200	50	30	Sand	----	Quasi-Elastic stiffness parameters in HC and TX testing	AP	NO
74	Naughton and O'Kelly	2004	200	50	35.5	Sand	----	Induced anisotropy	WP	NO
75	Brown and Richardson	2004	500	140	112	Sand and granulated crushed slate	----	Cyclic loading behavior of dry granular material	AP	NO
76	Lin and Penumadu	2005	230	25.4	17.8	Clay	----	Effect of principal stress rotation on Kaolin clay behavior	One-dimensional slurry consolidation	In terms of water content
77	Lin and Penumadu	2005	230	25.4	17.8	Clay	----	Strain localization in combined axial-torsional loading	One-dimensional slurry consolidation	NO
78	Silvestri et al.	2005	100	50-63.5	19-25	Clay	----	Expansion tests in clay using HC apparatus	Cutting with the technique of electroosmosis	NO
79	O'Kelly and Naughton	2005	200	50	35.5	Sand	----	Development of a hollow cylinder apparatus	WP	NO
80	O'Kelly and Naughton	2005	200	50	35.5	Sand	----	Engineering properties of wet pluviated HC specimens	WP	NO
81	Altun et al.	2005	200	50	30	Silty sand	$P_o = P_i$	Effect of fines content on liquefaction resistance	AP	NO
82	Yang et al.	2007	314	100	75	Sand	----	Anisotropic behavior in rotational shear	AP	NO

F_z = axial load, P_o & P_i = outer and inner cell pressures, T_h = torque, ε_z = axial strain, ε_2 = intermediate principal strain, σ_z = axial stress, AP = air pluviation, MT= moist tamping, SD= slurry deposition

Appendix F - Description and Method to Project Stress points onto the Same Octahedral Plane

True Triaxial and Torsion Shear tests are conducted with three unequal principal stresses. Therefore, if the tests do not keep a constant mean confining stress, the specimens will not all fail on the same octahedral plane. The principal stresses however, can be modified so that they all fall on the same plane. This procedure will be described in the pages that follow.

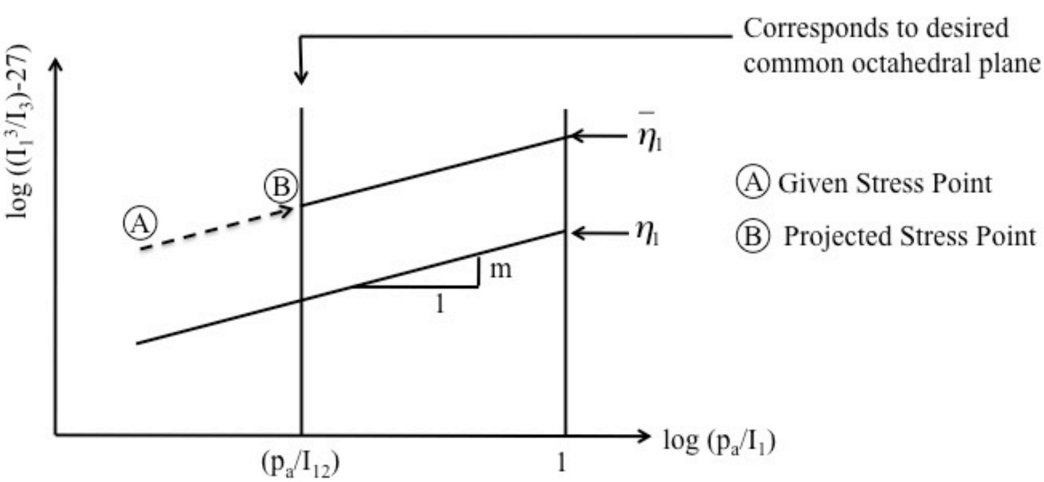

Figure 1. Schematic Illustration of the Projection Procedure

Point A in Figure 1 shows the stress state, (σ'_1, σ'_2, σ'_3) which is known. Point B is where the stress state will be adjusted and projected to, (σ^*_1, σ^*_2, σ^*_2). This is done by projecting Point A along a line with slope m to obtain a desired value of the first stress invariant, I_{12}. I_{12} is the octahedral plane that is desired. m is the geometric slope attained from plotting three triaxial compression tests. The failure state of Point A is defined by

$$\left(\frac{I_1^3}{I_3} - 27\right)_1 * \left(\frac{I_1}{p_a}\right)_1^m = \bar{\eta}_1 \qquad \text{Eq. F.1}$$

where pa=1 kg/cm2; Therefore, Eq. F.1 can be simplified to be

$$\left(\frac{I_1^3}{I_3} - 27\right)_1 * \left(I_1\right)_1^m = \bar{\eta}_1 \qquad \text{Eq. F.2}$$

Similarly, the failure state at Point B can be written as

$$\left(\frac{I_1^3}{I_3} - 27\right)_2 * \left(I_{12}\right)^m = \bar{\eta}_1 \qquad \text{Eq. F.3}$$

which can be rearranged as

$$\left(\frac{I_1^3}{I_3} - 27\right)_2 = \frac{\bar{\eta}_1}{\left(I_{12}\right)^m}$$

$$\left(\frac{I_1^3}{I_3}\right)_2 = \frac{\bar{\eta}_1}{\left(I_{12}\right)^m} + 27$$

$$\left(I_3\right)_2 = \frac{1}{\dfrac{\bar{\eta}_1}{\left(I_{12}\right)^m} + 27} * I_{12}^3$$

Eq. F.4

The intermediate stress ratio parameter, b can be defined as

$$b = \frac{(\sigma_2^* - \sigma_3^*)}{(\sigma_1^* - \sigma_3^*)} \qquad \text{Eq. F.5}$$

Rearranging the above equation, the intermediate principal stress, σ^*_2 can be expressed as:

$$\sigma_2^* = \sigma_3^* + b(\sigma_1^* - \sigma_3^*) \qquad \text{Eq. F.6}$$

The desired first stress invariant, I12 is expressed by

$$I_{12} = \sigma_1^* + \sigma_2^* + \sigma_3^* \qquad \text{Eq. F.7}$$

Substituting the last two equations, the following is attained:

$$\begin{aligned} I_{12} &= \sigma_1^* + \sigma_3^* + b(\sigma_1^* - \sigma_3^*) + \sigma_3^* \\ I_{12} &= (1+b)\sigma_1^* + (2-b)\sigma_3^* \end{aligned} \qquad \text{Eq. F.8}$$

Rearranging equation D.8, the desired major principal stress, σ^*_1 can be expressed as

$$\sigma_1^* = \frac{1}{(1+b)}\left\{I_{12} - (2-b)\sigma_3^*\right\} \qquad \text{Eq. F.9}$$

The desired third stress invariant I_{32} can be calculated as:

$$I_{32} = \sigma_1^* * \sigma_2^* * \sigma_3^* \qquad \text{Eq. F.10}$$

Substituting Equation F.6 into F.10 yields:

$$I_{32} = \sigma_1^* * \left\{\sigma_3^* + b*(\sigma_1^* - \sigma_3^*)\right\} * \sigma_3^*$$

$$I_{32} = \sigma_1^*(\sigma_3^*)^2 + b(\sigma_1^*)^2 * \sigma_3^* - b(\sigma_1^*)(\sigma_3^*)^2 \qquad \text{Eq. F. 11}$$

$$I_{32} = (1-b)\sigma_1^*(\sigma_3^*)^2 + b(\sigma_1^*)^2 * \sigma_3^*$$

Substituting Eq. F.9 into F.11:

$$I_{32} = (1-b) * \frac{1}{(1+b)} * \left\{I_{12} - (2-b)\sigma_3^*\right\}(\sigma_3^*)^2 + b\frac{1}{(1+b)^2}\left\{I_{12} - (2-b)\sigma_3^*\right\}(\sigma_3^*)$$

Eq. F. 12

Further rearrangement results in:

$$I_{32} = \frac{b(2-b)^2 - (1+b)(1-b)(2-b)}{(1+b)^2}(\sigma_3^*)^3 + \frac{(1+b)(1-b) - 2b(2-b)}{(1+b)^2}(I_{12}^2)(\sigma_3^*)^2$$

$$+\frac{b(I_{12}^2)}{(1+b)^2}(\sigma_3^*)$$

or

$$\left\{b(2-b)^2 - (1+b)(1-b)(2-b)\right\}(\sigma_3^*)^3 + \left\{(1+b)(1-b) - 2b(2-b)\right\}(I_{12}^2)(\sigma_3^*)^2$$

$$+b(I_{12}^2)(\sigma_3^*) - (1+b)^2(I_{32}) = 0$$

Eq. F. 13

Equation F. 13 can be simplified into a cubical equation of σ^*_3 by

$$(\sigma_3^*)^3 + \frac{(b^2 - 4b + 1)I_{12}}{(2-b)(2b-1)}(\sigma_3^*)^2 + \frac{(b)I_{12}^2}{(2-b)(2b-1)}(\sigma_3^*) + \frac{-(1+b)^2 I_{32}}{(2-b)(2b-1)} = 0 \qquad \text{Eq. F. 14}$$

The cubical equation in the form of x^3, + Ax^2+Bx+C=0 can be solved by saying that

$$A = \frac{(b^2 - 4b + 1)I_{12}}{(2-b)(2b-1)} \qquad \text{Eq. F. 15}$$

$$B = \frac{(b)I_{12}^2}{(2-b)(2b-1)} \qquad \text{Eq. F. 16}$$

$$C = \frac{-(1+b)^2 I_{32}}{(2-b)(2b-1)} \qquad \text{Eq. F. 17}$$

The solution to the cubical equation is given by (Korn and Korn, 1961):

$$p = -\frac{A^2}{3} + B \qquad \text{Eq. F. 18}$$

$$q = 2\left(\frac{A}{3}\right)^3 - \frac{AB}{3} + C \qquad \text{Eq. F. 19}$$

$$x_1 = 2\sqrt{\frac{-p}{3}}\cos\left(\frac{\alpha}{3}\right) - \left(\frac{A}{3}\right) \qquad \text{Eq. F. 20}$$

and

$$x_{2,3} = -2\sqrt{\frac{-p}{3}}\cos\left(\frac{\alpha}{3} \pm 60°\right) - \left(\frac{A}{3}\right) \qquad \text{Eq. F. 21}$$

where

$$\cos(\alpha) = -\frac{q}{2\sqrt{-\left(\frac{p}{3}\right)^3}} \qquad \text{Eq. F. 22}$$

The solution to F.21 depends on the b-value.

For b<0.5,

$$\sigma_3^* = x_2 = -2\sqrt{\frac{-p}{3}}\cos\left(\frac{\alpha}{3} + 60°\right) - \left(\frac{A}{3}\right) \qquad \text{Eq. F. 23}$$

For b>0.5,

$$\sigma_3^* = x_3 = -2\sqrt{\frac{-p}{3}}\cos\left(\frac{\alpha}{3} - 60°\right) - \left(\frac{A}{3}\right) \qquad \text{Eq. F. 24}$$

and for b=0.5, Equation F. 14 can be simplified to be

$$(b^2 - 4b + 1)(I_{12})(\sigma_3^*)^2 + b(I_{12}^2)(\sigma_3^*) - (1+b)^2(I_{32}) = 0 \qquad \text{Eq. F. 25}$$

where

$$\sigma_3^* = \frac{1}{3}I_{12} - \frac{1}{3}\sqrt{\frac{I_{32}}{I_{12}}}\sqrt{\frac{I_{12}^3}{I_{32}} - 27} \qquad \text{Eq. F. 26}$$

Once σ^*_3 has been calculated, the major and intermediate principal stresses can also be determined by solving Eq. F.6 and F.7 simultaneously.

Appendix G - Plotting Lade's Cross Anisotropic Failure Criterion (Lade, 2007)

In order to plot the failure criterion (Lade 2007) in terms of friction angle/stress ratio and b-value, equations must be combined and rearranged. The steps for doing so are described in detail in the pages that follow.

As stated in Lade (2007), combining Pietrusczak's function for a cross-anisotropic material and Lade's (1977) isotropic three-dimensional failure criterion for soils results in

$$f = \left(\frac{I_1^3}{I_3} - 27\right)\left(\frac{I_1}{p_a}\right)^m = \eta_0\left[1 + \Omega_1\left(1 - 3l_2^2\right)\right] \quad \text{Eq. G. 1}$$

where I_1 and I_3 are first and the third invariants of the stress tensor, pa is the atmospheric pressure (in the same units as I_1), η_0 and Ω_1 are constant material properties and l_2 is the loading direction relative to the material axis in which up to three different orthogonal normal stresses and one shear stress are applied. The expression for l_2 is

$$l_2 = \sqrt{\frac{\sigma_y^2 \sin^2\beta + \sigma_z^2 \cos^2\beta}{\sigma_x^2 + \sigma_y^2 + \sigma_z^2}} \quad \text{Eq. G. 2}$$

where σ_x, σ_y, and σ_z are principal stresses and β is the major principal stress direction.

Rearranging the terms in equation G.1 in order to isolate the I_1, the equation becomes,

$$\left(\frac{I_1^3}{I_3} - 27\right) = \frac{\eta_0\left[1 + \Omega_1\left(1 - 3l_2^2\right)\right]}{\left(\frac{I_1}{p_a}\right)^m}$$

$$\left(\frac{I_1^3}{I_3}\right) = \frac{\eta_0\left[1 + \Omega_1\left(1 - 3l_2^2\right)\right]}{\left(\frac{I_1}{p_a}\right)^m} + 27 = K \qquad \text{Eq. G. 3}$$

$$I_1^3 = K * I_3$$

Recalling that

$$b = \frac{(\sigma_2 - \sigma_3)}{(\sigma_1 - \sigma_3)} \qquad \text{Eq. G. 4}$$

$$I_1 = \sigma_1 + \sigma_2 + \sigma_3 \qquad \text{Eq. G. 5}$$

$$I_1 = \sigma_1 * \sigma_2 * \sigma_3 \qquad \text{Eq. G. 6}$$

Equation G. 3 can be rearranged so that it is in terms of b-value and stresses.

$$I_1^3 = K * I_3$$

$$(\sigma_1 + \sigma_2 + \sigma_3)^3 = K(\sigma_1 * \sigma_2 * \sigma_3) \qquad \text{Eq. G. 7}$$

$$(\sigma_1 + \sigma_2 + \sigma_3)^3 = K * \sigma_1\sigma_3(b(\sigma_1 - \sigma_3) + \sigma_3)$$

Rearranging the above equations in terms of σ_1/σ_3 results in

$$\frac{\sigma_1}{\sigma_3} = \frac{(\sigma_1 + \sigma_2 + \sigma_3)^3}{K * \sigma_3^2 (b(\sigma_1 - \sigma_3) + \sigma_3)}$$

$$\frac{\sigma_1}{\sigma_3} = \frac{(\sigma_1 + (b(\sigma_1 - \sigma_3) + \sigma_3) + \sigma_3)^3}{K * \sigma_3^2 (b(\sigma_1 - \sigma_3) + \sigma_3)}$$

$$SR = \frac{(SR + (b(SR - 1) + 1) + 1)^3}{(b(SR - 1) + 1)}$$

$$where$$

$$SR = \frac{\sigma_1}{\sigma_3}$$

$$0 = \left[SR + (b(SR - 1) + 1) + 1\right]^3 - SR * K(b(SR - 1) + 1)$$

Eq. G. 8

Equation G. 8 can be set to zero and the cubical equation can be solved only with inputting the values of k (equation G. 3) and b-value. The stress ratios can then be converted into friction angles if desired.

Appendix H – Equations used during Torsion Shear Testing where alpha, b-value and mean confining stress are kept constant.

The torsion shear experimental program involved conditions that kept b-value, alpha, and mean normal stress constant throughout the entire test. The inner pressure, outer pressure and vertical force therefore, had to be functions of the inputs given. By inputting the specific alpha, b-value and mean confining stress, while knowing the real-time inner and outer radius (calculated by inner volume change and specimen volume change), the stress path could be held constant. The mean normal stress was kept constant at 101.4 kPa. B-values varied in increments of 0.25 from 0 to 1 for each test and alpha values varied in 22.5 degree increments from 0 to 90 degrees. In the pages that follow, the equations used to derive the inner and outer pressure, as well as the vertical force required for the testing program is given.

As previously stated, in order to calculate stresses in a torsion shear specimen, the following equations are used:

$$\sigma_1 = \frac{\sigma_z + \sigma_\theta}{2} + \sqrt{\left(\frac{\sigma_z + \sigma_\theta}{2}\right)^2 + \tau_{z\theta}^{\ 2}} \qquad \text{Eq. H.1}$$

$$\sigma_3 = \frac{\sigma_z + \sigma_\theta}{2} - \sqrt{\left(\frac{\sigma_z + \sigma_\theta}{2}\right)^2 + \tau_{z\theta}^{\ 2}} \qquad \text{Eq. H.2}$$

$$\sigma_2 = \sigma_r = \frac{p_o r_o + p_i r_i}{r_o + r_i} \qquad \text{Eq. H.3}$$

$$\sigma_\theta = \frac{p_o r_o - p_i r_i}{r_o - r_i} \qquad \text{Eq. H.4}$$

$$\sigma_z = \frac{F_v}{\pi(r_o^2 - r_i^2)} + \frac{p_o r_o^2 - p_i r_i^2}{(r_o^2 - r_i^2)} \qquad \text{Eq. H.5}$$

$$\tau_{z\theta} = \frac{3M}{2\pi(r_o^3 - r_i^3)} \qquad \text{Eq. H.6}$$

The equations that were kept constant in the torsion shear experiments are:

$$\sigma_m = \frac{\sigma_1 + \sigma_2 + \sigma_3}{3} \qquad \text{Eq. H.7}$$

$$b = \frac{\sigma_2 - \sigma_3}{\sigma_1 - \sigma_3} \qquad \text{Eq. H.8}$$

$$\alpha = \frac{1}{2}\tan^{-1}\left(\frac{2\tau_{z\theta}}{\sigma_z - \sigma_\theta}\right) \qquad \text{Eq. H.9}$$

In order to express the vertical force (F_v), the inner pressure (p_i) and the outer pressure (p_o) as a function of moment (M), b-value, alpha (α), and mean confining stress (σ_m), the following equations were obtained.

$$\frac{\sigma_z + \sigma_\theta}{2} = \frac{F_v}{2\pi(r_o^2 - r_i^2)} + \frac{p_o r_o^2 - p_i r_i^2}{2(r_o^2 - r_i^2)} + \frac{p_o r_o - p_i r_i}{2(r_o - r_i)} \qquad \text{Eq. H.10}$$

which when simplified equals

$$\frac{\sigma_z + \sigma_\theta}{2} = \frac{F_v}{2\pi(r_o^2 - r_i^2)} + \frac{2p_o r_o^2 - 2p_i r_i^2 + r_i r_o(p_o - p_i)}{2(r_o^2 - r_i^2)} \qquad \text{Eq. H.11}$$

Similarly,

$$\frac{\sigma_z - \sigma_\theta}{2} = \frac{F_v}{2\pi(r_o^2 - r_i^2)} + \frac{p_o r_o^2 - p_i r_i^2}{2(r_o^2 - r_i^2)} - \frac{p_o r_o - p_i r_i}{2(r_o - r_i)}$$
$$\frac{\sigma_z - \sigma_\theta}{2} = \frac{F_v + \pi r_i r_o(p_i - p_o)}{2\pi(r_o^2 - r_i^2)} \qquad \text{Eq. H.12}$$

Using Equation H.11, the mean normal stress can be simplified by a rearrangement of terms where,

$$\sigma_m = \frac{1}{3}\left[(\sigma_1 + \sigma_3) + \sigma_2\right] = \frac{1}{3}\left[2\left(\frac{\sigma_z + \sigma_\theta}{2}\right) + \sigma_r\right] \qquad \text{Eq. H. 13}$$

Substituting equations H. 11 and H.3 into H.13 results in

$$\sigma_m = \frac{1}{3}\left[\frac{F_v}{\pi(r_o^2 - r_i^2)} + \frac{2p_o r_o^2 - 2p_i r_i^2 + r_i r_o(p_o - p_i)}{(r_o^2 - r_i^2)} + \frac{p_o r_o + p_i r_i}{(r_o + r_i)}\right]$$
$$\sigma_m = \frac{1}{3(r_o^2 - r_i^2)}\left[\frac{F_v}{\pi} + 3(p_o r_o^2 - pir_i^2)\right]$$

Eq. H. 14

Equation H.9 can be rearranged to get

$$\tan 2\alpha = \left(\frac{\tau_{z\theta}}{\frac{\sigma_z - \sigma_\theta}{2}} \right) = \frac{3M}{2\pi(r_o^3 - r_i^3)} \frac{2\pi(r_o^2 - r_i^2)}{F_v + \pi r_i r_o (p_i - p_o)}$$

$$3M \frac{(r_o^2 - r_i^2)}{(r_o^3 - r_i^3)} = \left[F_v + \pi r_i r_o (p_i - p_o) \right] \tan 2\alpha \qquad \text{Eq. H. 15}$$

In order to get Eq. H.8 in terms of p_o, p_i and F_v, the numerator and denominator of the b-value equation can be broken down into the following equations such that:

$$\sigma_1 - \sigma_3 = 2\sqrt{\left(\frac{\sigma_z - \sigma_\theta}{2} \right)^2 + \tau_{z\theta}^2} \qquad \text{Eq. H. 16}$$

$$(\sigma_1-\sigma_3)^2 = 4\left[\left(\frac{\sigma_z-\sigma_\theta}{2}\right)^2 + \tau_{z\theta}^2\right]$$
$$(\sigma_1-\sigma_3)^2 = 4\left[\left(\frac{F_v+\pi r_i r_o(p_i-p_o)}{2\pi(r_o^2-r_i^2)}\right)^2 + \left(\frac{3M}{2\pi(r_o^3-r_i^3)}\right)^2\right]$$
$$(\sigma_1-\sigma_3)^2 = \frac{1}{\pi^2(r_o^2-r_i^2)^2}\left[\left(F_v+\pi r_i r_o(p_i-p_o)\right)^2 + \left(F_v+\pi r_i r_o(p_i-p_o)\right)^2\tan^2 2\alpha\right]$$
$$(\sigma_1-\sigma_3)^2 = \frac{1}{\pi^2(r_o^2-r_i^2)^2}\left[\left(F_v+\pi r_i r_o(p_i-p_o)\right)^2 * \left(1+\tan^2 2\alpha\right)\right]$$
$$(\sigma_1-\sigma_3)^2 = \frac{1}{\pi^2(r_o^2-r_i^2)^2}\left[\left(F_v+\pi r_i r_o(p_i-p_o)\right)^2 * \frac{1}{\cos^2 2\alpha}\right]$$
$$(\sigma_1-\sigma_3) = \frac{\frac{F_v}{\pi}+r_i r_o(p_i-p_o)}{\cos 2\alpha(r_o^2-r_i^2)}$$

Eq. H. 17

In order to isolate σ_3, equations H.11 and H.17 can be used with Eq. H.2 such that

$$\sigma_3 = \frac{F_v}{2\pi(r_o^2-r_i^2)} + \frac{2p_o r_o^2 - 2p_i r_i^2 + r_i r_o(p_o-p_i)}{2(r_o^2-r_i^2)} - \frac{\frac{F_v}{\pi}+r_i r_o(p_i-p_o)}{\cos 2\alpha(r_o^2-r_i^2)}$$
$$\sigma_3 = \frac{\frac{F_v}{\pi}(\cos 2\alpha - 1) + 2\cos 2\alpha(p_o r_o^2 - p_i r_i^2) + r_i r_o(p_o-p_i)(\cos 2\alpha + 1)}{2(r_o^2-r_i^2)\cos 2\alpha}$$

Eq. H. 18

Combining Eq. H.3 and H.18, (σ_2-σ_3) is simplified to become

$$\sigma_2 - \sigma_3 = \frac{p_o r_o + p_i r_i}{r_o + r_i} - \frac{\frac{F_v}{\pi}(\cos 2\alpha - 1) + 2\cos 2\alpha (p_o r_o^2 - p_i r_i^2) + r_i r_o (p_o - p_i)(\cos 2\alpha + 1)}{2(r_o^2 - r_i^2)\cos 2\alpha}$$

$$\sigma_2 - \sigma_3 = \frac{\frac{F_v}{\pi}(1 - \cos 2\alpha) + 3\cos 2\alpha * r_i r_o (p_i - p_o) + r_i r_o (p_i - p_o)}{2(r_o^2 - r_i^2)\cos 2\alpha}$$

Eq. H. 19

Equation H. 19 can be combined with Equation H. 17 to solve for b, where

$$\frac{\sigma_2 - \sigma_3}{\sigma_1 - \sigma_3} = \frac{\dfrac{\frac{F_v}{\pi}(1 - \cos 2\alpha) + 3\cos 2\alpha * r_i r_o (p_i - p_o) + r_i r_o (p_i - p_o)}{2(r_o^2 - r_i^2)\cos 2\alpha}}{\dfrac{\frac{F_v}{\pi} + r_i r_o (p_i - p_o)}{\cos 2\alpha (r_o^2 - r_i^2)}}$$

$$b = \frac{\frac{F_v}{\pi}(1 - \cos 2\alpha) + (3\cos 2\alpha + 1) r_i r_o (p_i - p_o)}{2\left(\frac{F_v}{\pi} + r_i r_o (p_i - p_o)\right)}$$

Eq. H. 20

Equations H. 14, H. 15 and H. 20 are a set of three linear equations with three unknowns (p_i, p_o, and F_v). The three can be solved simultaneously resulting in three equations for p_i, p_o, and F_v :

$$p_i = \frac{3(r_o^2 - r_i^2)\sigma_m - \left[\frac{3r_o}{3r_o + r_i} + \frac{3\cos 2\alpha - 2b + 1}{1 - 2b - \cos 2\alpha} * \frac{r_i}{3r_o + r_i}\right]\left(3(r_o^2 - r_{i\ i}^2)\sigma_m - \left(\frac{3(r_o^2 - r_i^2)}{\pi(r_o^3 - r_i^3)}\right)\left(\frac{M}{\tan 2\alpha}\right)\right)}{\frac{3r_i(r_o^2 - r_i^2)}{3r_o + r_i} * \frac{4\cos 2\alpha}{\cos 2\alpha + 2b - 1}}$$

Eq. H. 21

$$p_o = \frac{3(r_o^2 - r_i^2)}{r_o(3r_o + r_i)}\sigma_m - \left(\frac{3(r_o^2 - r_i^2)}{\pi(r_o^3 - r_i^3)}\right)\left(\frac{1}{r_o(3r_o + r_i)}\right)\left(\frac{M}{\tan 2\alpha}\right) + \left(\frac{r_i(3r_i + r_o)}{r_o(3r_o + r_i)}\right)p_i$$

Eq, H. 22

$$F_v = \frac{3(r_o^2 - r_i^2)}{r_o(3r_o + r_i)}\pi\sigma_m - 3\pi r_o^2 p_o + 3\pi r_i^2 p_i$$

Eq. H. 23

Appendix Ia --- Measurement Error Corrections on Friction Angle for Torsion Shear Tests

Due to inaccuracies in the measurement devices in the torsion shear apparatus used, errors in the friction angle were calculated. The error estimation was calculated as follows.

The friction angle was calculated as

$$\sin\phi = \frac{(\sigma_1 - \sigma_3)}{(\sigma_1 + \sigma_3)} \qquad \text{Eq. I. 1}$$

From Equation H.17 found in Appendix H, we know that

$$\left(\sigma_1 - \sigma_3\right)^2 = 4\left[\left(\frac{F_v + \pi r_i r_o (p_i - p_o)}{2\pi(r_o^2 - r_i^2)}\right)^2 + \left(\frac{3M}{2\pi(r_o^3 - r_i^3)}\right)^2\right] \qquad \text{Eq. I.2}$$

which simplifies to

$$\left(\sigma_1 - \sigma_3\right) = \frac{\sqrt{\left(F_v + \pi r_i r_o (p_i - p_o)\right)^2 + \left(3M\,\frac{(r_o^2 - r_i^2)}{(r_o^3 - r_i^3)}\right)^2}}{\pi(r_o^2 - r_i^2)} \qquad \text{Eq.I.3}$$

We can also combine equations H.1 and H.2 to get

$$\sigma_1 + \sigma_3 = 2\left(\frac{\sigma_z + \sigma_\theta}{2}\right) \qquad \text{Eq. I.4}$$

Combining the above equation and Equation H.11 results in

$$\sigma_1 + \sigma_3 = \frac{F_v + \pi\left[2p_o r_o^2 - 2p_i r_i^2 + r_i r_o (p_o - p_i)\right]}{\pi\left(r_o^2 - r_i^2\right)} \qquad \text{Eq. I.5}$$

Substituting Equations I.3 and I.5 into I.1, the friction angle can be calculated as shown below.

$$\sin\phi = \frac{(\sigma_1 - \sigma_3)}{(\sigma_1 + \sigma_3)} = \frac{\sqrt{\left(F_v + \pi r_i r_o (p_i - p_o)\right)^2 + \left(3M\frac{(r_o^2 - r_i^2)}{(r_o^3 - r_i^3)}\right)^2}}{F_v + \pi\left[2p_o r_o^2 - 2p_i r_i^2 + r_i r_o (p_o - p_i)\right]} \qquad \text{Eq. I.5}$$

As previously defined, Fv is the vertical force. r_o and r_i are the outer and inner radii, respectively. P_o and P_i are the outer and inner cell pressures, respectively and alpha is the principal stress direction angle, measured from vertical. Because the radii do not change much throughout the test, they are considered to be constant in the error analysis. Therefore, Eq. I.5. can be simplified to

$$\sin\phi = \frac{(\sigma_1 - \sigma_3)}{(\sigma_1 + \sigma_3)} = \frac{\sqrt{\left(F_v + A(p_i - p_o)\right)^2 + (3MB)^2}}{\left(F_v + (Cp_o - Dp_i) + A(p_o - p_i)\right)} \qquad \text{Eq. I.6}$$

when

$A = \pi r_i r_o$

$B = \dfrac{(r_o^2 - r_i^2)}{(r_o^3 - r_i^3)}$

$C = 2\pi r_o^2$

$D = 2\pi r_i^2$

The error in friction angle can be calculated using the Least Squares Method where

$$\partial \sin\phi = \left[\left(\frac{\partial \sin\phi}{\partial F_v} \Delta F_v \right)^2 + \left(\frac{\partial \sin\phi}{\partial p_o} \Delta p_o \right)^2 + \left(\frac{\partial \sin\phi}{\partial p_i} \Delta p_i \right)^2 + \left(\frac{\partial \sin\phi}{\partial M} \Delta M \right)^2 \right]^{\frac{1}{2}} \qquad \text{Eq. I.7}$$

where

$$\frac{\partial \sin\phi}{\partial F_v} = \frac{(F_v + A(p_i - p_o))\left(F_v + (Cp_o - Dp_i) + A(p_o - p_i)\right)}{\sqrt{\left(F_v + A(p_i - p_o)\right)^2 + \left(3MB\right)^2}\left[\left(F_v + (Cp_o - Dp_i) + A(p_o - p_i)\right)\right]^2} - \frac{1\sqrt{\left(F_v + A(p_i - p_o)\right)^2 + \left(3MB\right)^2}}{\left[\left(F_v + (Cp_o - Dp_i) + A(p_o - p_i)\right)\right]^2}$$

Eq. I.8

$$\frac{\partial \sin\phi}{\partial p_i} = \frac{(F_v A + A^2(p_i - p_o))\left(F_v + (Cp_o - Dp_i) + A(p_o - p_i)\right)}{\sqrt{\left(F_v + A(p_i - p_o)\right)^2 + \left(3MB\right)^2}\left[\left(F_v + (Cp_o - Dp_i) + A(p_o - p_i)\right)\right]^2} - \frac{(-D - A)\sqrt{\left(F_v + A(p_i - p_o)\right)^2 + \left(3MB\right)^2}}{\left[\left(F_v + (Cp_o - Dp_i) + A(p_o - p_i)\right)\right]^2}$$

Eq. I. 9

$$\frac{\partial \sin\phi}{\partial p_o} = \frac{(-F_v A + A^2(p_o - p_i))\left(F_v + (Cp_o - Dp_i) + A(p_o - p_i)\right)}{\sqrt{\left(F_v + A(p_i - p_o)\right)^2 + \left(3MB\right)^2}\left[\left(F_v + (Cp_o - Dp_i) + A(p_o - p_i)\right)\right]^2} - \frac{(C + A)\sqrt{\left(F_v + A(p_i - p_o)\right)^2 + \left(3MB\right)^2}}{\left[\left(\left(F_v + (Cp_o - Dp_i) + A(p_o - p_i)\right)\right)\right]^2}$$

Eq. I.10

$$\frac{\partial \sin\phi}{\partial M} = \frac{(9B^2M)\left(F_v + (Cp_o - Dp_i) + A(p_o - p_i)\right)}{\sqrt{\left(F_v + A(p_i - p_o)\right)^2 + \left(3MB\right)^2}\left[\left(F_v + (Cp_o - Dp_i) + A(p_o - p_i)\right)\right]^2}$$

Eq. I.11

and

ΔF_v is the estimated error in F_v (vertical force)

Δp_i is the estimated error in p_i (inner pressure)

Δp_o is the estimated error in p_o (outer pressure)

ΔM is the estimated error in M (moment)

The derivative of $\sin\phi$ is calculated by

$$\partial \sin\phi = \cos\phi \Delta\phi$$

Eq. I. 12

The error $\Delta\phi$ can be calculated by combining Equation I. 7 and I. 15.

$$\Delta\phi = \frac{180}{\pi\cos\phi}\partial\sin\phi$$

$$\Delta\phi = \frac{180}{\pi\cos\phi}\left[\left(\frac{\partial\sin\phi}{\partial F_v}\Delta F_v\right)^2 + \left(\frac{\partial\sin\phi}{\partial p_o}\Delta p_o\right)^2 + \left(\frac{\partial\sin\phi}{\partial p_i}\Delta p_i\right)^2 + \left(\frac{\partial\sin\phi}{\partial M}\Delta M\right)^2\right]^{\frac{1}{2}}$$

Eq. I. 13

Appendix Ib --- Measurement Error Corrections on b-value for Torsion Shear Tests

In a similar way as the error was calculated for friction angle, the error on the b-value can also be calculated by following a similar process. For the torsion shear tests, the b-value, $(\sigma_2-\sigma_3)/(\sigma_1-\sigma_3)$ can be written out in terms of Fv, M, r_o, r_i, p_o and p_i. In order to get the numerator from the b-value equation, it is necessary to combine the terms as done below.

$$\left(\sigma_2-\sigma_3\right)=\frac{p_o r_o+p_i r_i}{r_o+r_i}-\left[\frac{F_v}{2\pi(r_o^2-r_i^2)}-\frac{2p_o r_o^2-2p_i r_i^2+r_i r_o(p_o-p_i)}{2(r_o^2-r_i^2)}\right]+\sqrt{\left(\frac{F_v+\pi r_i r_o(p_i-p_o)}{2\pi(r_o^2-r_i^2)}\right)^2+\left(\frac{3M}{2\pi(r_o^3-r_i^3)}\right)^2}$$

Eq. I.14

When terms are combined,

$$\left(\sigma_2-\sigma_3\right)=\left[\frac{-F_v+3\pi r_i r_o(p_i-p_o)+\sqrt{\left(F_v+\pi r_i r_o(p_i-p_o)\right)^2+\left(\frac{3M(r_o^2-r_i^2)}{(r_o^3-r_i^3)}\right)^2}}{2\pi(r_o^2-r_i^2)}\right]$$

Eq. I.15

By combining Eq. I.3 and I.15, the b-value can be written as,

$$\frac{(\sigma_2-\sigma_3)}{(\sigma_1-\sigma_3)}=\left[\frac{-F_v+3\pi r_i r_o(p_i-p_o)+\sqrt{\left(F_v+\pi r_i r_o(p_i-p_o)\right)^2+\left(\dfrac{3M(r_o^2-r_i^2)}{(r_o^3-r_i^3)}\right)^2}}{2\sqrt{\left(F_v+\pi r_i r_o(p_i-p_o)\right)^2+\left(\dfrac{3M(r_o^2-r_i^2)}{(r_o^3-r_i^3)}\right)^2}}\right]$$

Eq. I.16

or

$$\frac{(\sigma_2-\sigma_3)}{(\sigma_1-\sigma_3)}=\left[\frac{-F_v+3\pi r_i r_o(p_i-p_o)}{2\sqrt{\left(F_v+\pi r_i r_o(p_i-p_o)\right)^2+\left(\dfrac{3M(r_o^2-r_i^2)}{(r_o^3-r_i^3)}\right)^2}}+\frac{1}{2}\right]$$

Eq. I.17

Using the same substituions used when calculating the friction angle measurement error, equation I.17 can be simplified to become

$$\frac{(\sigma_2-\sigma_3)}{(\sigma_1-\sigma_3)}=\left[\frac{-F_v+3A(p_i-p_o)}{2\sqrt{\left(F_v+A(p_i-p_o)\right)^2+\left(3MB\right)^2}}+\frac{1}{2}\right]$$ Eq. I. 18

$$A=\pi r_i r_o$$
$$B=\frac{(r_o^2-r_i^2)}{(r_o^3-r_i^3)}$$
$$C=2\pi r_o^2$$
$$D=2\pi r_i^2$$

Using the Least Squares Method, the error in b-value can be calculated by:

$$\partial b = \left[\left(\frac{\partial b}{\partial F_v} \Delta F_v \right)^2 + \left(\frac{\partial b}{\partial p_o} \Delta p_o \right)^2 + \left(\frac{\partial b}{\partial p_i} \Delta p_i \right)^2 + \left(\frac{\partial b}{\partial M} \Delta M \right)^2 \right]^{\frac{1}{2}}$$

Eq. I.19

Where

$$\frac{\partial b}{\partial F_v} = \frac{-1\left(2\sqrt{\left(F_v + A(p_i - p_o)\right)^2 + \left(3MB\right)^2}\right)}{\left[2\sqrt{\left(F_v + A(p_i - p_o)\right)^2 + \left(3MB\right)^2}\right]^2} - \frac{\left(2F_v + 2A(p_i - p_o)\right)\left(-F_v + 3A(p_i - p_o)\right)}{\sqrt[3]{\left(F_v + A(p_i - p_o)\right)^2 + \left(3MB\right)^2}\left[2\sqrt{\left(F_v + A(p_i - p_o)\right)^2 + \left(3MB\right)^2}\right]^2}$$

Eq. I. 20

$$\frac{\partial b}{\partial p_i} = \frac{3A\left(2\sqrt{\left(F_v + A(p_i - p_o)\right)^2 + \left(3MB\right)^2}\right)}{\left[2\sqrt{\left(F_v + A(p_i - p_o)\right)^2 + \left(3MB\right)^2}\right]^2} - \frac{\left(2F_vA + 2A^2(p_i - p_o)\right)\left(-F_v + 3A(p_i - p_o)\right)}{\sqrt[3]{\left(F_v + A(p_i - p_o)\right)^2 + \left(3MB\right)^2}\left[2\sqrt{\left(F_v + A(p_i - p_o)\right)^2 + \left(3MB\right)^2}\right]^2}$$

Eq. I.21

$$\frac{\partial b}{\partial p_o} = \frac{-3A\left(2\sqrt{\left(F_v + A(p_i - p_o)\right)^2 + \left(3MB\right)^2}\right)}{\left[2\sqrt{\left(F_v + A(p_i - p_o)\right)^2 + \left(3MB\right)^2}\right]^2} - \frac{\left(-2F_vA + 2A^2(p_o - p_i)\right)\left(-F_v + 3A(p_i - p_o)\right)}{\sqrt[3]{\left(F_v + A(p_i - p_o)\right)^2 + \left(3MB\right)^2}\left[2\sqrt{\left(F_v + A(p_i - p_o)\right)^2 + \left(3MB\right)^2}\right]^2}$$

Eq. I.22

$$\frac{\partial b}{\partial M} = -\frac{\left(18B^2M\right)\left(-F_v + 3A(p_i - p_o)\right)}{\sqrt[3]{\left(F_v + A(p_i - p_o)\right)^2 + \left(3MB\right)^2}\left[2\sqrt{\left(F_v + A(p_i - p_o)\right)^2 + \left(3MB\right)^2}\right]^2}$$

Eq. I. 23

and

ΔF_v is the estimated error in F_v (vertical force)

Δp_i is the estimated error in p_i (inner pressure)

Δp_o is the estimated error in p_o (outer pressure)

ΔM is the estimated error in M (moment)

Appendix Ic --- Measurement Error Corrections on alpha for Torsion Shear Tests

Similarly, error analysis can be performed to get the error on alpha for torsion shear tests. Below is the process for this error calculation.

Combining equations H.6 and H.12, alpha can be written in terms of moment, inner and outer radii, inner and outer pressure and vertical force. This simplifies to:

$$\alpha = \frac{1}{2}\tan^{-1}\left(\frac{3M(r_o^2 - r_i^2)}{(r_o^3 - r_i^3)\left(F_v + \pi r_i r_o (p_i - p_o)\right)}\right) \qquad \text{Eq. I. 23}$$

Using the same substitutions shown in Appendix Ia and Ib, we can set the radii as constants and get

$$\alpha = \frac{1}{2}\tan^{-1}\left(\frac{3MB}{\left(F_v + A(p_i - p_o)\right)}\right) \qquad \text{Eq. I. 24}$$

where

$$A = \pi r_i r_o$$
$$B = \frac{(r_o^2 - r_i^2)}{(r_o^3 - r_i^3)}$$

Using the Least Squares Method, the error in alpha can be calculated by

$$\partial\alpha = \left[\left(\frac{\partial\alpha}{\partial F_v}\Delta F_v\right)^2 + \left(\frac{\partial\alpha}{\partial p_o}\Delta p_o\right)^2 + \left(\frac{\partial\alpha}{\partial p_i}\Delta p_i\right)^2 + \left(\frac{\partial\alpha}{\partial M}\Delta M\right)^2\right]^{\frac{1}{2}} \qquad \text{Eq. I. 25}$$

where

$$\frac{\partial a}{\partial F_v} = \frac{1}{2}\left(\frac{1}{1+\left(\frac{3MB}{\left(F_v + A(p_i - p_o)\right)}\right)^2}\right)\left(\frac{-3MB}{\left(F_v + A(p_i - p_o)\right)^2}\right) \qquad \text{Eq. I. 26}$$

$$\frac{\partial a}{\partial p_i} = \frac{1}{2}\left(\frac{1}{1+\left(\frac{3MB}{\left(F_v + A(p_i - p_o)\right)}\right)^2}\right)\left(\frac{-3MBA}{\left(F_v + A(p_i - p_o)\right)^2}\right) \qquad \text{Eq. I. 27}$$

$$\frac{\partial a}{\partial p_o} = \frac{1}{2}\left(\frac{1}{1+\left(\frac{3MB}{\left(F_v + A(p_i - p_o)\right)}\right)^2}\right)\left(\frac{3MBA}{\left(F_v + A(p_i - p_o)\right)^2}\right) \qquad \text{Eq. I. 28}$$

$$\frac{\partial a}{\partial M} = \frac{1}{2}\left(\frac{1}{1+\left(\frac{3MB}{\left(F_v + A(p_i - p_o)\right)}\right)^2}\right)\left(\frac{3B\left(F_v + A(p_i - p_o)\right)}{\left(F_v + A(p_i - p_o)\right)^2}\right) \qquad \text{Eq. I. 29}$$

and

ΔF_v is the estimated error in F_v (vertical force)

Δp_i is the estimated error in p_i (inner pressure)

Δp_o is the estimated error in p_o (outer pressure)

ΔM is the estimated error in M (moment)

Appendix Ja ---Measurement Error Corrections for True Triaxial Tests

As described in Appendix I, when doing true triaxial tests, it is important to calculate the possible measurement error on the friction angle. In the true triaxial apparatus the minor principal stress, σ_3, is applied by a constant cell pressure. The major and intermediate principal stress, σ_1 and σ_2, respectively, are applied by the cell pressure and the deviator load. It is necessary to calculate the error as follows.

$$\sin\phi = \frac{\sigma_1 - \sigma_3}{\sigma_1 + \sigma_3} = \frac{\left(\frac{F_v}{A} + \sigma_{cell}\right) - \sigma_{cell}}{\left(\frac{F_v}{A} + \sigma_{cell}\right) + \sigma_{cell}} = \frac{F_v}{F_v + 2A\sigma_{cell}} \qquad \text{Eq. J.1.}$$

where F_v is the vertical load, A is the specimen area where the deviator load is applied and σ_{cell} is the cell pressure.

Using the Least Squares Method (as done in Appendix I), the error in friction angle can be calculated by:

$$\partial \sin\phi = \left(\left(\frac{\partial \sin\phi}{\partial F_v} \Delta F_v \right)^2 + \left(\frac{\partial \sin\phi}{\partial A} \Delta A \right)^2 + \left(\frac{\partial \sin\phi}{\partial \sigma_{cell}} \Delta \sigma_{cell} \right)^2 \right)^{\frac{1}{2}} \qquad \text{Eq. J.2}$$

where

$$\frac{\partial \sin\phi}{\partial F_v} = \frac{2A\sigma_{cell}}{(F + 2A\sigma_{cell})^2} \qquad \text{Eq. J.3}$$

$$\frac{\partial \sin\phi}{\partial A} = \frac{-2F_v\sigma_{cell}}{(F + 2A\sigma_{cell})^2} \qquad \text{Eq. J.4}$$

$$\frac{\partial \sin\phi}{\partial \sigma_{cell}} = \frac{-2F_vA}{(F + 2A\sigma_{cell})^2} \qquad \text{Eq. J.5}$$

where

ΔF_v is the estimated error in F_v

ΔA is the estimated error in A

$\Delta\sigma_{cell}$ is the estimated error in σ_{cell}

The derivative of $\sin\varphi$ gives,

$$\partial \sin\phi = \cos\phi \Delta\phi \qquad \text{Eq. J. 6}$$

The error can be calculated by

$$\Delta\phi = \frac{180}{\pi\cos(\phi)}\left(\left(\frac{\partial\sin\phi}{\partial F_v}\Delta F_v\right)^2 + \left(\frac{\partial\sin\phi}{\partial A}\Delta A\right)^2 + \left(\frac{\partial\sin\phi}{\partial\sigma_{cell}}\Delta\sigma_{cell}\right)^2\right)^{\frac{1}{2}} \qquad \text{Eq. J. 7}$$

Appendix Jb --- Measurement Error Corrections on b-value for True Triaxial Tests

In a similar way as the error was calculated for friction angle, the error on the b-value can also be calculated by following a similar process. For the true triaxial tests, the b-value, $(\sigma_2-\sigma_3)/(\sigma_1-\sigma_3)$ can be written out in terms of F_v, F_h, A_v, A_h and σ_{cell} as follows:

$$b=\frac{(\sigma_2-\sigma_3)}{(\sigma_1-\sigma_3)}=\frac{\left(\frac{F_h}{A_v}+\sigma_{cell}\right)-\sigma_{cell}}{\left(\frac{F_v}{A_h}+\sigma_{cell}\right)-\sigma_{cell}}=\frac{\frac{F_h}{A_v}}{\frac{F_v}{A_h}}=\frac{F_hA_h}{F_vA_v} \qquad \text{Eq. J. 8}$$

Therefore, the error in b-value using the Least Squares Method can be calculated by

$$\partial b=\left(\left(\frac{\partial b}{\partial F_h}\Delta F_h\right)^2+\left(\frac{\partial b}{\partial F_v}\Delta F_v\right)^2+\left(\frac{\partial b}{\partial A_h}\Delta A_h\right)^2+\left(\frac{\partial b}{\partial A_v}\Delta A_v\right)^2\right)^{\frac{1}{2}} \qquad \text{Eq. J. 9}$$

where

$$\frac{\partial b}{\partial F_h}=\frac{A_hF_vA_v}{(F_vA_v)^2} \qquad \text{Eq. J. 10}$$

$$\frac{\partial b}{\partial F_v}=-\frac{A_vF_hA_h}{(F_vA_v)^2} \qquad \text{Eq. J. 11}$$

$$\frac{\partial b}{\partial A_h} = \frac{F_h F_v A_v}{\left(F_v A_v\right)^2} \qquad \text{Eq. J. 12}$$

$$\frac{\partial b}{\partial A_v} = -\frac{F_v F_h A_v}{\left(F_v A_v\right)^2} \qquad \text{Eq. J. 13}$$

and

ΔF_v is the estimated error in vertical force, F_v

ΔF_h is the estimated error in horiziontal force, F_h

ΔA_v is the estimated error in vertical area, A_v (length times height)

ΔA_h is the estimated error in vertical area, A_h (length times width)

Appendix K --- Polynomial Regression Explanation (after Chapra and Canale 2010).

In order to represent certain engineering data which cannot be captured with a straight line, a curve can be used to fit the data. A method to get this curve is to fit polynomial expressions to the data using a polynomial regression. By using the Least Squares procedure, the data can be fit to a higher order polynomial. The equations used that can be set to zero are shown below. In the case of a fourth order polynomial with 5 unknowns, 5 equations are required to solve the matrix. This is the case when using the fourth order Pietrusczack (2011) equation.

$$
\begin{aligned}
&(n)a_0 + \left(\sum x_i\right)a_1 + \left(\sum x_i^2\right)a_2 + \left(\sum x_i^3\right)a_3 + \left(\sum x_i^4\right)a_4 = \left(\sum y_i\right) \\
&\left(\sum x_i\right)a_0 + \left(\sum x_i^2\right)a_1 + \left(\sum x_i^3\right)a_2 + \left(\sum x_i^4\right)a_3 + \left(\sum x_i^5\right)a_4 = \left(\sum x_i y_i\right) \\
&\left(\sum x_i^2\right)a_0 + \left(\sum x_i^3\right)a_1 + \left(\sum x_i^4\right)a_2 + \left(\sum x_i^5\right)a_3 + \left(\sum x_i^6\right)a_4 = \left(\sum x_i^2 y_i\right) \\
&\left(\sum x_i^3\right)a_0 + \left(\sum x_i^4\right)a_1 + \left(\sum x_i^5\right)a_2 + \left(\sum x_i^6\right)a_3 + \left(\sum x_i^7\right)a_4 = \left(\sum x_i^3 y_i\right) \\
&\left(\sum x_i^4\right)a_0 + \left(\sum x_i^5\right)a_1 + \left(\sum x_i^6\right)a_2 + \left(\sum x_i^7\right)a_3 + \left(\sum x_i^8\right)a_4 = \left(\sum x_i^4 y_i\right) \\
&\left(\sum x_i^5\right)a_0 + \left(\sum x_i^6\right)a_1 + \left(\sum x_i^7\right)a_2 + \left(\sum x_i^8\right)a_3 + \left(\sum x_i^9\right)a_4 = \left(\sum x_i^5 y_i\right)
\end{aligned}
\qquad \text{Eq. K.1}
$$

where n is the number of data points used, a_1 through a_4 are the coefficients of the polynomial expression that is being solved.

Solving the coefficients of an mth order polynomial is equivalent to solving a system of m+1 simultaneous linear equations. Therefore, for this case, the standard error is

$$s_{y/x} = \sqrt{\frac{S_r}{n-(m+1)}} \qquad \text{Eq. K.2}$$

S_r is the sums of the residuals and n is the number of points used. As can be seen in the equation, when using only 5 points, a 4th order equation cannot be attained. For the particular case of this thesis (in Chapter 11), Equation K.3 was separated so that

$$\eta_f = \eta_0\left[1+\Omega_1(1-3l_2^2)+a_1\left(\Omega_1(1-3l_2^2)\right)^2+a_2\left(\Omega_1(1-3l_2^2)\right)^3+a_3\left(\Omega_1(1-3l_2^2)\right)^4+\ldots\right] \qquad \text{Eq. K.3}$$

$$\eta_f = \eta_0+\eta_0\Omega_1 x+\eta_0\Omega_1 a_1 x^2+\eta_0\Omega_1 a_2 x^3+\eta_0\Omega_1 a_3 x^4$$

where

$$\eta_f = \left(\frac{I_1^3}{I_3}-27\right)\left(\frac{I_1}{p_a}\right)^m \qquad \text{Eq. K.4}$$

and

$$x = (1-3l_2^2)$$

By plugging in the corresponding values of points from the torsion shear results and solving the matrix, all the parameters can be determined.

Appendix L –Test Data Sheets

Torsion Shear Test on Fine Nevada Sand with a Target Void Ratio = 0.530 (D_r = 91.28%)

Test No.:	1*	
Test Date:	5/10/10	
Initial Height, h_i:	39.85	cm
Initial Void Ratio, e:	0.510	
Final Mean Princpal Stress, σ_m :	98.0	kPa
Max Friction Angle, ϕ:	38.0	deg
b-value at failure:	0.00	
Stress direction at failure, α:	0	deg

Shear Band Notes	27
Point of Observation:	
none observed.	
Inclination (from Vertical)	
n/a	
Failure Notes:	
n/a	

Point (No.)	ε_z (%)	ε_r (%)	ε_θ (%)	ε_v (%)	$\gamma_{\theta z}$ (%)	σ_z (kPa)	σ_r (kPa)	σ_θ (kPa)	$\tau_{\theta z}$ (kPa)	b	α (°)	φ (°)
1	0.000	0.000	0.000	0.000	0.000	89.203	101.239	101.540	0.000	0.024	0.000	-3.708
2	0.013	-0.005	-0.003	0.005	0.000	103.472	94.687	94.382	0.000	0.034	0.000	2.633
3	0.027	-0.013	-0.008	0.006	0.000	115.123	89.179	88.589	0.000	0.022	0.000	7.484
4	0.045	-0.022	-0.011	0.011	0.000	125.568	84.190	84.404	0.000	-0.005	0.000	11.306
5	0.063	-0.037	-0.016	0.010	0.000	134.376	79.958	79.996	0.000	-0.001	0.000	14.695
6	0.083	-0.051	-0.022	0.010	0.000	142.313	76.114	75.851	0.000	0.004	0.000	17.737
7	0.106	-0.067	-0.028	0.011	0.000	149.787	72.417	72.202	0.000	0.003	0.000	20.457
8	0.124	-0.081	-0.033	0.010	0.000	154.925	70.114	70.159	0.000	-0.001	0.000	22.123
9	0.141	-0.094	-0.038	0.009	0.000	158.391	68.226	67.706	0.000	0.006	0.000	23.646
10	0.173	-0.118	-0.046	0.008	0.000	164.618	65.388	65.225	0.000	0.002	0.000	25.622
11	0.207	-0.144	-0.057	0.007	0.000	169.411	62.910	62.555	0.000	0.003	0.000	27.429
12	0.246	-0.174	-0.070	0.003	0.000	173.827	60.697	60.543	0.000	0.001	0.000	28.905
13	0.291	-0.208	-0.085	-0.002	0.000	177.997	58.750	58.755	0.000	0.000	0.000	30.243
14	0.346	-0.252	-0.105	-0.011	0.000	181.373	56.763	56.568	0.000	0.002	0.000	31.636
15	0.396	-0.293	-0.125	-0.022	0.000	184.445	55.504	55.294	0.000	0.002	0.000	32.596
16	0.459	-0.346	-0.151	-0.038	0.000	187.059	54.105	53.748	0.000	0.003	0.000	33.614
17	0.520	-0.398	-0.178	-0.056	0.000	189.303	52.945	52.791	0.000	0.001	0.000	34.324
18	0.589	-0.456	-0.211	-0.078	0.000	191.351	51.954	51.621	0.000	0.002	0.000	35.106
19	0.667	-0.525	-0.248	-0.106	0.000	193.114	50.930	50.840	0.000	0.001	0.000	35.676
20	0.746	-0.595	-0.288	-0.137	0.000	194.448	50.133	49.917	0.000	0.001	0.000	36.261
21	0.820	-0.661	-0.325	-0.166	0.000	195.865	49.579	49.712	0.000	-0.001	0.000	36.523
22	0.894	-0.726	-0.368	-0.201	0.000	196.581	49.025	48.607	0.000	0.003	0.000	37.122
23	0.976	-0.802	-0.411	-0.236	0.000	197.565	48.516	48.421	0.000	0.001	0.000	37.323
24	1.075	-0.891	-0.464	-0.281	0.000	198.346	47.935	47.669	0.000	0.002	0.000	37.769
25	1.149	-0.959	-0.505	-0.315	0.000	198.566	47.649	47.339	0.000	0.002	0.000	37.951
26	1.239	-1.042	-0.553	-0.356	0.000	199.217	47.377	47.407	0.000	0.000	0.000	37.992
27	1.350	-1.146	-0.608	-0.404	0.000	199.582	47.232	47.402	0.000	-0.001	0.000	38.036

Torsion Shear Test on Fine Nevada Sand with a Target Void Ratio = 0.530 (D_r = 91.28%)

Test No.:	2	
Test Date:	10/25/11	
Initial Height, h_i:	39.96	cm
Initial Void Ratio, e:	0.529	
Final Mean Princpal Stress, σ_m :	101.5	kPa
Max Friction Angle, ϕ:	56.9	deg
b-value at failure:	0.75	
Stress direction at failure, α:	0	deg

Shear Band Notes	33
Point of Observation:	
Inclination (from Vertical)	
7@65°, 67°, 68°, 75°, 90°	
Failure Notes:	
deep zig-zag patterns and vertical trough	

Point (No.)	ε_z (%)	ε_r (%)	ε_θ (%)	ε_v (%)	$\gamma_{\theta z}$ (%)	σ_z (kPa)	σ_r (kPa)	σ_θ (kPa)	$\tau_{\theta z}$ (kPa)	b	α (°)	φ (°)
1	0.000	-0.001	0.000	-0.001	0.000	100.540	101.315	101.401	0.000	0.900	0.000	0.244
2	0.001	0.002	-0.001	0.002	0.000	102.952	102.105	98.779	0.000	0.797	0.000	1.185
3	0.038	0.031	-0.043	0.026	0.000	134.866	114.985	53.710	0.000	0.755	0.000	25.491
4	0.048	0.034	-0.055	0.027	0.000	139.094	116.736	47.973	0.000	0.755	0.000	29.150
5	0.052	0.036	-0.061	0.027	0.000	140.615	117.426	45.427	0.000	0.756	0.000	30.773
6	0.058	0.037	-0.068	0.026	0.000	142.514	118.022	43.310	0.000	0.753	0.000	32.267
7	0.064	0.038	-0.076	0.025	0.000	144.165	118.667	41.107	0.000	0.753	0.000	33.797
8	0.069	0.040	-0.084	0.024	0.000	145.559	119.215	39.343	0.000	0.752	0.000	35.061
9	0.074	0.041	-0.093	0.022	0.000	146.719	119.658	37.753	0.000	0.752	0.000	36.206
10	0.080	0.044	-0.103	0.021	0.000	147.757	120.074	36.127	0.000	0.752	0.000	37.378
11	0.088	0.047	-0.115	0.020	0.000	148.922	120.576	34.325	0.000	0.753	0.000	38.710
12	0.094	0.050	-0.125	0.018	0.000	149.756	120.959	33.094	0.000	0.753	0.000	39.645
13	0.100	0.051	-0.136	0.016	0.000	150.734	121.301	31.998	0.000	0.752	0.000	40.525
14	0.107	0.055	-0.148	0.013	0.000	151.594	121.675	30.675	0.000	0.753	0.000	41.560
15	0.114	0.058	-0.161	0.010	0.000	152.316	121.932	29.782	0.000	0.752	0.000	42.291
16	0.127	0.066	-0.188	0.005	0.000	153.624	122.437	27.975	0.000	0.752	0.000	43.781
17	0.136	0.071	-0.207	0.001	0.000	154.231	122.764	26.792	0.000	0.753	0.000	44.749
18	0.151	0.080	-0.236	-0.005	0.000	155.226	123.132	25.430	0.000	0.753	0.000	45.929
19	0.158	0.083	-0.250	-0.009	0.000	155.838	123.366	24.786	0.000	0.752	0.000	46.515
20	0.166	0.087	-0.266	-0.014	0.000	156.627	123.617	24.090	0.000	0.751	0.000	47.172
21	0.182	0.096	-0.303	-0.024	0.000	157.515	123.994	22.641	0.000	0.751	0.000	48.474
22	0.193	0.103	-0.328	-0.032	0.000	158.029	124.180	22.112	0.000	0.751	0.000	48.982
23	0.207	0.113	-0.362	-0.043	0.000	158.190	124.475	21.017	0.000	0.754	0.000	49.947
24	0.227	0.125	-0.407	-0.055	0.000	159.225	124.688	20.236	0.000	0.752	0.000	50.758
25	0.252	0.141	-0.467	-0.074	0.000	160.225	125.137	19.228	0.000	0.751	0.000	51.786
26	0.255	0.142	-0.474	-0.077	0.000	160.395	125.169	19.025	0.000	0.751	0.000	51.992
27	0.309	0.176	-0.609	-0.123	1.000	161.312	125.561	17.230	0.000	0.752	0.000	53.804
28	0.317	0.180	-0.627	-0.130	2.000	161.648	125.609	17.113	0.000	0.751	0.000	53.953
29	0.375	0.216	-0.778	-0.187	3.000	162.832	126.107	15.597	0.000	0.751	0.000	55.606
30	0.389	0.225	-0.816	-0.202	4.000	163.065	126.203	15.351	0.000	0.750	0.000	55.885
31	0.408	0.238	-0.866	-0.221	5.000	163.315	126.283	15.023	0.000	0.750	0.000	56.256
32	0.424	0.248	-0.911	-0.239	6.000	163.487	126.378	14.735	0.000	0.751	0.000	56.579
33	0.441	0.258	-0.956	-0.256	7.000	163.736	126.435	14.452	0.000	0.750	0.000	56.907

Torsion Shear Test on Fine Nevada Sand with a Target Void Ratio = 0.530 (D_r = 91.28%)

Test No.:	3	
Test Date:	7/28/11	
Initial Height, h_i:	40.15	cm
Initial Void Ratio, e:	0.523	
Final Mean Princpal Stress, σ_m :	100.8	kPa
Max Friction Angle, ϕ:	39.9	deg
b-value at failure:	0.00	
Stress direction at failure, α:	22.4	deg

Shear Band Notes	
Point of Observation:	24
Inclination (from Vertical)	
19°, 20°, 23°	
Failure Notes:	
One thick shear band wrapping around	

Point (No.)	ε_z (%)	ε_r (%)	ε_θ (%)	ε_v (%)	$\gamma_{\theta z}$ (%)	σ_z (kPa)	σ_r (kPa)	σ_θ (kPa)	$\tau_{\theta z}$ (kPa)	b	α (°)	φ (°)
1	0.000	0.000	0.000	0.000	0.017	102.617	100.056	101.076	2.500	0.158	36.436	1.472
2	0.001	-0.001	0.000	0.000	0.018	105.370	98.310	99.539	4.308	0.102	27.957	2.910
3	0.030	-0.062	0.012	-0.020	0.245	155.886	65.996	81.373	40.069	0.019	23.541	27.465
4	0.050	-0.089	0.006	-0.033	0.327	160.685	62.858	79.788	43.191	0.015	23.439	29.482
5	0.095	-0.132	-0.013	-0.050	0.421	165.095	59.909	77.787	44.981	0.009	22.929	31.074
6	0.119	-0.162	-0.023	-0.066	0.499	167.730	58.287	76.810	46.285	0.007	22.758	32.046
7	0.245	-0.315	-0.083	-0.153	0.786	174.531	53.872	74.373	50.371	0.003	22.583	34.802
8	0.331	-0.417	-0.130	-0.216	0.980	177.238	52.196	73.702	51.844	0.000	22.521	35.727
9	0.394	-0.501	-0.166	-0.273	1.135	179.002	50.970	72.864	52.582	-0.002	22.368	36.387
10	0.427	-0.535	-0.185	-0.293	1.194	179.265	50.892	72.979	53.083	-0.001	22.484	36.553
11	0.488	-0.612	-0.221	-0.345	1.328	180.367	50.183	72.759	53.852	-0.002	22.513	36.975
12	0.518	-0.650	-0.240	-0.372	1.397	180.871	49.869	72.450	53.998	-0.002	22.444	37.164
13	0.582	-0.729	-0.280	-0.427	1.537	181.693	49.404	72.178	54.587	-0.001	22.455	37.526
14	0.619	-0.782	-0.304	-0.467	1.632	182.254	49.071	72.129	54.969	-0.002	22.476	37.713
15	0.680	-0.855	-0.344	-0.518	1.751	182.768	48.674	71.740	55.317	-0.001	22.449	38.014
16	0.736	-0.928	-0.381	-0.572	1.881	183.353	48.368	71.496	55.707	-0.001	22.443	38.279
17	0.796	-1.004	-0.421	-0.629	2.011	183.844	47.963	71.296	56.065	-0.001	22.447	38.512
18	0.823	-1.042	-0.440	-0.658	2.078	183.986	47.809	71.235	56.200	-0.001	22.455	38.594
19	0.894	-1.130	-0.489	-0.725	2.228	184.639	47.512	71.215	56.515	-0.002	22.450	38.745
20	0.916	-1.161	-0.505	-0.749	2.282	184.570	47.344	71.174	56.580	-0.003	22.470	38.785
21	0.966	-1.224	-0.538	-0.796	2.388	184.939	47.203	71.064	56.786	-0.002	22.462	38.920
22	1.029	-1.303	-0.584	-0.858	2.525	185.322	46.975	70.738	56.999	-0.001	22.426	39.141
23	1.122	-1.417	-0.649	-0.944	2.722	185.793	46.655	70.203	56.497	-0.003	22.175	39.156
24	1.222	-1.556	-0.727	-1.061	2.957	186.050	46.337	70.052	57.610	0.000	22.404	39.673
25	1.225	-1.560	-0.729	-1.064	2.965	186.037	46.338	70.087	57.605	0.000	22.408	39.657
26	1.265	-1.615	-0.760	-1.110	3.063	186.203	46.190	70.278	57.777	-0.001	22.454	39.656
27	1.322	-1.681	-0.799	-1.158	3.168	186.539	46.121	70.460	57.880	-0.003	22.461	39.634
28	1.358	-1.732	-0.827	-1.201	3.259	186.787	46.034	70.483	57.986	-0.003	22.459	39.673
29	1.423	-1.808	-0.872	-1.257	3.381	186.943	45.944	70.434	58.065	-0.003	22.453	39.728
30	1.466	-1.868	-0.904	-1.306	3.486	187.282	45.883	70.480	58.091	-0.004	22.424	39.728
31	1.501	-1.909	-0.929	-1.337	3.554	187.143	45.859	70.313	58.171	-0.003	22.440	39.823
32	1.545	-1.964	-0.963	-1.382	3.653	187.045	45.869	70.297	58.245	-0.002	22.468	39.857
33	1.620	-2.057	-1.020	-1.456	3.813	187.571	45.754	70.368	58.244	-0.004	22.412	39.839

Torsion Shear Test on Fine Nevada Sand with a Target Void Ratio = 0.530 (D_r = 91.28%)

Test No.:	4*	
Test Date:	8/1/10	
Initial Height, h_i:	40	cm
Initial Void Ratio, e:	0.548	
Final Mean Princpal Stress, σ_m :	97.5	kPa
Max Friction Angle, ϕ:	46.5	deg
b-value at failure:	0.27	
Stress direction at failure, α:	24.0	deg

Shear Band Notes

Point of Observation: 30

Inclination (from Vertical)
along middle at 40° and at 90°

Failure Notes: specimen bulged before shearing

Point (No.)	ε_z (%)	ε_r (%)	ε_θ (%)	ε_v (%)	$\gamma_{\theta z}$ (%)	σ_z (kPa)	σ_r (kPa)	σ_θ (kPa)	$\tau_{\theta z}$ (kPa)	b	α (°)	φ (°)
1	0.000	0.000	0.000	0.000	-0.003	89.995	101.394	101.498	0.779	0.986	86.142	3.475
2	0.001	-0.001	-0.001	-0.001	-0.003	90.825	100.594	100.006	2.440	0.998	76.003	3.123
3	0.022	-0.008	-0.008	0.006	0.006	111.812	93.042	87.841	17.397	0.339	27.717	12.218
4	0.026	-0.007	-0.010	0.009	0.018	116.891	91.202	84.646	21.485	0.322	26.558	15.460
5	0.027	-0.004	-0.012	0.011	0.039	121.624	89.398	81.619	25.853	0.313	26.136	18.763
6	0.028	0.000	-0.014	0.013	0.071	125.426	87.968	79.595	30.732	0.310	26.645	21.960
7	0.030	0.005	-0.021	0.013	0.113	129.511	86.551	77.222	34.566	0.306	26.449	24.789
8	0.037	0.008	-0.034	0.011	0.176	134.327	84.728	74.169	38.198	0.299	25.891	27.800
9	0.048	0.015	-0.055	0.008	0.295	138.767	82.993	71.321	41.575	0.294	25.477	30.638
10	0.062	0.021	-0.085	-0.001	0.422	143.087	81.333	68.975	44.431	0.287	25.086	33.069
11	0.078	0.028	-0.122	-0.016	0.554	146.508	80.003	66.540	46.670	0.284	24.706	35.234
12	0.103	0.032	-0.171	-0.036	0.697	149.177	78.905	64.770	48.597	0.282	24.514	36.991
13	0.161	0.037	-0.304	-0.106	1.031	154.148	76.874	61.193	51.625	0.278	24.002	40.177
14	0.198	0.034	-0.379	-0.147	1.210	156.793	76.103	61.151	53.365	0.271	24.068	41.115
15	0.248	0.022	-0.451	-0.181	1.335	157.886	75.680	60.103	53.888	0.271	23.892	41.880
16	0.259	0.022	-0.485	-0.203	1.410	158.183	75.473	59.581	54.144	0.272	23.840	42.263
17	0.293	0.015	-0.547	-0.239	1.537	159.183	75.181	59.224	55.147	0.271	23.907	42.963
18	0.309	0.016	-0.601	-0.275	1.646	160.181	74.843	58.721	55.644	0.270	23.822	43.469
19	0.326	0.016	-0.641	-0.300	1.728	160.591	74.610	58.684	55.985	0.269	23.847	43.667
20	0.333	0.017	-0.665	-0.315	1.780	160.581	74.557	58.541	56.222	0.269	23.888	43.864
21	0.384	0.002	-0.747	-0.361	1.917	161.475	74.291	57.892	56.540	0.269	23.755	44.352
22	0.387	0.002	-0.756	-0.366	1.936	161.400	74.292	57.658	56.678	0.271	23.768	44.545
23	0.399	0.002	-0.798	-0.396	2.020	161.779	74.130	57.349	56.898	0.271	23.729	44.817
24	0.402	0.002	-0.806	-0.402	2.037	161.933	74.121	57.648	56.922	0.269	23.755	44.677
25	0.440	-0.006	-0.887	-0.453	2.194	162.734	73.877	57.696	57.523	0.267	23.802	44.969
26	0.456	-0.006	-0.942	-0.492	2.306	162.738	73.778	57.255	57.796	0.269	23.809	45.343
27	0.502	-0.020	-1.025	-0.543	2.449	163.404	73.536	56.930	58.054	0.267	23.739	45.642
28	0.530	-0.021	-1.116	-0.606	2.626	163.914	73.380	56.485	58.292	0.268	23.670	45.997
29	0.554	-0.030	-1.182	-0.658	2.754	163.666	73.316	56.120	58.388	0.270	23.678	46.246
30	0.656	-0.133	-1.356	-0.833	3.255	162.734	73.457	56.304	58.996	0.273	23.975	46.506
31	0.727	-0.140	-1.567	-0.981	3.667	163.030	73.379	56.134	58.790	0.272	23.863	46.475

Torsion Shear Test on Fine Nevada Sand with a Target Void Ratio = 0.530 (D_r = 91.28%)

Test No.:	5*	
Test Date:	12/3/10	
Initial Height, h_i:	39.96	cm
Initial Void Ratio, e:	0.524	
Final Mean Princpal Stress, σ_m :	98.0	kPa
Max Friction Angle, ϕ:	42.0	deg
b-value at failure:	0.27	
Stress direction at failure, α:	23.5	deg

Shear Band Notes	
Point of Observation:	33
Inclination (from Vertical)	
2@34°	
Failure Notes:	

Point (No.)	ε_z (%)	ε_r (%)	ε_θ (%)	ε_v (%)	$\gamma_{\theta z}$ (%)	σ_z (kPa)	σ_r (kPa)	σ_θ (kPa)	$\tau_{\theta z}$ (kPa)	b	α (°)	φ (°)
1	0.001	0.000	0.000	0.001	0.001	92.963	100.025	99.151	3.698	0.912	64.958	2.877
2	0.001	0.001	0.000	0.002	0.002	95.382	99.307	98.249	5.574	0.716	52.212	3.408
3	0.004	0.004	0.004	0.012	0.043	111.140	93.322	88.249	17.237	0.346	28.208	11.978
4	0.005	0.005	0.004	0.014	0.078	116.277	91.416	85.120	21.781	0.327	27.214	15.422
5	0.013	0.003	0.000	0.016	0.120	120.116	89.946	82.715	26.004	0.321	27.139	18.411
6	0.032	-0.001	-0.011	0.019	0.204	125.989	87.718	79.135	31.013	0.309	26.466	22.269
7	0.045	-0.005	-0.021	0.020	0.260	129.507	86.468	77.195	33.502	0.301	26.010	24.283
8	0.060	-0.008	-0.032	0.020	0.316	132.580	85.283	75.143	35.447	0.296	25.493	26.056
9	0.073	-0.010	-0.042	0.021	0.361	135.228	84.411	73.984	36.845	0.289	25.135	27.258
10	0.084	-0.012	-0.054	0.018	0.407	136.857	83.731	72.681	38.016	0.289	24.917	28.349
11	0.100	-0.013	-0.074	0.013	0.496	139.797	82.683	71.125	40.027	0.284	24.688	30.004
12	0.125	-0.017	-0.103	0.005	0.589	141.901	81.832	69.649	41.637	0.283	24.527	31.409
13	0.146	-0.021	-0.130	-0.004	0.667	143.789	81.199	68.663	42.751	0.280	24.348	32.394
14	0.165	-0.024	-0.155	-0.014	0.739	144.993	80.759	68.149	43.829	0.279	24.380	33.156
15	0.191	-0.029	-0.193	-0.031	0.842	146.484	80.212	66.937	44.744	0.279	24.183	34.126
16	0.244	-0.031	-0.284	-0.072	1.075	148.877	79.273	65.212	46.732	0.279	24.083	35.868
17	0.300	-0.083	-0.331	-0.114	1.296	149.900	78.727	64.700	48.064	0.278	24.224	36.767
18	0.320	-0.088	-0.371	-0.138	1.376	151.743	78.106	62.929	48.222	0.277	23.679	37.643
19	0.361	-0.096	-0.448	-0.183	1.547	152.683	77.629	62.710	49.359	0.275	23.827	38.324
20	0.397	-0.100	-0.519	-0.223	1.692	154.092	77.327	61.964	49.865	0.274	23.634	38.933
21	0.426	-0.104	-0.574	-0.252	1.803	154.451	77.082	61.567	50.249	0.274	23.627	39.309
22	0.490	-0.120	-0.711	-0.341	2.078	155.781	76.635	60.850	51.167	0.273	23.575	40.117
23	0.525	-0.125	-0.787	-0.388	2.233	156.399	76.407	60.630	51.651	0.272	23.584	40.471
24	0.685	-0.140	-1.169	-0.625	2.985	158.441	75.764	59.645	53.114	0.271	23.538	41.697
25	0.692	-0.142	-1.186	-0.636	3.016	158.410	75.724	59.491	53.044	0.271	23.501	41.734
26	0.694	-0.142	-1.192	-0.640	3.027	158.410	75.730	59.490	53.112	0.271	23.519	41.769
27	0.732	-0.151	-1.292	-0.711	3.223	158.714	75.586	59.336	53.338	0.271	23.514	41.961
28	0.759	-0.148	-1.359	-0.748	3.353	158.999	75.544	59.452	53.502	0.270	23.534	41.992
29	0.869	-0.152	-1.583	-0.866	3.723	157.671	75.728	59.434	52.685	0.272	23.503	41.571
30	0.916	-0.159	-1.675	-0.919	3.877	158.189	75.735	59.707	52.992	0.270	23.551	41.603
31	0.967	-0.169	-1.769	-0.971	4.022	158.630	75.712	59.946	53.164	0.269	23.568	41.581
32	1.017	-0.176	-1.861	-1.020	4.158	158.819	75.645	59.948	53.275	0.268	23.570	41.639
33	1.117	-0.180	-2.045	-1.108	4.426	158.938	75.549	59.481	53.045	0.269	23.424	41.742

Torsion Shear Test on Fine Nevada Sand with a Target Void Ratio = 0.530 (D_r = 91.28%)

Test No.:	6
Test Date:	8/31/11
Initial Height, h_i:	39.96 cm
Initial Void Ratio, e:	0.526
Final Mean Princpal Stress, σ_m :	101.3 kPa
Max Friction Angle, ϕ:	45.9 deg
b-value at failure:	0.50
Stress direction at failure, α:	22.5 deg

Shear Band Notes	
Point of Observation:	30
Inclination (from Vertical)	
28°, 43°, 2@48°, 49°, 50°	
Failure Notes:	
6 parallel shear bands	

Point (No.)	ε_z (%)	ε_r (%)	ε_θ (%)	ε_v (%)	$\gamma_{\theta z}$ (%)	σ_z (kPa)	σ_r (kPa)	σ_θ (kPa)	$\tau_{\theta z}$ (kPa)	b	α (°)	φ (°)
1	0.000	0.000	0.000	0.000	0.001	101.463	101.328	100.228	0.397	0.829	16.361	0.417
2	0.001	-0.001	0.000	0.000	0.004	102.508	101.378	98.849	3.712	0.584	31.883	2.356
3	0.005	0.001	-0.003	0.003	0.021	114.183	101.352	89.081	13.378	0.492	23.413	10.398
4	0.008	0.002	-0.005	0.005	0.031	118.598	101.346	84.666	17.398	0.494	22.860	13.834
5	0.002	0.008	-0.004	0.006	0.043	122.726	101.382	80.345	21.000	0.497	22.371	17.087
6	0.020	0.002	-0.014	0.007	0.056	125.993	101.334	77.145	25.174	0.497	22.933	20.202
7	0.015	0.006	-0.014	0.007	0.066	128.475	101.400	74.640	27.286	0.498	22.695	22.173
8	0.016	0.010	-0.017	0.009	0.080	131.249	101.366	71.945	29.984	0.497	22.660	24.524
9	0.030	0.007	-0.029	0.008	0.104	133.551	101.389	68.858	32.445	0.502	22.544	26.916
10	0.039	0.008	-0.040	0.007	0.138	135.103	101.310	67.114	35.425	0.502	23.090	29.051
11	0.040	0.012	-0.048	0.004	0.172	136.107	101.258	64.598	36.942	0.509	22.968	30.818
12	0.044	0.017	-0.057	0.004	0.201	139.332	101.359	63.642	38.434	0.499	22.721	32.106
13	0.047	0.021	-0.070	-0.001	0.244	140.920	101.365	61.985	40.099	0.499	22.727	33.682
14	0.064	0.015	-0.082	-0.003	0.263	141.842	101.379	61.138	40.559	0.499	22.573	34.314
15	0.066	0.027	-0.106	-0.012	0.324	143.200	101.347	59.236	42.305	0.501	22.610	36.074
16	0.070	0.034	-0.124	-0.021	0.361	144.229	101.370	58.376	43.280	0.501	22.618	36.995
17	0.087	0.032	-0.146	-0.027	0.397	144.881	101.363	57.453	43.959	0.502	22.580	37.792
18	0.099	0.037	-0.175	-0.039	0.451	145.898	101.376	56.347	44.862	0.502	22.528	38.814
19	0.106	0.050	-0.216	-0.060	0.543	147.254	101.344	55.475	45.856	0.500	22.490	39.792
20	0.124	0.050	-0.248	-0.073	0.597	147.238	101.351	54.757	46.603	0.503	22.612	40.543
21	0.133	0.070	-0.310	-0.108	0.725	148.709	101.307	53.912	47.591	0.500	22.558	41.528
22	0.153	0.075	-0.360	-0.131	0.808	149.269	101.329	53.238	48.147	0.501	22.539	42.187
23	0.161	0.091	-0.412	-0.160	0.904	149.877	101.366	52.564	48.715	0.501	22.517	42.861
24	0.191	0.095	-0.474	-0.188	0.998	150.655	101.368	52.038	49.303	0.500	22.498	43.474
25	0.201	0.118	-0.548	-0.229	1.134	151.073	101.364	51.394	49.771	0.501	22.480	44.088
26	0.236	0.132	-0.645	-0.276	1.289	151.610	101.374	50.793	50.240	0.501	22.452	44.688
27	0.268	0.151	-0.750	-0.332	1.455	152.004	101.362	50.541	50.885	0.501	22.543	45.195
28	0.310	0.181	-0.893	-0.402	1.670	152.209	101.395	49.954	50.675	0.502	22.373	45.411
29	0.345	0.211	-1.022	-0.466	1.879	152.824	101.349	49.804	51.077	0.500	22.379	45.725
30	0.372	0.214	-1.075	-0.489	1.953	152.810	101.351	49.822	51.411	0.500	22.477	45.906

Torsion Shear Test on Fine Nevada Sand with a Target Void Ratio = 0.530 (D_r = 91.28%)

Test No.:	7*	
Test Date:	8/31/10	
Initial Height, h_i:	40.13	cm
Initial Void Ratio, e:	0.552	
Final Mean Princpal Stress, σ_m :	96.67	kPa
Max Friction Angle, ϕ:	43.1	deg
b-value at failure:	0.89	
Stress direction at failure, α:	24.5	deg

Shear Band Notes	
Point of Observation:	26
Inclination (from Vertical)	
1SB at 57°-67°	
30°, 65°, 66°, 67°	
Failure Notes:	
Deep trough varying direction	

Point (No.)	ε_z (%)	ε_r (%)	ε_θ (%)	ε_v (%)	$\gamma_{\theta z}$ (%)	σ_z (kPa)	σ_r (kPa)	σ_θ (kPa)	$\tau_{\theta z}$ (kPa)	b	α (°)	φ (°)
1	-0.003	0.032	-0.013	0.016	0.094	98.211	113.992	81.894	13.378	0.791	29.312	12.138
2	-0.003	0.034	-0.014	0.018	0.096	98.451	114.534	80.850	13.238	0.780	28.192	12.508
3	0.008	0.056	-0.033	0.031	0.167	101.073	119.289	73.827	19.587	0.857	27.590	17.732
4	0.012	0.066	-0.043	0.036	0.196	102.158	121.387	70.563	21.214	0.860	26.663	19.821
5	0.014	0.085	-0.056	0.043	0.273	103.219	123.539	67.020	23.825	0.876	26.388	22.479
6	0.013	0.102	-0.068	0.048	0.323	104.103	125.041	65.088	25.174	0.881	26.114	23.993
7	0.013	0.118	-0.079	0.052	0.366	104.756	126.229	62.992	26.462	0.886	25.861	25.544
8	0.011	0.140	-0.094	0.057	0.428	105.380	127.612	61.160	28.012	0.892	25.858	27.181
9	0.009	0.161	-0.109	0.060	0.482	105.880	128.805	59.067	29.085	0.892	25.587	28.750
10	0.006	0.193	-0.135	0.064	0.557	106.621	129.970	57.034	30.311	0.897	25.359	30.377
11	0.000	0.232	-0.166	0.065	0.641	107.189	131.198	55.228	30.826	0.893	24.938	31.651
12	-0.001	0.259	-0.193	0.065	0.709	107.823	132.046	53.939	32.280	0.902	25.075	33.057
13	-0.001	0.280	-0.215	0.064	0.760	107.916	132.599	53.068	32.797	0.901	25.049	33.841
14	-0.002	0.334	-0.275	0.057	0.895	108.647	133.778	51.623	34.412	0.909	25.178	35.527
15	-0.003	0.362	-0.308	0.051	0.954	108.890	134.367	50.560	34.638	0.906	24.951	36.294
16	-0.008	0.395	-0.343	0.044	1.033	109.357	134.825	49.918	35.192	0.910	24.909	36.959
17	-0.011	0.418	-0.369	0.038	1.082	109.183	135.139	49.156	35.256	0.905	24.796	37.498
18	-0.010	0.465	-0.433	0.022	1.200	109.568	135.726	48.321	35.913	0.908	24.773	38.379
19	-0.015	0.521	-0.503	0.003	1.334	109.827	136.328	47.725	36.642	0.910	24.861	39.194
20	-0.020	0.565	-0.559	-0.015	1.437	110.016	136.756	46.988	36.988	0.910	24.784	39.873
21	-0.022	0.615	-0.631	-0.038	1.560	110.403	137.086	46.336	37.416	0.912	24.716	40.515
22	-0.026	0.676	-0.719	-0.069	1.710	110.850	137.690	45.517	37.747	0.912	24.564	41.252
23	-0.030	0.730	-0.797	-0.098	1.843	110.798	137.979	45.028	38.221	0.913	24.646	41.891
24	-0.038	0.797	-0.902	-0.144	2.002	108.332	138.223	43.445	36.990	0.882	24.373	42.559
25	-0.046	0.835	-0.953	-0.164	2.083	108.355	138.393	43.186	37.540	0.885	24.521	43.083
26	-0.046	0.874	-1.011	-0.182	2.139	108.304	138.494	42.850	36.537	0.876	24.074	42.728

Torsion Shear Test on Fine Nevada Sand with a Target Void Ratio = 0.530 (D_r = 91.28%)

Test No.:	8	
Test Date:	9/2/11	
Initial Height, h_i:	39.96	cm
Initial Void Ratio, e:	0.541	
Final Mean Princpal Stress, σ_m :	102.3	kPa
Max Friction Angle, ϕ:	42.1	deg
b-value at failure:	0.99	
Stress direction at failure, α:	22.5	deg

Shear Band Notes

Point of Observation: 27

Inclination (from Vertical)

67°

Failure Notes:

Thick trough through specimen

Point (No.)	ε_z (%)	ε_r (%)	ε_θ (%)	ε_v (%)	$\gamma_{\theta z}$ (%)	σ_z (kPa)	σ_r (kPa)	σ_θ (kPa)	$\tau_{\theta z}$ (kPa)	b	α (°)	φ (°)
1	0.000	0.000	0.000	0.000	0.000	14.818	14.868	14.478	0.170	0.956	22.494	0.941
2	0.006	0.006	-0.007	0.005	0.017	15.271	15.707	13.212	1.407	0.920	26.902	7.031
3	0.007	0.009	-0.009	0.006	0.025	15.534	16.039	12.767	1.777	0.919	26.045	9.158
4	0.007	0.014	-0.012	0.009	0.035	15.728	16.390	12.169	2.104	0.943	24.887	11.395
5	0.007	0.019	-0.014	0.011	0.044	15.885	16.691	11.666	2.310	0.966	23.799	13.126
6	0.006	0.026	-0.018	0.013	0.062	16.102	17.098	11.063	2.718	0.974	23.584	15.834
7	0.005	0.031	-0.021	0.015	0.074	16.189	17.290	10.741	2.970	0.975	23.737	17.413
8	0.004	0.037	-0.024	0.016	0.088	16.325	17.521	10.423	3.186	0.977	23.598	18.950
9	0.003	0.043	-0.027	0.018	0.102	16.444	17.726	10.084	3.324	0.985	23.131	20.292
10	0.000	0.048	-0.029	0.019	0.117	16.531	17.864	9.890	3.538	0.979	23.409	21.550
11	0.001	0.054	-0.036	0.020	0.137	16.627	18.058	9.565	3.720	0.984	23.247	23.058
12	0.003	0.061	-0.043	0.021	0.163	16.758	18.238	9.350	4.003	0.975	23.609	24.692
13	0.006	0.074	-0.059	0.021	0.213	16.913	18.509	8.905	4.301	0.977	23.524	27.080
14	0.007	0.094	-0.083	0.018	0.268	17.018	18.786	8.390	4.502	0.988	23.111	29.395
15	0.008	0.115	-0.109	0.014	0.343	17.182	18.979	8.187	4.861	0.975	23.614	31.473
16	0.009	0.157	-0.168	-0.003	0.443	17.362	19.318	7.625	5.018	0.988	22.931	34.029
17	0.008	0.190	-0.217	-0.020	0.538	17.469	19.475	7.453	5.233	0.984	23.131	35.541
18	0.006	0.242	-0.302	-0.054	0.666	17.543	19.678	7.071	5.330	0.993	22.755	37.382
19	0.005	0.279	-0.363	-0.079	0.761	17.630	19.778	6.955	5.457	0.990	22.816	38.388
20	0.002	0.322	-0.437	-0.113	0.868	17.688	19.895	6.779	5.519	0.994	22.670	39.370
21	0.003	0.356	-0.500	-0.140	0.953	17.719	19.954	6.669	5.565	0.995	22.602	40.020
22	0.002	0.391	-0.561	-0.168	1.040	17.743	19.997	6.620	5.654	0.993	22.737	40.621
23	0.005	0.429	-0.637	-0.203	1.137	17.828	20.085	6.541	5.709	0.992	22.665	41.208
24	0.008	0.474	-0.726	-0.243	1.247	17.843	20.137	6.439	5.732	0.995	22.574	41.754
25	0.008	0.500	-0.773	-0.265	1.306	17.866	20.155	6.410	5.748	0.994	22.551	41.955
26	0.008	0.502	-0.777	-0.267	1.311	17.870	20.155	6.409	5.751	0.994	22.552	41.974
27	0.012	0.502	-0.784	-0.270	1.317	17.957	20.153	6.399	5.766	0.988	22.469	42.096

Torsion Shear Test on Fine Nevada Sand with a Target Void Ratio = 0.530 (D_r = 91.28%)

Test No.:	9	
Test Date:	9/9/11	
Initial Height, h_i:	39.96	cm
Initial Void Ratio, e:	0.526	
Final Mean Princpal Stress, σ_m :	101.3	kPa
Max Friction Angle, ϕ:	38.7	deg
b-value at failure:	0.25	
Stress direction at failure, α:	45.0	deg

Shear Band Notes	
Point of Observation:	28
Inclination (from Vertical)	
16°, 17°,2@19°,21°, 2@21.5°	
Failure Notes:	

Point (No.)	ε_z (%)	ε_r (%)	ε_θ (%)	ε_v (%)	$\gamma_{\theta z}$ (%)	σ_z (kPa)	σ_r (kPa)	σ_θ (kPa)	$\tau_{\theta z}$ (kPa)	b	α (°)	φ (°)
1	0.000	0.000	0.000	0.000	0.000	101.371	100.975	101.330	1.322	0.358	44.555	0.747
2	0.000	-0.003	0.004	0.001	0.036	103.052	98.165	102.480	12.565	0.317	44.349	7.025
3	0.000	-0.005	0.007	0.003	0.062	104.076	96.178	103.828	18.185	0.286	44.805	10.075
4	0.001	-0.007	0.012	0.006	0.106	105.224	93.551	104.964	25.269	0.272	44.853	13.913
5	0.001	-0.010	0.018	0.009	0.162	106.564	91.394	106.185	31.914	0.265	44.830	17.459
6	0.003	-0.013	0.022	0.012	0.207	107.351	89.867	106.914	36.143	0.261	44.827	19.717
7	0.001	-0.014	0.028	0.015	0.258	107.958	88.549	107.651	40.089	0.260	44.890	21.831
8	-0.002	-0.016	0.036	0.018	0.360	108.886	87.073	108.411	44.845	0.259	44.848	24.378
9	-0.005	-0.017	0.041	0.019	0.414	108.977	86.166	109.002	46.851	0.256	45.008	25.459
10	-0.012	-0.019	0.050	0.019	0.516	110.069	84.953	109.667	50.089	0.251	44.885	27.123
11	-0.019	-0.021	0.057	0.018	0.611	110.386	84.006	109.816	52.527	0.252	44.845	28.496
12	-0.027	-0.023	0.065	0.015	0.704	110.727	83.267	110.320	54.517	0.250	44.893	29.556
13	-0.036	-0.025	0.071	0.011	0.810	111.090	82.491	110.865	56.470	0.248	44.943	30.587
14	-0.048	-0.028	0.079	0.003	0.947	111.444	81.758	111.406	58.559	0.247	44.991	31.705
15	-0.060	-0.030	0.086	-0.004	1.054	111.811	81.267	111.502	60.160	0.247	44.927	32.602
16	-0.082	-0.039	0.095	-0.026	1.307	112.091	80.261	112.306	62.674	0.245	45.049	33.959
17	-0.088	-0.048	0.093	-0.043	1.458	112.129	79.964	112.176	64.037	0.249	45.011	34.819
18	-0.101	-0.054	0.094	-0.061	1.610	112.573	79.477	112.548	65.057	0.246	44.994	35.308
19	-0.109	-0.062	0.091	-0.080	1.770	112.737	79.161	112.755	66.047	0.246	45.004	35.860
20	-0.117	-0.067	0.091	-0.094	1.881	112.783	78.943	112.859	66.630	0.246	45.016	36.198
21	-0.131	-0.073	0.088	-0.116	2.055	113.045	78.675	112.979	67.646	0.246	44.986	36.768
22	-0.152	-0.086	0.081	-0.157	2.350	113.156	78.227	113.209	68.676	0.246	45.011	37.357
23	-0.171	-0.100	0.064	-0.207	2.691	113.272	77.965	113.154	69.449	0.246	44.976	37.838
24	-0.174	-0.109	0.052	-0.231	2.861	113.252	77.755	113.480	69.805	0.245	45.047	38.006
25	-0.188	-0.113	0.045	-0.256	3.026	113.190	77.696	113.642	70.169	0.245	45.092	38.221
26	-0.194	-0.120	0.033	-0.281	3.196	113.356	77.598	113.293	70.422	0.246	44.987	38.420
27	-0.202	-0.127	0.024	-0.305	3.357	113.406	77.515	113.376	70.691	0.246	44.994	38.567
28	-0.205	-0.130	0.019	-0.316	3.436	113.416	77.465	113.301	70.868	0.247	44.977	38.695
29	-0.224	-0.141	0.016	-0.348	3.707	113.554	77.395	113.528	70.852	0.245	44.995	38.610
30	-0.229	-0.149	0.014	-0.363	3.874	113.436	77.396	113.242	70.579	0.245	44.961	38.515
31	-0.235	-0.154	0.013	-0.377	4.044	113.575	77.432	113.380	70.523	0.244	44.960	38.424
32	-0.240	-0.160	0.012	-0.388	4.209	113.184	77.488	113.107	70.171	0.246	44.984	38.329
33	-0.244	-0.165	0.013	-0.396	4.376	113.500	77.613	113.558	70.077	0.244	45.012	38.116

Torsion Shear Test on Fine Nevada Sand with a Target Void Ratio = 0.530 (D_r = 91.28%)

Test No.:	10*	
Test Date:	8/7/10	
Initial Height, h_i:	40.09	cm
Initial Void Ratio, e:	0.555	
Final Mean Princpal Stress, σ_m :	98.2	kPa
Max Friction Angle, ϕ:	38.9	deg
b-value at failure:	0.54	
Stress direction at failure, α:	47.4	deg

Shear Band Notes	
Point of Observation:	24
Inclination (from Vertical)	
10°,3@12°	
Failure Notes:	
One SB along top cap	

Point (No.)	ε_z (%)	ε_r (%)	ε_θ (%)	ε_v (%)	$\gamma_{\theta z}$ (%)	σ_z (kPa)	σ_r (kPa)	σ_θ (kPa)	$\tau_{\theta z}$ (kPa)	b	α (°)	φ (°)
1	0.000	0.000	0.000	0.000	0.000	91.442	101.335	101.429	1.290	0.975	82.758	3.066
2	-0.006	0.002	0.005	0.000	0.047	91.554	101.345	101.569	10.642	0.703	57.599	6.996
3	-0.013	0.002	0.011	0.000	0.106	91.657	101.330	101.628	17.520	0.629	52.942	10.865
4	-0.019	0.005	0.017	0.003	0.158	91.387	101.353	101.526	22.103	0.608	51.458	13.597
5	-0.022	0.008	0.019	0.005	0.212	91.392	101.373	101.509	25.964	0.593	50.512	15.918
6	-0.032	0.015	0.025	0.008	0.279	91.656	101.372	101.422	30.049	0.579	49.615	18.382
7	-0.042	0.023	0.029	0.011	0.356	91.113	101.321	101.264	33.654	0.575	49.288	20.722
8	-0.050	0.033	0.032	0.014	0.437	91.596	101.352	101.335	37.073	0.565	48.741	22.806
9	-0.060	0.041	0.035	0.015	0.497	91.434	101.354	101.282	39.179	0.563	48.581	24.192
10	-0.067	0.052	0.034	0.018	0.592	91.585	101.343	101.615	42.031	0.556	48.402	25.989
11	-0.083	0.064	0.038	0.019	0.683	91.561	101.378	101.594	44.322	0.554	48.229	27.507
12	-0.096	0.075	0.037	0.015	0.769	91.554	101.362	101.651	46.166	0.551	48.120	28.734
13	-0.120	0.094	0.038	0.012	0.898	91.423	101.341	101.493	48.046	0.551	47.991	30.055
14	-0.147	0.112	0.039	0.004	1.024	91.462	101.343	101.621	49.701	0.548	47.918	31.164
15	-0.172	0.129	0.038	-0.006	1.141	91.275	101.392	101.014	51.051	0.551	47.724	32.235
16	-0.205	0.151	0.033	-0.021	1.317	91.388	101.389	101.330	52.884	0.547	47.685	33.452
17	-0.234	0.168	0.030	-0.036	1.446	91.446	101.377	101.450	53.948	0.545	47.648	34.176
18	-0.264	0.186	0.022	-0.057	1.619	91.266	101.382	101.250	55.308	0.546	47.579	35.234
19	-0.314	0.215	0.020	-0.079	1.783	91.454	101.385	101.186	56.446	0.545	47.463	36.030
20	-0.367	0.243	0.008	-0.116	2.040	91.488	101.321	101.507	57.957	0.541	47.470	37.074
21	-0.382	0.251	0.003	-0.128	2.118	91.545	101.355	101.515	58.471	0.541	47.437	37.440
22	-0.427	0.277	-0.012	-0.162	2.347	91.504	101.346	101.421	59.266	0.541	47.391	38.064
23	-0.492	0.313	-0.030	-0.208	2.642	91.314	101.322	100.967	60.056	0.543	47.297	38.806
24	-0.522	0.327	-0.037	-0.231	2.788	91.534	101.365	101.688	60.431	0.539	47.401	38.882

Torsion Shear Test on Fine Nevada Sand with a Target Void Ratio = 0.530 (D_r = 91.28%)

Test No.:	11	
Test Date:	9/22/11	
Initial Height, h_i:	39.99	cm
Initial Void Ratio, e:	0.540	
Final Mean Princpal Stress, σ_m :	101.6	kPa
Max Friction Angle, ϕ:	39.6	deg
b-value at failure:	0.75	
Stress direction at failure, α:	45.0	deg

Shear Band Notes	
Point of Observation:	23, 25
Inclination (from Vertical)	
25°, 40°, 50°, 3@60°, 65°, 69°, 5@70°, 73°	
Failure Notes:	

Point (No.)	ε_z (%)	ε_r (%)	ε_θ (%)	ε_v (%)	$\gamma_{\theta z}$ (%)	σ_z (kPa)	σ_r (kPa)	σ_θ (kPa)	$\tau_{\theta z}$ (kPa)	b	α (°)	φ (°)
1	0.000	0.001	0.001	0.002	0.005	100.860	101.643	101.450	1.710	0.641	49.889	0.983
2	0.000	0.007	0.000	0.007	0.038	99.992	104.435	99.872	10.187	0.721	44.831	5.851
3	0.000	0.014	0.002	0.016	0.076	98.665	106.978	98.565	17.094	0.745	44.917	9.982
4	0.002	0.019	0.001	0.022	0.124	98.137	108.853	97.971	23.786	0.727	44.900	14.039
5	-0.001	0.026	0.002	0.027	0.164	97.265	110.399	97.183	27.914	0.736	44.958	16.685
6	-0.007	0.038	0.004	0.035	0.228	96.808	111.870	96.741	33.196	0.727	44.971	20.062
7	-0.012	0.047	0.003	0.038	0.268	96.159	112.950	96.196	35.743	0.735	45.015	21.816
8	-0.023	0.065	0.002	0.044	0.356	95.270	114.220	95.199	39.202	0.742	44.974	24.308
9	-0.035	0.081	0.001	0.048	0.430	94.936	114.985	94.845	41.426	0.743	44.968	25.885
10	-0.048	0.098	-0.002	0.048	0.515	94.470	115.695	94.280	43.373	0.746	44.937	27.360
11	-0.065	0.119	-0.005	0.049	0.617	94.410	116.512	94.359	45.674	0.742	44.984	28.942
12	-0.085	0.141	-0.011	0.045	0.723	93.810	117.071	93.590	47.128	0.748	44.933	30.197
13	-0.114	0.171	-0.018	0.039	0.870	93.559	117.682	93.521	49.050	0.746	44.989	31.626
14	-0.142	0.197	-0.026	0.030	0.999	93.387	118.143	93.288	50.326	0.746	44.972	32.628
15	-0.189	0.238	-0.039	0.010	1.221	93.624	118.588	93.680	52.776	0.736	45.015	34.300
16	-0.201	0.249	-0.045	0.004	1.272	93.076	119.044	93.090	52.631	0.747	45.004	34.432
17	-0.241	0.283	-0.059	-0.017	1.439	92.831	119.236	92.643	53.551	0.747	44.950	35.271
18	-0.280	0.315	-0.074	-0.039	1.604	92.714	119.540	92.586	54.520	0.747	44.967	36.047
19	-0.337	0.360	-0.092	-0.069	1.818	92.435	119.890	92.356	55.380	0.748	44.980	36.826
20	-0.375	0.390	-0.107	-0.092	1.969	92.303	120.088	92.238	56.050	0.748	44.983	37.406
21	-0.424	0.429	-0.125	-0.120	2.157	92.352	120.327	92.102	56.819	0.747	44.937	38.030
22	-0.467	0.466	-0.150	-0.151	2.362	92.332	120.656	92.054	57.664	0.747	44.931	38.717
23	-0.504	0.498	-0.171	-0.178	2.532	92.309	120.819	91.988	58.145	0.747	44.921	39.124
24	-0.543	0.532	-0.202	-0.213	2.743	92.094	120.976	92.062	58.580	0.747	44.992	39.509
25	-0.561	0.545	-0.208	-0.224	2.816	91.992	120.956	91.925	58.675	0.747	44.984	39.648
26	-0.600	0.567	-0.213	-0.246	3.002	92.080	120.553	91.720	56.614	0.753	44.909	38.028
27	-0.608	0.572	-0.216	-0.252	3.104	92.492	120.272	92.238	55.953	0.749	44.935	37.285
28	-0.621	0.578	-0.213	-0.257	3.210	92.469	120.000	92.211	55.477	0.749	44.933	36.927
29	-0.628	0.581	-0.212	-0.259	3.265	92.417	120.028	92.069	55.377	0.751	44.910	36.894

Torsion Shear Test on Fine Nevada Sand with a Target Void Ratio = 0.530 (D_r = 91.28%)

Test No.:	12*
Test Date:	12/28/10
Initial Height, h_i:	40.09 cm
Initial Void Ratio, e:	0.559
Final Mean Princpal Stress, σ_m :	98.2 kPa
Max Friction Angle, ϕ:	38.9 deg
b-value at failure:	0.80
Stress direction at failure, α:	47.9 deg

Shear Band Notes	
Point of Observation:	28
Inclination (from Vertical)	
14°, 15°,18°, 19°, 2@20°, 22°, 30°	
Failure Notes:	
SBs spriraled through specimen height	

Point (No.)	ε_z (%)	ε_r (%)	ε_θ (%)	ε_v (%)	$\gamma_{\theta z}$ (%)	σ_z (kPa)	σ_r (kPa)	σ_θ (kPa)	$\tau_{\theta z}$ (kPa)	b	α (°)	φ (°)
1	0.000	0.000	0.000	0.000	0.019	91.135	101.709	101.079	0.742	0.946	85.759	2.998
2	0.000	0.007	0.002	0.009	0.046	90.117	104.372	100.273	9.092	0.941	59.591	6.281
3	0.000	0.015	0.003	0.019	0.067	88.856	105.931	99.015	13.222	0.923	55.508	8.672
4	0.000	0.021	0.006	0.027	0.093	88.461	107.389	98.704	17.589	0.877	53.117	11.289
5	0.004	0.027	0.003	0.035	0.121	87.884	108.508	98.107	21.283	0.854	51.753	13.614
6	0.009	0.032	0.002	0.043	0.150	86.997	109.604	97.228	24.364	0.851	50.928	15.681
7	0.013	0.036	0.000	0.049	0.181	86.368	110.483	96.962	26.985	0.842	50.553	17.458
8	0.015	0.044	-0.005	0.055	0.216	86.039	111.328	96.377	29.502	0.836	49.969	19.171
9	0.021	0.051	-0.011	0.061	0.256	85.456	112.046	95.905	31.741	0.832	49.673	20.778
10	0.023	0.058	-0.015	0.065	0.296	85.382	112.819	95.974	33.715	0.824	49.464	22.109
11	0.024	0.069	-0.024	0.069	0.351	85.156	113.428	95.350	35.813	0.820	49.050	23.629
12	0.026	0.080	-0.035	0.072	0.421	85.003	114.052	95.315	38.051	0.811	48.858	25.208
13	0.022	0.091	-0.041	0.072	0.466	84.754	114.598	95.381	39.205	0.810	48.859	26.057
14	0.015	0.110	-0.054	0.071	0.557	84.300	115.189	94.596	41.023	0.811	48.576	27.530
15	0.000	0.126	-0.061	0.064	0.620	84.078	115.700	94.762	42.175	0.809	48.609	28.386
16	-0.008	0.139	-0.072	0.059	0.700	83.708	116.028	94.311	43.284	0.810	48.492	29.335
17	-0.020	0.156	-0.088	0.048	0.803	83.344	116.492	94.141	44.566	0.809	48.453	30.389
18	-0.030	0.172	-0.103	0.039	0.901	83.178	116.823	93.761	45.588	0.809	48.311	31.249
19	-0.062	0.207	-0.133	0.012	1.111	82.941	117.483	93.452	47.461	0.807	48.159	32.780
20	-0.078	0.225	-0.150	-0.004	1.233	82.938	117.811	93.755	48.494	0.802	48.182	33.525
21	-0.101	0.247	-0.171	-0.024	1.375	82.551	118.088	93.177	49.210	0.805	48.081	34.286
22	-0.158	0.297	-0.210	-0.071	1.681	82.671	118.652	93.480	50.865	0.799	48.033	35.504
23	-0.184	0.319	-0.228	-0.093	1.819	82.263	118.820	93.088	51.405	0.801	48.005	36.125
24	-0.281	0.396	-0.285	-0.170	2.250	81.934	119.139	92.884	52.472	0.801	47.978	37.126
25	-0.388	0.482	-0.347	-0.253	2.705	81.917	119.609	92.805	53.580	0.799	47.901	38.059
26	-0.445	0.533	-0.386	-0.298	2.957	81.920	119.790	92.781	54.011	0.799	47.871	38.421
27	-0.574	0.653	-0.474	-0.394	3.484	81.917	120.145	92.385	54.634	0.801	47.736	39.032
28	-0.582	0.663	-0.482	-0.402	3.528	82.129	120.185	92.993	54.748	0.796	47.833	38.927
29	-0.619	0.697	-0.503	-0.425	3.662	82.079	120.214	93.168	54.760	0.796	47.891	38.913
30	-0.661	0.738	-0.530	-0.453	3.821	81.967	120.101	92.680	54.418	0.800	47.811	38.769
31	-0.709	0.792	-0.568	-0.485	4.032	81.806	119.931	92.627	53.990	0.801	47.861	38.473
32	-0.728	0.814	-0.582	-0.496	4.116	82.023	119.910	92.871	53.804	0.800	47.878	38.199
33	-0.756	0.862	-0.623	-0.517	4.311	81.112	119.820	92.867	52.989	0.808	48.165	37.798

Torsion Shear Test on Fine Nevada Sand with a Target Void Ratio = 0.530 (D_r = 91.28%)

Test No.:	13*	
Test Date:	9/3/11	
Initial Height, h_i:	40.03	cm
Initial Void Ratio, e:	0.553	
Final Mean Princpal Stress, σ_m :	97.98	kPa
Max Friction Angle, ϕ:	39.3	deg
b-value at failure:	0.96	
Stress direction at failure, α:	48.2	deg

Shear Band Notes	
Point of Observation:	31
Inclination (from Vertical)	
top cap slip none observed	
Failure Notes:	

Point (No.)	ε_z (%)	ε_r (%)	ε_θ (%)	ε_v (%)	$\gamma_{\theta z}$ (%)	σ_z (kPa)	σ_r (kPa)	σ_θ (kPa)	$\tau_{\theta z}$ (kPa)	b	α (°)	φ (°)
1	0.000	0.000	0.000	0.000	0.011	91.758	101.378	101.416	1.483	0.974	81.464	2.924
2	-0.002	0.007	-0.001	0.004	0.021	89.212	105.418	99.737	7.445	0.909	62.627	6.036
3	-0.003	0.009	-0.001	0.005	0.027	88.590	106.719	98.649	9.932	0.919	58.429	7.359
4	-0.004	0.013	0.000	0.008	0.032	87.445	108.364	97.732	11.895	0.902	56.692	8.792
5	-0.008	0.019	0.000	0.012	0.041	86.536	110.538	96.904	14.894	0.912	54.596	10.689
6	-0.010	0.023	0.000	0.013	0.046	86.114	111.752	96.464	16.727	0.922	53.596	11.810
7	-0.014	0.029	0.001	0.017	0.053	85.176	112.983	95.995	18.688	0.930	53.072	13.139
8	-0.019	0.036	0.001	0.018	0.070	84.095	114.291	95.163	21.000	0.936	52.382	14.747
9	-0.027	0.045	0.004	0.021	0.096	83.508	115.969	93.933	23.738	0.943	51.193	16.606
10	-0.045	0.065	0.007	0.027	0.166	82.419	117.755	93.281	28.187	0.980	50.453	19.349
11	-0.070	0.093	0.009	0.032	0.267	80.750	120.676	91.884	31.821	0.969	49.962	22.433
12	-0.087	0.113	0.008	0.034	0.354	79.803	123.139	90.683	33.792	0.949	49.573	24.465
13	-0.113	0.139	0.008	0.034	0.434	78.455	123.892	90.787	35.564	0.958	49.918	25.919
14	-0.146	0.170	0.007	0.032	0.535	78.587	125.645	89.892	37.507	0.956	49.285	27.476
15	-0.216	0.233	0.002	0.019	0.739	77.988	126.877	89.384	40.338	0.971	49.020	29.618
16	-0.324	0.322	-0.006	-0.007	1.013	76.400	128.770	87.911	42.345	0.957	48.870	32.089
17	-0.420	0.403	-0.027	-0.045	1.295	76.018	130.175	87.783	44.372	0.962	48.776	33.782
18	-0.525	0.487	-0.052	-0.090	1.582	75.205	131.539	86.877	45.744	0.955	48.635	35.477
19	-0.609	0.552	-0.070	-0.127	1.794	74.359	132.378	85.923	46.157	0.942	48.570	36.506
20	-0.625	0.565	-0.065	-0.124	1.809	74.385	132.794	85.833	43.110	0.904	48.782	34.588
21	-0.623	0.564	-0.065	-0.124	1.809	75.686	130.833	86.521	42.795	0.929	48.607	33.378
22	-0.623	0.565	-0.065	-0.122	1.809	75.543	130.672	87.058	42.714	0.932	48.838	33.202
23	-0.623	0.565	-0.065	-0.122	1.809	75.184	130.687	86.614	41.874	0.918	48.886	32.931
24	-0.620	0.564	-0.059	-0.115	1.794	75.704	130.056	87.135	36.422	0.862	49.459	29.320
25	-0.619	0.561	-0.058	-0.116	1.794	77.784	126.387	88.651	37.294	0.932	49.145	28.055
26	-0.617	0.562	-0.059	-0.115	1.794	77.730	126.852	88.387	37.533	0.928	49.040	28.360
27	-0.557	0.548	-0.025	-0.034	1.683	78.058	125.684	89.759	40.787	0.993	49.081	29.524
28	-0.603	0.575	-0.041	-0.069	1.836	76.785	129.138	88.236	47.575	0.987	48.431	35.272
29	-0.756	0.683	-0.081	-0.154	2.204	74.139	133.955	85.434	47.653	0.939	48.379	38.047
30	-0.786	0.701	-0.082	-0.167	2.370	74.123	133.951	85.684	48.126	0.946	48.425	38.309
31	-0.862	0.756	-0.110	-0.216	2.859	74.274	134.156	85.449	49.396	0.956	48.227	39.271

Torsion Shear Test on Fine Nevada Sand with a Target Void Ratio = 0.530 (D_r = 91.28%)

Test No.:	14	
Test Date:	9/30/11	
Initial Height, h_i:	39.99	cm
Initial Void Ratio, e:	0.538	
Final Mean Princpal Stress, σ_m :	101.7	kPa
Max Friction Angle, ϕ:	34.7	deg
b-value at failure:	0.01	
Stress direction at failure, α:	67.3	deg

Shear Band Notes	
Point of Observation:	33
Inclination (from Vertical)	
0°	
Failure Notes:	
Slip along top cap	

Point (No.)	ε_z (%)	ε_r (%)	ε_θ (%)	ε_v (%)	$\gamma_{\theta z}$ (%)	σ_z (kPa)	σ_r (kPa)	σ_θ (kPa)	$\tau_{\theta z}$ (kPa)	b	α (°)	φ (°)
1	-0.003	0.001	0.001	0.000	0.005	100.717	100.199	102.485	1.243	0.040	62.706	0.860
2	-0.018	0.000	0.018	0.001	0.038	98.311	94.999	111.187	7.686	0.014	64.974	5.493
3	-0.031	0.000	0.034	0.002	0.073	95.421	90.913	116.904	12.639	0.040	65.180	8.989
4	-0.044	-0.005	0.055	0.006	0.114	93.151	86.776	123.456	16.784	0.024	66.038	12.051
5	-0.058	-0.012	0.082	0.012	0.165	90.805	82.697	129.802	21.016	0.019	66.428	15.064
6	-0.070	-0.023	0.111	0.017	0.238	89.162	79.368	134.969	23.993	0.007	66.835	17.217
7	-0.083	-0.035	0.140	0.021	0.316	87.214	76.583	139.267	27.179	0.013	66.879	19.409
8	-0.102	-0.053	0.181	0.026	0.415	85.819	73.517	144.078	30.696	0.010	66.750	21.601
9	-0.120	-0.068	0.217	0.029	0.489	84.615	71.367	147.770	32.067	0.002	67.280	22.788
10	-0.138	-0.087	0.255	0.029	0.570	83.644	69.821	149.861	34.406	0.009	66.950	24.140
11	-0.163	-0.112	0.303	0.027	0.659	82.356	68.019	152.370	36.128	0.010	67.049	25.381
12	-0.194	-0.145	0.362	0.022	0.764	81.312	66.283	155.039	37.727	0.008	67.169	26.509
13	-0.245	-0.193	0.448	0.010	0.914	80.406	64.417	158.163	39.748	0.007	67.183	27.782
14	-0.276	-0.225	0.500	-0.001	1.003	79.926	63.357	159.983	40.640	0.004	67.283	28.395
15	-0.331	-0.271	0.583	-0.020	1.144	78.881	62.040	161.366	41.835	0.006	67.296	29.278
16	-0.378	-0.311	0.651	-0.038	1.256	78.450	61.202	162.795	42.748	0.005	67.306	29.856
17	-0.446	-0.377	0.755	-0.068	1.428	77.597	59.602	165.267	43.463	-0.001	67.622	30.554
18	-0.491	-0.418	0.820	-0.089	1.542	77.057	59.165	165.455	44.336	0.004	67.456	31.084
19	-0.535	-0.458	0.882	-0.110	1.650	77.108	58.719	166.675	45.092	0.003	67.401	31.425
20	-0.590	-0.509	0.962	-0.137	1.787	77.047	58.132	168.070	45.822	0.001	67.403	31.800
21	-0.645	-0.558	1.037	-0.166	1.918	76.457	57.638	168.221	46.507	0.005	67.306	32.277
22	-0.714	-0.625	1.135	-0.205	2.082	76.301	56.944	169.723	47.094	0.002	67.383	32.631
23	-0.770	-0.677	1.211	-0.236	2.211	76.162	56.533	170.464	47.577	0.002	67.371	32.902
24	-0.953	-0.844	1.454	-0.343	2.630	75.376	55.449	171.895	48.667	0.003	67.380	33.667
25	-1.009	-0.894	1.526	-0.377	2.753	75.145	55.234	172.181	48.973	0.004	67.366	33.880
26	-1.059	-0.965	1.606	-0.418	2.902	75.126	54.957	172.781	49.328	0.003	67.354	34.052
27	-1.140	-1.053	1.719	-0.473	3.103	74.792	54.490	173.412	49.480	0.002	67.451	34.255
28	-1.171	-1.093	1.766	-0.498	3.197	74.905	54.543	173.270	49.863	0.004	67.303	34.362
29	-1.226	-1.169	1.853	-0.542	3.357	74.750	54.165	174.131	49.764	0.000	67.479	34.411
30	-1.268	-1.223	1.918	-0.574	3.488	74.502	54.106	174.082	49.854	0.002	67.481	34.533
31	-1.314	-1.288	1.990	-0.613	3.636	74.495	54.042	174.083	50.133	0.003	67.403	34.646
32	-1.365	-1.354	2.066	-0.652	3.786	74.419	53.996	173.813	50.205	0.004	67.354	34.692
33	-1.367	-1.356	2.069	-0.654	3.791	74.346	54.002	173.691	50.259	0.005	67.332	34.735

Torsion Shear Test on Fine Nevada Sand with a Target Void Ratio = 0.530 (D_r = 91.28%)

Test No.:	15	
Test Date:	10/7/11	
Initial Height, h_i:	39.96	cm
Initial Void Ratio, e:	0.525	
Final Mean Princpal Stress, σ_m :	101.3	kPa
Max Friction Angle, ϕ:	39.5	deg
b-value at failure:	0.50	
Stress direction at failure, α:	67.5	deg

Shear Band Notes	
Point of Observation:	28
Inclination (from Vertical)	
Failure Notes:	
Slip along top cap and bottom ring	

Point (No.)	ε_z (%)	ε_r (%)	ε_θ (%)	ε_v (%)	$\gamma_{\theta z}$ (%)	σ_z (kPa)	σ_r (kPa)	σ_θ (kPa)	$\tau_{\theta z}$ (kPa)	b	α (°)	φ (°)
1	0.000	0.000	0.000	0.000	0.000	100.756	101.328	102.781	1.256	0.364	64.433	0.909
2	0.007	-0.005	0.000	0.002	0.006	94.352	101.466	107.409	7.008	0.531	66.486	5.448
3	-0.001	-0.002	0.008	0.006	0.021	90.281	101.353	112.283	11.523	0.502	66.837	9.050
4	-0.003	-0.002	0.014	0.009	0.046	86.629	101.366	116.150	15.458	0.499	66.839	12.169
5	-0.007	-0.002	0.022	0.013	0.080	83.089	101.364	119.268	19.124	0.504	66.704	15.080
6	-0.014	0.000	0.032	0.019	0.134	79.488	101.362	122.691	22.666	0.504	66.811	18.043
7	-0.019	0.001	0.040	0.022	0.174	77.459	101.384	124.716	24.655	0.504	66.891	19.744
8	-0.027	0.000	0.055	0.028	0.232	74.784	101.311	127.680	26.648	0.501	67.392	21.770
9	-0.037	-0.001	0.072	0.035	0.293	72.902	101.378	129.902	29.094	0.500	67.204	23.681
10	-0.047	0.002	0.084	0.039	0.359	70.892	101.382	131.521	30.857	0.502	67.246	25.303
11	-0.069	0.008	0.103	0.043	0.438	68.791	101.384	133.645	32.445	0.502	67.492	26.949
12	-0.111	0.022	0.131	0.043	0.531	67.612	101.372	135.105	34.253	0.500	67.287	28.320
13	-0.157	0.035	0.165	0.042	0.627	66.399	101.305	136.777	35.645	0.497	67.316	29.542
14	-0.221	0.051	0.208	0.038	0.754	65.194	101.317	138.769	37.238	0.494	67.326	30.882
15	-0.269	0.064	0.236	0.031	0.847	63.691	101.349	138.903	38.068	0.500	67.325	31.887
16	-0.328	0.078	0.271	0.021	0.962	62.745	101.360	139.926	39.118	0.500	67.306	32.837
17	-0.396	0.094	0.308	0.006	1.087	61.727	101.399	141.063	40.052	0.500	67.362	33.777
18	-0.486	0.116	0.354	-0.016	1.251	60.640	101.378	142.017	41.002	0.500	67.390	34.755
19	-0.572	0.137	0.396	-0.040	1.419	59.749	101.427	142.885	41.732	0.501	67.444	35.547
20	-0.635	0.156	0.423	-0.057	1.561	59.138	101.405	143.143	42.402	0.502	67.364	36.164
21	-0.702	0.175	0.453	-0.075	1.689	58.508	101.410	144.183	43.285	0.501	67.351	36.934
22	-0.787	0.188	0.491	-0.108	1.859	57.870	101.407	144.774	43.967	0.501	67.331	37.596
23	-0.874	0.212	0.529	-0.133	2.037	57.054	101.429	145.376	44.389	0.502	67.426	38.216
24	-0.984	0.239	0.580	-0.166	2.268	56.591	101.374	146.460	44.859	0.499	67.524	38.711
25	-1.095	0.264	0.627	-0.204	2.532	55.921	101.356	146.612	45.139	0.501	67.566	39.185
26	-1.183	0.285	0.663	-0.235	2.752	55.807	101.403	146.523	45.583	0.502	67.429	39.468
27	-1.211	0.291	0.673	-0.247	2.833	55.774	101.397	146.874	45.658	0.501	67.466	39.532
28	-1.230	0.296	0.681	-0.253	2.875	55.857	101.436	146.864	45.612	0.501	67.466	39.467
29	-1.235	0.296	0.682	-0.257	2.905	55.948	101.431	146.938	45.704	0.500	67.434	39.472

Torsion Shear Test on Fine Nevada Sand with a Target Void Ratio = 0.530 (D_r = 91.28%)

Test No.:	16*	
Test Date:	9/7/10	
Initial Height, h_i:	40.13	cm
Initial Void Ratio, e:	0.536	
Final Mean Princpal Stress, σ_m :	96.6	kPa
Max Friction Angle, ϕ:	29.2	deg
b-value at failure:	0.96	
Stress direction at failure, α:	71.5	deg

Shear Band Notes	
Point of Observation:	30
Inclination (from Vertical)	
top cap slip none observed	
Failure Notes:	

Point (No.)	ε_z (%)	ε_r (%)	ε_θ (%)	ε_v (%)	$\gamma_{\theta z}$ (%)	σ_z (kPa)	σ_r (kPa)	σ_θ (kPa)	$\tau_{\theta z}$ (kPa)	b	α (°)	φ (°)
1	0.000	0.000	0.000	0.000	0.012	91.467	101.356	101.210	1.076	0.997	83.771	2.969
2	-0.002	0.001	-0.001	-0.002	0.022	88.350	102.857	101.813	4.139	0.992	74.208	4.767
3	-0.006	0.006	0.001	0.001	0.031	83.817	105.941	103.642	5.731	0.968	74.984	7.017
4	-0.012	0.011	0.005	0.004	0.041	81.257	107.457	104.712	9.788	0.974	70.075	9.455
5	-0.021	0.021	0.010	0.011	0.051	77.023	110.477	106.707	9.898	0.979	73.150	11.198
6	-0.022	0.022	0.010	0.010	0.059	74.843	111.410	106.762	11.264	0.973	72.393	12.423
7	-0.030	0.028	0.013	0.012	0.072	72.706	112.628	107.118	12.542	0.968	71.955	13.698
8	-0.037	0.036	0.019	0.017	0.082	70.981	113.826	107.942	13.096	0.964	72.339	14.666
9	-0.043	0.040	0.022	0.019	0.091	70.168	114.303	108.562	13.774	0.973	72.171	15.331
10	-0.054	0.049	0.027	0.022	0.109	68.339	115.148	108.297	15.563	0.971	71.042	16.664
11	-0.068	0.061	0.034	0.026	0.133	66.279	116.699	109.857	16.924	0.981	71.081	18.257
12	-0.090	0.075	0.045	0.030	0.162	64.150	117.965	110.402	18.053	0.978	71.011	19.643
13	-0.114	0.095	0.054	0.035	0.193	62.396	119.031	110.924	18.876	0.974	71.059	20.778
14	-0.131	0.107	0.062	0.037	0.216	61.264	119.740	111.675	19.497	0.978	71.139	21.624
15	-0.151	0.120	0.069	0.038	0.239	60.103	120.424	111.424	19.664	0.965	71.268	22.145
16	-0.151	0.121	0.068	0.039	0.239	60.258	120.431	111.898	19.677	0.972	71.344	22.157
17	-0.152	0.122	0.069	0.039	0.241	60.200	120.442	111.795	19.633	0.970	71.364	22.146
18	-0.159	0.127	0.072	0.040	0.249	60.233	120.625	112.402	20.064	0.979	71.217	22.411
19	-0.201	0.153	0.089	0.041	0.302	58.769	121.685	113.014	21.413	0.982	70.855	23.724
20	-0.224	0.168	0.096	0.040	0.328	57.583	122.188	113.187	21.349	0.976	71.240	24.238
21	-0.247	0.183	0.105	0.041	0.355	57.637	122.421	113.481	21.965	0.982	70.905	24.533
22	-0.289	0.210	0.119	0.040	0.405	56.297	123.099	113.569	22.586	0.977	70.868	25.430
23	-0.322	0.231	0.127	0.036	0.452	55.555	123.617	114.002	22.981	0.978	70.909	26.009
24	-0.344	0.243	0.135	0.034	0.479	55.076	123.774	113.809	23.280	0.976	70.797	26.346
25	-0.401	0.275	0.153	0.027	0.544	53.826	124.401	114.230	23.613	0.974	70.990	27.145
26	-0.456	0.308	0.168	0.020	0.607	53.077	125.181	114.441	23.609	0.966	71.211	27.530
27	-0.498	0.332	0.178	0.013	0.660	52.278	125.506	114.421	23.780	0.963	71.286	27.997
28	-0.563	0.365	0.198	0.000	0.735	51.273	126.023	114.909	23.543	0.959	71.751	28.448
29	-0.670	0.421	0.221	-0.028	0.900	50.978	126.056	115.002	24.700	0.968	71.174	29.157
30	-0.722	0.448	0.229	-0.045	1.014	50.579	126.553	115.105	24.275	0.960	71.521	29.169

Torsion Shear Test on Fine Nevada Sand with a Target Void Ratio = 0.530 (D_r = 91.28%)

Test No.:	17	
Test Date:	10/5/11	
Initial Height, h_i:	39.96	cm
Initial Void Ratio, e:	0.532	
Final Mean Princpal Stress, σ_m :	101.8	kPa
Max Friction Angle, ϕ:	37.9	deg
b-value at failure:	1.01	
Stress direction at failure, α:	68.2	deg

Shear Band Notes	
Point of Observation:	29
Inclination (from Vertical)	
0°	
Failure Notes:	
Horizontal trough along specimen	

Point (No.)	ε_z (%)	ε_r (%)	ε_θ (%)	ε_v (%)	$\gamma_{\theta z}$ (%)	σ_z (kPa)	σ_r (kPa)	σ_θ (kPa)	$\tau_{\theta z}$ (kPa)	b	α (°)	φ (°)
1	-0.011	0.013	0.006	0.007	0.000	99.819	102.771	102.300	1.403	0.957	65.740	1.062
2	0.002	0.002	0.000	0.004	0.031	85.516	111.943	107.893	12.556	0.953	65.851	10.015
3	0.000	0.004	0.000	0.004	0.056	80.337	114.983	109.146	15.335	0.981	66.604	12.831
4	-0.003	0.006	0.002	0.005	0.082	77.585	116.930	110.699	17.742	0.969	66.511	14.938
5	-0.006	0.009	0.003	0.006	0.102	75.968	118.162	111.674	19.193	0.964	66.464	16.224
6	-0.017	0.017	0.009	0.009	0.160	70.991	120.901	112.751	21.776	0.981	66.898	19.171
7	-0.022	0.021	0.011	0.010	0.188	69.988	121.981	113.819	23.077	0.973	66.761	20.261
8	-0.030	0.027	0.015	0.012	0.235	67.442	123.257	113.975	24.502	0.982	66.759	21.870
9	-0.043	0.037	0.021	0.015	0.277	65.672	124.538	114.463	25.595	0.987	66.813	23.115
10	-0.062	0.052	0.029	0.019	0.327	64.160	125.558	115.485	26.762	0.982	66.899	24.380
11	-0.080	0.065	0.037	0.023	0.369	62.642	126.690	116.380	27.250	0.986	67.298	25.311
12	-0.088	0.072	0.041	0.025	0.400	61.557	127.136	116.187	27.689	0.992	67.305	25.954
13	-0.096	0.077	0.044	0.026	0.425	60.879	127.574	116.442	28.020	0.993	67.378	26.426
14	-0.101	0.081	0.047	0.027	0.445	60.242	127.829	116.311	28.252	0.997	67.389	26.799
15	-0.128	0.101	0.058	0.031	0.511	59.047	128.820	116.840	29.352	0.996	67.276	27.928
16	-0.155	0.120	0.069	0.035	0.571	57.782	129.618	117.426	29.928	0.997	67.449	28.834
17	-0.227	0.170	0.098	0.041	0.675	56.613	130.521	117.735	31.708	0.992	66.972	30.343
18	-0.257	0.190	0.109	0.042	0.715	55.240	131.447	118.381	31.310	1.002	67.619	30.810
19	-0.342	0.244	0.138	0.039	0.867	54.579	131.957	118.289	33.100	0.995	66.951	32.106
20	-0.382	0.267	0.150	0.035	0.917	52.906	132.772	119.098	32.322	1.005	67.839	32.541
21	-0.484	0.324	0.178	0.018	1.063	51.929	133.501	119.285	32.872	1.009	67.847	33.349
22	-0.582	0.373	0.201	-0.008	1.199	51.055	133.884	119.432	33.533	1.008	67.777	34.179
23	-0.648	0.410	0.214	-0.024	1.296	50.611	134.375	119.833	34.043	1.006	67.737	34.727
24	-0.709	0.444	0.225	-0.041	1.388	51.044	133.996	119.488	35.453	0.994	66.994	35.303
25	-0.850	0.527	0.244	-0.080	1.568	49.347	135.467	120.770	35.211	1.003	67.702	36.129
26	-0.986	0.614	0.255	-0.117	1.752	50.442	134.457	120.171	36.997	0.983	66.650	36.579
27	-1.076	0.676	0.258	-0.142	1.973	49.145	135.802	121.178	36.505	0.994	67.307	37.026
28	-1.183	0.752	0.259	-0.172	2.138	49.125	136.006	120.600	37.438	0.994	66.834	37.582
29	-1.267	0.816	0.256	-0.195	2.232	46.746	137.191	121.598	35.620	1.013	68.208	37.867

Torsion Shear Test on Fine Nevada Sand with a Target Void Ratio = 0.530 (D_r = 91.28%)

Test No.:	18	
Test Date:	10/13/11	
Initial Height, h_i:	39.96	cm
Initial Void Ratio, e:	0.53	
Final Mean Princpal Stress, σ_m :	100.1	kPa
Max Friction Angle, ϕ:	33.9	deg
b-value at failure:	0.00	
Stress direction at failure, α:	90.0	deg

Shear Band Notes	
Point of Observation:	30
Inclination (from Vertical)	
2@25°	
Failure Notes:	
lower half bulged inwards	

Point (No.)	ε_z (%)	ε_r (%)	ε_θ (%)	ε_v (%)	$\gamma_{\theta z}$ (%)	σ_z (kPa)	σ_r (kPa)	σ_θ (kPa)	$\tau_{\theta z}$ (kPa)	b	α (°)	φ (°)
1	0.000	0.000	0.000	0.000	0.000	94.902	101.305	101.611	0.000	0.954	90.000	1.956
2	-0.002	-0.012	0.009	-0.004	0.000	91.093	97.562	108.963	0.000	0.362	90.000	5.125
3	-0.007	-0.023	0.022	-0.008	0.000	87.734	94.173	115.920	0.000	0.228	90.000	7.955
4	-0.014	-0.033	0.037	-0.009	0.000	84.676	91.091	122.250	0.000	0.171	90.000	10.462
5	-0.023	-0.040	0.057	-0.007	0.000	81.875	88.119	128.292	0.000	0.135	90.000	12.759
6	-0.034	-0.049	0.079	-0.004	0.000	79.205	85.441	133.805	0.000	0.114	90.000	14.852
7	-0.045	-0.058	0.103	-0.001	0.000	76.668	83.051	138.810	0.000	0.103	90.000	16.762
8	-0.057	-0.067	0.127	0.003	0.000	74.356	80.812	143.139	0.000	0.094	90.000	18.436
9	-0.072	-0.079	0.159	0.007	0.000	72.198	78.460	148.017	0.000	0.083	90.000	20.139
10	-0.095	-0.091	0.198	0.012	0.000	70.301	76.551	151.691	0.000	0.077	90.000	21.508
11	-0.119	-0.105	0.241	0.017	0.000	68.787	74.819	155.527	0.000	0.070	90.000	22.749
12	-0.150	-0.119	0.291	0.022	0.000	67.081	73.209	158.617	0.000	0.067	90.000	23.927
13	-0.186	-0.137	0.349	0.026	0.000	65.550	71.647	161.784	0.000	0.063	90.000	25.044
14	-0.221	-0.156	0.405	0.028	0.000	64.163	70.373	164.138	0.000	0.062	90.000	25.970
15	-0.267	-0.176	0.473	0.030	0.000	63.180	69.302	166.604	0.000	0.059	90.000	26.750
16	-0.320	-0.202	0.553	0.030	0.000	61.972	68.040	168.975	0.000	0.057	90.000	27.602
17	-0.360	-0.223	0.612	0.028	0.000	61.100	67.220	170.671	0.000	0.056	90.000	28.213
18	-0.432	-0.261	0.715	0.023	0.000	59.822	66.015	172.847	0.000	0.055	90.000	29.063
19	-0.480	-0.283	0.782	0.019	0.000	59.385	65.508	174.190	0.000	0.053	90.000	29.440
20	-0.542	-0.314	0.867	0.011	0.000	58.802	64.762	175.853	0.000	0.051	90.000	29.922
21	-0.594	-0.341	0.938	0.003	0.000	57.979	64.134	176.872	0.000	0.052	90.000	30.414
22	-0.664	-0.378	1.031	-0.010	0.000	57.295	63.471	178.281	0.000	0.051	90.000	30.902
23	-0.713	-0.403	1.098	-0.019	0.000	56.969	63.043	179.293	0.000	0.050	90.000	31.181
24	-0.765	-0.432	1.167	-0.030	0.000	56.450	62.548	180.093	0.000	0.049	90.000	31.514
25	-0.844	-0.476	1.270	-0.050	0.000	55.495	61.855	180.968	0.000	0.051	90.000	32.048
26	-0.887	-0.501	1.326	-0.061	0.000	55.056	61.588	181.231	0.000	0.052	90.000	32.276
27	-1.016	-0.565	1.491	-0.089	0.000	54.826	61.062	183.609	0.000	0.048	90.000	32.692
28	-1.065	-0.594	1.555	-0.104	0.000	54.537	60.573	184.213	0.000	0.047	90.000	32.898
29	-1.104	-0.614	1.605	-0.113	0.000	54.405	60.353	184.685	0.000	0.046	90.000	33.018
30	-1.175	-0.653	1.694	-0.134	0.000	53.795	59.953	185.132	0.000	0.047	90.000	33.346
31	-1.222	-0.681	1.754	-0.149	0.000	53.481	59.729	185.355	0.000	0.047	90.000	33.515
32	-1.274	-0.710	1.819	-0.164	0.000	53.349	59.558	185.874	0.000	0.047	90.000	33.641
33	-1.400	-0.787	1.993	-0.194	0.000	53.365	59.068	187.747	0.000	0.042	90.000	33.872

Torsion Shear Test on Fine Nevada Sand with a Target Void Ratio = 0.530 (D_r = 91.28%)

Test No.:	19*	
Test Date:	7/5/10	
Initial Height, h_i:	39.99	cm
Initial Void Ratio, e:	0.523	
Final Mean Princpal Stress, σ_m :	96.7	kPa
Max Friction Angle, ϕ:	38.1	deg
b-value at failure:	0.04	
Stress direction at failure, α:	90.0	deg

Shear Band Notes	
Point of Observation:	33
Inclination (from Vertical)	
5@20°, 5@25°, 15°, 30°	
Failure Notes:	
middle caved inwards	

Point (No.)	ε_z (%)	ε_r (%)	ε_θ (%)	ε_v (%)	$\gamma_{\theta z}$ (%)	σ_z (kPa)	σ_r (kPa)	σ_θ (kPa)	$\tau_{\theta z}$ (kPa)	b	α (°)	φ (°)
1	0.000	0.004	0.000	0.004	0.000	91.352	101.284	101.575	0.000	0.972	90.000	3.037
2	0.000	-0.001	0.008	0.008	0.000	87.117	97.203	109.351	0.000	0.454	90.000	6.498
3	0.000	-0.006	0.018	0.012	0.000	83.587	93.439	116.949	0.000	0.295	90.000	9.576
4	-0.003	-0.012	0.028	0.014	0.000	80.284	89.848	124.096	0.000	0.218	90.000	12.378
5	-0.008	-0.017	0.044	0.019	0.000	77.312	86.856	130.132	0.000	0.181	90.000	14.751
6	-0.015	-0.024	0.061	0.022	0.000	74.534	83.998	135.880	0.000	0.154	90.000	16.951
7	-0.025	-0.032	0.082	0.026	0.000	71.768	81.241	140.793	0.000	0.137	90.000	18.949
8	-0.037	-0.038	0.107	0.031	0.000	69.458	78.774	145.962	0.000	0.122	90.000	20.802
9	-0.053	-0.048	0.136	0.036	0.000	67.185	76.415	151.158	0.000	0.110	90.000	22.618
10	-0.072	-0.057	0.169	0.041	0.000	65.360	74.444	154.851	0.000	0.102	90.000	23.978
11	-0.094	-0.067	0.207	0.045	0.000	63.501	72.434	158.841	0.000	0.094	90.000	25.391
12	-0.124	-0.080	0.253	0.049	0.000	61.803	70.601	162.356	0.000	0.088	90.000	26.653
13	-0.158	-0.094	0.303	0.051	0.000	60.038	69.056	165.439	0.000	0.086	90.000	27.869
14	-0.199	-0.110	0.361	0.051	0.000	58.654	67.595	168.457	0.000	0.081	90.000	28.913
15	-0.248	-0.131	0.427	0.049	0.000	57.390	66.106	171.131	0.000	0.077	90.000	29.850
16	-0.299	-0.153	0.496	0.044	0.000	56.016	64.954	173.423	0.000	0.076	90.000	30.778
17	-0.357	-0.178	0.572	0.037	0.000	54.889	63.741	175.762	0.000	0.073	90.000	31.605
18	-0.418	-0.206	0.651	0.027	0.000	53.819	62.700	177.712	0.000	0.072	90.000	32.351
19	-0.484	-0.237	0.734	0.012	0.000	53.076	61.773	179.864	0.000	0.069	90.000	32.977
20	-0.545	-0.268	0.810	-0.003	0.000	52.196	61.010	181.441	0.000	0.068	90.000	33.586
21	-0.649	-0.320	0.935	-0.033	0.000	51.345	60.290	183.282	0.000	0.068	90.000	34.217
22	-0.725	-0.352	1.023	-0.054	0.000	50.942	59.539	184.365	0.000	0.064	90.000	34.542
23	-0.795	-0.386	1.106	-0.075	0.000	50.292	58.875	185.536	0.000	0.063	90.000	34.993
24	-0.870	-0.426	1.194	-0.102	0.000	49.644	58.231	186.808	0.000	0.063	90.000	35.457
25	-0.944	-0.463	1.278	-0.128	0.000	49.139	57.762	187.534	0.000	0.062	90.000	35.785
26	-1.016	-0.503	1.362	-0.158	0.000	48.485	57.321	188.357	0.000	0.063	90.000	36.197
27	-1.127	-0.560	1.487	-0.200	0.000	48.131	56.812	189.590	0.000	0.061	90.000	36.517
28	-1.208	-0.604	1.580	-0.232	0.000	47.617	56.382	190.109	0.000	0.062	90.000	36.826
29	-1.288	-0.645	1.668	-0.266	0.000	47.383	56.043	190.959	0.000	0.060	90.000	37.042
30	-1.451	-0.722	1.841	-0.332	0.000	45.746	55.464	189.634	0.000	0.068	90.000	37.684
31	-1.500	-0.747	1.893	-0.354	0.000	45.436	55.418	189.617	0.000	0.069	90.000	37.835
32	-1.551	-0.773	1.947	-0.377	0.000	45.274	55.231	189.936	0.000	0.069	90.000	37.954
33	-1.624	-0.809	2.024	-0.409	0.000	45.073	55.098	190.087	0.000	0.069	90.000	38.073

Torsion Shear Test on Fine Nevada Sand with a Target Void Ratio = 0.530 (D_r = 91.28%)

Test No.:	20*	
Test Date:	4/22/10	
Initial Height, h_i:	39.99	cm
Initial Void Ratio, e:	0.53	
Final Mean Princpal Stress, σ_m :	97.6	kPa
Max Friction Angle, ϕ:	45.5	deg
b-value at failure:	0.54	
Stress direction at failure, α:	90.0	deg

Shear Band Notes	
Point of Observation:	33
Inclination (from Vertical)	
3@20°, 2@25°, 26°, 2@28°	
Failure Notes:	
Trough in X shape that spiraled through	

Point (No.)	ε_z (%)	ε_r (%)	ε_θ (%)	ε_v (%)	$\gamma_{\theta z}$ (%)	σ_z (kPa)	σ_r (kPa)	σ_θ (kPa)	$\tau_{\theta z}$ (kPa)	b	α (°)	φ (°)
1	-0.003	0.001	0.001	0.000	0.000	92.156	101.367	101.343	0.000	0.997	90.000	2.721
2	-0.003	0.001	0.001	0.000	0.000	91.956	101.395	100.822	0.000	0.939	90.000	2.636
3	-0.008	0.001	0.009	0.003	0.000	85.511	101.413	107.125	0.000	0.736	90.000	6.442
4	-0.012	0.002	0.015	0.005	0.000	79.771	101.341	111.957	0.000	0.670	90.000	9.664
5	-0.017	0.001	0.022	0.006	0.000	75.012	101.356	116.615	0.000	0.633	90.000	12.539
6	0.000	-0.010	0.019	0.009	0.000	71.154	101.390	121.397	0.000	0.602	90.000	15.125
7	-0.003	-0.012	0.027	0.011	0.000	67.286	101.347	124.611	0.000	0.594	90.000	17.381
8	-0.011	-0.010	0.038	0.017	0.000	63.941	101.344	127.707	0.000	0.587	90.000	19.434
9	-0.019	-0.011	0.050	0.020	0.000	61.119	101.400	131.025	0.000	0.576	90.000	21.335
10	-0.031	-0.011	0.065	0.023	0.000	58.248	101.360	133.552	0.000	0.573	90.000	23.117
11	-0.045	-0.007	0.079	0.026	0.000	55.753	101.368	135.813	0.000	0.570	90.000	24.704
12	-0.063	-0.003	0.097	0.031	0.000	53.621	101.348	137.970	0.000	0.566	90.000	26.120
13	-0.084	0.001	0.117	0.035	0.000	51.628	101.381	140.303	0.000	0.561	90.000	27.517
14	-0.110	0.007	0.140	0.037	0.000	49.371	101.362	141.962	0.000	0.562	90.000	28.942
15	-0.139	0.012	0.165	0.038	0.000	47.829	101.324	143.506	0.000	0.559	90.000	30.003
16	-0.176	0.019	0.197	0.040	0.000	46.430	101.366	145.286	0.000	0.556	90.000	31.040
17	-0.215	0.029	0.226	0.040	0.000	45.074	101.369	146.877	0.000	0.553	90.000	32.030
18	-0.259	0.039	0.259	0.039	0.000	43.786	101.363	147.861	0.000	0.553	90.000	32.892
19	-0.307	0.050	0.292	0.035	0.000	42.425	101.354	149.106	0.000	0.552	90.000	33.848
20	-0.359	0.060	0.328	0.030	0.000	41.245	101.357	150.065	0.000	0.552	90.000	34.668
21	-0.412	0.073	0.363	0.025	0.000	40.372	101.371	151.055	0.000	0.551	90.000	35.324
22	-0.481	0.089	0.409	0.018	0.000	39.458	101.381	152.314	0.000	0.549	90.000	36.050
23	-0.605	0.116	0.486	-0.003	0.000	37.607	101.401	154.001	0.000	0.548	90.000	37.406
24	-0.725	0.141	0.559	-0.026	0.000	36.699	101.409	155.260	0.000	0.546	90.000	38.144
25	-0.886	0.176	0.648	-0.062	0.000	35.317	101.361	156.444	0.000	0.545	90.000	39.172
26	-1.097	0.221	0.764	-0.112	0.000	33.771	101.364	157.844	0.000	0.545	90.000	40.354
27	-1.263	0.253	0.852	-0.158	0.000	32.610	101.379	158.771	0.000	0.545	90.000	41.240
28	-1.466	0.292	0.956	-0.218	0.000	31.784	101.388	159.963	0.000	0.543	90.000	41.950
29	-1.778	0.355	1.114	-0.310	0.000	30.490	101.360	161.199	0.000	0.542	90.000	42.990
30	-2.157	0.419	1.296	-0.442	0.000	28.889	101.360	162.352	0.000	0.543	90.000	44.257
31	-2.807	0.530	1.595	-0.682	0.000	27.474	101.396	163.984	0.000	0.542	90.000	45.479
32	-2.913	0.545	1.643	-0.726	0.000	27.810	101.411	164.242	0.000	0.539	90.000	45.267
33	-3.027	0.546	1.697	-0.784	0.000	27.819	101.494	164.239	0.000	0.540	90.000	45.260

Torsion Shear Test on Fine Nevada Sand with a Target Void Ratio = 0.530 (D_r = 91.28%)

Test No.:	21*	
Test Date:	6/26/10	
Initial Height, h_i:	39.96	cm
Initial Void Ratio, e:	0.52	
Final Mean Princpal Stress, σ_m :	97.0	kPa
Max Friction Angle, ϕ:	40.1	deg
b-value at failure:	0.78	
Stress direction at failure, α:	90.0	deg

Shear Band Notes	
Point of Observation:	32
Inclination (from Vertical)	
18°, 2@24°, 25°, 4@26°	
Failure Notes:	
SB crossed each other (not very deep)	

Point (No.)	ε_z (%)	ε_r (%)	ε_θ (%)	ε_v (%)	$\gamma_{\theta z}$ (%)	σ_z (kPa)	σ_r (kPa)	σ_θ (kPa)	$\tau_{\theta z}$ (kPa)	b	α (°)	φ (°)
1	0.000	0.000	0.000	0.000	0.000	91.924	101.262	101.153	0.000	0.988	90.000	2.740
2	0.006	-0.005	-0.002	-0.001	0.000	85.804	102.871	105.123	0.000	0.883	90.000	5.807
3	0.008	-0.007	0.001	0.002	0.000	80.574	104.322	108.869	0.000	0.839	90.000	8.590
4	0.004	-0.005	0.007	0.006	0.000	75.867	105.597	112.016	0.000	0.822	90.000	11.093
5	-0.007	0.001	0.017	0.011	0.000	71.810	106.792	115.016	0.000	0.810	90.000	13.371
6	-0.023	0.009	0.029	0.015	0.000	67.875	107.816	117.211	0.000	0.810	90.000	15.459
7	-0.049	0.022	0.046	0.019	0.000	64.625	108.710	119.976	0.000	0.796	90.000	17.448
8	-0.080	0.037	0.065	0.023	0.000	61.736	109.535	121.621	0.000	0.798	90.000	19.063
9	-0.116	0.056	0.088	0.028	0.000	59.267	110.344	124.036	0.000	0.789	90.000	20.692
10	-0.158	0.077	0.112	0.032	0.000	56.666	110.986	125.322	0.000	0.791	90.000	22.164
11	-0.195	0.096	0.136	0.037	0.000	54.704	111.655	127.457	0.000	0.783	90.000	23.540
12	-0.247	0.122	0.166	0.041	0.000	52.196	112.193	128.292	0.000	0.788	90.000	24.936
13	-0.308	0.153	0.199	0.044	0.000	50.652	112.650	129.848	0.000	0.783	90.000	26.025
14	-0.382	0.189	0.239	0.047	0.000	48.855	113.158	130.955	0.000	0.783	90.000	27.168
15	-0.459	0.227	0.281	0.050	0.000	47.131	113.565	131.514	0.000	0.787	90.000	28.187
16	-0.550	0.271	0.329	0.051	0.000	45.782	114.014	132.846	0.000	0.784	90.000	29.170
17	-0.639	0.315	0.377	0.053	0.000	44.273	114.357	134.115	0.000	0.780	90.000	30.241
18	-0.719	0.353	0.418	0.053	0.000	43.295	114.670	134.805	0.000	0.780	90.000	30.918
19	-0.818	0.400	0.470	0.052	0.000	42.163	114.919	135.376	0.000	0.781	90.000	31.670
20	-0.926	0.451	0.523	0.049	0.000	41.028	115.218	136.094	0.000	0.780	90.000	32.461
21	-1.030	0.499	0.577	0.045	0.000	40.022	115.505	136.480	0.000	0.783	90.000	33.127
22	-1.272	0.610	0.698	0.035	0.000	38.255	115.971	137.847	0.000	0.780	90.000	34.439
23	-1.553	0.739	0.834	0.020	0.000	36.567	116.426	138.803	0.000	0.781	90.000	35.660
24	-1.816	0.856	0.962	0.001	0.000	35.120	116.730	139.790	0.000	0.780	90.000	36.757
25	-1.923	0.905	1.012	-0.006	0.000	34.752	116.913	139.970	0.000	0.781	90.000	37.028
26	-2.083	0.977	1.089	-0.017	0.000	33.940	117.059	140.780	0.000	0.778	90.000	37.697
27	-2.157	1.009	1.124	-0.024	0.000	33.416	117.183	140.898	0.000	0.779	90.000	38.068
28	-2.268	1.057	1.176	-0.034	0.000	32.671	117.364	141.244	0.000	0.780	90.000	38.630
29	-2.407	1.118	1.241	-0.048	0.000	32.106	117.516	141.638	0.000	0.780	90.000	39.081
30	-2.546	1.177	1.306	-0.064	0.000	31.585	117.597	141.760	0.000	0.781	90.000	39.463
31	-2.687	1.239	1.371	-0.077	0.000	31.248	117.694	142.121	0.000	0.780	90.000	39.756
32	-2.819	1.296	1.433	-0.090	0.000	30.811	117.786	142.385	0.000	0.780	90.000	40.106

Torsion Shear Test on Fine Nevada Sand with a Target Void Ratio = 0.530 (D_r = 91.28%)

Test No.:	22*	
Test Date:	6/29/10	
Initial Height, h_i:	39.96	cm
Initial Void Ratio, e:	0.520	
Final Mean Princpal Stress, σ_m :	97.9	kPa
Max Friction Angle, ϕ:	37.4	deg
b-value at failure:	0.99	
Stress direction at failure, α:	90.0	deg

Shear Band Notes	
Point of Observation:	33
Inclination (from Vertical)	
vertical deep SB at top cap	
crossed SB at 20°and 25°	
Failure Notes:	

Point (No.)	ε_z (%)	ε_r (%)	ε_θ (%)	ε_v (%)	$\gamma_{\theta z}$ (%)	σ_z (kPa)	σ_r (kPa)	σ_θ (kPa)	$\tau_{\theta z}$ (kPa)	b	α (°)	φ (°)
1	-0.003	0.002	0.002	0.000	0.000	92.721	101.068	101.147	0.000	0.991	90.000	2.469
2	-0.007	0.004	0.004	0.001	0.000	87.188	103.814	103.959	0.000	0.991	90.000	4.994
3	-0.012	0.010	0.007	0.005	0.000	81.967	106.230	105.801	0.000	0.982	90.000	7.407
4	-0.017	0.017	0.011	0.010	0.000	77.650	108.305	107.991	0.000	0.990	90.000	9.489
5	-0.024	0.023	0.016	0.015	0.000	73.887	110.181	110.162	0.000	0.999	90.000	11.372
6	-0.035	0.032	0.023	0.020	0.000	70.343	111.914	111.948	0.000	0.999	90.000	13.185
7	-0.048	0.044	0.033	0.029	0.000	67.041	113.397	113.223	0.000	0.996	90.000	14.887
8	-0.061	0.056	0.042	0.037	0.000	64.370	114.903	115.059	0.000	0.997	90.000	16.372
9	-0.078	0.070	0.052	0.044	0.000	61.349	116.119	116.541	0.000	0.992	90.000	17.976
10	-0.093	0.081	0.062	0.049	0.000	59.104	117.355	117.448	0.000	0.998	90.000	19.275
11	-0.111	0.094	0.073	0.055	0.000	56.808	118.461	118.709	0.000	0.996	90.000	20.595
12	-0.131	0.108	0.083	0.061	0.000	54.612	119.463	119.519	0.000	0.999	90.000	21.873
13	-0.150	0.123	0.095	0.068	0.000	52.662	120.434	120.351	0.000	0.999	90.000	23.050
14	-0.174	0.140	0.107	0.073	0.000	50.919	121.325	121.252	0.000	0.999	90.000	24.127
15	-0.202	0.159	0.122	0.079	0.000	49.156	122.119	122.073	0.000	0.999	90.000	25.214
16	-0.232	0.179	0.137	0.083	0.000	47.417	122.857	122.245	0.000	0.992	90.000	26.299
17	-0.264	0.197	0.153	0.087	0.000	46.233	123.581	123.600	0.000	1.000	90.000	27.096
18	-0.307	0.224	0.171	0.089	0.000	44.756	124.245	124.059	0.000	0.998	90.000	28.057
19	-0.346	0.248	0.189	0.091	0.000	43.518	124.908	124.771	0.000	0.998	90.000	28.897
20	-0.388	0.272	0.208	0.092	0.000	42.208	125.450	125.456	0.000	1.000	90.000	29.769
21	-0.436	0.299	0.230	0.093	0.000	41.067	126.029	125.857	0.000	0.998	90.000	30.562
22	-0.488	0.329	0.251	0.091	0.000	40.036	126.541	126.608	0.000	0.999	90.000	31.286
23	-0.544	0.358	0.274	0.088	0.000	39.205	127.011	127.202	0.000	0.998	90.000	31.888
24	-0.602	0.389	0.297	0.085	0.000	38.105	127.436	127.621	0.000	0.998	90.000	32.658
25	-0.676	0.428	0.325	0.077	0.000	37.287	127.927	128.165	0.000	0.997	90.000	33.272
26	-0.751	0.467	0.352	0.068	0.000	36.236	128.389	128.533	0.000	0.998	90.000	34.040
27	-0.816	0.500	0.375	0.059	0.000	35.506	128.712	128.984	0.000	0.997	90.000	34.581
28	-0.879	0.530	0.398	0.049	0.000	34.819	129.083	129.272	0.000	0.998	90.000	35.108
29	-0.965	0.574	0.426	0.035	0.000	34.063	129.467	129.727	0.000	0.997	90.000	35.690
30	-1.051	0.618	0.452	0.019	0.000	33.370	129.791	129.889	0.000	0.999	90.000	36.225
31	-1.247	0.722	0.502	-0.022	0.000	32.593	130.189	130.626	0.000	0.996	90.000	36.838
32	-1.439	0.829	0.546	-0.064	0.000	32.071	130.430	130.981	0.000	0.994	90.000	37.249
33	-1.565	0.912	0.556	-0.097	0.000	31.884	130.568	131.218	0.000	0.993	90.000	37.407

Torsion Shear Test on Fine Nevada Sand with a Target Void Ratio = 0.530 (D_r = 91.28%)

Test No.:	23	
Test Date:	9/22/11	
Initial Height, h_i:	39.94	cm
Initial Void Ratio, e:	0.531	
Final Mean Princpal Stress, σ_m :	101.4	kPa
Max Friction Angle, ϕ:	41.4	deg
b-value at failure:	0.00	
Stress direction at failure, α:	0	deg

Shear Band Notes	
Point of Observation:	29
Inclination (from Vertical):	
6@70°, 3@60°, 65°, 73°, 50°, 25°, 40°	
Failure Notes:	
Large bulge around middle of specimen	

Point (No.)	ε_z (%)	ε_r (%)	ε_θ (%)	ε_v (%)	$\gamma_{\theta z}$ (%)	σ_z (kPa)	σ_r (kPa)	σ_θ (kPa)	$\tau_{\theta z}$ (kPa)	b	α (°)	φ (°)
1	0.000	0.000	0.000	0.000	0.000	101.486	101.355	101.145	0.000	0.616	0.000	0.097
2	0.051	-0.003	-0.009	0.039	0.000	156.852	73.764	73.743	0.000	0.000	0.000	21.125
3	0.101	-0.034	-0.027	0.040	0.000	177.032	63.542	63.414	0.000	0.001	0.000	28.199
4	0.152	-0.074	-0.047	0.031	0.000	188.959	57.530	57.456	0.000	0.001	0.000	32.253
5	0.201	-0.116	-0.071	0.014	0.000	194.107	54.839	54.736	0.000	0.001	0.000	34.061
6	0.250	-0.158	-0.097	-0.005	0.000	197.833	53.048	53.246	0.000	-0.001	0.000	35.160
7	0.302	-0.202	-0.125	-0.026	0.000	200.331	51.657	52.138	0.000	-0.003	0.000	35.943
8	0.358	-0.251	-0.159	-0.052	0.000	202.631	50.598	50.475	0.000	0.001	0.000	36.953
9	0.414	-0.300	-0.193	-0.080	0.000	204.019	49.829	49.652	0.000	0.001	0.000	37.483
10	0.458	-0.339	-0.220	-0.101	0.000	205.124	49.306	49.393	0.000	-0.001	0.000	37.725
11	0.507	-0.381	-0.250	-0.125	0.000	206.241	48.796	48.921	0.000	-0.001	0.000	38.065
12	0.563	-0.430	-0.285	-0.153	0.000	206.963	48.321	48.240	0.000	0.001	0.000	38.459
13	0.620	-0.479	-0.322	-0.182	0.000	207.940	47.825	47.840	0.000	0.000	0.000	38.750
14	0.658	-0.513	-0.348	-0.203	0.000	208.604	47.580	47.548	0.000	0.000	0.000	38.958
15	0.731	-0.576	-0.396	-0.241	0.000	209.450	47.076	47.078	0.000	0.000	0.000	39.269
16	0.761	-0.604	-0.416	-0.259	0.000	209.986	46.843	47.022	0.000	-0.001	0.000	39.352
17	0.825	-0.663	-0.459	-0.297	0.000	210.563	46.461	46.531	0.000	0.000	0.000	39.645
18	0.873	-0.707	-0.492	-0.327	0.000	211.124	46.275	46.413	0.000	-0.001	0.000	39.759
19	0.926	-0.755	-0.529	-0.358	0.000	211.587	46.082	46.229	0.000	-0.001	0.000	39.895
20	0.993	-0.814	-0.576	-0.397	0.000	211.764	45.852	45.670	0.000	0.001	0.000	40.180
21	1.049	-0.864	-0.614	-0.429	0.000	212.451	45.651	45.739	0.000	-0.001	0.000	40.218
22	1.115	-0.923	-0.661	-0.469	0.000	212.790	45.387	45.517	0.000	-0.001	0.000	40.359
23	1.196	-0.997	-0.719	-0.519	0.000	213.216	45.163	45.217	0.000	0.000	0.000	40.547
24	1.266	-1.059	-0.769	-0.562	0.000	213.720	44.949	45.138	0.000	-0.001	0.000	40.636
25	1.341	-1.128	-0.823	-0.610	0.000	214.137	44.773	44.864	0.000	-0.001	0.000	40.810
26	1.446	-1.226	-0.899	-0.679	0.000	214.539	44.507	44.911	0.000	-0.002	0.000	40.829
27	1.542	-1.314	-0.972	-0.744	0.000	215.073	44.349	44.669	0.000	-0.002	0.000	41.000
28	1.719	-1.470	-1.109	-0.860	0.000	214.568	44.071	43.782	0.000	0.002	0.000	41.381
29	1.759	-1.506	-1.139	-0.886	0.000	215.460	44.077	44.101	0.000	0.000	0.000	41.314
30	1.900	-1.634	-1.240	-0.975	0.000	215.708	43.890	43.975	0.000	0.000	0.000	41.401

Torsion Shear Test on Fine Nevada Sand with a Target Void Ratio = 0.530 (D_r = 91.28%)

Test No.:	24*
Test Date:	5/17/10
Initial Height, h_i:	39.93 cm
Initial Void Ratio, e:	0.530
Final Mean Princpal Stress, σ_m :	97.28 kPa
Max Friction Angle, ϕ:	46.1 deg
b-value at failure:	0.27
Stress direction at failure, α:	0 deg

Shear Band Notes	33
Point of Observation:	
Inclination (from Vertical):	
6@62°, 2@63°, 2@64°,	
2@65°, 66°, 67°, 68°, 70°, 71°	
Failure Notes:	
zig-zag paattern in middle of specimen	

Point (No.)	ε_z (%)	ε_r (%)	ε_θ (%)	ε_v (%)	$\gamma_{\theta z}$ (%)	σ_z (kPa)	σ_r (kPa)	σ_θ (kPa)	$\tau_{\theta z}$ (kPa)	b	α (°)	φ (°)
1	0.000	0.000	0.000	0.000	0.000	89.056	101.298	101.759	0.000	0.036	0.000	-3.817
2	0.080	-0.021	-0.052	0.008	0.000	145.957	85.647	61.874	0.000	0.283	0.000	23.864
3	0.121	-0.031	-0.083	0.007	0.000	155.755	82.947	54.934	0.000	0.278	0.000	28.590
4	0.160	-0.040	-0.117	0.003	0.000	162.345	81.049	50.381	0.000	0.274	0.000	31.758
5	0.201	-0.050	-0.154	-0.003	0.000	167.011	79.701	46.848	0.000	0.273	0.000	34.186
6	0.281	-0.067	-0.232	-0.019	0.000	173.203	77.892	42.716	0.000	0.270	0.000	37.181
7	0.321	-0.078	-0.274	-0.031	0.000	175.442	77.290	41.171	0.000	0.269	0.000	38.307
8	0.401	-0.095	-0.361	-0.056	0.000	178.360	76.358	38.799	0.000	0.269	0.000	39.991
9	0.480	-0.115	-0.453	-0.087	0.000	180.476	75.760	36.955	0.000	0.270	0.000	41.306
10	0.521	-0.124	-0.499	-0.103	0.000	181.572	75.507	36.427	0.000	0.269	0.000	41.744
11	0.602	-0.142	-0.597	-0.137	0.000	183.130	74.974	35.560	0.000	0.267	0.000	42.438
12	0.684	-0.162	-0.698	-0.176	0.000	184.242	74.538	34.413	0.000	0.268	0.000	43.254
13	0.720	-0.169	-0.743	-0.191	0.000	184.049	74.511	33.844	0.000	0.271	0.000	43.579
14	0.800	-0.183	-0.843	-0.225	0.000	184.191	74.473	33.488	0.000	0.272	0.000	43.814
15	0.925	-0.212	-1.008	-0.295	0.000	186.143	73.898	32.341	0.000	0.270	0.000	44.745
16	0.968	-0.222	-1.066	-0.319	0.000	186.328	73.826	32.097	0.000	0.271	0.000	44.919
17	1.006	-0.229	-1.115	-0.339	0.000	186.537	73.723	31.878	0.000	0.271	0.000	45.080
18	1.121	-0.250	-1.267	-0.396	0.000	186.379	73.664	31.434	0.000	0.273	0.000	45.346
19	1.161	-0.260	-1.320	-0.419	0.000	186.737	73.523	31.514	0.000	0.271	0.000	45.334
20	1.200	-0.268	-1.374	-0.441	0.000	187.166	73.483	31.485	0.000	0.270	0.000	45.399
21	1.285	-0.283	-1.489	-0.486	0.000	187.528	73.310	31.378	0.000	0.269	0.000	45.506
22	1.331	-0.295	-1.552	-0.515	0.000	187.586	73.267	31.174	0.000	0.269	0.000	45.643
23	1.365	-0.300	-1.601	-0.535	0.000	187.576	73.189	31.062	0.000	0.269	0.000	45.714
24	1.419	-0.306	-1.675	-0.562	0.000	187.546	73.159	31.211	0.000	0.268	0.000	45.615
25	1.475	-0.303	-1.781	-0.610	0.000	186.726	72.909	30.265	0.000	0.273	0.000	46.141
26	1.539	-0.310	-1.871	-0.641	0.000	186.828	73.095	30.441	0.000	0.273	0.000	46.036
27	1.578	-0.320	-1.923	-0.665	0.000	186.779	73.093	30.340	0.000	0.273	0.000	46.098
28	1.617	-0.325	-1.974	-0.682	0.000	186.862	73.087	30.629	0.000	0.272	0.000	45.918
29	1.657	-0.333	-2.026	-0.703	0.000	186.930	73.088	30.760	0.000	0.271	0.000	45.840
30	1.735	-0.347	-2.127	-0.739	0.000	187.183	73.093	31.303	0.000	0.268	0.000	45.517
31	1.775	-0.353	-2.178	-0.756	0.000	187.262	73.071	31.488	0.000	0.267	0.000	45.407
32	1.814	-0.362	-2.229	-0.776	0.000	187.141	73.070	31.288	0.000	0.268	0.000	45.522
33	1.882	-0.373	-2.315	-0.807	0.000	187.353	73.094	31.703	0.000	0.266	0.000	45.280

Torsion Shear Test on Fine Nevada Sand with a Target Void Ratio = 0.530 (D_r = 91.28%)

Test No.:	25*	
Test Date:	6/5/10	
Initial Height, h_i:	39.99	cm
Initial Void Ratio, e:	0.530	
Final Mean Princpal Stress, σ_m :	96.69	kPa
Max Friction Angle, ϕ:	53.2	deg
b-value at failure:	0.55	
Stress direction at failure, α:	0	deg

Shear Band Notes	32
Point of Observation:	
Inclination (from Vertical)	
63°, 3@64°, 3@65°, 66°, 2@67°, 2@68°, 3@70°, 2@80°	
Failure Notes:	
zig-zag pattern across middle of specimen	

Point (No.)	ε_z (%)	ε_r (%)	ε_θ (%)	ε_v (%)	$\gamma_{\theta z}$ (%)	σ_z (kPa)	σ_r (kPa)	σ_θ (kPa)	$\tau_{\theta z}$ (kPa)	b	α (°)	φ (°)
1	0.000	0.000	0.000	0.000	0.000	89.751	101.394	101.675	0.000	0.976	0.000	3.571
2	0.020	-0.003	-0.017	0.000	0.000	123.051	101.340	68.858	0.000	0.599	0.000	16.403
3	0.040	0.003	-0.044	-0.001	0.000	141.797	101.317	50.105	0.000	0.559	0.000	28.542
4	0.061	0.017	-0.090	-0.012	0.000	152.767	101.303	39.010	0.000	0.548	0.000	36.382
5	0.081	0.027	-0.129	-0.021	0.000	156.789	101.333	34.937	0.000	0.545	0.000	39.461
6	0.101	0.037	-0.170	-0.033	0.000	158.914	101.363	32.401	0.000	0.545	0.000	41.398
7	0.122	0.045	-0.213	-0.046	0.000	160.862	101.386	30.444	0.000	0.544	0.000	42.979
8	0.142	0.053	-0.255	-0.061	0.000	162.424	101.412	29.106	0.000	0.542	0.000	44.113
9	0.161	0.061	-0.297	-0.075	0.000	163.402	101.335	28.132	0.000	0.541	0.000	44.931
10	0.181	0.068	-0.342	-0.093	0.000	164.427	101.337	27.065	0.000	0.541	0.000	45.834
11	0.200	0.074	-0.383	-0.109	0.000	165.071	101.337	26.322	0.000	0.541	0.000	46.464
12	0.223	0.084	-0.437	-0.129	0.000	165.820	101.397	25.486	0.000	0.541	0.000	47.185
13	0.244	0.094	-0.487	-0.149	0.000	166.663	101.383	24.866	0.000	0.540	0.000	47.760
14	0.272	0.104	-0.554	-0.179	0.000	166.909	101.401	23.796	0.000	0.542	0.000	48.629
15	0.281	0.109	-0.578	-0.188	0.000	167.106	101.390	23.475	0.000	0.542	0.000	48.907
16	0.307	0.119	-0.636	-0.210	0.000	167.737	101.355	22.937	0.000	0.542	0.000	49.412
17	0.325	0.126	-0.681	-0.229	0.000	168.159	101.354	22.730	0.000	0.541	0.000	49.628
18	0.363	0.144	-0.779	-0.272	0.000	168.211	101.415	21.878	0.000	0.544	0.000	50.337
19	0.370	0.146	-0.795	-0.279	0.000	168.267	101.390	21.702	0.000	0.544	0.000	50.490
20	0.382	0.151	-0.826	-0.292	0.000	168.713	101.372	21.748	0.000	0.542	0.000	50.500
21	0.401	0.158	-0.870	-0.312	0.000	169.204	101.359	21.518	0.000	0.541	0.000	50.747
22	0.422	0.165	-0.925	-0.338	0.000	169.513	101.351	21.056	0.000	0.541	0.000	51.171
23	0.452	0.178	-1.003	-0.373	0.000	169.096	101.380	20.257	0.000	0.545	0.000	51.817
24	0.466	0.184	-1.040	-0.390	0.000	169.383	101.353	20.289	0.000	0.544	0.000	51.819
25	0.508	0.202	-1.151	-0.441	0.000	169.300	101.409	19.483	0.000	0.547	0.000	52.522
26	0.516	0.205	-1.172	-0.451	0.000	169.554	101.378	19.314	0.000	0.546	0.000	52.700
27	0.524	0.208	-1.192	-0.461	0.000	170.011	101.380	19.780	0.000	0.543	0.000	52.332
28	0.551	0.220	-1.266	-0.495	0.000	169.794	101.390	19.245	0.000	0.546	0.000	52.787
29	0.567	0.226	-1.307	-0.514	0.000	169.843	101.373	19.158	0.000	0.546	0.000	52.870
30	0.583	0.231	-1.347	-0.533	0.000	169.984	101.351	19.276	0.000	0.545	0.000	52.779
31	0.606	0.239	-1.405	-0.560	0.000	169.835	101.335	18.833	0.000	0.546	0.000	53.164
32	0.629	0.250	-1.470	-0.591	0.000	169.940	101.375	18.759	0.000	0.546	0.000	53.242

Torsion Shear Test on Fine Nevada Sand with a Target Void Ratio = 0.530 (D_r = 91.28%)

Test No.:	26	
Test Date:	10/19/11	
Initial Height, h_i:	39.99	cm
Initial Void Ratio, e:	0.532	
Final Mean Princpal Stress, σ_m :	101.8	kPa
Max Friction Angle, ϕ:	53.1	deg
b-value at failure:	1.00	
Stress direction at failure, α:	0	deg

Shear Band Notes	25
Point of Observation:	
Inclination (from Vertical)	
90°	
Failure Notes:	
deep vertical trough	

Point (No.)	ε_z (%)	ε_r (%)	ε_θ (%)	ε_v (%)	$\gamma_{\theta z}$ (%)	σ_z (kPa)	σ_r (kPa)	σ_θ (kPa)	$\tau_{\theta z}$ (kPa)	b	α (°)	φ (°)
1	0.000	0.000	0.000	0.000	0.000	101.522	101.416	101.420	0.000	-0.040	0.000	0.029
2	0.010	0.009	-0.012	0.007	0.000	112.146	111.676	80.616	0.000	0.985	0.000	9.414
3	0.020	0.028	-0.037	0.011	0.000	124.980	124.531	55.338	0.000	0.994	0.000	22.719
4	0.030	0.039	-0.061	0.008	0.000	130.227	130.001	44.592	0.000	0.997	0.000	29.331
5	0.040	0.053	-0.090	0.003	0.000	133.686	133.310	37.748	0.000	0.996	0.000	34.029
6	0.051	0.070	-0.123	-0.002	0.000	136.156	135.757	33.140	0.000	0.996	0.000	37.481
7	0.061	0.086	-0.156	-0.009	0.000	138.020	137.343	30.142	0.000	0.994	0.000	39.904
8	0.071	0.102	-0.190	-0.017	0.000	138.900	138.342	28.033	0.000	0.995	0.000	41.617
9	0.081	0.119	-0.225	-0.026	0.000	139.927	139.193	26.384	0.000	0.994	0.000	43.056
10	0.091	0.136	-0.264	-0.037	0.000	140.231	139.800	25.017	0.000	0.996	0.000	44.205
11	0.102	0.153	-0.304	-0.049	0.000	141.165	140.575	23.739	0.000	0.995	0.000	45.405
12	0.110	0.170	-0.342	-0.061	0.000	141.389	141.036	22.675	0.000	0.997	0.000	46.351
13	0.121	0.189	-0.384	-0.075	0.000	142.034	141.423	21.896	0.000	0.995	0.000	47.126
14	0.133	0.209	-0.432	-0.090	0.000	142.398	141.857	20.927	0.000	0.996	0.000	48.051
15	0.142	0.224	-0.467	-0.101	0.000	142.978	142.144	20.421	0.000	0.993	0.000	48.595
16	0.152	0.242	-0.510	-0.116	0.000	142.771	142.428	19.701	0.000	0.997	0.000	49.243
17	0.160	0.257	-0.544	-0.127	0.000	142.990	142.553	19.362	0.000	0.996	0.000	49.594
18	0.170	0.272	-0.583	-0.140	0.000	143.509	142.882	19.032	0.000	0.995	0.000	49.980
19	0.183	0.293	-0.633	-0.158	0.000	144.002	143.338	18.414	0.000	0.995	0.000	50.647
20	0.193	0.311	-0.679	-0.175	0.000	144.273	143.575	17.887	0.000	0.994	0.000	51.205
21	0.201	0.325	-0.714	-0.188	0.000	144.425	143.736	17.616	0.000	0.995	0.000	51.497
22	0.216	0.352	-0.782	-0.214	0.000	144.590	143.958	17.074	0.000	0.995	0.000	52.071
23	0.227	0.371	-0.829	-0.231	0.000	144.694	144.088	16.740	0.000	0.995	0.000	52.430
24	0.235	0.387	-0.870	-0.247	0.000	144.860	144.208	16.513	0.000	0.995	0.000	52.688
25	0.246	0.408	-0.920	-0.265	0.000	144.968	144.360	16.139	0.000	0.995	0.000	53.097

Torsion Shear Test on Fine Nevada Sand with a Target Void Ratio = 0.530 (D_r = 91.28%)

Test No.:	27*	
Test Date:	4/15/11	
Initial Height, h_i:	39.96	cm
Initial Void Ratio, e:	0.510	
Final Mean Princpal Stress, σ_m :	97.9	kPa
Max Friction Angle, ϕ:	37.6	deg
b-value at failure:	0.02	
Stress direction at failure, α:	24.0	deg

Shear Band Notes	
Point of Observation:	26
Inclination (from Vertical)	
30°	
Failure Notes:	

Point (No.)	ε_z (%)	ε_r (%)	ε_θ (%)	ε_v (%)	$\gamma_{\theta z}$ (%)	σ_z (kPa)	σ_r (kPa)	σ_θ (kPa)	$\tau_{\theta z}$ (kPa)	b	α (°)	φ (°)
1	0.000	0.000	0.000	0.000	0.000	88.632	101.375	101.240	-0.633	-0.008	2.865	-3.826
2	0.034	-0.026	-0.014	-0.006	0.056	113.698	86.174	92.744	20.770	0.134	31.616	13.024
3	0.039	-0.032	-0.014	-0.007	0.086	121.595	81.081	89.704	23.440	0.067	27.887	15.565
4	0.047	-0.040	-0.017	-0.010	0.142	130.701	75.340	86.449	28.145	0.036	25.914	19.253
5	0.052	-0.044	-0.020	-0.011	0.172	134.456	73.142	85.489	30.574	0.030	25.656	20.865
6	0.060	-0.050	-0.023	-0.013	0.226	136.727	71.772	84.810	34.619	0.049	26.568	22.994
7	0.071	-0.061	-0.027	-0.017	0.254	142.877	68.065	82.311	36.211	0.028	25.047	24.787
8	0.080	-0.067	-0.032	-0.020	0.285	145.356	66.556	81.676	37.747	0.025	24.926	25.787
9	0.097	-0.084	-0.039	-0.026	0.340	149.315	64.081	80.335	39.935	0.019	24.592	27.357
10	0.130	-0.111	-0.057	-0.038	0.413	153.089	61.720	78.984	42.096	0.016	24.323	28.901
11	0.163	-0.143	-0.076	-0.056	0.510	156.940	59.345	77.570	44.047	0.012	23.991	30.373
12	0.186	-0.166	-0.091	-0.071	0.579	158.676	58.273	77.144	45.416	0.011	24.044	31.170
13	0.239	-0.216	-0.123	-0.100	0.717	161.762	56.182	75.704	45.900	0.003	23.425	31.998
14	0.326	-0.301	-0.185	-0.160	0.962	163.799	55.051	75.179	49.446	0.015	24.068	33.756
15	0.356	-0.330	-0.205	-0.178	1.019	165.445	54.153	74.600	49.485	0.010	23.725	34.032
16	0.469	-0.436	-0.282	-0.249	1.287	165.326	54.041	74.681	49.257	0.007	23.691	33.902
17	0.506	-0.483	-0.320	-0.297	1.449	166.037	53.674	74.609	53.047	0.024	24.623	35.591
18	0.556	-0.539	-0.354	-0.338	1.550	170.759	50.710	72.602	50.851	-0.002	23.008	35.507
19	0.593	-0.569	-0.385	-0.360	1.643	167.633	52.691	73.824	53.106	0.020	24.274	35.936
20	0.672	-0.658	-0.443	-0.428	1.813	170.733	50.596	72.990	52.862	0.005	23.623	36.211
21	0.733	-0.726	-0.494	-0.487	1.973	171.464	50.455	72.582	53.433	0.008	23.611	36.626
22	0.838	-0.832	-0.575	-0.569	2.193	172.086	49.995	72.520	54.032	0.008	23.672	36.922
23	0.904	-0.906	-0.629	-0.631	2.352	173.098	49.632	72.307	54.254	0.007	23.556	37.120
24	1.000	-0.997	-0.707	-0.703	2.583	171.894	50.241	72.638	55.029	0.014	23.977	37.306
25	1.162	-1.159	-0.814	-0.811	2.853	173.304	48.794	71.477	53.313	0.001	23.159	37.037
26	1.187	-1.182	-0.842	-0.837	2.964	171.130	50.326	72.098	55.154	0.019	24.042	37.551
27	1.256	-1.253	-0.887	-0.883	3.101	172.412	49.797	73.131	55.130	0.008	24.000	37.176
28	1.347	-1.338	-0.954	-0.945	3.302	171.389	50.340	72.525	55.267	0.017	24.095	37.444
29	1.440	-1.438	-1.011	-1.009	3.456	174.422	48.636	71.881	53.265	-0.004	23.047	36.893
30	1.503	-1.494	-1.060	-1.051	3.614	171.072	50.402	72.281	55.038	0.018	24.046	37.430
31	1.635	-1.632	-1.134	-1.130	3.888	171.692	50.316	72.950	54.927	0.013	24.025	37.141

Torsion Shear Test on Fine Nevada Sand with a Target Void Ratio = 0.530 (D_r = 91.28%)

Test No.:	28	
Test Date:	8/29/11	
Initial Height, h_i:	40.06	cm
Initial Void Ratio, e:	0.531	
Final Mean Princpal Stress, σ_m :	103.5	kPa
Max Friction Angle, ϕ:	43.0	deg
b-value at failure:	0.23	
Stress direction at failure, α:	23.7	deg

Shear Band Notes	
Point of Observation:	32
Inclination (from Vertical)	
First SB: 43°, 30°, 41°	
Second SB: 32°, 43°	
Failure Notes:	
two parallel shear bands	

Point (No.)	ε_z (%)	ε_r (%)	ε_θ (%)	ε_v (%)	$\gamma_{\theta z}$ (%)	σ_z (kPa)	σ_r (kPa)	σ_θ (kPa)	$\tau_{\theta z}$ (kPa)	b	α (°)	φ (°)
1	0.000	0.000	0.000	0.000	0.000	103.082	100.437	100.856	1.847	0.145	29.464	1.212
2	0.010	0.000	-0.004	0.006	0.000	109.568	97.840	95.236	10.753	0.323	28.160	7.249
3	0.016	-0.002	-0.006	0.008	0.000	113.585	96.329	92.509	13.666	0.305	26.181	9.641
4	0.026	-0.008	-0.011	0.007	0.000	117.726	94.902	91.161	14.637	0.259	23.889	10.909
5	0.024	-0.005	-0.009	0.011	0.023	123.685	92.576	87.842	19.395	0.250	23.631	14.459
6	0.029	-0.007	-0.012	0.011	0.032	124.670	92.227	87.051	20.238	0.253	23.548	15.129
7	0.030	-0.005	-0.013	0.012	0.047	126.216	91.797	85.890	21.370	0.257	23.332	16.084
8	0.025	-0.004	-0.008	0.013	0.062	127.468	91.210	85.487	22.805	0.254	23.686	16.923
9	0.025	-0.002	-0.008	0.014	0.081	129.292	90.583	85.008	24.202	0.247	23.773	17.826
10	0.033	-0.005	-0.013	0.016	0.099	130.539	89.908	83.142	25.479	0.257	23.537	19.007
11	0.034	-0.005	-0.013	0.017	0.101	132.503	89.328	82.962	25.054	0.239	22.663	19.089
12	0.036	-0.004	-0.015	0.017	0.113	131.038	89.592	81.486	26.481	0.270	23.453	19.955
13	0.036	-0.004	-0.014	0.018	0.145	133.883	88.743	82.506	28.035	0.244	23.751	20.576
14	0.038	-0.004	-0.015	0.019	0.179	135.598	88.030	81.001	29.320	0.247	23.522	21.710
15	0.039	-0.003	-0.016	0.019	0.213	137.051	87.443	79.515	30.383	0.251	23.282	22.732
16	0.040	-0.004	-0.016	0.020	0.224	138.191	86.993	78.428	30.068	0.249	22.589	23.041
17	0.045	0.039	-0.013	0.071	0.244	138.353	86.897	78.843	31.504	0.250	23.318	23.518
18	0.051	0.038	-0.016	0.073	0.279	140.973	86.060	77.119	33.404	0.251	23.148	25.071
19	0.056	0.039	-0.020	0.075	0.318	143.229	85.065	76.436	34.140	0.241	22.815	25.774
20	0.057	0.041	-0.023	0.075	0.360	143.955	84.677	74.728	36.456	0.255	23.242	27.371
21	0.065	0.042	-0.030	0.077	0.404	148.327	83.176	73.157	37.919	0.242	22.627	28.824
22	0.069	0.044	-0.038	0.075	0.449	150.669	82.889	70.584	39.597	0.254	22.340	30.600
23	0.083	0.040	-0.050	0.073	0.510	151.781	81.971	71.315	42.416	0.247	23.257	31.608
24	0.089	0.042	-0.061	0.070	0.551	152.857	81.537	69.578	43.322	0.253	23.067	32.703
25	0.112	0.039	-0.090	0.061	0.660	155.334	80.491	68.555	45.525	0.250	23.188	34.180
26	0.141	0.037	-0.135	0.043	0.800	157.928	79.480	66.409	47.583	0.252	23.059	36.053
27	0.161	0.033	-0.168	0.026	0.911	159.231	78.945	65.822	49.443	0.253	23.316	37.187
28	0.198	0.029	-0.237	-0.010	1.087	162.402	78.159	64.835	51.371	0.250	23.240	38.574
29	0.234	0.029	-0.307	-0.043	1.253	163.164	77.588	62.942	52.016	0.254	23.034	39.708
30	0.311	0.014	-0.448	-0.122	1.569	167.634	76.665	63.035	54.594	0.244	23.115	40.958
31	0.414	0.001	-0.652	-0.238	1.988	167.640	75.761	60.118	55.360	0.253	22.920	42.659
32	0.515	-0.023	-0.889	-0.397	2.456	172.144	74.962	63.352	59.095	0.234	23.686	43.010

Torsion Shear Test on Fine Nevada Sand with a Target Void Ratio = 0.530 (D_r = 91.28%)

Test No.:	29	
Test Date:	9/1/11	
Initial Height, h_i:	39.96	cm
Initial Void Ratio, e:	0.531	
Final Mean Princpal Stress, σ_m :	101.4	kPa
Max Friction Angle, ϕ:	46.5	deg
b-value at failure:	0.75	
Stress direction at failure, α:	22.2	deg

Shear Band Notes	
Point of Observation:	32
Inclination (from Vertical)	
one SB at 20°, 48°, 60°, 76°	
Failure Notes:	
thick SB (two SB's crossing each other)	

Point (No.)	ε_z (%)	ε_r (%)	ε_θ (%)	ε_v (%)	$\gamma_{\theta z}$ (%)	σ_z (kPa)	σ_r (kPa)	σ_θ (kPa)	$\tau_{\theta z}$ (kPa)	b	α (°)	φ (°)
1	0.000	0.000	0.000	0.000	0.000	100.314	101.302	101.092	0.261	1.139	-16.924	0.267
2	0.017	0.010	-0.014	0.014	0.000	111.843	108.028	84.187	13.965	0.755	22.642	11.567
3	0.020	0.015	-0.017	0.017	0.000	113.970	109.536	80.317	17.846	0.753	23.341	14.625
4	0.025	0.022	-0.026	0.022	0.000	117.612	111.660	74.627	22.539	0.749	23.181	18.906
5	0.028	0.026	-0.029	0.025	0.000	118.440	112.371	72.791	25.191	0.746	23.911	20.826
6	0.030	0.032	-0.036	0.026	0.036	120.582	113.625	69.657	26.797	0.750	23.231	22.869
7	0.032	0.037	-0.041	0.028	0.064	121.768	114.401	67.657	28.059	0.753	23.022	24.302
8	0.033	0.042	-0.047	0.029	0.092	122.770	114.980	66.099	29.441	0.751	23.048	25.639
9	0.042	0.045	-0.057	0.030	0.121	123.966	115.683	64.428	30.933	0.750	23.049	27.114
10	0.039	0.056	-0.064	0.031	0.157	124.871	116.348	62.368	32.370	0.753	23.003	28.725
11	0.042	0.065	-0.077	0.031	0.192	126.112	117.069	60.719	33.797	0.752	22.974	30.225
12	0.046	0.074	-0.088	0.031	0.222	127.181	117.683	59.097	34.760	0.752	22.799	31.491
13	0.057	0.081	-0.109	0.028	0.266	127.940	118.143	57.845	36.233	0.750	22.976	32.866
14	0.062	0.098	-0.136	0.024	0.325	128.994	118.872	55.812	37.449	0.753	22.832	34.515
15	0.065	0.115	-0.162	0.018	0.384	129.979	119.414	54.456	38.553	0.752	22.797	35.817
16	0.078	0.127	-0.194	0.011	0.439	130.809	119.946	53.160	39.221	0.753	22.646	36.867
17	0.080	0.137	-0.211	0.006	0.474	131.587	120.253	52.513	39.693	0.752	22.556	37.490
18	0.083	0.147	-0.231	0.000	0.509	131.881	120.485	51.933	40.132	0.752	22.556	38.048
19	0.094	0.154	-0.255	-0.007	0.549	132.158	120.692	51.291	40.568	0.753	22.547	38.641
20	0.101	0.163	-0.279	-0.015	0.589	132.450	120.895	50.756	40.991	0.753	22.550	39.178
21	0.104	0.175	-0.303	-0.024	0.632	132.623	121.104	50.029	41.320	0.755	22.508	39.768
22	0.108	0.195	-0.343	-0.040	0.705	133.316	121.426	49.521	41.997	0.753	22.534	40.460
23	0.113	0.216	-0.386	-0.057	0.776	133.431	121.673	48.493	42.327	0.756	22.452	41.237
24	0.133	0.231	-0.441	-0.077	0.862	134.037	121.929	48.014	43.036	0.754	22.508	41.947
25	0.137	0.249	-0.478	-0.092	0.926	134.451	122.149	47.531	43.441	0.754	22.494	42.479
26	0.144	0.272	-0.528	-0.113	1.006	134.747	122.411	46.847	43.751	0.755	22.435	43.078
27	0.165	0.300	-0.612	-0.146	1.135	135.132	122.598	46.335	44.581	0.753	22.559	43.903
28	0.169	0.313	-0.640	-0.159	1.183	135.566	122.800	46.103	44.871	0.752	22.545	44.228
29	0.183	0.338	-0.707	-0.187	1.282	135.815	123.046	45.253	45.097	0.754	22.441	44.901
30	0.193	0.363	-0.771	-0.215	1.381	136.143	123.184	44.934	45.599	0.753	22.498	45.423
31	0.198	0.388	-0.829	-0.243	1.470	136.350	123.387	44.394	45.831	0.754	22.454	45.919
32	0.295	0.517	-1.242	-0.430	1.953	137.015	123.529	43.523	45.807	0.754	22.209	46.472

Torsion Shear Test on Fine Nevada Sand with a Target Void Ratio = 0.530 (D_r = 91.28%)

Test No.:	30*	
Test Date:	5/6/11	
Initial Height, h_i:	39.96	cm
Initial Void Ratio, e:	0.529	
Final Mean Princpal Stress, σ_m :	97.9	kPa
Max Friction Angle, ϕ:	46.4	deg
b-value at failure:	0.85	
Stress direction at failure, α:	22.9	deg

Shear Band Notes	
Point of Observation:	30
Inclination (from Vertical)	
big trough at 62°, 40° and 62°	
other SBs @ 40°, 49°, 2@ 62°, 70°	
Failure Notes:	
trough changed slope in middle of specimen	

Point (No.)	ε_z (%)	ε_r (%)	ε_θ (%)	ε_v (%)	$\gamma_{\theta z}$ (%)	σ_z (kPa)	σ_r (kPa)	σ_θ (kPa)	$\tau_{\theta z}$ (kPa)	b	α (°)	φ (°)
1	0.000	0.000	0.000	0.000	0.000	89.389	101.779	100.232	0.301	0.001	0.170	3.283
2	0.006	-0.002	-0.003	0.000	0.000	91.346	101.785	100.110	0.310	0.001	0.175	2.630
3	0.009	-0.004	-0.004	0.001	0.000	89.845	101.844	100.091	2.838	0.063	1.594	3.535
4	0.011	-0.002	-0.006	0.003	0.000	91.457	103.051	96.872	3.741	0.207	2.076	2.811
5	0.011	-0.002	-0.006	0.004	0.000	92.433	103.445	96.062	4.326	0.307	2.390	2.853
6	0.013	-0.002	-0.008	0.004	0.000	92.821	103.804	95.173	4.957	0.385	2.728	3.107
7	0.018	-0.003	-0.010	0.005	0.000	94.438	104.703	92.793	7.328	0.556	25.451	4.518
8	0.020	-0.003	-0.012	0.005	0.000	95.193	105.130	91.627	8.353	0.604	25.526	5.246
9	0.022	-0.003	-0.014	0.006	0.000	95.753	105.658	90.174	9.921	0.635	26.017	6.365
10	0.025	-0.002	-0.016	0.007	0.000	97.179	106.345	88.561	11.362	0.677	25.976	7.518
11	0.028	-0.002	-0.018	0.007	0.000	98.149	107.041	86.668	12.572	0.708	25.491	8.601
12	0.031	-0.002	-0.021	0.008	0.000	99.195	107.591	85.038	13.226	0.736	24.775	9.373
13	0.036	-0.003	-0.024	0.009	0.000	99.249	107.930	84.278	15.915	0.713	26.692	11.050
14	0.046	-0.001	-0.031	0.013	0.000	101.449	109.242	80.893	20.452	0.725	27.638	14.540
15	0.047	0.007	-0.038	0.016	0.055	104.873	111.317	75.364	24.485	0.758	26.857	18.494
16	0.047	0.018	-0.046	0.018	0.108	107.892	113.274	70.108	27.149	0.786	25.758	21.816
17	0.040	0.030	-0.050	0.020	0.145	109.965	114.541	67.151	29.994	0.790	25.846	24.589
18	0.042	0.040	-0.061	0.021	0.185	111.616	115.904	63.357	30.785	0.808	24.760	26.557
19	0.048	0.048	-0.076	0.020	0.237	112.953	116.313	63.048	34.301	0.794	26.086	28.816
20	0.055	0.069	-0.108	0.015	0.318	115.435	117.942	58.786	36.247	0.808	25.393	31.876
21	0.062	0.106	-0.170	-0.002	0.472	116.701	118.823	55.900	39.288	0.806	25.657	35.143
22	0.068	0.152	-0.250	-0.031	0.627	118.770	120.183	51.771	40.247	0.820	24.819	37.887
23	0.072	0.181	-0.305	-0.052	0.746	119.926	120.735	51.457	41.856	0.817	25.360	39.126
24	0.075	0.234	-0.396	-0.087	0.915	120.675	121.475	48.723	42.701	0.822	24.943	41.241
25	0.078	0.260	-0.453	-0.115	1.025	121.402	121.851	47.717	43.455	0.823	24.854	42.356
26	0.087	0.325	-0.589	-0.177	1.260	122.898	122.654	46.369	44.414	0.826	24.627	43.842
27	0.090	0.338	-0.613	-0.185	1.293	121.933	122.574	44.197	42.139	0.839	23.656	43.642
28	0.090	0.362	-0.661	-0.209	1.430	121.222	121.686	48.978	47.110	0.804	26.260	44.234
29	0.097	0.439	-0.809	-0.273	1.600	124.420	123.912	41.645	43.039	0.847	23.060	45.981
30	0.102	0.590	-1.074	-0.383	1.999	126.088	124.238	41.538	43.529	0.848	22.919	46.384
31	0.106	0.665	-1.202	-0.430	2.234	122.934	122.448	47.476	48.086	0.809	25.941	45.835
32	0.111	0.535	-1.217	-0.571	2.648	125.385	124.498	40.873	41.664	0.856	22.298	45.550
33	0.099	0.655	-1.368	-0.614	2.930	120.883	121.606	48.597	46.856	0.805	26.178	44.293

Torsion Shear Test on Fine Nevada Sand with a Target Void Ratio = 0.530 (D_r = 91.28%)

Test No.:	31	
Test Date:	9/6/11	
Initial Height, h_i:	39.99	cm
Initial Void Ratio, e:	0.535	
Final Mean Princpal Stress, σ_m :	101.1	kPa
Max Friction Angle, ϕ:	35.9	deg
b-value at failure:	0.00	
Stress direction at failure, α:	44.9	deg

Shear Band Notes	
Point of Observation:	27
Inclination (from Vertical)	
15°, 10°, 15°, 13°, 10°	
Failure Notes:	
SB's not so prominent	

Point (No.)	ε_z (%)	ε_r (%)	ε_θ (%)	ε_v (%)	$\gamma_{\theta z}$ (%)	σ_z (kPa)	σ_r (kPa)	σ_θ (kPa)	$\tau_{\theta z}$ (kPa)	b	α (°)	φ (°)
1	0.000	0.000	0.000	0.000	0.000	102.144	100.233	101.482	1.774	0.062	39.715	1.015
2	0.006	-0.015	0.006	-0.003	0.092	106.067	92.440	105.775	14.610	0.039	44.714	7.929
3	0.019	-0.034	0.012	-0.002	0.200	108.864	86.528	108.420	25.211	0.061	44.748	13.419
4	0.026	-0.059	0.034	0.001	0.355	113.725	78.464	112.820	35.035	0.003	44.630	18.019
5	0.031	-0.075	0.049	0.005	0.451	114.265	76.020	114.019	40.220	0.026	44.912	20.632
6	0.033	-0.087	0.060	0.006	0.504	114.710	74.228	114.538	42.668	0.027	44.942	21.854
7	0.035	-0.095	0.067	0.007	0.544	115.675	72.893	115.466	42.877	0.002	44.930	21.778
8	0.041	-0.129	0.095	0.007	0.711	116.871	69.987	116.353	49.278	0.027	44.849	24.998
9	0.045	-0.160	0.119	0.004	0.832	118.162	67.569	117.916	52.030	0.015	44.932	26.154
10	0.047	-0.178	0.132	0.001	0.905	118.715	66.603	118.285	53.457	0.015	44.885	26.815
11	0.052	-0.225	0.164	-0.009	1.082	119.607	64.186	119.144	56.368	0.010	44.882	28.177
12	0.058	-0.280	0.196	-0.025	1.281	120.686	62.673	120.208	58.665	0.008	44.883	29.148
13	0.056	-0.329	0.228	-0.044	1.463	121.186	61.330	120.962	60.540	0.007	44.947	30.002
14	0.060	-0.395	0.263	-0.072	1.692	121.918	59.967	121.484	62.416	0.005	44.900	30.855
15	0.060	-0.450	0.292	-0.097	1.877	122.366	58.978	121.871	63.698	0.004	44.889	31.440
16	0.057	-0.515	0.327	-0.131	2.107	122.547	58.127	122.377	65.453	0.009	44.963	32.309
17	0.056	-0.588	0.363	-0.168	2.355	123.436	57.121	123.098	66.461	0.002	44.927	32.627
18	0.053	-0.624	0.381	-0.190	2.501	122.664	57.501	122.583	67.303	0.016	44.983	33.289
19	0.044	-0.742	0.439	-0.259	2.891	124.005	55.668	123.671	68.528	0.003	44.930	33.598
20	0.044	-0.766	0.449	-0.273	2.971	124.068	55.510	123.638	68.793	0.003	44.911	33.741
21	0.051	-0.866	0.484	-0.331	3.280	124.351	54.722	123.874	69.882	0.004	44.902	34.267
22	0.058	-0.927	0.503	-0.366	3.461	124.632	54.442	124.105	70.345	0.003	44.893	34.446
23	0.062	-1.003	0.529	-0.412	3.699	124.900	54.059	124.578	70.884	0.001	44.935	34.629
24	0.079	-1.103	0.555	-0.469	3.989	126.129	53.635	124.629	71.574	-0.001	44.700	34.812
25	0.084	-1.175	0.573	-0.518	4.246	124.462	54.597	124.099	72.428	0.019	44.928	35.646
26	0.090	-1.231	0.591	-0.551	4.384	125.209	52.941	124.750	72.035	0.000	44.909	35.196
27	0.100	-1.292	0.604	-0.588	4.583	124.506	53.956	124.722	72.973	0.016	44.958	35.845
28	0.111	-1.410	0.639	-0.660	4.919	125.640	52.655	125.361	72.955	0.001	44.945	35.543
29	0.123	-1.485	0.656	-0.705	5.132	125.483	52.514	125.017	73.137	0.003	44.909	35.728
30	0.134	-1.564	0.677	-0.754	5.369	125.587	52.427	125.267	73.331	0.002	44.937	35.779
31	0.137	-1.626	0.697	-0.793	5.555	125.731	52.304	125.301	73.421	0.001	44.916	35.800
32	0.153	-1.717	0.718	-0.846	5.814	125.481	52.292	125.021	73.440	0.003	44.910	35.898
33	0.161	-1.779	0.735	-0.882	6.005	125.683	52.288	125.186	73.443	0.002	44.903	35.839

Torsion Shear Test on Fine Nevada Sand with a Target Void Ratio = 0.530 (D_r = 91.28%)

Test No.:	32*	
Test Date:	4/30/11	
Initial Height, h_i:	40.06	cm
Initial Void Ratio, e:	0.560	
Final Mean Princpal Stress, σ_m :	84.0	kPa
Max Friction Angle, ϕ:	40.9	deg
b-value at failure:	0.18	
Stress direction at failure, α:	31.6	deg

Shear Band Notes	
Point of Observation:	31
Inclination (from Vertical)	
3@15°,10°	
Failure Notes:	
One SB along top cap	

Point (No.)	ε_z (%)	ε_r (%)	ε_θ (%)	ε_v (%)	$\gamma_{\theta z}$ (%)	σ_z (kPa)	σ_r (kPa)	σ_θ (kPa)	$\tau_{\theta z}$ (kPa)	b	α (°)	φ (°)
1	0.000	0.000	0.000	0.000	0.000	90.037	101.355	101.552	2.082	0.843	43.646	4.116
2	0.040	-0.052	0.017	0.005	0.143	85.909	82.540	110.159	28.804	0.256	32.192	18.380
3	0.043	-0.066	0.032	0.009	0.239	85.031	78.914	111.636	33.863	0.239	32.106	21.350
4	0.043	-0.079	0.045	0.010	0.325	84.381	76.565	112.736	37.833	0.235	32.225	23.749
5	0.043	-0.088	0.054	0.010	0.384	84.188	75.085	113.641	40.002	0.228	32.135	25.015
6	0.044	-0.117	0.080	0.007	0.559	83.488	72.109	114.922	45.291	0.226	32.351	28.286
7	0.045	-0.144	0.100	0.001	0.680	82.844	68.851	116.556	48.002	0.205	31.789	29.971
8	0.046	-0.165	0.113	-0.005	0.774	82.362	67.360	116.883	49.984	0.204	31.824	31.313
9	0.049	-0.185	0.125	-0.011	0.864	82.161	66.142	117.595	51.692	0.200	31.770	32.390
10	0.052	-0.217	0.141	-0.024	1.000	81.875	64.699	118.292	53.728	0.197	31.746	33.717
11	0.048	-0.267	0.170	-0.050	1.218	81.415	62.623	119.149	56.448	0.193	31.702	35.551
12	0.042	-0.303	0.189	-0.072	1.380	80.907	61.864	119.743	57.908	0.194	31.723	36.656
13	0.039	-0.321	0.198	-0.083	1.454	80.797	61.391	119.932	58.425	0.193	31.695	37.019
14	0.036	-0.348	0.212	-0.101	1.575	80.552	60.727	120.062	59.282	0.193	31.707	37.670
15	0.033	-0.370	0.221	-0.116	1.673	80.548	60.428	120.274	60.232	0.194	31.791	38.304
16	0.025	-0.431	0.249	-0.157	1.931	80.481	59.178	121.041	61.431	0.188	31.637	39.049
17	0.024	-0.440	0.253	-0.163	1.970	80.428	59.034	121.053	61.595	0.188	31.639	39.180
18	0.022	-0.473	0.265	-0.186	2.114	80.344	58.622	121.247	62.207	0.188	31.640	39.614
19	0.011	-0.489	0.277	-0.201	2.199	80.250	58.262	121.374	62.656	0.187	31.634	39.947
20	0.011	-0.517	0.285	-0.221	2.318	80.213	57.995	121.489	62.987	0.186	31.625	40.178
21	0.010	-0.532	0.290	-0.232	2.384	80.313	57.900	121.531	63.246	0.186	31.648	40.315
22	0.010	-0.533	0.291	-0.232	2.388	80.371	57.890	121.643	63.248	0.186	31.626	40.279
23	0.010	-0.534	0.291	-0.234	2.391	80.408	57.890	121.697	63.277	0.185	31.622	40.278
24	0.009	-0.543	0.294	-0.240	2.426	80.347	57.753	121.710	63.371	0.185	31.612	40.365
25	0.009	-0.543	0.293	-0.240	2.430	80.291	57.745	121.599	63.384	0.186	31.633	40.411
26	0.009	-0.545	0.294	-0.242	2.433	80.311	57.747	121.634	63.389	0.186	31.628	40.402
27	0.009	-0.545	0.294	-0.242	2.437	80.300	57.752	121.595	63.397	0.186	31.637	40.418
28	0.009	-0.546	0.294	-0.243	2.441	80.255	57.740	121.510	63.390	0.186	31.649	40.441
29	-0.003	-0.623	0.322	-0.304	2.810	80.295	57.191	122.079	64.147	0.184	31.585	40.885
30	-0.003	-0.626	0.323	-0.306	2.825	80.315	57.177	122.061	64.128	0.183	31.583	40.865
31	-0.010	-0.662	0.336	-0.337	3.029	80.513	57.117	121.937	64.114	0.182	31.592	40.785
32	-0.016	-0.712	0.354	-0.374	3.360	79.984	57.369	121.803	63.144	0.182	31.484	40.326
33	-0.005	-0.642	0.327	-0.320	2.909	80.396	57.142	121.676	64.147	0.184	31.648	40.891

Torsion Shear Test on Fine Nevada Sand with a Target Void Ratio = 0.530 (D_r = 91.28%)

Test No.:	33
Test Date:	9/21/11
Initial Height, h_i:	39.96 cm
Initial Void Ratio, e:	0.540
Final Mean Princpal Stress, σ_m :	101.6 kPa
Max Friction Angle, ϕ:	45.0 deg
b-value at failure:	0.50
Stress direction at failure, α:	45.0 deg

Shear Band Notes

Point of Observation: 33

Inclination (from Vertical)

10°, 2@20°

Failure Notes:

Point (No.)	ε_z (%)	ε_r (%)	ε_θ (%)	ε_v (%)	$\gamma_{\theta z}$ (%)	σ_z (kPa)	σ_r (kPa)	σ_θ (kPa)	$\tau_{\theta z}$ (kPa)	b	α (°)	φ (°)
1	0.000	0.000	0.000	0.000	0.000	101.569	101.341	101.463	1.771	0.451	44.135	1.000
2	0.001	0.000	0.002	0.002	0.009	101.264	101.401	101.186	9.032	0.510	44.877	5.119
3	0.002	0.000	0.002	0.004	0.017	101.392	101.322	101.356	14.010	0.498	44.964	7.944
4	0.003	-0.001	0.003	0.006	0.044	101.351	101.419	101.299	18.356	0.503	44.960	10.437
5	0.005	-0.001	0.004	0.007	0.059	101.594	101.402	101.350	22.470	0.498	44.844	12.794
6	0.006	0.000	0.004	0.009	0.095	101.582	101.429	101.116	26.123	0.502	44.744	14.937
7	0.007	-0.001	0.006	0.012	0.133	101.359	101.302	101.494	29.253	0.498	44.934	16.763
8	0.007	0.000	0.007	0.014	0.194	101.570	101.295	101.537	32.244	0.496	44.985	18.512
9	0.007	0.001	0.008	0.016	0.266	101.634	101.308	101.538	34.819	0.496	44.961	20.045
10	0.005	0.003	0.011	0.019	0.335	101.723	101.383	101.224	39.598	0.499	44.819	22.969
11	0.005	0.003	0.010	0.019	0.339	101.801	101.384	101.236	39.727	0.498	44.796	23.038
12	0.003	0.005	0.011	0.019	0.406	101.915	101.393	101.522	42.195	0.496	44.867	24.508
13	0.001	0.007	0.013	0.020	0.464	101.862	101.374	101.270	44.122	0.498	44.808	25.749
14	-0.002	0.009	0.015	0.022	0.521	102.006	101.317	101.542	46.073	0.495	44.856	26.917
15	-0.004	0.011	0.016	0.022	0.565	101.953	101.280	101.523	47.580	0.495	44.870	27.883
16	-0.008	0.014	0.016	0.022	0.621	101.946	101.347	101.457	49.419	0.496	44.858	29.073
17	-0.012	0.017	0.017	0.022	0.676	101.762	101.341	101.237	51.120	0.498	44.853	30.242
18	-0.015	0.019	0.017	0.021	0.711	101.740	101.366	101.229	52.170	0.499	44.860	30.935
19	-0.019	0.022	0.017	0.020	0.761	101.493	101.375	101.442	53.553	0.499	44.987	31.856
20	-0.025	0.026	0.018	0.019	0.813	101.475	101.386	101.471	54.809	0.499	44.999	32.693
21	-0.032	0.030	0.017	0.016	0.869	101.435	101.420	101.471	56.082	0.500	44.991	33.559
22	-0.039	0.035	0.017	0.013	0.931	101.471	101.436	101.535	57.251	0.499	44.984	34.335
23	-0.047	0.039	0.017	0.009	0.988	101.546	101.461	101.642	58.378	0.499	44.976	35.073
24	-0.066	0.049	0.014	-0.002	1.125	101.909	101.426	101.732	60.539	0.497	44.958	36.481
25	-0.077	0.055	0.012	-0.010	1.200	101.857	101.460	101.515	61.465	0.498	44.920	37.190
26	-0.106	0.069	0.009	-0.028	1.356	101.548	101.301	101.487	63.115	0.498	44.986	38.442
27	-0.140	0.085	0.002	-0.053	1.545	101.821	101.400	101.733	64.781	0.497	44.981	39.531
28	-0.160	0.094	-0.002	-0.068	1.655	102.019	101.406	102.005	65.625	0.495	44.997	40.039
29	-0.199	0.112	-0.011	-0.098	1.853	101.876	101.435	101.722	66.894	0.497	44.967	41.080
30	-0.241	0.133	-0.023	-0.132	2.059	101.631	101.438	101.165	67.851	0.500	44.902	42.002
31	-0.334	0.177	-0.083	-0.240	2.676	102.001	101.419	101.810	70.208	0.497	44.961	43.548
32	-0.439	0.228	-0.169	-0.379	3.377	101.934	101.355	101.895	71.869	0.496	44.992	44.845
33	-0.456	0.236	-0.182	-0.402	3.490	102.033	101.382	102.065	72.118	0.495	44.994	44.967

Torsion Shear Test on Fine Nevada Sand with a Target Void Ratio = 0.530 (D_r = 91.28%)

Test No.:	34	
Test Date:	9/29/11	
Initial Height, h_i:	39.99	cm
Initial Void Ratio, e:	0.541	
Final Mean Princpal Stress, σ_m :	101.5	kPa
Max Friction Angle, ϕ:	34.9	deg
b-value at failure:	1.00	
Stress direction at failure, α:	48.7	deg

Shear Band Notes	
Point of Observation:	27
Inclination (from Vertical)	
2°, 5°, 10°, 20°, 25°	
Failure Notes:	

Point (No.)	ε_z (%)	ε_r (%)	ε_θ (%)	ε_v (%)	$\gamma_{\theta z}$ (%)	σ_z (kPa)	σ_r (kPa)	σ_θ (kPa)	$\tau_{\theta z}$ (kPa)	b	α (°)	φ (°)
1	0.000	0.000	0.000	0.000	0.000	101.564	102.066	101.639	1.344	0.673	44.205	0.758
2	-0.012	0.057	-0.008	0.036	0.221	91.553	122.113	91.642	32.286	0.973	44.961	20.639
3	-0.027	0.084	-0.014	0.043	0.330	89.771	125.335	89.755	36.650	0.985	44.994	24.098
4	-0.046	0.114	-0.021	0.047	0.445	88.713	127.298	88.727	39.533	0.988	44.995	26.461
5	-0.050	0.120	-0.023	0.047	0.474	88.514	127.684	88.460	39.982	0.990	44.981	26.862
6	-0.053	0.126	-0.026	0.047	0.502	88.222	128.020	88.258	40.457	0.992	44.987	27.289
7	-0.060	0.133	-0.027	0.047	0.528	88.217	128.342	88.078	40.875	0.992	44.951	27.627
8	-0.063	0.139	-0.030	0.047	0.557	87.986	128.600	87.882	41.325	0.992	44.964	28.032
9	-0.068	0.146	-0.032	0.046	0.587	87.817	128.905	87.754	41.779	0.992	44.978	28.420
10	-0.075	0.155	-0.034	0.046	0.616	87.636	129.247	87.539	42.175	0.994	44.967	28.785
11	-0.082	0.162	-0.036	0.044	0.646	87.629	129.469	87.551	42.621	0.991	44.974	29.117
12	-0.087	0.169	-0.039	0.044	0.675	87.460	129.795	87.196	43.015	0.994	44.912	29.510
13	-0.094	0.177	-0.041	0.042	0.708	87.408	130.043	87.454	43.475	0.990	44.985	29.818
14	-0.099	0.185	-0.045	0.040	0.742	87.296	130.346	87.283	43.804	0.991	44.996	30.121
15	-0.105	0.193	-0.049	0.038	0.775	86.972	130.579	86.943	44.015	0.996	44.991	30.409
16	-0.110	0.198	-0.051	0.036	0.798	87.014	130.708	86.942	44.244	0.994	44.977	30.576
17	-0.118	0.206	-0.054	0.035	0.827	86.942	130.883	86.818	44.525	0.994	44.960	30.830
18	-0.168	0.261	-0.077	0.016	1.044	86.241	132.247	85.935	46.443	0.997	44.906	32.649
19	-0.241	0.332	-0.110	-0.019	1.348	85.804	133.335	85.606	48.062	0.996	44.941	34.110
20	-0.261	0.349	-0.118	-0.029	1.427	85.629	133.446	85.431	48.212	0.997	44.941	34.311
21	-0.272	0.359	-0.120	-0.034	1.469	85.651	133.548	85.620	48.403	0.995	44.991	34.418
22	-0.273	0.359	-0.121	-0.035	1.472	85.679	133.554	85.620	48.422	0.995	44.983	34.427
23	-0.274	0.360	-0.121	-0.035	1.476	85.681	133.562	85.609	48.426	0.995	44.978	34.432
24	-0.280	0.368	-0.128	-0.040	1.519	85.551	133.669	85.425	48.546	0.996	44.963	34.602
25	-0.296	0.381	-0.134	-0.049	1.581	85.464	133.832	85.386	48.667	0.997	44.977	34.730
26	-0.296	0.381	-0.134	-0.049	1.584	85.504	133.818	85.444	48.697	0.996	44.982	34.731
27	-0.308	0.391	-0.138	-0.054	1.631	85.347	133.825	85.181	48.727	0.998	44.951	34.854

Torsion Shear Test on Fine Nevada Sand with a Target Void Ratio = 0.530 (D_r = 91.28%)

Test No.:	35*	
Test Date:	5/4/11	
Initial Height, h_i:	40.06	cm
Initial Void Ratio, e:	0.531	
Final Mean Princpal Stress, σ_m :	96.2	kPa
Max Friction Angle, ϕ:	38.1	deg
b-value at failure:	0.17	
Stress direction at failure, α:	65.1	deg

Shear Band Notes	
Point of Observation:	21
Inclination (from Vertical)	
0°	
Failure Notes:	
SB along top cap	

Point (No.)	ε_z (%)	ε_r (%)	ε_θ (%)	ε_v (%)	$\gamma_{\theta z}$ (%)	σ_z (kPa)	σ_r (kPa)	σ_θ (kPa)	$\tau_{\theta z}$ (kPa)	b	α (°)	φ (°)
1	0.000	0.000	0.000	0.000	0.000	89.142	101.408	101.417	0.480	0.925	89.738	0.271
2	-0.015	-0.001	0.020	0.003	0.068	85.654	95.103	110.925	10.699	0.132	71.760	7.421
3	-0.037	-0.001	0.043	0.006	0.068	83.282	90.543	118.196	14.804	0.020	68.478	11.191
4	-0.056	-0.002	0.069	0.011	0.069	81.059	86.698	124.058	18.739	0.040	67.545	14.542
5	-0.065	-0.010	0.086	0.012	0.069	79.532	82.933	130.070	19.176	0.056	64.567	16.576
6	-0.102	-0.013	0.130	0.015	0.166	77.639	79.925	134.545	25.752	0.106	66.659	20.490
7	-0.145	-0.028	0.188	0.015	0.215	75.982	76.326	140.391	29.631	0.129	66.385	23.747
8	-0.183	-0.047	0.242	0.012	0.215	73.949	72.623	145.903	28.450	0.119	63.914	25.123
9	-0.202	-0.049	0.258	0.008	0.215	74.209	73.650	143.746	32.046	0.137	66.219	25.906
10	-0.255	-0.073	0.325	-0.003	0.215	72.511	70.391	148.955	32.661	0.136	64.871	27.762
11	-0.334	-0.101	0.412	-0.024	0.214	71.682	68.584	151.895	34.659	0.144	64.881	29.443
12	-0.424	-0.131	0.504	-0.051	0.395	70.947	67.187	154.039	36.213	0.149	64.913	30.743
13	-0.487	-0.161	0.573	-0.076	0.536	70.383	65.939	156.164	37.091	0.152	64.713	31.729
14	-0.595	-0.195	0.675	-0.115	0.746	69.655	64.647	158.064	37.956	0.154	64.549	32.717
15	-0.650	-0.215	0.727	-0.137	0.903	69.534	64.426	158.246	39.030	0.157	64.881	33.237
16	-0.744	-0.184	0.773	-0.156	1.109	76.927	64.195	175.278	39.196	0.185	62.605	34.593
17	-0.932	-0.240	0.922	-0.251	1.252	67.364	62.458	159.103	41.054	0.158	65.175	34.916
18	-1.005	-0.265	0.986	-0.284	1.491	67.253	62.177	159.755	41.405	0.158	65.160	35.216
19	-1.101	-0.299	1.070	-0.330	1.816	67.000	61.726	160.287	41.868	0.160	65.175	35.629
20	-1.170	-0.330	1.133	-0.366	2.084	66.746	61.523	160.565	42.105	0.159	65.186	35.829
21	-1.258	-0.367	1.213	-0.412	2.398	66.629	60.942	161.668	42.647	0.162	65.129	36.364
22	-1.310	-0.392	1.261	-0.441	2.584	66.503	60.716	162.082	43.058	0.162	65.175	36.654
23	-1.394	-0.427	1.335	-0.486	2.875	66.077	60.410	162.094	43.291	0.162	65.207	36.886
24	-1.469	-0.462	1.401	-0.529	3.164	66.056	60.156	162.630	43.397	0.162	65.132	37.069
25	-1.528	-0.490	1.453	-0.565	3.382	65.904	59.965	162.907	43.716	0.163	65.171	37.301
26	-1.607	-0.523	1.521	-0.609	3.629	65.771	59.746	163.209	43.975	0.163	65.183	37.521
27	-1.675	-0.556	1.582	-0.649	3.892	65.702	59.455	163.744	44.236	0.164	65.155	37.788
28	-1.746	-0.591	1.645	-0.692	4.124	65.537	59.251	164.039	44.350	0.164	65.123	37.940
29	-1.818	-0.626	1.708	-0.737	4.373	65.414	59.027	164.213	44.480	0.165	65.111	38.105

Torsion Shear Test on Fine Nevada Sand with a Target Void Ratio = 0.530 (D_r = 91.28%)

Test No.:	36	
Test Date:	10/4/11	
Initial Height, h_i:	39.96	cm
Initial Void Ratio, e:	0.533	
Final Mean Princpal Stress, σ_m :	101.7	kPa
Max Friction Angle, ϕ:	37.2	deg
b-value at failure:	0.25	
Stress direction at failure, α:	67.8	deg

Shear Band Notes	
Point of Observation:	33
Inclination (from Vertical)	
Failure Notes:	
Slip along top cap	

Point (No.)	ε_z (%)	ε_r (%)	ε_θ (%)	ε_v (%)	$\gamma_{\theta z}$ (%)	σ_z (kPa)	σ_r (kPa)	σ_θ (kPa)	$\tau_{\theta z}$ (kPa)	b	α (°)	φ (°)
1	0.000	0.000	0.000	0.000	0.000	101.588	101.304	101.542	1.680	0.423	65.691	0.948
2	-0.001	-0.005	0.015	0.010	0.034	93.181	96.239	114.491	12.093	0.264	65.691	8.929
3	-0.004	-0.008	0.026	0.013	0.058	90.350	94.556	119.143	15.532	0.259	66.413	11.665
4	-0.010	-0.010	0.040	0.019	0.089	87.669	92.921	123.313	18.983	0.259	66.597	14.290
5	-0.020	-0.015	0.061	0.026	0.139	84.509	90.799	129.254	22.531	0.247	67.399	17.282
6	-0.024	-0.016	0.068	0.029	0.159	83.580	90.209	130.873	23.731	0.246	67.449	18.206
7	-0.029	-0.016	0.076	0.031	0.178	82.714	89.697	131.950	24.916	0.248	67.328	19.047
8	-0.032	-0.018	0.082	0.032	0.194	82.308	89.362	133.185	25.545	0.245	67.441	19.548
9	-0.038	-0.020	0.091	0.033	0.218	81.353	89.015	134.010	26.755	0.251	67.270	20.401
10	-0.043	-0.021	0.099	0.036	0.245	80.745	88.378	135.835	27.602	0.245	67.470	21.106
11	-0.049	-0.023	0.110	0.038	0.276	79.747	87.961	136.865	28.800	0.249	67.380	21.993
12	-0.056	-0.024	0.120	0.040	0.305	79.163	87.461	138.052	29.673	0.247	67.389	22.638
13	-0.059	-0.024	0.126	0.042	0.318	78.835	87.301	138.639	29.981	0.247	67.462	22.918
14	-0.063	-0.026	0.131	0.042	0.339	78.545	87.164	139.225	30.890	0.249	67.242	23.431
15	-0.070	-0.026	0.142	0.045	0.368	78.025	86.639	140.141	31.366	0.246	67.358	23.870
16	-0.073	-0.027	0.146	0.046	0.374	77.545	86.496	140.823	30.934	0.244	67.823	23.908
17	-0.077	-0.029	0.151	0.045	0.400	77.445	86.329	141.424	32.352	0.246	67.339	24.566
18	-0.085	-0.030	0.162	0.047	0.426	77.039	85.987	142.253	32.136	0.242	67.708	24.679
19	-0.091	-0.030	0.169	0.048	0.452	76.324	85.856	142.448	33.128	0.249	67.471	25.333
20	-0.095	-0.031	0.176	0.049	0.466	76.174	85.659	142.951	32.806	0.245	67.752	25.292
21	-0.110	-0.033	0.194	0.050	0.529	75.575	85.178	144.410	34.412	0.245	67.502	26.262
22	-0.129	-0.036	0.217	0.052	0.601	74.899	84.644	145.704	35.557	0.244	67.438	27.059
23	-0.161	-0.041	0.253	0.051	0.722	73.574	83.944	147.315	37.007	0.246	67.447	28.229
24	-0.187	-0.043	0.281	0.051	0.816	73.761	83.768	148.166	38.571	0.246	66.983	28.878
25	-0.227	-0.050	0.323	0.047	0.922	71.785	82.840	150.703	39.494	0.246	67.488	30.123
26	-0.272	-0.056	0.367	0.039	1.033	70.599	82.190	151.780	40.579	0.247	67.504	31.078
27	-0.325	-0.063	0.418	0.030	1.155	70.021	81.685	153.432	41.967	0.246	67.411	31.975
28	-0.386	-0.070	0.473	0.017	1.283	69.113	81.183	154.779	43.073	0.247	67.420	32.863
29	-0.443	-0.078	0.524	0.003	1.406	68.572	80.710	156.236	44.019	0.245	67.439	33.549
30	-0.547	-0.092	0.613	-0.026	1.612	67.379	80.046	157.925	45.257	0.245	67.505	34.628
31	-0.629	-0.100	0.680	-0.049	1.770	66.593	79.515	159.091	46.180	0.245	67.521	35.394
32	-0.747	-0.112	0.773	-0.086	2.001	65.745	78.987	160.553	47.286	0.245	67.536	36.282
33	-0.897	-0.132	0.883	-0.146	2.326	64.296	78.390	162.275	47.958	0.245	67.805	37.241

Torsion Shear Test on Fine Nevada Sand with a Target Void Ratio = 0.530 (D_r = 91.28%)

Test No.:	37*	
Test Date:	5/10/11	
Initial Height, h_i:	39.96	cm
Initial Void Ratio, e:	0.528	
Final Mean Princpal Stress, σ_m :	97.2	kPa
Max Friction Angle, ϕ:	38.7	deg
b-value at failure:	0.56	
Stress direction at failure, α:	65.0	deg

Shear Band Notes	
Point of Observation:	27
Inclination (from Vertical)	
One SB around bottom half at 0°, 10°, 15°	
Failure Notes:	
After SB developed, top cap slipped	

Point (No.)	ε_z (%)	ε_r (%)	ε_θ (%)	ε_v (%)	$\gamma_{\theta z}$ (%)	σ_z (kPa)	σ_r (kPa)	σ_θ (kPa)	$\tau_{\theta z}$ (kPa)	b	α (°)	φ (°)
1	0.000	0.000	0.000	0.000	0.000	89.243	101.364	101.377	1.723	0.980	52.926	3.794
2	-0.020	0.009	0.037	0.026	0.108	70.755	101.381	118.715	18.153	0.610	63.563	18.511
3	-0.033	0.015	0.049	0.031	0.143	68.559	101.366	120.531	20.010	0.604	63.799	20.298
4	-0.043	0.019	0.059	0.035	0.170	67.481	101.392	122.271	21.446	0.594	64.028	21.512
5	-0.059	0.025	0.072	0.038	0.203	65.530	101.367	123.732	22.988	0.591	64.153	23.073
6	-0.094	0.039	0.099	0.044	0.269	63.284	101.381	126.105	25.590	0.583	64.585	25.331
7	-0.118	0.049	0.116	0.047	0.310	62.077	101.396	127.263	26.668	0.580	64.645	26.413
8	-0.145	0.059	0.134	0.048	0.351	61.038	101.373	128.475	27.555	0.576	64.628	27.358
9	-0.164	0.067	0.145	0.048	0.382	60.343	101.367	129.035	28.182	0.575	64.685	27.982
10	-0.203	0.082	0.169	0.048	0.441	59.472	101.368	130.473	29.147	0.570	64.694	28.924
11	-0.287	0.113	0.215	0.042	0.559	57.818	101.355	132.129	30.608	0.566	64.740	30.455
12	-0.337	0.132	0.242	0.038	0.630	56.934	101.381	132.913	31.322	0.566	64.752	31.245
13	-0.386	0.150	0.267	0.030	0.701	56.191	101.373	133.633	32.054	0.564	64.809	31.980
14	-0.443	0.170	0.295	0.022	0.780	55.586	101.377	134.316	32.693	0.563	64.855	32.610
15	-0.485	0.185	0.314	0.015	0.835	55.021	101.367	134.623	33.099	0.563	64.874	33.088
16	-0.561	0.210	0.349	-0.002	0.940	54.311	101.365	135.673	33.779	0.560	64.852	33.824
17	-0.616	0.229	0.372	-0.015	1.020	53.707	101.378	135.808	34.159	0.562	64.882	34.304
18	-0.762	0.277	0.432	-0.054	1.253	52.773	101.361	136.915	35.117	0.559	64.926	35.296
19	-0.863	0.309	0.470	-0.083	1.487	52.601	101.408	137.530	35.459	0.557	64.931	35.587
20	-0.917	0.330	0.489	-0.098	1.704	52.259	101.358	137.509	35.560	0.558	64.918	35.806
21	-0.981	0.354	0.509	-0.117	1.903	51.847	101.369	138.083	36.041	0.557	64.946	36.282
22	-1.022	0.371	0.524	-0.128	2.029	51.646	101.372	137.927	36.360	0.558	65.063	36.529
23	-1.080	0.391	0.545	-0.144	2.205	51.330	101.371	138.573	36.653	0.556	65.019	36.874
24	-1.150	0.412	0.567	-0.171	2.463	50.989	101.388	139.159	37.101	0.555	65.042	37.304
25	-1.558	0.576	0.696	-0.286	3.675	49.400	101.383	140.301	38.073	0.555	64.976	38.689
26	-1.578	0.584	0.702	-0.291	3.733	49.731	101.363	140.382	38.296	0.553	65.097	38.626
27	-1.579	0.584	0.702	-0.292	3.739	49.709	101.371	140.367	38.266	0.553	65.085	38.622
28	-1.581	0.586	0.703	-0.293	3.746	49.749	101.360	140.500	38.300	0.553	65.083	38.625
29	-1.588	0.588	0.705	-0.295	3.766	49.787	101.374	140.531	38.326	0.552	65.094	38.619

Torsion Shear Test on Fine Nevada Sand with a Target Void Ratio = 0.530 (D_r = 91.28%)

Test No.:	38
Test Date:	10/11/11
Initial Height, h_i:	39.96 cm
Initial Void Ratio, e:	0.528
Final Mean Princpal Stress, σ_m :	101.5 kPa
Max Friction Angle, ϕ:	31.5 deg
b-value at failure:	0.75
Stress direction at failure, α:	65.1 deg

Shear Band Notes	
Point of Observation:	27
Inclination (from Vertical)	
Failure Notes:	
top cap SB (deep)	

Point (No.)	ε_z (%)	ε_r (%)	ε_θ (%)	ε_v (%)	$\gamma_{\theta z}$ (%)	σ_z (kPa)	σ_r (kPa)	σ_θ (kPa)	$\tau_{\theta z}$ (kPa)	b	α (°)	φ (°)
1	0.000	0.000	0.000	0.000	0.000	101.198	101.394	101.053	1.300	0.603	52.926	0.738
2	-0.014	0.020	0.015	0.022	0.052	86.608	107.195	111.688	14.227	0.712	63.563	11.027
3	-0.017	0.024	0.018	0.025	0.066	84.289	108.077	112.851	16.090	0.721	63.799	12.607
4	-0.026	0.031	0.026	0.031	0.093	80.302	109.526	114.717	18.474	0.738	64.028	15.005
5	-0.038	0.039	0.034	0.035	0.122	77.436	110.487	116.339	20.183	0.743	64.153	16.817
6	-0.045	0.044	0.039	0.039	0.140	76.880	110.912	116.935	21.490	0.738	64.585	17.646
7	-0.053	0.050	0.045	0.042	0.157	75.047	111.462	118.045	22.132	0.742	64.645	18.638
8	-0.063	0.057	0.052	0.045	0.181	73.471	112.035	118.695	23.124	0.747	64.628	19.670
9	-0.073	0.063	0.058	0.048	0.203	72.518	112.475	119.237	23.979	0.748	64.685	20.436
10	-0.086	0.071	0.066	0.051	0.229	71.298	112.915	120.136	24.827	0.747	64.694	21.335
11	-0.096	0.077	0.072	0.053	0.249	70.354	113.250	120.781	25.542	0.746	64.740	22.058
12	-0.113	0.088	0.081	0.056	0.283	69.294	113.655	121.139	26.468	0.749	64.752	22.898
13	-0.119	0.091	0.085	0.057	0.295	69.040	113.830	121.577	26.724	0.747	64.809	23.152
14	-0.133	0.100	0.093	0.059	0.320	68.273	114.117	121.880	27.200	0.749	64.855	23.681
15	-0.151	0.110	0.103	0.061	0.354	67.496	114.282	122.594	27.919	0.745	64.874	24.373
16	-0.162	0.117	0.107	0.062	0.373	67.074	114.498	122.854	28.257	0.746	64.852	24.713
17	-0.173	0.124	0.114	0.066	0.393	66.675	114.655	123.107	28.432	0.747	64.882	24.969
18	-0.185	0.130	0.120	0.065	0.415	66.302	114.837	123.338	28.830	0.747	64.926	25.320
19	-0.201	0.138	0.127	0.064	0.444	65.677	115.026	123.455	29.224	0.749	64.931	25.756
20	-0.216	0.146	0.135	0.065	0.472	65.292	115.227	123.768	29.648	0.749	64.918	26.135
21	-0.230	0.153	0.142	0.065	0.497	64.902	115.387	123.995	29.937	0.749	64.946	26.445
22	-0.243	0.161	0.148	0.066	0.519	64.516	115.544	124.317	30.233	0.748	65.063	26.767
23	-0.277	0.178	0.164	0.064	0.579	63.613	115.844	124.696	30.851	0.750	65.019	27.456
24	-0.329	0.205	0.187	0.063	0.669	62.631	116.229	125.411	31.685	0.749	65.042	28.319
25	-0.410	0.243	0.221	0.055	0.804	61.367	116.761	126.416	32.794	0.748	64.976	29.467
26	-0.488	0.280	0.252	0.044	0.934	60.156	117.162	126.955	33.559	0.749	65.097	30.403
27	-0.614	0.335	0.299	0.021	1.154	59.009	117.689	127.942	34.663	0.748	65.085	31.530

Torsion Shear Test on Fine Nevada Sand with a Target Void Ratio = 0.530 (D_r = 91.28%)

Test No.:	39*	
Test Date:	5/12/11	
Initial Height, h_i:	40.06	cm
Initial Void Ratio, e:	0.531	
Final Mean Princpal Stress, σ_m :	97.1	kPa
Max Friction Angle, ϕ:		deg
b-value at failure:		
Stress direction at failure, α:		deg

Shear Band Notes	
Point of Observation:	26
Inclination (from Vertical)	
Failure Notes:	

Point (No.)	ε_z (%)	ε_r (%)	ε_θ (%)	ε_v (%)	$\gamma_{\theta z}$ (%)	σ_z (kPa)	σ_r (kPa)	σ_θ (kPa)	$\tau_{\theta z}$ (kPa)	b	α (°)	φ (°)
1	0.000	0.000	0.000	0.000	0.000	88.455	101.542	101.656	-0.140	0.991	44.393	3.982
2	-0.077	0.033	0.075	0.031	0.169	63.609	110.740	116.793	20.385	0.806	63.737	21.806
3	-0.121	0.051	0.106	0.035	0.242	60.423	111.870	118.543	22.540	0.804	63.899	24.267
4	-0.175	0.073	0.139	0.036	0.324	57.626	112.974	120.152	24.420	0.804	63.997	26.506
5	-0.228	0.093	0.169	0.034	0.396	55.628	113.694	121.399	25.669	0.802	63.987	28.119
6	-0.229	0.093	0.170	0.034	0.397	55.606	113.696	121.340	25.680	0.802	64.001	28.128
7	-0.287	0.117	0.198	0.028	0.477	54.869	114.119	121.881	27.487	0.797	64.682	29.366
8	-0.418	0.165	0.258	0.005	0.645	52.002	115.180	124.029	29.144	0.793	64.491	31.761
9	-0.535	0.208	0.305	-0.021	0.798	50.332	115.728	124.861	29.874	0.795	64.359	33.041
10	-0.605	0.235	0.331	-0.039	0.895	49.851	115.868	125.055	29.988	0.795	64.286	33.364
11	-0.657	0.255	0.351	-0.051	0.975	49.611	115.885	124.878	30.410	0.796	64.470	33.682
12	-0.715	0.278	0.369	-0.068	1.106	49.321	116.167	125.524	30.609	0.794	64.389	33.990
13	-0.763	0.296	0.384	-0.083	1.231	49.171	116.165	125.295	30.583	0.796	64.391	34.037
14	-0.800	0.311	0.394	-0.095	1.358	48.837	116.248	125.458	30.933	0.796	64.459	34.404
15	-0.840	0.329	0.406	-0.105	1.476	48.518	116.387	125.804	31.180	0.794	64.450	34.728
16	-0.876	0.344	0.416	-0.117	1.587	48.352	116.521	126.093	31.328	0.793	64.434	34.916
17	-0.894	0.352	0.421	-0.122	1.642	48.397	116.526	126.113	31.346	0.793	64.446	34.902
18	-0.896	0.353	0.421	-0.122	1.647	48.419	116.532	126.151	31.380	0.793	64.459	34.910
19	-0.897	0.354	0.421	-0.123	1.652	48.407	116.527	126.152	31.398	0.793	64.464	34.926
20	-0.899	0.354	0.422	-0.123	1.655	48.452	116.523	126.209	31.439	0.792	64.480	34.927
21	-0.901	0.356	0.423	-0.122	1.661	48.454	116.529	126.249	31.449	0.792	64.478	34.934
22	-0.901	0.356	0.422	-0.123	1.667	48.457	116.530	126.247	31.390	0.792	64.453	34.903
23	-0.903	0.356	0.423	-0.123	1.671	48.442	116.540	126.195	31.464	0.792	64.492	34.944
24	-0.904	0.358	0.423	-0.124	1.675	48.486	116.556	126.262	31.445	0.792	64.480	34.916
25	-0.947	0.385	0.434	-0.128	1.800	48.160	116.624	126.466	31.490	0.792	64.405	35.132
26	-1.009	0.490	0.441	-0.078	1.999	47.965	116.596	126.534	31.665	0.791	64.435	35.332
27	-1.094	0.654	0.448	0.008	2.277	47.923	116.587	126.668	31.615	0.790	64.382	35.340
28	-1.222	1.772	0.363	0.913	2.793	47.800	116.469	125.778	31.038	0.798	64.261	35.044

Torsion Shear Test on Fine Nevada Sand with a Target Void Ratio = 0.530 (D_r = 91.28%)

Test No.:	40*	
Test Date:	9/19/10	
Initial Height, h_i:	40.03	cm
Initial Void Ratio, e:	0.541	
Final Mean Princpal Stress, σ_m :	97.35	kPa
Max Friction Angle, ϕ:	34.9	deg
b-value at failure:	0.80	
Stress direction at failure, α:	61.9	deg

Shear Band Notes	
Point of Observation:	28
Inclination (from Vertical)	
1SB @ 9.5°, 10°, 11°, 13°	
Failure Notes:	
One SB wrapping around specimen	

Point (No.)	ε_z (%)	ε_r (%)	ε_θ (%)	ε_v (%)	$\gamma_{\theta z}$ (%)	σ_z (kPa)	σ_r (kPa)	σ_θ (kPa)	$\tau_{\theta z}$ (kPa)	b	α (°)	φ (°)
1	0.000	0.000	0.000	0.000	0.000	86.365	103.111	102.776	1.060	0.976	48.608	5.111
2	-0.004	0.005	0.003	0.004	0.088	77.454	109.120	106.439	10.121	0.850	61.294	11.621
3	-0.011	0.014	0.005	0.008	0.105	72.721	111.764	108.078	10.862	0.854	59.546	14.016
4	-0.015	0.015	0.008	0.008	0.115	71.610	112.446	108.091	11.140	0.845	59.308	14.640
5	-0.017	0.016	0.008	0.008	0.125	70.838	112.715	107.689	11.510	0.833	59.399	15.091
6	-0.018	0.017	0.009	0.008	0.130	70.300	112.991	107.965	11.788	0.835	59.454	15.431
7	-0.023	0.024	0.011	0.012	0.158	68.924	113.918	108.557	12.991	0.830	60.003	16.509
8	-0.032	0.026	0.015	0.010	0.193	66.810	115.083	109.052	14.380	0.822	60.393	17.994
9	-0.041	0.031	0.019	0.010	0.227	65.172	116.386	109.685	15.492	0.816	60.587	19.250
10	-0.050	0.040	0.021	0.012	0.263	63.265	117.452	110.415	16.975	0.814	61.034	20.722
11	-0.061	0.046	0.027	0.012	0.301	61.240	118.724	111.352	18.273	0.814	61.223	22.241
12	-0.074	0.053	0.033	0.012	0.338	60.433	119.375	111.668	19.387	0.808	61.669	23.103
13	-0.085	0.059	0.036	0.010	0.358	58.560	120.440	112.398	19.667	0.812	61.221	24.182
14	-0.111	0.072	0.044	0.006	0.414	57.208	121.368	112.990	20.969	0.809	61.586	25.419
15	-0.125	0.082	0.047	0.004	0.444	56.226	122.019	113.305	21.713	0.807	61.713	26.249
16	-0.144	0.091	0.055	0.002	0.475	54.750	122.740	113.691	21.997	0.808	61.453	27.146
17	-0.174	0.106	0.062	-0.006	0.532	53.461	123.736	114.351	23.578	0.804	61.931	28.529
18	-0.203	0.121	0.070	-0.012	0.573	52.021	124.418	114.362	24.049	0.801	61.799	29.513
19	-0.222	0.129	0.076	-0.018	0.605	51.286	124.901	114.845	24.610	0.802	61.884	30.173
20	-0.045	0.034	0.021	0.010	0.244	64.341	116.869	110.168	16.233	0.817	60.860	19.924
21	-0.249	0.143	0.079	-0.028	0.649	50.581	125.484	115.091	24.986	0.801	61.854	30.758
22	-0.269	0.153	0.081	-0.035	0.682	49.993	125.828	115.435	25.360	0.802	61.888	31.258
23	-0.345	0.185	0.100	-0.059	0.785	48.303	126.787	115.721	26.306	0.798	61.918	32.660
24	-0.369	0.198	0.104	-0.067	0.821	47.987	127.101	116.369	26.683	0.802	62.001	33.028
25	-0.426	0.223	0.124	-0.079	0.898	47.750	127.614	116.547	26.886	0.800	61.976	33.300
26	-0.486	0.252	0.136	-0.098	0.975	46.835	127.821	116.752	27.365	0.801	62.025	34.031
27	-0.544	0.281	0.135	-0.128	1.056	46.056	128.266	116.858	27.558	0.800	61.920	34.595
28	-0.649	0.342	0.140	-0.167	1.324	45.833	128.649	117.570	27.764	0.804	61.921	34.852

Torsion Shear Test on Fine Nevada Sand with a Target Void Ratio = 0.530 (D_r = 91.28%)

Test No.:	41
Test Date:	10/21/11
Initial Height, h_i:	39.99 cm
Initial Void Ratio, e:	0.523
Final Mean Princpal Stress, σ_m :	101.8 kPa
Max Friction Angle, ϕ:	33.6 deg
b-value at failure:	0.00
Stress direction at failure, α:	90.0 deg

Shear Band Notes	
Point of Observation:	22
Inclination (from Vertical)	
2@16, 21, 21.5, 22.5, 23.5, 32	
Failure Notes:	
lower half bulged inwards, SBs crossed	

Point (No.)	ε_z (%)	ε_r (%)	ε_θ (%)	ε_v (%)	$\gamma_{\theta z}$ (%)	σ_z (kPa)	σ_r (kPa)	σ_θ (kPa)	$\tau_{\theta z}$ (kPa)	b	α (°)	φ (°)
1	0.000	0.000	0.000	0.000	0.000	101.597	101.317	101.512	0.000	0.698	90.000	0.024
2	-0.049	-0.025	0.101	0.027	0.000	80.939	80.978	141.832	0.000	0.001	90.000	15.863
3	-0.099	-0.061	0.201	0.041	0.000	73.698	73.669	156.439	0.000	0.000	90.000	21.071
4	-0.155	-0.099	0.302	0.048	0.000	69.790	69.955	163.668	0.000	0.002	90.000	23.711
5	-0.213	-0.138	0.402	0.051	0.000	67.511	67.620	168.335	0.000	0.001	90.000	25.309
6	-0.274	-0.182	0.504	0.047	0.000	65.390	65.726	171.955	0.000	0.003	90.000	26.679
7	-0.342	-0.229	0.611	0.040	0.000	64.132	64.339	174.813	0.000	0.002	90.000	27.594
8	-0.407	-0.277	0.712	0.028	0.000	62.989	63.166	177.245	0.000	0.002	90.000	28.399
9	-0.476	-0.329	0.816	0.011	0.000	61.913	62.146	179.177	0.000	0.002	90.000	29.104
10	-0.538	-0.374	0.908	-0.004	0.000	61.127	61.424	180.423	0.000	0.002	90.000	29.596
11	-0.670	-0.479	1.104	-0.045	0.000	59.709	59.953	183.459	0.000	0.002	90.000	30.591
12	-0.777	-0.566	1.258	-0.085	0.000	58.558	59.052	184.777	0.000	0.004	90.000	31.245
13	-0.821	-0.598	1.319	-0.099	0.000	58.588	58.884	185.606	0.000	0.002	90.000	31.343
14	-0.896	-0.653	1.425	-0.124	0.000	58.232	58.378	186.668	0.000	0.001	90.000	31.631
15	-0.967	-0.707	1.525	-0.150	0.000	57.700	57.918	187.562	0.000	0.002	90.000	31.971
16	-1.033	-0.761	1.618	-0.176	0.000	57.225	57.390	188.525	0.000	0.001	90.000	32.295
17	-1.112	-0.828	1.730	-0.210	0.000	56.621	56.999	189.037	0.000	0.003	90.000	32.617
18	-1.182	-0.885	1.827	-0.240	0.000	56.469	56.748	189.779	0.000	0.002	90.000	32.777
19	-1.266	-0.953	1.945	-0.275	0.000	56.175	56.427	190.431	0.000	0.002	90.000	32.985
20	-1.347	-1.019	2.049	-0.317	0.000	55.291	56.058	190.759	0.000	0.006	90.000	33.406
21	-1.432	-1.102	2.179	-0.356	0.000	55.340	55.653	191.383	0.000	0.002	90.000	33.463
22	-1.503	-1.154	2.271	-0.386	0.000	55.089	55.629	191.748	0.000	0.004	90.000	33.617
23	-1.576	-1.185	2.349	-0.412	0.000	56.092	55.403	194.419	0.000	-0.005	90.000	33.517

Torsion Shear Test on Fine Nevada Sand with a Target Void Ratio = 0.530 (D_r = 91.28%)

Test No.:	42*	
Test Date:	4/17/10	
Initial Height, h_i:	39.96	cm
Initial Void Ratio, e:	0.53	
Final Mean Princpal Stress, σ_m :	95.9	kPa
Max Friction Angle, ϕ:	45.5	deg
b-value at failure:	0.32	
Stress direction at failure, α:	90.0	deg

Shear Band Notes	
Point of Observation:	31
Inclination (from Vertical)	
2@24°, 6@25°, 2@26°	
Failure Notes:	
SB crossed along entire specimen	

Point (No.)	ε_z (%)	ε_r (%)	ε_θ (%)	ε_v (%)	$\gamma_{\theta z}$ (%)	σ_z (kPa)	σ_r (kPa)	σ_θ (kPa)	$\tau_{\theta z}$ (kPa)	b	α (°)	φ (°)
1	0.000	0.000	0.000	0.000	0.000	89.457	101.605	100.493	0.000	0.908	90.000	3.331
2	-0.034	-0.032	0.100	0.034	0.000	58.428	88.940	144.358	0.000	0.355	90.000	25.071
3	-0.071	-0.034	0.150	0.045	0.000	53.931	87.123	150.616	0.000	0.343	90.000	28.209
4	-0.113	-0.037	0.201	0.051	0.000	50.925	85.919	154.749	0.000	0.337	90.000	30.318
5	-0.158	-0.036	0.252	0.058	0.000	48.539	84.971	157.993	0.000	0.333	90.000	32.003
6	-0.207	-0.035	0.302	0.060	0.000	46.771	84.275	160.362	0.000	0.330	90.000	33.257
7	-0.255	-0.037	0.350	0.059	0.000	45.176	83.650	162.482	0.000	0.328	90.000	34.395
8	-0.313	-0.040	0.406	0.053	0.000	43.525	83.007	164.653	0.000	0.326	90.000	35.581
9	-0.381	-0.033	0.464	0.049	0.000	42.745	82.721	165.600	0.000	0.325	90.000	36.134
10	-0.423	-0.032	0.502	0.048	0.000	42.176	82.511	166.295	0.000	0.325	90.000	36.539
11	-0.486	-0.031	0.557	0.040	0.000	40.867	82.010	167.975	0.000	0.324	90.000	37.491
12	-0.545	-0.030	0.608	0.033	0.000	40.196	81.667	169.113	0.000	0.322	90.000	38.019
13	-0.601	-0.033	0.656	0.022	0.000	39.586	81.430	169.887	0.000	0.321	90.000	38.465
14	-0.671	-0.033	0.714	0.010	0.000	38.698	81.151	170.797	0.000	0.321	90.000	39.092
15	-0.733	-0.032	0.764	-0.001	0.000	38.144	80.968	171.381	0.000	0.321	90.000	39.487
16	-0.790	-0.031	0.808	-0.013	0.000	37.708	80.804	171.905	0.000	0.321	90.000	39.808
17	-0.860	-0.029	0.863	-0.026	0.000	37.100	80.603	172.551	0.000	0.321	90.000	40.247
18	-0.932	-0.028	0.918	-0.042	0.000	36.576	80.399	173.200	0.000	0.321	90.000	40.639
19	-0.989	-0.028	0.961	-0.056	0.000	36.150	80.249	173.675	0.000	0.321	90.000	40.952
20	-1.065	-0.028	1.018	-0.074	0.000	35.522	80.068	174.246	0.000	0.321	90.000	41.401
21	-1.128	-0.027	1.064	-0.091	0.000	35.096	79.885	174.830	0.000	0.321	90.000	41.731
22	-1.184	-0.026	1.107	-0.104	0.000	34.822	79.752	175.247	0.000	0.320	90.000	41.949
23	-1.349	-0.026	1.227	-0.149	0.000	33.785	79.478	176.071	0.000	0.321	90.000	42.689
24	-1.478	-0.028	1.317	-0.189	0.000	33.355	79.264	176.716	0.000	0.320	90.000	43.035
25	-1.544	-0.025	1.363	-0.207	0.000	32.968	79.208	176.868	0.000	0.321	90.000	43.296
26	-1.695	-0.027	1.468	-0.254	0.000	32.275	79.016	177.419	0.000	0.322	90.000	43.802
27	-1.818	-0.027	1.551	-0.293	0.000	31.821	78.832	177.967	0.000	0.322	90.000	44.158
28	-1.903	-0.024	1.609	-0.318	0.000	31.338	78.698	178.370	0.000	0.322	90.000	44.518
29	-2.132	-0.035	1.761	-0.406	0.000	30.722	78.502	178.881	0.000	0.322	90.000	44.979
30	-2.257	-0.040	1.843	-0.454	0.000	30.343	78.440	179.006	0.000	0.324	90.000	45.244
31	-2.408	-0.040	1.938	-0.510	0.000	30.057	78.369	179.155	0.000	0.324	90.000	45.452

Torsion Shear Test on Fine Nevada Sand with a Target Void Ratio = 0.530 (D_r = 91.28%)

Test No.:	43*	
Test Date:	5/13/11	
Initial Height, h_i:	39.96	cm
Initial Void Ratio, e:	0.520	
Final Mean Princpal Stress, σ_m :	96.9	kPa
Max Friction Angle, ϕ:	41.3	deg
b-value at failure:	0.78	
Stress direction at failure, α:	90.0	deg

Shear Band Notes
Point of Observation: 26

Inclination (from Vertical)
1SB @ 33°,32°,and 33°

Failure Notes:
thick continuous band around specimen

Point (No.)	ε_z (%)	ε_r (%)	ε_θ (%)	ε_v (%)	$\gamma_{\theta z}$ (%)	σ_z (kPa)	σ_r (kPa)	σ_θ (kPa)	$\tau_{\theta z}$ (kPa)	b	α (°)	φ (°)
1	0.000	0.000	0.000	0.000	0.000	90.074	101.251	101.287	0.000	0.997	90.000	3.359
2	-0.047	0.037	0.050	0.041	0.000	63.531	108.301	118.713	0.000	0.811	90.000	17.625
3	-0.108	0.068	0.101	0.061	0.000	56.616	110.205	123.593	0.000	0.800	90.000	21.818
4	-0.177	0.103	0.153	0.079	0.000	51.082	111.779	127.490	0.000	0.794	90.000	25.334
5	-0.251	0.138	0.203	0.090	0.000	48.243	112.554	129.407	0.000	0.792	90.000	27.185
6	-0.328	0.173	0.252	0.097	0.000	45.689	113.295	131.152	0.000	0.791	90.000	28.900
7	-0.410	0.208	0.302	0.100	0.000	43.468	113.833	132.814	0.000	0.788	90.000	30.453
8	-0.498	0.245	0.351	0.098	0.000	41.731	114.369	133.819	0.000	0.789	90.000	31.639
9	-0.592	0.283	0.401	0.092	0.000	40.084	114.769	134.890	0.000	0.788	90.000	32.808
10	-0.699	0.325	0.457	0.083	0.000	38.801	115.152	136.004	0.000	0.785	90.000	33.784
11	-0.797	0.362	0.506	0.070	0.000	37.699	115.471	136.713	0.000	0.785	90.000	34.590
12	-0.898	0.399	0.554	0.055	0.000	36.873	115.668	137.230	0.000	0.785	90.000	35.199
13	-0.997	0.435	0.600	0.039	0.000	36.042	115.898	137.666	0.000	0.786	90.000	35.805
14	-1.124	0.480	0.660	0.016	0.000	34.996	116.225	138.744	0.000	0.783	90.000	36.666
15	-1.244	0.520	0.713	-0.011	0.000	33.903	116.522	139.281	0.000	0.784	90.000	37.480
16	-1.384	0.566	0.773	-0.044	0.000	33.186	116.688	139.848	0.000	0.783	90.000	38.056
17	-1.465	0.591	0.807	-0.067	0.000	32.823	116.779	140.070	0.000	0.783	90.000	38.338
18	-1.601	0.639	0.863	-0.099	0.000	32.431	116.906	140.194	0.000	0.784	90.000	38.628
19	-1.717	0.681	0.913	-0.123	0.000	31.912	116.962	140.488	0.000	0.783	90.000	39.035
20	-1.810	0.711	0.952	-0.147	0.000	31.945	117.037	140.238	0.000	0.786	90.000	38.972
21	-2.056	0.793	1.053	-0.211	0.000	30.852	117.284	141.366	0.000	0.782	90.000	39.920
22	-2.186	0.836	1.105	-0.246	0.000	30.459	117.381	141.601	0.000	0.782	90.000	40.237
23	-2.314	0.882	1.156	-0.276	0.000	30.108	117.513	141.781	0.000	0.783	90.000	40.518
24	-2.396	0.908	1.187	-0.301	0.000	29.995	117.577	142.362	0.000	0.779	90.000	40.688
25	-2.514	0.941	1.232	-0.341	0.000	29.850	117.686	143.068	0.000	0.776	90.000	40.900
26	-2.731	1.006	1.315	-0.410	0.000	29.389	117.840	143.407	0.000	0.776	90.000	41.288

Torsion Shear Test on Fine Nevada Sand with a Target Void Ratio = 0.530 (D_r = 91.28%)

Test No.:	44*	
Test Date:	5/16/11	
Initial Height, h_i:	39.96	cm
Initial Void Ratio, e:	0.510	
Final Mean Princpal Stress, σ_m :	96.9	kPa
Max Friction Angle, ϕ:	37.9	deg
b-value at failure:	0.99	
Stress direction at failure, α:	90.0	deg

Shear Band Notes	
Point of Observation:	27
Inclination (from Vertical)	
0°	
Failure Notes:	
Deep trough SB along top cap	

Point (No.)	ε_z (%)	ε_r (%)	ε_θ (%)	ε_v (%)	$\gamma_{\theta z}$ (%)	σ_z (kPa)	σ_r (kPa)	σ_θ (kPa)	$\tau_{\theta z}$ (kPa)	b	α (°)	φ (°)
1	0.000	0.000	0.000	0.000	0.000	88.412	101.393	101.525	0.000	0.989	90.000	3.959
2	-0.019	0.023	0.021	0.025	0.000	62.027	114.095	114.086	0.000	1.000	90.000	17.193
3	-0.034	0.033	0.030	0.029	0.000	58.361	115.970	116.143	0.000	0.997	90.000	19.337
4	-0.051	0.043	0.040	0.032	0.000	55.380	117.361	116.887	0.000	1.008	90.000	20.919
5	-0.069	0.054	0.051	0.036	0.000	53.089	118.551	118.549	0.000	1.000	90.000	22.420
6	-0.088	0.066	0.061	0.038	0.000	51.091	119.530	119.681	0.000	0.998	90.000	23.681
7	-0.104	0.075	0.070	0.041	0.000	49.305	120.322	120.493	0.000	0.998	90.000	24.787
8	-0.125	0.086	0.081	0.042	0.000	47.433	121.243	121.300	0.000	0.999	90.000	25.962
9	-0.144	0.097	0.090	0.043	0.000	46.331	121.802	122.027	0.000	0.997	90.000	26.719
10	-0.169	0.110	0.102	0.042	0.000	45.430	122.239	122.296	0.000	0.999	90.000	27.276
11	-0.189	0.121	0.111	0.043	0.000	44.666	122.580	122.677	0.000	0.999	90.000	27.786
12	-0.211	0.132	0.120	0.042	0.000	43.805	123.004	122.885	0.000	1.002	90.000	28.321
13	-0.235	0.145	0.131	0.042	0.000	43.147	123.362	123.552	0.000	0.998	90.000	28.838
14	-0.285	0.170	0.153	0.038	0.000	41.719	123.974	123.934	0.000	1.000	90.000	29.756
15	-0.337	0.197	0.174	0.034	0.000	40.487	124.630	124.518	0.000	1.001	90.000	30.614
16	-0.377	0.216	0.190	0.030	0.000	39.568	125.020	125.116	0.000	0.999	90.000	31.296
17	-0.438	0.245	0.213	0.020	0.000	38.466	125.552	125.556	0.000	1.000	90.000	32.071
18	-0.490	0.269	0.233	0.011	0.000	37.655	125.942	126.093	0.000	0.998	90.000	32.690
19	-0.575	0.309	0.263	-0.003	0.000	36.794	126.384	126.495	0.000	0.999	90.000	33.322
20	-0.648	0.340	0.291	-0.017	0.000	35.982	126.848	127.103	0.000	0.997	90.000	33.968
21	-0.709	0.366	0.311	-0.031	0.000	35.224	127.152	127.312	0.000	0.998	90.000	34.511
22	-0.806	0.410	0.343	-0.053	0.000	34.460	127.504	127.786	0.000	0.997	90.000	35.115
23	-0.910	0.457	0.377	-0.076	0.000	33.509	127.936	127.833	0.000	1.001	90.000	35.776
24	-0.986	0.490	0.403	-0.093	0.000	32.665	128.392	128.535	0.000	0.999	90.000	36.493
25	-1.020	0.504	0.412	-0.103	0.000	32.252	128.571	128.673	0.000	0.999	90.000	36.811
26	-1.127	0.552	0.442	-0.133	0.000	31.682	128.941	129.211	0.000	0.997	90.000	37.314
27	-1.348	0.654	0.492	-0.203	0.000	31.116	129.368	130.161	0.000	0.992	90.000	37.889

True Triaxial Test on Fine Nevada Sand with a Target Void Ratio = 0.530 (D_r = 91.28%)

Test No.:	1	
Test Date:	3/21/11	
Sector:	I	
Initial Void Ratio, e:	0.522	
Final Mean Princpal Stress, σ_m :	121.4	kPa
Max Friction Angle, ϕ:	43.0	deg
b-value at failure:	0.00	
Stress direction at failure, α:	0.0	deg

Shear Band Notes

Point of Observation: 30

Inclination (from Vertical):
51°, 58°

Failure Notes:

Point (No.)	ε_z (%)	ε_x (%)	ε_y (%)	ε_v (%)	$\gamma_{\theta z}$ (%)	σ_z (kPa)	σ_x (kPa)	σ_y (kPa)	$\tau_{\theta z}$ (kPa)	b	α (°)	φ (°)
1	0.000	0.000	0.000	0.000	0.000	51.627	50.000	50.000	0.000	0.000	0.000	0.917
2	0.014	-0.005	-0.005	0.004	0.000	63.297	50.000	50.000	0.000	0.000	0.000	6.740
3	0.041	-0.014	-0.014	0.013	0.000	76.423	50.000	50.000	0.000	0.000	0.000	12.064
4	0.126	-0.045	-0.045	0.037	0.000	104.831	50.000	50.000	0.000	0.000	0.000	20.741
5	0.201	-0.075	-0.075	0.050	0.000	123.372	50.000	50.000	0.000	0.000	0.000	25.037
6	0.421	-0.181	-0.181	0.059	0.000	162.830	50.000	50.000	0.000	0.000	0.000	32.015
7	0.620	-0.296	-0.296	0.028	0.000	186.502	50.000	50.000	0.000	0.000	0.000	35.252
8	0.809	-0.415	-0.415	-0.020	0.000	202.092	50.000	50.000	0.000	0.000	0.000	37.108
9	1.053	-0.582	-0.582	-0.111	0.000	215.641	50.000	50.000	0.000	0.000	0.000	38.576
10	1.211	-0.693	-0.693	-0.176	0.000	222.463	50.000	50.000	0.000	0.000	0.000	39.270
11	1.421	-0.844	-0.844	-0.268	0.000	230.904	50.000	50.000	0.000	0.000	0.000	40.091
12	1.637	-1.007	-1.007	-0.376	0.000	237.817	50.000	50.000	0.000	0.000	0.000	40.735
13	1.811	-1.140	-1.140	-0.470	0.000	243.016	50.000	50.000	0.000	0.000	0.000	41.202
14	2.007	-1.292	-1.292	-0.577	0.000	248.111	50.000	50.000	0.000	0.000	0.000	41.648
15	2.237	-1.476	-1.476	-0.716	0.000	250.914	50.000	50.000	0.000	0.000	0.000	41.888
16	2.421	-1.618	-1.618	-0.816	0.000	254.573	50.000	50.000	0.000	0.000	0.000	42.196
17	2.611	-1.772	-1.772	-0.933	0.000	256.402	50.000	50.000	0.000	0.000	0.000	42.348
18	2.806	-1.931	-1.931	-1.055	0.000	258.896	50.000	50.000	0.000	0.000	0.000	42.553
19	3.053	-2.130	-2.130	-1.208	0.000	259.450	50.000	50.000	0.000	0.000	0.000	42.598
20	3.211	-2.255	-2.255	-1.299	0.000	261.012	50.000	50.000	0.000	0.000	0.000	42.724
21	3.421	-2.423	-2.423	-1.425	0.000	263.069	50.000	50.000	0.000	0.000	0.000	42.889
22	3.632	-2.594	-2.594	-1.556	0.000	263.024	50.000	50.000	0.000	0.000	0.000	42.886
23	3.842	-2.764	-2.764	-1.686	0.000	264.355	50.000	50.000	0.000	0.000	0.000	42.991
24	4.135	-3.000	-3.000	-1.865	0.000	262.299	50.000	50.000	0.000	0.000	0.000	42.828
25	4.263	-3.101	-3.101	-1.939	0.000	263.231	50.000	50.000	0.000	0.000	0.000	42.902
26	4.421	-3.223	-3.223	-2.026	0.000	263.039	50.000	50.000	0.000	0.000	0.000	42.887
27	4.668	-3.417	-3.417	-2.165	0.000	261.858	50.000	50.000	0.000	0.000	0.000	42.792
28	4.881	-3.584	-3.584	-2.287	0.000	261.135	50.000	50.000	0.000	0.000	0.000	42.734
29	5.026	-3.696	-3.696	-2.365	0.000	258.281	50.000	50.000	0.000	0.000	0.000	42.502
30	5.250	-3.866	-3.866	-2.482	0.000	257.552	50.000	50.000	0.000	0.000	0.000	42.443

True Triaxial Test on Fine Nevada Sand with a Target Void Ratio = 0.530 (D_r = 91.28%)

Test No.:	2	
Test Date:	3/22/11	
Sector:	I	
Initial Void Ratio, e:	0.527	
Final Mean Princpal Stress, σ_m :	158.3	kPa
Max Friction Angle, ϕ:	46.3	deg
b-value at failure:	0.24	
Stress direction at failure, α:	0.0	deg

Shear Band Notes	
Point of Observation:	18
Inclination (from Vertical):	
61°, 62°	
Failure Notes:	

Point (No.)	ε_z (%)	ε_x (%)	ε_y (%)	ε_v (%)	$\gamma_{\theta z}$ (%)	σ_z (kPa)	σ_x (kPa)	σ_y (kPa)	$\tau_{\theta z}$ (kPa)	b	α (°)	φ (°)
1	0.000	0.000	0.000	0.000	0.000	51.617	50.404	50.000	0.000	0.250	0.000	0.911
2	0.000	0.002	0.002	0.003	0.000	60.631	52.497	50.000	0.000	0.235	0.000	5.514
3	0.023	0.000	-0.008	0.015	0.000	72.888	55.563	50.000	0.000	0.243	0.000	10.734
4	0.049	0.000	-0.024	0.026	0.000	85.862	58.809	50.000	0.000	0.246	0.000	15.305
5	0.208	0.206	-0.350	0.065	0.000	136.227	71.397	50.000	0.000	0.248	0.000	27.582
6	0.406	0.253	-0.584	0.075	0.000	174.880	81.108	50.000	0.000	0.249	0.000	33.733
7	0.602	0.253	-0.799	0.056	0.000	204.021	88.480	50.000	0.000	0.250	0.000	37.325
8	0.807	0.253	-1.047	0.013	0.000	230.115	95.120	50.000	0.000	0.251	0.000	40.016
9	1.009	0.253	-1.305	-0.043	0.000	251.423	100.580	50.000	0.000	0.251	0.000	41.931
10	1.201	0.253	-1.565	-0.112	0.000	269.414	105.220	50.000	0.000	0.252	0.000	43.387
11	1.422	0.253	-1.877	-0.202	0.000	286.130	109.573	50.000	0.000	0.252	0.000	44.628
12	1.628	0.253	-2.186	-0.305	0.000	294.965	111.938	50.000	0.000	0.253	0.000	45.244
13	1.813	0.253	-2.466	-0.400	0.000	304.174	113.556	50.000	0.000	0.250	0.000	45.861
14	2.082	0.253	-2.881	-0.546	0.000	309.824	113.473	50.000	0.000	0.244	0.000	46.227
15	2.205	0.253	-3.073	-0.615	0.000	311.095	113.435	50.000	0.000	0.243	0.000	46.308
16	2.408	0.253	-3.405	-0.744	0.000	310.257	113.363	50.000	0.000	0.243	0.000	46.255
17	2.623	0.253	-3.762	-0.886	0.000	298.910	112.225	50.000	0.000	0.250	0.000	45.512
18	2.810	0.253	-4.052	-0.989	0.000	273.898	106.351	50.000	0.000	0.252	0.000	43.730
19	3.012	0.253	-4.319	-1.054	0.000	249.415	98.391	50.000	0.000	0.243	0.000	41.760
20	3.239	0.253	-4.582	-1.091	0.000	239.581	96.796	50.000	0.000	0.247	0.000	40.895
21	3.452	0.253	-4.823	-1.119	0.000	233.627	95.734	50.000	0.000	0.249	0.000	40.348

True Triaxial Test on Fine Nevada Sand with a Target Void Ratio = 0.530 (D_r = 91.28%)

Test No.:	3	**Shear Band Notes**	
Test Date:	3/24/11	Point of Observation:	24
Sector:	I		
Initial Void Ratio, e:	0.527	Inclination (from Vertical):	
Final Mean Princpal Stress, σ_m :	217.7 kPa	61°, 63°	
Max Friction Angle, ϕ:	50.3 deg		
b-value at failure:	0.51	Failure Notes:	
Stress direction at failure, α:	0.0 deg		

Point (No.)	ε_z (%)	ε_x (%)	ε_y (%)	ε_v (%)	$\gamma_{\theta z}$ (%)	σ_z (kPa)	σ_x (kPa)	σ_y (kPa)	$\tau_{\theta z}$ (kPa)	b	α (°)	φ (°)
1	0.000	0.000	0.000	0.000	0.000	51.616	50.808	50.000	0.000	0.500	0.000	0.911
2	0.008	0.000	-0.001	0.006	1.000	59.909	54.955	50.000	0.000	0.500	0.000	5.173
3	0.022	0.000	-0.005	0.017	2.000	72.888	61.446	50.000	0.000	0.500	0.000	10.734
4	0.052	0.399	-0.415	0.037	3.000	85.503	67.690	50.000	0.000	0.498	0.000	15.189
5	0.077	0.599	-0.626	0.049	4.000	97.034	73.394	50.000	0.000	0.497	0.000	18.656
6	0.103	0.143	-0.185	0.060	6.000	107.117	78.547	50.000	0.000	0.500	0.000	21.317
7	0.203	0.238	-0.361	0.080	0.000	138.040	94.005	50.000	0.000	0.500	0.000	27.917
8	0.316	0.314	-0.545	0.086	0.000	165.286	109.897	50.000	0.000	0.520	0.000	32.378
9	0.402	0.352	-0.677	0.077	0.000	186.023	118.408	50.000	0.000	0.503	0.000	35.192
10	0.536	0.400	-0.885	0.052	0.000	215.590	133.289	50.000	0.000	0.503	0.000	38.571
11	0.618	0.429	-1.014	0.032	0.000	232.273	142.578	50.000	0.000	0.508	0.000	40.221
12	0.746	0.467	-1.222	-0.009	0.000	260.241	156.088	50.000	0.000	0.505	0.000	42.662
13	0.809	0.486	-1.329	-0.034	0.000	272.215	162.431	50.000	0.000	0.506	0.000	43.602
14	0.927	0.524	-1.537	-0.086	0.000	293.620	173.504	50.000	0.000	0.507	0.000	45.152
15	1.000	0.552	-1.673	-0.120	0.000	305.131	179.277	50.000	0.000	0.507	0.000	45.924
16	1.131	0.610	-1.942	-0.202	0.000	320.972	188.661	50.000	0.000	0.512	0.000	46.923
17	1.209	0.638	-2.087	-0.241	0.000	334.882	195.204	50.000	0.000	0.510	0.000	47.747
18	1.305	0.667	-2.262	-0.290	0.000	350.095	202.255	50.000	0.000	0.507	0.000	48.596
19	1.416	0.705	-2.478	-0.357	0.000	364.460	209.520	50.000	0.000	0.507	0.000	49.352
20	1.532	0.752	-2.715	-0.430	0.000	377.325	217.275	50.000	0.000	0.511	0.000	49.995
21	1.623	0.781	-2.890	-0.486	0.000	383.217	219.788	50.000	0.000	0.510	0.000	50.279
22	1.729	0.798	-3.091	-0.564	0.000	374.871	215.679	50.000	0.000	0.510	0.000	49.874
23	1.810	0.798	-3.236	-0.628	0.000	354.699	206.345	50.000	0.000	0.513	0.000	48.842
24	1.911	0.845	-3.444	-0.688	0.000	317.671	187.735	50.000	0.000	0.515	0.000	46.720
25	2.091	0.845	-3.641	-0.705	0.000	297.165	175.155	50.000	0.000	0.506	0.000	45.394
26	2.177	0.845	-3.770	-0.748	0.000	274.431	165.538	50.000	0.000	0.515	0.000	43.770
27	2.245	0.798	-3.805	-0.761	0.000	264.447	162.680	50.000	0.000	0.525	0.000	42.999
28	2.330	0.798	-3.898	-0.770	0.000	257.608	156.086	50.000	0.000	0.511	0.000	42.447
29	2.439	0.798	-4.013	-0.776	0.000	257.029	155.823	50.000	0.000	0.511	0.000	42.400
30	2.787	0.798	-4.375	-0.789	0.000	252.482	153.461	50.000	0.000	0.511	0.000	42.021
31	2.842	0.798	-4.430	-0.789	0.000	251.679	152.961	50.000	0.000	0.511	0.000	41.953
32	3.000	0.798	-4.590	-0.791	0.000	252.760	153.681	50.000	0.000	0.511	0.000	42.044

True Triaxial Test on Fine Nevada Sand with a Target Void Ratio = 0.530 (D_r = 91.28%)

Test No.:	4
Test Date:	3/25/11
Sector:	I
Initial Void Ratio, e:	0.528
Final Mean Princpal Stress, σ_m :	263.2 kPa
Max Friction Angle, ϕ:	51.7 deg
b-value at failure:	0.75
Stress direction at failure, α:	0.0 deg

Shear Band Notes	
Point of Observation:	24
Inclination (from Vertical):	
64°	
Failure Notes:	

Point (No.)	ε_z (%)	ε_x (%)	ε_y (%)	ε_v (%)	$\gamma_{\theta z}$ (%)	σ_z (kPa)	σ_x (kPa)	σ_y (kPa)	$\tau_{\theta z}$ (kPa)	b	α (°)	φ (°)
1	0.000	0.000	0.000	0.000	0.000	50.000	50.161	50.000	0.000	0.750	0.000	0.000
2	0.002	0.000	0.011	0.013	1.000	59.914	57.449	50.000	0.000	0.751	0.000	5.175
3	0.009	0.000	0.012	0.022	2.000	71.096	65.851	50.000	0.000	0.751	0.000	10.033
4	0.049	0.000	-0.004	0.045	3.000	87.684	78.318	50.000	0.000	0.751	0.000	15.884
5	0.111	0.452	-0.490	0.073	0.000	107.862	93.496	50.000	0.000	0.752	0.000	21.502
6	0.213	0.703	-0.812	0.103	0.000	135.925	114.636	50.000	0.000	0.752	0.000	27.526
7	0.312	0.879	-1.076	0.114	0.000	161.051	133.608	50.000	0.000	0.753	0.000	31.748
8	0.406	1.029	-1.334	0.101	0.000	185.389	152.038	50.000	0.000	0.754	0.000	35.112
9	0.507	1.180	-1.607	0.080	0.000	210.733	171.281	50.000	0.000	0.755	0.000	38.058
10	0.605	1.406	-1.959	0.052	0.000	234.199	189.169	50.000	0.000	0.756	0.000	40.401
11	0.709	1.531	-2.229	0.011	0.000	257.254	206.786	50.000	0.000	0.756	0.000	42.418
12	0.825	1.632	-2.501	-0.045	0.000	283.389	226.842	50.000	0.000	0.758	0.000	44.431
13	0.900	1.682	-2.666	-0.084	0.000	300.290	239.851	50.000	0.000	0.759	0.000	45.604
14	1.019	1.782	-2.962	-0.161	0.000	323.730	256.414	50.000	0.000	0.754	0.000	47.090
15	1.101	1.908	-3.234	-0.226	0.000	336.177	264.456	50.000	0.000	0.749	0.000	47.821
16	1.203	2.008	-3.518	-0.308	0.000	353.824	280.540	50.000	0.000	0.759	0.000	48.796
17	1.322	2.134	-3.862	-0.407	0.000	373.437	295.284	50.000	0.000	0.758	0.000	49.804
18	1.400	2.234	-4.105	-0.471	0.000	387.532	304.667	50.000	0.000	0.754	0.000	50.484
19	1.526	2.334	-4.457	-0.596	0.000	399.823	315.390	50.000	0.000	0.759	0.000	51.050
20	1.619	2.410	-4.719	-0.691	0.000	409.103	320.751	50.000	0.000	0.754	0.000	51.461
21	1.737	2.514	-5.010	-0.759	0.000	414.832	324.772	50.000	0.000	0.753	0.000	51.709
22	1.807	2.614	-5.288	-0.867	0.000	410.724	320.751	50.000	0.000	0.751	0.000	51.531
23	1.909	2.660	-5.527	-0.957	0.000	384.446	301.986	50.000	0.000	0.753	0.000	50.338
24	2.123	2.660	-5.852	-1.069	0.000	309.558	245.691	50.000	0.000	0.754	0.000	46.210
25	2.224	2.660	-5.984	-1.099	0.000	287.210	229.607	50.000	0.000	0.757	0.000	44.704
26	2.327	2.614	-6.047	-1.106	0.000	278.923	221.565	50.000	0.000	0.749	0.000	44.105
27	2.461	2.614	-6.182	-1.108	0.000	274.794	218.884	50.000	0.000	0.751	0.000	43.798
28	2.533	2.614	-6.257	-1.110	0.000	274.986	218.884	50.000	0.000	0.751	0.000	43.812
29	2.643	2.614	-6.369	-1.112	0.000	275.793	218.884	50.000	0.000	0.748	0.000	43.873
30	2.705	2.614	-6.431	-1.112	0.000	277.052	218.884	50.000	0.000	0.744	0.000	43.967

True Triaxial Test on Fine Nevada Sand with a Target Void Ratio = 0.530 (D_r = 91.28%)

Test No.:	5
Test Date:	3/26/11
Sector:	I
Initial Void Ratio, e:	0.530
Final Mean Princpal Stress, σ_m :	272.6 kPa
Max Friction Angle, ϕ:	52.8 deg
b-value at failure:	0.70
Stress direction at failure, α:	0.0 deg

Shear Band Notes	
Point of Observation:	24
Inclination (from Vertical):	
64°, 65°	
Failure Notes:	

Point (No.)	ε_z (%)	ε_x (%)	ε_y (%)	ε_v (%)	$\gamma_{\theta z}$ (%)	σ_z (kPa)	σ_x (kPa)	σ_y (kPa)	$\tau_{\theta z}$ (kPa)	b	α (°)	φ (°)
1	0.000	0.000	0.000	0.000	0.000	51.632	51.632	50.000	0.000	1.000	0.000	0.920
2	0.007	0.000	0.006	0.013	0.000	59.275	59.276	50.000	0.000	1.000	0.000	4.869
3	0.033	0.000	0.006	0.039	0.000	73.106	73.114	50.000	0.000	1.000	0.000	10.818
4	0.065	0.721	-0.716	0.069	0.000	86.939	86.696	50.000	0.000	0.993	0.000	15.649
5	0.101	0.541	-0.551	0.091	0.000	102.945	102.677	50.000	0.000	0.995	0.000	20.253
6	0.206	0.811	-0.913	0.104	0.000	141.806	143.401	50.000	0.000	1.017	0.000	28.597
7	0.316	1.081	-1.332	0.065	0.000	188.153	191.245	50.000	0.000	1.022	0.000	35.458
8	0.402	1.284	-1.677	0.009	0.000	224.954	229.345	50.000	0.000	1.025	0.000	39.517
9	0.511	1.555	-2.152	-0.087	0.000	260.450	265.706	50.000	0.000	1.025	0.000	42.679
10	0.622	1.791	-2.649	-0.237	0.000	289.179	295.181	50.000	0.000	1.025	0.000	44.843
11	0.702	1.926	-2.953	-0.326	0.000	305.744	311.731	50.000	0.000	1.023	0.000	45.964
12	0.804	2.095	-3.412	-0.512	0.000	312.241	320.002	50.000	0.000	1.030	0.000	46.381
13	0.905	2.265	-3.738	-0.569	0.000	347.405	327.115	50.000	0.000	0.932	0.000	48.449
14	1.002	2.311	-3.916	-0.604	0.000	374.276	327.244	50.000	0.000	0.855	0.000	49.845
15	1.138	2.365	-4.171	-0.669	0.000	397.287	326.822	50.000	0.000	0.797	0.000	50.935
16	1.223	2.410	-4.345	-0.712	0.000	408.298	326.720	50.000	0.000	0.772	0.000	51.426
17	1.328	2.458	-4.555	-0.769	0.000	420.245	323.024	50.000	0.000	0.737	0.000	51.938
18	1.404	2.458	-4.665	-0.803	0.000	428.410	323.674	50.000	0.000	0.723	0.000	52.277
19	1.501	2.458	-4.814	-0.855	0.000	435.005	324.942	50.000	0.000	0.714	0.000	52.544
20	1.614	2.505	-5.035	-0.916	0.000	441.831	325.998	50.000	0.000	0.704	0.000	52.814
21	1.726	2.505	-5.234	-1.003	0.000	438.252	322.984	50.000	0.000	0.703	0.000	52.673
22	1.830	2.505	-5.403	-1.068	0.000	428.434	320.325	50.000	0.000	0.714	0.000	52.278
23	1.918	2.505	-5.547	-1.125	0.000	409.524	304.627	50.000	0.000	0.708	0.000	51.479
24	2.075	2.552	-5.808	-1.181	0.000	369.264	273.393	50.000	0.000	0.700	0.000	49.595
25	2.156	2.552	-5.910	-1.203	0.000	352.382	262.987	50.000	0.000	0.704	0.000	48.719
26	2.268	2.552	-6.049	-1.229	0.000	336.138	252.581	50.000	0.000	0.708	0.000	47.819
27	2.368	2.552	-6.158	-1.237	0.000	329.865	247.394	50.000	0.000	0.705	0.000	47.455
28	2.469	2.552	-6.267	-1.246	0.000	325.711	242.208	50.000	0.000	0.697	0.000	47.209
29	2.586	2.552	-6.389	-1.250	0.000	323.289	242.220	50.000	0.000	0.703	0.000	47.064
30	2.725	2.552	-6.531	-1.255	0.000	322.572	242.235	50.000	0.000	0.705	0.000	47.020
31	2.870	2.552	-6.685	-1.263	0.000	322.179	242.245	50.000	0.000	0.706	0.000	46.997

True Triaxial Test on Fine Nevada Sand with a Target Void Ratio = 0.530 (D_r = 91.28%)

Test No.:	6	
Test Date:	3/28/11	
Sector:	I	
Initial Void Ratio, e:	0.530	
Final Mean Princpal Stress, σ_m :	267.8	kPa
Max Friction Angle, ϕ:	52.3	deg
b-value at failure:	0.72	
Stress direction at failure, α:	0.0	deg

Shear Band Notes	
Point of Observation:	22
Inclination (from Vertical):	
62°	
Failure Notes:	

Point (No.)	ε_z (%)	ε_x (%)	ε_y (%)	ε_v (%)	$\gamma_{\theta z}$ (%)	σ_z (kPa)	σ_x (kPa)	σ_y (kPa)	$\tau_{\theta z}$ (kPa)	b	α (°)	φ (°)
1	0.000	0.000	0.000	0.000	0.000	51.631	51.631	50.000	0.000	1.000	0.000	0.920
2	0.005	0.000	-0.003	0.002	1.000	54.178	54.178	50.000	0.000	1.000	0.000	2.298
3	0.016	0.856	-0.007	0.865	3.000	65.820	65.822	50.000	0.000	1.000	0.000	7.851
4	0.029	4.174	-0.003	4.200	6.000	75.280	75.288	50.000	0.000	1.000	0.000	11.642
5	0.044	4.709	-0.348	4.405	9.000	87.288	87.175	50.000	0.000	0.997	0.000	15.760
6	0.063	5.030	-0.888	4.205	12.000	100.023	99.613	50.000	0.000	0.992	0.000	19.477
7	0.079	5.244	-1.187	4.136	14.000	108.756	108.111	50.000	0.000	0.989	0.000	21.722
8	0.106	0.200	0.076	0.382	0.000	121.482	121.211	50.000	0.000	1.000	0.000	24.636
9	0.218	0.426	-0.560	0.085	0.000	165.056	164.954	50.000	0.000	1.000	0.000	32.344
10	0.309	0.748	-0.986	0.071	0.000	195.113	195.367	50.000	0.000	1.000	0.000	36.301
11	0.405	0.962	-1.319	0.048	0.000	229.805	228.965	50.000	0.000	1.000	0.000	39.987
12	0.517	1.283	-1.806	-0.007	0.000	259.990	259.628	50.000	0.000	1.000	0.000	42.641
13	0.615	1.497	-2.203	-0.091	0.000	288.232	288.105	50.000	0.000	1.000	0.000	44.777
14	0.706	1.711	-2.560	-0.143	0.000	298.429	297.328	50.000	0.000	1.000	0.000	45.479
15	0.817	1.925	-3.011	-0.269	0.000	314.859	315.942	50.000	0.000	1.000	0.000	46.546
16	0.901	2.139	-3.417	-0.378	0.000	329.917	326.106	50.000	0.000	0.999	0.000	47.458
17	1.017	2.353	-3.839	-0.469	0.000	367.845	325.009	50.000	0.000	0.997	0.000	49.524
18	1.101	2.460	-4.078	-0.517	0.000	391.889	325.255	50.000	0.000	0.995	0.000	50.687
19	1.215	2.550	-4.248	-0.483	0.000	415.370	323.402	50.000	0.000	0.993	0.000	51.732
20	1.307	2.567	-4.499	-0.625	0.000	429.566	323.781	50.000	0.000	0.992	0.000	52.324
21	1.455	2.674	-4.898	-0.768	0.000	415.344	324.226	50.000	0.000	0.990	0.000	51.730
22	1.675	2.674	-5.278	-0.929	0.000	339.025	260.409	50.000	0.000	0.989	0.000	47.983
23	1.841	2.674	-5.491	-0.977	0.000	306.144	234.843	50.000	0.000	1.003	0.000	45.990

True Triaxial Test on Fine Nevada Sand with a Target Void Ratio = 0.530 (D_r = 91.28%)

Test No.:	7	
Test Date:	3/30/11	
Sector:	I	
Initial Void Ratio, e:	0.530	
Final Mean Princpal Stress, σ_m :	170.0	kPa
Max Friction Angle, ϕ:	50.6	deg
b-value at failure:	1.00	
Stress direction at failure, α:	0.0	deg

Shear Band Notes	29
Point of Observation:	
Inclination (from Vertical):	
90	
Failure Notes:	
failed in vertical direction	

Point (No.)	ε_z (%)	ε_x (%)	ε_y (%)	ε_v (%)	$\gamma_{\theta z}$ (%)	σ_z (kPa)	σ_x (kPa)	σ_y (kPa)	$\tau_{\theta z}$ (kPa)	b	α (°)	φ (°)
1	0.000	0.000	0.000	0.000	0.000	72.723	72.440	30.000	0.000	1.000	0.000	1.517
2	0.001	0.000	-0.001	0.000	1.000	33.086	33.086	30.000	0.000	1.000	0.000	2.804
3	0.002	0.000	0.003	0.004	2.000	34.906	34.906	30.000	0.000	1.000	0.000	4.335
4	0.007	0.000	0.002	0.009	3.000	37.816	37.817	30.000	0.000	1.000	0.000	6.618
5	0.012	0.000	-0.003	0.009	4.000	40.726	40.728	30.000	0.000	1.000	0.000	8.723
6	0.018	0.000	-0.007	0.011	5.000	43.272	43.275	30.000	0.000	1.000	0.000	10.436
7	0.026	0.000	-0.009	0.017	6.000	46.183	46.187	30.000	0.000	1.000	0.000	12.264
8	0.035	0.000	-0.009	0.026	7.000	49.820	49.827	30.000	0.000	1.000	0.000	14.378
9	0.049	0.000	-0.017	0.033	8.000	54.911	54.924	30.000	0.000	1.000	0.000	17.061
10	0.062	0.247	-0.268	0.041	9.000	58.548	58.495	30.000	0.000	0.998	0.000	18.808
11	0.073	0.448	-0.475	0.046	10.000	61.456	61.339	30.000	0.000	0.996	0.000	20.118
12	0.081	0.548	-0.577	0.052	11.000	64.002	63.844	30.000	0.000	0.995	0.000	21.206
13	0.090	0.648	-0.684	0.054	12.000	66.183	65.981	30.000	0.000	0.994	0.000	22.098
14	0.097	0.702	-0.742	0.056	13.000	68.000	67.770	30.000	0.000	0.994	0.000	22.815
15	0.114	0.777	-0.830	0.061	1.000	99.204	99.520	30.000	0.000	0.993	0.000	24.576
16	0.221	1.110	-1.266	0.065	2.000	116.180	117.121	30.000	0.000	1.005	0.000	32.386
17	0.312	1.150	-1.611	-0.149	3.000	142.846	143.812	30.000	0.000	1.011	0.000	36.125
18	0.435	1.609	-2.066	-0.022	4.000	153.934	155.446	30.000	0.000	1.009	0.000	40.758
19	0.504	1.771	-2.353	-0.078	5.000	167.426	168.811	30.000	0.000	1.012	0.000	42.361
20	0.607	2.125	-2.916	-0.184	6.000	187.397	189.381	30.000	0.000	1.010	0.000	44.114
21	0.701	2.332	-3.302	-0.269	7.000	196.377	198.841	30.000	0.000	1.013	0.000	46.386
22	0.803	2.787	-4.032	-0.443	8.000	217.168	218.971	30.000	0.000	1.015	0.000	47.303
23	0.924	3.041	-4.546	-0.582	9.000	222.145	223.330	30.000	0.000	1.010	0.000	49.222
24	1.024	3.348	-5.101	-0.729	10.000	226.399	231.608	30.000	0.000	1.006	0.000	49.644
25	1.105	3.595	-5.586	-0.885	11.000	228.045	230.613	30.000	0.000	1.027	0.000	49.995
26	1.215	3.936	-6.227	-1.076	12.000	234.420	236.540	30.000	0.000	1.013	0.000	50.128
27	1.325	4.076	-6.590	-1.189	13.000	230.536	234.786	30.000	0.000	1.010	0.000	50.632
28	1.507	4.576	-7.702	-1.619	14.000	206.690	208.343	30.000	0.000	1.021	0.000	50.327
29	1.613	5.010	-8.490	-1.866	0.000	165.056	164.954	50.000	0.000	1.009	0.000	48.288

True Triaxial Test on Fine Nevada Sand with a Target Void Ratio = 0.530 (D_r = 91.28%)

Test No.:	8	
Test Date:	3/12/11	
Sector:	II	
Initial Void Ratio, e:	0.527	
Final Mean Princpal Stress, σ_m :	158.3	kPa
Max Friction Angle, ϕ:	46.3	deg
b-value at failure:	0.25	
Stress direction at failure, α:	90.0	deg

Shear Band Notes	
Point of Observation:	25
Inclination (from Vertical):	
65°, 64°	
Failure Notes:	

Point (No.)	ε_z (%)	ε_x (%)	ε_y (%)	ε_v (%)	$\gamma_{\theta z}$ (%)	σ_z (kPa)	σ_x (kPa)	σ_y (kPa)	$\tau_{\theta z}$ (kPa)	b	α (°)	φ (°)
1	0.000	0.000	0.000	0.000	0.000	51.616	50.404	50.000	0.000	0.250	90.000	0.911
2	0.009	0.000	-0.008	0.001	1.000	59.907	52.477	50.000	0.000	0.250	90.000	5.172
3	0.023	0.000	-0.017	0.006	2.000	71.440	55.361	50.000	0.000	0.250	90.000	10.169
4	0.046	0.000	-0.033	0.013	3.000	85.491	58.877	50.000	0.000	0.250	90.000	15.185
5	0.069	0.000	-0.051	0.018	4.000	96.654	61.672	50.000	0.000	0.250	90.000	18.550
6	0.100	0.076	-0.151	0.025	0.000	109.611	64.906	50.000	0.000	0.250	90.000	21.930
7	0.210	0.132	-0.313	0.029	0.000	146.612	76.187	50.000	0.000	0.271	90.000	29.432
8	0.304	0.157	-0.442	0.019	0.000	172.036	80.554	50.000	0.000	0.250	90.000	33.341
9	0.411	0.198	-0.609	0.000	0.000	193.425	85.933	50.000	0.000	0.251	90.000	36.100
10	0.500	0.239	-0.760	-0.022	0.000	209.406	89.956	50.000	0.000	0.251	90.000	37.916
11	0.608	0.284	-0.946	-0.054	0.000	225.300	93.968	50.000	0.000	0.251	90.000	39.551
12	0.721	0.385	-1.205	-0.099	0.000	237.188	96.955	50.000	0.000	0.251	90.000	40.677
13	0.809	0.432	-1.370	-0.129	0.000	246.971	99.430	50.000	0.000	0.251	90.000	41.550
14	0.908	0.432	-1.512	-0.172	0.000	256.682	101.919	50.000	0.000	0.251	90.000	42.371
15	1.002	0.478	-1.691	-0.211	0.000	264.252	103.846	50.000	0.000	0.251	90.000	42.983
16	1.116	0.478	-1.857	-0.262	0.000	271.725	105.789	50.000	0.000	0.252	90.000	43.565
17	1.216	0.478	-2.004	-0.310	0.000	277.088	107.196	50.000	0.000	0.252	90.000	43.969
18	1.517	0.525	-2.513	-0.471	0.000	289.500	110.478	50.000	0.000	0.253	90.000	44.866
19	1.737	0.525	-2.847	-0.585	0.000	298.236	111.830	50.000	0.000	0.249	90.000	45.466
20	2.110	0.478	-3.352	-0.763	0.000	310.576	114.406	50.000	0.000	0.247	90.000	46.275
21	2.226	0.478	-3.591	-0.886	0.000	305.780	115.088	50.000	0.000	0.254	90.000	45.966
22	2.331	0.478	-3.773	-0.963	0.000	289.623	109.012	50.000	0.000	0.246	90.000	44.874
23	2.421	0.478	-3.936	-1.036	0.000	262.760	102.380	50.000	0.000	0.246	90.000	42.864
24	2.536	0.478	-4.103	-1.088	0.000	235.279	95.767	50.000	0.000	0.247	90.000	40.501
25	2.632	0.432	-4.180	-1.116	0.000	225.325	93.141	50.000	0.000	0.246	90.000	39.553
26	2.717	0.432	-4.280	-1.131	0.000	218.906	90.500	50.000	0.000	0.240	90.000	38.912
27	2.810	0.432	-4.390	-1.148	0.000	214.566	90.496	50.000	0.000	0.246	90.000	38.464
28	2.935	0.385	-4.479	-1.159	0.000	210.885	89.986	50.000	0.000	0.249	90.000	38.075
29	3.006	0.385	-4.562	-1.170	0.000	210.413	88.929	50.000	0.000	0.243	90.000	38.024
30	3.106	0.385	-4.674	-1.183	0.000	208.857	88.927	50.000	0.000	0.245	90.000	37.857
31	3.211	0.385	-4.787	-1.191	0.000	208.686	88.927	50.000	0.000	0.245	90.000	37.838

True Triaxial Test on Fine Nevada Sand with a Target Void Ratio = 0.530 (D_r = 91.28%)

Test No.:	9	
Test Date:	3/13/11	
Sector:	II	
Initial Void Ratio, e:	0.528	
Final Mean Princpal Stress, σ_m :	203.0	kPa
Max Friction Angle, ϕ:	49.1	deg
b-value at failure:	0.49	
Stress direction at failure, α:	90.0	deg

Shear Band Notes	
Point of Observation:	27
Inclination (from Vertical):	
60°	
Failure Notes:	

Point (No.)	ε_z (%)	ε_x (%)	ε_y (%)	ε_v (%)	$\gamma_{\theta z}$ (%)	σ_z (kPa)	σ_x (kPa)	σ_y (kPa)	$\tau_{\theta z}$ (kPa)	b	α (°)	φ (°)
1	0.000	0.000	0.000	0.000	0.000	51.617	50.808	50.000	0.000	0.500	90.000	0.912
2	0.005	0.000	0.003	0.009	0.000	60.633	55.317	50.000	0.000	0.500	90.000	5.515
3	0.021	0.000	0.005	0.026	0.000	73.617	61.811	50.000	0.000	0.500	90.000	11.014
4	0.039	0.499	-0.495	0.043	0.000	85.880	67.858	50.000	0.000	0.498	90.000	15.311
5	0.079	0.951	-0.962	0.068	0.000	104.270	76.898	50.000	0.000	0.496	90.000	20.596
6	0.111	0.125	-0.159	0.077	0.000	116.511	83.151	50.000	0.000	0.498	90.000	23.543
7	0.211	0.275	-0.387	0.099	0.000	143.480	96.569	50.000	0.000	0.498	90.000	28.891
8	0.302	0.375	-0.565	0.112	0.000	165.727	107.647	50.000	0.000	0.498	90.000	32.442
9	0.412	0.500	-0.800	0.112	0.000	187.180	118.322	50.000	0.000	0.498	90.000	35.337
10	0.519	0.575	-0.991	0.103	0.000	207.498	128.468	50.000	0.000	0.498	90.000	37.709
11	0.617	0.675	-1.196	0.097	0.000	225.281	137.325	50.000	0.000	0.498	90.000	39.549
12	0.703	0.775	-1.392	0.086	0.000	240.177	144.732	50.000	0.000	0.498	90.000	40.949
13	0.816	0.875	-1.631	0.060	0.000	260.330	154.784	50.000	0.000	0.498	90.000	42.669
14	0.951	0.975	-1.909	0.017	0.000	288.205	168.713	50.000	0.000	0.498	90.000	44.775
15	1.033	1.025	-2.071	-0.013	0.000	304.015	174.646	50.000	0.000	0.491	90.000	45.851
16	1.110	1.100	-2.257	-0.047	0.000	316.942	179.793	50.000	0.000	0.486	90.000	46.675
17	1.211	1.150	-2.447	-0.086	0.000	330.475	187.593	50.000	0.000	0.491	90.000	47.491
18	1.316	1.203	-2.653	-0.133	0.000	343.225	192.731	50.000	0.000	0.487	90.000	48.219
19	1.421	1.250	-2.854	-0.183	0.000	355.930	200.498	50.000	0.000	0.492	90.000	48.908
20	1.505	1.350	-3.087	-0.232	0.000	358.741	200.286	50.000	0.000	0.487	90.000	49.056
21	1.644	1.350	-3.308	-0.314	0.000	358.791	200.178	50.000	0.000	0.486	90.000	49.058
22	1.755	1.350	-3.479	-0.374	0.000	354.499	197.498	50.000	0.000	0.484	90.000	48.832
23	1.846	1.350	-3.615	-0.419	0.000	348.985	194.835	50.000	0.000	0.484	90.000	48.535
24	1.901	1.350	-3.694	-0.443	0.000	344.573	192.185	50.000	0.000	0.483	90.000	48.293
25	2.000	1.350	-3.832	-0.482	0.000	336.843	190.571	50.000	0.000	0.490	90.000	47.859
26	2.105	1.350	-3.971	-0.516	0.000	327.306	184.235	50.000	0.000	0.484	90.000	47.304
27	2.211	1.350	-4.107	-0.546	0.000	316.736	178.957	50.000	0.000	0.483	90.000	46.663
28	2.417	1.350	-4.354	-0.587	0.000	307.961	176.308	50.000	0.000	0.490	90.000	46.107
29	2.494	1.350	-4.444	-0.600	0.000	305.625	173.673	50.000	0.000	0.484	90.000	45.956
30	2.895	1.350	-4.903	-0.658	0.000	299.993	171.036	50.000	0.000	0.484	90.000	45.584
31	3.229	1.350	-5.280	-0.701	0.000	298.730	171.028	50.000	0.000	0.487	90.000	45.500
32	3.684	1.350	-5.757	-0.723	0.000	297.644	168.378	50.000	0.000	0.478	90.000	45.426

True Triaxial Test on Fine Nevada Sand with a Target Void Ratio = 0.530 (D_r = 91.28%)

Test No.:	10	
Test Date:	3/15/11	
Sector:	II	
Initial Void Ratio, e:	0.528	
Final Mean Princpal Stress, σ_m :	265.3	kPa
Max Friction Angle, ϕ:	52.4	deg
b-value at failure:	0.70	
Stress direction at failure, α:	90.0	deg

Shear Band Notes

Point of Observation: 27

Inclination (from Vertical):
62°

Failure Notes:

Point (No.)	ε_z (%)	ε_x (%)	ε_y (%)	ε_v (%)	$\gamma_{\theta z}$ (%)	σ_z (kPa)	σ_x (kPa)	σ_y (kPa)	$\tau_{\theta z}$ (kPa)	b	α (°)	φ (°)
1	0.000	0.000	0.000	0.000	0.000	51.617	51.213	50.000	0.000	0.750	90.000	0.912
2	0.056	0.000	-0.047	0.009	0.000	76.492	69.880	50.000	0.000	0.750	90.000	12.089
3	0.061	0.000	-0.048	0.013	0.000	80.097	72.586	50.000	0.000	0.750	90.000	13.376
4	0.066	0.000	-0.040	0.026	0.000	85.507	76.648	50.000	0.000	0.750	90.000	15.191
5	0.070	0.485	-0.521	0.034	0.000	89.115	79.214	50.000	0.000	0.747	90.000	16.330
6	0.073	0.685	-0.721	0.037	0.000	92.361	81.576	50.000	0.000	0.745	90.000	17.311
7	0.077	0.785	-0.819	0.043	0.000	95.968	84.232	50.000	0.000	0.745	90.000	18.356
8	0.081	0.885	-0.920	0.045	0.000	99.214	86.613	50.000	0.000	0.744	90.000	19.258
9	0.086	0.984	-1.021	0.049	0.000	103.902	90.063	50.000	0.000	0.743	90.000	20.502
10	0.106	0.209	-0.255	0.060	0.000	115.789	99.291	50.000	0.000	0.749	90.000	23.380
11	0.201	0.419	-0.542	0.077	0.000	157.167	130.200	50.000	0.000	0.748	90.000	31.151
12	0.303	0.609	-0.833	0.080	0.000	193.053	156.961	50.000	0.000	0.748	90.000	36.055
13	0.405	0.780	-1.121	0.065	0.000	224.526	180.402	50.000	0.000	0.747	90.000	39.475
14	0.519	0.914	-1.384	0.049	0.000	243.338	194.429	50.000	0.000	0.747	90.000	41.231
15	0.612	1.142	-1.764	-0.011	0.000	277.478	217.981	50.000	0.000	0.738	90.000	43.998
16	0.707	1.277	-2.036	-0.052	0.000	300.814	234.861	50.000	0.000	0.737	90.000	45.639
17	0.813	1.423	-2.353	-0.116	0.000	322.573	248.981	50.000	0.000	0.730	90.000	47.020
18	0.923	1.569	-2.699	-0.207	0.000	340.612	261.677	50.000	0.000	0.728	90.000	48.073
19	1.022	1.716	-3.030	-0.293	0.000	361.834	276.949	50.000	0.000	0.728	90.000	49.217
20	1.113	1.862	-3.343	-0.368	0.000	377.358	289.562	50.000	0.000	0.732	90.000	49.996
21	1.219	1.955	-3.648	-0.473	0.000	389.128	298.522	50.000	0.000	0.733	90.000	50.559
22	1.316	2.055	-3.921	-0.551	0.000	406.297	308.285	50.000	0.000	0.725	90.000	51.338
23	1.416	2.254	-4.316	-0.645	0.000	418.764	316.676	50.000	0.000	0.723	90.000	51.876
24	1.504	2.301	-4.528	-0.723	0.000	428.785	315.853	50.000	0.000	0.702	90.000	52.292
25	1.626	2.394	-4.846	-0.826	0.000	430.464	315.530	50.000	0.000	0.698	90.000	52.360
26	1.719	2.440	-5.054	-0.895	0.000	428.130	315.825	50.000	0.000	0.703	90.000	52.265
27	1.812	2.487	-5.262	-0.964	0.000	408.588	310.165	50.000	0.000	0.726	90.000	51.438
28	1.919	2.533	-5.473	-1.020	0.000	365.239	278.430	50.000	0.000	0.725	90.000	49.392
29	2.013	2.533	-5.581	-1.035	0.000	346.690	263.361	50.000	0.000	0.719	90.000	48.410
30	2.113	2.533	-5.690	-1.043	0.000	332.378	253.015	50.000	0.000	0.719	90.000	47.602

True Triaxial Test on Fine Nevada Sand with a Target Void Ratio = 0.530 (D_r = 91.28%)

Test No.:	11
Test Date:	3/17/11
Sector:	II
Initial Void Ratio, e:	0.534
Final Mean Princpal Stress, σ_m :	265.6 kPa
Max Friction Angle, ϕ:	52.4 deg
b-value at failure:	0.69
Stress direction at failure, α:	90.0 deg

Shear Band Notes	
Point of Observation:	23
Inclination (from Vertical):	
62°	
Failure Notes:	

Point (No.)	ε_z (%)	ε_x (%)	ε_y (%)	ε_v (%)	$\gamma_{\theta z}$ (%)	σ_z (kPa)	σ_x (kPa)	σ_y (kPa)	$\tau_{\theta z}$ (kPa)	b	α (°)	φ (°)
1	0.000	0.000	0.000	0.000	0.000	51.611	51.611	50.000	0.000	1.000	90.000	0.908
2	0.010	0.000	-0.006	0.004	1.000	59.516	59.517	50.000	0.000	1.000	90.000	4.985
3	0.019	0.000	-0.004	0.015	2.000	68.858	68.861	50.000	0.000	1.000	90.000	9.129
4	0.035	0.000	-0.001	0.034	3.000	80.357	80.367	50.000	0.000	1.000	90.000	13.466
5	0.064	0.000	-0.004	0.060	4.000	105.867	105.903	50.000	0.000	1.000	90.000	21.004
6	0.085	0.000	-0.016	0.069	5.000	120.231	120.291	50.000	0.000	1.000	90.000	24.366
7	0.104	0.394	-0.429	0.069	0.000	130.995	130.760	50.000	0.000	0.997	90.000	26.583
8	0.209	0.604	-0.756	0.058	0.000	168.936	168.465	50.000	0.000	0.996	90.000	32.905
9	0.309	0.841	-1.111	0.039	0.000	202.848	202.032	50.000	0.000	0.995	90.000	37.193
10	0.402	1.078	-1.492	-0.013	0.000	231.271	230.041	50.000	0.000	0.993	90.000	40.126
11	0.506	1.288	-1.899	-0.105	0.000	261.296	256.093	50.000	0.000	0.975	90.000	42.747
12	0.609	1.498	-2.319	-0.212	0.000	287.617	280.406	50.000	0.000	0.970	90.000	44.733
13	0.702	1.629	-2.657	-0.326	0.000	307.788	299.511	50.000	0.000	0.968	90.000	46.096
14	0.804	1.813	-3.093	-0.476	0.000	321.734	313.074	50.000	0.000	0.968	90.000	46.969
15	0.909	1.997	-3.567	-0.660	0.000	331.973	318.239	50.000	0.000	0.951	90.000	47.578
16	1.008	2.098	-3.899	-0.793	0.000	354.322	315.881	50.000	0.000	0.874	90.000	48.822
17	1.112	2.198	-4.185	-0.874	0.000	380.952	316.314	50.000	0.000	0.805	90.000	50.171
18	1.211	2.251	-4.405	-0.943	0.000	400.503	316.587	50.000	0.000	0.761	90.000	51.080
19	1.314	2.351	-4.698	-1.033	0.000	416.748	314.672	50.000	0.000	0.722	90.000	51.790
20	1.421	2.351	-4.882	-1.110	0.000	431.542	315.165	50.000	0.000	0.695	90.000	52.404
21	1.506	2.503	-5.175	-1.166	0.000	428.621	315.118	50.000	0.000	0.700	90.000	52.285
22	1.628	2.450	-5.339	-1.260	0.000	403.350	296.738	50.000	0.000	0.698	90.000	51.208
23	1.706	2.450	-5.459	-1.303	0.000	384.084	283.769	50.000	0.000	0.700	90.000	50.321
24	1.837	2.450	-5.637	-1.350	0.000	366.783	270.810	50.000	0.000	0.697	90.000	49.470
25	1.918	2.450	-5.740	-1.372	0.000	358.116	265.628	50.000	0.000	0.700	90.000	49.023
26	2.017	2.450	-5.857	-1.389	0.000	353.253	260.460	50.000	0.000	0.694	90.000	48.765
27	2.155	2.450	-6.012	-1.406	0.000	348.640	257.873	50.000	0.000	0.696	90.000	48.517
28	2.244	2.450	-6.111	-1.417	0.000	350.442	260.442	50.000	0.000	0.700	90.000	48.614
29	2.313	2.450	-6.188	-1.425	0.000	351.265	257.862	50.000	0.000	0.690	90.000	48.659
30	2.421	2.450	-6.307	-1.436	0.000	351.274	259.404	50.000	0.000	0.695	90.000	48.659
31	2.504	2.450	-6.399	-1.445	0.000	352.054	259.402	50.000	0.000	0.693	90.000	48.701

True Triaxial Test on Fine Nevada Sand with a Target Void Ratio = 0.530 (D_r = 91.28%)

Test No.:	12	
Test Date:	3/31/11	
Sector:	II	
Initial Void Ratio, e:	0.530	
Final Mean Princpal Stress, σ_m :	158.6	kPa
Max Friction Angle, ϕ:	50.4	deg
b-value at failure:	1.00	
Stress direction at failure, α:	90.0	deg

Shear Band Notes	
Point of Observation:	28
Inclination (from Vertical):	
90°	
Failure Notes:	
vertical failure	

Point (No.)	ε_z (%)	ε_x (%)	ε_y (%)	ε_v (%)	$\gamma_{\theta z}$ (%)	σ_z (kPa)	σ_x (kPa)	σ_y (kPa)	$\tau_{\theta z}$ (kPa)	b	α (°)	φ (°)
1	0.000	0.000	0.000	0.000	0.000	30.631	30.631	29.000	0.000	1.000	90.000	1.567
2	0.004	0.000	0.000	0.004	1.000	32.449	32.449	29.000	0.000	1.000	90.000	3.218
3	0.008	0.000	0.000	0.009	2.000	34.268	34.268	29.000	0.000	1.000	90.000	4.776
4	0.015	0.000	-0.002	0.013	3.000	37.177	37.178	29.000	0.000	1.000	90.000	7.098
5	0.022	0.000	-0.005	0.017	4.000	40.086	40.089	29.000	0.000	1.000	90.000	9.234
6	0.034	0.380	-0.386	0.028	5.000	44.087	44.034	29.000	0.000	0.997	90.000	11.913
7	0.043	0.574	-0.582	0.035	6.000	46.269	46.177	29.000	0.000	0.995	90.000	13.263
8	0.050	0.721	-0.728	0.044	7.000	48.451	48.321	29.000	0.000	0.993	90.000	14.545
9	0.053	0.868	-0.875	0.046	8.000	50.634	50.458	29.000	0.000	0.992	90.000	15.764
10	0.066	0.968	-0.981	0.052	9.000	52.815	52.600	29.000	0.000	0.991	90.000	16.923
11	0.075	1.122	-1.140	0.057	10.000	55.724	55.444	29.000	0.000	0.990	90.000	18.387
12	0.085	1.168	-1.193	0.061	11.000	58.269	57.951	29.000	0.000	0.989	90.000	19.596
13	0.095	1.315	-1.345	0.065	12.000	59.723	59.347	29.000	0.000	0.988	90.000	20.260
14	0.103	0.616	-0.651	0.068	0.000	61.898	61.729	29.000	0.000	0.995	90.000	21.218
15	0.200	0.700	-1.069	-0.169	0.000	84.396	83.981	29.000	0.000	0.993	90.000	29.243
16	0.319	1.232	-1.485	0.065	0.000	110.452	110.273	29.000	0.000	0.998	90.000	35.739
17	0.423	1.421	-1.812	0.033	0.000	127.379	127.628	29.000	0.000	1.003	90.000	38.984
18	0.529	1.563	-2.101	-0.009	0.000	146.421	146.654	29.000	0.000	1.002	90.000	42.018
19	0.615	1.753	-2.437	-0.070	0.000	155.296	155.655	29.000	0.000	1.003	90.000	43.258
20	0.741	1.957	-2.847	-0.148	0.000	171.286	171.715	29.000	0.000	1.003	90.000	45.269
21	0.810	2.058	-3.068	-0.201	0.000	178.693	179.961	29.000	0.000	1.008	90.000	46.116
22	0.904	2.258	-3.436	-0.275	0.000	189.257	190.370	29.000	0.000	1.007	90.000	47.245
23	1.025	2.512	-3.923	-0.386	0.000	201.127	201.628	29.000	0.000	1.003	90.000	48.414
24	1.125	2.712	-4.317	-0.480	0.000	209.790	210.315	29.000	0.000	1.003	90.000	49.210
25	1.205	2.866	-4.638	-0.567	0.000	216.319	219.050	29.000	0.000	1.015	90.000	49.780
26	1.311	3.120	-5.128	-0.698	0.000	223.076	223.572	29.000	0.000	1.003	90.000	50.346
27	1.405	3.467	-5.744	-0.872	0.000	218.365	218.738	29.000	0.000	1.002	90.000	49.954
28	1.534	3.808	-6.433	-1.090	0.000	209.636	208.739	29.000	0.000	0.995	90.000	49.196
29	1.633	4.148	-7.046	-1.265	0.000	203.212	202.757	29.000	0.000	0.997	90.000	48.610
30	1.704	4.342	-7.385	-1.339	0.000	204.431	203.614	29.000	0.000	0.995	90.000	48.723
31	1.852	4.629	-7.981	-1.500	0.000	206.812	208.008	29.000	0.000	1.007	90.000	48.942
32	1.907	4.722	-8.200	-1.570	0.000	207.685	207.748	29.000	0.000	1.000	90.000	49.021
33	2.031	4.909	-8.632	-1.692	0.000	218.238	221.219	29.000	0.000	1.016	90.000	49.943

True Triaxial Test on Fine Nevada Sand with a Target Void Ratio = 0.530 (D_r = 91.28%)

Test No.:	13
Test Date:	2/25/11
Sector:	III
Initial Void Ratio, e:	0.535
Final Mean Princpal Stress, σ_m :	102.2 kPa
Max Friction Angle, ϕ:	37.6 deg
b-value at failure:	0.00
Stress direction at failure, α:	90.0 deg

Shear Band Notes	
Point of Observation:	25
Inclination (from Vertical):	
63°	
Failure Notes:	

Point (No.)	ε_z (%)	ε_x (%)	ε_y (%)	ε_v (%)	$\gamma_{\theta z}$ (%)	σ_z (kPa)	σ_x (kPa)	σ_y (kPa)	$\tau_{\theta z}$ (kPa)	b	α (°)	φ (°)
1	0.000	0.000	0.000	0.000	0.000	52.164	50.000	50.000	0.000	0.000	90.000	1.213
2	0.017	-0.006	-0.006	0.004	0.000	59.669	50.000	50.000	0.000	0.000	90.000	5.058
3	0.031	-0.011	-0.011	0.009	0.000	70.658	50.000	50.000	0.000	0.000	90.000	9.858
4	0.072	-0.019	-0.019	0.035	0.000	87.137	50.000	50.000	0.000	0.000	90.000	15.712
5	0.155	-0.049	-0.049	0.057	0.000	106.515	50.000	50.000	0.000	0.000	90.000	21.167
6	0.246	-0.084	-0.084	0.079	0.000	120.010	50.000	50.000	0.000	0.000	90.000	24.318
7	0.541	-0.222	-0.222	0.096	0.000	141.338	50.000	50.000	0.000	0.000	90.000	28.513
8	0.615	-0.260	-0.260	0.096	0.000	144.915	50.000	50.000	0.000	0.000	90.000	29.141
9	0.876	-0.399	-0.399	0.079	0.000	155.554	50.000	50.000	0.000	0.000	90.000	30.898
10	1.077	-0.510	-0.510	0.057	0.000	161.845	50.000	50.000	0.000	0.000	90.000	31.867
11	1.215	-0.590	-0.590	0.035	0.000	165.647	50.000	50.000	0.000	0.000	90.000	32.431
12	1.421	-0.711	-0.711	0.000	0.000	171.145	50.000	50.000	0.000	0.000	90.000	33.217
13	1.846	-0.967	-0.967	-0.087	0.000	177.703	50.000	50.000	0.000	0.000	90.000	34.113
14	2.221	-1.200	-1.200	-0.179	0.000	184.610	50.000	50.000	0.000	0.000	90.000	35.013
15	2.647	-1.470	-1.470	-0.293	0.000	190.629	50.000	50.000	0.000	0.000	90.000	35.762
16	2.942	-1.670	-1.670	-0.398	0.000	192.537	50.000	50.000	0.000	0.000	90.000	35.993
17	3.307	-1.909	-1.909	-0.511	0.000	197.127	50.000	50.000	0.000	0.000	90.000	36.538
18	3.736	-2.194	-2.194	-0.651	0.000	199.425	50.000	50.000	0.000	0.000	90.000	36.804
19	4.018	-2.385	-2.385	-0.752	0.000	201.979	50.000	50.000	0.000	0.000	90.000	37.095
20	4.402	-2.645	-2.645	-0.887	0.000	204.640	50.000	50.000	0.000	0.000	90.000	37.394
21	5.038	-3.077	-3.077	-1.115	0.000	205.674	50.000	50.000	0.000	0.000	90.000	37.508
22	5.286	-3.242	-3.242	-1.198	0.000	206.513	50.000	50.000	0.000	0.000	90.000	37.601
23	5.856	-3.629	-3.629	-1.403	0.000	205.256	50.000	50.000	0.000	0.000	90.000	37.462
24	6.362	-3.961	-3.961	-1.561	0.000	194.047	50.000	50.000	0.000	0.000	90.000	36.174
25	6.685	-4.155	-4.155	-1.626	0.000	187.065	50.000	50.000	0.000	0.000	90.000	35.322
26	6.886	-4.271	-4.271	-1.657	0.000	183.708	50.000	50.000	0.000	0.000	90.000	34.898
27	7.104	-4.391	-4.391	-1.679	0.000	181.023	50.000	50.000	0.000	0.000	90.000	34.551
28	7.803	-4.767	-4.767	-1.731	0.000	175.653	50.000	50.000	0.000	0.000	90.000	33.838
29	8.442	-5.097	-5.097	-1.753	0.000	170.470	50.000	50.000	0.000	0.000	90.000	33.122
30	8.839	-5.301	-5.301	-1.764	0.000	170.262	50.000	50.000	0.000	0.000	90.000	33.093
31	9.088	-5.428	-5.428	-1.768	0.000	169.601	50.000	50.000	0.000	0.000	90.000	32.999

True Triaxial Test on Fine Nevada Sand with a Target Void Ratio = 0.530 (D_r = 91.28%)

Test No.:	14	
Test Date:	3/5/11	
Sector:	III	
Initial Void Ratio, e:	0.530	
Final Mean Princpal Stress, σ_m :	151.6	kPa
Max Friction Angle, ϕ:	45.1	deg
b-value at failure:	0.25	
Stress direction at failure, α:	90.0	deg

Shear Band Notes	
Point of Observation:	23
Inclination (from Vertical):	
59°, 60°	
Failure Notes:	

Point (No.)	ε_z (%)	ε_x (%)	ε_y (%)	ε_v (%)	$\gamma_{\theta z}$ (%)	σ_z (kPa)	σ_x (kPa)	σ_y (kPa)	$\tau_{\theta z}$ (kPa)	b	α (°)	φ (°)
1	0.000	0.000	0.000	0.000	0.000	51.606	50.000	50.000	0.000	0.000	90.000	0.905
2	0.005	0.000	-0.003	0.002	0.000	53.789	50.486	50.000	0.000	0.128	90.000	2.092
3	0.016	0.000	-0.008	0.009	0.000	67.977	54.053	50.000	0.000	0.225	90.000	8.765
4	0.028	0.000	-0.015	0.013	0.000	76.343	56.160	50.000	0.000	0.234	90.000	12.035
5	0.038	0.000	-0.018	0.020	0.000	83.618	57.998	50.000	0.000	0.238	90.000	14.572
6	0.067	0.000	-0.032	0.035	0.000	108.347	64.161	50.000	0.000	0.243	90.000	21.622
7	0.108	0.047	-0.107	0.048	0.000	126.155	68.650	50.000	0.000	0.245	90.000	25.615
8	0.168	0.084	-0.186	0.065	0.000	154.467	75.715	50.000	0.000	0.246	90.000	30.725
9	0.311	0.134	-0.376	0.069	0.000	183.360	82.992	50.000	0.000	0.247	90.000	34.853
10	0.461	0.184	-0.585	0.060	0.000	203.443	88.046	50.000	0.000	0.248	90.000	37.260
11	0.603	0.228	-0.787	0.044	0.000	218.762	91.961	50.000	0.000	0.249	90.000	38.897
12	0.758	0.267	-1.004	0.022	0.000	231.469	95.171	50.000	0.000	0.249	90.000	40.145
13	0.902	0.301	-1.209	-0.007	0.000	243.060	98.162	50.000	0.000	0.249	90.000	41.206
14	1.061	0.334	-1.437	-0.041	0.000	253.850	100.931	50.000	0.000	0.250	90.000	42.136
15	1.210	0.373	-1.664	-0.081	0.000	262.454	103.099	50.000	0.000	0.250	90.000	42.840
16	1.351	0.407	-1.876	-0.118	0.000	269.255	104.946	50.000	0.000	0.251	90.000	43.375
17	1.524	0.488	-2.184	-0.172	0.000	275.213	106.488	50.000	0.000	0.251	90.000	43.829
18	1.655	0.488	-2.356	-0.214	0.000	280.907	108.024	50.000	0.000	0.251	90.000	44.251
19	1.831	0.541	-2.647	-0.275	0.000	289.998	110.377	50.000	0.000	0.252	90.000	44.901
20	1.964	0.440	-2.726	-0.323	0.000	292.779	111.156	50.000	0.000	0.252	90.000	45.094
21	2.116	0.440	-2.938	-0.382	0.000	293.345	111.393	50.000	0.000	0.252	90.000	45.133
22	2.270	0.440	-3.156	-0.445	0.000	284.330	109.219	50.000	0.000	0.253	90.000	44.499
23	2.452	0.440	-3.399	-0.506	0.000	275.297	107.050	50.000	0.000	0.253	90.000	43.835
24	2.569	0.440	-3.543	-0.535	0.000	263.334	104.042	50.000	0.000	0.253	90.000	42.910
25	2.725	0.440	-3.724	-0.559	0.000	255.917	102.215	50.000	0.000	0.254	90.000	42.308
26	2.927	0.440	-3.947	-0.580	0.000	252.662	101.516	50.000	0.000	0.254	90.000	42.036
27	3.045	0.440	-4.076	-0.591	0.000	252.412	101.515	50.000	0.000	0.255	90.000	42.015
28	3.211	0.440	-4.256	-0.604	0.000	252.063	101.515	50.000	0.000	0.255	90.000	41.986
29	3.317	0.440	-4.370	-0.613	0.000	252.543	101.675	50.000	0.000	0.255	90.000	42.026
30	3.602	0.440	-4.673	-0.631	0.000	251.608	101.625	50.000	0.000	0.256	90.000	41.947
31	3.780	0.440	-4.859	-0.639	0.000	251.947	101.789	50.000	0.000	0.256	90.000	41.976

True Triaxial Test on Fine Nevada Sand with a Target Void Ratio = 0.530 (D_r = 91.28%)

Test No.:	15	**Shear Band Notes**	
Test Date:	3/8/11	Point of Observation:	25
Sector:	III		
Initial Void Ratio, e:	0.533	Inclination (from Vertical):	
Final Mean Princpal Stress, σ_m :	165.0 kPa	59°, 60°	
Max Friction Angle, ϕ:	44.3 deg		
b-value at failure:	0.49	Failure Notes:	
Stress direction at failure, α:	90.0 deg		

Point (No.)	ε_z (%)	ε_x (%)	ε_y (%)	ε_v (%)	$\gamma_{\theta z}$ (%)	σ_z (kPa)	σ_x (kPa)	σ_y (kPa)	$\tau_{\theta z}$ (kPa)	b	α (°)	φ (°)
1	0.000	0.000	0.000	0.000	0.000	51.602	48.282	50.000	0.000	0.517	90.000	0.903
2	0.009	0.325	0.000	0.333	0.000	63.814	54.349	50.000	0.000	0.315	90.000	6.971
3	0.018	2.124	-0.007	2.135	0.000	69.201	57.946	50.000	0.000	0.414	90.000	9.270
4	0.028	2.529	-0.416	2.141	0.000	74.229	59.359	50.000	0.000	0.386	90.000	11.247
5	0.037	2.489	-0.383	2.143	0.000	79.255	62.038	50.000	0.000	0.411	90.000	13.081
6	0.050	2.596	-0.496	2.150	0.000	84.640	64.698	50.000	0.000	0.424	90.000	14.909
7	0.060	2.603	-0.509	2.154	0.000	88.947	66.836	50.000	0.000	0.432	90.000	16.278
8	0.071	2.656	-0.569	2.159	0.000	92.894	68.804	50.000	0.000	0.438	90.000	17.468
9	0.101	0.249	-0.305	0.045	0.000	102.219	73.520	50.000	0.000	0.450	90.000	20.063
10	0.205	0.454	-0.588	0.071	0.000	126.572	85.672	50.000	0.000	0.466	90.000	25.700
11	0.305	0.635	-0.861	0.080	0.000	146.216	95.436	50.000	0.000	0.472	90.000	29.364
12	0.403	0.794	-1.113	0.084	0.000	161.885	103.203	50.000	0.000	0.476	90.000	31.873
13	0.520	0.930	-1.370	0.080	0.000	177.134	110.797	50.000	0.000	0.478	90.000	34.037
14	0.601	1.043	-1.570	0.073	0.000	187.392	115.884	50.000	0.000	0.480	90.000	35.363
15	0.710	1.134	-1.783	0.060	0.000	200.080	122.246	50.000	0.000	0.481	90.000	36.879
16	0.837	1.247	-2.058	0.026	0.000	212.321	128.298	50.000	0.000	0.482	90.000	38.228
17	0.925	1.293	-2.211	0.006	0.000	222.477	133.392	50.000	0.000	0.483	90.000	39.272
18	1.052	1.361	-2.439	-0.026	0.000	234.654	139.511	50.000	0.000	0.485	90.000	40.443
19	1.137	1.406	-2.595	-0.052	0.000	242.981	143.739	50.000	0.000	0.486	90.000	41.199
20	1.357	1.474	-2.954	-0.123	0.000	261.916	153.347	50.000	0.000	0.488	90.000	42.797
21	1.445	1.497	-3.097	-0.155	0.000	267.684	156.255	50.000	0.000	0.488	90.000	43.253
22	1.935	1.613	-3.883	-0.336	0.000	281.402	163.565	50.000	0.000	0.491	90.000	44.287
23	1.973	1.610	-3.962	-0.379	0.000	280.173	162.936	50.000	0.000	0.491	90.000	44.197
24	2.127	1.610	-4.185	-0.448	0.000	271.628	158.772	50.000	0.000	0.491	90.000	43.557
25	2.237	1.610	-4.338	-0.491	0.000	264.305	155.212	50.000	0.000	0.491	90.000	42.987
26	2.353	1.610	-4.497	-0.534	0.000	253.499	149.920	50.000	0.000	0.491	90.000	42.106
27	2.452	1.610	-4.622	-0.560	0.000	244.880	145.698	50.000	0.000	0.491	90.000	41.367
28	2.587	1.610	-4.783	-0.586	0.000	235.871	141.270	50.000	0.000	0.491	90.000	40.556
29	2.691	1.610	-4.902	-0.601	0.000	231.135	139.005	50.000	0.000	0.491	90.000	40.113
30	2.804	1.610	-5.026	-0.612	0.000	227.446	137.217	50.000	0.000	0.492	90.000	39.760
31	2.880	1.610	-5.108	-0.618	0.000	225.918	136.534	50.000	0.000	0.492	90.000	39.611
32	2.981	1.610	-5.215	-0.625	0.000	225.045	136.168	50.000	0.000	0.492	90.000	39.526
33	3.336	1.610	-5.588	-0.642	0.000	222.704	135.249	50.000	0.000	0.494	90.000	39.294

True Triaxial Test on Fine Nevada Sand with a Target Void Ratio = 0.530 (D_r = 91.28%)

Test No.:	16
Test Date:	3/10/11
Sector:	III
Initial Void Ratio, e:	0.533
Final Mean Princpal Stress, σ_m :	232.1 kPa
Max Friction Angle, ϕ:	49.5 deg
b-value at failure:	0.72
Stress direction at failure, α:	90.0 deg

Shear Band Notes	
Point of Observation:	28
Inclination (from Vertical):	
none observed	
Failure Notes:	
vacuum was not held after failure	

Point (No.)	ε_z (%)	ε_x (%)	ε_y (%)	ε_v (%)	$\gamma_{\theta z}$ (%)	σ_z (kPa)	σ_x (kPa)	σ_y (kPa)	$\tau_{\theta z}$ (kPa)	b	α (°)	φ (°)
1	0.000	0.000	0.000	0.000	0.000	51.610	49.168	50.000	0.000	0.341	90.000	0.908
2	0.003	0.000	0.000	0.002	0.000	54.125	51.054	50.000	0.000	0.255	90.000	4.461
3	0.009	0.000	-0.007	0.002	0.000	58.435	54.287	50.000	0.000	0.508	90.000	6.814
4	0.029	0.000	-0.013	0.015	0.000	73.160	65.334	50.000	0.000	0.662	90.000	10.839
5	0.042	0.000	-0.016	0.026	0.000	86.807	75.576	50.000	0.000	0.695	90.000	15.607
6	0.075	0.199	-0.226	0.047	0.000	103.322	87.905	50.000	0.000	0.711	90.000	20.351
7	0.099	0.451	-0.494	0.056	0.000	113.368	95.326	50.000	0.000	0.715	90.000	22.823
8	0.107	0.385	-0.432	0.060	0.000	116.237	97.506	50.000	0.000	0.717	90.000	23.481
9	0.203	0.650	-0.776	0.078	0.000	141.302	116.141	50.000	0.000	0.724	90.000	28.507
10	0.317	0.819	-1.059	0.078	0.000	161.270	131.008	50.000	0.000	0.728	90.000	31.781
11	0.414	0.963	-1.303	0.074	0.000	180.139	145.044	50.000	0.000	0.730	90.000	34.436
12	0.502	1.108	-1.538	0.071	0.000	196.125	156.907	50.000	0.000	0.732	90.000	36.420
13	0.605	1.228	-1.792	0.041	0.000	211.658	168.467	50.000	0.000	0.733	90.000	38.157
14	0.707	1.445	-2.145	0.006	0.000	226.797	179.601	50.000	0.000	0.733	90.000	39.697
15	0.809	1.589	-2.431	-0.032	0.000	240.104	189.449	50.000	0.000	0.734	90.000	40.942
16	0.910	1.758	-2.737	-0.069	0.000	251.963	198.172	50.000	0.000	0.734	90.000	41.977
17	1.012	1.878	-2.998	-0.108	0.000	265.561	208.254	50.000	0.000	0.734	90.000	43.087
18	1.114	1.975	-3.235	-0.146	0.000	278.410	217.818	50.000	0.000	0.735	90.000	44.067
19	1.311	2.119	-3.682	-0.252	0.000	296.519	231.382	50.000	0.000	0.736	90.000	45.350
20	1.510	2.288	-4.168	-0.370	0.000	313.438	244.030	50.000	0.000	0.737	90.000	46.456
21	1.724	2.432	-4.673	-0.517	0.000	325.920	253.467	50.000	0.000	0.737	90.000	47.222
22	1.907	2.504	-5.058	-0.646	0.000	335.985	261.204	50.000	0.000	0.739	90.000	47.810
23	2.116	2.649	-5.558	-0.793	0.000	346.588	265.416	50.000	0.000	0.726	90.000	48.404
24	2.204	2.721	-5.780	-0.855	0.000	351.769	268.270	50.000	0.000	0.723	90.000	48.686
25	2.434	2.890	-6.332	-1.008	0.000	366.033	276.964	50.000	0.000	0.718	90.000	49.432
26	2.531	2.962	-6.557	-1.064	0.000	368.030	278.260	50.000	0.000	0.718	90.000	49.533
27	2.623	3.013	-6.764	-1.129	0.000	366.886	278.032	50.000	0.000	0.720	90.000	49.475
28	2.804	3.112	-7.153	-1.236	0.000	339.765	258.041	50.000	0.000	0.718	90.000	48.025
29	2.917	3.159	-7.351	-1.275	0.000	318.638	241.570	50.000	0.000	0.713	90.000	46.780
30	3.004	3.159	-7.463	-1.301	0.000	308.692	234.690	50.000	0.000	0.714	90.000	46.154
31	3.122	3.159	-7.601	-1.320	0.000	297.676	226.954	50.000	0.000	0.714	90.000	45.429
32	3.361	3.205	-7.915	-1.348	0.000	291.915	223.273	50.000	0.000	0.716	90.000	45.034
33	3.633	3.205	-8.208	-1.370	0.000	294.345	224.321	50.000	0.000	0.713	90.000	45.202

True Triaxial Test on Fine Nevada Sand with a Target Void Ratio = 0.530 (D_r = 91.28%)

Test No.:	17
Test Date:	3/11/11
Sector:	III
Initial Void Ratio, e:	0.533
Final Mean Princpal Stress, σ_m :	238.7 kPa
Max Friction Angle, ϕ:	50.1 deg
b-value at failure:	0.72
Stress direction at failure, α:	90.0 deg

Shear Band Notes

Point of Observation: 28

Inclination (from Vertical):
63°

Failure Notes:

Point (No.)	ε_z (%)	ε_x (%)	ε_y (%)	ε_v (%)	$\gamma_{\theta z}$ (%)	σ_z (kPa)	σ_x (kPa)	σ_y (kPa)	$\tau_{\theta z}$ (kPa)	b	α (°)	φ (°)
1	0.000	0.000	0.000	0.000	0.000	51.610	51.020	50.000	0.000	0.633	90.000	0.908
2	0.012	0.000	-0.010	0.002	0.000	59.871	59.282	50.000	0.000	0.940	90.000	5.155
3	0.024	0.000	-0.015	0.009	0.000	67.054	66.467	50.000	0.000	0.966	90.000	8.377
4	0.026	0.000	-0.009	0.017	0.000	74.238	73.654	50.000	0.000	0.976	90.000	11.250
5	0.028	0.000	-0.002	0.026	0.000	81.424	80.842	50.000	0.000	0.981	90.000	13.834
6	0.029	0.000	0.006	0.034	0.000	90.407	89.828	50.000	0.000	0.986	90.000	16.725
7	0.030	0.000	0.006	0.037	0.000	98.310	97.734	50.000	0.000	0.988	90.000	19.010
8	0.032	0.000	0.006	0.039	0.000	105.136	104.563	50.000	0.000	0.990	90.000	20.818
9	0.037	0.252	-0.248	0.041	0.000	110.882	110.162	50.000	0.000	0.988	90.000	22.236
10	0.106	0.300	-0.358	0.047	0.000	142.438	141.514	50.000	0.000	0.990	90.000	28.708
11	0.204	0.710	-0.885	0.028	0.000	172.814	171.582	50.000	0.000	0.990	90.000	33.449
12	0.305	1.055	-1.365	-0.004	0.000	195.578	194.043	50.000	0.000	0.989	90.000	36.356
13	0.404	1.300	-1.752	-0.047	0.000	216.128	214.214	50.000	0.000	0.988	90.000	38.626
14	0.508	1.539	-2.155	-0.108	0.000	234.443	232.132	50.000	0.000	0.987	90.000	40.424
15	0.605	1.785	-2.566	-0.177	0.000	251.990	249.212	50.000	0.000	0.986	90.000	41.979
16	0.703	1.977	-2.935	-0.254	0.000	270.884	267.691	50.000	0.000	0.986	90.000	43.500
17	0.813	2.216	-3.391	-0.362	0.000	282.524	275.632	50.000	0.000	0.970	90.000	44.368
18	0.916	2.362	-3.735	-0.457	0.000	301.603	289.808	50.000	0.000	0.953	90.000	45.691
19	1.012	2.508	-4.028	-0.508	0.000	319.685	289.728	50.000	0.000	0.889	90.000	46.844
20	1.104	2.554	-4.227	-0.569	0.000	332.028	289.493	50.000	0.000	0.849	90.000	47.582
21	1.204	2.654	-4.492	-0.633	0.000	343.608	287.411	50.000	0.000	0.809	90.000	48.240
22	1.323	2.700	-4.735	-0.711	0.000	353.992	288.445	50.000	0.000	0.784	90.000	48.805
23	1.422	2.747	-4.948	-0.780	0.000	363.370	288.716	50.000	0.000	0.762	90.000	49.296
24	1.621	2.840	-5.378	-0.918	0.000	374.668	286.771	50.000	0.000	0.729	90.000	49.864
25	1.711	2.840	-5.524	-0.974	0.000	375.619	287.333	50.000	0.000	0.729	90.000	49.911
26	1.825	2.886	-5.754	-1.043	0.000	378.562	287.507	50.000	0.000	0.723	90.000	50.055
27	1.904	2.886	-5.902	-1.111	0.000	372.167	287.366	50.000	0.000	0.737	90.000	49.741
28	2.011	2.886	-6.064	-1.167	0.000	348.659	263.839	50.000	0.000	0.716	90.000	48.518
29	2.101	2.886	-6.184	-1.198	0.000	332.298	253.455	50.000	0.000	0.721	90.000	47.597
30	2.248	2.886	-6.364	-1.230	0.000	316.522	240.497	50.000	0.000	0.715	90.000	46.649
31	2.453	2.886	-6.589	-1.249	0.000	310.754	237.911	50.000	0.000	0.721	90.000	46.286
32	2.529	2.886	-6.669	-1.254	0.000	312.291	237.657	50.000	0.000	0.715	90.000	46.384
33	2.622	2.886	-6.766	-1.258	0.000	315.170	237.665	50.000	0.000	0.708	90.000	46.565

True Triaxial Test on Fine Nevada Sand with a Target Void Ratio = 0.530 (D_r = 91.28%)

Test No.:	18
Test Date:	3/18/11
Sector:	III
Initial Void Ratio, e:	0.526
Final Mean Princpal Stress, σ_m :	224.0 kPa
Max Friction Angle, ϕ:	46.8 deg
b-value at failure:	0.95
Stress direction at failure, α:	90.0 deg

Shear Band Notes	
Point of Observation:	31
Inclination (from Vertical):	
none observed	
Failure Notes:	
vacuum was not held at failure	

Point (No.)	ε_z (%)	ε_x (%)	ε_y (%)	ε_v (%)	$\gamma_{\theta z}$ (%)	σ_z (kPa)	σ_x (kPa)	σ_y (kPa)	$\tau_{\theta z}$ (kPa)	b	α (°)	φ (°)
1	0.000	0.000	0.000	0.000	0.000	51.611	51.611	50.000	0.000	1.000	90.000	0.908
2	0.001	0.000	-0.001	0.000	0.000	53.048	51.389	50.000	0.000	0.456	90.000	1.695
3	0.009	0.000	-0.007	0.002	0.000	58.077	58.078	50.000	0.000	1.000	90.000	4.286
4	0.017	0.000	-0.013	0.004	0.000	63.106	63.108	50.000	0.000	1.000	90.000	6.654
5	0.023	0.000	-0.016	0.008	0.000	68.854	68.858	50.000	0.000	1.000	90.000	9.127
6	0.031	0.000	-0.020	0.011	0.000	73.882	73.889	50.000	0.000	1.000	90.000	11.115
7	0.036	0.000	-0.019	0.017	0.000	78.193	78.203	50.000	0.000	1.000	90.000	12.705
8	0.043	0.000	-0.015	0.028	0.000	84.301	84.315	50.000	0.000	1.000	90.000	14.797
9	0.052	0.297	-0.310	0.039	0.000	89.690	89.593	50.000	0.000	0.998	90.000	16.507
10	0.105	0.519	-0.543	0.081	0.000	112.676	112.416	50.000	0.000	0.996	90.000	22.661
11	0.165	0.631	-0.691	0.105	0.000	129.173	128.803	50.000	0.000	0.995	90.000	26.224
12	0.201	0.779	-0.866	0.114	0.000	138.487	137.974	50.000	0.000	0.994	90.000	27.999
13	0.258	0.928	-1.066	0.120	0.000	149.927	149.256	50.000	0.000	0.993	90.000	29.988
14	0.316	1.076	-1.271	0.121	0.000	161.351	160.502	50.000	0.000	0.992	90.000	31.793
15	0.358	1.187	-1.427	0.119	0.000	169.550	166.798	50.000	0.000	0.977	90.000	32.992
16	0.402	1.262	-1.552	0.111	0.000	175.584	172.514	50.000	0.000	0.976	90.000	33.828
17	0.461	1.341	-1.700	0.102	0.000	185.528	182.432	50.000	0.000	0.977	90.000	35.129
18	0.511	1.487	-1.908	0.090	0.000	192.968	189.604	50.000	0.000	0.976	90.000	36.045
19	0.646	1.832	-2.431	0.047	0.000	217.035	212.697	50.000	0.000	0.974	90.000	38.720
20	0.678	1.932	-2.565	0.045	0.000	221.987	216.994	50.000	0.000	0.971	90.000	39.223
21	0.762	2.131	-2.882	0.011	0.000	236.793	231.006	50.000	0.000	0.969	90.000	40.641
22	0.858	2.377	-3.269	-0.034	0.000	243.688	236.763	50.000	0.000	0.964	90.000	41.262
23	0.906	2.430	-3.391	-0.056	0.000	252.468	246.016	50.000	0.000	0.968	90.000	42.020
24	1.059	2.729	-3.925	-0.137	0.000	267.331	259.597	50.000	0.000	0.964	90.000	43.225
25	1.200	2.981	-4.430	-0.249	0.000	276.417	267.940	50.000	0.000	0.963	90.000	43.919
26	1.281	3.127	-4.721	-0.313	0.000	283.566	273.971	50.000	0.000	0.959	90.000	44.444
27	1.404	3.326	-5.148	-0.418	0.000	294.759	284.931	50.000	0.000	0.960	90.000	45.230
28	1.561	3.625	-5.752	-0.566	0.000	312.448	299.355	50.000	0.000	0.950	90.000	46.394
29	1.665	3.970	-6.381	-0.746	0.000	318.516	304.524	50.000	0.000	0.948	90.000	46.773
30	1.706	4.169	-6.724	-0.849	0.000	318.209	303.812	50.000	0.000	0.946	90.000	46.754
31	1.771	5.590	-9.091	-1.730	0.000	267.555	232.427	50.000	0.000	0.839	90.000	43.243
32	1.858	9.123	-12.233	-1.252	0.000	213.973	201.835	50.000	0.000	0.926	90.000	38.402

Triaxial Test on Fine Nevada Sand with a Target Void Ratio = 0.530 (D_r = 91.28%)

Test No.:	1, TT#1	
Test Date:	3/21/11	
Sector:	I	
Initial Void Ratio, e:	0.522	
Final Mean Princpal Stress, σ_m :	121.4	kPa
Max Friction Angle, ϕ:	43.0	deg
b-value at failure:	0.00	
Stress direction at failure, α:	0.0	deg

Shear Band Notes	
Point of Observation:	30
Inclination (from Vertical):	
51°, 58°	
Failure Notes:	

Point (No.)	ε_z (%)	ε_x (%)	ε_y (%)	ε_v (%)	$\gamma_{\theta z}$ (%)	σ_z (kPa)	σ_x (kPa)	σ_y (kPa)	$\tau_{\theta z}$ (kPa)	b	α (°)	φ (°)
1	0.000	0.000	0.000	0.000	0.000	51.627	50.000	50.000	0.000	0.000	0.000	0.917
2	0.014	-0.005	-0.005	0.004	0.000	63.297	50.000	50.000	0.000	0.000	0.000	6.740
3	0.041	-0.014	-0.014	0.013	0.000	76.423	50.000	50.000	0.000	0.000	0.000	12.064
4	0.126	-0.045	-0.045	0.037	0.000	104.831	50.000	50.000	0.000	0.000	0.000	20.741
5	0.201	-0.075	-0.075	0.050	0.000	123.372	50.000	50.000	0.000	0.000	0.000	25.037
6	0.421	-0.181	-0.181	0.059	0.000	162.830	50.000	50.000	0.000	0.000	0.000	32.015
7	0.620	-0.296	-0.296	0.028	0.000	186.502	50.000	50.000	0.000	0.000	0.000	35.252
8	0.809	-0.415	-0.415	-0.020	0.000	202.092	50.000	50.000	0.000	0.000	0.000	37.108
9	1.053	-0.582	-0.582	-0.111	0.000	215.641	50.000	50.000	0.000	0.000	0.000	38.576
10	1.211	-0.693	-0.693	-0.176	0.000	222.463	50.000	50.000	0.000	0.000	0.000	39.270
11	1.421	-0.844	-0.844	-0.268	0.000	230.904	50.000	50.000	0.000	0.000	0.000	40.091
12	1.637	-1.007	-1.007	-0.376	0.000	237.817	50.000	50.000	0.000	0.000	0.000	40.735
13	1.811	-1.140	-1.140	-0.470	0.000	243.016	50.000	50.000	0.000	0.000	0.000	41.202
14	2.007	-1.292	-1.292	-0.577	0.000	248.111	50.000	50.000	0.000	0.000	0.000	41.648
15	2.237	-1.476	-1.476	-0.716	0.000	250.914	50.000	50.000	0.000	0.000	0.000	41.888
16	2.421	-1.618	-1.618	-0.816	0.000	254.573	50.000	50.000	0.000	0.000	0.000	42.196
17	2.611	-1.772	-1.772	-0.933	0.000	256.402	50.000	50.000	0.000	0.000	0.000	42.348
18	2.806	-1.931	-1.931	-1.055	0.000	258.896	50.000	50.000	0.000	0.000	0.000	42.553
19	3.053	-2.130	-2.130	-1.208	0.000	259.450	50.000	50.000	0.000	0.000	0.000	42.598
20	3.211	-2.255	-2.255	-1.299	0.000	261.012	50.000	50.000	0.000	0.000	0.000	42.724
21	3.421	-2.423	-2.423	-1.425	0.000	263.069	50.000	50.000	0.000	0.000	0.000	42.889
22	3.632	-2.594	-2.594	-1.556	0.000	263.024	50.000	50.000	0.000	0.000	0.000	42.886
23	3.842	-2.764	-2.764	-1.686	0.000	264.355	50.000	50.000	0.000	0.000	0.000	42.991
24	4.135	-3.000	-3.000	-1.865	0.000	262.299	50.000	50.000	0.000	0.000	0.000	42.828
25	4.263	-3.101	-3.101	-1.939	0.000	263.231	50.000	50.000	0.000	0.000	0.000	42.902
26	4.421	-3.223	-3.223	-2.026	0.000	263.039	50.000	50.000	0.000	0.000	0.000	42.887
27	4.668	-3.417	-3.417	-2.165	0.000	261.858	50.000	50.000	0.000	0.000	0.000	42.792
28	4.881	-3.584	-3.584	-2.287	0.000	261.135	50.000	50.000	0.000	0.000	0.000	42.734
29	5.026	-3.696	-3.696	-2.365	0.000	258.281	50.000	50.000	0.000	0.000	0.000	42.502
30	5.250	-3.866	-3.866	-2.482	0.000	257.552	50.000	50.000	0.000	0.000	0.000	42.443

Triaxial Test on Fine Nevada Sand with a Target Void Ratio = 0.530 (D_r = 91.28%)

Test No.:	2
Test Date:	4/1/11
Sector:	I
Initial Void Ratio, e:	0.537
Final Mean Princpal Stress, σ_m :	69.1 kPa
Max Friction Angle, ϕ:	46.5 deg
b-value at failure:	0.00
Stress direction at failure, α:	0.0 deg

Shear Band Notes

Point of Observation: 28

Inclination (from Vertical):
57.4°, 56.9°

Failure Notes:

Point (No.)	ε_z (%)	ε_x (%)	ε_y (%)	ε_v (%)	$\gamma_{\theta z}$ (%)	σ_z (kPa)	σ_x (kPa)	σ_y (kPa)	$\tau_{\theta z}$ (kPa)	b	α (°)	φ (°)
1	0.000	0.000	0.000	0.000	0.000	27.190	25.000	25.000	0.000	0.000	0.000	2.405
2	0.001	0.002	0.002	0.004	0.000	30.315	25.000	25.000	0.000	0.000	0.000	5.514
3	0.002	0.001	0.001	0.004	0.000	34.024	25.000	25.000	0.000	0.000	0.000	8.795
4	0.012	-0.002	-0.002	0.009	0.000	41.443	25.000	25.000	0.000	0.000	0.000	14.328
5	0.024	-0.005	-0.005	0.013	0.000	46.263	25.000	25.000	0.000	0.000	0.000	17.360
6	0.037	-0.010	-0.010	0.018	0.000	51.083	25.000	25.000	0.000	0.000	0.000	20.049
7	0.230	-0.095	-0.095	0.040	0.000	86.278	25.000	25.000	0.000	0.000	0.000	33.413
8	0.421	-0.201	-0.201	0.020	0.000	102.416	25.000	25.000	0.000	0.000	0.000	37.415
9	0.737	-0.394	-0.394	-0.051	0.000	119.064	25.000	25.000	0.000	0.000	0.000	40.763
10	0.842	-0.465	-0.465	-0.089	0.000	123.347	25.000	25.000	0.000	0.000	0.000	41.525
11	1.005	-0.575	-0.575	-0.146	0.000	129.740	25.000	25.000	0.000	0.000	0.000	42.600
12	1.263	-0.760	-0.760	-0.257	0.000	135.946	25.000	25.000	0.000	0.000	0.000	43.578
13	1.477	-0.918	-0.918	-0.358	0.000	141.436	25.000	25.000	0.000	0.000	0.000	44.394
14	1.615	-1.018	-1.018	-0.420	0.000	144.483	25.000	25.000	0.000	0.000	0.000	44.828
15	1.806	-1.158	-1.158	-0.509	0.000	147.783	25.000	25.000	0.000	0.000	0.000	45.285
16	2.065	-1.362	-1.362	-0.659	0.000	149.463	25.000	25.000	0.000	0.000	0.000	45.513
17	2.204	-1.469	-1.469	-0.735	0.000	152.085	25.000	25.000	0.000	0.000	0.000	45.861
18	2.603	-1.775	-1.775	-0.947	0.000	154.195	25.000	25.000	0.000	0.000	0.000	46.135
19	2.737	-1.880	-1.880	-1.022	0.000	155.360	25.000	25.000	0.000	0.000	0.000	46.284
20	2.921	-2.020	-2.020	-1.120	0.000	156.427	25.000	25.000	0.000	0.000	0.000	46.420
21	3.191	-2.235	-2.235	-1.279	0.000	156.232	25.000	25.000	0.000	0.000	0.000	46.395
22	3.290	-2.311	-2.311	-1.332	0.000	156.390	25.000	25.000	0.000	0.000	0.000	46.415
23	3.427	-2.415	-2.415	-1.403	0.000	157.183	25.000	25.000	0.000	0.000	0.000	46.515
24	3.961	-2.828	-2.828	-1.695	0.000	156.468	25.000	25.000	0.000	0.000	0.000	46.425
25	4.095	-2.926	-2.926	-1.757	0.000	156.564	25.000	25.000	0.000	0.000	0.000	46.437
26	4.282	-3.077	-3.077	-1.872	0.000	153.734	25.000	25.000	0.000	0.000	0.000	46.075
27	4.528	-3.260	-3.260	-1.991	0.000	152.924	25.000	25.000	0.000	0.000	0.000	45.970
28	4.737	-3.406	-3.406	-2.076	0.000	145.976	25.000	25.000	0.000	0.000	0.000	45.037
29	4.911	-3.524	-3.524	-2.138	0.000	134.643	25.000	25.000	0.000	0.000	0.000	43.377
30	5.191	-3.691	-3.691	-2.191	0.000	124.300	25.000	25.000	0.000	0.000	0.000	41.690
31	5.439	-3.828	-3.828	-2.217	0.000	120.254	25.000	25.000	0.000	0.000	0.000	40.978
32	6.050	-4.151	-4.151	-2.253	0.000	117.254	25.000	25.000	0.000	0.000	0.000	40.430
33	6.664	-4.467	-4.467	-2.270	0.000	116.330	25.000	25.000	0.000	0.000	0.000	40.257

Triaxial Test on Fine Nevada Sand with a Target Void Ratio = 0.530 (D_r = 91.28%)

Test No.:	3	
Test Date:	4/4/11	
Sector:	I	
Initial Void Ratio, e:	0.542	
Final Mean Princpal Stress, σ_m :	284.6	kPa
Max Friction Angle, ϕ:	39.9	deg
b-value at failure:	0.00	
Stress direction at failure, α:	0.0	deg

Shear Band Notes	
Point of Observation:	26
Inclination (from Vertical):	
57.0°, 58.9°	
Failure Notes:	

Point (No.)	ε_z (%)	ε_x (%)	ε_y (%)	ε_v (%)	$\gamma_{\theta z}$ (%)	σ_z (kPa)	σ_x (kPa)	σ_y (kPa)	$\tau_{\theta z}$ (kPa)	b	α (°)	φ (°)
1	0.000	0.000	0.000	0.000	0.000	130.000	130.000	25.000	0.000	0.000	0.000	0.000
2	0.000	-0.005	-0.005	-0.011	0.000	151.214	130.000	25.000	0.000	0.000	0.000	5.45
3	0.000	-0.015	-0.015	-0.029	0.000	187.606	130.000	25.000	0.000	0.000	0.000	10.3
4	0.000	-0.030	-0.030	-0.060	0.000	217.430	130.000	25.000	0.000	0.000	0.000	15.7
5	0.039	-0.041	-0.041	-0.043	0.000	238.876	130.000	25.000	0.000	0.000	0.000	18.2
6	0.017	-0.045	-0.045	-0.073	0.000	250.143	130.000	25.000	0.000	0.000	0.000	19.5
7	0.205	-0.062	-0.062	0.081	0.000	276.283	130.000	25.000	0.000	0.000	0.000	21.103
8	0.412	-0.150	-0.150	0.112	0.000	351.891	130.000	25.000	0.000	0.000	0.000	27.417
9	0.619	-0.253	-0.253	0.114	0.000	406.486	130.000	25.000	0.000	0.000	0.000	31.022
10	0.875	-0.394	-0.394	0.087	0.000	453.011	130.000	25.000	0.000	0.000	0.000	33.645
11	1.130	-0.548	-0.548	0.035	0.000	486.208	130.000	25.000	0.000	0.000	0.000	35.315
12	1.417	-0.739	-0.739	-0.061	0.000	513.871	130.000	25.000	0.000	0.000	0.000	36.598
13	1.656	-0.896	-0.896	-0.135	0.000	533.381	130.000	25.000	0.000	0.000	0.000	37.450
14	1.853	-1.029	-1.029	-0.205	0.000	546.547	130.000	25.000	0.000	0.000	0.000	38.002
15	2.227	-1.292	-1.292	-0.358	0.000	564.165	130.000	25.000	0.000	0.000	0.000	38.715
16	3.145	-1.966	-1.966	-0.786	0.000	592.484	130.000	25.000	0.000	0.000	0.000	39.802
17	3.514	-2.238	-2.238	-0.961	0.000	593.722	130.000	25.000	0.000	0.000	0.000	39.847
18	3.966	-2.581	-2.581	-1.197	0.000	593.897	130.000	25.000	0.000	0.000	0.000	39.854
19	4.231	-2.779	-2.779	-1.328	0.000	592.688	130.000	25.000	0.000	0.000	0.000	39.809
20	4.410	-2.921	-2.921	-1.433	0.000	588.587	130.000	25.000	0.000	0.000	0.000	39.656
21	4.725	-3.158	-3.158	-1.590	0.000	585.317	130.000	25.000	0.000	0.000	0.000	39.533
22	4.843	-3.247	-3.247	-1.651	0.000	584.471	130.000	25.000	0.000	0.000	0.000	39.501
23	5.053	-3.398	-3.398	-1.743	0.000	579.305	130.000	25.000	0.000	0.000	0.000	39.305
24	5.293	-3.573	-3.573	-1.852	0.000	574.286	130.000	25.000	0.000	0.000	0.000	39.112
25	5.437	-3.682	-3.682	-1.926	0.000	570.236	130.000	25.000	0.000	0.000	0.000	38.954
26	5.641	-3.812	-3.812	-1.983	0.000	558.920	130.000	25.000	0.000	0.000	0.000	38.506
27	5.929	-4.011	-4.011	-2.092	0.000	486.676	130.000	25.000	0.000	0.000	0.000	35.337
28	6.036	-4.075	-4.075	-2.114	0.000	464.747	130.000	25.000	0.000	0.000	0.000	34.252
29	6.355	-4.248	-4.248	-2.141	0.000	429.453	130.000	25.000	0.000	0.000	0.000	32.362
30	6.639	-4.391	-4.391	-2.143	0.000	420.202	130.000	25.000	0.000	0.000	0.000	31.833
31	6.903	-4.522	-4.522	-2.141	0.000	417.716	130.000	25.000	0.000	0.000	0.000	31.689
32	7.106	-4.621	-4.621	-2.136	0.000	417.751	130.000	25.000	0.000	0.000	0.000	31.691
33	7.446	-4.788	-4.788	-2.130	0.000	418.019	130.000	25.000	0.000	0.000	0.000	31.706

Triaxial Test on Fine Nevada Sand with a Target Void Ratio = 0.530 (D_r = 91.28%)

Test No.:	4
Test Date:	4/5/11
Sector:	I
Initial Void Ratio, e:	0.542
Final Mean Princpal Stress, σ_m :	159.7 kPa
Max Friction Angle, ϕ:	41.1 deg
b-value at failure:	0.00
Stress direction at failure, α:	0.0 deg

Shear Band Notes	
Point of Observation:	25
Inclination (from Vertical):	
53.0°, 60.3°	
Failure Notes:	

Point (No.)	ε_z (%)	ε_x (%)	ε_y (%)	ε_v (%)	$\gamma_{\theta z}$ (%)	σ_z (kPa)	σ_x (kPa)	σ_y (kPa)	$\tau_{\theta z}$ (kPa)	b	α (°)	φ (°)
1	0.000	0.000	0.000	0.000	0.000	72.151	70.000	70.000	0.000	0.000	0.000	0.867
2	0.015	-0.005	-0.005	0.004	0.000	85.797	70.000	70.000	0.000	0.000	0.000	5.820
3	0.043	-0.013	-0.013	0.017	0.000	103.636	70.000	70.000	0.000	0.000	0.000	11.170
4	0.079	-0.022	-0.022	0.035	0.000	120.012	70.000	70.000	0.000	0.000	0.000	15.260
5	0.132	-0.040	-0.040	0.052	0.000	138.918	70.000	70.000	0.000	0.000	0.000	19.262
6	0.206	-0.068	-0.068	0.070	0.000	159.611	70.000	70.000	0.000	0.000	0.000	22.972
7	0.461	-0.180	-0.180	0.100	0.000	207.675	70.000	70.000	0.000	0.000	0.000	29.723
8	0.637	-0.277	-0.277	0.083	0.000	230.226	70.000	70.000	0.000	0.000	0.000	32.255
9	0.815	-0.372	-0.372	0.070	0.000	248.353	70.000	70.000	0.000	0.000	0.000	34.072
10	1.005	-0.494	-0.494	0.017	0.000	262.342	70.000	70.000	0.000	0.000	0.000	35.362
11	1.265	-0.654	-0.654	-0.044	0.000	278.614	70.000	70.000	0.000	0.000	0.000	36.756
12	1.467	-0.784	-0.784	-0.100	0.000	289.900	70.000	70.000	0.000	0.000	0.000	37.662
13	1.602	-0.873	-0.873	-0.144	0.000	295.229	70.000	70.000	0.000	0.000	0.000	38.074
14	1.886	-1.063	-1.063	-0.240	0.000	307.196	70.000	70.000	0.000	0.000	0.000	38.965
15	2.023	-1.175	-1.175	-0.328	0.000	308.793	70.000	70.000	0.000	0.000	0.000	39.080
16	2.259	-1.348	-1.348	-0.437	0.000	318.236	70.000	70.000	0.000	0.000	0.000	39.747
17	2.609	-1.610	-1.610	-0.612	0.000	325.734	70.000	70.000	0.000	0.000	0.000	40.258
18	3.112	-1.984	-1.984	-0.856	0.000	329.742	70.000	70.000	0.000	0.000	0.000	40.525
19	3.700	-2.420	-2.420	-1.140	0.000	337.151	70.000	70.000	0.000	0.000	0.000	41.007
20	4.148	-2.764	-2.764	-1.380	0.000	339.067	70.000	70.000	0.000	0.000	0.000	41.129
21	4.727	-3.207	-3.207	-1.686	0.000	338.002	70.000	70.000	0.000	0.000	0.000	41.061
22	4.813	-3.280	-3.280	-1.747	0.000	337.259	70.000	70.000	0.000	0.000	0.000	41.014
23	5.058	-3.446	-3.446	-1.835	0.000	335.664	70.000	70.000	0.000	0.000	0.000	40.911
24	5.412	-3.697	-3.697	-1.983	0.000	334.626	70.000	70.000	0.000	0.000	0.000	40.844
25	5.493	-3.756	-3.756	-2.018	0.000	334.307	70.000	70.000	0.000	0.000	0.000	40.823
26	5.929	-4.041	-4.041	-2.154	0.000	322.677	70.000	70.000	0.000	0.000	0.000	40.051
27	6.167	-4.173	-4.173	-2.180	0.000	301.238	70.000	70.000	0.000	0.000	0.000	38.527
28	6.278	-4.229	-4.229	-2.180	0.000	285.930	70.000	70.000	0.000	0.000	0.000	37.349
29	6.476	-4.330	-4.330	-2.184	0.000	272.464	70.000	70.000	0.000	0.000	0.000	36.242
30	6.781	-4.483	-4.483	-2.184	0.000	258.514	70.000	70.000	0.000	0.000	0.000	35.018
31	7.117	-4.651	-4.651	-2.184	0.000	251.545	70.000	70.000	0.000	0.000	0.000	34.375
32	7.337	-4.760	-4.760	-2.184	0.000	251.116	70.000	70.000	0.000	0.000	0.000	34.334
33	7.945	-5.065	-5.065	-2.184	0.000	249.598	70.000	70.000	0.000	0.000	0.000	34.191

Triaxial Test on Fine Nevada Sand with a Target Void Ratio = 0.530 (D_r = 91.28%)

Test No.:	5	
Test Date:	11/19/10	
Sector:	III	
Initial Void Ratio, e:	0.533	
Final Mean Princpal Stress, σ_m :	53.9	kPa
Max Friction Angle, ϕ:	39.4	deg
b-value at failure:	0.00	
Stress direction at failure, α:	90.0	deg

Shear Band Notes	
Point of Observation:	29
Inclination (from Vertical):	
60.0°	
Failure Notes:	

Point (No.)	ε_z (%)	ε_x (%)	ε_y (%)	ε_v (%)	$\gamma_{\theta z}$ (%)	σ_z (kPa)	σ_x (kPa)	σ_y (kPa)	$\tau_{\theta z}$ (kPa)	b	α (°)	φ (°)
1	0.000	0.000	0.000	0.000	0.000	25.000	25.000	25.000	0.000	0.000	90.000	0.000
2	0.017	-0.008	-0.008	0.000	0.000	31.377	25.000	25.000	0.000	0.000	90.000	6.495
3	0.036	-0.015	-0.015	0.007	0.000	39.043	25.000	25.000	0.000	0.000	90.000	12.666
4	0.056	-0.022	-0.022	0.013	0.000	43.221	25.000	25.000	0.000	0.000	90.000	15.491
5	0.105	-0.040	-0.040	0.026	0.000	48.787	25.000	25.000	0.000	0.000	90.000	18.807
6	0.224	-0.090	-0.090	0.044	0.000	56.766	25.000	25.000	0.000	0.000	90.000	22.861
7	0.324	-0.137	-0.137	0.050	0.000	60.212	25.000	25.000	0.000	0.000	90.000	24.408
8	0.403	-0.175	-0.175	0.052	0.000	64.005	25.000	25.000	0.000	0.000	90.000	25.991
9	0.506	-0.225	-0.225	0.057	0.000	67.437	25.000	25.000	0.000	0.000	90.000	27.328
10	0.632	-0.288	-0.288	0.056	0.000	71.195	25.000	25.000	0.000	0.000	90.000	28.700
11	0.738	-0.343	-0.343	0.052	0.000	73.567	25.000	25.000	0.000	0.000	90.000	29.520
12	0.895	-0.426	-0.426	0.044	0.000	76.942	25.000	25.000	0.000	0.000	90.000	30.632
13	0.998	-0.482	-0.482	0.035	0.000	78.954	25.000	25.000	0.000	0.000	90.000	31.266
14	1.147	-0.565	-0.565	0.017	0.000	81.965	25.000	25.000	0.000	0.000	90.000	32.178
15	1.442	-0.732	-0.732	-0.022	0.000	86.581	25.000	25.000	0.000	0.000	90.000	33.497
16	1.623	-0.838	-0.838	-0.052	0.000	89.191	25.000	25.000	0.000	0.000	90.000	34.204
17	2.007	-1.074	-1.074	-0.140	0.000	92.295	25.000	25.000	0.000	0.000	90.000	35.010
18	2.463	-1.356	-1.356	-0.249	0.000	96.996	25.000	25.000	0.000	0.000	90.000	36.168
19	2.871	-1.615	-1.615	-0.358	0.000	101.002	25.000	25.000	0.000	0.000	90.000	37.098
20	3.662	-2.134	-2.134	-0.607	0.000	105.871	25.000	25.000	0.000	0.000	90.000	38.166
21	4.006	-2.344	-2.344	-0.681	0.000	107.849	25.000	25.000	0.000	0.000	90.000	38.582
22	4.851	-2.904	-2.904	-0.956	0.000	109.853	25.000	25.000	0.000	0.000	90.000	38.993
23	4.975	-2.983	-2.983	-0.991	0.000	110.369	25.000	25.000	0.000	0.000	90.000	39.097
24	5.236	-3.161	-3.161	-1.087	0.000	110.053	25.000	25.000	0.000	0.000	90.000	39.034
25	5.487	-3.331	-3.331	-1.174	0.000	111.057	25.000	25.000	0.000	0.000	90.000	39.235
26	5.665	-3.450	-3.450	-1.236	0.000	111.818	25.000	25.000	0.000	0.000	90.000	39.387
27	6.002	-3.682	-3.682	-1.362	0.000	108.814	25.000	25.000	0.000	0.000	90.000	38.781
28	6.298	-3.874	-3.874	-1.450	0.000	105.258	25.000	25.000	0.000	0.000	90.000	38.035
29	6.542	-4.024	-4.024	-1.506	0.000	102.116	25.000	25.000	0.000	0.000	90.000	37.348
30	6.777	-4.172	-4.172	-1.567	0.000	99.956	25.000	25.000	0.000	0.000	90.000	36.860
31	6.938	-4.267	-4.267	-1.596	0.000	99.487	25.000	25.000	0.000	0.000	90.000	36.752
32	7.144	-4.386	-4.386	-1.629	0.000	98.980	25.000	25.000	0.000	0.000	90.000	36.635
33	7.636	-4.667	-4.667	-1.698	0.000	95.055	25.000	25.000	0.000	0.000	90.000	35.699

Triaxial Test on Fine Nevada Sand with a Target Void Ratio = 0.530 (D_r = 91.28%)

Test No.:	6	
Test Date:	11/24/10	
Sector:	III	
Initial Void Ratio, e:	0.538	
Final Mean Princpal Stress, σ_m :	155.9	kPa
Max Friction Angle, ϕ:	38.2	deg
b-value at failure:	0.00	
Stress direction at failure, α:	90.0	deg

Shear Band Notes	
Point of Observation:	27
Inclination (from Vertical):	
67.1°	
Failure Notes:	

Point (No.)	ε_z (%)	ε_x (%)	ε_y (%)	ε_v (%)	$\gamma_{\theta z}$ (%)	σ_z (kPa)	σ_x (kPa)	σ_y (kPa)	$\tau_{\theta z}$ (kPa)	b	α (°)	φ (°)
1	0.000	0.000	0.000	0.000	0.000	74.977	75.000	75.000	0.000	0.000	90.000	-0.009
2	0.044	-0.019	-0.019	0.007	0.000	90.702	75.000	75.000	0.000	0.000	90.000	5.437
3	0.055	-0.021	-0.021	0.013	0.000	97.980	75.000	75.000	0.000	0.000	90.000	7.634
4	0.068	-0.025	-0.025	0.017	0.000	103.869	75.000	75.000	0.000	0.000	90.000	9.288
5	0.106	-0.037	-0.037	0.033	0.000	120.148	75.000	75.000	0.000	0.000	90.000	13.377
6	0.215	-0.070	-0.070	0.074	0.000	151.626	75.000	75.000	0.000	0.000	90.000	19.762
7	0.304	-0.102	-0.102	0.100	0.000	169.572	75.000	75.000	0.000	0.000	90.000	22.748
8	0.420	-0.149	-0.149	0.122	0.000	186.768	75.000	75.000	0.000	0.000	90.000	25.276
9	0.551	-0.204	-0.204	0.143	0.000	201.495	75.000	75.000	0.000	0.000	90.000	27.226
10	0.610	-0.231	-0.231	0.148	0.000	207.638	75.000	75.000	0.000	0.000	90.000	27.988
11	0.803	-0.315	-0.315	0.174	0.000	224.642	75.000	75.000	0.000	0.000	90.000	29.960
12	0.902	-0.362	-0.362	0.178	0.000	232.073	75.000	75.000	0.000	0.000	90.000	30.765
13	1.070	-0.448	-0.448	0.174	0.000	242.452	75.000	75.000	0.000	0.000	90.000	31.836
14	1.171	-0.502	-0.502	0.167	0.000	247.763	75.000	75.000	0.000	0.000	90.000	32.362
15	1.368	-0.608	-0.608	0.152	0.000	257.668	75.000	75.000	0.000	0.000	90.000	33.305
16	1.725	-0.815	-0.815	0.096	0.000	270.547	75.000	75.000	0.000	0.000	90.000	34.465
17	2.303	-1.156	-1.156	-0.009	0.000	287.485	75.000	75.000	0.000	0.000	90.000	35.887
18	2.526	-1.291	-1.291	-0.056	0.000	293.318	75.000	75.000	0.000	0.000	90.000	36.352
19	3.083	-1.640	-1.640	-0.198	0.000	303.502	75.000	75.000	0.000	0.000	90.000	37.135
20	4.048	-2.267	-2.267	-0.487	0.000	313.821	75.000	75.000	0.000	0.000	90.000	37.895
21	4.625	-2.643	-2.643	-0.660	0.000	317.889	75.000	75.000	0.000	0.000	90.000	38.186
22	4.934	-2.849	-2.849	-0.765	0.000	317.179	75.000	75.000	0.000	0.000	90.000	38.135
23	5.110	-2.967	-2.967	-0.825	0.000	317.238	75.000	75.000	0.000	0.000	90.000	38.140
24	5.384	-3.146	-3.146	-0.908	0.000	317.314	75.000	75.000	0.000	0.000	90.000	38.145
25	5.685	-3.347	-3.347	-1.008	0.000	314.038	75.000	75.000	0.000	0.000	90.000	37.911
26	5.945	-3.516	-3.516	-1.086	0.000	309.646	75.000	75.000	0.000	0.000	90.000	37.592
27	6.207	-3.681	-3.681	-1.155	0.000	298.545	75.000	75.000	0.000	0.000	90.000	36.758
28	6.500	-3.864	-3.864	-1.227	0.000	279.432	75.000	75.000	0.000	0.000	90.000	35.225
29	6.755	-4.010	-4.010	-1.264	0.000	266.348	75.000	75.000	0.000	0.000	90.000	34.095
30	7.016	-4.151	-4.151	-1.286	0.000	261.633	75.000	75.000	0.000	0.000	90.000	33.670
31	7.165	-4.230	-4.230	-1.295	0.000	260.365	75.000	75.000	0.000	0.000	90.000	33.554
32	7.320	-4.311	-4.311	-1.301	0.000	260.043	75.000	75.000	0.000	0.000	90.000	33.525
33	8.068	-4.692	-4.692	-1.316	0.000	260.096	75.000	75.000	0.000	0.000	90.000	33.530

Triaxial Test on Fine Nevada Sand with a Target Void Ratio = 0.530 (D_r = 91.28%)

Test No.:	7	
Test Date:	12/4/10	
Sector:	III	
Initial Void Ratio, e:	0.532	
Final Mean Princpal Stress, σ_m :	260.5	kPa
Max Friction Angle, ϕ:	36.9	deg
b-value at failure:	0.00	
Stress direction at failure, α:	90.0	deg

Shear Band Notes	
Point of Observation:	27
Inclination (from Vertical):	
66.9°, 60.6°	
Failure Notes:	

Point (No.)	ε_z (%)	ε_x (%)	ε_y (%)	ε_v (%)	$\gamma_{\theta z}$ (%)	σ_z (kPa)	σ_x (kPa)	σ_y (kPa)	$\tau_{\theta z}$ (kPa)	b	α (°)	φ (°)
1	0.000	0.000	0.000	0.000	0.000	129.977	130.000	130.000	0.000	0.000	90.000	-0.005
2	0.042	-0.017	-0.017	0.009	0.000	157.682	130.000	130.000	0.000	0.000	90.000	5.522
3	0.061	-0.018	-0.018	0.024	0.000	174.088	130.000	130.000	0.000	0.000	90.000	8.336
4	0.090	-0.028	-0.028	0.035	0.000	197.463	130.000	130.000	0.000	0.000	90.000	11.889
5	0.104	-0.030	-0.030	0.044	0.000	207.231	130.000	130.000	0.000	0.000	90.000	13.239
6	0.224	-0.068	-0.068	0.088	0.000	260.526	130.000	130.000	0.000	0.000	90.000	19.526
7	0.305	-0.096	-0.096	0.114	0.000	285.549	130.000	130.000	0.000	0.000	90.000	21.982
8	0.428	-0.142	-0.142	0.144	0.000	313.958	130.000	130.000	0.000	0.000	90.000	24.479
9	0.501	-0.172	-0.172	0.158	0.000	329.856	130.000	130.000	0.000	0.000	90.000	25.760
10	0.620	-0.223	-0.223	0.175	0.000	345.294	130.000	130.000	0.000	0.000	90.000	26.934
11	0.935	-0.371	-0.371	0.193	0.000	382.777	130.000	130.000	0.000	0.000	90.000	29.535
12	1.048	-0.427	-0.427	0.195	0.000	393.571	130.000	130.000	0.000	0.000	90.000	30.226
13	1.134	-0.470	-0.470	0.195	0.000	401.300	130.000	130.000	0.000	0.000	90.000	30.706
14	1.213	-0.510	-0.510	0.193	0.000	407.645	130.000	130.000	0.000	0.000	90.000	31.092
15	1.460	-0.640	-0.640	0.179	0.000	425.527	130.000	130.000	0.000	0.000	90.000	32.139
16	1.783	-0.818	-0.818	0.147	0.000	446.103	130.000	130.000	0.000	0.000	90.000	33.277
17	2.242	-1.082	-1.082	0.079	0.000	466.958	130.000	130.000	0.000	0.000	90.000	34.365
18	2.710	-1.364	-1.364	-0.018	0.000	487.440	130.000	130.000	0.000	0.000	90.000	35.374
19	2.952	-1.513	-1.513	-0.074	0.000	495.831	130.000	130.000	0.000	0.000	90.000	35.771
20	3.169	-1.648	-1.648	-0.127	0.000	502.251	130.000	130.000	0.000	0.000	90.000	36.070
21	3.719	-1.999	-1.999	-0.278	0.000	513.660	130.000	130.000	0.000	0.000	90.000	36.588
22	4.112	-2.251	-2.251	-0.390	0.000	519.341	130.000	130.000	0.000	0.000	90.000	36.841
23	4.850	-2.731	-2.731	-0.613	0.000	521.105	130.000	130.000	0.000	0.000	90.000	36.919
24	5.020	-2.842	-2.842	-0.665	0.000	517.896	130.000	130.000	0.000	0.000	90.000	36.777
25	5.229	-2.980	-2.980	-0.731	0.000	509.562	130.000	130.000	0.000	0.000	90.000	36.404
26	5.483	-3.142	-3.142	-0.801	0.000	492.563	130.000	130.000	0.000	0.000	90.000	35.618
27	5.774	-3.318	-3.318	-0.862	0.000	471.327	130.000	130.000	0.000	0.000	90.000	34.585
28	6.166	-3.541	-3.541	-0.917	0.000	438.878	130.000	130.000	0.000	0.000	90.000	32.885
29	6.245	-3.584	-3.584	-0.923	0.000	432.761	130.000	130.000	0.000	0.000	90.000	32.547
30	6.667	-3.800	-3.800	-0.932	0.000	416.838	130.000	130.000	0.000	0.000	90.000	31.637
31	6.761	-3.847	-3.847	-0.934	0.000	416.868	130.000	130.000	0.000	0.000	90.000	31.639
32	6.929	-3.931	-3.931	-0.934	0.000	415.063	130.000	130.000	0.000	0.000	90.000	31.533
33	7.150	-4.040	-4.040	-0.930	0.000	411.826	130.000	130.000	0.000	0.000	90.000	31.342

Triaxial Test on Fine Nevada Sand with a Target Void Ratio = 0.530 (D_r = 91.28%)

Test No.:	8, TT# 13
Test Date:	2/25/11
Sector:	III
Initial Void Ratio, e:	0.535
Final Mean Princpal Stress, σ_m :	102.2 kPa
Max Friction Angle, ϕ:	37.6 deg
b-value at failure:	0.00
Stress direction at failure, α:	90.0 deg

Shear Band Notes	
Point of Observation:	26
Inclination (from Vertical):	
63°	
Failure Notes:	

Point (No.)	ε_z (%)	ε_x (%)	ε_y (%)	ε_v (%)	$\gamma_{\theta z}$ (%)	σ_z (kPa)	σ_x (kPa)	σ_y (kPa)	$\tau_{\theta z}$ (kPa)	b	α (°)	φ (°)
1	0.000	0.000	0.000	0.000	0.000	52.164	50.000	50.000	0.000	0.000	90.000	1.213
2	0.017	-0.006	-0.006	0.004	0.000	59.669	50.000	50.000	0.000	0.000	90.000	5.058
3	0.031	-0.011	-0.011	0.009	0.000	70.658	50.000	50.000	0.000	0.000	90.000	9.858
4	0.072	-0.019	-0.019	0.035	0.000	87.137	50.000	50.000	0.000	0.000	90.000	15.712
5	0.155	-0.049	-0.049	0.057	0.000	106.515	50.000	50.000	0.000	0.000	90.000	21.167
6	0.246	-0.084	-0.084	0.079	0.000	120.010	50.000	50.000	0.000	0.000	90.000	24.318
7	0.541	-0.222	-0.222	0.096	0.000	141.338	50.000	50.000	0.000	0.000	90.000	28.513
8	0.615	-0.260	-0.260	0.096	0.000	144.915	50.000	50.000	0.000	0.000	90.000	29.141
9	0.876	-0.399	-0.399	0.079	0.000	155.554	50.000	50.000	0.000	0.000	90.000	30.898
10	1.077	-0.510	-0.510	0.057	0.000	161.845	50.000	50.000	0.000	0.000	90.000	31.867
11	1.215	-0.590	-0.590	0.035	0.000	165.647	50.000	50.000	0.000	0.000	90.000	32.431
12	1.421	-0.711	-0.711	0.000	0.000	171.145	50.000	50.000	0.000	0.000	90.000	33.217
13	1.846	-0.967	-0.967	-0.087	0.000	177.703	50.000	50.000	0.000	0.000	90.000	34.113
14	2.221	-1.200	-1.200	-0.179	0.000	184.610	50.000	50.000	0.000	0.000	90.000	35.013
15	2.647	-1.470	-1.470	-0.293	0.000	190.629	50.000	50.000	0.000	0.000	90.000	35.762
16	2.942	-1.670	-1.670	-0.398	0.000	192.537	50.000	50.000	0.000	0.000	90.000	35.993
17	3.307	-1.909	-1.909	-0.511	0.000	197.127	50.000	50.000	0.000	0.000	90.000	36.538
18	3.736	-2.194	-2.194	-0.651	0.000	199.425	50.000	50.000	0.000	0.000	90.000	36.804
19	4.018	-2.385	-2.385	-0.752	0.000	201.979	50.000	50.000	0.000	0.000	90.000	37.095
20	4.402	-2.645	-2.645	-0.887	0.000	204.640	50.000	50.000	0.000	0.000	90.000	37.394
21	5.038	-3.077	-3.077	-1.115	0.000	205.674	50.000	50.000	0.000	0.000	90.000	37.508
22	5.286	-3.242	-3.242	-1.198	0.000	206.513	50.000	50.000	0.000	0.000	90.000	37.601
23	5.856	-3.629	-3.629	-1.403	0.000	205.256	50.000	50.000	0.000	0.000	90.000	37.462
24	6.362	-3.961	-3.961	-1.561	0.000	194.047	50.000	50.000	0.000	0.000	90.000	36.174
25	6.685	-4.155	-4.155	-1.626	0.000	187.065	50.000	50.000	0.000	0.000	90.000	35.322
26	6.886	-4.271	-4.271	-1.657	0.000	183.708	50.000	50.000	0.000	0.000	90.000	34.898
27	7.104	-4.391	-4.391	-1.679	0.000	181.023	50.000	50.000	0.000	0.000	90.000	34.551
28	7.803	-4.767	-4.767	-1.731	0.000	175.653	50.000	50.000	0.000	0.000	90.000	33.838
29	8.442	-5.097	-5.097	-1.753	0.000	170.470	50.000	50.000	0.000	0.000	90.000	33.122
30	8.839	-5.301	-5.301	-1.764	0.000	170.262	50.000	50.000	0.000	0.000	90.000	33.093
31	9.088	-5.428	-5.428	-1.768	0.000	169.601	50.000	50.000	0.000	0.000	90.000	32.999

Triaxial Test on Fine Nevada Sand with a Target Void Ratio = 0.530 (D_r = 91.28%)

Test No.:	9, W1	
Test Date:	1/17/11	
Sector:	III	
Initial Void Ratio, e:	0.534	
Final Mean Princpal Stress, σ_m :	206.9	kPa
Max Friction Angle, ϕ:	37.7	deg
b-value at failure:	0.00	
Stress direction at failure, α:	90.0	deg

Shear Band Notes	
Point of Observation:	26
Inclination (from Vertical):	
60°, 55°	
Failure Notes:	

Point (No.)	ε_z (%)	ε_x (%)	ε_y (%)	ε_v (%)	$\gamma_{\theta z}$ (%)	σ_z (kPa)	σ_x (kPa)	σ_y (kPa)	$\tau_{\theta z}$ (kPa)	b	α (°)	φ (°)
1	0.000	0.000	0.000	0.000	0.000	96.246	101.000	101.000	0.000	0.000	90.000	-1.381
2	0.007	0.000	0.000	0.007	0.000	121.991	101.000	101.000	0.000	0.000	90.000	5.401
3	0.057	-0.015	-0.015	0.026	0.000	153.796	101.000	101.000	0.000	0.000	90.000	11.959
4	0.141	-0.042	-0.042	0.057	0.000	189.367	101.000	101.000	0.000	0.000	90.000	17.718
5	0.240	-0.079	-0.079	0.081	0.000	217.317	101.000	101.000	0.000	0.000	90.000	21.433
6	0.329	-0.114	-0.114	0.101	0.000	235.399	101.000	101.000	0.000	0.000	90.000	23.548
7	0.638	-0.254	-0.254	0.130	0.000	277.855	101.000	101.000	0.000	0.000	90.000	27.828
8	0.964	-0.419	-0.419	0.125	0.000	307.549	101.000	101.000	0.000	0.000	90.000	30.369
9	1.268	-0.588	-0.588	0.092	0.000	328.212	101.000	101.000	0.000	0.000	90.000	31.963
10	1.549	-0.748	-0.748	0.053	0.000	343.540	101.000	101.000	0.000	0.000	90.000	33.066
11	1.893	-0.955	-0.955	-0.018	0.000	358.147	101.000	101.000	0.000	0.000	90.000	34.059
12	2.145	-1.110	-1.110	-0.075	0.000	367.723	101.000	101.000	0.000	0.000	90.000	34.683
13	2.468	-1.313	-1.313	-0.158	0.000	378.989	101.000	101.000	0.000	0.000	90.000	35.391
14	3.006	-1.661	-1.661	-0.317	0.000	391.497	101.000	101.000	0.000	0.000	90.000	36.146
15	3.312	-1.865	-1.865	-0.418	0.000	398.863	101.000	101.000	0.000	0.000	90.000	36.576
16	3.921	-2.281	-2.281	-0.642	0.000	409.714	101.000	101.000	0.000	0.000	90.000	37.191
17	4.281	-2.527	-2.527	-0.774	0.000	413.913	101.000	101.000	0.000	0.000	90.000	37.423
18	4.802	-2.889	-2.889	-0.976	0.000	418.192	101.000	101.000	0.000	0.000	90.000	37.657
19	5.135	-3.124	-3.124	-1.113	0.000	418.077	101.000	101.000	0.000	0.000	90.000	37.651
20	5.775	-3.576	-3.576	-1.376	0.000	418.112	101.000	101.000	0.000	0.000	90.000	37.653
21	6.096	-3.800	-3.800	-1.504	0.000	417.336	101.000	101.000	0.000	0.000	90.000	37.611
22	6.355	-3.978	-3.978	-1.601	0.000	416.509	101.000	101.000	0.000	0.000	90.000	37.566
23	6.697	-4.219	-4.219	-1.741	0.000	412.839	101.000	101.000	0.000	0.000	90.000	37.364
24	7.022	-4.441	-4.441	-1.860	0.000	410.008	101.000	101.000	0.000	0.000	90.000	37.207
25	7.337	-4.658	-4.658	-1.979	0.000	403.268	101.000	101.000	0.000	0.000	90.000	36.828
26	7.611	-4.843	-4.843	-2.076	0.000	397.975	101.000	101.000	0.000	0.000	90.000	36.525
27	8.162	-5.202	-5.202	-2.243	0.000	365.256	101.000	101.000	0.000	0.000	90.000	34.525
28	8.489	-5.396	-5.396	-2.304	0.000	347.709	101.000	101.000	0.000	0.000	90.000	33.355
29	9.083	-5.723	-5.723	-2.364	0.000	341.082	101.000	101.000	0.000	0.000	90.000	32.893
30	9.637	-6.015	-6.015	-2.392	0.000	338.883	101.000	101.000	0.000	0.000	90.000	32.737
31	9.637	-6.015	-6.015	-2.392	0.000	339.218	101.000	101.000	0.000	0.000	90.000	32.761
32	10.877	-6.670	-6.670	-2.462	0.000	339.579	101.000	101.000	0.000	0.000	90.000	32.787

Triaxial Test on Fine Nevada Sand with a Target Void Ratio = 0.530 (D_r = 91.28%)

Test No.:	10, A7	**Shear Band Notes**	29
Test Date:	12/21/10	Point of Observation:	
Sector:	III		
Initial Void Ratio, e:	0.532	Inclination (from Vertical):	
Final Mean Princpal Stress, σ_m :	200.0 kPa	58°	
Max Friction Angle, ϕ:	37.2 deg		
b-value at failure:	0.00	Failure Notes:	
Stress direction at failure, α:	90.0 deg		

Point (No.)	ε_z (%)	ε_x (%)	ε_y (%)	ε_v (%)	$\gamma_{\theta z}$ (%)	σ_z (kPa)	σ_x (kPa)	σ_y (kPa)	$\tau_{\theta z}$ (kPa)	b	α (°)	φ (°)
1	0.000	0.000	0.000	0.000	0.000	98.977	99.000	99.000	0.000	0.000	90.000	-0.007
2	0.023	-0.006	-0.006	0.011	0.000	121.459	99.000	99.000	0.000	0.000	90.000	5.847
3	0.067	-0.018	-0.018	0.031	0.000	146.596	99.000	99.000	0.000	0.000	90.000	11.175
4	0.122	-0.034	-0.034	0.053	0.000	172.064	99.000	99.000	0.000	0.000	90.000	15.637
5	0.171	-0.051	-0.051	0.070	0.000	189.489	99.000	99.000	0.000	0.000	90.000	18.280
6	0.256	-0.081	-0.081	0.095	0.000	211.058	99.000	99.000	0.000	0.000	90.000	21.187
7	0.516	-0.188	-0.188	0.141	0.000	253.622	99.000	99.000	0.000	0.000	90.000	26.008
8	0.793	-0.315	-0.315	0.163	0.000	284.120	99.000	99.000	0.000	0.000	90.000	28.894
9	1.023	-0.432	-0.432	0.158	0.000	302.729	99.000	99.000	0.000	0.000	90.000	30.473
10	1.299	-0.586	-0.586	0.128	0.000	319.359	99.000	99.000	0.000	0.000	90.000	31.784
11	1.505	-0.701	-0.701	0.102	0.000	329.865	99.000	99.000	0.000	0.000	90.000	32.569
12	1.926	-0.940	-0.940	0.046	0.000	347.259	99.000	99.000	0.000	0.000	90.000	33.801
13	2.147	-1.067	-1.067	0.013	0.000	354.481	99.000	99.000	0.000	0.000	90.000	34.290
14	2.681	-1.385	-1.385	-0.088	0.000	368.453	99.000	99.000	0.000	0.000	90.000	35.200
15	2.796	-1.459	-1.459	-0.123	0.000	370.076	99.000	99.000	0.000	0.000	90.000	35.303
16	3.040	-1.612	-1.612	-0.185	0.000	377.682	99.000	99.000	0.000	0.000	90.000	35.777
17	3.275	-1.763	-1.763	-0.251	0.000	383.226	99.000	99.000	0.000	0.000	90.000	36.115
18	3.623	-1.990	-1.990	-0.356	0.000	391.969	99.000	99.000	0.000	0.000	90.000	36.635
19	3.836	-2.134	-2.134	-0.431	0.000	394.115	99.000	99.000	0.000	0.000	90.000	36.760
20	4.066	-2.284	-2.284	-0.502	0.000	397.539	99.000	99.000	0.000	0.000	90.000	36.959
21	4.294	-2.435	-2.435	-0.576	0.000	399.598	99.000	99.000	0.000	0.000	90.000	37.077
22	4.736	-2.731	-2.731	-0.726	0.000	400.410	99.000	99.000	0.000	0.000	90.000	37.123
23	5.197	-3.043	-3.043	-0.889	0.000	402.735	99.000	99.000	0.000	0.000	90.000	37.255
24	5.528	-3.272	-3.272	-1.016	0.000	401.943	99.000	99.000	0.000	0.000	90.000	37.211
25	5.679	-3.374	-3.374	-1.069	0.000	401.954	99.000	99.000	0.000	0.000	90.000	37.211
26	6.509	-3.930	-3.930	-1.351	0.000	398.452	99.000	99.000	0.000	0.000	90.000	37.011
27	6.676	-4.042	-4.042	-1.408	0.000	395.823	99.000	99.000	0.000	0.000	90.000	36.860
28	6.794	-4.116	-4.116	-1.439	0.000	390.541	99.000	99.000	0.000	0.000	90.000	36.551
29	7.065	-4.296	-4.296	-1.527	0.000	368.339	99.000	99.000	0.000	0.000	90.000	35.192
30	7.422	-4.494	-4.494	-1.566	0.000	347.776	99.000	99.000	0.000	0.000	90.000	33.836
31	8.479	-5.033	-5.033	-1.586	0.000	339.222	99.000	99.000	0.000	0.000	90.000	33.242
32	9.623	-5.606	-5.606	-1.588	0.000	337.768	99.000	99.000	0.000	0.000	90.000	33.139
32	10.117	-5.852	-5.852	-1.586	0.000	335.849	99.000	99.000	0.000	0.000	90.000	33.002

Triaxial Test on Fine Nevada Sand with a Target Void Ratio = 0.530 (D_r = 91.28%)

Test No.:	11, W5 (ext)
Test Date:	2/9/11
Sector:	III
Initial Void Ratio, e:	0.534
Final Mean Princpal Stress, σ_m :	51.2 kPa
Max Friction Angle, ϕ:	35.9 deg
b-value at failure:	0.00
Stress direction at failure, α:	90.0 deg

Shear Band Notes	
Point of Observation:	32
Inclination (from Vertical):	
20°	
Failure Notes:	

Point (No.)	ε_z (%)	ε_x (%)	ε_y (%)	ε_v (%)	$\gamma_{\theta z}$ (%)	σ_z (kPa)	σ_x (kPa)	σ_y (kPa)	$\tau_{\theta z}$ (kPa)	b	α (°)	φ (°)
1	0.000	0.000	0.000	0.000	0.000	114.587	101.000	101.000	0.000	0.000	90.000	-3.613
2	0.002	-0.003	-0.003	-0.004	0.000	96.611	101.000	101.000	0.000	0.000	90.000	1.273
3	0.009	-0.008	-0.008	-0.007	0.000	80.785	101.000	101.000	0.000	0.000	90.000	6.385
4	0.021	-0.014	-0.014	-0.007	0.000	71.626	101.000	101.000	0.000	0.000	90.000	9.797
5	0.038	-0.019	-0.019	0.000	0.000	62.859	101.000	101.000	0.000	0.000	90.000	13.460
6	0.054	-0.023	-0.023	0.009	0.000	58.992	101.000	101.000	0.000	0.000	90.000	15.222
7	0.100	-0.031	-0.031	0.039	0.000	52.477	101.000	101.000	0.000	0.000	90.000	18.431
8	0.154	-0.036	-0.036	0.083	0.000	48.026	101.000	101.000	0.000	0.000	90.000	20.822
9	0.203	-0.043	-0.043	0.117	0.000	46.443	101.000	101.000	0.000	0.000	90.000	21.717
10	0.275	-0.061	-0.061	0.152	0.000	41.956	101.000	101.000	0.000	0.000	90.000	24.395
11	0.303	-0.071	-0.071	0.161	0.000	40.772	101.000	101.000	0.000	0.000	90.000	25.139
12	0.365	-0.097	-0.097	0.172	0.000	38.912	101.000	101.000	0.000	0.000	90.000	26.344
13	0.402	-0.116	-0.116	0.169	0.000	37.560	101.000	101.000	0.000	0.000	90.000	27.248
14	0.472	-0.158	-0.158	0.156	0.000	35.008	101.000	101.000	0.000	0.000	90.000	29.026
15	0.501	-0.179	-0.179	0.143	0.000	34.835	101.000	101.000	0.000	0.000	90.000	29.150
16	0.556	-0.219	-0.219	0.117	0.000	32.913	101.000	101.000	0.000	0.000	90.000	30.560
17	0.606	-0.259	-0.259	0.087	0.000	32.113	101.000	101.000	0.000	0.000	90.000	31.165
18	0.664	-0.306	-0.306	0.052	0.000	31.436	101.000	101.000	0.000	0.000	90.000	31.686
19	0.747	-0.378	-0.378	-0.009	0.000	30.180	101.000	101.000	0.000	0.000	90.000	32.675
20	0.782	-0.406	-0.406	-0.030	0.000	29.396	101.000	101.000	0.000	0.000	90.000	33.307
21	0.811	-0.432	-0.432	-0.052	0.000	29.336	101.000	101.000	0.000	0.000	90.000	33.356
22	0.852	-0.470	-0.470	-0.087	0.000	28.619	101.000	101.000	0.000	0.000	90.000	33.946
23	0.915	-0.526	-0.526	-0.137	0.000	28.356	101.000	101.000	0.000	0.000	90.000	34.165
24	0.963	-0.571	-0.571	-0.178	0.000	27.608	101.000	101.000	0.000	0.000	90.000	34.797
25	1.008	-0.613	-0.613	-0.217	0.000	26.921	101.000	101.000	0.000	0.000	90.000	35.387
26	1.158	-0.753	-0.753	-0.348	0.000	26.433	101.000	101.000	0.000	0.000	90.000	35.813
27	1.195	-0.789	-0.789	-0.382	0.000	26.419	101.000	101.000	0.000	0.000	90.000	35.826
28	1.246	-0.838	-0.838	-0.430	0.000	26.307	101.000	101.000	0.000	0.000	90.000	35.924
29	1.295	-0.891	-0.891	-0.487	0.000	26.393	101.000	101.000	0.000	0.000	90.000	35.849
30	1.375	-0.955	-0.955	-0.534	0.000	28.276	101.000	101.000	0.000	0.000	90.000	34.232
31	1.375	-0.955	-0.955	-0.534	0.000	28.276	101.000	101.000	0.000	0.000	90.000	34.232
32	1.478	-1.026	-1.026	-0.574	0.000	33.490	101.000	101.000	0.000	0.000	90.000	30.131
33	1.562	-1.072	-1.072	-0.582	0.000	34.874	101.000	101.000	0.000	0.000	90.000	29.122

Varying σ_3 Test on Fine Nevada Sand with a Target Void Ratio = 0.530 (D_r = 91.28%)

Test No.:	W1, Triaxial 9
Test Date:	1/17/11
Sector:	III
Initial Void Ratio, e:	0.534
Final Mean Princpal Stress, σ_m :	206.9 kPa
Max Friction Angle, ϕ:	37.7 deg
b-value at failure:	0.00
Stress direction at failure, α:	90.0 deg

Shear Band Notes	
Point of Observation:	26
Inclination (from Vertical):	
60°, 55°	
Failure Notes:	

Point (No.)	ε_z (%)	ε_x (%)	ε_y (%)	ε_v (%)	$\gamma_{\theta z}$ (%)	σ_z (kPa)	σ_x (kPa)	σ_y (kPa)	$\tau_{\theta z}$ (kPa)	b	α (°)	φ (°)
1	0.000	0.000	0.000	0.000	0.000	96.246	101.000	101.000	0.000	0.000	90.000	-1.381
2	0.329	-0.114	-0.114	0.101	0.000	235.399	101.000	101.000	0.000	0.000	90.000	23.548
3	0.638	-0.254	-0.254	0.130	0.000	277.855	101.000	101.000	0.000	0.000	90.000	27.828
4	0.964	-0.419	-0.419	0.125	0.000	307.549	101.000	101.000	0.000	0.000	90.000	30.369
5	1.268	-0.588	-0.588	0.092	0.000	328.212	101.000	101.000	0.000	0.000	90.000	31.963
6	1.549	-0.748	-0.748	0.053	0.000	343.540	101.000	101.000	0.000	0.000	90.000	33.066
7	1.893	-0.955	-0.955	-0.018	0.000	358.147	101.000	101.000	0.000	0.000	90.000	34.059
8	2.145	-1.110	-1.110	-0.075	0.000	367.723	101.000	101.000	0.000	0.000	90.000	34.683
9	2.468	-1.313	-1.313	-0.158	0.000	378.989	101.000	101.000	0.000	0.000	90.000	35.391
10	3.006	-1.661	-1.661	-0.317	0.000	391.497	101.000	101.000	0.000	0.000	90.000	36.146
11	3.072	-1.705	-1.705	-0.339	0.000	393.249	101.000	101.000	0.000	0.000	90.000	36.249
12	3.312	-1.865	-1.865	-0.418	0.000	398.863	101.000	101.000	0.000	0.000	90.000	36.576
13	3.703	-2.131	-2.131	-0.558	0.000	406.680	101.000	101.000	0.000	0.000	90.000	37.021
14	3.921	-2.281	-2.281	-0.642	0.000	409.714	101.000	101.000	0.000	0.000	90.000	37.191
15	4.281	-2.527	-2.527	-0.774	0.000	413.913	101.000	101.000	0.000	0.000	90.000	37.423
16	4.579	-2.736	-2.736	-0.893	0.000	415.615	101.000	101.000	0.000	0.000	90.000	37.517
17	4.802	-2.889	-2.889	-0.976	0.000	418.192	101.000	101.000	0.000	0.000	90.000	37.657
18	5.135	-3.124	-3.124	-1.113	0.000	418.077	101.000	101.000	0.000	0.000	90.000	37.651
19	5.537	-3.404	-3.404	-1.271	0.000	418.536	101.000	101.000	0.000	0.000	90.000	37.676
20	5.775	-3.576	-3.576	-1.376	0.000	418.112	101.000	101.000	0.000	0.000	90.000	37.653
21	6.096	-3.800	-3.800	-1.504	0.000	417.336	101.000	101.000	0.000	0.000	90.000	37.611
22	6.355	-3.978	-3.978	-1.601	0.000	416.509	101.000	101.000	0.000	0.000	90.000	37.566
23	6.697	-4.219	-4.219	-1.741	0.000	412.839	101.000	101.000	0.000	0.000	90.000	37.364
24	7.022	-4.441	-4.441	-1.860	0.000	410.008	101.000	101.000	0.000	0.000	90.000	37.207
25	7.337	-4.658	-4.658	-1.979	0.000	403.268	101.000	101.000	0.000	0.000	90.000	36.828
26	7.611	-4.843	-4.843	-2.076	0.000	397.975	101.000	101.000	0.000	0.000	90.000	36.525
27	8.162	-5.202	-5.202	-2.243	0.000	365.256	101.000	101.000	0.000	0.000	90.000	34.525
28	8.489	-5.396	-5.396	-2.304	0.000	347.709	101.000	101.000	0.000	0.000	90.000	33.355
29	9.083	-5.723	-5.723	-2.364	0.000	341.082	101.000	101.000	0.000	0.000	90.000	32.893
30	9.637	-6.015	-6.015	-2.392	0.000	338.883	101.000	101.000	0.000	0.000	90.000	32.737
31	9.637	-6.015	-6.015	-2.392	0.000	339.218	101.000	101.000	0.000	0.000	90.000	32.761
32	10.877	-6.670	-6.670	-2.462	0.000	339.579	101.000	101.000	0.000	0.000	90.000	32.787

Varying σ_3 Test on Fine Nevada Sand with a Target Void Ratio = 0.530 (D_r = 91.28%)

Test No.:	W2	
Test Date:	1/20/11	
Sector:	III	
Initial Void Ratio, e:	0.528	
Final Mean Princpal Stress, σ_m :	96.5	kPa
Max Friction Angle, ϕ:	37.6	deg
b-value at failure:	0.00	
Stress direction at failure, α:	90.0	deg

Shear Band Notes
Point of Observation:
n/a
Inclination (from Vertical):
n/a
Failure Notes:
n/a

Point (No.)	ε_z (%)	ε_x (%)	ε_y (%)	ε_v (%)	$\gamma_{\theta z}$ (%)	σ_z (kPa)	σ_x (kPa)	σ_y (kPa)	$\tau_{\theta z}$ (kPa)	b	α (°)	φ (°)
1	0.000	0.000	0.000	0.000	0.000	101.014	101.036	101.036	0.000	0.000	90.000	-0.006
2	0.028	-0.012	-0.012	0.004	0.000	118.519	91.418	91.418	0.000	0.000	90.000	7.417
3	0.061	-0.027	-0.027	0.006	0.000	130.722	84.566	84.566	0.000	0.000	90.000	12.380
4	0.096	-0.044	-0.044	0.008	0.000	139.864	79.610	79.610	0.000	0.000	90.000	15.935
5	0.163	-0.073	-0.073	0.017	0.000	149.934	74.506	74.506	0.000	0.000	90.000	19.638
6	0.233	-0.106	-0.106	0.021	0.000	153.888	69.353	69.353	0.000	0.000	90.000	22.251
7	0.343	-0.160	-0.160	0.023	0.000	160.108	65.967	65.967	0.000	0.000	90.000	24.608
8	0.470	-0.223	-0.223	0.023	0.000	165.223	63.710	63.710	0.000	0.000	90.000	26.322
9	0.616	-0.301	-0.301	0.015	0.000	169.293	61.551	61.551	0.000	0.000	90.000	27.822
10	0.759	-0.377	-0.377	0.004	0.000	172.644	59.784	59.784	0.000	0.000	90.000	29.050
11	0.917	-0.468	-0.468	-0.019	0.000	174.457	58.165	58.165	0.000	0.000	90.000	29.995
12	1.084	-0.564	-0.564	-0.044	0.000	176.389	56.693	56.693	0.000	0.000	90.000	30.900
13	1.243	-0.659	-0.659	-0.074	0.000	178.344	55.613	55.613	0.000	0.000	90.000	31.640
14	1.419	-0.765	-0.765	-0.112	0.000	180.073	54.534	54.534	0.000	0.000	90.000	32.351
15	1.574	-0.862	-0.862	-0.150	0.000	181.175	53.896	53.896	0.000	0.000	90.000	32.783
16	1.737	-0.964	-0.964	-0.191	0.000	182.699	53.159	53.159	0.000	0.000	90.000	33.314
17	1.888	-1.059	-1.059	-0.231	0.000	183.934	52.669	52.669	0.000	0.000	90.000	33.696
18	2.046	-1.161	-1.161	-0.277	0.000	184.115	51.687	51.687	0.000	0.000	90.000	34.167
19	2.213	-1.271	-1.271	-0.328	0.000	185.040	51.295	51.295	0.000	0.000	90.000	34.466
20	2.397	-1.390	-1.390	-0.383	0.000	184.715	51.295	51.295	0.000	0.000	90.000	34.424
21	2.549	-1.491	-1.491	-0.434	0.000	185.953	50.313	50.313	0.000	0.000	90.000	35.036
22	2.699	-1.590	-1.590	-0.481	0.000	186.920	49.773	49.773	0.000	0.000	90.000	35.410
23	2.869	-1.703	-1.703	-0.536	0.000	187.662	49.234	49.234	0.000	0.000	90.000	35.757
24	3.025	-1.808	-1.808	-0.591	0.000	188.772	48.694	48.694	0.000	0.000	90.000	36.149
25	3.180	-1.913	-1.913	-0.646	0.000	189.973	49.136	49.136	0.000	0.000	90.000	36.087
26	3.336	-2.016	-2.016	-0.697	0.000	192.045	49.037	49.037	0.000	0.000	90.000	36.369
27	3.481	-2.116	-2.116	-0.750	0.000	192.868	48.743	48.743	0.000	0.000	90.000	36.632
28	3.642	-2.224	-2.224	-0.807	0.000	193.284	48.252	48.252	0.000	0.000	90.000	36.965
29	3.789	-2.327	-2.327	-0.864	0.000	194.423	47.418	47.418	0.000	0.000	90.000	37.355
30	3.937	-2.427	-2.427	-0.917	0.000	195.032	47.124	47.124	0.000	0.000	90.000	37.613

Varying σ_3 Test on Fine Nevada Sand with a Target Void Ratio = 0.530 (D_r = 91.28%)

Test No.:	W3
Test Date:	1/24/11
Sector:	III
Initial Void Ratio, e:	0.530
Final Mean Princpal Stress, σ_m :	100.8 kPa
Max Friction Angle, ϕ:	35.3 deg
b-value at failure:	0.00
Stress direction at failure, α:	90.0 deg

Shear Band Notes
Point of Observation:
n/a
Inclination (from Vertical):
n/a

Failure Notes:
n/a

Point (No.)	ε_z (%)	ε_x (%)	ε_y (%)	ε_v (%)	$\gamma_{\theta z}$ (%)	σ_z (kPa)	σ_x (kPa)	σ_y (kPa)	$\tau_{\theta z}$ (kPa)	b	α (°)	φ (°)
1	0.000	0.000	0.000	0.000	0.000	100.277	100.300	100.300	0.000	0.000	90.000	-0.007
2	0.025	-0.009	-0.009	0.007	0.000	117.064	90.945	90.945	0.000	0.000	90.000	7.213
3	0.055	-0.023	-0.023	0.009	0.000	130.658	85.547	85.547	0.000	0.000	90.000	12.043
4	0.112	-0.047	-0.047	0.017	0.000	141.748	79.168	79.168	0.000	0.000	90.000	16.456
5	0.196	-0.083	-0.083	0.030	0.000	151.010	74.751	74.751	0.000	0.000	90.000	19.742
6	0.292	-0.127	-0.127	0.039	0.000	157.579	71.807	71.807	0.000	0.000	90.000	21.958
7	0.423	-0.189	-0.189	0.046	0.000	163.902	68.666	68.666	0.000	0.000	90.000	24.173
8	0.531	-0.241	-0.241	0.048	0.000	167.948	66.066	66.066	0.000	0.000	90.000	25.809
9	0.710	-0.331	-0.331	0.048	0.000	174.192	64.446	64.446	0.000	0.000	90.000	27.380
10	0.845	-0.401	-0.401	0.043	0.000	177.062	62.238	62.238	0.000	0.000	90.000	28.675
11	0.981	-0.474	-0.474	0.034	0.000	179.497	61.109	61.109	0.000	0.000	90.000	29.475
12	1.158	-0.570	-0.570	0.017	0.000	182.922	59.735	59.735	0.000	0.000	90.000	30.508
13	1.274	-0.636	-0.636	0.002	0.000	184.939	58.754	58.754	0.000	0.000	90.000	31.185
14	1.452	-0.739	-0.739	-0.026	0.000	187.396	57.576	57.576	0.000	0.000	90.000	32.001
15	1.612	-0.832	-0.832	-0.052	0.000	189.195	56.840	56.840	0.000	0.000	90.000	32.544
16	1.790	-0.938	-0.938	-0.087	0.000	190.604	55.760	55.760	0.000	0.000	90.000	33.184
17	1.948	-1.035	-1.035	-0.122	0.000	191.854	55.613	55.613	0.000	0.000	90.000	33.404
18	2.113	-1.141	-1.141	-0.169	0.000	192.075	55.024	55.024	0.000	0.000	90.000	33.686
19	2.263	-1.234	-1.234	-0.204	0.000	192.601	54.337	54.337	0.000	0.000	90.000	34.050
20	2.421	-1.333	-1.333	-0.246	0.000	193.517	53.699	53.699	0.000	0.000	90.000	34.442
21	2.592	-1.441	-1.441	-0.290	0.000	194.378	53.123	53.123	0.000	0.000	90.000	34.801
22	2.742	-1.537	-1.537	-0.332	0.000	195.264	52.644	52.644	0.000	0.000	90.000	35.120
23	2.880	-1.627	-1.627	-0.374	0.000	195.994	52.607	52.607	0.000	0.000	90.000	35.224
24	3.063	-1.740	-1.740	-0.417	0.000	196.593	52.423	52.423	0.000	0.000	90.000	35.377
25	3.225	-1.846	-1.846	-0.467	0.000	196.891	52.730	52.730	0.000	0.000	90.000	35.276
26	3.415	-1.982	-1.982	-0.550	0.000	194.942	55.490	55.490	0.000	0.000	90.000	33.838

Varying σ_3 Test on Fine Nevada Sand with a Target Void Ratio = 0.530 (D_r = 91.28%)

Test No.:	W4
Test Date:	1/27/11
Sector:	III
Initial Void Ratio, e:	0.554
Final Mean Princpal Stress, σ_m :	52.3 kPa
Max Friction Angle, ϕ:	34.7 deg
b-value at failure:	0.00
Stress direction at failure, α:	90.0 deg

Shear Band Notes
Point of Observation:
n/a
Inclination (from Vertical):
n/a
Failure Notes:
n/a

Point (No.)	ε_z (%)	ε_x (%)	ε_y (%)	ε_v (%)	$\gamma_{\theta z}$ (%)	σ_z (kPa)	σ_x (kPa)	σ_y (kPa)	$\tau_{\theta z}$ (kPa)	b	α (°)	φ (°)
1	0.000	0.000	0.000	0.000	0.000	100.977	101.000	101.000	0.000	0.000	90.000	-0.007
2	0.004	-0.007	-0.007	-0.009	0.000	102.031	79.100	79.100	0.000	0.000	90.000	7.273
3	0.012	-0.021	-0.021	-0.031	0.000	101.033	68.812	68.812	0.000	0.000	90.000	10.936
4	0.012	-0.028	-0.028	-0.044	0.000	101.693	60.809	60.809	0.000	0.000	90.000	14.572
5	0.024	-0.043	-0.043	-0.062	0.000	100.992	54.149	54.149	0.000	0.000	90.000	17.574
6	0.051	-0.062	-0.062	-0.073	0.000	100.967	49.021	49.021	0.000	0.000	90.000	20.263
7	0.115	-0.098	-0.098	-0.081	0.000	101.024	44.793	44.793	0.000	0.000	90.000	22.682
8	0.220	-0.154	-0.154	-0.088	0.000	101.028	41.698	41.698	0.000	0.000	90.000	24.563
9	0.346	-0.222	-0.222	-0.097	0.000	100.964	39.308	39.308	0.000	0.000	90.000	26.075
10	0.470	-0.291	-0.291	-0.112	0.000	100.959	37.497	37.497	0.000	0.000	90.000	27.281
11	0.641	-0.389	-0.389	-0.137	0.000	100.983	36.296	36.296	0.000	0.000	90.000	28.113
12	0.784	-0.473	-0.473	-0.161	0.000	101.034	35.214	35.214	0.000	0.000	90.000	28.888
13	0.921	-0.553	-0.553	-0.185	0.000	101.063	34.301	34.301	0.000	0.000	90.000	29.551
14	1.043	-0.626	-0.626	-0.209	0.000	100.961	33.570	33.570	0.000	0.000	90.000	30.062
15	1.189	-0.716	-0.716	-0.242	0.000	101.024	32.770	32.770	0.000	0.000	90.000	30.673
16	1.370	-0.824	-0.824	-0.278	0.000	100.091	32.292	32.292	0.000	0.000	90.000	30.806
17	1.417	-0.857	-0.857	-0.297	0.000	101.132	31.417	31.417	0.000	0.000	90.000	31.732
18	1.530	-0.926	-0.926	-0.322	0.000	101.414	30.249	30.249	0.000	0.000	90.000	32.718
19	1.667	-1.016	-1.016	-0.366	0.000	101.172	29.959	29.959	0.000	0.000	90.000	32.893
20	1.816	-1.117	-1.117	-0.417	0.000	101.816	29.586	29.586	0.000	0.000	90.000	33.346
21	2.055	-1.266	-1.266	-0.477	0.000	100.774	29.505	29.505	0.000	0.000	90.000	33.164
22	2.116	-1.309	-1.309	-0.503	0.000	100.858	29.815	29.815	0.000	0.000	90.000	32.933
23	2.247	-1.406	-1.406	-0.566	0.000	102.218	31.908	31.908	0.000	0.000	90.000	33.336
24	2.335	-1.458	-1.458	-0.581	0.000	101.068	28.227	28.227	0.000	0.000	90.000	34.289
25	2.474	-1.551	-1.551	-0.629	0.000	100.771	28.128	28.128	0.000	0.000	90.000	34.303
26	2.384	-1.491	-1.491	-0.599	0.000	101.344	27.769	27.769	0.000	0.000	90.000	34.740

Varying σ_3 Test on Fine Nevada Sand with a Target Void Ratio = 0.530 (D_r = 91.28%)

Test No.:	W5, Triaxial 11
Test Date:	2/9/11
Sector:	III
Initial Void Ratio, e:	0.534
Final Mean Princpal Stress, σ_m :	51.2 kPa
Max Friction Angle, ϕ:	35.9 deg
b-value at failure:	0.00
Stress direction at failure, α:	90.0 deg

Shear Band Notes	
Point of Observation:	32
n/a	
Inclination (from Vertical):	
n/a	
Failure Notes:	
n/a	

Point (No.)	ε_z (%)	ε_x (%)	ε_y (%)	ε_v (%)	$\gamma_{\theta z}$ (%)	σ_z (kPa)	σ_x (kPa)	σ_y (kPa)	$\tau_{\theta z}$ (kPa)	b	α (°)	φ (°)
1	0.000	0.000	0.000	0.000	0.000	114.587	101.000	101.000	0.000	0.000	90.000	-3.613
2	0.002	-0.003	-0.003	-0.004	0.000	96.611	101.000	101.000	0.000	0.000	90.000	1.273
3	0.009	-0.008	-0.008	-0.007	0.000	80.785	101.000	101.000	0.000	0.000	90.000	6.385
4	0.021	-0.014	-0.014	-0.007	0.000	71.626	101.000	101.000	0.000	0.000	90.000	9.797
5	0.038	-0.019	-0.019	0.000	0.000	62.859	101.000	101.000	0.000	0.000	90.000	13.460
6	0.054	-0.023	-0.023	0.009	0.000	58.992	101.000	101.000	0.000	0.000	90.000	15.222
7	0.100	-0.031	-0.031	0.039	0.000	52.477	101.000	101.000	0.000	0.000	90.000	18.431
8	0.154	-0.036	-0.036	0.083	0.000	48.026	101.000	101.000	0.000	0.000	90.000	20.822
9	0.203	-0.043	-0.043	0.117	0.000	46.443	101.000	101.000	0.000	0.000	90.000	21.717
10	0.275	-0.061	-0.061	0.152	0.000	41.956	101.000	101.000	0.000	0.000	90.000	24.395
11	0.303	-0.071	-0.071	0.161	0.000	40.772	101.000	101.000	0.000	0.000	90.000	25.139
12	0.365	-0.097	-0.097	0.172	0.000	38.912	101.000	101.000	0.000	0.000	90.000	26.344
13	0.402	-0.116	-0.116	0.169	0.000	37.560	101.000	101.000	0.000	0.000	90.000	27.248
14	0.472	-0.158	-0.158	0.156	0.000	35.008	101.000	101.000	0.000	0.000	90.000	29.026
15	0.501	-0.179	-0.179	0.143	0.000	34.835	101.000	101.000	0.000	0.000	90.000	29.150
16	0.556	-0.219	-0.219	0.117	0.000	32.913	101.000	101.000	0.000	0.000	90.000	30.560
17	0.606	-0.259	-0.259	0.087	0.000	32.113	101.000	101.000	0.000	0.000	90.000	31.165
18	0.664	-0.306	-0.306	0.052	0.000	31.436	101.000	101.000	0.000	0.000	90.000	31.686
19	0.747	-0.378	-0.378	-0.009	0.000	30.180	101.000	101.000	0.000	0.000	90.000	32.675
20	0.782	-0.406	-0.406	-0.030	0.000	29.396	101.000	101.000	0.000	0.000	90.000	33.307
21	0.811	-0.432	-0.432	-0.052	0.000	29.336	101.000	101.000	0.000	0.000	90.000	33.356
22	0.852	-0.470	-0.470	-0.087	0.000	28.619	101.000	101.000	0.000	0.000	90.000	33.946
23	0.915	-0.526	-0.526	-0.137	0.000	28.356	101.000	101.000	0.000	0.000	90.000	34.165
24	0.963	-0.571	-0.571	-0.178	0.000	27.608	101.000	101.000	0.000	0.000	90.000	34.797
25	1.008	-0.613	-0.613	-0.217	0.000	26.921	101.000	101.000	0.000	0.000	90.000	35.387
26	1.158	-0.753	-0.753	-0.348	0.000	26.433	101.000	101.000	0.000	0.000	90.000	35.813
27	1.195	-0.789	-0.789	-0.382	0.000	26.419	101.000	101.000	0.000	0.000	90.000	35.826
28	1.246	-0.838	-0.838	-0.430	0.000	26.307	101.000	101.000	0.000	0.000	90.000	35.924
29	1.295	-0.891	-0.891	-0.487	0.000	26.393	101.000	101.000	0.000	0.000	90.000	35.849
30	1.375	-0.955	-0.955	-0.534	0.000	28.276	101.000	101.000	0.000	0.000	90.000	34.232
31	1.375	-0.955	-0.955	-0.534	0.000	28.276	101.000	101.000	0.000	0.000	90.000	34.232
32	1.478	-1.026	-1.026	-0.574	0.000	33.490	101.000	101.000	0.000	0.000	90.000	30.131
33	1.562	-1.072	-1.072	-0.582	0.000	34.874	101.000	101.000	0.000	0.000	90.000	29.122

Varying σ_3 Test on Fine Nevada Sand with a Target Void Ratio = 0.530 (D_r = 91.28%)

Test No.:	W6
Test Date:	1/31/11
Sector:	I
Initial Void Ratio, e:	0.534
Final Mean Princpal Stress, σ_m :	98.4 kPa
Max Friction Angle, ϕ:	39.6 deg
b-value at failure:	0.00
Stress direction at failure, α:	0.0 deg

Shear Band Notes
Point of Observation:
n/a
Inclination (from Vertical):
n/a
Failure Notes:
n/a

Point (No.)	ε_z (%)	ε_x (%)	ε_y (%)	ε_v (%)	$\gamma_{\theta z}$ (%)	σ_z (kPa)	σ_x (kPa)	σ_y (kPa)	$\tau_{\theta z}$ (kPa)	b	α (°)	φ (°)
1	0.000	0.000	0.000	0.000	0.000	101.013	101.036	101.036	0.000	0.000	0.000	-0.007
2	0.046	-0.022	-0.022	0.003	0.000	120.076	90.945	90.945	0.000	0.000	0.000	7.935
3	0.076	-0.035	-0.035	0.007	0.000	132.285	85.057	85.057	0.000	0.000	0.000	12.551
4	0.107	-0.049	-0.049	0.009	0.000	141.467	80.149	80.149	0.000	0.000	0.000	16.062
5	0.156	-0.073	-0.073	0.011	0.000	152.063	75.340	75.340	0.000	0.000	0.000	19.718
6	0.208	-0.098	-0.098	0.013	0.000	159.533	71.611	71.611	0.000	0.000	0.000	22.357
7	0.290	-0.140	-0.140	0.010	0.000	167.279	67.440	67.440	0.000	0.000	0.000	25.173
8	0.372	-0.185	-0.185	0.002	0.000	173.368	64.299	64.299	0.000	0.000	0.000	27.317
9	0.488	-0.255	-0.255	-0.022	0.000	179.600	60.619	60.619	0.000	0.000	0.000	29.690
10	0.590	-0.311	-0.311	-0.033	0.000	183.503	59.343	59.343	0.000	0.000	0.000	30.749
11	0.701	-0.380	-0.380	-0.059	0.000	187.347	57.674	57.674	0.000	0.000	0.000	31.954
12	0.837	-0.466	-0.466	-0.095	0.000	190.969	55.466	55.466	0.000	0.000	0.000	33.357
13	0.981	-0.561	-0.561	-0.141	0.000	193.818	54.043	54.043	0.000	0.000	0.000	34.328
14	1.102	-0.643	-0.643	-0.185	0.000	196.138	53.012	53.012	0.000	0.000	0.000	35.061
15	1.259	-0.753	-0.753	-0.247	0.000	198.448	51.687	51.687	0.000	0.000	0.000	35.925
16	1.441	-0.883	-0.883	-0.326	0.000	200.041	50.853	50.853	0.000	0.000	0.000	36.486
17	1.586	-0.990	-0.990	-0.394	0.000	201.871	49.823	49.823	0.000	0.000	0.000	37.164
18	1.741	-1.105	-1.105	-0.469	0.000	203.438	48.939	48.939	0.000	0.000	0.000	37.747
19	1.947	-1.264	-1.264	-0.581	0.000	203.676	48.743	48.743	0.000	0.000	0.000	37.864
20	2.090	-1.373	-1.373	-0.656	0.000	204.876	48.056	48.056	0.000	0.000	0.000	38.317
21	2.253	-1.499	-1.499	-0.744	0.000	205.781	47.320	47.320	0.000	0.000	0.000	38.761
22	2.429	-1.634	-1.634	-0.839	0.000	205.422	47.025	47.025	0.000	0.000	0.000	38.862
23	2.590	-1.760	-1.760	-0.929	0.000	206.421	46.584	46.584	0.000	0.000	0.000	39.180
24	2.775	-1.905	-1.905	-1.035	0.000	206.661	46.191	46.191	0.000	0.000	0.000	39.393
25	2.958	-2.050	-2.050	-1.142	0.000	205.301	45.799	45.799	0.000	0.000	0.000	39.436
26	3.123	-2.182	-2.182	-1.241	0.000	205.324	44.977	44.977	0.000	0.000	0.000	39.838

Varying σ_3 Test on Fine Nevada Sand with a Target Void Ratio = 0.530 (D_r = 91.28%)

Test No.:	A1	
Test Date:	12/9/10	
Sector:	III	
Initial Void Ratio, e:	0.522	
Final Mean Princpal Stress, σ_m :	200.1	kPa
Max Friction Angle, ϕ:	32.5	deg
b-value at failure:	0.00	
Stress direction at failure, α:	90.0	deg

Shear Band Notes
Point of Observation:
n/a
Inclination (from Vertical):
n/a
Failure Notes:
n/a

Point (No.)	ε_z (%)	ε_x (%)	ε_y (%)	ε_v (%)	$\gamma_{\theta z}$ (%)	σ_z (kPa)	σ_x (kPa)	σ_y (kPa)	$\tau_{\theta z}$ (kPa)	b	α (°)	φ (°)
1	0.000	0.000	0.000	0.000	0.000	100.786	102.088	102.088	0.000	0.000	90.000	-0.368
2	0.015	-0.003	-0.003	0.009	0.000	111.526	91.243	91.243	0.000	0.000	90.000	5.741
3	0.037	-0.011	-0.011	0.015	0.000	124.753	85.680	85.680	0.000	0.000	90.000	10.701
4	0.057	-0.020	-0.020	0.017	0.000	132.871	83.461	83.461	0.000	0.000	90.000	13.203
5	0.086	-0.031	-0.031	0.024	0.000	140.311	80.400	80.400	0.000	0.000	90.000	15.750
6	0.127	-0.048	-0.048	0.030	0.000	146.492	76.842	76.842	0.000	0.000	90.000	18.172
7	0.176	-0.070	-0.070	0.036	0.000	152.151	74.962	74.962	0.000	0.000	90.000	19.869
8	0.225	-0.092	-0.092	0.041	0.000	156.538	72.932	72.932	0.000	0.000	90.000	21.367
9	0.316	-0.135	-0.135	0.045	0.000	161.792	70.156	70.156	0.000	0.000	90.000	23.270
10	0.406	-0.179	-0.179	0.048	0.000	165.769	67.775	67.775	0.000	0.000	90.000	24.809
11	0.492	-0.222	-0.222	0.047	0.000	169.213	65.788	65.788	0.000	0.000	90.000	26.111
12	0.616	-0.287	-0.287	0.043	0.000	172.199	63.950	63.950	0.000	0.000	90.000	27.284
13	0.725	-0.346	-0.346	0.032	0.000	175.519	62.259	62.259	0.000	0.000	90.000	28.446
14	0.822	-0.403	-0.403	0.017	0.000	177.371	63.303	63.303	0.000	0.000	90.000	28.291
15	0.854	-0.418	-0.418	0.017	0.000	178.198	61.612	61.612	0.000	0.000	90.000	29.088
16	1.042	-0.528	-0.528	-0.013	0.000	181.338	60.069	60.069	0.000	0.000	90.000	30.155
17	1.188	-0.613	-0.613	-0.039	0.000	183.228	59.969	59.969	0.000	0.000	90.000	30.453
18	1.309	-0.684	-0.684	-0.060	0.000	184.916	58.376	58.376	0.000	0.000	90.000	31.340
19	1.411	-0.748	-0.748	-0.086	0.000	185.178	59.521	59.521	0.000	0.000	90.000	30.898
20	1.503	-0.786	-0.786	-0.069	0.000	186.253	57.429	57.429	0.000	0.000	90.000	31.915
21	1.648	-0.880	-0.880	-0.112	0.000	186.167	59.571	59.571	0.000	0.000	90.000	31.009
22	1.772	-0.952	-0.952	-0.133	0.000	187.884	55.907	55.907	0.000	0.000	90.000	**32.776**
23	1.854	-1.006	-1.006	-0.159	0.000	188.539	53.738	53.738	0.000	0.000	90.000	33.807
24	1.937	-1.056	-1.056	-0.176	0.000	188.577	52.340	52.340	0.000	0.000	90.000	34.437
25	2.014	-1.105	-1.105	-0.197	0.000	189.125	50.378	50.378	0.000	0.000	90.000	35.402
26	2.124	-1.169	-1.169	-0.214	0.000	191.642	47.815	47.815	0.000	0.000	90.000	37.130
27	2.209	-1.220	-1.220	-0.232	0.000	170.998	59.607	59.607	0.000	0.000	90.000	34.525

Varying σ_3 Test on Fine Nevada Sand with a Target Void Ratio = 0.530 (D_r = 91.28%)

Test No.:	A2
Test Date:	12/11/10
Sector:	III
Initial Void Ratio, e:	0.536
Final Mean Princpal Stress, σ_m :	136.8 kPa
Max Friction Angle, ϕ:	37.1 deg
b-value at failure:	0.00
Stress direction at failure, α:	90.0 deg

Shear Band Notes
Point of Observation:
n/a
Inclination (from Vertical):
n/a
Failure Notes:
n/a

Point (No.)	ε_z (%)	ε_x (%)	ε_y (%)	ε_v (%)	$\gamma_{\theta z}$ (%)	σ_z (kPa)	σ_x (kPa)	σ_y (kPa)	$\tau_{\theta z}$ (kPa)	b	α (°)	φ (°)
1	0.000	0.000	0.000	0.000	0.000	100.282	100.305	100.305	0.000	0.000	90.000	-0.006
2	0.006	-0.001	-0.001	0.004	0.000	115.905	96.677	96.677	0.000	0.000	90.000	5.190
3	0.054	-0.016	-0.016	0.022	0.000	149.778	90.735	90.735	0.000	0.000	90.000	14.211
4	0.084	-0.027	-0.027	0.030	0.000	161.439	88.570	88.570	0.000	0.000	90.000	16.946
5	0.141	-0.047	-0.047	0.048	0.000	177.527	85.616	85.616	0.000	0.000	90.000	20.443
6	0.231	-0.084	-0.084	0.063	0.000	193.247	82.905	82.905	0.000	0.000	90.000	23.551
7	0.307	-0.119	-0.119	0.069	0.000	203.149	80.931	80.931	0.000	0.000	90.000	25.482
8	0.436	-0.179	-0.179	0.078	0.000	214.321	79.005	79.005	0.000	0.000	90.000	27.472
9	0.555	-0.239	-0.239	0.078	0.000	222.741	77.523	77.523	0.000	0.000	90.000	28.923
10	0.726	-0.326	-0.326	0.074	0.000	232.699	75.644	75.644	0.000	0.000	90.000	30.621
11	0.838	-0.387	-0.387	0.063	0.000	237.151	74.902	74.902	0.000	0.000	90.000	31.328
12	0.995	-0.475	-0.475	0.045	0.000	242.924	73.912	73.912	0.000	0.000	90.000	32.238
13	1.243	-0.624	-0.624	-0.004	0.000	250.891	72.031	72.031	0.000	0.000	90.000	33.634
14	1.330	-0.676	-0.676	-0.022	0.000	251.283	72.427	72.427	0.000	0.000	90.000	33.540
15	1.521	-0.793	-0.793	-0.065	0.000	256.001	71.486	71.486	0.000	0.000	90.000	34.293
16	1.685	-0.894	-0.894	-0.104	0.000	258.155	70.891	70.891	0.000	0.000	90.000	34.688
17	1.857	-1.010	-1.010	-0.164	0.000	260.001	70.792	70.792	0.000	0.000	90.000	34.889
18	2.014	-1.113	-1.113	-0.212	0.000	262.725	70.247	70.247	0.000	0.000	90.000	35.314
19	2.166	-1.210	-1.210	-0.255	0.000	265.003	69.801	69.801	0.000	0.000	90.000	35.664
20	2.329	-1.318	-1.318	-0.307	0.000	267.861	69.255	69.255	0.000	0.000	90.000	36.095
21	2.484	-1.421	-1.421	-0.358	0.000	268.934	69.106	69.106	0.000	0.000	90.000	36.238
22	2.689	-1.560	-1.560	-0.432	0.000	270.297	68.858	68.858	0.000	0.000	90.000	**36.437**
23	2.857	-1.673	-1.673	-0.488	0.000	272.072	68.561	68.561	0.000	0.000	90.000	36.688
24	3.112	-1.843	-1.843	-0.574	0.000	274.215	68.164	68.164	0.000	0.000	90.000	37.000
25	3.228	-1.921	-1.921	-0.613	0.000	274.230	67.966	67.966	0.000	0.000	90.000	37.068
26	3.354	-2.014	-2.014	-0.674	0.000	273.267	68.114	68.114	0.000	0.000	90.000	36.938
27	3.502	-2.116	-2.116	-0.730	0.000	272.938	68.214	68.214	0.000	0.000	90.000	36.877
28	3.660	-2.221	-2.221	-0.782	0.000	273.602	68.065	68.065	0.000	0.000	90.000	36.983
29	3.817	-2.325	-2.325	-0.834	0.000	274.571	67.866	67.866	0.000	0.000	90.000	37.130
30	4.001	-2.458	-2.458	-0.916	0.000	273.415	68.164	68.164	0.000	0.000	90.000	36.934
31	4.146	-2.555	-2.555	-0.963	0.000	274.232	67.966	67.966	0.000	0.000	90.000	37.069
32	4.320	-2.671	-2.671	-1.021	0.000	274.407	67.916	67.916	0.000	0.000	90.000	37.100

Varying σ_3 Test on Fine Nevada Sand with a Target Void Ratio = 0.530 (D_r = 91.28%)

Test No.:	A3
Test Date:	12/14/11
Sector:	III
Initial Void Ratio, e:	0.533
Final Mean Princpal Stress, σ_m :	61.4 kPa
Max Friction Angle, ϕ:	29.9 deg
b-value at failure:	0.00
Stress direction at failure, α:	90.0 deg

Shear Band Notes
Point of Observation:
n/a
Inclination (from Vertical):
n/a
Failure Notes:
n/a

Point (No.)	ε_z (%)	ε_x (%)	ε_y (%)	ε_v (%)	$\gamma_{\theta z}$ (%)	σ_z (kPa)	σ_x (kPa)	σ_y (kPa)	$\tau_{\theta z}$ (kPa)	b	α (°)	φ (°)
1	0.000	0.000	0.000	0.000	0.000	104.295	104.318	104.318	0.000	0.000	90.000	-0.006
2	0.012	-0.002	-0.002	0.009	0.000	105.146	93.929	93.929	0.000	0.000	90.000	3.230
3	0.012	-0.001	-0.001	0.009	0.000	104.831	85.419	85.419	0.000	0.000	90.000	5.856
4	0.015	-0.008	-0.008	-0.001	0.000	104.964	79.647	79.647	0.000	0.000	90.000	7.882
5	0.016	-0.010	-0.010	-0.004	0.000	104.977	77.375	77.375	0.000	0.000	90.000	8.706
6	0.023	-0.015	-0.015	-0.008	0.000	105.058	71.932	71.932	0.000	0.000	90.000	10.787
7	0.027	-0.018	-0.018	-0.009	0.000	104.876	68.511	68.511	0.000	0.000	90.000	12.107
8	0.037	-0.024	-0.024	-0.011	0.000	105.345	64.888	64.888	0.000	0.000	90.000	13.748
9	0.048	-0.028	-0.028	-0.009	0.000	105.114	61.706	61.706	0.000	0.000	90.000	15.082
10	0.060	-0.035	-0.035	-0.009	0.000	105.147	59.268	59.268	0.000	0.000	90.000	16.203
11	0.078	-0.043	-0.043	-0.009	0.000	105.266	56.728	56.728	0.000	0.000	90.000	17.435
12	0.094	-0.047	-0.047	-0.001	0.000	105.155	54.335	54.335	0.000	0.000	90.000	18.581
13	0.113	-0.056	-0.056	0.001	0.000	105.245	52.338	52.338	0.000	0.000	90.000	19.617
14	0.141	-0.071	-0.071	0.000	0.000	105.268	50.091	50.091	0.000	0.000	90.000	20.803
15	0.173	-0.087	-0.087	0.000	0.000	105.364	48.491	48.491	0.000	0.000	90.000	21.694
16	0.213	-0.105	-0.105	0.002	0.000	105.476	46.340	46.340	0.000	0.000	90.000	22.925
17	0.238	-0.116	-0.116	0.007	0.000	105.300	45.740	45.740	0.000	0.000	90.000	23.225
18	0.287	-0.140	-0.140	0.007	0.000	105.273	44.087	44.087	0.000	0.000	90.000	24.183
19	0.331	-0.162	-0.162	0.007	0.000	105.406	43.486	43.486	0.000	0.000	90.000	24.574
20	0.375	-0.182	-0.182	0.011	0.000	105.269	42.233	42.233	0.000	0.000	90.000	25.300
21	0.425	-0.207	-0.207	0.011	0.000	105.284	41.331	41.331	0.000	0.000	90.000	25.861
22	0.477	-0.234	-0.234	0.009	0.000	105.346	40.478	40.478	0.000	0.000	90.000	26.413
23	0.527	-0.260	-0.260	0.007	0.000	105.279	39.876	39.876	0.000	0.000	90.000	26.780
24	0.575	-0.285	-0.285	0.004	0.000	104.773	39.023	39.023	0.000	0.000	90.000	27.209
25	0.626	-0.312	-0.312	0.002	0.000	105.311	38.270	38.270	0.000	0.000	90.000	27.834
26	0.676	-0.337	-0.337	0.001	0.000	105.277	38.270	38.270	0.000	0.000	90.000	27.803
27	0.706	-0.359	-0.359	-0.011	0.000	105.205	39.174	39.174	0.000	0.000	90.000	27.193
28	0.779	-0.392	-0.392	-0.004	0.000	108.923	36.312	36.312	0.000	0.000	90.000	29.973

Varying σ_3 Test on Fine Nevada Sand with a Target Void Ratio = 0.530 (D_r = 91.28%)

Test No.:	A4
Test Date:	12/15/10
Sector:	III
Initial Void Ratio, e:	0.534
Final Mean Princpal Stress, σ_m :	49.1 kPa
Max Friction Angle, ϕ:	27.8 deg
b-value at failure:	0.00
Stress direction at failure, α:	90.0 deg

Shear Band Notes
Point of Observation:
n/a
Inclination (from Vertical):
n/a
Failure Notes:
n/a

Point (No.)	ε_z (%)	ε_x (%)	ε_y (%)	ε_v (%)	$\gamma_{\theta z}$ (%)	σ_z (kPa)	σ_x (kPa)	σ_y (kPa)	$\tau_{\theta z}$ (kPa)	b	α (°)	φ (°)
1	0.000	0.000	0.000	0.000	0.000	103.045	103.067	103.067	0.000	0.000	90.000	-0.006
2	0.002	-0.003	-0.003	-0.004	0.000	100.596	98.364	98.364	0.000	0.000	90.000	0.643
3	0.008	-0.005	-0.005	-0.002	0.000	97.655	85.088	85.088	0.000	0.000	90.000	3.943
4	0.016	-0.012	-0.012	-0.009	0.000	92.328	65.291	65.291	0.000	0.000	90.000	9.877
5	0.023	-0.027	-0.027	-0.030	0.000	88.893	51.341	51.341	0.000	0.000	90.000	15.533
6	0.032	-0.044	-0.044	-0.057	0.000	88.623	48.641	48.641	0.000	0.000	90.000	16.934
7	0.045	-0.054	-0.054	-0.062	0.000	87.343	45.913	45.913	0.000	0.000	90.000	18.114
8	0.058	-0.063	-0.063	-0.067	0.000	87.778	45.462	45.462	0.000	0.000	90.000	18.517
9	0.066	-0.068	-0.068	-0.070	0.000	87.241	43.334	43.334	0.000	0.000	90.000	19.649
10	0.078	-0.074	-0.074	-0.070	0.000	86.921	42.080	42.080	0.000	0.000	90.000	20.340
11	0.092	-0.082	-0.082	-0.072	0.000	86.762	41.177	41.177	0.000	0.000	90.000	20.873
12	0.103	-0.089	-0.089	-0.074	0.000	86.529	40.575	40.575	0.000	0.000	90.000	21.195
13	0.120	-0.097	-0.097	-0.074	0.000	86.382	39.873	39.873	0.000	0.000	90.000	21.616
14	0.134	-0.105	-0.105	-0.076	0.000	86.362	39.672	39.672	0.000	0.000	90.000	21.744
15	0.153	-0.114	-0.114	-0.076	0.000	86.200	38.768	38.768	0.000	0.000	90.000	22.306
16	0.192	-0.135	-0.135	-0.078	0.000	85.798	37.261	37.261	0.000	0.000	90.000	23.230
17	0.206	-0.143	-0.143	-0.079	0.000	85.778	37.060	37.060	0.000	0.000	90.000	23.366
18	0.217	-0.148	-0.148	-0.079	0.000	85.568	36.105	36.105	0.000	0.000	90.000	23.986
19	0.237	-0.160	-0.160	-0.082	0.000	85.526	35.980	35.980	0.000	0.000	90.000	24.065
20	0.259	-0.173	-0.173	-0.086	0.000	85.441	35.628	35.628	0.000	0.000	90.000	24.296
21	0.267	-0.177	-0.177	-0.087	0.000	85.337	35.389	35.389	0.000	0.000	90.000	24.440
22	0.279	-0.183	-0.183	-0.087	0.000	85.239	35.062	35.062	0.000	0.000	90.000	24.652
23	0.289	-0.190	-0.190	-0.090	0.000	85.076	34.257	34.257	0.000	0.000	90.000	25.205
24	0.361	-0.230	-0.230	-0.098	0.000	84.878	33.339	33.339	0.000	0.000	90.000	25.847
25	0.397	-0.253	-0.253	-0.109	0.000	84.788	32.999	32.999	0.000	0.000	90.000	26.084
26	0.449	-0.284	-0.284	-0.119	0.000	84.725	32.634	32.634	0.000	0.000	90.000	26.350
27	0.463	-0.295	-0.295	-0.127	0.000	84.569	32.219	32.219	0.000	0.000	90.000	26.632
28	0.512	-0.322	-0.322	-0.132	0.000	84.308	31.563	31.563	0.000	0.000	90.000	27.078
29	0.582	-0.360	-0.360	-0.139	0.000	84.384	31.625	31.625	0.000	0.000	90.000	27.051
30	0.607	-0.379	-0.379	-0.150	0.000	84.417	31.497	31.497	0.000	0.000	90.000	27.165
31	0.633	-0.396	-0.396	-0.160	0.000	84.521	32.133	32.133	0.000	0.000	90.000	26.686
32	0.760	-0.462	-0.462	-0.164	0.000	84.223	30.549	30.549	0.000	0.000	90.000	27.882
33	0.789	-0.486	-0.486	-0.184	0.000	84.153	30.601	30.601	0.000	0.000	90.000	27.818

Varying σ_3 Test on Fine Nevada Sand with a Target Void Ratio = 0.530 (D_r = 91.28%)

Test No.:	A5
Test Date:	12/17/10
Sector:	III
Initial Void Ratio, e:	0.534
Final Mean Princpal Stress, σ_m :	89.02 kPa
Max Friction Angle, ϕ:	22.6 deg
b-value at failure:	0.00
Stress direction at failure, α:	90.0 deg

Shear Band Notes
Point of Observation:
n/a
Inclination (from Vertical):
n/a

Failure Notes:
n/a

Point (No.)	ε_z (%)	ε_x (%)	ε_y (%)	ε_v (%)	$\gamma_{\theta z}$ (%)	σ_z (kPa)	σ_x (kPa)	σ_y (kPa)	$\tau_{\theta z}$ (kPa)	b	α (°)	φ (°)
1	0.000	0.000	0.000	0.000	0.000	101.478	101.501	101.501	0.000	0.000	90.000	-0.006
2	0.001	0.002	0.002	0.004	0.000	102.800	99.737	99.737	0.000	0.000	90.000	0.867
3	0.002	0.001	0.001	0.004	0.000	105.946	95.763	95.763	0.000	0.000	90.000	2.894
4	0.004	0.000	0.000	0.004	0.000	108.773	92.472	92.472	0.000	0.000	90.000	4.646
5	0.010	-0.001	-0.001	0.007	0.000	113.038	86.961	86.961	0.000	0.000	90.000	7.492
6	0.011	-0.003	-0.003	0.004	0.000	113.193	87.059	87.059	0.000	0.000	90.000	7.499
7	0.016	-0.004	-0.004	0.009	0.000	117.260	81.832	81.832	0.000	0.000	90.000	10.250
8	0.017	-0.007	-0.007	0.004	0.000	117.322	81.832	81.832	0.000	0.000	90.000	10.265
9	0.022	-0.007	-0.007	0.009	0.000	120.534	77.188	77.188	0.000	0.000	90.000	12.664
10	0.030	-0.010	-0.010	0.009	0.000	121.934	75.457	75.457	0.000	0.000	90.000	13.619
11	0.035	-0.013	-0.013	0.009	0.000	123.413	73.724	73.724	0.000	0.000	90.000	14.599
12	0.039	-0.015	-0.015	0.009	0.000	123.757	72.783	72.783	0.000	0.000	90.000	15.032
13	0.045	-0.018	-0.018	0.009	0.000	124.892	71.990	71.990	0.000	0.000	90.000	15.587
14	0.048	-0.020	-0.020	0.009	0.000	125.042	71.842	71.842	0.000	0.000	90.000	15.677
15	0.053	-0.020	-0.020	0.013	0.000	126.783	69.710	69.710	0.000	0.000	90.000	16.885
16	0.059	-0.023	-0.023	0.013	0.000	126.726	69.759	69.759	0.000	0.000	90.000	16.854
17	0.066	-0.025	-0.025	0.015	0.000	127.906	68.333	68.333	0.000	0.000	90.000	17.672
18	0.072	-0.028	-0.028	0.017	0.000	128.792	67.377	67.377	0.000	0.000	90.000	18.244
19	0.079	-0.031	-0.031	0.018	0.000	129.533	66.496	66.496	0.000	0.000	90.000	18.758
20	0.088	-0.035	-0.035	0.019	0.000	130.254	65.552	65.552	0.000	0.000	90.000	19.296
21	0.093	-0.036	-0.036	0.020	0.000	130.582	65.166	65.166	0.000	0.000	90.000	19.523
22	0.099	-0.039	-0.039	0.021	0.000	131.469	64.058	64.058	0.000	0.000	90.000	20.167
23	0.110	-0.043	-0.043	0.023	0.000	131.912	63.557	63.557	0.000	0.000	90.000	20.469
24	0.134	-0.054	-0.054	0.027	0.000	133.243	64.276	64.276	0.000	0.000	90.000	20.436
25	0.147	-0.052	-0.052	0.042	0.000	140.617	62.702	62.702	0.000	0.000	90.000	22.533
26	0.160	-0.056	-0.056	0.048	0.000	141.417	62.819	62.819	0.000	0.000	90.000	22.634
27	0.271	-0.173	-0.173	-0.075	0.000	166.093	73.957	73.957	0.000	0.000	90.000	22.570

Varying σ_3 Test on Fine Nevada Sand with a Target Void Ratio = 0.530 (D_r = 91.28%)

Test No.:	A6	
Test Date:	12/18/10	
Sector:	III	
Initial Void Ratio, e:	0.538	
Final Mean Princpal Stress, σ_m :	155.9	kPa
Max Friction Angle, ϕ:	38.2	deg
b-value at failure:	0.00	
Stress direction at failure, α:	90.0	deg

Shear Band Notes
Point of Observation:
n/a
Inclination (from Vertical):
n/a
Failure Notes:
n/a

Point (No.)	ε_z (%)	ε_x (%)	ε_y (%)	ε_v (%)	$\gamma_{\theta z}$ (%)	σ_z (kPa)	σ_x (kPa)	σ_y (kPa)	$\tau_{\theta z}$ (kPa)	b	α (°)	φ (°)
1	0.000	0.000	0.000	0.000	0.000	101.086	101.109	101.109	0.000	0.000	90.000	-0.006
2	0.012	-0.004	-0.004	0.004	0.000	111.297	95.518	95.518	0.000	0.000	90.000	4.376
3	0.023	-0.007	-0.007	0.009	0.000	120.430	91.292	91.292	0.000	0.000	90.000	7.910
4	0.036	-0.012	-0.012	0.013	0.000	126.786	88.241	88.241	0.000	0.000	90.000	10.326
5	0.058	-0.018	-0.018	0.022	0.000	135.686	84.348	84.348	0.000	0.000	90.000	13.492
6	0.078	-0.024	-0.024	0.030	0.000	141.911	81.734	81.734	0.000	0.000	90.000	15.609
7	0.107	-0.034	-0.034	0.039	0.000	147.800	79.165	79.165	0.000	0.000	90.000	17.602
8	0.143	-0.049	-0.049	0.046	0.000	153.202	76.496	76.496	0.000	0.000	90.000	19.508
9	0.181	-0.063	-0.063	0.054	0.000	157.596	74.516	74.516	0.000	0.000	90.000	20.973
10	0.240	-0.087	-0.087	0.065	0.000	162.989	72.238	72.238	0.000	0.000	90.000	22.693
11	0.315	-0.119	-0.119	0.076	0.000	167.733	69.710	69.710	0.000	0.000	90.000	24.383
12	0.380	-0.149	-0.149	0.083	0.000	171.375	67.775	67.775	0.000	0.000	90.000	25.671
13	0.442	-0.178	-0.178	0.086	0.000	173.751	66.831	66.831	0.000	0.000	90.000	26.386
14	0.529	-0.221	-0.221	0.087	0.000	176.567	65.987	65.987	0.000	0.000	90.000	27.123
15	0.600	-0.256	-0.256	0.087	0.000	178.543	65.043	65.043	0.000	0.000	90.000	27.772
16	0.710	-0.313	-0.313	0.085	0.000	180.868	63.751	63.751	0.000	0.000	90.000	28.605
17	0.789	-0.354	-0.354	0.080	0.000	182.556	63.104	63.104	0.000	0.000	90.000	29.094
18	0.889	-0.410	-0.410	0.070	0.000	183.397	62.209	62.209	0.000	0.000	90.000	29.566
19	0.988	-0.466	-0.466	0.057	0.000	184.517	61.413	61.413	0.000	0.000	90.000	30.037
20	1.093	-0.525	-0.525	0.043	0.000	185.887	61.065	61.065	0.000	0.000	90.000	30.361
21	1.200	-0.585	-0.585	0.030	0.000	187.051	60.517	60.517	0.000	0.000	90.000	30.738
22	1.269	-0.623	-0.623	0.022	0.000	187.867	59.571	59.571	0.000	0.000	90.000	31.232
23	1.369	-0.682	-0.682	0.004	0.000	188.889	59.073	59.073	0.000	0.000	90.000	31.569
24	1.478	-0.747	-0.747	-0.015	0.000	189.645	58.973	58.973	0.000	0.000	90.000	31.708
25	1.580	-0.811	-0.811	-0.041	0.000	189.735	59.160	59.160	0.000	0.000	90.000	31.643
26	1.693	-0.877	-0.877	-0.061	0.000	190.256	59.795	59.795	0.000	0.000	90.000	31.449
27	1.758	-0.915	-0.915	-0.072	0.000	191.994	57.977	57.977	0.000	0.000	90.000	32.421
28	1.828	-0.957	-0.957	-0.087	0.000	192.554	57.728	57.728	0.000	0.000	90.000	32.595

Varying σ_3 Test on Fine Nevada Sand with a Target Void Ratio = 0.530 (D_r = 91.28%)

Test No.:	A7, Triaxial 10
Test Date:	12/21/10
Sector:	III
Initial Void Ratio, e:	0.532
Final Mean Princpal Stress, σ_m :	200.0 kPa
Max Friction Angle, ϕ:	37.2 deg
b-value at failure:	0.00
Stress direction at failure, α:	90.0 deg

Shear Band Notes
Point of Observation:
Inclination (from Vertical):
58°
Failure Notes:

Point (No.)	ε_z (%)	ε_x (%)	ε_y (%)	ε_v (%)	$\gamma_{\theta z}$ (%)	σ_z (kPa)	σ_x (kPa)	σ_y (kPa)	$\tau_{\theta z}$ (kPa)	b	α (°)	φ (°)
1	0.000	0.000	0.000	0.000	0.000	98.977	99.000	99.000	0.000	0.000	90.000	-0.007
2	0.023	-0.006	-0.006	0.011	0.000	121.459	99.000	99.000	0.000	0.000	90.000	5.847
3	0.067	-0.018	-0.018	0.031	0.000	146.596	99.000	99.000	0.000	0.000	90.000	11.175
4	0.122	-0.034	-0.034	0.053	0.000	172.064	99.000	99.000	0.000	0.000	90.000	15.637
5	0.171	-0.051	-0.051	0.070	0.000	189.489	99.000	99.000	0.000	0.000	90.000	18.280
6	0.256	-0.081	-0.081	0.095	0.000	211.058	99.000	99.000	0.000	0.000	90.000	21.187
7	0.516	-0.188	-0.188	0.141	0.000	253.622	99.000	99.000	0.000	0.000	90.000	26.008
8	0.793	-0.315	-0.315	0.163	0.000	284.120	99.000	99.000	0.000	0.000	90.000	28.894
9	1.023	-0.432	-0.432	0.158	0.000	302.729	99.000	99.000	0.000	0.000	90.000	30.473
10	1.299	-0.586	-0.586	0.128	0.000	319.359	99.000	99.000	0.000	0.000	90.000	31.784
11	1.505	-0.701	-0.701	0.102	0.000	329.865	99.000	99.000	0.000	0.000	90.000	32.569
12	1.926	-0.940	-0.940	0.046	0.000	347.259	99.000	99.000	0.000	0.000	90.000	33.801
13	2.147	-1.067	-1.067	0.013	0.000	354.481	99.000	99.000	0.000	0.000	90.000	34.290
14	2.681	-1.385	-1.385	-0.088	0.000	368.453	99.000	99.000	0.000	0.000	90.000	35.200
15	2.796	-1.459	-1.459	-0.123	0.000	370.076	99.000	99.000	0.000	0.000	90.000	35.303
16	3.040	-1.612	-1.612	-0.185	0.000	377.682	99.000	99.000	0.000	0.000	90.000	35.777
17	3.275	-1.763	-1.763	-0.251	0.000	383.226	99.000	99.000	0.000	0.000	90.000	36.115
18	3.623	-1.990	-1.990	-0.356	0.000	391.969	99.000	99.000	0.000	0.000	90.000	36.635
19	3.836	-2.134	-2.134	-0.431	0.000	394.115	99.000	99.000	0.000	0.000	90.000	36.760
20	4.066	-2.284	-2.284	-0.502	0.000	397.539	99.000	99.000	0.000	0.000	90.000	36.959
21	4.294	-2.435	-2.435	-0.576	0.000	399.598	99.000	99.000	0.000	0.000	90.000	37.077
22	4.736	-2.731	-2.731	-0.726	0.000	400.410	99.000	99.000	0.000	0.000	90.000	37.123
23	5.197	-3.043	-3.043	-0.889	0.000	402.735	99.000	99.000	0.000	0.000	90.000	37.255
24	5.528	-3.272	-3.272	-1.016	0.000	401.943	99.000	99.000	0.000	0.000	90.000	37.211
25	5.679	-3.374	-3.374	-1.069	0.000	401.954	99.000	99.000	0.000	0.000	90.000	37.211
26	6.509	-3.930	-3.930	-1.351	0.000	398.452	99.000	99.000	0.000	0.000	90.000	37.011
27	6.676	-4.042	-4.042	-1.408	0.000	395.823	99.000	99.000	0.000	0.000	90.000	36.860
28	6.794	-4.116	-4.116	-1.439	0.000	390.541	99.000	99.000	0.000	0.000	90.000	36.551
29	7.065	-4.296	-4.296	-1.527	0.000	368.339	99.000	99.000	0.000	0.000	90.000	35.192
30	7.422	-4.494	-4.494	-1.566	0.000	347.776	99.000	99.000	0.000	0.000	90.000	33.836
31	8.479	-5.033	-5.033	-1.586	0.000	339.222	99.000	99.000	0.000	0.000	90.000	33.242
32	9.623	-5.606	-5.606	-1.588	0.000	337.768	99.000	99.000	0.000	0.000	90.000	33.139
32	10.117	-5.852	-5.852	-1.586	0.000	335.849	99.000	99.000	0.000	0.000	90.000	33.002

References

Abelev, A., & Lade , P. V. (2004). Characterization of Failure in Cross-Anisotropic Soils. *Journal of Engineering Mechanics , 130* (5), 599-606.

Arthur, J. R. (1988). Cubical Devices: Versatility and Constraints. In R. C. Robert Donaghe, *Advanced Triaxial Testing of Soil and Rock, ASTM STP 977* (pp. 743-765). Philadelphia : American Society of Testing and Materials .

Arthur, J., & Dunstan, T. (1982). Rupture layers in granular media. *IUTAM Con. Def. Fail Gran Media,* (pp. 453-459). Balkema: Amsterdam.

Arthur, J., & Phillips, A. (1975). Homogeneous and Layered Sand in triaxial compression. Geotechnique 25, 799-815.

Arthur, J., & Menzies, B. (1972). Inherent Anisotropy in a sand. *Geotechnique ,* 22 (1), 115-128.

Arthur, J., Chua, K. S., & Dunstan, T. (1977). Induced Anisotropy in a Sand. *Geotechnique , 27* (1), 115-128.

Baldi, G. & Nova, R. (1985). Membrane Penetration Effects in Triaxial Testing. Journal of Geotechnical Engineering, 111. Pp. 1047-1049

Bardet, J. (1991). Orientation of Shear Bands in Frictional Soils. *Journal of Engineering Mechanics , 117* (7), 1466-1484.

Broms, B., & Casbarian, A. (1965). Effects of rotation of the principal stress axes and of the intermediate principal stress on the shear strength. *Proceedings of the 6th International Conference on Soil Mechanics and Foundation Engineering (ICSMFE). 1*, pp. 179-183. Montreal, Quebec: Pergamon Press.

Casagrande, A. (1938). The Shear Resistance of Soils and its Relation to the Stability of Earth Dams. *Soil and Foundation Conference of the U.S. Engineering Department.* Boston.

Casagrande, A., & Carillo, N. (1944). Shear Failure of Anisotropic Materials. *Journal of the Boston Society of Civil Engineers , 31* (4), 122-135.

Chapra, S.C. & Canale, Raymond P. Numerical Methods for Engineers, 6th Edition (New York: Mc-Grill Hall, 2010), 470-471.

Dafalias, Y., & Popov, E. (1975). A model of nonlinearly hardening materials for complex loading. *Acta Mech , 21* (3), 173-192.

Degroff, W., Donague, R., Lade, P.V., & La Rochelle, P.L. (1988). Correction of Strength Membrane Effects in the Triaxial Test. *Geotechnical Testing Journal GTODJ*, 11(1), 78-82.

Duncan, J.M., & Dunlop, P. (1969). Behavior of Soils in Simple Shear Tests. *Proceedings of 7th International Conference on Soil Mechanics and Foundation Engineering,* Vol. 1, 101-108.

Germaine, J.T. & Germaine, A.V. Geotechnical Laboratory Measurements for Engineers, (New Jersey: John Wiley & Sons, Inc., 2009).

Green, G. (1971). Stress Strain Behavior of Soils. *Proceedings, Roscoe Memorial Symposium* (pp. 285-324). Henley on Thames: G.T. Foulis.

Gutierrez, M., Ishihara, K., & Towhata, I. (1991). Flow Theory for Sand during Rotation of Principal Stress Direction. *Soils and Foundations , 31* (4), 121-132.

Hambly, E. (1969). A new triaxial apparatus. *Geotechnique , 19* (2), 307-309.

Han, C., & Drescher, A. (1993). Shear Bands in Biaxial Tests on Dry Coarse Sand. *Soils and Foundations , 33* (1), 118-132.

Hight, D., Gens, A., & Symes, M. (1983). The development of a new hollow cylinder apparatus for investigating the effects of principal stress rotation in soils. *Geotechnique , 33* (4), 355-383.

Hong, W.P., & Lade, P.V. (1989) "Elasto-Plastic Behavior of K0-Consolidated Clay in Torsion Shear Tests, *Soils and Foundations*, Japanese Society of Soil Mechanics and Foundation Engineering. 29(2), 127-140.

Hvorslev, M.J. (1937). Uber die Festigkeitseigenschaften gestoerter bindiger Boden." Ingeniorridenskabelige Skriften. A, No. 45.

Johansson, C.E. (1965). Structural studies of Sedimentary Deposits. *Geol. For. Stockh*. 87, 3-61.

Kirkgard, M.M. (1988). An Experimental Study on the Three-Dimensional Behavior of Natural Normally Consolidated Anisotropic Clay. Ph.D Thesis, University of California, Los Angeles.

Ko, H.-Y., & Scott, R. (1967). A new soil testing apparatus. *Geotechnique , 17* (1), 40-57.

Koenders, M. (1990). Localised deformation using higher order deformation gradients. *J. Energy Res. Technol. (Trans ASME) , 112*, 51-53.

Lade, P. (1975). Torsion Shear Tests on Cohesionless Soil. *Proceedings of the 5th Panamerican Conference on Soil Mechanics and Foundation Engineering*, *1*, pp. 117-127. Buenos Aires, Argentina.

Lade, P.V. (1977). Elasto-Plastic Stress-Strain Theory for Cohesionless Soil with Curved Yield Surfaces," *International Journal of Solids and Structures*, Pergamon Press, Vol. 13, November, pp. 1019-1035.

Lade, P.V. (1978). Cubical Triaxial Apparatus for Soil Testing. *Geotechnical Testing Journal , 1* (2), 93-101.

Lade, P.V. (1981). Torsion Shear Apparatus for Soil Testing. *ASTM STP 740, American Society of Testing and Materials* , 145-163.

Lade, P.V. (1982), "Localization Effects in Triaxial Tests on Sand," IUTAM Symposium on Deformation and Failure of Granular Materials, Delft, Holland, Sept. 2,.

Lade, P.V. (2006). Assessment of Test Data for selection of 3-D Failure Criterion for sand. *International Journal for Numerical and Analytical methods in geomechanics , 30*, 307-333.

Lade, P.V. (2007). Modeling failure in cross-anisotropic frictional materials. *International Journal of Solids and Structures , 44*, 5146-5162.

Lade, P.V. (2008). Failure Criterion for Cross-Anisotropic Soils. *Journal of Geotechnical and Geoenvironmental Engineering , 134* (1), 117-124.

Lade, P.V., & Abelev, A. (2003). Effects of Cross Anisotropy on Three-Dimensional Behavior of Sand. II: Volume Change Behavior and Failure. *Journal of Engineering Mechanics , 129* (2), 167-174.

Lade, P.V. & Duncan, J. (1973). Cubical Triaxial Tests on Cohesionless Soil. *Journal of Soil Mechanics and Foundation Division , American Society of Civil Engineers , 99* (SM10), 793-812.

Lade, P.V. & Duncan, J. (1975). Elastoplastic Stress Strain Theory for Cohesionless Soils. *Journal of Geotechnical Engineering Division, ASCE , 101* (GT10), 1037-1053.

Lade, P.V. & Prabucki, M. (1995). Softening and Preshearing Effects in Sand. *Soils and Foundations , 35* (4), 93-104.

Lade, P.V., Nam, J., & Hong, W. (2008). Shear banding and cross-anisotropic behavior observed in laboratory sand tests with stress rotation. *Canadian Geotechnical Journal , 45*, 74-84.

Lade, P.V., Nam, J. & Hong, W.P. (2009). Interpretation of strains in torsion shear tests *Computers and Geotechnics,* Vol. 36, No. 1-2, January/March 2009, pp. 211-225.

Lade, P.V., Nelson, R.B. & Ito, Y.M. (1987). Nonassociated Flow and Stability of Granular Materials, *Journal of Engineering Mechanics*, ASCE, Vol. 113, No. 9, September 1987, pp. 1302-1328.

Lade, P., & Wang, Q. (2001). Analysis of Shear Banding in True Triaxial Tests on Sand. *Journal of Engineering Mechanics , 127* (8), 762-768.

Lade, P. & Wang, Q. (2012a). Method for Uniform Strain Extension Tests on Sand, *Geotechnical Testing Journal, ASTM*, Vol. 35.

Lade, P. & Wang, Q. (2012b). Effects of Stiff and Flexible Boundary Conditions in Triaxial Extension Tests on Cross-Anisotropic Sand Behavior. *Geotechnical Testing Journal, ASTM,* Vol. 35.

Lade, P. & Wasif, U. (1988). Effects of Height-to-Diameter Raio in Triaxial Specimens on the Behavior of Cross-Anisotropic Sand. Advanced Triaxial Testing of Soil and Rock, ASTM STP 977, Philadephia. Pp. 706-714.

Lade, P., Yamamuro, J., & Skyers, B. (1996). Effects of Shear Band Formation in Triaxial Extension Tests. *Geotechnical Testing Journal, GTJODJ , 19* (4), 398-410.

Logan, D. L. (1981). Mechanics of Materials HarperCollins Publishers Inc. New York, NY.

Lomize, G., & Kryzhanovsky, A. (1967). On the stength of sand. *Proceedings Geotechnical Conference, Norwegian Geotechnical Institute*, *1*, pp. 215-219. Oslo.

Martin, G.R., Finn, W.D.L., & Seed, H.B. (1978) Effects of system compliance of liquefaction tests. Journal of Geotechnical Engineering, ASCE, 104(4): 463-479.

Meier, R., Ko, H.-Y., & Sture, S. (1985). A direct tensile loading apparatus combined with a cubical test cell for testing rocks and concrete. *Geotechnical Testing Journal , 8*, 71-78.

Miura, K., Miura, S., & Toki, S. (1986). Deformation Behavior of Anisotropic Dense Sand Under Principal Stress Axes Rotation. *Soils and Foundations , 26* (1): 36-52.

Miura, N., & Yamamoto, N. (1982). On the yield curve of a sand in a particle crushing region. *Proceedings JSCE (in Japanese)* (326), 83-90.

Morshedian J. (1992). Stress Analysis in Elastic Bending Beams and Thick Hollow Cylinders, Iranian Journal of Polymer Science and Technology , Vol.1, No.2. 78- 83.

Naughton, P.J. & O'Kelly, B.C. (2007) "Stress non-uniformity in a hollow cylinder torsional sand specimen" *Geomechanics and Geoengineering: An International Journal*. Vol 2, no. 2. June 117-122.

Ng, T.T. (2004). Macro-and Micro-behaviors of granular materials under different sample preparation methods and stress paths. *International Journal of Solids and Structures*. (41) 5871-5884.

Ng, T.T. (2005). Behavior of Gravity Deposited granular material under different stress paths. *Canadian Geotechnical Journal* (42), 1644-1655.

Oda, M., Koishikawa, I., & Higuchi, T. (1978). Experimental Study of Anisotropic Shear Strength of Sand by Plane Strain Tests. *Soils and Foundations , 18* (1), 25-38.

O'Kelly, B., & Naughton, P. (2005). Development of a New Hollow Cylinder Apparatus for Stress Path Measurements over a Wide Strain Range. *Geotechnical Testing Journal, GTJODJ , 28* (4), 1-10.

O'Kelly, B., & Naughton, P. (2009). Study of Yielding of Sand under generalized Stress Conditions using a Versatile Hollow Cylinder Torsional Apparatus. *Mechanics of Materials , 41* (3), 187-198.

Parkin, A.K., Gerrard, C.M. & Willoughby, D.R. (1968). Discussion: Deformation of sand in shear. Journal of Soil Mechanics, Fdn. Div. ASCE, 94. SM1. 336-340.

Phillips, A.B., & May, P.H., (1967) "A Form of Anisotropy in Granular Media", *Special Task Report,* Dept. of Civil and Municipal Engineering, University College, London.

Pietrusczak, S. & Mroz, Z. (2000), Formulation of anisotropic failure criteria incorporating a microstructure tensor, Computers and Geotechnics, 26, 105-112.

Pietrusczak, S. & Mroz, Z. (2001), On Failure Criteria for anisotropic cohesive-frictional materials", International Journal for Numerical and Analytical Methods in Geomechanics, 25, 509-524.

Pietrusczak, S. & Peijun, G. (2011), Description of deformation process in inherently anisotropic granular materials, International Journal for Numerical and Analytical Methods in Geomechanics, 35 (published online Nov. 15, 2011).

Poorooshasb, H. (1989). Description of Flow of Sand using State Parameters. *Computers and Geotechnics , 8*, 195-218.

Poorooshasb, H., & Pietruszak, S. (1986). A Generalized Flow Theory for Sand. *Soils and Foundations , 26* (2), 1-15.

Poorooshasb, H., Holubec, I., & Sherbourne, A. (1966). Yielding and Flow of Sand in Triaxial Compression Part I. *Canadian Geotechnical Journal , 3* (4), 179-190.

Poorooshasb, H., Holubec, I., & Sherbourne, A. (1967). Yielding and Flow of Sand in Triaxial Compression Part II and III. *Canadian Geotechnical Journal , 4* (4), 376-397.

Pradel, D., Ishihara, K., & and Gutierrez, M. (1990). Yielding and Flow of Sand under Principal Stress Axes Rotation. *Soils and Foundations , 30* (1), 87-99.

Pradhan, T.B.S., Tatsuoka, F., & Horii, N. (1988). Simple Shear Testing on Sand in a Torsional Shear Apparatus. *Soils and Foundations*. 28(2), 95-112.

Rechenmacher, A. (2005). Onset, Growth, Progression and Uniformity of Shear Bands in Dilative Sands. *Proceedings from the 11th International Conference on Fracture.* Turin, Italy.

Roscoe, K.H. (1953). An apparatus for the application of simple shear to soil samples*. Proc. 3rd International Conference in Soil Mechanics,* 1:186-191.

Roscoe, K.H. (1970) “Tenth Rankine Lecture: The Influence of strains in soil mechanics.” Geotechnique 20 129-170.

Roscoe, K., Schofield, A. N., & and Wroth, C. (1958). On the Yielding of Soils. *Geotechnique , 8* (1), 27-53.

Rudnicki, J., & Rice, J. (1975). Conditions for the localisation of deformation in pressure sensitive dilatant materials. *JMPS , 23*, 371-394.

Saada, A. S., Liang, L., Figueroa, J. L., & Cope, C. T. (1999). Bifurcation and shear band propagation in sands. *Geotechnique , 49* (3), 367-385.

Sayao, A., & Vaid, Y. (1991). A Critical Assessment of Stress Nonuniformities in Hollow Cylinder Test Specimens. *Soils and Foundations , 31* (1), 60-72.

Scarpelli, G., & Wood, D. M. (1982). Experimental Observations of Shear Band Patterns in Direct Shear Tests. *IUTAM Conference of Deformation and Failure of Granular Materials*, (pp. 473-493). Delft.

Shibuya, S. (1988). A servo system for hollow cylinder testing of soils. *Geotechnical Testing Journal, GTJODJ , 11* (2), 109-118.

Suzuki, K., & Yamada, T. (2006). Double Strain Softening and Diagonally Crossing Shear Bands of Sand in Drained Triaxial Tests. *International Journal of Geomechanics , 6* (6), 440-446.

Tastan, E. (2009). *Effects of Principal Stress Rotation and Intermediate Principal Stress Changes on the Drained Monotonic and Undrained Cyclic Behavior of Clean and Nonplastic Silty Ottowa Sands formed Underwater* (Vol. PhD Thesis). Colorado State University.

Tatsuoka, F., & Ishihara, K. (1974). Yielding of Sand in Triaxial Compression. *Soils and Foundations , 14* (2), 63-74.

Tatsuoka, F., Sonoda, S., Hara, K., Fukushima, S., & Pradhan, T.B.S., (1986) Failure and Deformation of Sand in Torsional Shear *Soils and Foundations.* 26 (4), 79-97.

Taylor, D. (1948). *Fundamentals of Soil Mechanics.* New York: John Wiley & Sons.

Van Dyck, E. (2012). Effect of Principal Stress Direction and the Intermediate Principal Stress on the Stress-Strain Behavior of a Cross-Anisotropic Fine Sand Deposit, PhD Thesis. The Catholic University of America

Vardoulakis, I. (1980). Shear band inclination and shear modulus of sand in biaxial tests. *International Journal of Numerical Analysis Methods Geomechanics , 4*, 103-119.

Vermeer, P. (1990). The Orientation of Shear Bands in Biaxial Tests. Geotechnique , 40 (2), 223-236.

Wijewickreme, D. (1990) Behavior of Sand Under Simultaneous Increase in Stress Ratio and Rotation of Principal Stresses, Ph.D., The University of British Columbia, Vancouver, B.C. (Chairman: Y.P. Vaid)
1990.

Wijewickreme, D. & Vaid, Y.P. (1991), Stress non-uniformities in Hollow Cylinder Torsional Specimens, *Geotechnical Testing Journal, GTJODJ*, 14 (4): 349-362.

Wong, R.T., Seed, H.B., & Chan, C.K. (1975), Cyclic loading liquefaction of gravelly soils. *Journal of Geotechnical Engineering, ASCE,* 101(6): 571-583.

Yamada, Y., & Ishihara, K. (1979). Anisotropic Deformation Characteristics of Sand under Three Dimensional Stress Conditions. *Soils and Foundations ,* 19 (2), 79-94.

Yamamuro, J.A. & Lade, P.V. Strain Localization in Extension Tests on Granular Materials, *Journal of Engineering Mechanics, ASCE,* Vol. 121, No. 7, July 1995, pp. 828-836.

Yang, Z., Li, X., & Yang, J. (2007). Undrained Anisotropy and Rotational Shera in Granular Soil. *Geotechnique , 57* (4), 371-384.

Yasufuku, N., Murata, H., & Hyodo, M. (1991). Yield Characteristics of Anisotropically Consolidated Sand under Low and High Stresses. *Soils and Foundations ,31* (1), 95-109.

Zitouni, Z. (1988). *Comportement tridimensionnel des sables.* UJF Grenoble: Ph.D Thesis Univerte Joseph Fourier.